frontiers | Research Topics

Natural methane emissions in a changing arctic - implications for climate and environment

Edited by
Karin Andreassen, Jochen Knies, Susanne Liebner,
Andrew Jonathan Hodson and Carolyn Ruppel

Published in
Frontiers in Earth Science
Frontiers in Environmental Science

ISSN 1664-8714
ISBN 978-2-8325-5635-1
DOI 10.3389/978-2-8325-5635-1

About Frontiers

Frontiers is more than just an open access publisher of scholarly articles: it is a pioneering approach to the world of academia, radically improving the way scholarly research is managed. The grand vision of Frontiers is a world where all people have an equal opportunity to seek, share and generate knowledge. Frontiers provides immediate and permanent online open access to all its publications, but this alone is not enough to realize our grand goals.

Frontiers journal series

The Frontiers journal series is a multi-tier and interdisciplinary set of open-access, online journals, promising a paradigm shift from the current review, selection and dissemination processes in academic publishing. All Frontiers journals are driven by researchers for researchers; therefore, they constitute a service to the scholarly community. At the same time, the *Frontiers journal series* operates on a revolutionary invention, the tiered publishing system, initially addressing specific communities of scholars, and gradually climbing up to broader public understanding, thus serving the interests of the lay society, too.

Dedication to quality

Each Frontiers article is a landmark of the highest quality, thanks to genuinely collaborative interactions between authors and review editors, who include some of the world's best academicians. Research must be certified by peers before entering a stream of knowledge that may eventually reach the public - and shape society; therefore, Frontiers only applies the most rigorous and unbiased reviews. Frontiers revolutionizes research publishing by freely delivering the most outstanding research, evaluated with no bias from both the academic and social point of view. By applying the most advanced information technologies, Frontiers is catapulting scholarly publishing into a new generation.

What are Frontiers Research Topics?

Frontiers Research Topics are very popular trademarks of the *Frontiers journals series*: they are collections of at least ten articles, all centered on a particular subject. With their unique mix of varied contributions from Original Research to Review Articles, Frontiers Research Topics unify the most influential researchers, the latest key findings and historical advances in a hot research area.

Find out more on how to host your own Frontiers Research Topic or contribute to one as an author by contacting the Frontiers editorial office: frontiersin.org/about/contact

Natural methane emissions in a changing arctic - implications for climate and environment

Topic editors

Karin Andreassen — UiT The Arctic University of Norway, Norway
Jochen Knies — Geological Survey of Norway, Norway
Susanne Liebner — GFZ German Research Centre for Geosciences, Germany
Andrew Jonathan Hodson — The University Centre in Svalbard, Norway
Carolyn Ruppel — US Geological Survey (USGS), United States

Citation

Andreassen, K., Knies, J., Liebner, S., Hodson, A. J., Ruppel, C., eds. (2024). *Natural methane emissions in a changing arctic - implications for climate and environment*. Lausanne: Frontiers Media SA. doi: 10.3389/978-2-8325-5635-1

Table of contents

frontiers | Frontiers in Earth Science

TYPE Editorial
PUBLISHED 23 October 2024
DOI 10.3389/feart.2024.1508196

OPEN ACCESS

EDITED AND REVIEWED BY
Michael Lehning,
Swiss Federal Institute of Technology Lausanne, Switzerland

*CORRESPONDENCE
Karin Andreassen,
karin.andreassen@uit.no

RECEIVED 09 October 2024
ACCEPTED 14 October 2024
PUBLISHED 23 October 2024

CITATION
Andreassen K, Ruppel C, Liebner S, Hodson A and Knies J (2024) Editorial: Natural methane emissions in a changing arctic – implications for climate and environment.
Front. Earth Sci. 12:1508196.
doi: 10.3389/feart.2024.1508196

Editorial: Natural methane emissions in a changing arctic – implications for climate and environment

Karin Andreassen[1,2]*, Carolyn Ruppel[3], Susanne Liebner[4], Andrew Hodson[5] and Jochen Knies[1,2,6]

[1]CAGE - Former Centre for Arctic Gas Hydrate, Environment and Climate, UiT - The Arctic University of Norway, Tromsø, Norway, [2]iC3 – Centre for ice, Cryosphere, Carbon and Climate, UiT–The Arctic University of Norway, Tromsø, Norway, [3]U.S. Geological Survey, Woods Hole, MA, United States, [4]Geomicrobiology Section, GFZ – German Research Centre for Geosciences, Potsdam, Germany, [5]Arctic Geology Department, UNIS – The University Centre in Svalbard, Longyearbyen, Norway, [6]NGU - Geological Survey of Norway, Trondheim, Norway

KEYWORDS

methane, arctic, climate, cryosphere, atmosphere

Editorial on the Research Topic
Natural methane emissions in a changing arctic – implications for climate and environment

Introduction

Natural methane emissions have received significant attention in recent years due to the documented increase in atmospheric concentrations of methane and its elevated global warming potential relative to CO_2. Over the past decades, the Arctic has been warming nearly four times faster than the rest of the planet (Rantanen et al., 2022). Arctic amplification of global warming drives a pressing need to assess the current and future vulnerability of natural methane accumulations under continued high latitude warming.

Methane accumulations exist in a variety of Arctic settings, including deep-water marine environments, shallow-water continental shelves and fjords hosting relict subsea permafrost and gas hydrate, in and beneath onshore permafrost, and beneath glaciers and the Greenland Ice Sheet. Continued climate warming is making increased methane leakage from these accumulations more likely. Even deeper conventional gas reservoirs could leak methane as the overlying permafrost and gas hydrates degrade. These Research Topic were the focus of "Methane in a Changing Arctic," a conference convened by the Centre for Arctic Gas Hydrates, Environment and Climate (CAGE) at UiT—The Arctic University of Norway from 14–16 September 2022. CAGE was a Norwegian Centre of Excellence funded by the Research Council of Norway from 2013 to 2023, and a key focus of CAGE's research was related to the interaction between Arctic climate change and methane emissions.

CAGE's research legacy, along with the 2022 conference, sparked interest in developing the Frontiers Research Topic that has now produced 15 original research articles. These

studies cover all aspects of methane migration, starting with the geosphere (e.g., sub-seafloor methane reservoirs) through the biosphere (e.g., microbes consuming this methane and acting as a critical sink) to the hydrosphere (e.g., ocean, other waters), the cryosphere (e.g., permafrost sediments, ice sheets, and glaciers) and potentially into the atmosphere. The papers collectively contribute to improved understanding of complex high-latitude methane emissions. The studies investigate timescales from the Pleistocene Ice Ages to the present, demonstrating how past methane seepage histories may inform future climate scenarios.

Methane in the geosphere: subsurface thermogenic, biogenic and abiotic sources

Methane emitted from seafloor or terrestrial seeps has long been known to originate with biotic processes. At lower temperatures, microbial decomposition of organic matter produces gas that has sometimes been referred to as biogenic. At higher temperatures, thermal cracking of heavier hydrocarbons at deeper depths generates thermogenic gas. Both microbial and thermogenic gases are considered biotic in origin owing to their ultimate reliance on organic matter as a substrate. It has also been suggested that methane can be generated abiotically during serpentinization of ultramafic rocks (Proskurowski et al., 2008; Cannat et al., 2010) in slow-to ultraslow-spreading mid-oceanic ridge environments and also during serpentinization in certain backarc systems (Wheat et al., 2020).

In the Barents Sea, widespread seafloor seeps regularly emit thermogenic gases, reflecting the basin's status as a major hydrocarbon province characterized by deep oil and gas reservoirs. Serov et al. explore the origin of Barents Sea seeps, underscoring the role that Cenozoic tectonic uplift and extensive Quaternary glacial erosion (Lasabuda et al., 2021; Patton et al., 2022) have played in reducing the thickness of unlithified overburden sediment that could host widespread microbial methane generation. Analyses by Chand et al. of seep emissions at the Loppa High in the Southwest Barents Sea confirm a deep-seated thermogenic origin but also suggest significant microbial modification of gas chemistry during syn- and post-glacial storage of gas that had migrated into shallow sediments. The study postulates that water percolation through open faults could play a role in some seep gases being characterized by less than purely thermogenic composition.

Studies of abiotic methane remain relatively novel. In the eastern Fram Strait, Johnson et al. (2015) have suggested abiotic methane as the gas source for a long-lived hydrate system on young oceanic crust. Chand et al. investigate gas flares in this area, concluding that the gas primarily originates from thermal cracking of organic material (thermogenic process), with a minor contribution from possible abiotic crustal/mantle sources.

Methane in the hydrosphere: seep distribution and controlling processes

Extensive seafloor methane seepage has been detected in a variety of settings, including at high latitudes. Although seafloor gas releases at greater than ~100 m below sea level (mbsl) are unlikely to have a direct impact on atmospheric methane concentrations owing to the strong sink of water column aerobic methane oxidation (e.g., Ruppel and Kessler, 2017), the seeps still play a critical role in the carbon cycle and ocean chemistry and as hosts for seafloor chemosynthetic communities. A key difference between seafloor seep systems at temperate and high latitudes (e.g., in Scandinavia and surrounding areas) is the impact of past glaciations and loading/unloading cycles on the latter locations.

Gas seeps and fluid flow in Norwegian offshore regions have long been linked to previous glaciations (Crémière et al., 2016). The predominance of glaciological and geological controls on gas seepage is evident in new results from a 5,000 km^2 area of the northern Barents Sea shelf. In this area, Serov et al. document 21,700 seeps located on glacially eroded, exhumed, and highly faulted structural highs and leaking oil and thermogenic methane from deep reservoirs. They estimate seabed methane flux to be one to two orders of magnitude higher than at other seafloor seep provinces and predict that vigorous methane emissions will continue in the Barents Sea in the future.

Glaciations over the past 2.7 million years have strongly affected both the Barents Sea, which was repeatedly covered by grounded ice, and Vestnesa Ridge west of Svalbard, which was located seaward of ice sheets that terminated at the continental shelf break (Patton et al., 2016). A new seepage chronology for the Barents Sea reveals episodic emissions throughout the Holocene and suggests gas hydrate decomposition and post-glacial seismic activity as potential trigger mechanisms (Himmler et al.). For the deep-water gas hydrate system on Vestnesa Ridge, glacial cycles have partially controlled seepage histories by affecting fracture formation (Cooke et al.) and oceanographic and depositional patterns (Rasmussen and Nielsen).

Geological control also plays a role for the evolution of active gas seeps in western Svalbard fjords, where Rodes et al. describe widespread emissions for which the gas may originate in organic-rich rock sequences that also crop out in the fjords. Southwest of Svalbard, Bellec et al. describe seafloor indicators of seepage (e.g., carbonate crusts, bacterial mats, chemosynthetic organisms), but no active gas flares, at 800 mbsl, near the confluence of two fans associated with the mouths of glacial troughs. Sediment loading from these fans and the consequent evolution of overpressures may drive the seafloor seepage, which occurs in an area where a gas-charged seafloor dome is postulated to have developed and then subsequently deflated. This is a new setting for seepage on the Svalbard margin, where previous studies have focused on seepage from the continental slope and shelf. On the Norwegian shelf, Sinner et al. report an unusual seep site with active hydrocarbon leakage, yet lacking chemosymbiotrophic fauna, possibly due to highly localized methane flow pathways.

Methane in the cryosphere

The cryosphere (i.e., permafrost, ice sheets, and glaciers) forms a frozen cap that traps underlying gas, preventing it from reaching the surface (Walter Anthony et al., 2012; Andreassen et al., 2017). Permafrost formed during past glaciations persists today across vast swaths of Arctic regions, and Birchall et al. highlight the widespread existence of vapor phase gas accumulations below permafrost-bearing sediments in some areas. In recent years, a surprising finding has been that circulating water transports dissolved gas from sub-permafrost and subglacial locations to the forefields

of glaciers (Kleber et al., 2023). A paper in this Research Topic (Kleber et al.) adds to this narrative, describing the complex and interconnected hydrologic system that is crucial to these gas transport processes.

Ice sheets and offshore grounded ice have long been known to interact with methane systems in the underlying sediments. Damm et al. demonstrate that sea ice may also play a crucial role in the Arctic methane cycle. They present new insights showing that sea-ice leads may serve as sinks for atmospheric methane as they refreeze and suggest that this process may take on added importance as the Arctic Ocean transitions into a regime of only seasonal ice cover.

Methane in the biosphere: the microbial filter

Anaerobic methane-oxidizing bacteria present in seafloor sediments (Hinrichs et al., 1999) and aerobic oxidizers in the water column (e.g., Mau et al., 2013) constitute powerful microbial biofilters that mitigate emissions from water-covered areas. In Arctic marine cold seep provinces, De Groot et al. show that bubble-mediated transport and translocation via ocean currents shape microbial community structure and affect the efficiency of the aerobic water column methane sink. In a very different setting, Kleber et al. demonstrate that microbial oxidation is a strong summertime sink mitigating the release of methane from gas-charged subglacial groundwaters. In winter, shallow groundwater systems freeze, reducing subsurface methane oxidation and leading to higher methane emissions. Based on laboratory incubation experiments, Sert et al. reveal that water column aerobic methane oxidation alters dissolved organic matter (DOM) composition towards increased molecular diversity. They show that addition of methane affects DOM characteristics even if the water column was previously associated with a non-seep site and low methane oxidation rates.

Methane in the atmosphere

Continued Arctic warming is liberating carbon that is currently trapped in the cryosphere, and a fraction of this carbon will ultimately be released to the atmosphere as methane. Due to methane's potency as a greenhouse gas, appropriate attribution of natural methane emissions to various sources and geographic regions has taken on greater significance. In a contribution focused on determining if Arctic methane emissions are increasing, Lan and Dlugokencky summarize direct measurements of Arctic methane concentrations, calculate changes in interpolar differences, and apply atmospheric tracer transport models. They conclude that most of the increase in global atmospheric methane can be attributed to emissions from microbial sources in the tropics and that Arctic contributions have not increased significantly in the past four decades.

Author contributions

KA: Writing–original draft, Writing–review and editing. CR: Writing–original draft, Writing–review and editing. SL: Writing–original draft, Writing–review and editing. AH: Writing–original draft, Writing–review and editing. JK: Writing–original draft, Writing–review and editing.

Funding

The author(s) declare that financial support was received for the research, authorship, and/or publication of this article. This is a contribution to CAGE: Centre for Arctic Gas Hydrate, Environment and Climate, and to iC3: Centre for ice, Cryosphere, Carbon and Climate, and was supported by the Research Council of Norway (RCN) through its Centres of Excellence funding scheme, project numbers 223259 and 332635.

Acknowledgments

We thank Peter Swarzenski (USGS) and Pam Swarzenski (USGS) for comments that improved the manuscript. Any use of trade, firm, or product names is for descriptive purposes only and does not imply endorsement by the U.S. Government.

Conflict of interest

The authors declare that the research was conducted in the absence of any commercial or financial relationships that could be construed as a potential conflict of interest.

Publisher's note

References

Andreassen, K., Hubbard, A., Winsborrow, M., Patton, H., Vadakkepuliyambatta, S., Plaza-Faverola, A., et al. (2017). Massive blow-out craters formed by hydrate-controlled methane expulsion from the Arctic seafloor. *Science* 356, 948–953. doi:10.1126/science.aal4500

Cannat, M., Fontaine, F., and Escartín, J. (2010). "Serpentinization and associated hydrogen and methane fluxes at slow spreading ridges," in *Geophysical monograph series (Washington DC, USA: American geophysical union)*, 188. doi:10.1029/2008GM000760

Crémière, A., Lepland, A., Chand, S., Sahy, D., Condon, D. J., Noble, S. R., et al. (2016). Timescales of methane seepage on the Norwegian margin following collapse of the Scandinavian Ice Sheet. *Nat. Commun.* 7, 11509. doi:10.1038/ncomms11509

Hinrichs, K. U., Hayes, J. M., Sylva, S. P., Brewer, P. G., and DeLong, E. F. (1999). Methane-consuming archaebacteria in marine sediments. *Nature* 398 (6730):802–805. doi:10.1038/19751

Johnson, J. E., Mienert, J., Plaza-Faverola, A., Vadakkepuliyambatta, S., Knies, J., Buenz, S., et al. (2015). Abiotic methane from ultraslow-spreading ridges can charge Arctic gas hydrates. *Geology* 43, 371–374. doi:10.1130/G36440.1

Kleber, G. E., Hodson, A. J., Magerl, L., Mannerfelt, E. S., Bradbury, H. J., Zhu, Y., et al. (2023). Groundwater springs formed during glacial retreat are a large source of methane in the high Arctic. *Nat. Geosci.* 16, 597–604. doi:10.1038/s41561-023-01210-6

Lasabuda, A. P. E., Johansen, N. S., Laberg, J. S., Faleide, J. I., Senger, K., Rydningen, T. A., et al. (2021). Cenozoic uplift and erosion of the Norwegian Barents shelf—a review. *Earth Sci. Rev.* 217, 103609. doi:10.1016/j.earscirev.2021.103609

Mau, S., Blees, J., Helmke, E., Niemann, H., and Damm, E. (2013). Vertical distribution of methane oxidation and methanotrophic response to elevated methane concentrations in stratified waters of the Arctic fjord Storfjorden (Svalbard, Norway). *Biogeosciences* 10, 6267–6278. doi:10.5194/bg-10-6267-2013

Patton, H., Hubbard, A., Andreassen, K., Winsborrow, M., and Stroeven, A. P. (2016). The build-up, configuration, and dynamical sensitivity of the Eurasian ice-sheet complex to Late Weichselian climatic and oceanic forcing. *Quat. Sci. Rev.* 153, 97–121. doi:10.1016/j.quascirev.2016.10.009

Patton, H., Hubbard, A., Heyman, J., Alexandropoulou, N., Lasabuda, A. P. E., Stroeven, A. P., et al. (2022). The extreme yet transient nature of glacial erosion. *Nat. Commun.* 13, 7377. doi:10.1038/s41467-022-35072-0

Proskurowski, G., Lilley, M. D., Seewald, J. S., Früh-Green, G. L., Olson, E. J., Lupton, J. E., et al. (2008). Abiogenic hydrocarbon production at Lost City hydrothermal field. *Science* 319 (5863), 604–607. doi:10.1126/science.1151194

Rantanen, M., Karpechko, A. Y., Lipponen, A., Nordling, K., Hyvärinen, O., Ruosteenoja, K., et al. (2022). The Arctic has warmed nearly four times faster than the globe since 1979. *Commun. Earth Environ.* 3, 168. doi:10.1038/s43247-022-00498-3

Ruppel, C. D., and Kessler, J. D. (2017). The interaction of climate change and methane hydrates. *Rev. Geophys.* 55, 126–168. doi:10.1002/2016RG000534

Walter Anthony, K., Anthony, P., Grosse, G., and Chanton, J. (2012). Geologic methane seeps along boundaries of Arctic permafrost thaw and melting glaciers. *Nat. Geosci.* 5 (6), 419–426. doi:10.1038/ngeo1480

Wheat, C., Seewald, J., and Takai, K. (2020). Fluid transport and reaction processes within a serpentinite mud volcano: South Chamorro Seamount. *Geochim. Cosmochim. Acta.* 269, 413–428. doi:10.1016/j.gca.2019.10.037

frontiers | Frontiers in Earth Science

TYPE Original Research
PUBLISHED 30 May 2023
DOI 10.3389/feart.2023.1188737

OPEN ACCESS

EDITED BY
Jacek Raddatz,
Goethe University Frankfurt, Germany

REVIEWED BY
André Bahr,
Heidelberg University, Germany
Wang Yun,
China University of Geosciences, China

*CORRESPONDENCE
Frances Cooke,
frances.a.cooke@uit.no

RECEIVED 17 March 2023
ACCEPTED 16 May 2023
PUBLISHED 30 May 2023

CITATION
Cooke F, Plaza-Faverola A, Bünz S, Sultan N, Ramachandran H, Bedle H, Patton H, Singhroha S and Knies J (2023), Sedimentary deformation relating to episodic seepage in the last 1.2 million years: a multi-scale seismic study from the Vestnesa Ridge, eastern Fram Strait. *Front. Earth Sci.* 11:1188737. doi: 10.3389/feart.2023.1188737

Sedimentary deformation relating to episodic seepage in the last 1.2 million years: a multi-scale seismic study from the Vestnesa Ridge, eastern Fram Strait

Frances Cooke[1]*, Andreia Plaza-Faverola[1], Stefan Bünz[1], Nabil Sultan[2], Hariharan Ramachandran[3], Heather Bedle[4], Henry Patton[1], Sunny Singhroha[1] and Jochen Knies[5]

[1]CAGE—Centre for Arctic Gas Hydrate, Environment and Climate, UiT (The Arctic University of Norway), The Arctic University of Norway, Tromsø, Norway, [2]Geo-Ocean, UMR6538, Ifremer, CNRS, UBO, UBS, Plouzané, France, [3]Institute of GeoEnergy Engineering, Heriot-Watt University, Edinburgh, United Kingdom, [4]School of Geosciences, The University of Oklahoma, Norman, OK, United States, [5]NGU—Geological Survey of Norway, Trondheim, Norway

Seafloor hydrocarbon seepage is a natural fluid release process that occurs worldwide on continental shelves, slopes, and in deep oceanic basins. The Vestnesa sedimentary ridge in the eastern Fram Strait hosts a deep-water gas hydrate system that became charged with hydrocarbons ~2.7 Ma and has experienced episodic seepage along the entire ridge until a few thousand years ago, when seepage activity apparently ceased in the west but persisted in the east. Although it has been documented that faults and fractures play a key role in feeding the seeps with thermogenic gases, the mechanisms controlling seepage periodicity remain poorly understood. Here we integrate high-resolution P-cable 3D seismic and Chirp data to investigate the spatial and temporal evolution of high-resolution fractures and fluid flow features in the west of the Vestnesa Ridge. We characterize sediment deformation using a fracture density seismic attribute workflow revealing two highly deformed stratigraphic intervals and associated small-scale pockmarks (<20 m diameter). Chronostratigraphic constraints from the region show that these two highly deformed intervals are influenced by at least three major climatic and oceanic events during the last 1.2 million years: the Mid-Pleistocene Transition (~1.25–0.7 Ma), the penultimate deglaciation (~130 ka) and the last deglaciation (Heinrich Stadial 1: ~16 ka). These periods of deformation appear associated with seismic anomalies potentially correlated with buried methane-derived authigenic carbonate and have been sensitive to shifts in the boundary of the free gas-gas hydrate interface. Our results show shifts (up to ~30 m) in the depth of the base of the gas hydrate stability zone (GHSZ) associated with major changes in ocean bottom water temperatures. This ocean-driven effect on the base of the GHSZ since the Last Glacial Maximum coincides with the already highly deformed Mid-Pleistocene Transition sedimentary interval and likely enhanced deformation and gas leakage along the ridge. Our results have implications for understanding how glacial cycles impact fracture formation and associated seepage activity.

KEYWORDS

sediment fracturing, episodic seepage, high-resolution seismic attributes, glacial dynamics, Fram Strait

1 Introduction

The release of gas-rich fluids to the oceans and the atmosphere is a natural process that occurs worldwide in marine settings, including at sites of gas hydrate accumulations (Hovland, 1988; Anderson and Bryant, 1989; Mazurenko and Soloviev, 2003). Such fluid release is often associated with hydrocarbon leakage pathways that are detected in seismic data as vertical zones of deteriorated strata (Arntsen et al., 2007; Hustoft et al., 2007; Gay et al., 2012; Cartwright and Santamarina, 2015; Ma et al., 2021). These 'gas chimneys' (or pipes) are sedimentary disturbances formed through hydrofracturing (Moss and Cartwright, 2010) when the excess fluid pressure exceeds the effective least principal stress plus the tensile strength of the medium (Alfaro and Wong, 2001). The subsequent fluid flow through fractured zones depends on the fluid pressure, which is governed by two critical thresholds: the 'shut-in pressure,' which stops the flow, and the 're-opening pressure,' which allows it to restart (Sano et al., 2005). Hydrofractures are known to develop at the base of the gas hydrate stability zone (GHSZ) where overpressure exists at the free gas-gas hydrate interface (e.g., Elger et al., 2018). When fluids migrate vertically towards the seafloor—preferably along gas chimneys during hydrogeological pumping—a cycle of pressure build-up and release occurs (Powers, 1967) leading to the formation of collapse features (Ligtenberg, 2005; Judd and Hovland, 2007; Løseth et al., 2009; Moss and Cartwright, 2010). These seafloor features were first described in the literature by King and Maclean. (1970) as pockmarks, and typically range in size from a few meters to >1 km (Andreassen et al., 2007; Rise et al., 2015). The presence of pockmarks is associated with fluid release related to various geological processes (i.e., compaction and dewatering/degassing, active faulting/tectonics, or gas hydrate dissolution and dissociation (Sultan et al., 2014)). These different geological processes are expressed in the seismic data in different ways and are highly dependent on the resolution of the dataset. Seepage can be episodically active, before slowing down and/or becoming dormant (e.g., Gay and Berndt, 2007) due to a shifting balance between gas pressure build up, and fluid migration from beneath the base of the GHSZ, over geological time scales (Gay and Berndt, 2007; Etiope, 2015).

Such periodic seepage through existing permeable pathways have been documented globally, including across the North Sea (e.g., Hovland, 2008), the mid-Norwegian margin (Plaza-Faverola et al., 2012) Canterbury basin (Bertoni et al., 2019), and Arctic margins (Plaza-Faverola et al., 2015; Himmler et al., 2019). In formerly glaciated domains episodic seepage events are known to span millennial time scales, hypothetically driven by the changing pressure, temperature and tectonic-stress conditions associated with the repeated growth and retreat of continental-scale ice sheets through the Late Quaternary (Crémière et al., 2016; Serov et al., 2017; Himmler et al., 2019; Vachon et al., 2022), evidenced by subsurface pockmarks and buried authigenic carbonate concretions at multiple stratigraphic levels (e.g., Plaza-Faverola et al., 2015, 2011; Moss et al., 2012; Riboulot et al., 2014; Chand et al., 2017; Himmler et al., 2019).

Despite documentation of periodic gas release through vertical pathways at numerous continental margins, the exact mechanisms controlling the periodicity remains poorly investigated. So far, it is known that the slightest pressure perturbations may drive local seepage events (Wiprut and Zoback, 2000). However, it is not known whether the reactivation of pre-existing faults and fractures triggering the seepage are dependent on very small pore-pressure or stress changes (Oye et al., 2022), with a time-transgressive understanding of seepage pathways and periodicity in marine environments primarily limited by the frequency of (i.e., conventional) seismic acquisition and the inattention to data conditioning in seismic post processing.

Here, we conduct integrated analyses of high-resolution (6.25 x 6.25 m) P-cable 3D seismic and Chirp data to constrain deformation structures and fluid flow features at an unprecedented level of detail along the Vestnesa Ridge, an active deep-water gas hydrate and seepage system in the eastern Fram Strait. We pay close attention to the small (<20 m) geological features in the post-stack processing (see Supplementary Appendix SA) and maintain a high signal-to-noise ratio to avoid removing key information in the seismic data. Our results reveal new insights into spatial and temporal variations in the amount of sediment deformation and associated gas migration related to episodic seepage events since the start of the Mid-Pleistocene Transition [~1.2 million years ago (Ma)]. The integration of advanced seismic attributes with chronostratigraphic information from this region also allows key time intervals of enhanced sediment fracturing to be constrained. We discuss the influence of gas hydrate and glacial dynamics on sediment deformation and seepage periodicity, and how key transitions in the climate and ocean systems have potentially impacted sub-seafloor fracture formation and seepage activity at Arctic deep-marine fluid flow systems.

2 Study area

2.1 The Vestnesa Ridge

The Vestnesa Ridge is a 100 km long and 3–5 km wide contourite drift in the eastern Fram Strait at ~1,200–1700 m water depth. Located approximately 100 km to the north of the Molloy Transform Fault (MTF), the Vestnesa Ridge lies between the ultra-slow spreading Molloy Ridge and the Knipovich Ridge (Figure 1). Beneath the contourite drift lies a young (<20 Ma) relatively hot oceanic crust (Vanneste et al., 2005; Bünz et al., 2012). Young oceanic crust has higher geothermal gradients, which leads to more buoyant fluid and more active flow. Geothermal gradients increase from 70°C/km over Vestnesa Ridge to 115°C/km closer towards the MTF (Crane et al., 1991; Vanneste et al., 2005). The Knipovich Ridge is the northernmost extension of the Mid-Atlantic Ridge system that propagated northwards and is now buried by thick contourite deposits in the study area (Crane et al., 2001; Vanneste et al., 2005). Extensional faults propagate northwards from the Knipovich Ridge, changing in orientation (~N–S to NW–SE) further from the Knipovich Ridge spreading center towards the southern rim of the Vestnesa Ridge (Crane et al., 2001; Vanneste et al., 2005; Hustoft et al., 2009; Plaza-Faverola et al., 2015).

The Vestnesa Ridge has a sediment thickness of ~5 km (Lebedeva-Ivanova et al., 2019) on the ridge and decreases in thickness to hundreds of meters towards the Knipovich and MTF (Breivik et al., 1999; Ritzmann et al., 2004; Bünz et al., 2012). The

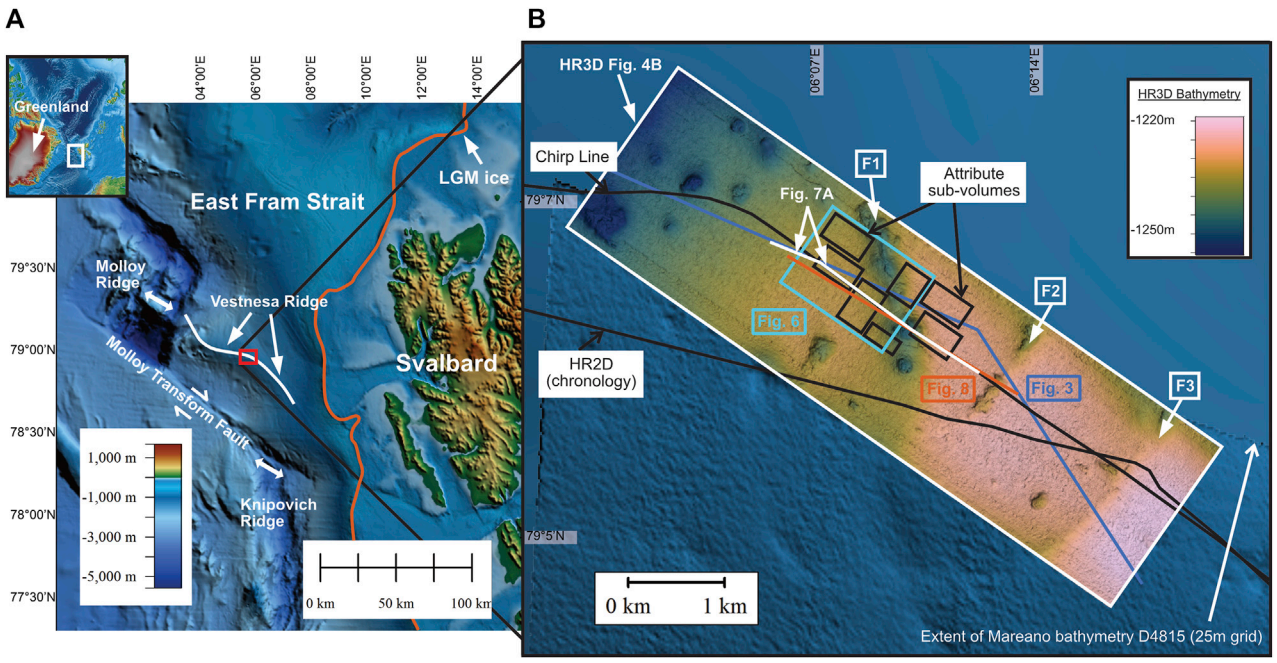

FIGURE 1
Location map of the Vestnesa Ridge in the eastern Fram Strait **(A)** with IBCAO (200 m x 200 m) bathymetry; the orange line **(A)** corresponds to the maximum extent of the Barents Sea ice sheet during the Last Glacial Maximum (LGM) adapted from Patton et al., 2015a. Study area **(B)** displays the HR3D seismic bathymetry (white box); a HR2D line connecting the chronostratigraphy from the east of the Vestnesa Ridge and the Chirp data (black lines); 7 sub-volume selections for fracture density attribute work (black boxes), 1 K1 attribute sub-volume selection (cyan box) (Figure 6); 3 HR3D and Chirp composite lines (orange, lilac and white lines). Overlying the IBCAO bathymetry **(A)** is the higher resolution (25x25 m) bathymetry **(B)** available from the region (e.g., from Mareano, and UiT multiple surveys) which overlaps the HR3D bathymetry **(B)**. The seafloor was converted to depth using the water column velocity (CAGE 18-4 cruise report: Bünz, 2022).

reflection characteristics of the seismic sections are typical of a slope-sheeted drift, as described in the area northwards, towards the north east of the Spitsbergen Fracture Zone (Osti et al., 2019). The drift is influenced by bottom current controlled sediment activity that began during the opening of the Fram Strait during the middle and late Miocene (Eiken and Hinz, 1993; Osti et al., 2019). Three main stratigraphic units are defined for the Yermak Plateau and the Vestnesa Ridge: YP-1, YP-2, and YP-3 (Eiken and Hinz, 1993). The base of the youngest unit (of main interest for this study), YP-3, is associated to an age estimate of 2.7 Ma, constrained by the Ocean Drilling Program Leg 151 on the Yermak Plateau (ODP Hole 912 (Mattingsdal et al., 2014)). The boundary between YP-2 and YP-3 thus marks the transition of pure contourite deposition to the deposition of glacially transported sediments (Knies et al., 2018; Osti et al., 2019). Characteristic sediments of YP-3 include extensive, regional ice-rafted debris (IRD) (Howe et al., 2008; Sztybor and Rasmussen., 2017) and laminated silty turbidites (Jessen et al., 2010), attributed to an increase in sediment supply from beneath fast flowing ice streams during periods of rapid melting.

The Vestnesa Ridge consists of an eastern segment with a narrow peak forming an anticline that strikes NW–SE, parallel to the MTF. The ridge crest flattens towards the west and extends E–W towards the Molloy Ridge (Figure 1A). Gas hydrates are an important component of the Quaternary sedimentary system along the entire ridge. A widespread bottom-simulating reflection (BSR) has been mapped and it extends from the ridge crest towards the ridge flanks (e.g., Plaza-Faverola et al., 2017). Gas hydrates have been sampled as thin, small flakes and as more massive several cm-long concentrations from sediment cores within the upper 6 m at sites on the eastern end of the sedimentary ridge (e.g., Panieri et al., 2017; Sultan et al., 2020). Head space gas samples along the ridge indicate the presence of methane and heavier hydrocarbons with a thermogenic signature in addition to microbial methane (Plaza-Faverola et al., 2017; Pape et al., 2020).

Hydrocarbon migration modelling at the Vestnesa Ridge suggests large scale fluid migration started around 6 Ma and reached the seafloor around 2 Ma (Knies et al., 2018; Daszinnies et al., 2021). High-resolution P-Cable 3D seismic reveals multi-stage buried pockmarks indicating that recurrent seepage events have occurred episodically with the onset of northern hemisphere glaciations ~2.7 Ma (Plaza-Faverola et al., 2015). Several periodic events of seepage have also been reported via paleontological proxies since the Last Glacial Maximum (LGM) (Panieri et al., 2014; Consolaro et al., 2015; Sztybor and Rasmussen, 2017; Schneider et al., 2018; Himmler et al., 2019). Seepage has remained active along the entire ridge until a few thousand years ago (Bünz et al., 2012) when high flux seepage ceased in the west but remained active in the east (Plaza-Faverola et al., 2015). Despite the absence of acoustic flare activity in the west, piezometer data reveal shallow (<10 m) high-pressured sediments (e.g., Sultan et al., 2020) suggesting the presence of gas in the near-surface sub-seafloor.

Pockmarks are widespread on the present day seafloor (e.g., Vogt et al., 1994). All pockmarks at the Vestnesa Ridge are seafloor expressions of focused fluid flow identified as chimneys and pipes in subsurface seismic data (Petersen et al., 2010; Bünz et al., 2012). Gas hydrate and fluid flow studies at the Vestnesa Ridge have largely focused on the active pockmarks in the east. Two large (ca. 500 m in diameter) pockmarks (i.e., Lunde and Lomvi), have been used to study paleo-methane seepage and methane transport mechanisms (Smith et al., 2014; Panieri et al., 2017; Dessandier et al., 2019; Yao et al., 2019; Hong et al., 2021; Sauer et al., 2021; Domel et al., 2022). Previous studies suggest that the regional stress regime is the main external factor controlling the long-term pattern of gas seepage here (Plaza-Faverola and Keiding, 2019). However, shorter periodicity seepage is not included in these studies. To the west of the Vestnesa Ridge, pockmarks are more widespread, yet less well studied. Here, they are referred to as inactive or dormant because gas bubbles have not yet been observed in echosounder data, despite decades of acoustic surveying (Bünz et al., 2012). The inactivity of pockmarks in the west, however, does not rule out the possibility that seepage is occurring as micro-seepage or intermittently. Recent studies suggest that seepage periodicity at the Vestnesa Ridge may be related to pressure changes induced by sea-level changes or other external mechanisms able to generate seismicity (Domel et al., 2022); other studies suggest that external pressure is generated by sediment compaction, gravity sliding, and glacial isostatic adjustment (controlled by varying ice sheet thicknesses) (Himmler et al., 2019; Vachon et al., 2022).

3 Data and methods

A high-resolution 3D (HR3D) seismic data volume is the primary dataset for this study. The data were acquired and processed on board the RV Helmer Hanssen in July 2018 during the Centre for Arctic Gas Hydrate, Environment and Climate (CAGE) 18-4 cruise (Bünz, 2022), using the P-cable seismic system (e.g., Planke et al., 2009; Petersen et al., 2010).

The HR3D volume covers an area of ~2 x 7 km. Data were acquired using 14, 25 m long streamers, with eight channels per streamer. The source consisted of 2 mini-GI guns (30/30 in^3 and 15/15 in^3) firing every 6 s at a ship speed of 4-5 knots and with a sampling rate of 0.25 s. Onboard processing included geometry assignment, bandpass-filtering with a frequency of 18-25-400–500 Hz, spherical divergence, noise attenuation, de-ghosting, CDP binning at 6.25 x 6.25 m, static corrections, NMO correction, stacking and 3D post stack Stolt migration, using a stacking velocity of 1,480 m/s. The lateral resolution after migration is given by a bin size of 6.25 x 6.25 m, and the vertical resolution is ~4–5 m at the seafloor (calculated as $\lambda/4$ using a water velocity of 1,480 m/s and for a dominant frequency of 138 Hz).

A high-resolution (20–300 Hz) 2D (HR2D) seismic line was collected along the crest of the ridge (Figure 1B) documented in Plaza-Faverola et al. (2017). The HR2D line is used in this study to establish chronostratigraphic constraints based on previous studies (Plaza-Faverola et al., 2015; Plaza-Faverola et al., 2017; Knies et al., 2018; Himmler et al., 2019; Alexandropoulou et al., 2021; Dessandier et al., 2021).

Chirp data was acquired during the CAGE 19-3 cruise on board the R/V Kronprins Haakon (Knies and Vadakkepuliyambatta, 2023) (Figure 1B). The data were acquired using the hull-mounted Kongsberg SBP300 (MK2) with frequencies between 2.5 and 7 kHz. Instantaneous amplitude was applied during the recording of the processed sequence. The frequency sweep of the Chirp source pulse suppresses source ringing and enhances the vertical resolution (Quinn et al., 1998). The maximum vertical resolution of the system is 0.3 m, and the bin size is approximately 10 m, given the average distance between traces.

3.1 Seismic attributes

Seismic attribute analyses allow us to extract additional information from seismic data, leading to enhanced seismic data interpretation and understanding of subsurface geological processes (e.g., Li and Zhao, 2014). A 'fracture density' attribute workflow (Supplementary Appendix SA2; Figure 2, section 3.1.3) is used in this study on multiple sub-volumes of HR3D seismic data (areas outlined in Figure 1B) and interpreted in conjunction with two additional seismic discontinuity attributes (section 3.1.2): 'variance' (Supplementary Appendix SA1, SA2) and 'most positive principal structural curvature (K1)' (e.g., Al-Dossary and Marfurt, 2006) (Supplementary Appendix SA1, SA2).

3.1.1 Data conditioning

Post stack seismic data should be optimally processed prior to the computation of seismic attributes. This is referred to as data conditioning or image enhancement (e.g., Al-Dossary and Marfurt, 2006; Chávez-Pérez and Vargas-Meleza, 2008). Despite high-resolution static corrections applied in the pre-processing, some residual statics remained in the datasets, revealing an undesirable acquisition footprint. Without footprint removal, artifacts are enhanced in further data conditioning steps and problems arise during the detection of real amplitude discontinuities (Chopra and Marfurt, 2013). In this study, the seismic data is first conditioned with geostatistical filtering using the M-GS Destriping (see Supplementary Appendix SA2) which removes the acquisition geometry footprint from the post stack cube. In addition to geostatistical filtering, a recommendation in structural interpretation is to apply a structure-oriented filter (Fehmers and Höcker, 2003) or dip-steered median filter prior to fault characterization (e.g., Ashraf et al., 2020; Acuña-Uribe et al., 2021). In our fracture density attribute workflow, dip estimation was calculated using the dip steered median filter (DSMF) (principal component analysis (PCA) + median filter (MF)) (Supplementary Appendix SA2). The DSMF decreased the random noise and smoothed the seismic reflectors slightly, keeping the desired geological features intact.

3.1.2 Seismic discontinuity

Coherence and curvature-related seismic attributes are referred to as discontinuity attributes in this work (see Supplementary Appendix SA1). Coherence measures the similarity between waveforms on neighboring traces, while curvature measures lateral changes in dip and azimuth. Both these attributes are widely used as edge detection methods for fault and fracture

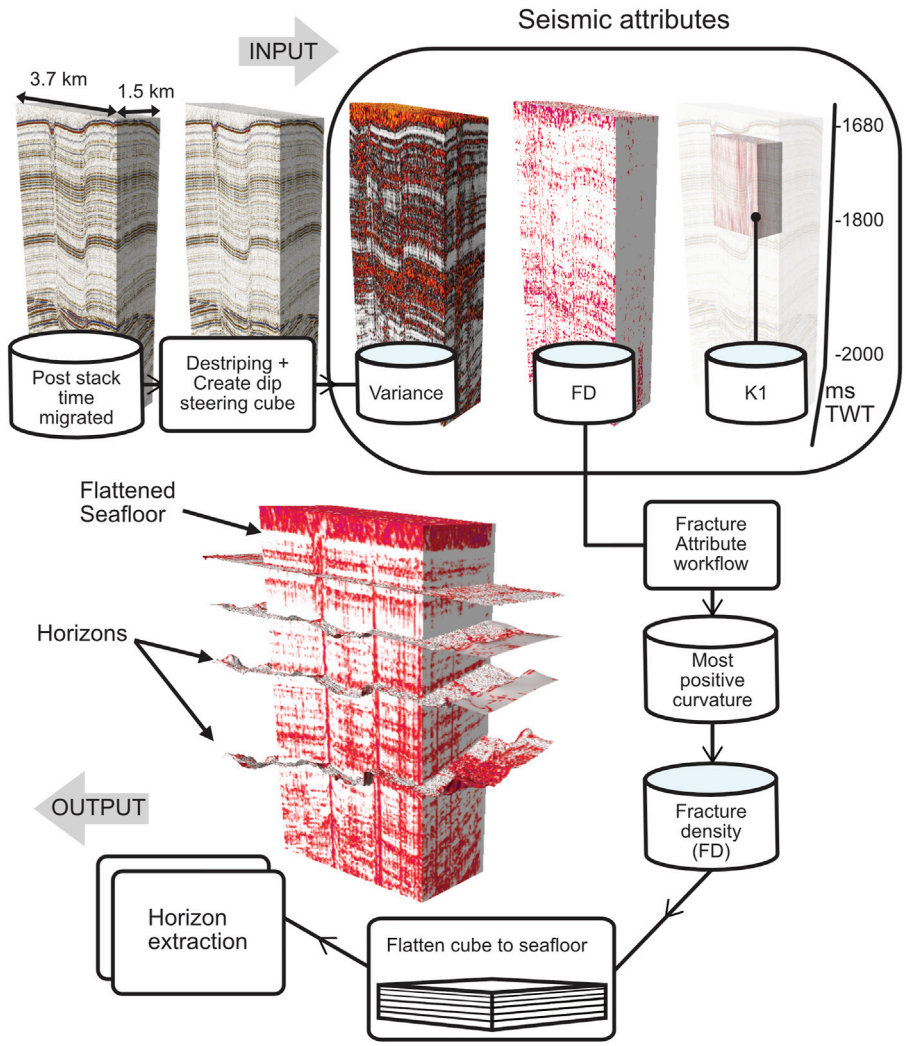

FIGURE 2
Seismic attribute workflow detailing steps used in the fracture attribute processing prior to horizon extraction. The input for the attributes consists of the original seismic volume after removing the residual statics (MGS-destriping). The fracture density (FD) attribute volume requires the calculation of most positive curvature first, prior to calculating FD. A set of horizons were extracted from the FD volume, after seafloor flattening (see Supplementary Appendix SA2 for information on parameters used in the workflow).

characterization (e.g., Lisle, 1994; Bahorich and Farmer, 1995; Marfurt et al., 1999; Roberts, 2001; Hart, 2002; Al-Dossary and Marfurt, 2006). They may also be used to detect subtle stratigraphic features (e.g., channels and turbidites, Blumentritt et al., 2003). Falsely interpreted features caused by velocity pull-ups and push-downs and apparent faulting created by noise contamination may also be present (Roberts, 2001).

A plethora of different coherence algorithms exist, and their availability varies between various software packages. In this study we used 'variance' which is the inverse of coherence (Supplementary Appendix SA1). High variance (low coherence) can suggest faults or high fracture intensity. Coherence will fail when the offset (or difference in waveform) is below the seismic resolution, causing the seismic reflector to appear continuous (Gao, 2013). Most positive and most negative curvature-related attributes are known to provide some of the best illumination of faults and fractures over other discontinuity attributes (Chopra and Marfurt, 2007). To extract as much detail as possible from the HR3D dataset we use most positive curvature, in the fracture density attribute workflow (Supplementary Appendix SA2; Figure 2) and qualitatively compare the result with the variance and K1 attribute. Most positive curvature is computed on the full HR3D dataset followed by fracture density in separate sub-volumes. K1 was computed on a single sub-volume that areally encompasses the fracture density sub-volumes (Figure 1B).

3.1.3 Fracture density

The fracture density attribute is used to highlight regions of high density fractures. It improves the visualization of potential fracture anomalies by computing the ratio of the number of traces classified as being fractures to the total number of traces present (e.g., Klokov et al., 2017; Ashraf et al., 2020). A radius for scanning is required for the computation and a discontinuity attribute as input to define the fracture anomalies. Most positive curvature was used as the attribute

input, with a radius of scanning set to 20 m (Supplementary Appendix SA2).

Prior to horizon extraction, the fracture density volume was flattened to the seafloor (Figure 2). To verify that the resulting fracture density trends were robust we divided the whole volume into 7 fracture density sub-volumes (Figure 1). These sub-volumes were selected with the aim of covering key areas with seafloor structures of relevance (e.g., potential weakness zones associated with major faults in the region; zones mainly free of large fluid flow structures and areas of minimum velocity seismic disturbance for ease of horizon mapping). 24 fracture density horizons were extracted from each 7 sub-volumes with a total of 168 extractions. The 24 horizons represent the ~170 m interval from the seafloor to the base of the GHSZ. For a more quantitative approach, the mean fracture density was extracted for each horizon. The mean was then multiplied by the respective sub-volume surface to calculate the weighted mean value, giving an overview of fracture density for each horizon.

3.2 Extraction of seafloor and buried pockmark diameters

The shape of the pockmarks was systematically extracted from 5 (10 x 10 m) digital elevation model (DEM) surfaces (H0, H0.3, H1, H2, H2.25), using a rule-based GIS methodology, which defines the pockmark perimeter by analysis of closed-contour properties (Patton et al., 2015). A 1 m contour interval was used, as well as a minimum depth threshold of 2 m for defining pockmarks; other default parameter values remained unchanged. Reflection sags from velocity push-down effects were also extracted from the DEM data and investigated. The size and shape of the pockmarks can provide information about the strength of the fluid flow at each selected horizon and the directionality of the flow if the pockmarks are elongated.

3.3 Chirp data analyses

Chirp data was used to validate fine-scale structures revealed by the various attributes from the HR3D seismic data. The Chirp data provides a higher vertical resolution than the HR3D by a factor of ~20, in the upper 40 m of the sedimentary column, while the HR3D seismic data provides better penetration (~200 m i.e., beyond the base of the GHSZ). The high vertical resolution in the Chirp aids the interpretation of fine <0.5 m layering, displayed as the reflection strength, referred to as the envelope of the acoustic wave (Schock, 2004; Zhang and Digby, 2013). The envelope display highlights geological features, such as gas accumulation and faults with only positive values, where peaks reveal high impedance and troughs low impedance.

3.4 Gas hydrate stability zone modelling

To constrain the range of variability of the GHSZ and its effect on fluid dynamics along the investigated transect of the Vestnesa Ridge we ran a 2D transient heat equation model with the temperature and pressure of hydrate-phase equilibrium calculated at each time step using the van der Waals and Platteeuw model (Sultan et al., 2020). We implemented the approach by Sultan et al. (2020) using constraints from cross-disciplinary studies in the area for the last ca. 35 ka (i.e., the constraints for bottom water temperatures and sea-level changes for the Fram Strait are restricted to ca. 33 ka which is the length of available analysed sedimentary records (Ezat et al., 2014; Sessford et al., 2018). Our initial model is an 8-layer model constrained using porosities, thermal conductivity and corresponding sea-level (Peltier and Fairbanks, 2006; Daszinnies et al., 2021) (Supplementary Appendix SB). We generated a simplified bottom water temperature function for the last 35 ka by integrating the data in El bani Altuna et al. (2021), Ezat et al. (2014) and Ezat et al. (2021) (Supplementary Appendix SB). We used an average geothermal gradient (GTG) of 90°C/km (Plaza-Faverola, 2020). Sensitivity tests for reasonable variations in the GTG, bottom water temperatures and salinity conducted for a BSR model along the entire Vestnesa Ridge shows that modelling uncertainties at our study site is in the range of −/+ 20 m (Plaza-Faverola et al., 2017). To compare the modelled BSR depth with the observed BSR, the seismic transect was depth converted following the approach in Plaza-Faverola et al. (2017). For this area they used P-wave interval velocity constraints from two ocean bottom seismometers (OBSs) located >20 km apart from each other along the Vestnesa Ridge used by Petersen et al. (2010). Their sensitivity test for a range of interval velocities showed that the estimated depth of the reflections may have an uncertainty of −/+ 8 m (Plaza-Faverola et al., 2017).

These experiments provide a sense of the shift of the BSR depth in response to the simultaneous effect of changing pressures (sea-level) and temperatures (ocean bottom temperatures) during major climatic transformations (i.e., glacial-interglacial transitions) within the last 35 ka. Gas hydrate dissociation may have occurred after the LGM initiated by elevated bottom water temperatures during oceanic warming (i.e., Heinrich Stadial 1: ~16 ka) in the last deglacial period (El bani Altuna et al., 2021). We use the BSR behaviour modelled for this period as a reference to discuss the magnitude of changes that can be expected during other comparable major paleoclimatic events and the implications for understanding sediment deformation processes.

4 Results and interpretation

4.1 Seafloor morphology and outcropping sedimentary faults

The depth of the bathymetry for the HR3D survey area ranges from 1,217 to 1,264 m and deepens gradually from east to west (Figure 1B). The investigated sedimentary sequences extend to ca. 1,400 m below the sea surface. The deepest interpreted surface (H2.25) is closest to the gas hydrate related bottom-simulating reflection (BSR) (section 4.2).

There are two main faults (F1 and F2) that display large depressions along the strike (Figure 3, Figure 4B, Figure 1B), located in the center of the survey area. A third major fault (F3) lies 1.6 km to the east of F2 with the same strike (~NE–SW) orientation. F1 and F2 are located between bathymetric highs

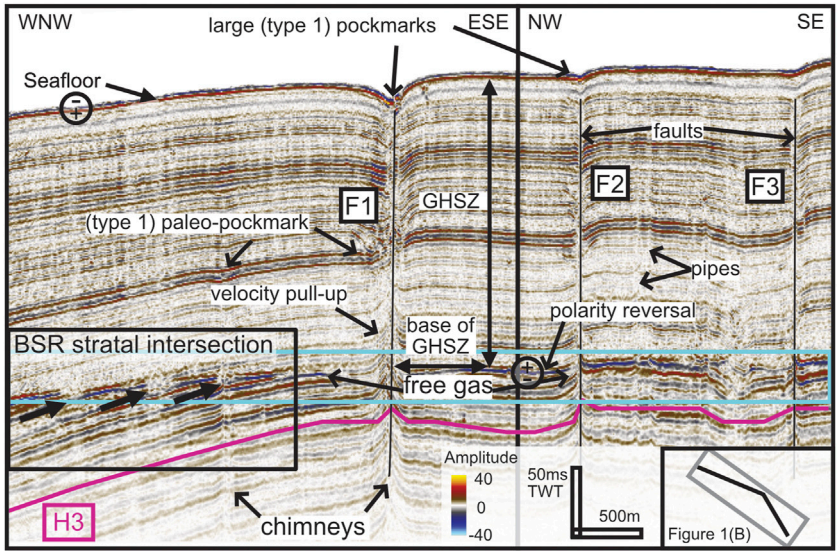

FIGURE 3
HR3D composite seismic section displays faults F1, F2 and F3 (vertical black lines) and the base of the gas hydrate stability zone (GHSZ) revealed by the bottom-simulating reflection (BSR) (enclosed in the cyan box). Where the bathymetry dips downwards towards the WNW the dipping lithology intersects the BSR indicated by the upward dipping black arrows also marking vertical disturbances (i.e., gas chimneys) originating from beneath the BSR. The magenta line beneath the BSR marks the ~1.5 Ma chronostratigraphic event used to calculate sediment ages marked as horizon H3. The magenta line (horizon H3) beneath the BSR marks the ~1.5 Ma chronostratigraphic event used to calculate sediment ages (between ~0.4 and ~1.5 Ma), (see Figure 8). Chimneys/pipes and type 1 buried (paleo) and present day, pockmarks are indicated. Velocity pull-up features are expressed in the seismic above, at, and below the BSR (revealed most clearly at Fault F1).

BH1 and BH2 which have their long axis in line with the orientation of faults F1 and F2 respectively (Figure 4B, Figure 1B).

4.2 Gas hydrate and fluid flow indicators

We observe typical direct hydrocarbon indicators (DHIs) as amplitude anomalies due to the presence of hydrocarbons in the sediments. The first prominent indication of sub-seabed fluid flow dynamics is the presence of the BSR that can be imaged within the entire area at depths ranging from ~1875–1915 ms TWT ((~165–170 m beneath the seafloor (mbsf)) (Figure 3). The BSR is characterized by anomalously high amplitudes and a phase reversal with respect to the seafloor polarity indicating the presence of free gas trapped beneath gas hydrate bearing strata (Figure 3). The BSR gets shallower westward with respect to the seafloor (Figure 3, Figure 4A) and is most clearly defined where it cross cuts stratal reflections (Figure 3). In sections, the high amplitude reflections are punctured and locally disturbed creating a discontinuous BSR (Figure 3). The disturbances extend vertically through the seismic data and terminate at the seafloor. They are interpreted as vertical focused fluid migration features (i.e., chimneys or pipes, Løseth et al., 2009; Bünz et al., 2012). The distribution of the chimneys is reflected on the seafloor as pockmarks (Figure 1B, Figure 3, Figure 4).

We observe bright spots (Figure 4A) inside some of the chimneys potentially indicating trapping of fluids at preferential sedimentary or structural features or representing real morphological features such as buried authigenic carbonate domes or infilled buried pockmarks often documented from other margins (e.g., Løseth et al., 2011; Heggland, 2005; Hustoft et al., 2007; Plaza-Faverola et al., 2015).

Gas chimneys provide evidence for gas transport and release into paleo and present day seafloors. The present day seafloor is characterized by two types of fluid seepage indicators. Type 1: large pockmarks (<50 and >250 m width and 5–10 m deep) (Figure 4B) and type 2: small-scale pockmarks (<20–50 m width and very shallow ~1–3 m deep/minimum resolution of seismic) (Figures 5, 6).

The large pockmarks (type 1) (e.g., pockmarks P1–P8) are distributed within the investigated 3D volume area (Figure 4B) with some of them following structural lineaments and faults (Figure 4B). The pockmarks with the largest areal surfaces are prominently expressed within F1, in the center of the 3D volume. Here several pockmarks have merged forming irregular shapes (Figure 1B; Figure 4B).

The chimneys vary in character throughout the sedimentary column. The areal surfaces of the chimney structure at each horizon are highly varied in many cases (e.g., P3, P4 and P7: Figure 4B). The seismic disturbance zone sometimes displays narrowing at the surface compared to a much broader buried surface at depth (e.g., P3: Figures 4A, B). Some chimneys display a pull-up effect (e.g., P2: Figures 4A, B) resulting in an apparent pockmark extracted from the DEM surfaces, offset from the central chimney (Figure 4B). The velocity pull-up effect at the P2 chimney starts nearby horizon H2 and affects the seismic below until the BSR. Above horizon H2 the only true pockmark is revealed on the seafloor (Figure 4B).

The variation in the areal extent of the chimney area is shown most clearly in pockmark P3 (Figures 4A–C). A broadened chimney

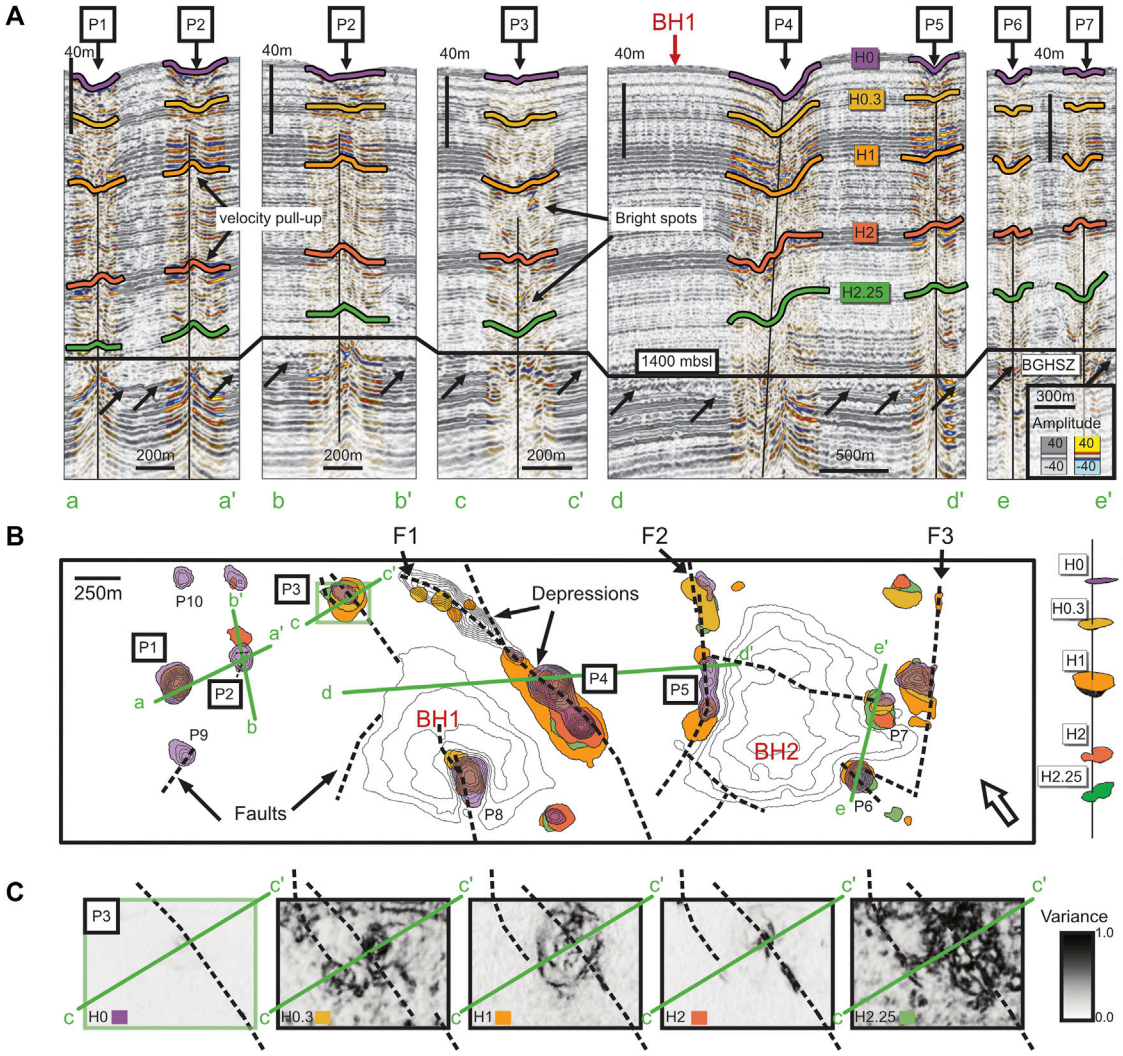

FIGURE 4
(A) Depth converted HR3D vertical sections (a—a', b—b', c— c', d— d', e—e') across 7 present day, type 1 pockmarks on the seafloor (see Figure 1B for the HR3D seafloor bathymetry). Five horizon surfaces (H0/Seafloor, H0.3, H1, H2 and H2.25) above the base of the gas hydrate stability zone/bottom-simulating reflection (BGHSZ/BSR), are indicated. **(B)** Extracted pockmarks from 5 (10 x 10 m) digital elevation model (DEM) surfaces (H0/Seafloor, H0.3, H1, H2, H2.25) using a rule-based GIS methodology (Patton et al., 2015). Bathymetric highs (BH1 and BH2) as well as faults (F2 and F3) are indicated together with extracted seafloor and buried pockmarks. **(C)** Variance surface extractions at pockmark P3 (H0/Seafloor, H0.3, H1, H2 and H2.25) show differences in fluid activity at each horizon surface.

unit is represented by horizon H1 while chimney narrowing is represented by horizons H0 and H2 (Figure 4C). Another notable characteristic is the high level of variance at horizons H0.3 and H2.25 (Figure 4C). The chimney typically broadens at more laterally disturbed seismic reflections and narrows at more laterally continuous seismic reflections (possibly related to the type of sedimentary deposit).

4.3 Sub-seismic scale indications for fracturing and fluid flow

The small-scale pockmarks (type 2) are widely distributed in the seismic volume yet vary in size and density between stratigraphic units (Figure 5). It is difficult to interpret the character of each type 2 feature on a large scale, owing to their small size (<20 m) and high density. However, patterns are observed in variance maps (Figure 5, Figure 6). Higher densities of type 2 features are observed within and at the outer limits of fault zones (Figure 6). In some instances, type 2 features form circular rings, they may be elongated or aligned forming short chains (Figure 5B).

The approach used to visualize only the positive peaks of curvature represented in the seismic (referred to as anticlinal flexures), (relating to both large-scale and small-scale features), was to use fracture density and K1 attributes. The fracture density attribute reveals where fractures intersect, or where there are a high number of them. The anticlinal flexures of the K1 attribute fill in the white spaces (high coherence) between the small-scale pockmarks (type 2) in the variance attribute. We therefore use the three attributes combined, to understand the distribution of small-

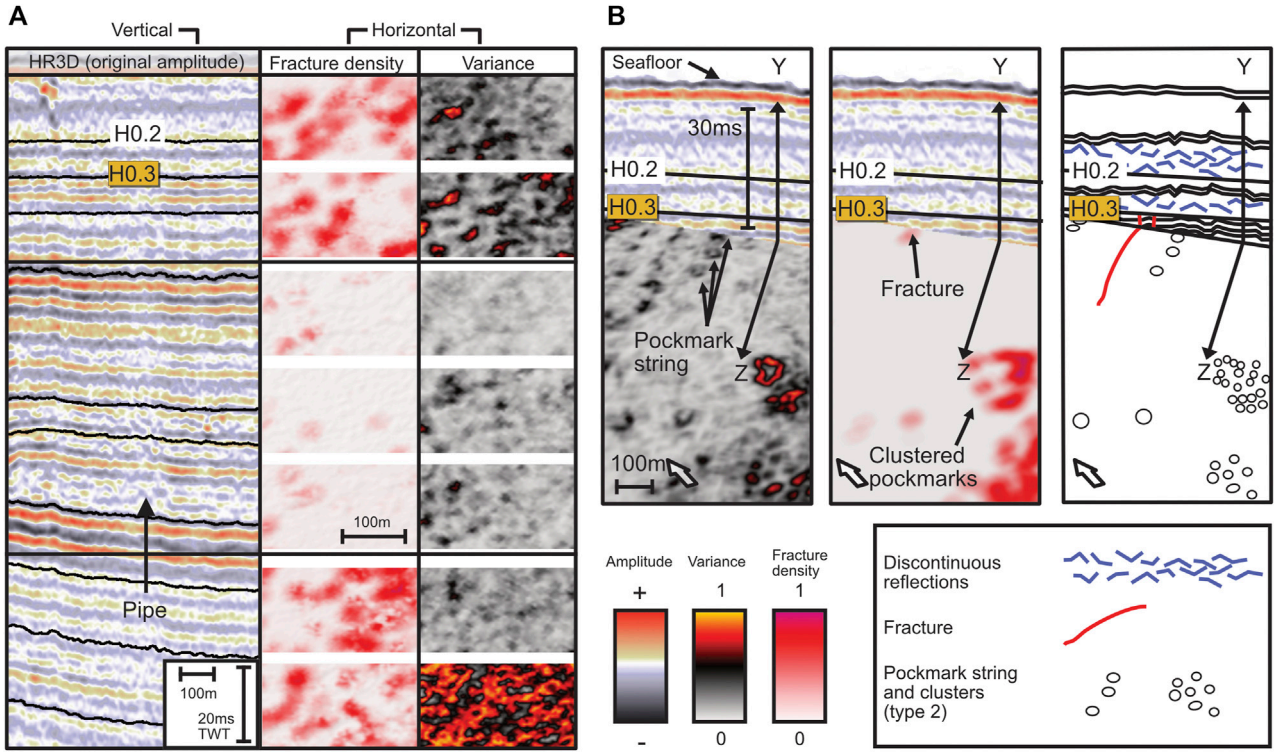

FIGURE 5
(A) Seismic inset from a HR3D inline after seafloor flattening illustrating changes in the seismic character of the fluid flow system. Key seismic horizons are displayed for reference. The insets to the right correspond to fracture density and variance extracted along the indicated horizons. Notice the vertical change in the seismic response across the three indicated regions. **(B)** Chair views, zoomed in on the same inline (88) as in **(A)** with (left to right) horizontal variance volume slice (Z: 1720.50), horizontal fracture density (Z: 1720.50), and cartoon combining features observed in the original amplitude, variance and fracture density volumes.

scale pockmarks (type 2) and their placement, with respect to fractures and faults (Figure 6).

The K1 attribute demonstrates an enhanced curvature inside of the main fault F1 at horizon H0.3 and slightly less outside of the fault zone (Figure 6C). Similar spatial trends can be observed also in the fracture density and the variance attributes (Figures 6A,B). All three attributes document a high degree of disturbance along H0.3 interpreted as small-scale deformation. Along horizon H1 (Figures 6D–F), the three attributes clearly show the fault zone belonging to F1 as deformed, with high variance (low coherence) and curvature. However, the strata outside of it is much less disturbed than it is at H0.3. The key difference between the horizons containing high fracture anomalies and those of an overall low fracture anomaly is the lateral spread of deformation (reflected by an increase in small-scale pockmark intensity (Figure 4C H0.3 and H2.25, Figure 5A, Figures 6A–C). HR3D horizons displaying less defined small-scale pockmarks (e.g., H1) display weaker fracture density anomalies and a thinner main fault zone (Figures 6D, E, F). Those horizons displaying the most defined fracture density anomalies (e.g., H0.3) display strongly defined small-scale pockmarks that extend outwards from the thicker main fault zone and appear connected to the change in the strength of the fluid activity (Figures 6A–C).

Considering that the pattern of discontinuity in the K1 attribute map appears as interconnected joints (best represented in Figure 6C) and that high anomalies are similarly represented in all the discontinuity attributes (Figures 6A–C), we choose the fracture density anomalies to indicate the most likely deformation by 'fracturing' and identify sedimentary intervals that are 'highly deformed' (from hereon, also referred to as 'highly fractured').

There are two highly deformed intervals (HDIs) located, 1) near the seafloor surface at ~20 to 30 mbsf (Figures 7, 8) and 2) at 20–40 m above the present day BSR (~170 mbsf) (Figure 8). Of the 24 interpreted horizons in our study, there are three that are contained within the upper highly deformed interval. Between the seafloor and horizon H1, there are three fracture density peaks (I–II, III and IV) (Figure 7); and between horizon H1 and the base of the GHSZ, there are also three fracture density peaks V, VI and VII (Figure 8). Between the two highly deformed intervals (HDIs; Figure 8) there is a significantly less deformed interval (LDI; Figures 6D–F, Figure 8). Fracture density values remain consistently at lower ranges within the less deformed interval. Fracture density peaks contained within the highly deformed intervals are characterized by highly discontinuous seismic responses relative to the less deformed units (Figure 5A, Figure 7D).

The sub-volumes used in the fracture density study (Figure 1B) were positioned across the major fault (F1). As expected, the sub-volumes in close range of the fault are among those displaying the highest fracture density peaks (Figure 8). In the upper highly deformed interval (HDI), the three sub-volumes (closest to F1)

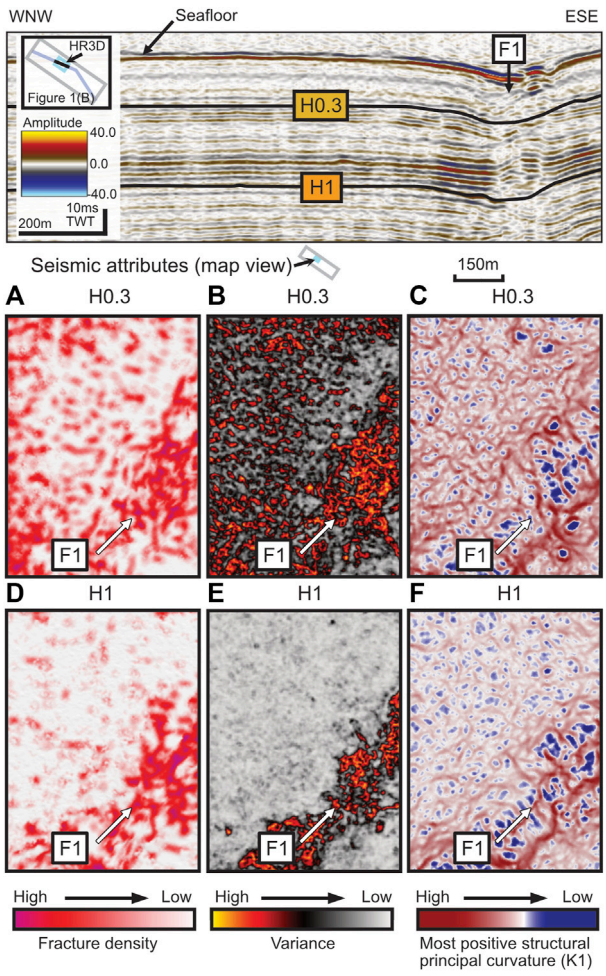

FIGURE 6
Above: HR3D composite seismic section displaying fault F1 indicating location of 2 horizons H0.3 and H1. Below: Comparing three surface attribute extractions (see Figure 1B for location of the area) for both horizons H0.3 **(A–C)** and H1 **(D–F)**. Fracture density: H0.3 **(A)** and H1 **(D)**; variance H0.3 **(B)** and H1 **(E)** and most positive structural principal curvature (K1) H0.3 **(C)** and H1 **(F)**.

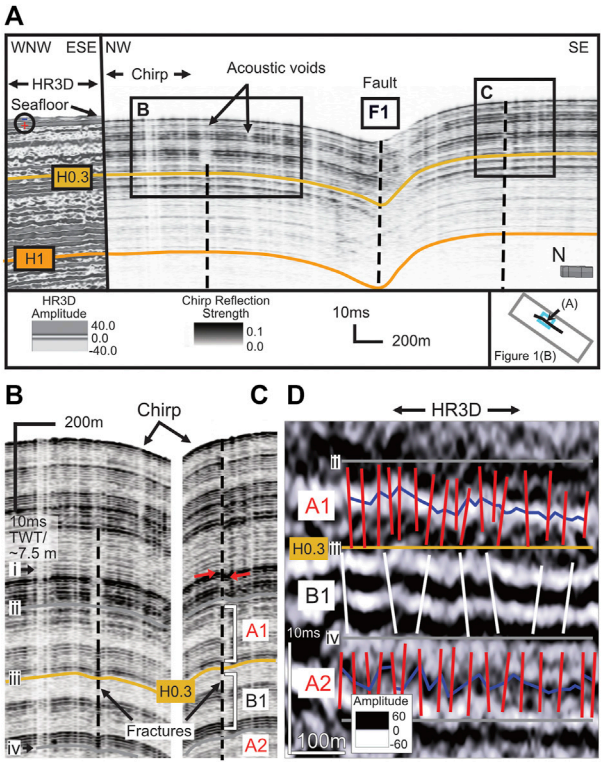

FIGURE 7
(A) Intersecting composite HR3D and Chirp lines to compare seismic character between the two separate datasets and locations of horizons H0.3 and H1. Acoustic voids and small-scale fractures (red arrows in (C) display offset) are clearly revealed in insets **(B)** and **(C)** either side of fault F1. Fracture density peaks, specifically (II-IV) (see Figure 8) are marked in the Chirp section in **(B)** and in the sampled HR3D vertically exaggerated seismic section in **(D)**. The fractures indicated by the vertical broken black line **(C)** are visible only in the Chirp dataset. Highly fractured units (A1, A2) (indicated by sub-vertical red lines which disrupt the manually traced (purple) horizon **(D)**) are also marked by the white square brackets in the Chirp section **(C)**. The acoustic void (center of inset B) is contained within the highly fractured unit A1. Horizon H0.3 is at the base of unit A1. Unit B1 **(C)**, **(D)** contains more continuous seismic reflections and less interpreted fracturing, indicated by fewer sub-vertical (white) lines.

show a higher overall average of fracture density than the sub-volumes located in a completely fault free zone. However, the fracture density trend with depth matches for each 7 sub-volumes. The varying trends resulting from repeating the approach along given horizons for each sub-volume confirms the veracity of the fracture density patterns.

Highly deformed intervals extend to the present day seafloor. This is evidenced by abundant acoustic masking in the Chirp data (Figures 7A, B). Columnar masking is abundant within the upper ~30 mbsf. There are narrow (single to multiple trace; 10–20 m) and broad (~50 m wide x ~10 m depth) masking events that have either significantly reduced the acoustic energy from the seafloor or from a specific depth (Figures 7A, B, C). The broad events, referred to as acoustic voids or vertical disturbances, are confined within a series of stratigraphic units. The base of the acoustic void appears within the highly reflective unit A1 (Figures 7B–D). Within the same series of fracture density peaks (I-II to III; Figure 7B) there is a <10 m fracture to the east of F1 (Figure 7C). The fracture is displayed on the crest of an acoustic reflection. We may be unable to identify fracturing through displacement if the seismic is disturbed, however we can infer fracture presence from curvature on the edges of acoustic disturbance zones. The disturbance zones are represented in the HR3D variance maps (Figures 5A, B, Figures 6B, E) as small-scale pockmarks.

We argue that the highly deformed events are highly fractured and give way to fluid expulsion forming small-scale (<20 m diameter) pockmarks. The distribution of the small pockmarks also varies between stratigraphic intervals (Figure 5A, Figure 6) providing additional evidence for sporadic fluid discharge. We treat the pockmarks and faulting revealed in the different attributes (i.e., seismic anomalies) to be genetically related and consider the probability of fluid seepage based on fracture density. Within the highly deformed interval, fluid flow mechanisms significantly alter and revert to widespread deformation. The small-scale pockmarks (Figure 6) appear associated with this widespread deformation. The

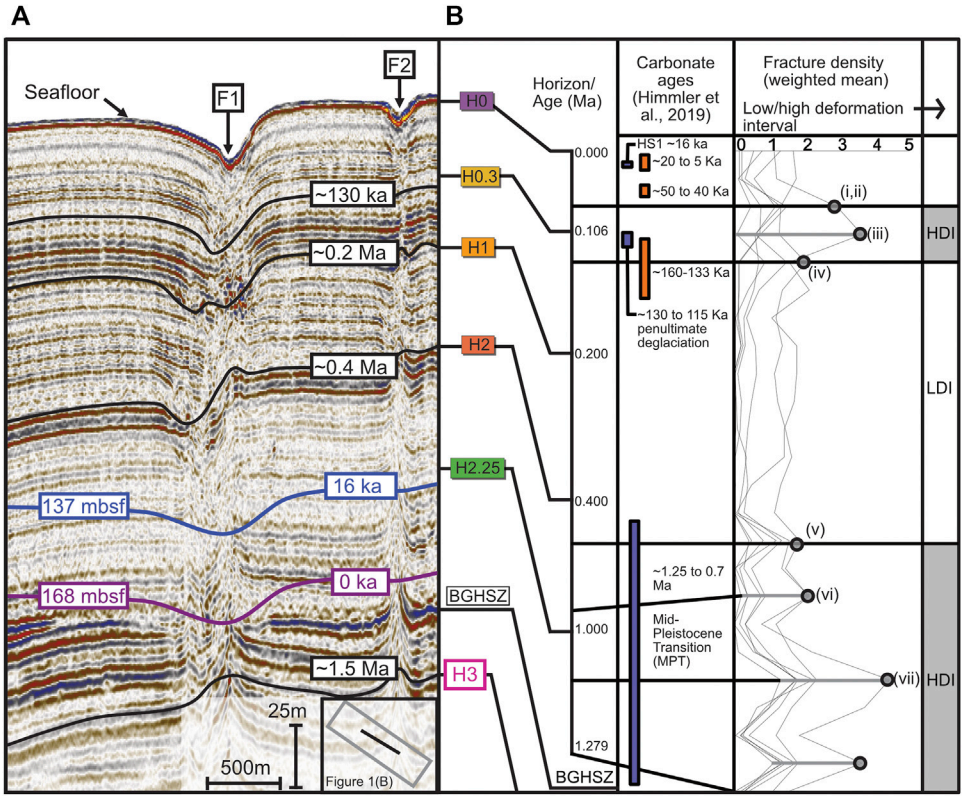

FIGURE 8
(A) Depth converted HR3D composite line with chronostratigraphic markers (black lines) (~130 ka, ~0.2 Ma, ~0.4 Ma and 1.5 Ma). The purple line (168 m below sea floor (mbsf)) indicates the depth to the present day (0 ka) base of the gas hydrate stability zone (BGHSZ), and the blue line (137 mbsf) indicates how much the BGHSZ has shifted from the present day to the peak oceanic warming during Heinrich Stadial 1 (HS1) following the Last Glacial Maximum (LGM)) (see Figure 9). **(B)** Two highly deformed intervals (HDI) interpreted from the peaks in the fracture density plots, correspond to two significant climatic periods (the penultimate deglaciation and the Mid-Pleistocene Transition (MPT). Between the two major climatic events is a low deformation interval (LDI). Horizon ages are calculated based on rates of sedimentation using established seismic chronostratigraphy. Carbonates are present during the penultimate deglaciation (~130 ka) (Himmler et al., 2019) coinciding with the (younger) HDI. Fracture density peaks are indicated by filled grey circles.

more significant the deformation (as displayed in the fracture density and K1 attribute) the higher the density of the small-scale pockmarks (as seen in the variance attribute) (Figure 5A, Figure 6). This is notable in horizons H0.3 (Figure 4C, Figure 5A, Figure 6B) and H2.25 (Figure 4C) for both major deformation events.

It is possible that the observed deformation features may represent a stage of fracturing that precedes polygonal deformation (Berndt et al., 2003; Cartwright and Santamarina, 2004; Gay and Berndt, 2007) captured at the edge of the resolution of the available seismic data.

5 Discussion

5.1 Chronological framework of sediment deformation and seepage at the Vestnesa Ridge

We identify two major deformation events (HDI: Figure 8) as fluid-leakage-prone intervals that correspond to at least two key climatic events (not yet considering the ocean-driven warming effect, section 5.3) based on existing chronostratigraphic constraints. The HR3D/2D and Chirp surveys were tied to available chronological markers along the Vestnesa Ridge (e.g., Mattingsdal et al., 2014; Plaza-Faverola et al., 2015; Alexandropoulou et al., 2021; Dessandier et al., 2021). We continue the chronostratigraphic reflections marked at drill sites MeBo 125 and MeBo 126 (Dessandier et al., 2021) from the east of the Vestnesa Ridge to the west. In addition, we also continue the 1.5 Ma reflection (Mattingsdal et al., 2014; Alexandropoulou et al., 2021) that dips beneath the base of the GHSZ within our HR3D study area.

The youngest highly fractured interval corresponds to ~140–70 ka (Figure 8) and coincides with the start of a major seepage event inferred by Dessandier et al. (2021) that began at the end of the penultimate glacial period (Late Saalian) through to the last interglacial period (~130 ka). The oldest highly fractured interval corresponds to ~1.2 Ma—0.8 Ma (i.e., coinciding with the Mid-Pleistocene Transition e.g., Head and Gibbard, 2005) and it is situated above the present day base of the GHSZ (Figure 8, Figure 9). Between these two major climatic periods, there is a gap in deformation, where the sediment appears less impacted (LDI: Figure 8).

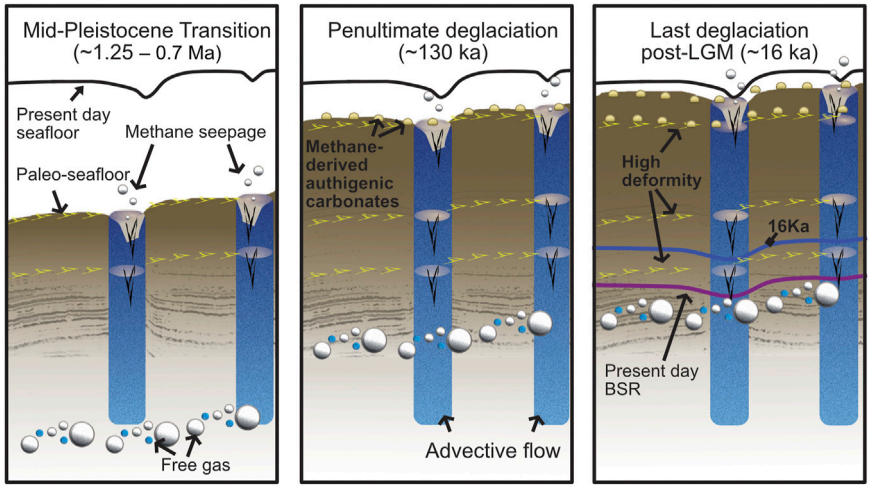

FIGURE 9
A three-stage sequence (left to right) depicting two types of fracture expression: vertical blue columns highlight zones of vertical fluid flow (i.e., chimneys/pipes) that reach the present day seafloor, and horizontal fractures (irregular yellow shapes) that propagate outwards from the chimneys during significant climatic-oceanic events (i.e., during the Mid-Pleistocene Transition (MPT), followed by the penultimate deglaciation, and the significant oceanic warming period (i.e., Heinrich Stadial 1 (HS1)) during the last deglaciation (post-LGM). In the younger sequences (~130 ka and post-LGM), enhanced fracturing promoted gas transport, seepage and methane-derived authigenic carbonate formation (yellow filled semi-circles). The older sequences (MPT fractured intervals) are disturbed possibly a second time by localized pressure changes at the free gas zone due to the upward shift of the base of the gas hydrate stability zone (GHSZ) post-LGM, (i.e., blue line). The calculated base of the GHSZ for today (i.e., present day BSR) is represented by the purple line.

5.2 Seepage evolution from the Mid-Pleistocene Transition to the present day

The correlation of highly fractured sedimentary intervals characterized by high density pockmarks with two major climatic events (i.e., the Mid-Pleistocene Transition and the penultimate deglaciation) is in line with studies that associate paleo-seepage in the region with regional glacial dynamics (Consolaro et al., 2015; Plaza-Faverola et al., 2015; Portnov et al., 2016; Schneider et al., 2018; Walmann et al., 2018; Himmler et al., 2019; Plaza-Faverola and Keiding, 2019).

Assuming that the documented fracturing was contemporaneous with the transition from glacial to interglacial periods, we can elucidate the history of glacially influenced Quaternary deformation and associated seepage along the Vestnesa Ridge (Figure 9).

Various studies have suggested that seepage episodes inferred from sedimentary proxies were related to glacial isostasy at the forebulge region of the Barents Sea ice sheet (Schneider et al., 2018; Himmler et al., 2019; Dessandier et al., 2021).

Kinematic fault modelling on land shows that post-glacial rebound transfers stresses to the near-surface and triggers fault reactivation and deformation (e.g., Lund et al., 2009). Whether the same mechanism is valid in offshore regions beyond the ice sheet edge remains to be proven. However, recent glacial stress models show that the Vestnesa Ridge lies in a lithospheric zone (i.e., the forebulge) prone to considerable uplift and subsidence during glacial transitions (Vachon et al., 2022). We propose that the highly fractured sedimentary intervals documented here are evidence of glacial stress transfer to the Quaternary sedimentary succession during maximum uplift and initiation of the subsidence.

The best constrained time intervals and seepage events in the region are over the last ~130 ka (e.g., Consolaro et al., 2015; Sztybor and Rasmunssen, 2017; Schneider et al., 2018; Himmler et al., 2019) because that is where sedimentary proxies are available. Nevertheless, it is sensible to assume that similar mechanisms would have favored fracturing and seepage at older major glacial transitions.

From bottom to top, the first major glacially induced fracturing and associated seepage event in our model is the Mid-Pleistocene Transition (Figure 9). This significant climatic period represents a time of glacial expansion and increasing ice sheet volumes across the Eurasian Arctic that is tied to a general shift in the duration of glacial cycles from 41 kyr to 100 kyr (Knies et al., 2009; Hjelstuen and Sejrup, 2021; Panieri et al., 2023). The shift towards larger continental-scale ice sheets may have also affected the Vestnesa Ridge, with greater isostatic loading imposing greater mantle uplift in shelf-adjacent forebulge areas (Vachon et al., 2022).

The second and best constrained fracture-controlled seepage event in our model (Figure 9) is that at ~130 ka, around the transition period between the penultimate glacial maximum and the last interglacial (i.e., the penultimate deglaciation). This seepage event has been recognized at the mid-Norwegian margin (Plaza-Faverola et al., 2012) and on the eastern Vestnesa Ridge segment, where buried authigenic carbonate dating confirmed paleo-seepage events in this area for the first time (Himmler et al., 2019).

For each of the above periods we envision a cyclic process including fracturing, gas seepage, carbonate precipitation, self-sealing, burial, reactivation. Similar processes have been inferred from observations along the mid-Norwegian margin (Hovland, 2002; Hovland et al., 2010). During a period of glacially induced fracturing and sustained methane flux, carbonate precipitation would be expected, as observed

and sampled at present day from this and other margins (e.g., Hovland, 2002; Crémière et al., 2016; Mazzini et al., 2017; Himmler et al., 2019). The high fracture density intervals documented here might reveal fractures that have formed after the extensive growth of the carbonates, which have subsequently changed the property of the sediments. Post-glacial fracture development preconditions the system for carbonate growth, and carbonate precipitation eventually seals the sediments, changing the sediment permeability, as demonstrated for vertical fluid migration systems along other margins (e.g., mid-Norwegian margin, Hovland, 2002). This model is relevant to explain why the highly deformed events are confined to specific stratigraphic intervals. Sediment deformation may be reflected by an enhanced precipitated carbonate environment.

Based on this model and the observations of abundant pockmarks on the present day seafloor, we envision that a major seepage event similarly followed the Last Glacial Maximum in the region (Figure 9), with evidence provided from foraminiferal data indicating seepage from 14 to 8 kyr (Consolaro et al., 2015). Today, no active seepage has been observed and the system is believed to be at hydrostatic pressure equilibrium (Ramachandran et al., 2022).

The intensification of glacially induced fracturing would also provide a pathway for a sudden release of gas (Greinert et al., 2001). We suspect that an increase in the density of the small pockmarks is linked to an increase in fluid flow, but it is difficult to determine whether the fracturing forms before, after, or during the release. Despite this uncertainty, we infer that the high fracture density anomalies reveal a high probability of fluid flow at the time of their formation.

5.3 Gas hydrate dynamics during glacial/interglacial transitions

The Vestnesa Ridge has been charged with significant amounts of thermogenic gas since at least 2 Ma (Knies et al., 2018; Daszinnies et al., 2021). A gas hydrate system was already in place at the Mid-Pleistocene Transition at 1.2 Ma. Therefore, gas hydrate dynamics were likely to play a role in enhancing glacially induced seepage in the area.

The effect of isostasy resulting from ice sheet growth and collapse is considered to contribute to shifts in the gas hydrate system (e.g., Wallmann et al., 2018). Stress modelling suggests that the Vestnesa Ridge, which is located on the peripheral forebulge of the Barents Sea and Greenland ice sheets, has experienced uplift and a more tensile stress regime during glacial maximums, and subsidence following ice sheet retreat (Vachon et al., 2022).

The highly deformed interval corresponding to the Mid-Pleistocene Transition exists today at the boundary of the base of the GHSZ (Figure 8, Figure 9), and is most susceptible to hydrofracturing by gas hydrate recycling at the base of the GHSZ (e.g., Haacke et al., 2007; Plaza-Faverola et al., 2012). We imply an adjusted position of the base of the GHSZ in the three-stage sequence (Figure 9), as sediment progressively accumulated from the Mid-Pleistocene Transition (first stage) until the penultimate deglaciation and last deglaciation (second and third stages). In addition, the thickness of the GHSZ fluctuated a few meters in response to the balanced effect of hydrostatic pressure (affected by sea-level changes, sedimentation, and isostasy) and temperature (Ruppel and Kessler., 2017; Serov et al., 2017; Wallmann et al., 2018; Daigle et al., 2020; Trivedi et al., 2022).

Our transient 2D modelling accounts for the balanced effect of sea-level and temperature changes. It shows that during the last deglaciation, elevated and rapid changes in bottom water temperatures (5.5 °C) that initiated ~16 ka during Heinrich Stadial 1 (HS1) (El bani Altuna et al., 2021) resulted in a maximum upwards shift of the base of the GHSZ by approximately 30 m (Figure 8, Figure 9). However, this model does not account for the effect of isostasy tied to the collapse of the Barents Sea and Greenland ice sheets. This (~30 m) maximum shift was thus potentially partially compensated by the effect of post-LGM forebulge subsidence, though at 16 ka BP the surrounding ice sheets were still in relatively advanced positions (Vachon et al., 2022).

Nonetheless, even small fluctuations at the base of the GHSZ associated with the HS1 oceanic warming would have affected the already deformed sediments above the base of the GHSZ (Figure 9), as well as impacted near-surface sediments through further authigenic carbonate precipitation after gas hydrate dissolution and gas release (e.g., Sultan et al., 2020) (Figure 9). Additionally, as the system is critically stressed, small increases in free gas amounts beneath the base of the GHSZ would have been enough to trigger gas release through pre-existing fractures within the GHSZ along the Vestnesa Ridge (Ramachandran et al., 2022; Plaza-Faverola et al., 2023). This process reconciles the observation of small-scale buried pockmarks at highly deformed intervals (Figure 4, Figure 5, Figure 6).

The gas beneath the base of the GHSZ may have become depleted after a period of sustained methane flux. The low fracture density observed in the period between the two highly deformed intervals could therefore be a response to gas saturation build up, which will depend on the rate of gas generated from beneath the base of the GHSZ and on the permeability of the sediments that controls the gas flow out (Jung et al., 2012; Ramachandran et al., 2022). We propose that gas may have been depleted after the Mid-Pleistocene Transition interval. Following the Mid-Pleistocene Transition, gas saturation build-up was potentially required before the fracture criterion could be reached, to re-fracture younger authigenic carbonate intervals. This could explain why we do not see more highly deformed intervals associated with younger glaciations after the Mid-Pleistocene Transition and before the Late Saalian period (~0.7 Ma–140 ka).

Our study focuses on widespread, small-scale sediment deformation; however, we do not disregard the advective flow (i.e., vertical expulsion) through gas chimneys originating at or beneath the base of the GHSZ. The presence of the larger pockmarks at various stratigraphic intervals (Figure 4B) indicates that the vertical migration of fluids has been important in this segment of the Vestnesa Ridge in the past as suggested in previous studies (e.g., Plaza-Faverola et al., 2015). The size of the lateral chimney disturbance zones (Figure 4C) may also reflect the strength in the migration of fluids from beneath the GHSZ or a contrast in sediment properties.

6 Conclusion

We integrate multiple resolution acoustic data sets and available cross-disciplinary observations to constrain the spatial and temporal

evolution of highly deformed Quaternary sedimentary strata along the Vestnesa Ridge in the eastern Fram Strait. A new high-resolution 3D seismic attribute workflow to quantify sediment deformation reveals both large- and small-scale fluid flow features mapped out at 5 horizons (seafloor to ~1.2 Ma). In addition, we supply chronological constraints for the main 5 horizons, that align with major climatic events over the past ~1.2 Ma.

The variance attribute clearly displays large faults that correlate well with large (~50 m to >200 m) pockmarks and chimneys. However, the smaller pockmarks (<20 m) are more difficult to connect to potential smaller fractures if we consider only variance. We are unable to match specific small-scale fluid flow features to a unique set of fractures and can only deduce that our choice of attributes reveals fluid flow associated with fractures at a much smaller scale.

The most positive curvature-related attributes provide information where coherency does not; furthermore, the fracture density attribute which is based on most positive curvature (with a 20 m scanning radius) helps to delineate weakness zones susceptible to fluid flow. We indicate that the fracture density anomalies highlight focal points of disturbance.

The fracture density attribute is used to detect where deformation is most pronounced in the sedimentary column. Chronological markers constrain high fracture density peaks following the end of the penultimate glacial (~130 ka deglaciation) and during the Mid-Pleistocene Transition. We propose that high fracturing that occurred during the Mid-Pleistocene Transition was initially triggered by extensive glacial build up, and accompanied by methane-derived authigenic carbonate growth, further disturbing sediments. The highly fractured sediments may have reactivated during subsequent tectonic events related to younger glacial isostatic adjustment. We also imply re-deformation of highly fractured sediments found ~30 m above the base of the GHSZ within the Mid-Pleistocene Transition interval. While our first (oldest) process links the formation of authigenic carbonate to deformation during, or after, extensive glacial build up and seepage; the second (youngest) process, considers a pumping mechanism attributed to the shift of the base of the gas hydrate stability zone associated with bottom water temperature variations during the last deglaciation. We suggest that highly fractured sediments at the Mid-Pleistocene Transition may also be affected by climatic-oceanic events during the last deglaciation.

Our results help to advance the current understanding of the effects and interplay of glacial dynamics on sub-seabed deformation, gas hydrates and associated fluid migration systems in Quaternary sedimentary strata at an Arctic margin.

Data availability statement

The datasets presented in this study can be found in online repositories. The names of the repository/repositories and accession number(s) can be found below: https://doi.org/10.18710/NMGLRL.

Author contributions

SB and AP-F planned and acquired the HR3D seismic data set. JK and FC planned and acquired the Chirp data. FC prepared the manuscript with significant contributions from AP-F, JK, NS, SB, and HP. FC processed the data and conceived as well as implemented the working flow with seismic attributes, with contributions from HB and HR. HP contributed to the methodology required for the pockmark extractions. NS prepared the gas hydrate model. All authors contributed to the article and approved the submitted version.

Funding

The SEAMSTRESS project (Tectonic Stress Effects on Arctic Methane Seepage) is supported by grants from the Tromsø Research Foundation (project nr. A31680), the Research Council of Norway (project nr. 287865) and UiT—The Arctic University of Norway through its PhD fellowship programs. Data acquisition was also supported by CAGE - Centre for Arctic Gas Hydrate, Environment and Climate (funding scheme grant nr. 223259).

Acknowledgments

This work is part of the SEAMSTRESS project, supported by grants from the Tromsø Research Foundation (project nr. A31680) and the Research Council of Norway (project nr. 287865). The work has been also supported by the Research Council of Norway through its Center of Excellence CAGE. We are thankful to the ship and scientific crew on board R/V Helmer Hanssen and R/V Kronprins Haakon, for the seismic and Chirp data acquisition. We thank OpendTect and Schlumberger (Petrel) for software and support, and Thang Ha at the Attribute Assisted Seismic Processing and Interpretation (AASPI) research consortium for running volume attribute computations and for providing the K1 dataset. FC is particularly grateful to Jean-Baptiste Koehl for his advice and feedback. AP-F, SB, HP and JK are currently affiliated with the new Norwegian Center of Excellence iC3 (Centre for ice, Cryosphere, Carbon and Climate), project number 332635.

Conflict of interest

The authors declare that the research was conducted in the absence of any commercial or financial relationships that could be construed as a potential conflict of interest.

Publisher's note

Supplementary material

The Supplementary Material for this article can be found online at: https://www.frontiersin.org/articles/10.3389/feart.2023.1188737/full#supplementary-material

References

Acuña-Uribe, M., Pico-Forero, M. C., Goyes-Peñafiel, P., and Mateus, D. (2021). Enhanced ant tracking: Using a multispectral seismic attribute workflow to improve 3D fault detection. *Lead. Edge* 40, 502–512. doi:10.1190/tle40070502.1

Al-Dossary, S., and Marfurt, K. (2006). 3D volumetric multispectral estimates of reflector curvature and rotation. *Geophysics* 71, P41–P51. doi:10.1190/1.2242449

Alexandropoulou, N., Winsborrow, M., Andreassen, K., Plaza-Faverola, A., Dessandier, P.-A., Mattingsdal, R., et al. (2021). A continuous seismostratigraphic framework for the western svalbard-barents sea margin over the last 2.7 Ma: Implications for the late cenozoic glacial history of the svalbard-barents Sea ice sheet. *Front. Earth Sci.* 9, 1. doi:10.3389/feart.2021.656732

Alfaro, M. C., and Wong, R. C. (2001). Laboratory studies on fracturing of low-permeability soils. *Can. Geotech. J.* 38, 303–315. doi:10.1139/t00-096

Anderson, A. L., and Bryant, W. R. (1989). Acoustic properties of shallow seafloor gas. *OnePetro*. Paper presented at the Offshore Technology Conference, Houston, Texas, May 1–4, 1989. doi:10.4043/5955-MS

Andreassen, K., Ødegaard, C. M., and Rafaelsen, B. (2007). Imprints of former ice streams, imaged and interpreted using industry three-dimensional seismic data from the south-Western Barents Sea. *Geol. Soc. Lond. Spec. Publ.* 277, 151–169. doi:10.1144/GSL.SP.2007.277.01.09

Arntsen, B., Wensaas, L., Løseth, H., and Hermanrud, C. (2007). Seismic modeling of gas chimneys. *GEOPHYSICS* 72, SM251–SM259. doi:10.1190/1.2749570

Ashraf, U., Zhang, H., Anees, A., Nasir Mangi, H., Ali, M., Ullah, Z., et al. (2020). Application of unconventional seismic attributes and unsupervised machine learning for the identification of fault and fracture network. *Appl. Sci.* 10, 3864. doi:10.3390/app10113864

Bahorich, M. S., and Farmer, S. L. (1995). "3D seismic discontinuity for faults and stratigraphic features: The coherence cube," in *SEG technical program expanded abstracts 1995, SEG technical program expanded abstracts* (Society of Exploration Geophysicists. The Leading Edge) 14 (10), 1021–1098. doi:10.1190/1.1437077

Bertoni, C., Gan, Y., Philomena)Paganoni, M., Mayer, J., Cartwright, J., et al. (2019). Late paleocene pipe swarm in the great south – Canterbury basin (New Zealand). *Mar. Petroleum Geol.* 107, 451–466. doi:10.1016/j.marpetgeo.2019.05.039

Berndt, C., Bünz, S., and Mienert, J. (2003). Polygonal fault systems on the mid-Norwegian margin: a long-term source for fluid flow. *Geological Society*. London: Special Publications 216, 283–290. doi:10.1144/GSL.SP.2003.216.01.18

Blumentritt, C. H., Sullivan, E. C., and Marfurt, K. J. (2003). "Channel detection using seismic attributes on the Central Basin Platform, west Texas," in Paper presented at the 2003 SEG Annual Meeting, Dallas, Texas (Society of Exploration Geophysicists), 466–469. doi:10.1190/1.1817953

Breivik, A. J., Verhoef, J., and Faleide, J. I. (1999). Effect of thermal contrasts on gravity modeling at passive margins: Results from the Western Barents Sea. *J. Geophys. Res. Solid Earth* 104, 15293–15311. doi:10.1029/1998JB900022

Bünz, S. (2022). Cruise CAGE-18-4. *Environ. Clim. Rep. Ser.* 6, 1. doi:10.7557/cage.6850

Bünz, S., Polyanov, S., Vadakkepuliyambatta, S., Consolaro, C., and Mienert, J. (2012). Active gas venting through hydrate-bearing sediments on the Vestnesa Ridge, offshore W-Svalbard. *Mar. Geol.* 332, 189–197. doi:10.1016/j.margeo.2012.09.012

Cartwright, J., and Santamarina, C. (2015). Seismic characteristics of fluid escape pipes in sedimentary basins: Implications for pipe Genesis. *Mar. Petroleum Geol.* 65, 126–140. doi:10.1016/j.marpetgeo.2015.03.023

Chand, S., Crémière, A., Lepland, A., Thorsnes, T., Brunstad, H., and Stoddart, D. (2017). Long-term fluid expulsion revealed by carbonate crusts and pockmarks connected to subsurface gas anomalies and palaeo-channels in the central North Sea. *Geo-Mar Lett.* 37, 215–227. doi:10.1007/s00367-016-0487-x

Chávez-Pérez, S., and Vargas-Meleza, L. (2008). Enhanced imaging workflow of seismic data from Chicontepec Basin, Mexico. *Lead. Edge* 27, 352–359. doi:10.1190/1.2896626

Chopra, S., and Marfurt, K. J. (2013). "Preconditioning seismic data with 5D interpolation for computing geometric attributes," in Paper presented at the 2013 SEG Annual Meeting, Houston, Texas (Society of Exploration Geophysicists), 1368–1373. doi:10.1190/segam2013-0169.1

Chopra, S., and Marfurt, K. J. (2007). "Seismic attributes for fault/fracture characterization," in Paper presented at the 2007 SEG Annual Meeting, San Antonio, Texas (Society of Exploration Geophysicists), 1520–1524. doi:10.1190/1.2792785

Consolaro, C., Rasmussen, T. L., Panieri, G., Mienert, J., Bünz, S., and Sztybor, K. (2015). Carbon isotope (δ13C) excursions suggest times of major methane release during the last 14 kyr in Fram Strait, the deep-water gateway to the Arctic. *Clim. Past* 11, 669–685. doi:10.5194/cp-11-669-2015

Crane, K., Doss, H., Vogt, P., Sundvor, E., Cherkashov, G., Poroshina, I., et al. (2001). The role of the Spitsbergen shear zone in determining morphology, segmentation and evolution of the Knipovich Ridge. *Mar. Geophys. Res.* 22, 153–205. doi:10.1023/A:1012288309435

Crane, K., Sundvor, E., Buck, R., and Martinez, F. (1991). Rifting in the northern Norwegian-Greenland Sea: Thermal tests of asymmetric spreading. *J. Geophys. Res. Solid Earth* 96, 14529–14550. doi:10.1029/91JB01231

Crémière, A., Lepland, A., Chand, S., Sahy, D., Condon, D. J., Noble, S. R., et al. (2016). Timescales of methane seepage on the Norwegian margin following collapse of the Scandinavian Ice Sheet. *Nat. Commun.* 7, 11509. doi:10.1038/ncomms11509

Daigle, H., Cook, A., Fang, Y., Bihani, A., Song, W., and Flemings, P. B. (2020). Gas-driven tensile fracturing in shallow marine sediments. *J. Geophys. Res. Solid Earth* 125, e2020JB020835. doi:10.1029/2020JB020835

Daszinnies, M., Plaza-Faverola, A., Sylta, Ø., Bünz, S., Mattingsdal, R., Tømmerås, A., et al. (2021). The Plio-Pleistocene seepage history off Western Svalbard inferred from 3D petroleum systems modelling. *Mar. Petroleum Geol.* 128, 105023. doi:10.1016/j.marpetgeo.2021.105023

Dessandier, P.-A., Borrelli, C., Kalenitchenko, D., and Panieri, G. (2019). Benthic foraminifera in arctic methane hydrate bearing sediments. *Front. Mar. Sci.* 6. doi:10.3389/fmars.2019.00765

Dessandier, P.-A., Knies, J., Plaza-Faverola, A., Labrousse, C., Renoult, M., and Panieri, G. (2021). Ice-sheet melt drove methane emissions in the Arctic during the last two interglacials. *Geology* 49, 799–803. doi:10.1130/G48580.1

Domel, P., Singhroha, S., Plaza-Faverola, A., Schlindwein, V., Ramachandran, H., and Buenz, S. (2022). Origin and periodic behavior of short duration signals recorded by seismometers at Vestnesa Ridge, an active seepage site on the west-Svalbard continental margin. *Front. Earth Sci.* 10. doi:10.3389/feart.2022.831526

Eiken, O., and Hinz, K. (1993). Contourites in the Fram Strait. *Sediment. Geol.* 82, 15–32. doi:10.1016/0037-0738(93)90110-Q

El bani Altuna, N., Ezat, M. M., Greaves, M., and Rasmussen, T. L. (2021). Millennial-scale changes in bottom water temperature and water mass exchange through the Fram Strait 79°N, 63-13 ka. *Paleoceanogr. Paleoclimatology* 36, e2020PA004061. doi:10.1029/2020PA004061

Elger, J., Berndt, C., Rüpke, L., Krastel, S., Gross, F., and Geissler, W. H. (2018). Submarine slope failures due to pipe structure formation. *Nat. Commun.* 9, 715. doi:10.1038/s41467-018-03176-1

Etiope, G. (2015). *Natural gas seepage*. Cham: Springer International Publishing. doi:10.1007/978-3-319-14601-0

Ezat, M. M., Rasmussen, T. L., and Groeneveld, J. (2014). Persistent intermediate water warming during cold stadials in the southeastern Nordic seas during the past 65 k.y. *Y. Geol.* 42, 663–666. doi:10.1130/G35579.1

Ezat, M. M., Rasmussen, T. L., Hain, M. P., Greaves, M., Rae, J. W. B., Zamelczyk, K., et al. (2021). Deep Ocean storage of heat and CO2 in the Fram Strait, arctic ocean during the last glacial period. *Paleoceanogr. Paleoclimatology* 36, e2021PA004216. doi:10.1029/2021PA004216

Fehmers, G. C., and Höcker, C. F. W. (2003). Fast structural interpretation with structure-oriented filtering. *GEOPHYSICS* 68, 1286–1293. doi:10.1190/1.1598121

Gao, D. (2013). Integrating 3D seismic curvature and curvature gradient attributes for fracture characterization: Methodologies and interpretational implications. *Geophysics* 78, O21–O31. doi:10.1190/geo2012-0190.1

Gay, A., and Berndt, C. (2007). Cessation/reactivation of polygonal faulting and effects on fluid flow in the Vøring Basin, Norwegian Margin. *J. Geol. Soc.* 164, 129–141. doi:10.1144/0016-76492005-178

Gay, A., Mourgues, R., Berndt, C., Bureau, D., Planke, S., Laurent, D., et al. (2012). Anatomy of a fluid pipe in the Norway Basin: Initiation, propagation and 3D shape. *Mar. Geol. Hydrocarbon leakage through Focus. fluid flow Syst. Cont. margins 332–* 334, 75–88. doi:10.1016/j.margeo.2012.08.010

Greinert, J., Bohrmann, G., and Suess, E. (2001). "Gas hydrate-associated carbonates and methane-venting at hydrate ridge: Classification, distribution, and origin of authigenic lithologies," in *Natural gas hydrates: Occurrence, distribution, and detection* (American Geophysical Union (AGU), 99–113. doi:10.1029/GM124p0099

Haacke, R. R., Westbrook, G. K., and Hyndman, R. D. (2007). Gas hydrate, fluid flow and free gas: Formation of the bottom-simulating reflector. *Earth Planet. Sci. Lett.* 261, 407–420. doi:10.1016/j.epsl.2007.07.008

Hart, B. S. (2002). Validating seismic attribute studies: Beyond statistics. *Lead. Edge* 21, 1016–1021. doi:10.1190/1.1518439

Head, M. J., and Gibbard, P. L. (2005). Early-middle pleistocene transitions: An overview and recommendation for the defining boundary. *SP* 247, 1–18. doi:10.1144/GSL.SP.2005.247.01.01

Heggland, R. (2005). "Using gas chimneys in seal integrity analysis: A discussion basedon case histories," in Editors P. Boult and J. Kaldi. *Evaluating fault andcap rock seals: AAPG Hedberg Series*. The American Association of Petroleum Geologists 2, 237–245. doi:10.1306/1060767H23170

Himmler, T., Sahy, D., Martma, T., Bohrmann, G., Plaza-Faverola, A., Bünz, S., et al. (2019). A 160,000-year-old history of tectonically controlled methane seepage in the Arctic. *Sci. Adv.* 5, eaaw1450. doi:10.1126/sciadv.aaw1450

Hjelstuen, B. O., and Sejrup, H. P. (2021). Latitudinal variability in the quaternary development of the eurasian ice sheets—evidence from the marine domain. *Geology* 49, 346–351. doi:10.1130/G48106.1

Hong, W.-L., Pape, T., Schmidt, C., Yao, H., Wallmann, K., Plaza-Faverola, A., et al. (2021). Interactions between deep formation fluid and gas hydrate dynamics inferred from pore fluid geochemistry at active pockmarks of the Vestnesa Ridge, west Svalbard margin. *Mar. Petroleum Geol.* 127, 104957. doi:10.1016/j.marpetgeo.2021.104957

Hovland, M. (2008). *Deep-water coral reefs: Unique biodiversity hot-spots*. Germany: Springer Science & Business Media.

Hovland, M., Heggland, R., De Vries, M. H., and Tjelta, T. I. (2010). Unit-pockmarks and their potential significance for predicting fluid flow. *Mar. Petroleum Geol.* 27, 1190–1199. doi:10.1016/j.marpetgeo.2010.02.005

Hovland, M., 2002. On the self-sealing nature of marine seeps. *Cont. Shelf Res. Gas Mar. Sediments Contributions 5th Int. Conf. orgainsed by Shallow Gas Group*, Bologna, Italy, 22, 2387–2394. doi:10.1016/S0278-4343(02)00063-8

Hovland, M. (1988). *Seabed pockmarks and seepages: Impact on geology, biology and the marine environment*. London: Graham & Trotman.

Howe, J. A., Shimmield, T. M., Harland, R., and Eyles, N. (2008). Late quaternary contourites and glaciomarine sedimentation in the Fram Strait. *Sedimentology* 55, 179–200. doi:10.1111/j.1365-3091.2007.00897.x

Hustoft, S., Bünz, S., Mienert, J., and Chand, S. (2009). Gas hydrate reservoir and active methane-venting province in sediments on <20 Ma young oceanic crust in the Fram Strait, offshore NW-Svalbard. *Earth Planet. Sci. Lett.* 284, 12–24. doi:10.1016/j.epsl.2009.03.038

Hustoft, S., Mienert, J., Bünz, S., and Nouzé, H. (2007). High-resolution 3D-seismic data indicate focussed fluid migration pathways above polygonal fault systems of the mid-Norwegian margin. *Mar. Geol.* 245, 89–106. doi:10.1016/j.margeo.2007.07.004

Jessen, S. P., Rasmussen, T. L., Nielsen, T., and Solheim, A. (2010). A new Late Weichselian and Holocene marine chronology for the Western Svalbard slope 30,000–0 cal years BP. *Quat. Sci. Rev.* 29, 1301–1312. doi:10.1016/j.quascirev.2010.02.020

Judd, A., and Hovland, M. (2007). *Seabed fluid flow: The impact on geology, biology, and the marine environment*. Cambridge: Cambridge University Press. doi:10.1017/CBO9780511535918

Jung, J. W., Jang, J., Santamarina, J. C., Tsouris, C., Phelps, T. J., and Rawn, C. J. (2012). Gas production from hydrate-bearing sediments: The role of fine particles. *Energy fuels.* 26, 480–487. doi:10.1021/ef101651b

King, L. H., and MacLEAN, B. (1970). Pockmarks on the scotian shelf. *Geol. Soc. Am. Bull.* 81, 3141. doi:10.1130/0016-7606(1970)81[3141

Klokov, A., Treviño, R. H., and Meckel, T. A. (2017). Diffraction imaging for seal evaluation using ultra high resolution 3D seismic data. *Mar. Petroleum Geol.* 82, 85–96. doi:10.1016/j.marpetgeo.2017.02.002

Knies, J., Daszinnies, M., Plaza-Faverola, A., Chand, S., Sylta, Ø., Bünz, S., et al. (2018). Modelling persistent methane seepage offshore Western Svalbard since early Pleistocene. *Mar. Petroleum Geol.* 91, 800–811. doi:10.1016/j.marpetgeo.2018.01.020

Knies, J., Matthiessen, J., Vogt, C., Laberg, J. S., Hjelstuen, B. O., Smelror, M., et al. (2009). The plio-pleistocene glaciation of the Barents Sea–svalbard region: A new model based on revised chronostratigraphy. *Quat. Sci. Rev.* 28, 812–829. doi:10.1016/j.quascirev.2008.12.002

Knies, J., and Vadakkepuliyambatta, S. (2023). CAGE19-3 Cruise Report: Calypso giant piston coring in the Atlantic-Arctic gateway – investigation of continental margin development and effect of tectonic stress on methane release. *CAGE – Centre Arct. Gas Hydrate, Environ. Clim. Rep. Ser.* 7, 1. doi:10.7557/cage.6911

Lebedeva-Ivanova, N., Gaina, C., Minakov, A., and Kashubin, S. (2019). ArcCRUST: Arctic crustal thickness from 3-D gravity inversion. *Geochem. Geophys. Geosystems* 20, 3225–3247. doi:10.1029/2018GC008098

Li, M., and Zhao, Y. (2014). "Chapter 5 - seismic attribute analysis," in *Geophysical exploration technology* M. Li and Y. Zhao (Oxford: Elsevier), 103–131. doi:10.1016/B978-0-12-410436-5.00005-8

Ligtenberg, J. H. (2005). Detection of fluid migration pathways in seismic data: Implications for fault seal analysis. *Basin Res.* 17, 141–153. doi:10.1111/j.1365-2117.2005.00258.x

Lisle, R. J. (1994). Detection of zones of abnormal strains in structures using Gaussian curvature analysis. *AAPG Bull.* 78. doi:10.1306/a25ff305-171b-11d7-8645000102c1865d

Løseth, H., Wensaas, L., Arntsen, B., Hanken, N.-M., Basire, C., Graue, K., et al. 2011. 1000 m long gas blow-out pipes. *Mar. Pet. Geol.* 28, 1047–1060. doi:10.1016/j.marpetgeo.2010.10.001

Løseth, H., Gading, M., and Wensaas, L. (2009). Hydrocarbon leakage interpreted on seismic data. *Mar. Petroleum Geol.* 26, 1304–1319. doi:10.1016/j.marpetgeo.2008.09.008

Lund, B., Schmidt, P., and Hieronymus, C. (2009). *Swedish Nuclear Fuel and Waste Management Co*. SKB Technical Report, 106.

Ma, G., Zhan, L., Lu, H., and Hou, G. (2021). Structures in shallow marine sediments associated with gas and fluid migration. *JMSE* 9, 396. doi:10.3390/jmse9040396

Marfurt, K. J., Sudhaker, V., Gersztenkorn, A., Crawford, K. D., and Nissen, S. E. (1999). Coherency calculations in the presence of structural dip. *GEOPHYSICS* 64, 104–111. doi:10.1190/1.1444508

Mattingsdal, R., Knies, J., Andreassen, K., Fabian, K., Husum, K., Grøsfjeld, K., et al. (2014). A new 6 Myr stratigraphic framework for the Atlantic–Arctic Gateway. *Quat. Sci. Rev.* 92, 170–178. doi:10.1016/j.quascirev.2013.08.022

Mazurenko, L. L., and Soloviev, V. A. (2003). Worldwide distribution of deep-water fluid venting and potential occurrences of gas hydrate accumulations. *Geo-Marine Lett.* 23, 162–176. doi:10.1007/s00367-003-0146-x

Mazzini, A., Svensen, H. H., Forsberg, C. F., Linge, H., Lauritzen, S.-E., Haflidason, H., et al. (2017). A climatic trigger for the giant Troll pockmark field in the northern North Sea. *Earth Planet. Sci. Lett.* 464, 24–34. doi:10.1016/j.epsl.2017.02.014

Moss, J. L., Cartwright, J., and Moore, R. (2012). Evidence for fluid migration following pockmark formation: Examples from the nile deep sea fan. *Mar. Geol.* 303, 1–13. doi:10.1016/j.margeo.2012.01.010

Moss, J. L., and Cartwright, J. (2010). The spatial and temporal distribution of pipe formation, offshore Namibia. *Mar. Petroleum Geol.* 27, 1216–1234. doi:10.1016/j.marpetgeo.2009.12.013

Osti, G., Waghorn, K. A., Waage, M., Plaza-Faverola, A., and Ferré, B. (2019). Evolution of contourite drifts in regions of slope failures at eastern Fram Strait. *Arktos* 5, 105–120. doi:10.1007/s41063-019-00070-y

Oye, V., Stanchits, S., Babarinde, O., Bauer, R., Dichiarante, A. M., Langet, N., et al. (2022). Cubic-meter scale laboratory fault re-activation experiments to improve the understanding of induced seismicity risks. *Sci. Rep.* 12, 8015. doi:10.1038/s41598-022-11715-6

Panieri, G., Bünz, S., Fornari, D. J., Escartin, J., Serov, P., Jansson, P., et al. (2017). An integrated view of the methane system in the pockmarks at Vestnesa Ridge, 79°N. *Mar. Geol.* 390, 282–300. doi:10.1016/j.margeo.2017.06.006

Panieri, G., James, R. H., Camerlenghi, A., Westbrook, G. K., Consolaro, C., Cacho, I., et al. (2014). Record of methane emissions from the West Svalbard continental margin during the last 23.500yrs revealed by δ13C of benthic foraminifera. *Glob. Planet. Change* 122, 151–160. doi:10.1016/j.gloplacha.2014.08.014

Panieri, G., Knies, J., Vadakkepuliyambatta, S., Lee, A. L., and Schubert, C. J. (2023). Evidence of Arctic methane emissions across the mid-Pleistocene. *Commun. Earth Environ.* 4, 109. doi:10.1038/s43247-023-00772-y

Pape, T., Bünz, S., Hong, W.-L., Torres, M. E., Riedel, M., Panieri, G., et al. (2020). Origin and transformation of light hydrocarbons ascending at an active pockmark on Vestnesa Ridge, arctic ocean. *J. Geophys. Res. Solid Earth* 125, e2018JB016679. doi:10.1029/2018JB016679

Patton, H., Andreassen, K., Bjarnadóttir, L. R., Dowdeswell, J. A., Winsborrow, M. C. M., Noormets, R., et al. (2015a). Geophysical constraints on the dynamics and retreat of the Barents Sea ice sheet as a paleobenchmark for models of marine ice sheet deglaciation. *Rev. Geophys.* 53, 1051–1098. doi:10.1002/2015RG000495

Patton, H., Swift, D. A., Clark, C. D., Livingstone, S. J., Cook, S. J., and Hubbard, A. (2015). Automated mapping of glacial overdeepenings beneath contemporary ice sheets: Approaches and potential applications. *Geomorphology* 232, 209–223. doi:10.1016/j.geomorph.2015.01.003

Peltier, W. R., and Fairbanks, R. G. (2006). Global glacial ice volume and Last Glacial Maximum duration from an extended Barbados sea level record. *Quat. Sci. Rev. Crit. Quat. Stratigr.* 25, 3322–3337. doi:10.1016/j.quascirev.2006.04.010

Petersen, C. J., Bünz, S., Hustoft, S., Mienert, J., and Klaeschen, D. (2010). High-resolution P-Cable 3D seismic imaging of gas chimney structures in gas hydrated sediments of an Arctic sediment drift. *Mar. Petroleum Geol.* 27, 1981–1994. doi:10.1016/j.marpetgeo.2010.06.006

Planke, S., Erikson, F. N., Berndt, C., Mienert, J., and Masson, D. (2009). P-cable high-resolution seismic. *Oceanog* 22, 85. doi:10.5670/oceanog.2009.09

Plaza-Faverola, A., Bünz, S., Johnson, J. E., Chand, S., Knies, J., Mienert, J., et al. (2015). Role of tectonic stress in seepage evolution along the gas hydrate-charged Vestnesa Ridge, Fram Strait: Arctic seepage modulated by tectonics. *Geophys. Res. Lett.* 42, 733–742. doi:10.1002/2014GL062474

Plaza-Faverola, A., Bünz, S., and Mienert, J. (2011). Repeated fluid expulsion through sub-seabed chimneys offshore Norway in response to glacial cycles. *Earth Planet. Sci. Lett.* 305, 297–308. doi:10.1016/j.epsl.2011.03.001

Plaza-Faverola, A., Bünz, S., and Mienert, J. (2012). The free gas zone beneath gas hydrate bearing sediments and its link to fluid flow: 3-D seismic imaging offshore mid-Norway. *Mar. Geol.* 291, 211–226. doi:10.1016/j.margeo.2011.07.002

Plaza-Faverola, A. (2020). CAGE20-6 Cruise Report: Pore-fluid pressure and heat flow surveys along the Vestnesa Ridge, west-Svalbard continental margin. *CAGE – Centre Arct. Gas Hydrate, Environ. Clim. Rep. Ser.* 8, 1. doi:10.7557/cage.6918

Plaza-Faverola, A., and Keiding, M. (2019). Correlation between tectonic stress regimes and methane seepage on the Western Svalbard margin. *Solid earth.* 10, 79–94. doi:10.5194/se-10-79-2019

Plaza-Faverola, A., Vadakkepuliyambatta, S., Hong, W.-L., Mienert, J., Bünz, S., Chand, S., et al. (2017). Bottom-simulating reflector dynamics at Arctic thermogenic gas provinces: An example from Vestnesa Ridge, offshore west Svalbard. *J. Geophys. Res. Solid Earth* 122, 4089–4105. doi:10.1002/2016JB013761

Plaza-Faverola, A., Sultan, N., Lucchi, R. G., El bani Altuna, N., Ramachandran, H., Singhroha, S., et al. (2023). Spatial Changes in Gas Transport and Sediment Stiffness Influenced by Regional Stress: Observations From Piezometer Data Along Vestnesa Ridge, Eastern Fram Strait. *J. Geophys. Res. Solid Earth* 128, e2022JB025868. doi:10.1029/2022JB025868

Portnov, A., Vadakkepuliyambatta, S., Mienert, J., and Hubbard, A. (2016). Ice-sheet-driven methane storage and release in the Arctic. *Nat. Commun.* 7, 10314. doi:10.1038/ncomms10314

Powers, M. C. (1967). Fluid-Release Mechanisms in Compacting Marine Mudrocks and Their Importance in Oil Exploration. *AAPG Bulletin* 51, 1240–1254. doi:10.1306/5D25C137-16C1-11D7-8645000102C1865D

Quinn, R., Bull, J., and Dix, J. (1998). Optimal processing of marine high-resolution seismic reflection (chirp) data. *Mar. Geophys. Res.* 20, 13–20. doi:10.1023/A:1004349805280

Ramachandran, H., Plaza-Faverola, A., and Daigle, H. (2022). Impact of gas saturation and gas column height at the base of the gas hydrate stability zone on fracturing and seepage at Vestnesa Ridge, west-svalbard margin. *Energies* 15, 3156. doi:10.3390/en15093156

Riboulot, V., Thomas, Y., Berné, S., Jouet, G., and Cattaneo, A. (2014). Control of Quaternary sea-level changes on gas seeps: Kiboulot et al.: Control of eustatism on gas seeps. *Geophys. Res. Lett.* 41, 4970–4977. doi:10.1002/2014GL060460

Rise, L., Bellec, V. K., Chand, S., and Bøe, R. (2015). Pockmarks in the southwestern Barents Sea and finnmark fjords. *NJG*. doi:10.17850/njg94-4-02

Ritzmann, O., Jokat, W., Czuba, W., Guterch, A., Mjelde, R., and Nishimura, Y. (2004). A deep seismic transect from hovgård Ridge to northwestern svalbard across the continental-ocean transition: A sheared margin study. *Geophys. J. Int.* 157, 683–702. doi:10.1111/j.1365-246X.2004.02204.x

Roberts, A. (2001). Curvature attributes and their application to 3D interpreted horizons. *First Break* 19, 85–100. doi:10.1046/j.0263-5046.2001.00142.x

Ruppel, C. D., and Kessler, J. D. (2017). The interaction of climate change and methane hydrates. *Rev. Geophys.* 55, 126–168. doi:10.1002/2016RG000534

Sano, O., Ito, H., Hirata, A., and Mizuta, Y. (2005). Review of methods of measuring stress and its variations. *Bull. Earthq. Res. Inst. Univ. Tokyo* 80, 87–103.

Sauer, S., Hong, W.-L., Yao, H., Lepland, A., Klug, M., Eichinger, F., et al. (2021). Methane transport and sources in an Arctic deep-water cold seep offshore NW Svalbard (Vestnesa Ridge, 79°N). *Deep Sea Res. Part I Oceanogr. Res. Pap.* 167, 103430. doi:10.1016/j.dsr.2020.103430

Schneider, A., Panieri, G., Lepland, A., Consolaro, C., Crémière, A., Forwick, M., et al. (2018). Methane seepage at Vestnesa Ridge (NW svalbard) since the last glacial maximum. *Quat. Sci. Rev.* 193, 98–117. doi:10.1016/j.quascirev.2018.06.006

Schock, S. G. (2004). A method for estimating the physical and acoustic properties of the sea bed using chirp sonar data. *IEEE J. Ocean. Eng.* 29, 1200–1217. doi:10.1109/JOE.2004.841421

Serov, P., Vadakkepuliyambatta, S., Mienert, J., Patton, H., Portnov, A., Silyakova, A., et al. (2017). Postglacial response of Arctic Ocean gas hydrates to climatic amelioration. *Proc. Natl. Acad. Sci.* 114, 6215–6220. doi:10.1073/pnas.1619288114

Sessford, E. G., Tisserand, A. A., Risebrobakken, B., Andersson, C., Dokken, T., and Jansen, E. (2018). High-resolution benthic Mg/Ca temperature record of the intermediate water in the Denmark strait across D-O stadial-interstadial cycles. *Paleoceanogr. paleoclimatology* 33 (11), 1169–1185. doi:10.1029/2018pa003370

Smith, A. J., Mienert, J., Bünz, S., and Greinert, J. (2014). Thermogenic methane injection via bubble transport into the upper Arctic Ocean from the hydrate-charged Vestnesa Ridge, Svalbard. *Geochem. Geophys. Geosystems* 15, 1945–1959. doi:10.1002/2013GC005179

Sultan, N., Bohrmann, G., Ruffine, L., Pape, T., Riboulot, V., Colliat, J.-L., et al. (2014). Pockmark formation and evolution in deep water Nigeria: Rapid hydrate growth versus slow hydrate dissolution. *J. Geophys. Res. Solid Earth* 119, 2679–2694. doi:10.1002/2013JB010546

Sultan, N., Plaza-Faverola, A., Vadakkepuliyambatta, S., Buenz, S., and Knies, J. (2020). Impact of tides and sea-level on deep-sea Arctic methane emissions. *Nat. Commun.* 11, 5087. doi:10.1038/s41467-020-18899-3

Sztybor, K., and Rasmussen, T. L. (2017). Diagenetic disturbances of marine sedimentary records from methane-influenced environments in the Fram Strait as indications of variation in seep intensity during the last 35 000 years. *Boreas* 46, 212–228. doi:10.1111/bor.12202

Trivedi, A., Sarkar, S., Marin-Moreno, H., Minshull, T. A., Whitehouse, P. L., and Singh, U. (2022). Reassessment of hydrate destabilization mechanisms offshore west svalbard confirms link to recent ocean warming. *J. Geophys. Res. Solid Earth* 127, e2022JB025231. doi:10.1029/2022JB025231

Vachon, R., Schmidt, P., Lund, B., Plaza-Faverola, A., Patton, H., and Hubbard, A. (2022). Glacially induced stress across the arctic from the eemian interglacial to the present—implications for faulting and methane seepage. *J. Geophys. Res. Solid Earth* 127, e2022JB024272. doi:10.1029/2022JB024272

Vanneste, M., Guidard, S., and Mienert, J. (2005). Bottom-simulating reflections and geothermal gradients across the Western Svalbard margin. *Terra nova.* 17, 510–516. doi:10.1111/j.1365-3121.2005.00643.x

Vogt, P. R., Crane, K., Sundvor, E., Max, M. D., and Pfirman, S. L. (1994). Methane-generated(?) pockmarks on young, thickly sedimented oceanic crust in the Arctic: Vestnesa ridge, Fram strait. *Geology* 22, 255–258. doi:10.1130/0091-7613(1994)022<0255:MGPOYT>2.3

Wallmann, K., Riedel, M., Hong, W. L., Patton, H., Hubbard, A., Pape, T., et al. (2018). Gas hydrate dissociation off Svalbard induced by isostatic rebound rather than global warming. *Nat. Commun.* 9, 83. doi:10.1038/s41467-017-02550-9

Wiprut, D., and Zoback, M. (2000). Constraining the stress tensor in the Visund field, Norwegian North Sea: Application to wellbore stability and sand production. *Int. J. Rock Mech. Min. Sci.* 37, 317–336. doi:10.1016/s1365-1609(99)00109-4

Yao, H., Hong, W.-L., Panieri, G., Sauer, S., Torres, M. E., Lehmann, M. F., et al. (2019). Fracture-controlled fluid transport supports microbial methane-oxidizing communities at Vestnesa Ridge. *Biogeosciences* 16, 2221–2232. doi:10.5194/bg-16-2221-2019

Zhang, Z., and Digby, A. (2013). "Analysis of amplitude, reflection strength, and acoustic impedance of AUV sub-bottom profiles with application to deepwater near-surface sediments," in *All days. Presented at the offshore technology conference* (Houston, Texas, USA: OTC). doi:10.4043/23978-MS

frontiers | Frontiers in Earth Science

TYPE Original Research
PUBLISHED 20 June 2023
DOI 10.3389/feart.2023.1173477

OPEN ACCESS

EDITED BY
Jochen Knies,
Geological Survey of Norway, Norway

REVIEWED BY
Shyam Chand, Geological Survey of Norway, Norway
Pavel Serov,
UiT The Arctic University of Norway, Norway

*CORRESPONDENCE
Nil Rodes,
nilrodes@yahoo.com

RECEIVED 24 February 2023
ACCEPTED 09 June 2023
PUBLISHED 20 June 2023

CITATION
Rodes N, Betlem P, Senger K, Römer M, Hodson A, Liira M, Birchall T, Roy S, Noormets R, Smyrak-Sikora A, Olaussen S and Bohrmann G (2023), Active gas seepage in western Spitsbergen fjords, Svalbard archipelago: spatial extent and geological controls.
Front. Earth Sci. 11:1173477.
doi: 10.3389/feart.2023.1173477

Active gas seepage in western Spitsbergen fjords, Svalbard archipelago: spatial extent and geological controls

Nil Rodes[1]*, Peter Betlem[1,2], Kim Senger[1], Miriam Römer[3,4], Andy Hodson[1,5], Martin Liira[6,7], Tom Birchall[1], Srikumar Roy[8], Riko Noormets[1], Aleksandra Smyrak-Sikora[1], Snorre Olaussen[1] and Gerhard Bohrmann[3,4]

[1]Department of Arctic Geology, The University Centre in Svalbard, Longyearbyen, Norway, [2]Department of Geosciences, University of Oslo, Oslo, Norway, [3]Department of Geosciences, University of Bremen, Bremen, Germany, [4]General Geology–Marine Geology, MARUM–Center for Marine Environmental Sciences, Bremen, Germany, [5]Department of Environmental Sciences, Western Norway University of Applied Sciences, Bergen, Norway, [6]Department of Geology, University of Tartu, Tartu, Estonia, [7]The Geological Survey of Estonia, Rakvere, Estonia, [8]Irish Centre for Research in Applied Geosciences, University College Dublin, School of Earth Sciences, Dublin, Ireland

This study presents the first systematic observations of active gas seepage from the seafloor in the main fjords of western Spitsbergen in the Svalbard archipelago. High-resolution acoustic water column data were acquired throughout two research cruises in August 2015 and June 2021. 883 gas flares have been identified and characterized in Isfjorden, and 115 gas flares in Van Mijenfjorden. The hydroacoustic data indicate active fluid migration into the water column. Interpretation of 1943 km of regional offshore 2D seismic profiles supplemented the water column and existing gas geochemical data by providing geological control on the distribution of source rocks and potential migration pathways for fluids. In the study area, bedrock architecture controls the fluid migration from deep source rocks. Faults, high permeability layers, heavily fractured units and igneous intrusions channel the gas seepage into the water column. The observations of gas seepage presented in this study are an important step towards the assessment of how near-shore seepage impacts upon the carbon budget of Svalbard fjords, which constitute a globally recognized early climate change warning system for the High Arctic.

KEYWORDS

gas seepage, gas flares, hydrocarbon sources, hydroacoustic mapping, water column anomalies, Arctic fjord systems, Svalbard archipelago

1 Introduction

Methane is a potent greenhouse gas that strongly influences the global climate (Shindell et al., 2009). When averaged over a 100-year timescale, the warming effect of methane per unit mass is 28 times higher than that of carbon dioxide (CO_2) (Stocker et al., 2013), and its emissions constitute the second-largest contribution to historical warming after CO_2. Contrary to the well-studied deep-water sites on the continental slope west of Svalbard (Gentz et al., 2014; Sahling et al., 2014; Mau et al., 2017), gas seepage is poorly constrained in the fjords. In the shallow waters of the fjords, gas seepage is more likely to avoid complete

removal by dissolution and microbial oxidation of methane in the water column, and thus reach the water-atmosphere interface (Judd and Hovland, 2007). It is estimated that global CH_4 emissions from marine seeps account for up to 65 Tg CH_4 yr^{-1}, but the flux of oceanic methane reaching the atmosphere is uncertain (Saunois et al., 2020). In Svalbard, microbial methane oxidation effects in near-surface sediments greatly reduce the flux of diffusive methane reaching the water column (Liira et al., 2019). However, Adventfjorden, Tempelfjorden and Van Mijenfjorden exhibit perennial supersaturation with respect to methane and the local conditions typically support a sea-air flux (Damm et al., 2021). Understanding the causes and effects of gas seepage into shallow waters is crucial as it provides valuable knowledge to constrain the contribution of gas emissions emanating from shallow Arctic water and fjords to the global atmospheric carbon pool. Herein, establishing the origin and composition of the gas forms an important first step to study climate feedbacks in Svalbard's near-shore Arctic waters. This is important because Svalbard is warming faster than elsewhere in the Arctic (Nordli et al., 2014). Findings in Svalbard's fjords may therefore tell us what to expect elsewhere in the Arctic, which itself is an important early warning system for climate change (Hassol et al., 2004).

Svalbard's fjord and onshore geology consist of thick sedimentary units comprising both hydrocarbon source and reservoir rocks, along with documented onshore secondary and tertiary migrated hydrocarbons (Abay et al., 2017; Nicolaisen et al., 2019; Ohm et al., 2019) and offshore gas seeps (Roy et al., 2019). Multiple technical gas discoveries (predominantly methane) have been made in Late Palaeozoic-Mesozoic successions (Senger et al., 2019). The organic-rich Botneheia Formation (Middle Triassic) and the organic-rich Agardhfjellet Formation (Upper Jurassic to Lower Cretaceous) are both known gas sources in central Spitsbergen (Abay et al., 2017; Ohm et al., 2019; Senger et al., 2019; Birchall et al., 2021). Studying seabed methane leakage in Svalbard fjords has the advantage that the geological conditions conform to the well-known and easily accessible onshore geology. This facilitates direct onshore-offshore correlations for deciphering the controlling mechanisms of gas leakage. It also helps to demonstrate how fjords differ from the further offshore provinces, such as the well-studied Vestnesa Ridge (Bünz et al., 2012; Panieri et al., 2017; Sauer et al., 2021), the continental slope west of Svalbard and in particular the continental slope west of Prins Karls Forland, where thousands of gas flares have been described (Bünz et al., 2012; Gentz et al., 2014; Sahling et al., 2014; Mau et al., 2017).

Onshore natural gas in Svalbard is present beneath glaciers and permafrost (Hodson et al., 2020; Kleber et al., 2023) and as shale gas in thick organic-rich source rocks (Ohm et al., 2019). Late Pliocene to Holocene glaciations have formed large fjord systems in Svalbard, exposing excellent outcrops nearly identical to the subsurface geology. Deglaciation has also initiated isostatic uplift, exposing marine sediments to freezing and thus permafrost aggradation, trapping much of the deeper gas beneath (Hornum et al., 2020). Active gas seepage has therefore been identified in numerous terrestrial springs where gas-charged groundwaters are able to discharge through the permafrost layer (Hodson et al., 2020) or exploit the forefields of retreating glaciers (Kleber et al., 2023). Hodson et al. (2020) report that biogenic gas can contribute to the emissions from the pingos in Central Svalbard, but the overwhelming source of gas in terrestrial seeps is geogenic in origin (Kleber et al., 2023). In nearby marine settings, Mau and Rohardt (2016) identified 8 gas flares along a transect in Isfjorden in 2015 (Figure 1). Roy et al. (2019) also documented active seeps observed during a 2015 cruise in Nordfjorden and linked them to subsurface geological conditions.

In Isfjorden, the largest fjord system in western Spitsbergen, over 1,300 crater-like depression features on the seafloor have been mapped and interpreted as pockmarks. Over 50% of the pockmarks are related to source rocks, alluding to the presence of an underlying petroleum system (Roy et al., 2015). Different acoustic features such as enhanced reflections, acoustic turbidity zones and acoustic blankings have been interpreted on high-resolution sub-bottom acoustic profiles, preferentially distributed over regional faults (Roy et al., 2019; Roy et al., 2016; Roy et al., 2014). Integrated geophysical data analysis suggested that faults and igneous intrusions could have acted as migration pathways of fluids and gas, facilitating the seepage of the buoyant fluids into the water column and creating pockmarks on the seabed (Roy et al., 2015; Roy et al., 2014).

Modeling of the gas hydrate stability zone by Betlem et al. (2021) suggested that the deeper parts of Isfjorden currently lie close to the hydrate stability phase boundary. Here the authors assumed a 5% contribution of higher order hydrocarbons (ethane equivalent) to the gas feed and year-around bottom-water temperatures near the freezing point to identify the potential gas hydrate stability zone. These temperatures are consistent with the decadal temperature trends observed from 1987 to 2017 in Isfjorden (Skogseth et al., 2020). However, the waters of Svalbard and the Arctic are warming at unprecedented rates (Skogseth et al., 2020). Decadal water column thermal trends indicate heat transfer from the North Atlantic into the fjord waters of western Svalbard, raising the mean water temperatures by 0.7°C per decade in winter and 0.6°C per decade in summer (Skogseth et al., 2020). This temperature increase could result in the thawing of subsea permafrost and natural gas hydrate dissociation (Mienert et al., 2005; Betlem et al., 2021), causing additional methane release into the water column.

In the fjords of Spitsbergen, further knowledge needs to be acquired to ascertain ongoing fluid migration and assess the causes of the seepage in the shallow waters of this region in the Arctic. This is important as the spatial variation of active (ebullitive) gas seepage and the underlying geological controlling factors are unknown. Furthermore, the seasonal and yearly variation of ebullition (gas flaring) at individual seeps is virtually unknown in the study area. Moreover, there needs to be a an improved understanding of how gas seepage is governed by the major stratigraphic units and structural elements in the bedrock, different seabed morphologic expressions, and the effects of potentially widespread gas hydrate stability zone (GHSZ).

Here we present new acoustic flare data documenting active gas emissions in Isfjorden and Van Mijenfjorden based on two research cruises in 2015 and 2021. We characterize the gas flares using multibeam bathymetry and geological maps to investigate potential correlations between source rock intervals and flares. We have utilized 2D seismic and bathymetry data to correlate flares with the underlying geology, specifically migration pathways along fault zones. Additionally, we integrate all published marine gas geochemical data from and around

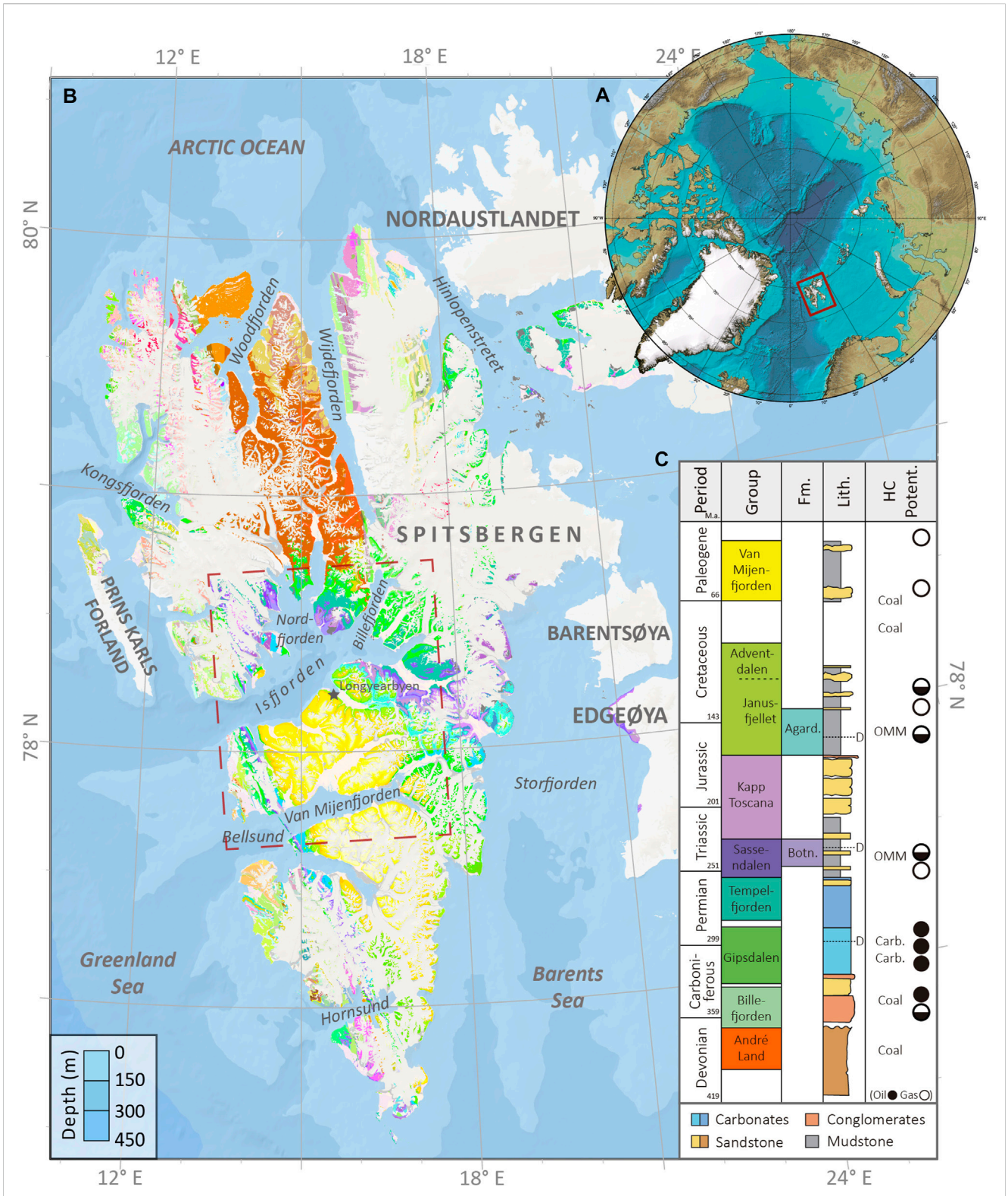

FIGURE 1
(A). Inset of the location of Svalbard (red square) on Jakobsson et al., 2020. **(B)**. Bedrock map of the Svalbard archipelago. The geological map is courtesy of the Norwegian Polar Institute, 2016. The polygon marked with a red dashed line defines the area shown in Figure 2. **(C)**. The stratigraphic log is based on an unpublished figure by Arild Andresen (University of Oslo), further updated with source rocks and hydrocarbon potential by Betlem et al. (2021) and Olaussen et al. (2022). Abbreviations: Fm.: Formation; Lith.; Lithology; HC Potent.: Hydrocarbon Potential; Agard.: Agardhfjellet Formation; Botn.: Botneheia Formation, Carb.: Carbonates; D.: Decollement; OMM: Organic Marine Mudstone.

Svalbard to better constrain the gas source. Finally, we address the significance of the regional onshore-offshore gas seepage in terms of potential gas hydrate occurrences and the observed climatic forcing in the region.

2 Geological setting

Svalbard represents the uplifted and exposed northwestern corner of the Eurasian plate. A nearly complete sedimentary succession from Devonian to Paleogene (with the exception of Upper Cretaceous) is exposed across the Archipelago (Harland et al., 1997; Dallmann, 2015) in addition to metamorphic basement rocks in the northwest (Figure 1). The Upper Palaeozoic and Mesozoic successions are linked to the stratigraphy of the prolific southwestern Barents Sea Hydrocarbon Province (Worsley et al., 1986; Nøttvedt et al., 1993; Henriksen et al., 2011).

The continental Upper Devonian Andrée Land Group succession is unconformably overlain by the Lower Carboniferous alluvial, lacustrine and coal-bearing deposits of the Billefjorden Group (Gjelberg and Steel, 1981; Harland et al., 1997). Subsequently, the Late Carboniferous-Early Permian succession of mixed siliciclastics, evaporites, and warm-water organic-rich carbonates of the Gipsdalen Group were deposited (Stemmerik, 2008; Sorento et al., 2020; Smyrak-Sikora et al., 2021) before transitioning to cool water carbonates of the Tempelfjorden Group (Matysik et al., 2018).

The entire siliciclastic dominated Mesozoic and Paleogene stratigraphic sequence began with the marine mudstones and subordinate deltaic sandstones of the Lower Triassic Sassendalen Group (Mørk et al., 1982; Steel and Worsley, 1984). The uppermost part of the Sassendalen Group hosts the organic-rich Botneheia Formation (Mørk et al., 1999; Krajewski, 2008). In Svalbard this marine basin was filled in from the east and southeast with the early Late Triassic deltaic succession of the lower Kapp Toscana Group (Mørk et al., 1982; Anell et al., 2014; Lord et al., 2017). In contrast, the Late Triassic-Middle Jurassic succession of the Wilhelmøya Subgroup is highly condensed with multiple hiatuses, forming up-to-25-m thick outcrops in central and western Spitsbergen (Rismyhr et al., 2019). The Adventdalen Group begins with the organic-rich, Middle Jurassic to Lower Cretaceous Agardhfjellet Formation (Koevoets et al., 2018), overlaid by regressive to transgressive Early Cretaceous deposits (Steel and Worsley, 1984; Olaussen et al., 2022). The Upper Cretaceous succession in Svalbard is missing, likely due to the emplacement of the High Arctic Large Igneous Province (HALIP) (Maher, 2001; Senger and Galland, 2022) and uplift related to the opening of the Arctic Ocean.

The Paleogene succession of the Van Mijenfjorden Group was deposited in the Central Spitsbergen Basin -a foreland basin formed in the front of the West Spitsbergen fold-thrust belt (Harland et al., 1997; Helland-Hansen and Grundvåg, 2021). The lowermost part of the Van Mijenfjorden Group consists of coal-bearing formations mined in Spitsbergen. Evidence of past and present faulting is widespread throughout the archipelago (Lowell, 1972; Harland et al., 1974). During the Palaeocene/Eocene, the western and central Spitsbergen was affected by transpression and structural shortening, followed by extensional faulting in the Oligocene, resulting in different migration pathways. Structural heterogeneities and permeable zones such as faults and decollements, permeable reservoir rocks, igneous intrusions, and near-shore permafrost are implied to have a crucial role in directing the flow from deep source rocks and terminating on the seafloor (Henriksen et al., 2011; Ogata et al., 2014; Roy et al., 2014).

Several organic-rich rocks are regionally widespread in Svalbard. The Upper Jurassic to Lower Cretaceous Organic Rich Marine Mudstone (OMM) Agardhfjellet Formation and the Middle Triassic OMM Botneheia Formation are the most important regional source rocks, with proven migration of hydrocarbons found throughout Spitsbergen (Nøttvedt et al., 1993; Abay et al., 2017; Ohm et al., 2019). These two units are also linked to the two prolific time-equivalent oil and gas-prone source rocks in the southwestern Barents Sea hydrocarbon province; the Hekkingen and Steinkobbe formations, respectively (Worsley, 2008; Abay et al., 2018; Lutz et al., 2021; Wesenlund et al., 2021). The maturation of Agardhfjellet and Botneheia formations decreases from west to east. In the westernmost part of Spitsbergen they are overmature, they are oil-prone in the east coast of Spitsbergen and are immature to the far east of the archipelago in Kong Karls Land (Olaussen et al., 2022). Additional hydrocarbon source rocks occur in the upper Palaeozoic, Lower Cretaceous and particularly Paleocene coal deposits (Gjelberg and Steel, 1995; Van Koeverdenet al., 2011; Uguna et al., 2017). All these organic-rich rocks are in the state of having expelled or are currently capable of expelling hydrocarbons in our study area (Abay et al., 2017; Nicolaisen et al., 2019; Olaussen et al., 2022).

2.1 Source rock characterization

The Middle Triassic Botneheia Formation is comprised predominantly of black shale with abundant small phosphate nodules and silty dolomite becoming calcareous in the upper part with numerous bivalves and reptile bone fragments (Mørk et al., 1982). The formation presents a varying thickness between 80 and 168 m. The upper part is very rich in organic material, presenting lateral variations in maturity, with total organic carbon (TOC) values (5%–10%), hydrogen index (HI) values of 400–600 mg HC/g TOC, low production index (PI) (0.04–0.1) and Tmax (439°C–446°C) suggesting excellent source rocks composed of oil-prone Type II kerogen. The Botneheia Formation was deposited in a offshore to prodelta depositional environment under periodically anoxic sea floe conditions (Wesenlund et al., 2021).

The Middle Jurassic to Lower Cretaceous Agardhfjellet Formation is 90–350 m thick and is largely missing in the east due to erosion related to Late Jurassic and Early Cretaceous inversion (Olaussen et al., 2022). Its dominant lithology is siltstone, sandstone, and beds of black organic-rich shales. Core data in central western Spitsbergen shows that the formation is dominated by type III kerogen in the silty part, while the clay dominated part has a higher amount of type II kerogen (Ohm et al., 2019). It is very rich in organic material with a TOC of 6%–10% and a high HI of 50–200 mgHC/g TOC. Average Tmax values are 455°C in the black paper shale in the lower part of the Agardhfjellet Formation (Koevoets et al., 2016; Ohm et al., 2019; Olaussen et al., 2022). The Agardhfjellet Formation is gas saturated in the lower part of Adventdalen. Open hole test in Borehole DH5R, near

the base of the Formation, i.e., 640 m.b.s.l. produced thermogenic gas dominated by methane (Ohm et al., 2019). Up valley another dry gas was discovered in Cretaceous strata, This gas was suggested to be a mixture of biogenic thermogenic origin of the methane as seen in the fjords c.f. (Liira et al., 2019).

Multiple coal seams are present in sedimentary successions in Svalbard. Organic geochemical/petrological data on Carboniferous and Tertiary strata (Van Koeverden et al., 2011; Marshall et al., 2015) and Triassic–Lower Cretaceous units (Abay et al., 2017) suggest that most coals have the potential for gas generation, which makes them another potential source for the natural gas observed seeping into the water column.

3 Data and methods

In this study we provide new hydroacoustic data and integrate these with a broad range of seabed data (e.g., multibeam bathymetry and backscatter) and sub-seabed data (e.g., 2D seismic data and borehole data), to discuss the controlling mechanisms behind seepage into the fjords (Supplementary Table S1).

3.1 Water column imaging and bathymetry: spatial and temporal extent of active flaring

The multibeam bathymetric, seafloor backscatter and acoustic water column datasets were acquired during two research cruises. First, in August 2015, data were acquired using R/V Heincke during cruise HE-449 (Mau and Rohardt, 2016) across an area of 176 km^2 in Isfjorden and 20 km^2 in Van Mijenfjorden. The R/V Heincke was equipped with a Kongsberg EM710 multibeam echosounder operating at 70–100 kHz, which makes it suitable for the water depths encountered in the fjords and provides high-quality swath beam images and clear backscatter anomalies across the entire water column.

A second cruise was conducted in June 2021 onboard the R/V Clione motor sailer, with the intention of revisiting the sites used in the data from 2015. The vessel was equipped with a Norbit iWBMSh high-end turnkey multibeam sonar system, which was operated at frequencies of 200 kHz (deeper than 200 m.b.s.l.) or 400 kHz (shallower than 200 m.b.s.l.) for the acquisition of high-resolution hydrographic data. The high-frequency operational range provided a very fine depth resolution of 10 mm in shallow waters. It had a maximum depth range of 300 m.b.s.l., however, we experienced that the signal quality decreased greatly where water depths exceeded 150 m.b.s.l. Consequently, the survey in 2021 targeted the shallower waters of Isfjorden and the tributary fjords where data acquisition would be optimal. As a result, deep-water coverage across the deeper parts of Isfjorden was not as extensive as that surveyed in 2015 using a multibeam system Kongsberg EM710. The resulting hydroacoustic profiles in 2021 delivered high-resolution swath beam images showing sharp flares in waters shallower than 150 m.b.s.l. 16 CTD profiles were acquired across 4 main transects to calculate Sound Velocity Profiles (SVP) for calibrating the hydrographic data, which were inserted in the Data Collection Tool (DCT; Norbit Subsea). In total, 110 km^2 of the seafloor was covered in Isfjorden and tributary fjords.

While technical differences in multibeam systems and survey design exist, the multibeam used equiangular swath width in both cruises, which enabled wide lateral coverage for bathymetric and seafloor backscatter mapping and facilitated the detection of acoustic flares. QPS FMMidwater 7.7.2 was used to identify anomalies from the hydroacoustic profiles attributed to the presence of gas bubbles, which relied on the observation of acoustic anomalies in the water column appearing in several successive swath beam images in the hydrographic profiles. A criterion used to differentiate gas flares from other anomalies, such as fish schools, is that the anomaly has to present a narrow and vertically oriented shape, often originating from the seafloor, and showing a constant upward movement over time, as do gas bubbles in the water column. We used the FMGeopicking Tool to extract the reference information related to the gas flares.

The ship track made during the hydroacoustic data acquisition did not cover the entirety of the fjords. Consequently, we computed the real footprint by buffering the depth-dependent points from the ship track based on the opening angle of the multibeam. Continuedly, we normalized the results with the real footprint and adjusted the data measured during the transects to see if there were statistically significant distribution anomalies. The 2021 dataset presented variable data qualities resulting from instrumental limitations. Depth range and bad weather days resulted in very low data confidence in deep areas as a consequence of high background noise. In order to maximize the data confidence, we only used binned values shallower than 150 m.b.s.l. to normalize the 2021 results.

In addition to the acoustic data acquired during the R/V Heincke and R/V Clione cruises, we used existing bathymetry data (resolution 5 m; Figure 2) (Roy et al., 2015) to characterize different seabed morphologies in Isfjorden.

3.2 2D seismic data interpretation: identifying subsea migration pathways

We have interpreted the available 2D seismic data in Isfjorden and Van Mijenfjorden using Schlumberger's Petrel E&P Software Platform v2019.1. The seismic data we used came from multiple surveys conducted by industry and academia (Supplementary Table S1), which are widely documented in the literature (Austegard et al., 1994; Blinova et al., 2012; Bælum and Braathen, 2012; Senger et al., 2013; Knudsen, 2015). The interpretations of deep stratigraphic units are based on the structure described by (Bælum and Braathen, 2012) from the petroleum exploration borehole 7816/12-1 Reindalspasset I (Figure 2) (Senger et al., 2019). Two land-based seismic tie lines linked the borehole onshore with the seismic profiles in Van Mijenfjorden, which were further extended to Isfjorden through the 7815/10-1 Colesbukta near-shore well (Figure 2). By extrapolating the borehole-constrained seismic reflectors we yielded regional stratigraphic surfaces.

The 2D seismic data were acquired using a relatively low frequency (0.01—180 Hz), resulting in deep penetration and moderately low resolution of the seismic profiles. The sedimentary packages feature abnormally high seismic velocity due to extensive diagenesis associated with compaction and cementation (Mørk, 2013). This complicates differentiation of

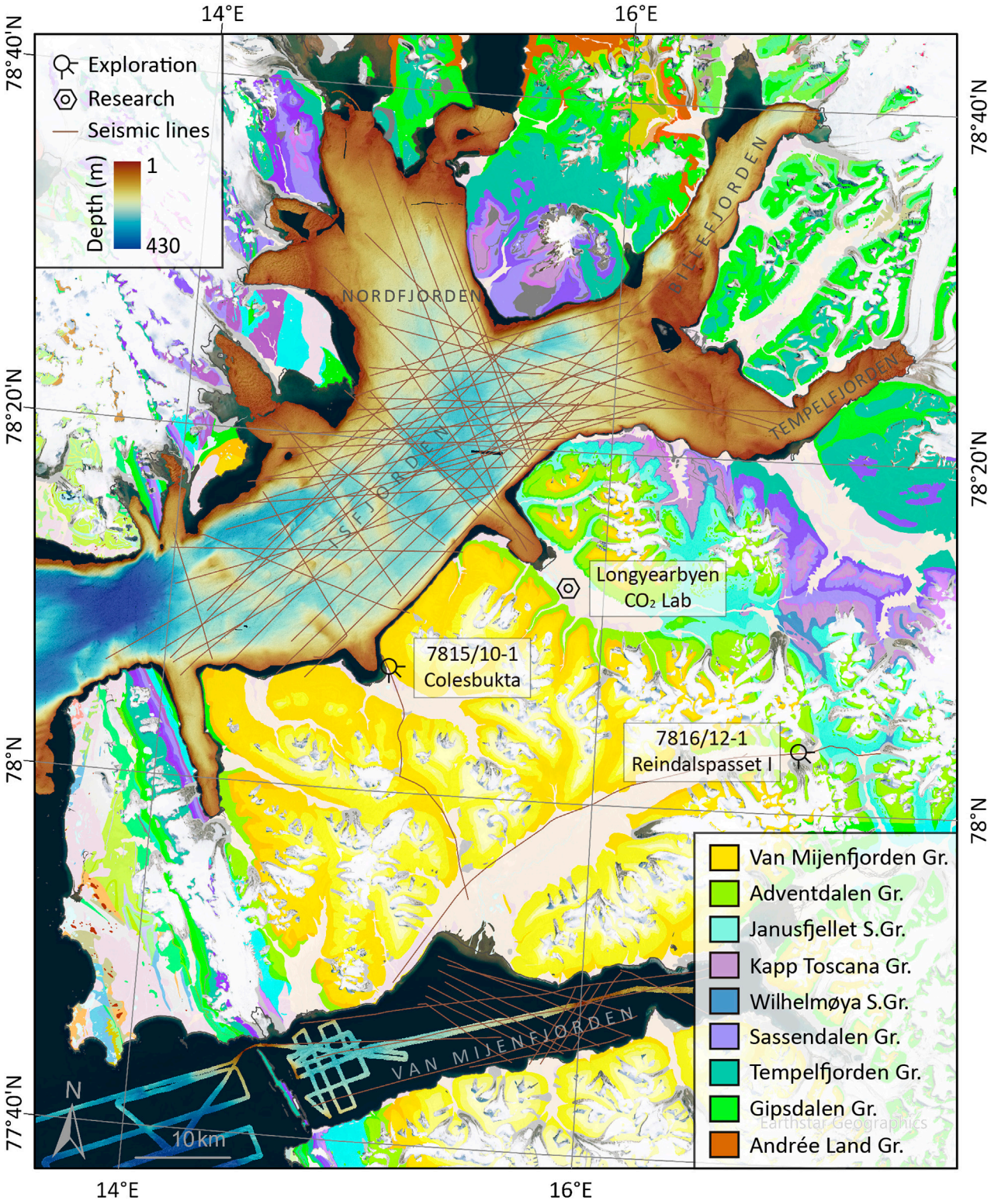

FIGURE 2
Regional map of the study area and the datasets used in this study. The geological map is courtesy of the Norwegian Polar Institute, 2016. The bathymetry in Isfjorden was provided by the Norwegian Hydrographic Service, and acquired during the HE-449 cruise in Van Mijenfjorden by the University of Bremen and MARUM. Seismic lines were interpreted in this work and tied by exploration wells onshore. EPSG:32633 projection. Abbreviations: Gr.: Group; S.Gr.: Subgroup.

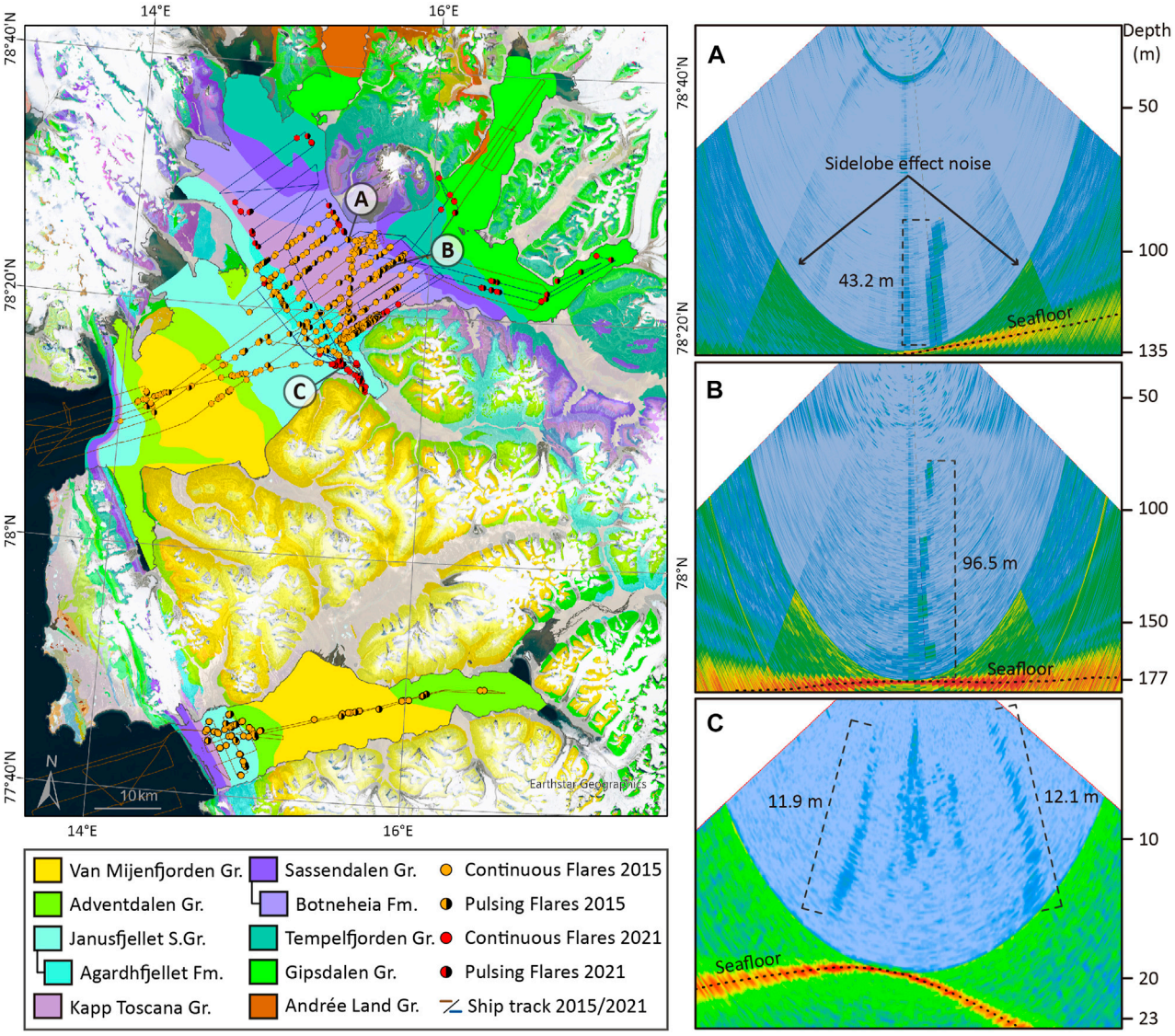

FIGURE 3
Geological map of western Spitsbergen showing the flare distribution and the stratigraphic units outcropping in the fjord result from the seismic profiles' interpretations. In orange are the flares interpretations along the transect lines of the 2015 dataset, and in red are the flares observed in the 2021 dataset. **(A,B)** are examples of flares observed in the echograms using the Kongsberg EM710 multibeam echosounder. **(C)** is an example of flare observed in the echogram with the Norbit iWBMSh high-end turnkey multibeam sonar system. Onshore geological information is courtesy of the Norwegian Polar Institute, 2016. EPSG:32633 projection and base map courtesy of Earthstar Geographics.

fluid-related anomalies and reflectors, such as potential bottom-simulating reflectors (BSRs). Limitations to the 2D seismic data extent prevented a seismic-based interpretation of unit boundaries along the mouth and northern coast in Isfjorden, including parts of Nordfjorden, Billefjorden and Tempelfjorden. There, we interpreted the geology to follow general stratigraphical trends and onshore geology. We calibrated the Agardhfjellet Formation's boundaries based on the sequence's thickness in onshore exploration boreholes and outcrops.

Not all interpreted seismic horizons represent major stratigraphic boundaries. To define the different units, we followed the observations and descriptions made by Bælum and Braathen (2012) and Knudsen (2015). The reflectors representing the Van Mijenfjorden Group are continuous, parallel and layered, with a series of strong reflections at the bottom, representing the Firkanten Formation. A combination of strong reflectors characterizes the Helvetiafjellet Formation and weak discontinuous reflectors part of the Carolinefjellet Formation. The reflector defining the top of the Agardhfjellet Formation features high amplitude values and the base shows cutting reflectors corresponding to the unconformity between the Kapp Toscana Group and the Adventdalen Group. The base reflector of the Kapp Toscana Group is characterized by low amplitude values, interpreted as a dolerite sill. In the upper-Sassendalen Group, the Botneheia Formation is affected by a thick intrusion presenting strong reflectors. The base reflector of the Sassendalen Group is

TABLE 1 Synthesis of flare characteristics from the different hydroacoustic datasets.

Dataset	Number of flares	Area (km^2)	Depth range (m.b.s.l.)	Flare height range (m)	Median intensity (dB)	Continuous/Pulsing nature (%)
Isfjorden 2015	681	172	13–280	1.2–192.2	−55	67/33
Van Mijenfjorden 2015	115	20	30–120	0.9–69.7	−50	71/29
Isfjorden 2021	152	110	13–232	3.5–44.9	No data	58/42

interpreted as an impedance contrast between weak amplitude reflectors above and strong amplitudes below, corresponding to the boundary between the Triassic shales and the silicified sandstones of Tempelfjorden Group. The base of the Tempelfjorden Group is more or less discontinuous with a slight amplitude contrast. Finally, the base of the Gipsdalen Group is characterized by a contrast of amplitudes between low values above and high amplitude values below from the carbonate/evaporite sequences. The interpretations of the older units have higher uncertainty as a result of their greater depths.

3.3 Data integration and visualization

Geographical visualization, statistical analysis, and data georeferencing were performed using the ESRI ArcGIS Pro v2.7.0 software package (Supplementary Figure S1). The geostatistics and spatial analyses of the data were conducted programmatically. To determine the area of occurrence, we combined the locations of gas flares, pockmarks, and faults with the ship track's footprint and geological units in the fjords. A minimal working example detailing the use of Python is provided in Supplementary Material.

4 Results

4.1 Hydroacoustic flare characterization

In 2015, 681 flares were detected in Isfjorden over an area of 176 km^2, and 115 flares were identified in Van Mijenfjorden over 20 km^2 (Figure 3; Table 1). A total of 152 gas flares were identified in Isfjorden in 2021 over an area of 110 km^2 and targeting shallower waters. Gas column heights for the combined data sets varied from 1.2 m to 192.2 m (Figures 3A–C). Bottom water depths ranged from 13 to 280 m.b.s.l. in Isfjorden, and from 30 to 120 m.b.s.l. in Van Mijenfjorden. The footprint of the flares for the combined data sets was between 2 m^2 for small individual flares and 458 m^2 for clusters comprising multiple flares.

The intensities of the flares are related to the bubble size, volume and rate of gas discharge. In Isfjorden, the intensity values for the first and third quartile were −60 dB and −45 dB, respectively. The median value of the flares was −55 dB. In Van Mijenfjorden, the intensity ranged between −60 dB for the first quartile and −40 dB for the third quartile. The median value of the flares was −50 dB.

Most of the flares were observed continuously flowing (Figure 3A). However, 33% of the flares detected in 2015 in Isfjorden and 42% in 2021 exhibit a pulsing nature (Figure 3B). In Van Mijenfjorden the pulsing flares account for 29% of the total.

4.2 Subsurface geology and stratigraphy of the fjords

The 2D-seismic interpretation facilitated mapping the major stratigraphic elements outcropping in the fjords (Figure 4). The geology below Isfjorden forms a large ~southerly plunging syncline (the Central Spitsbergen foreland Basin) with an almost vertical outcropping angle on the western side and a lower angle (~10°) towards the east. We interpreted the major groups outcropping in the fjord: Van Mijenfjorden Group (250 km^2), Adventdalen Group (690 km^2), Kapp Toscana Group (275 km^2), Sassendalen Group (335 km^2), Tempelfjorden Group (225 km^2) and Gipsdalen Group (390 km^2). As part of the Adventdalen Group, we could identify the seismic boundaries of the Janusfjellet Subgroup (490 km^2), which features large thickness variations caused by folding related to compressional tectonics from the Paleogene.

The Agardhfjellet Formation (the lower part of the Janusfjellet Subgroup) is of high interest in this study due to its potential as a source rock. The seismic data exhibit chaotic reflectors across the upper boundary of the formation. We estimated the total outcropping area of the formation in the fjord at 80 km^2 (Figure 3). The Botneheia Formation, the youngest unit of the Sassendalen Group, is also a primary unit of interest in our study for its hydrocarbon potential and it outcrops over 195 km^2 in the inner part of Isfjorden.

In Van Mijenfjorden, the stratigraphy of the syncline and the fjord's general structure limit the seafloor exposures to mainly the Van Mijenfjorden Group and Adventdalen Group, covering 260 km^2 and 210 km^2, respectively. The Janusfjellet Subgroup (60 km^2), Kapp Toscana Group (12 km^2), Sassendalen Group (25 km^2) and Tempelfjorden Group (2.5 km^2) outcrop in the western part of the fjord.

4.3 Seepage correlation with geological setting and seabed morphologies

In the 2015 dataset, the largest concentration of normalized flares in Isfjorden was within the outcropping Kapp Toscana Group (9.69 flares/km^2), and the organic-rich formations Agardhfjellet Formation (7.96 flares/km^2) and Botneheia Formation (7.13 flares/km^2). A different distribution is found for the 2021 dataset, with 3.94 flares/km^2 observed within Janusfjellet

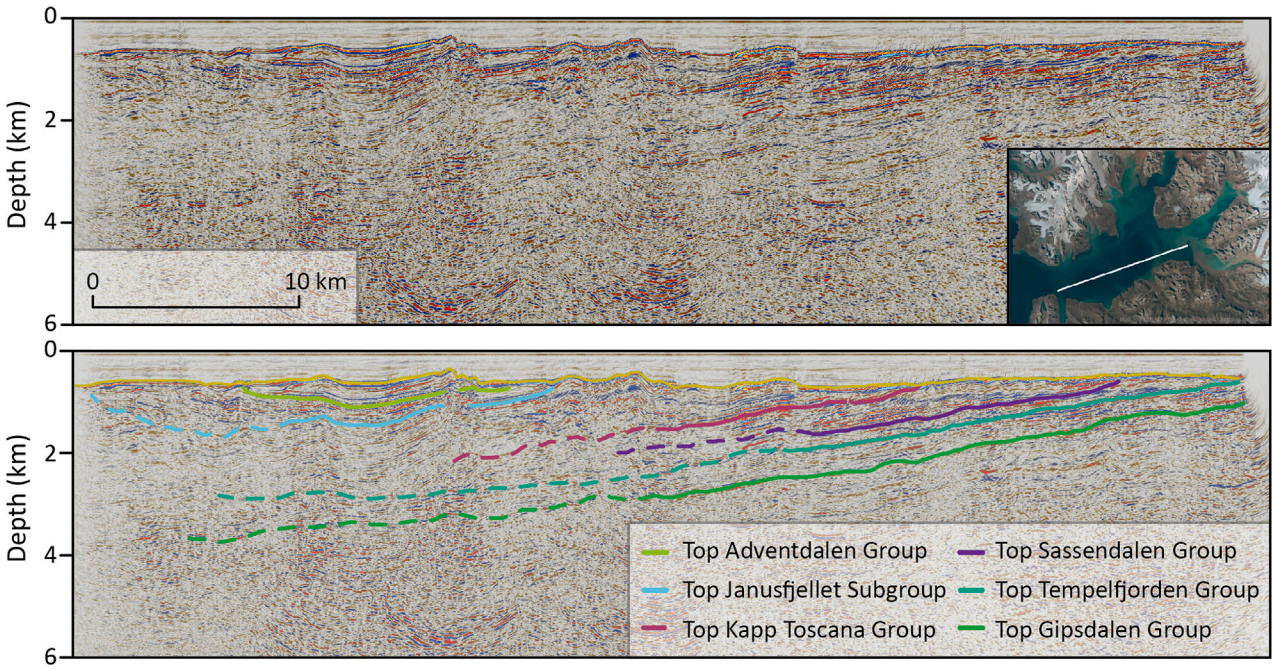

FIGURE 4
Interpretation of the seismic profile NH8509-NH8509-202-mig080001 crossing the main trunk of Isfjorden. The seismic profile is a central section of Isfjorden, and it is representative of the structures that are present on all profiles. It has a vertical exaggeration x10 and a depth scale converted from seismic assuming 4 km/s as constant velocity for the compacted rocks in Svalbard. The map shows the seismic line's location in the fjord's regional setting.

Subgroup, followed by the Gipsdalen Group (3.3 flares/km^2) and the Tempelfjorden Group (1.74 flares/km^2) (Figure 5). In Van Mijenfjorden, the largest concentration of flares was within Janusfjellet Subgroup (11.06 flares/km^2), followed by Adventdalen Group (4.64 flares/km^2), Van Mijenfjorden Group (2.44 flares/km^2) and Kapp Toscana Group (1.21 flares/km^2). No flares were detected across the seafloor extent of the Sassendalen and Tempelfjorden groups. Quantitative comparison of the distributions of outcropping geological units, pockmarks, gas flares, and structural elements relied on the normalization of the data sets to account for the limited area covered by the cruises in Isfjorden. The occurrence of these geological features was normalized according to the interpreted outcrop area of each geological unit in Isfjorden. The results firstly show that the geological units located in the inner part of Isfjorden concentrate a higher number of pockmarks per outcropping area. Secondly, the distribution of faults per outcropping area shows higher concentrations of faults in the Kapp Toscana and Sassendalen groups and the Janusfjellet Subgroup. Finally, the highest flare concentrations (per outcropping area of ship track) were found in the central parts of Isfjorden, across the areas corresponding to the Janusfjellet Subgroup, Agardhfjellet Formation, and the Kapp Toscana Group.

5 Discussion

The differences in water depth settings and acquisition parameters between the two surveys limit the comparison of spatial and temporal aspects. However, as a single Supplementary Dataset, they prove pivotal in correlating seepage within the underlying geology. Consequently, in this section, we discuss the main reasons for the distribution of flares by comparing them with the geological units and organic-rich formations, migration pathways, seafloor surface expressions, oceanographic setting, and gas geochemistry characteristics. In addition, we discuss the implications of shallow seepage for the atmospheric greenhouse gas budget in the High Arctic.

5.1 Fluid flow: driving factors for gas seepage distribution

Geochemical studies show that the Middle Jurassic to Lower Cretaceous OMM Agardhfjellet Formation and Middle Triassic Botneheia Formation have the potential to generate mixed oil and gas, and are likely the two most important regional source rocks for gas generation in Spitsbergen (Ohm et al., 2019; Wesenlund et al., 2022; 2021; Olaussen et al., 2022). Roy et al. (2014), suggest secondary migration of gas from the source rocks to the seafloor. Knies et al. (2004) found high concentrations of adsorbed methane and ethane in the southern part of Nordfjorden, implying a thermogenic gas origin from the organic-rich source rocks.

Faults are common migration routes for fluids in many basins worldwide, providing direct routes for the buoyant hydrocarbon fluids to migrate from deeper stratigraphy (Ligtenberg, 2005). In the

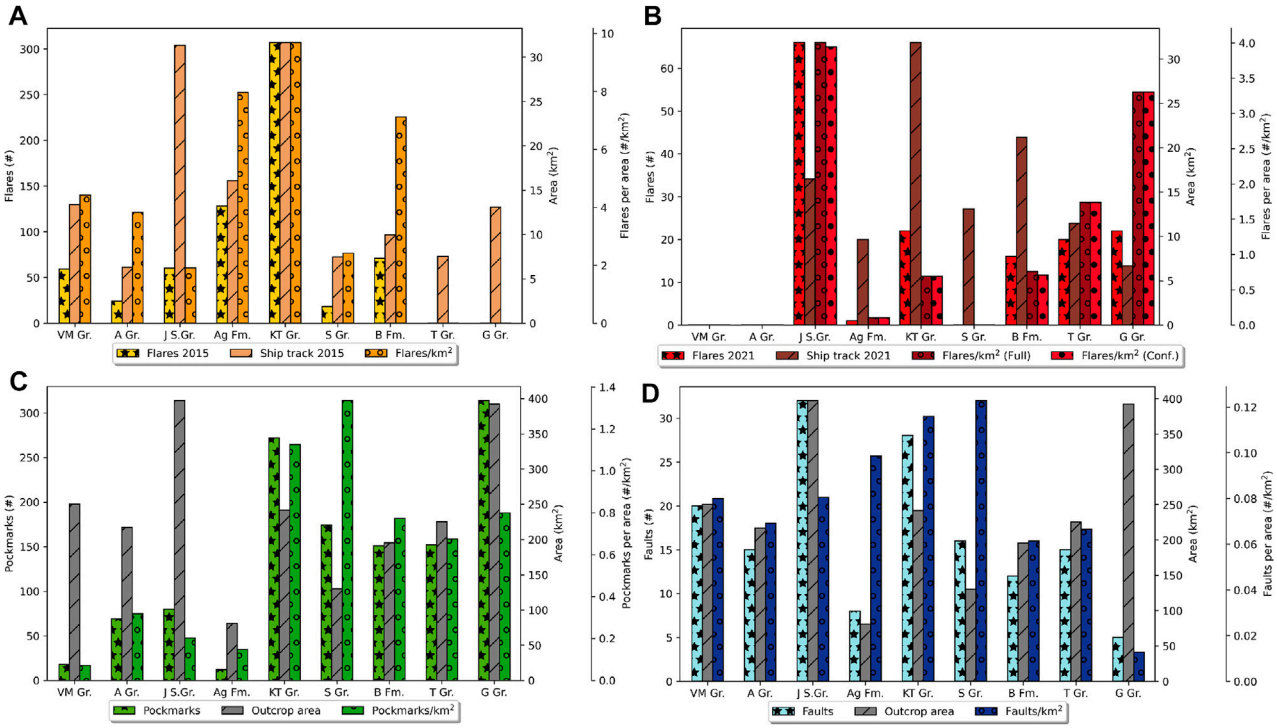

FIGURE 5
(A,B): Bar charts of the percentage of flares, ship track, and normalized flares within each stratigraphic unit (youngest to oldest from left to right) in Isfjorden for the 2015 and 2021 datasets. **(C,D)**: Bar charts of the percentage of pockmarks and faults normalized with the outcropping stratigraphic units in Isfjorden. VM Gr.: Van Mijenfjorden Group; A Gr.: Adventdalen Group; J S.Gr.: Janusfjellet Subgroup; Ag Fm.: Agardhfjellet Formation; KT Gr.: Kapp Toscana Group; B. Fm.: Botneheia Formation; S Gr.: Sassendalen Group; T Gr.: Tempelfjorden Group; G Gr.: Gipsdalen Group.

West Spitsbergen Fold-and-thrust Belt complex, various types of faults and fracture networks have been documented (Teyssier et al., 1995; Braathen et al., 2012), revealing an important role in the migration of fluids ascending from deep source rocks and seeping into the marine environment (Roy et al., 2015). The Kapp Toscana Group is highly fractured and heavily faulted (Figures 5, 6) (Roy et al., 2015). The spatial pockmark distribution on the seafloor over this unit correlates with the faults interpreted by Blinova et al. (2012), and so they most likely act as conduits for gas coming from the underlying Botneheia Formation. Similarly, the Janusfjellet Subgroup consists of highly fractured shale (Braathen et al., 2012; Ogata et al., 2014) with over 25% of the total faults interpreted in Isfjorden. These likely serve as migration pathways for the gas coming from the underlying Agardhfjellet Formation.

The results from the geostatistical analyses show that in Isfjorden, gas occurrences described in 2015 are in close association with Agardhfjellet Formation, Kapp Toscana Group and Botneheia Formation. In June 2021, the highest flare concentrations were over the mapped Janusfjellet Subgroup (mainly distributed in Adventfjorden) and Kapp Toscana Group. Therefore we find that collectively, both surveys support the conclusion of Knies et al. (2004) and Roy et al. (2015), who suggested that stratigraphy, lithology and faulting control the fluid flow migration from source rocks in Isfjorden.

Pingos and pockmarks are morphological features related to the expulsion of fluids on land or the seabed (Hovland and Judd, 1988). In high latitudes, pore-water seepage, thawing permafrost, gas hydrate dissociation, and up-drifting ice detached from the seafloor are important factors for pockmark formation (Roy et al., 2015). In Isfjorden, the abundance of pockmarks aligned along the outcropping edge of doleritic intrusions from the Early Cretaceous (Senger et al., 2013; Roy et al., 2014), suggesting that they act as crucial conduits channeling the buoyant fluid flow toward the surface (Figures 7, 8). There are also numerous pockmark occurrences aligned with steep faults suggesting that these could provide direct routes for the methane-rich fluids from organic-rich formations (Agardhfjellet and Botneheia formations), which would then seep through the seafloor, remobilizing the soft, fine-grained sediments and forming pockmarks (Forwick et al., 2009; Roy et al., 2014).

No correlation was observed between the occurrence of pockmarks and flares, as evidenced by the complete absence of flares in areas with high pockmark concentrations (Figure 7B). Neither did we observe high backscatter in the data, which may be associated with coarser sediments that prevent pockmark development (Forwick et al., 2009). A plausible explanation for the notable absence relates to the phase of the fluid outflows. Acoustic flares are detected in the water column only when the outflows contain gases or are in a gaseous phase. The pockmarks may thus still be features affected by ongoing fluid flow, such as pore-water escape, but the gas remains dissolved. In Isfjorden, however, the pockmarks are concentrated in the inner part of the fjord where the oldest stratigraphical units outcrop. Previous findings by Roy et al. (2015) indicate no ongoing fluid seepage of

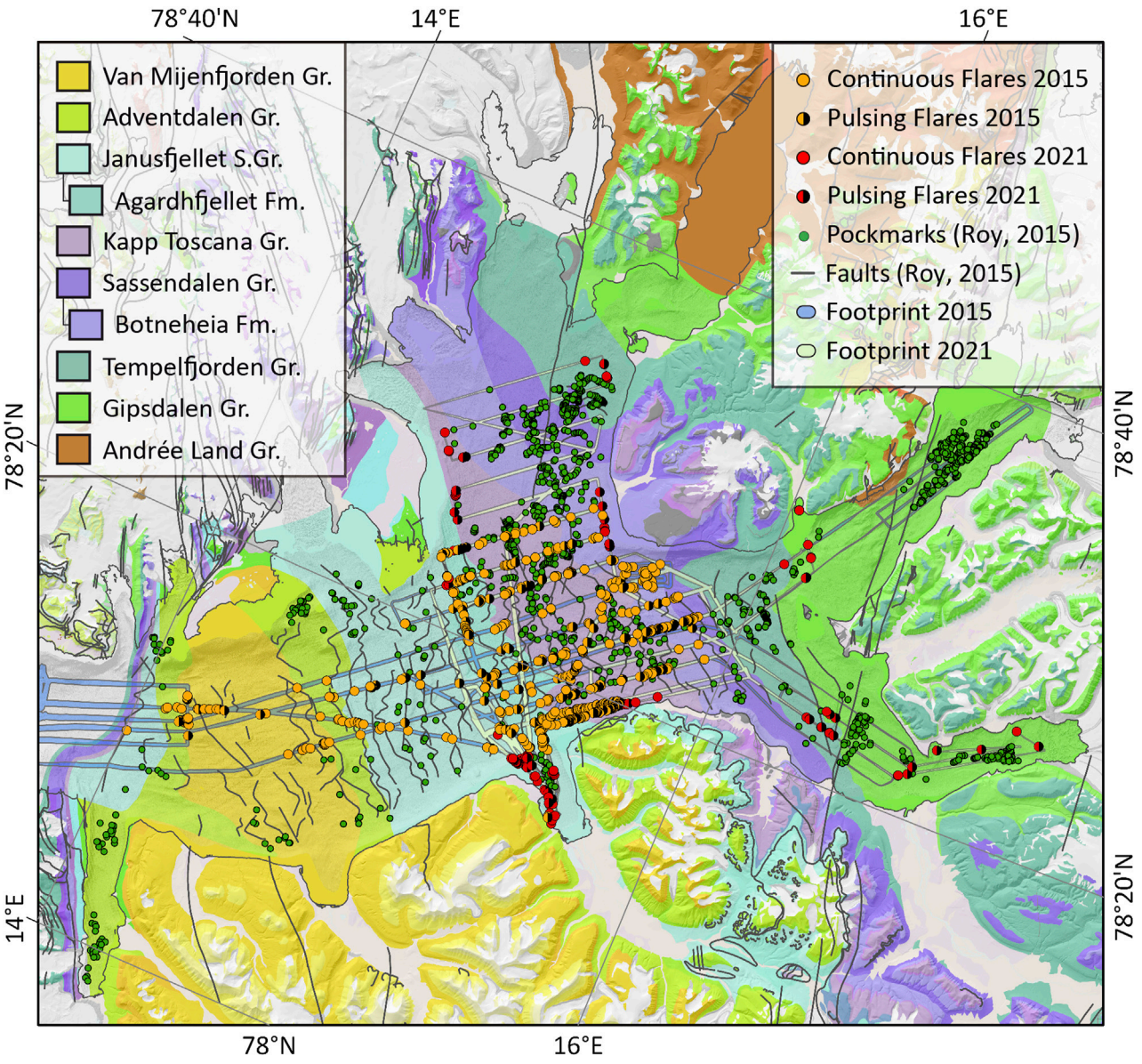

FIGURE 6
Flare distribution in Isfjorden on top of the geological units outcropping in the fjords. In orange are the flares interpretations from the 2015 dataset and in red are the flares interpretation from the 2021 dataset. Pockmark and fault distribution described by (Roy et al., 2015). Stratigraphic units outcropping in Isfjorden result from the interpretations of the seismic profiles. Onshore is the Geological map of the study area from Norwegian Polar Institute, 2016. EPSG:32633 projection.

any fluid. The paleo-pockmarks were therefore caused by fluid seepage that most likely migrated along fault zones, doleritic intrusions, and geological unconformities towards the seabed. Since then, however, the escaping fluids may have migrated to new seep locations in the seabed, ceased to flow, or become sealed by changing thermobaric conditions.

High organic matter deposition rates of 5–17 g m^{-2} yr^{-1} were reported in the fjords of Svalbard (Winkelmann and Knies, 2005), favoring biogenic methane production by the degradation of organic matter in near-surface sediments (Damm et al., 2021). Therefore, *in-situ* microbial activity could produce gas accumulations that form bubbles when methane concentrations in the sediment are high enough. For example, a mixture of thermogenic and microbial methane was found in the surface sediments of Isfjorden (Knies et al., 2004; Liira et al., 2019). These gases are proven to seep from the seafloor, suggesting a slow and steady degassing of the fjord subsurface. Most importantly, the geochemical characterization corroborates the occurrence of thermogenic gas migration in Isfjorden (Knies et al., 2004; Liira et al., 2019).

The fjords undergo significant seasonal variability in the water column temperature (Skogseth et al., 2020). In June (late spring/early summer conditions), the water column becomes stratified, with a warm surface and cold water at depth (Skogseth et al., 2020). However, in August (late summer/early autumn), with the water

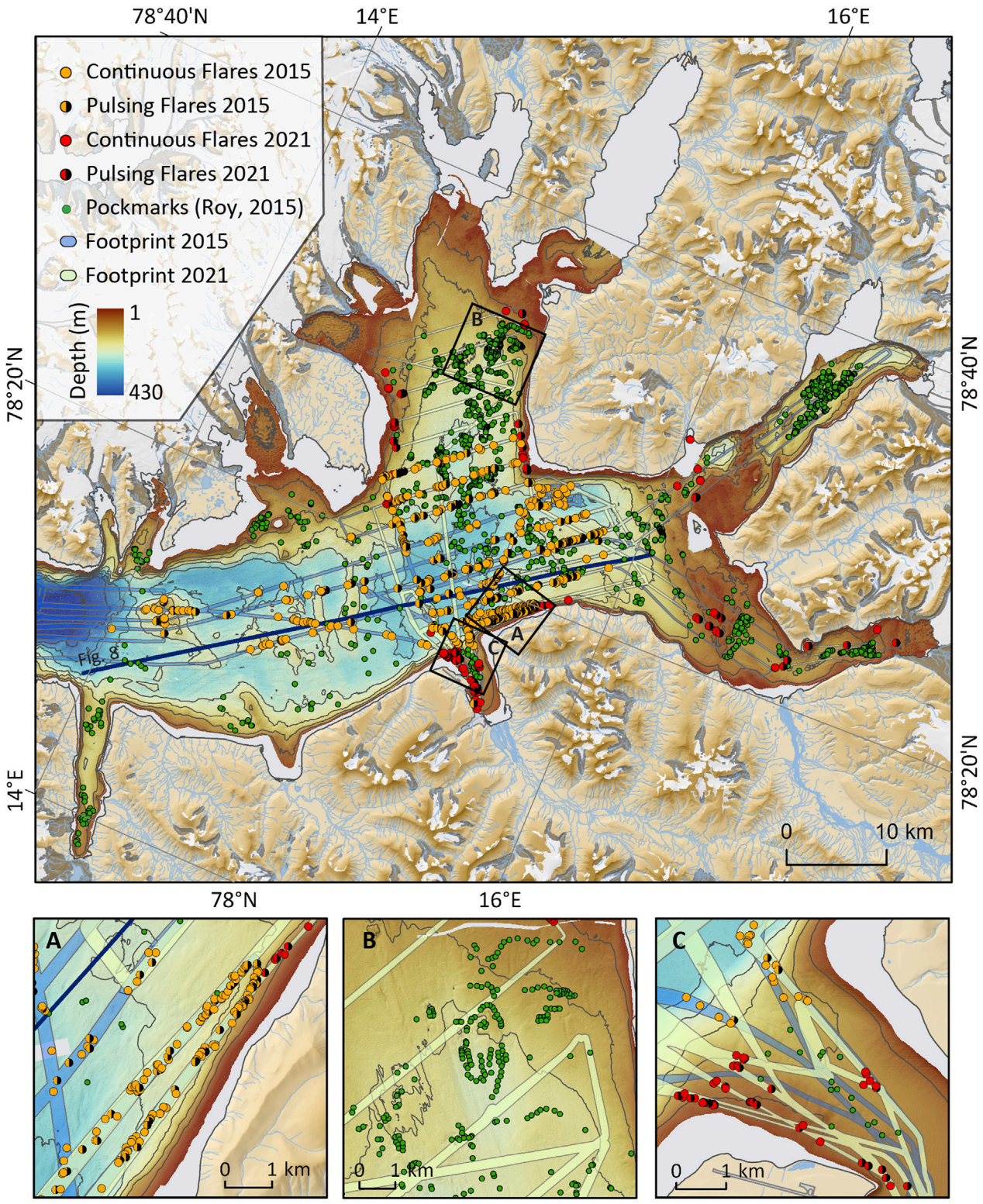

FIGURE 7
Flare distribution in Isfjorden overlain on bathymetry. In orange are the interpreted flares from the 2015 dataset and in red are the flares interpreted from the 2021 dataset. The pockmark distribution described by Roy et al. (2015) is displayed in green. The bathymetry has a 50 m isobath interval. **(A)**. No correlation between areas with high concentrations of flares and pockmarks. **(B)**. Clusters of pockmarks follow the trends of interpreted faults. No flares were detected in the ship transects. **(C)**. Temporal and spatial variation of the seepage detected in 2015 and 2021. The blue line defines the transect represented in Figure 8. EPSG:32633 projection.

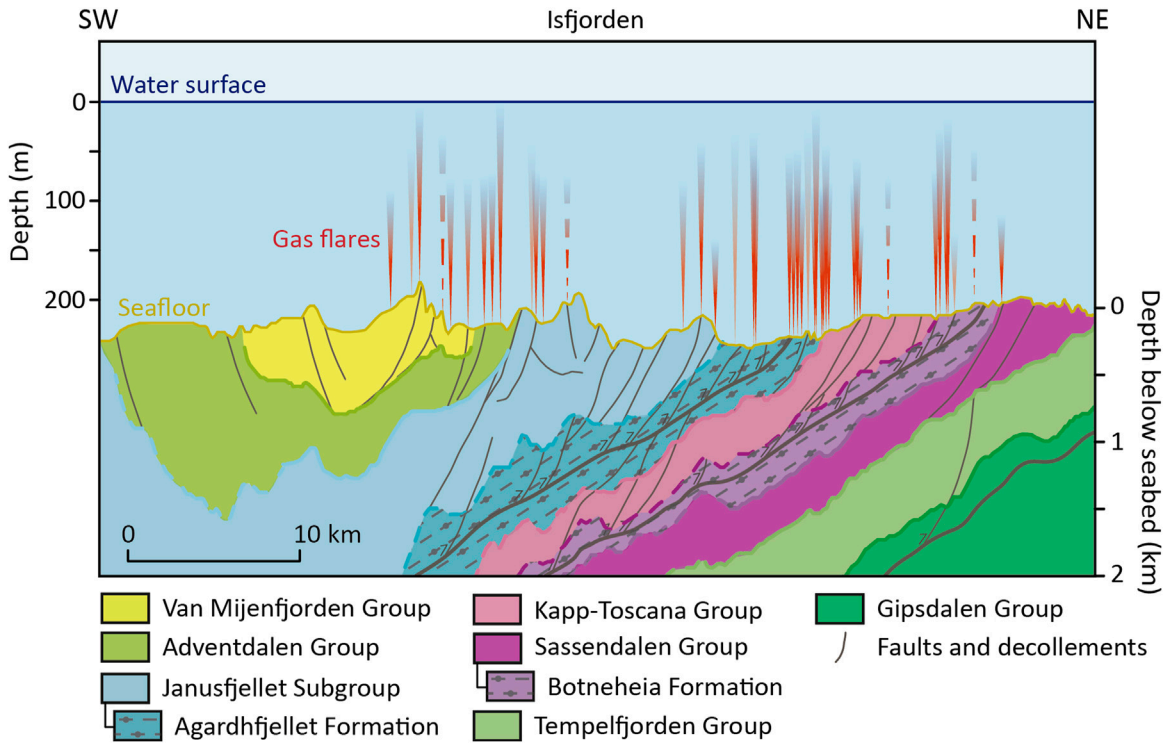

FIGURE 8
Conceptual model of the gas system across Isfjorden demonstrating the main stratigraphic groups outcropping beneath the fjord. The seismic is depth converted assuming 4 km/s as constant velocity. The organic-rich units are the source of the thermogenic gas that migrates through the fault system (Leever et al., 2011; Roy et al., 2015) to the surface. The organic-rich source rocks display a clear spatial correlation with the frequency of the gas flares interpreted in the dataset from 2015 along the transect.

column mixing, the temperature rises in the deeper parts of the fjords. On the one hand, the temperature increase in June may affect the microbial activity in the superficial sediments, favoring the methane production by the degradation of organic matter in near-surface sediments, as suggested by Damm et al. (2021). On the other hand, the summer temperature increase may contribute to the gradual thinning and degradation of near-shore permafrost leading to captured or trapped gas release, as discussed by Roy et al. (2014). The fluids may migrate beneath the onshore impermeable permafrost and then seep through to the seabed, where the permafrost is absent or discontinuous.

Methane fluxes into the atmosphere increase with shallower water depths (Greinert et al., 2010). Shallow sites (depths <100 m.b.s.l.) may represent a significant source of methane to the surface water and direct local emissions into the atmosphere (Schmale et al., 2005; Graves et al., 2015). The flares observed in the deep parts of Isfjorden do not reach the water surface but contribute to keeping the fjord waters supersaturated with methane. Methane is mixed within the water column and transported along vertical isopycnals until it reaches the water-atmosphere interface (Damm et al., 2021) enabling diffusion into the atmosphere, or it is removed by methane-consuming processes in the sediments or water column such as microbial oxidation. Shallow sites with large flares clusters are likely to contribute methane directly into the atmosphere via ebullition (i.e., bubble bursts at the water surface).

5.2 Origins of gas: insights from gas geochemistry

Studies from offshore and onshore Svalbard demonstrate the existence of active hydrocarbon systems in the region (Abay et al., 2017; Betlem et al., 2021; Blinova et al., 2012; Blumenberg et al., 2018; Hornum et al., 2020; Knies et al., 2004; Liira et al., 2019; Mau et al., 2017; Ohm et al., 2019; Roy et al., 2016; Roy et al., 2015; Roy et al., 2019; Senger et al., 2019; Weniger et al., 2019, and references therein). Although methane is the most common hydrocarbon gas in on- and offshore sediments (Forster et al., 2007; Judd and Hovland, 2007), gas samples, proven source rocks outcropping in the fjords and an active petroleum system indicate input from deeper thermogenic hydrocarbon sources. This is unsurprising given the existence of numerous prolific source rocks throughout the Barents Shelf (Henriksen et al., 2011) and 45% of wellbores drilled on the Barents Shelf are classified as discoveries (Senger et al., 2019).

Blumenberg et al. (2016) reported hydrocarbons from near-surface sediments of the Barents Sea north of Svalbard, where thermogenic methane gas adsorbed to the sediment matrix was found. Similarly Weniger et al., (2019), found that near-surface sediment-bound gases in the northern Barents Sea generally have compositional and stable carbon isotope signatures of thermogenic gas. Knies et al. (2004) presented geochemical evidence from Isfjorden and east of Spitsbergen that proposed that thermogenic

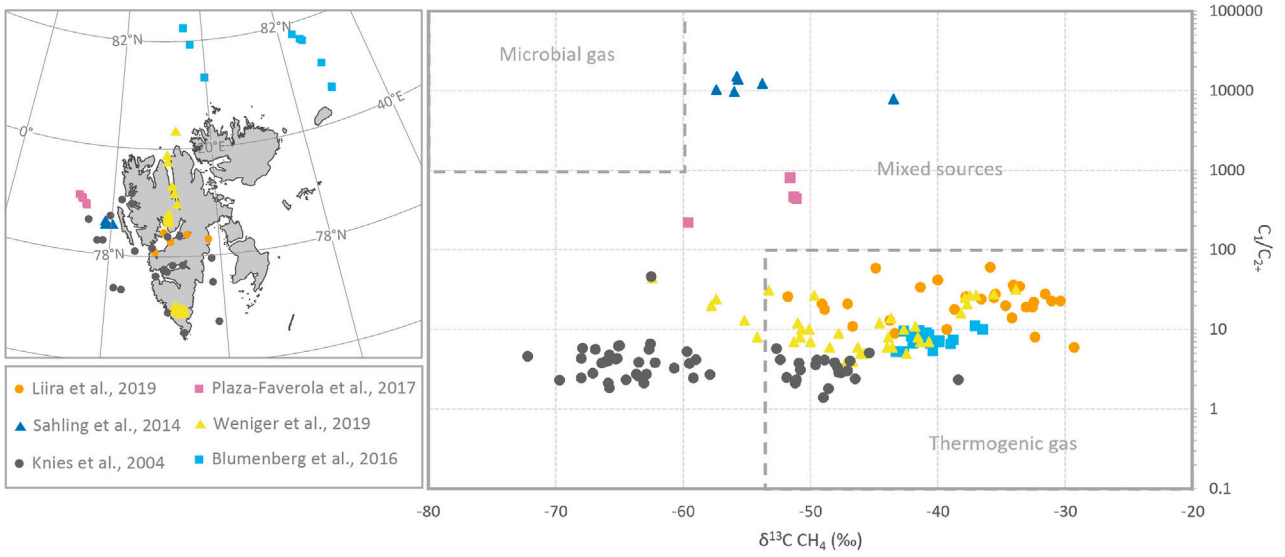

FIGURE 9
Compilation of the published sorbed and free gas geochemical analysis data from offshore sediments around Svalbard. The plot C_1/C_{2+} versus the isotopic composition of CH_4 illustrates the predominantly thermogenic signature of the analyzed gas.

hydrocarbons from deep sources had migrated to near-seafloor sediments. Liira et al. (2019) reported slow and steady hydrocarbon gas emissions of the Isfjorden pockmarks and surrounding undisturbed seafloor, having elevated concentrations of the higher hydrocarbon homologies, indicating, at least to some extent, input from thermogenic sources to the overall seeping gas budget (Figure 9).

Onshore gas analyses from the Longyearbyen CO_2 lab boreholes in Adventdalen (Huq et al., 2017; Ohm et al., 2019) show that methane encountered in the shallow subsurface is from a microbial source, based on $\delta^{13}C$ values of degassed methane and CO_2 (Huq et al., 2017). Hodson et al. (2020) revealed year-round sub-permafrost methane migration in Adventdalen, central Spitsbergen, via open system pingos where isotope data mostly suggests a microbial origin. In Adventdalen, the shallow gas accumulations are composed of methane with a significant contribution of higher order hydrocarbons (wet gas) encountered through the Jurassic source rock and underlying reservoirs (Huq et al., 2017; Ohm et al., 2019). The wetter gas is likely due to its thermogenic origin from the marine source rock of the Agardhfjellet Formation (Ohm et al., 2019), while the methane-dominated shallower gas is a likely result of microbial or coalbed (coal is prolific in the upper parts of the wellbore) origin. Kleber et al., (2023) show that the thermogenic methane is by far the most common gas source in the terrestrial seeps found in glacier forefields.

Spatially, gas has been frequently encountered in shallow intervals throughout Svalbard (Birchall et al., 2021) and shows little prevalence in any particular stratigraphic interval, except where there is no prolific source rock present due to erosion. Although samples are limited, the shallow gas composition varies, with samples from Spitsbergen appearing to be more methane dominated. In contrast, gas sampled from Hopen Island in the southeasternmost part of Svalbard revealed wet gas (C_2 and heavier making up > 31%). Given the large variations in gas composition, further studies are required to better understand the origins of the gas encountered throughout the onshore and nearshore areas of Svalbard. However, the variability and existence of numerous prolific source rocks and coal seams suggests that gas is common in the shallow subsurface of the archipelago. Ongoing migration is also evident in numerous seeps and flares, with some gas accumulations having been encountered in sediments less than 600 years old (Birchall et al., 2021).

5.3 Implications for a changing Arctic

An increased inflow of Atlantic Water results in temperature and salinity rise in the water column from Isfjorden (Skogseth et al., 2020). This increment in temperature would reduce the extent of potential sub-marine permafrost, releasing the gas trapped underneath. Methane release from such sub-permafrost stores represents a significant uncertainty in the Arctic greenhouse gas budget (Hodson et al., 2020). In addition, although the presence of gas hydrates from the fjords of Svalbard has to date not been documented to our knowledge, modelling shows that parts of central Isfjorden present favorable thermobaric conditions for natural gas hydrate formation down from the seafloor (Betlem et al., 2021). Given the numerous gas flares observed in the area, together with the organic-rich units outcropping there, the occurrence of gas hydrates is not unlikely. Where present, temperature variations may affect their stability. Further investigations are needed to assess the extent of natural gas hydrates in the fjords, and the effects hereon of bottom-water temperature change, especially in the context of the recentness of shallow gas accumulations. This is equally important for close-to-shore areas that may host sub-sea permafrost but have not been surveyed yet (Birchall et al., 2021).

Most of the Circum Arctic has a shared geological and glacial history with Svalbard and is equally exposed to the effects of climate change (Batchelor et al., 2019). Svalbard's fjords which are extensively studied due to their easy accessibility, present a similar and exposed geology to the Barents Sea (Worsley, 2008). Hence, due to its easy access and data availability, Svalbard may be an excellent place to study the mechanisms that result in the release of methane from the sub-surface into the water column and the atmosphere in the High Arctic. Shallow fjord methane emissions are likely to be particularly important in Arctic regions like Svalbard, and their climate-sensitivity means they could contribute to the atmospheric carbon pool, thus enhancing the Arctic amplification of global warming (Westbrook et al., 2009).

6 Conclusion

In this study, we document widespread active gas seepage in Svalbard's fjord system with 948 individual gas flares observed during two research cruises in 2015 and 2021. We have integrated the hydroacoustic data to decipher the likely source and migration pathways of the gas and conclude that:

- Gas seepage is widespread in the fjords of western Svalbard, proving an active fluid flow system.
- Geostatistical analyses prove that gas flares in Isfjorden are found within or close to organic-rich stratigraphic sequences -Botneheia Fm and Agardhfjellet Fm- outcropping in the fjord.
- Gas migration towards the seafloor occurs along faults, high permeability layers, and heavily fractured rock units.
- There is no spatial correlation between the distribution of pockmarks and the observed active gas flares, suggesting that the pockmarks observed throughout the seabed are not the result of present-day gas emissions.

Data availability statement

The datasets generated and analyzed in this study can be found in Zenodo repository, https://doi.org/10.5281/zenodo.7822180. We provide a minimal working example as a Python script to calculate the flare density per multibeam area of outcropping geological units. This information has also been included in the Supplementary Material.

Author contributions

NR: Conceptualization, Methodology, Software, Validation, Formal analysis, Investigation, Resources, Data Curation, Writing—Original Draft, Visualization, Project administration, Funding acquisition, Writing—Review and Editing. PB: Conceptualization, Methodology, Software, Validation, Formal analysis, Investigation, Data Curation, Writing—Original Draft, Visualization, Project administration, Supervision, Funding acquisition, Writing—Review and Editing. KS: Conceptualization, Investigation, Resources, Data Curation, Writing—Original Draft, Supervision, Funding acquisition, Writing—Review and Editing. MR: Conceptualization, Methodology, Investigation, Resources, Data Curation, Funding acquisition, Writing—Review and Editing, Supervision. AH: Resources, Writing—Review and Editing, Funding acquisition. ML: Investigation, Visualization, Writing—Original Draft, Writing—Review and Editing. TB: Investigation, Writing—Original Draft. SR: Investigation, Data Curation, Writing—Review and Editing. RN: Data Curation, Writing—Review and Editing. AS-S: Investigation, Writing—Review and Editing. SO: Writing—Review and Editing. GB: Resources, Funding acquisition, Supervision. All authors contributed to the article and approved the submitted version.

Funding

This study was partly funded by the Svalbard Science Forum (SSF) via an Arctic Field Grant 2021 (RCN #322189) and The Research Council of Norway (RCN) through the CLIMAGAS project (RCN #294764), the Norwegian CCS Research Centre (NCCS; industry partners and RCN #257579) and the Research Centre for Arctic Petroleum Exploration (ARCEx; industry partners and RCN #228107).

Acknowledgments

We sincerely thank Norbit Subsea for lending us an excellent multibeam system for the GASGEM2021 cruise. We thank the crew and chief scientist Dr. Susan Mau for their support in enabling and conducting hydroacoustic water column mapping during R/V Heincke cruise HE449. Depth data from the Mapping Authority sea division, reproduced with permission no. 13/G706, provided by the Norwegian Hydrographic Service. We also acknowledge the Czech Arctic Research Station and the crew of RV Clione for their assistance during the GASGEM2021 cruise. Finally, we sincerely appreciate the constructive feedback provided by Shyam Chand and Pavel Serov, as well as the excellent editorial handling by Jochen Knies.

Conflict of interest

The authors declare that the research was conducted in the absence of any commercial or financial relationships that could be construed as a potential conflict of interest.

Publisher's note

Supplementary material

The Supplementary Material for this article can be found online at: https://www.frontiersin.org/articles/10.3389/feart.2023.1173477/full#supplementary-material

References

Abay, T. B., Karlsen, D. A., Lerch, B., Olaussen, S., Pedersen, J. H., and Backer-Owe, K. (2017). Migrated petroleum in outcropping mesozoic sedimentary rocks in spitsbergen: Organic geochemical characterization and implications for regional exploration. *J. Pet. Geol.* 40, 5–36. doi:10.1111/jpg.12662

Abay, T. B., Karlsen, D. A., Pedersen, J. H., Olaussen, S., and Backer-Owe, K. (2018). Thermal maturity, hydrocarbon potential and kerogen type of some triassic-lower cretaceous sediments from the SW Barents Sea and Svalbard. *Pet. Geosci.* 24, 349–373. doi:10.1144/petgeo2017-035

Anell, I., Braathen, A., and Olaussen, S. (2014). The triassic – early jurassic of the northern Barents shelf: A regional understanding of the longyearbyen CO2 reservoir. *Nor. J. Geol.* Available at: https://www.duo.uio.no/handle/10852/62025 94, 83–98.

Austegard, A., Baturin, D., Eiken, O., Faleide, J. I., Thor, S., Peter, G., et al. (1994). *Seismic Atlas of Western Svalbard. selection of regional seismic transects*. Oslo.

Bælum, K., and Braathen, A. (2012). Along-strike changes in fault array and rift basin geometry of the Carboniferous Billefjorden Trough, Svalbard, Norway. *Tectonophysics* 546–547, 38–55. doi:10.1016/j.tecto.2012.04.009

Batchelor, C. L., Dowdeswell, J. A., Rignot, E., and Millan, R. (2019). Submarine moraines in southeast Greenland fjords reveal contrasting outlet-glacier behavior since the last glacial maximum. *Geophys Res. Lett.* 46, 3279–3286. doi:10.1029/2019GL082556

Betlem, P., Roy, S., Birchall, T., Hodson, A., Noormets, R., Römer, M., et al. (2021). Modelling of the gas hydrate potential in Svalbard's fjords. *J. Nat. Gas. Sci. Eng.* 94, 104127. doi:10.1016/j.jngse.2021.104127

Birchall, T., Jochmann, M., Betlem, P., Senger, K., and Olaussen, S. (2021). Permafrost trapped natural gas in svalbard, Norway. *Cryosphere Discuss*. doi:10.5194/tc-2021-226

Blinova, M., Inge Faleide, J., Gabrielsen, R. H., and Mjelde, R. (2012). Seafloor expression and shallow structure of a fold-and-thrust system, Isfjorden, west Spitsbergen. *Polar Res.* 31, 11209. doi:10.3402/polar.v31i0.11209

Blumenberg, M., Lutz, R., Schlömer, S., Krüger, M., Scheeder, G., Berglar, K., et al. (2016). Hydrocarbons from near-surface sediments of the Barents Sea north of Svalbard - indication of subsurface hydrocarbon generation? *Mar. Pet. Geol.* 76, 432–443. doi:10.1016/j.marpetgeo.2016.05.031

Blumenberg, M., Weniger, P., Kus, J., Scheeder, G., Piepjohn, K., Zindler, M., et al. (2018). Geochemistry of a middle Devonian cannel coal (Munindalen) in comparison with Carboniferous coals from Svalbard. *arktos* 4, 1–8. doi:10.1007/s41063-018-0038-y

Braathen, A., Bælum, K., Christiansen, H. H., Dahl, T., Eiken, O., Elvebakk, H., et al. (2012). The longyearbyen CO2 lab of svalbard, Norway—Initial assessment of the geological conditions for CO2 sequestration. *Nor. J. Geol.* Available at: https://d1wqtxts1xzle7.cloudfront.net/33078163/Braathen_et_al_2012_%28CO2%29.pdf?1393332456=&response-content-disposition=inline%3B+filename%3DBraathen_et_al_2012_CO2_sequestration.pdf&Expires=1686585036&Signature=hSCoxonW2pnEgNSQAOAMEbKVw~qiPFpXX65jtHc63EqRoPBPR7CCir-aGdidIZGlHP1tH1c-2WbhVDDnxsN3FXYB8tqbaS~RE~2CU8Tc5r9rtKCSc4Hp9w12EVZDiuEXj85WfHLnD50Fh0sLoFENXLT1gXOl3qaTFNtZvPowJ0V6PZC~0V5Vsm7qEAoXA8o9aizOOCibjCbxhbv~VoDHQdscDButHkVrDEeNV~Ekfxif6tKcQogpxvsN~0dAsP-zQoSB78u8KMOxv3PuGnX7J50lpzIG83Dn0Qxc2SqazC7Cc6~u-nGGN-~rpgMj5mFfZCAzOQGEUADA7bHFdud6uA__&Key-Pair-Id=APKAJLOHF5GGSLRBV4ZA 92, 353–376.

Bünz, S., Polyanov, S., Vadakkepuliyambatta, S., Consolaro, C., and Mienert, J. (2012). Active gas venting through hydrate-bearing sediments on the Vestnesa Ridge, offshore W-Svalbard. *Mar. Geol.* 332–334, 189–197. doi:10.1016/j.margeo.2012.09.012

Dallmann, W. K. (2015). *Geoscience atlas of svalbard*. Norsk Polarinstitutt.

Damm, E., Ericson, Y., and Falck, E. (2021). Waterside convection and stratification control methane spreading in supersaturated Arctic fjords (Spitsbergen). *Cont. Shelf Res.* 224, 104473. doi:10.1016/j.csr.2021.104473

Forster, P., Ramaswamy, V., Artaxo, P., Berntsen, T., Betts, R., Fahley, D. W., et al. (2007). "Changes in atmospheric constituents and in radiative forcing," in *Climate change 2007: The physical science basis. Contribution of working group I to the 4th assessment report of the intergovernmental panel on climate change* (Cambridge).

Forwick, M., Baeten, N., and Vorren, T. (2009). Pockmarks in spitsbergen fjords. *Nor. J. Geology/Norsk Geol. Forening* 89, 65–77. doi:10.1016/j.palaeo.2009.06.026

Gentz, T., Damm, E., Schneider von Deimling, J., Mau, S., McGinnis, D. F., and Schlüter, M. (2014). A water column study of methane around gas flares located at the West Spitsbergen continental margin. *Cont. Shelf Res.* 72, 107–118. doi:10.1016/j.csr.2013.07.013

Gjelberg, J. G., and Steel, R. J. (1981). *An outline of lower-middle carboniferous sedimentation on svalbard: Effects of tectonic, climatic and sea level changes in rift basin sequences*. Available at: https://www.sciencedirect.com/science/article/pii/S0928893706800871.

Gjelberg, J., and Steel, R. J. (1995). Helvetiafjellet Formation (Barremian-Aptian), spitsbergen: Characteristics of a transgressive succession. *Nor. Pet. Soc. Spec. Publ.* 5, 571–593.

Graves, C. A., Steinle, L., Rehder, G., Niemann, H., Connelly, D. P., Lowry, D., et al. (2015). Fluxes and fate of dissolved methane released at the seafloor at the landward limit of the gas hydrate stability zone offshore Western Svalbard. *J. Geophys Res. Oceans* 120, 6185–6201. doi:10.1002/2015JC011084

Greinert, J., McGinnis, D. F., Naudts, L., Linke, P., and De Batist, M. (2010). Atmospheric methane flux from bubbling seeps: Spatially extrapolated quantification from a Black Sea shelf area. *J. Geophys Res. Oceans* 115, C01002. doi:10.1029/2009JC005381

Harland, W. B., Cutbill, J. L., Friend, P. F., Gobbett, D. J., Holliday, D. W., Maton, P. I., et al. (1974). *The Billefjorden Fault Zone, Spitsbergen the lang history of a major tectonic lineament* NORSK POLARINSTITUTT, OSLO.

Harland, W. B., Anderson, L. M., Manasrah, D., Butterfield, N. J., Challinor, A., Doubleday, P. A., et al. (1997). *The geology of svalbard* The Geological Society, London.

Hassol, S. J., Salomons, E., Zijderveld, J., and Corell, R. (2004). *Impacts of a warming arctic–arctic climate impact assessment* Cambridge University Press.

Helland-Hansen, W., and Grundvåg, S. A. (2021). The svalbard eocene-oligocene (?) central basin succession: Sedimentation patterns and controls. *Basin Res.* 33, 729–753. doi:10.1111/bre.12492

Henriksen, E., Bjørnseth, H. M., Hals, T. K., Heide, T., Kiryukhina, T., Kløvjan, O. S., et al. (2011). Chapter 17: Uplift and erosion of the greater Barents Sea: Impact on prospectivity and petroleum systems. *Geol. Soc. Mem.* 35, 271–281. doi:10.1144/M35.17

Hodson, A. J., Nowak, A., Hornum, M. T., Senger, K., Redeker, K., Christiansen, H. H., et al. (2020). Sub-permafrost methane seepage from open-system pingos in Svalbard. *Cryosphere* 14, 3829–3842. doi:10.5194/tc-14-3829-2020

Hornum, M. T., Hodson, A. J., Jessen, S. R., Bense, V., and Senger, K. (2020). Numerical modelling of permafrost spring discharge and open-system pingo formation induced by basal permafrost aggradation. *Cryosphere* 14, 4627–4651. doi:10.5194/tc-14-4627-2020

Hovland, M., and Judd, A. (1988). *Seabed pockmarks and seepages: Impact on geology, biology and the marine environment* London: Graham & Trotman. doi:10.1111/j.1749-6632.1993.tb18844.x

Huq, F., Smalley, P. C., Mørkved, P. T., Johansen, I., Yarushina, V., and Johansen, H. (2017). The Longyearbyen CO2 Lab: Fluid communication in reservoir and caprock. *Int. J. Greenh. Gas Control* 63, 59–76. doi:10.1016/j.ijggc.2017.05.005

Jakobsson, M., Mayer, L. A., Bringensparr, C., Castro, C. F., Mohammad, R., Johnson, P., et al. (2020). The international bathymetric chart of the Arctic Ocean version 4.0. *Scientific data* 7(1), 176.

Judd, A., and Hovland, M. (2007). *Seabed fluid flow: The impact on geology, biology and the marine environment* Cambridge University Press.

Kleber, G. E., Hodson, A. J., Magerl, L., Mannerfelt, E. S., Bradbury, H., Zhu, Y., et al. (2023). Groundwater springs formed during glacial retreat are a large source of methane in the high Arctic. *Nat. Geosci.* doi:10.1038/s41561-023-01210-6

Knies, J., Damm, E., Gutt, J., Mann, U., and Pinturier, L. (2004). Near-surface hydrocarbon anomalies in shelf sediments off Spitsbergen: Evidences for past seepages. *Geochem. Geophys. Geosystems* 5. doi:10.1029/2003GC000687

Knudsen, E. W. (2015). *Processing and interpretation of multichannel seismic data from van mijenfjorden*. Svalbard: University of Bergen.

Koevoets, M. J., Abay, T. B., and HammerOlaussen, S. (2016). High-resolution organic carbon-isotope stratigraphy of the middle jurassic-lower cretaceous Agardhfjellet Formation of central spitsbergen, svalbard. *Palaeogeogr. Palaeoclimatol. Palaeoecol.* 449, 266–274. doi:10.1016/j.palaeo.2016.02.029

Koevoets, M. J., Hammer, Ø., Olaussen, S., Senger, K., and Smelror, M. (2018). Integrating subsurface and outcrop data of the middle Jurassic to lower Cretaceous Agardhfjellet Formation in central Spitsbergen. *Nor. J. Geol.* 98, 1–34. doi:10.17850/njg98-4-01

Krajewski, K. P. (2008). The Botneheia Formation (middle triassic) in edgeøya and barentsøya, svalbard: Lithostratigraphy, facies, phosphogenesis, paleoenvironment. *Pol. Polar Res*. Available at: https://citeseerx.ist.psu.edu/document?repid=rep1&type=pdf&doi=8ab1828c4f15c775b9df05ab69600a31490b9a34 29, 319–364.

Leever, K. A., Gabrielsen, R. H., Faleide, J. I., and Braathen, A. (2011). A transpressional origin for the West Spitsbergen fold-and-thrust belt: Insight from analog modeling. *Tectonics* 30. doi:10.1029/2010TC002753

Ligtenberg, J. H. (2005). Detection of Fluid migration pathways in seismic data: Implications for fault seal analysis. *Basin Res.* 17, 141–153. doi:10.1111/j.1365-2117.2005.00258.x

Liira, M., Noormets, R., Sepp, H., Kekišev, O., Maddison, M., and Olaussen, S. (2019). Sediment geochemical study of hydrocarbon seeps in isfjorden and mohnbukta: A comparison between Western and eastern spitsbergen, svalbard. *Arktos* 5, 49–62. doi:10.1007/s41063-019-00067-7

Lord, G. S., Johansen, S. K., Støen, S. J., and Mørk, A. (2017). Facies development of the upper triassic succession on barentsøya, Wilhelmøya and NE spitsbergen, svalbard. *Nor. J. Geol.* 97, 33–62. doi:10.17850/njg97-1-03

Lowell, J. D. (1972). Spitsbergen tertiary orogenic belt and the spitsbergen fracture zone. *Geol. Soc. Am. Bull.* 83, 3091–3102. doi:10.1130/0016-7606(1972)83[3091:stobat]2.0.co;2

Lutz, R., Klitzke, P., Weniger, P., Blumenberg, M., Franke, D., Reinhardt, L., et al. (2021). Basin and petroleum systems modelling in the northern Norwegian Barents Sea. *Mar. Pet. Geol.* 130, 105128. doi:10.1016/j.marpetgeo.2021.105128

Maher, H. D. (2001). Manifestations of the cretaceous high arctic large igneous province in svalbard. *J. Geol.* 109, 91–104. doi:10.1086/317960

Marshall, C., Uguna, J., Large, D. J., Meredith, W., Jochmann, M., Friis, B., et al. (2015). Geochemistry and petrology of palaeocene coals from Spitzbergen - Part 2: Maturity variations and implications for local and regional burial models. *Int. J. Coal Geol.* 143, 1–10. doi:10.1016/j.coal.2015.03.013

Matysik, M., Stemmerik, L., Olaussen, S., and Brunstad, H. (2018). Diagenesis of spiculites and carbonates in a permian temperate ramp succession – tempelfjorden group, spitsbergen, arctic Norway. *Sedimentology* 65, 745–774. doi:10.1111/sed.12404

Mau, S., and Rohardt, G. (2016). *Physical oceanography during HEINCKE cruise HE449* Alfred Wegener Institute, Helmholtz Centre for Polar and Marine Research, Bremerhaven.

Mau, S., Römer, M., Torres, M. E., Bussmann, I., Pape, T., Damm, E., et al. (2017). Widespread methane seepage along the continental margin off Svalbard-from Bjørnøya to Kongsfjorden. *Sci. Rep.* 7, 42997. doi:10.1038/srep42997

Mienert, J., Vanneste, M., Bünz, S., Andreassen, K., Haflidason, H., and Sejrup, H. P. (2005). Ocean warming and gas hydrate stability on the mid-Norwegian margin at the Storegga Slide. *Mar. Pet. Geol.* 22, 233–244. doi:10.1016/j.marpetgeo.2004.10.018

Mørk, A., Knarud, R., and Worsley, D. (1982). *Depositional and diagenetic environments of the triassic and lower jurassic succession of svalbard*. Available at: https://archives.datapages.com/data/cspg_sp/data/008/008001/371_cspgsp0080371.htm.

Mørk, A., Elvebakk, G., Forsberg, A. W., Hounslow, M. W., Nakrem, H. A., Vigran, J. O., et al. (1999). The type section of the Vikinghogda formation: A new lower triassic unit in central and eastern svalbard. *Polar Res.* 18, 51–82. doi:10.1111/j.1751-8369.1999.tb00277.x

Mørk, M. B. E. (2013). Diagenesis and quartz cement distribution of low-permeability Upper Triassic-Middle Jurassic reservoir sandstones, Longyearbyen CO2 lab well site in Svalbard, Norway. *Am. Assoc. Pet. Geol. Bull.* 97, 577–596. doi:10.1306/10031211193

Nicolaisen, J. B., Elvebakk, G., Ahokas, J., Bojesen-Koefoed, J. A., Olaussen, S., Rinna, J., et al. (2019). Characterization of upper palaeozoic organic-rich units in svalbard: Implications for the petroleum systems of the Norwegian Barents shelf. *J. Pet. Geol.* 42, 59–78. doi:10.1111/jpg.12724

Nordli, Ø., Przybylak, R., Ogilvie, A. E. J., and Isaksen, K. (2014). Long-term temperature trends and variability on spitsbergen: The extended svalbard airport temperature series, 1898-2012. *Polar Res.* 33, 21349. doi:10.3402/polar.v33.21349

Norwegian Polar Institute (2016). *Geological map of svalbard (1:250000)*. [Data set].

Nøttvedt, A., Livbjerg, F., Midbøe, P. S., and Rasmussen, E. (1993). "Hydrocarbon potential of the central Spitsbergen Basin," in *Norwegian petroleum society special publications*, 333–361. doi:10.1016/B978-0-444-88943-0.50026-5

Ogata, K., Senger, K., Braathen, A., Tveranger, J., and Olaussen, S. (2014). Fracture systems and mesoscale structural patterns in the siliciclastic Mesozoic reservoir-caprock succession of the Longyearbyen CO2 Lab project: Implications for geological CO2 sequestration in Central Spitsbergen, Svalbard. *Nor. J. Geol.* Available at: https://www.researchgate.net/profile/Kei-Ogata/publication/271443183_Fracture_systems_and_mesoscale_structural_patterns_in_the_siliciclastic_Mesozoic_reservoir-caprock_succession_of_the_Longyearbyen_CO2_Lab_project_Implications_for_geological_CO2_sequestration_in_Centr/links/54c7b3100cf22d626a36e118/Fracture-systems-and-mesoscale-structural-patterns-in-the-siliciclastic-Mesozoic-reservoir-caprock-succession-of-the-Longyearbyen-CO2-Lab-project-Implications-for-geological-CO2-sequestration-in-Centr.pdf 94, 121–154.

Ohm, S. E., Larsen, L., Olaussen, S., Senger, K., Birchall, T., Demchuk, T., et al. (2019). Discovery of shale gas in organic-rich Jurassic successions, Adventdalen, central Spitsbergen, Norway. *Nor. J. Geol.* 99, 349–376. doi:10.17850/njg007

Olaussen, S., Grundvåg, S.-A., Senger, K., Anell, I., Betlem, P., Birchall, T., et al. (2022). *The svalbard carboniferous to cenozoic composite tectono-stratigraphic element*, 57. London: Geological Society. Memoirs. doi:10.1144/m57-2021-36

Panieri, G., Bünz, S., Fornari, D. J., Escartin, J., Serov, P., Jansson, P., et al. (2017). An integrated view of the methane system in the pockmarks at Vestnesa Ridge, 79°N. *Mar. Geol.* 390, 282–300. doi:10.1016/j.margeo.2017.06.006

Rismyhr, B., Bjærke, T., Olaussen, S., Mulrooney, M. J., and Senger, K. (2019). Facies, palynostratigraphy and sequence stratigraphy of the Wilhelmøya subgroup (upper triassic–middle jurassic) in western central spitsbergen, svalbard. *Nor. J. Geol.* 99, 189–218. doi:10.17850/njg001

Roy, S., Senger, K., Braathen, A., Noormets, R., Hovland, M., Olaussen, S., et al. (2014). BDNF mediated activity dependent maturation of visual Wulst following prenatal repetitive auditory stimulation at a critical developmental period in domestic chicks (*Gallus domesticus*). *Nor. Geol. Tidsskr.* 94, 99–108. doi:10.1016/j.brainresbull.2014.10.003

Roy, S., Hovland, M., Noormets, R., and Olaussen, S. (2015). Seepage in isfjorden and its tributary fjords, West Spitsbergen. *Mar. Geol.* 363, 146–159. doi:10.1016/j.margeo.2015.02.003

Roy, S., Hovland, M., and Braathen, A. (2016). Evidence of fluid seepage in Grønfjorden, Spitsbergen: Implications from an integrated acoustic study of seafloor morphology, marine sediments and tectonics. *Mar. Geol.* 380, 67–78. doi:10.1016/j.margeo.2016.07.002

Roy, S., Senger, K., Hovland, M., Römer, M., and Braathen, A. (2019). Geological controls on shallow gas distribution and seafloor seepage in an Arctic fjord of Spitsbergen, Norway. *Mar. Pet. Geol.* 107, 237–254. doi:10.1016/j.marpetgeo.2019.05.021

Sahling, H., Römer, M., Pape, T., Bergès, B., dos Santos Fereirra, C., Boelmann, J., et al. (2014). Gas emissions at the continental margin west of Svalbard: Mapping, sampling, and quantification. *Biogeosciences* 11, 6029–6046. doi:10.5194/bg-11-6029-2014

Sauer, S., Hong, W. L., Yao, H., Lepland, A., Klug, M., Eichinger, F., et al. (2021). Methane transport and sources in an Arctic deep-water cold seep offshore NW Svalbard (Vestnesa Ridge, 79°N). *Deep Sea Res.*167, 103430. doi:10.1016/j.dsr.2020.103430

Saunois, M., Stavert, R. A., Poulter, B., Bousquet, P., Canadell, J. G., Jackson, B., et al. (2020). The global methane budget 2000-2017. *Earth Syst. Sci. Data* 12, 1561–1623. doi:10.5194/essd-12-1561-2020

Schmale, O., Greinert, J., and Rehder, G. (2005). Methane emission from high-intensity marine gas seeps in the Black Sea into the atmosphere. *Geophys Res. Lett.* 32, 1–4. doi:10.1029/2004GL021138

Senger, K., and Galland, O. (2022). Stratigraphic and spatial extent of HALIP magmatism in central spitsbergen. *Geochem. Geophys. Geosyst.* 23. doi:10.1029/2021GC010300

Senger, K., Roy, S., Braathen, A., Buckley, S. J., Bælum, K., Gernigon, L., et al. (2013). Geometries of doleritic intrusions in central spitsbergen, svalbard: An integrated study of an onshore-offshore magmatic province with implications for CO2 sequestration. *Nor. J. Geol.* Available at: https://core.ac.uk/download/pdf/30908485.pdf 93, 143–166.

Senger, K., Brugmans, P., Grundvåg, S. A., Jochmann, M., Nøttvedt, A., Olaussen, S., et al. (2019). Petroleum, coal and research drilling onshore svalbard: A historical perspective. *Nor. J. Geol.* 99, 1–30. doi:10.17850/njg99-3-1

Shindell, D. T., Faluvegi, G., Koch, D. M., Schmidt, G. A., Unger, N., and Bauer, S. E. (2009). Improved attribution of climate forcing to emissions. *Sci. Rep.* 326, 716–718. doi:10.1126/science.1174760

Skogseth, R., Olivier, L. L. A., Nilsen, F., Falck, E., Fraser, N., Tverberg, V., et al. (2020). Variability and decadal trends in the Isfjorden (Svalbard) ocean climate and circulation – an indicator for climate change in the European Arctic. *Prog. Oceanogr.* 187, 102394. doi:10.1016/j.pocean.2020.102394

Smyrak-Sikora, A., Nicolaisen, J. B., Braathen, A., Johannessen, E. P., Olaussen, S., and Stemmerik, L. (2021). Impact of growth faults on mixed siliciclastic-carbonate-evaporite deposits during rift climax and reorganisation—Billefjorden Trough, svalbard, Norway. *Basin Res.* 33, 2643–2674. doi:10.1111/bre.12578

Sorento, T., Olaussen, S., and Stemmerik, L. (2020). Controls on deposition of shallow marine carbonates and evaporites – lower Permian Gipshuken Formation, central Spitsbergen, Arctic Norway. *Sedimentology* 67, 207–238. doi:10.1111/sed.12640

Steel, R. J., and Worsley, D. (1984). "Svalbard's post-caledonian strata — An atlas of sedimentational patterns and palaeogeographic evolution," in *Petroleum geology of the North European margin* (Dordrecht: Springer Netherlands), 109–135. doi:10.1007/978-94-009-5626-1_9

Stemmerik, L. (2008). "Influence of late paleozoic gondwana glaciations on the depositional evolution of the northern pangean shelf, north Greenland, svalbard, and the Barents Sea," in *Resolving the late paleozoic ice age in time and space*, 205–217.

Stocker, T. F., Qin, D., Plattner, G.-K., Tignor, M. M. B., Allen, S. K., Boschung, J., et al. (2013). *Climate change 2013: The physical science basis* Cambridge University press.

Teyssier, C., Kleinspehn, K., and Pershing, J. (1995). Analysis of fault populations in Western Spitsbergen: Implications for deformation partitioning along transform margins.

Uguna, J. O., Carr, A. D., Marshall, C., Large, D. J., Meredith, W., Jochmann, M., et al. (2017). Improving spatial predictability of petroleum resources within the central tertiary basin, spitsbergen: A geochemical and petrographic study of coals from the eastern and Western coalfields. *Int. J. Coal Geol.* 179, 278–294. doi:10.1016/j.coal.2017.06.007

Van Koeverden, J. H., Karlsen, D. A., and Backer-Owe, K. (2011). Carboniferous non-marine source rocks from spitsbergen and bjørnøya: Comparison with the Western arctic. *J. Pet. Geol.* 34(1), 53–66. doi:10.1111/j.1747-5457.2011.00493.x

Weniger, P., Blumenberg, M., and Kus, J. (2019). "Thermal maturity of Paleocene coal from Svalbard - influence of citrinite refletance suppression," in 29 th International Meeting on Organic Geochemistry (IMOG).

Wesenlund, F., Grundvåg, S. A., Engelschiøn, V. S., Thießen, O., and Pedersen, J. H. (2021). Linking facies variations, organic carbon richness and bulk bitumen content – a

case study of the organic-rich Middle Triassic shales from eastern Svalbard. *Mar. Pet. Geol.* 132, 105168. doi:10.1016/j.marpetgeo.2021.105168

Wesenlund, F., Grundvåg, S. A., Engelschiøn, V. S., Thießen, O., and Pedersen, J. H. (2022). Multi-elemental chemostratigraphy of Triassic mudstones in eastern Svalbard: Implications for source rock formation in front of the World's largest delta plain. *Depositional Rec.* 8, 718–753. doi:10.1002/dep2.182

Westbrook, G. K., Thatcher, K. E., Rohling, E. J., Piotrowski, A. M., Pälike, H., Osborne, A. H., et al. (2009). Escape of methane gas from the seabed along the West Spitsbergen continental margin. *Geophys Res. Lett.* 36. doi:10.1029/2009GL039191

Winkelmann, D., and Knies, J. (2005). Recent distribution and accumulation of organic carbon on the continental margin west off Spitsbergen. *Geochem. Geophys. Geosyst.* 6. doi:10.1029/2005GC000916

Worsley, D., Aga, O. J., Dalland, A., Elverhøi, A., and Thon, A. (1986). "Evolution of an arctic archipelago," in *The geological history of svalbard* (Stavanger, Norway: Den norske stats oljeselskap as), 121.

Worsley, D. (2008). "The post-caledonian development of svalbard and the Western Barents Sea," in *Polar research* (Norwegian Polar Institute), 298–317. doi:10.1111/j.1751-8369.2008.00085.x

frontiers | Frontiers in Earth Science

TYPE Original Research
PUBLISHED 20 July 2023
DOI 10.3389/feart.2023.1203998

OPEN ACCESS

EDITED BY
Dong Liu,
Chinese Academy of Sciences (CAS), China

REVIEWED BY
Erik Cordes,
Temple University, United States
Owen Sherwood,
Dalhousie University, Canada

*CORRESPONDENCE
Arunima Sen,
arunimas@unis.no

†PRESENT ADDRESS
Loïc N. Michel,
Animal Systematics and Diversity, Freshwater, and Oceanic Sciences Unit of Research (FOCUS), University of Liège, Liège, Belgium

RECEIVED 11 April 2023
ACCEPTED 07 July 2023
PUBLISHED 20 July 2023

CITATION
Sinner M, Hong WL, Michel LN, Vadakkepuliyambatta S, Knies J and Sen A (2023), Lack of detectable chemosynthesis at a sponge dominated subarctic methane seep.
Front. Earth Sci. 11:1203998.
doi: 10.3389/feart.2023.1203998

Lack of detectable chemosynthesis at a sponge dominated subarctic methane seep

Melina Sinner[1,2,3], Wei Li Hong[4], Loïc N. Michel[5†], Sunil Vadakkepuliyambatta[6], Jochen Knies[7,8] and Arunima Sen[9,10]*

[1]National Oceanography Center, University of Southampton, Southampton, United Kingdom, [2]Plentzia Marine Station, University of the Basque Country, Plentzia, Spain, [3]Faculty of Sciences, University of Liège, Liège, Belgium, [4]Department of Geological Sciences, Stockholm University, Stockholm, Sweden, [5]Centre national de la recherche scientifique (CNRS), Ifremer, UMR6197 BEEP (Biologie et Ecologie des Ecosystèmes marins Profonds), University Brest, Plouzané, France, [6]National Centre for Polar and Ocean Research (NCPOR), Ministry of Earth Sciences, Government of India, Vasco-da-Gama, Goa, India, [7]Geological Survey of Norway, Trondheim, Norway, [8]iC3: The Centre for ice, Cryosphere, Carbon, and Climate, The Department of Geosciences, UiT The Arctic University of Norway, Tromsø, Norway, [9]Department of Arctic Biology, The University Centre in Svalbard, Longyearbyen, Norway, [10]Department of Bioscience and Aquaculture, Nord University, Bodø, Norway

We used high-resolution imagery within a Geographic Information System (GIS), free gas and porewater analyses and animal bulk stable isotope measurements to characterize the biotic and abiotic aspects of the newly discovered Vestbrona Carbonate Field (VCF) seep site on the Norwegian shelf (63°28′N, 6° 31′E, ∿270 m water depth). Free gas was mainly composed of microbial methane. Sediment porewater sulfide concentrations were in the millimolar range and thus high enough to sustain seep chemosymbiotrophic animals. Nonetheless, the VCF lacked chemosymbiotrophic animals despite an abundance of methane-derived carbonate crusts which are formed by the same anaerobic processes that sustain chemosymbiotrophic animals at seeps. Furthermore, none of the sampled taxa, across various trophic guilds exhibited a detectable contribution of chemosynthetically fixed carbon to their diets based on bulk stable isotope values, suggesting a predominantly photosynthetic source of carbon to the VCF seep food web. We link the absence of chemosymbiotrophic animals to highly localized methane flow pathways, which may act as a "shunt-bypass" of the anaerobic oxidation of methane (AOM) and by extension sulfide generation, thus leading to sediment sulfide concentrations that are highly heterogeneous over very short lateral distances, inhibiting the successful colonization of chemosymbiotrophic animals at the VCF seep. Instead, the seep hosted diverse biological communities, consisting of heterotrophic benthic fauna, including long lived taxa, such as soft corals (e.g., *Paragorgia arborea*) and stony corals (i.e., *Desmophyllum pertusum*, formerly known as *Lophelia pertusa*). Compared to the surrounding non-seep seafloor, we measured heightened megafaunal density at the seep, which we attribute to increased habitat heterogeneity and the presence of a variety of hard substrates (i.e., methane-derived authigenic carbonates, dropstones and coral rubble), particularly since the most abundant taxa all belonged to the phylum Porifera. Compared to the surrounding non-seep seafloor, marine litter was denser within the VCF seep, which we link to the more variable local topography due to authigenic carbonates, which can rip off parts of bottom trawling nets thereby making the seep act as catchment area for marine litter.

KEYWORDS

seepage, GIS, imagery, megafauna, chemosynthesis, marine litter, benthos, sulfide

1 Introduction

One of the most striking characteristics of the deep sea (below the photic zone, ∿ −200 m) is probably how vast and barren the seafloor appears, seemingly lacking both life-sustaining habitats and life itself. Local fauna is sparse, as food is derived from low quantities of photosynthesis-based material, slowly descending through the water column (Levin and Michener, 2002; Sahling et al., 2003). On the contrary, in areas known as cold seeps, where fluids enriched with reduced compounds and hydrocarbons (predominantly sulfide and methane) escape from the geosphere into the seafloor sediment, chemosynthesis-based carbon fixation can occur, thereby sustaining unique oasis-type ecosystems which act as hotspots for geo-biosphere interactions that provide a local, deep-sea energy source in the otherwise desert-like environment (Carney, 1994; Sibuet and Olu, 1998; Cordes et al., 2010; Levin et al., 2016; Ceramicola et al., 2018). The methane emitted at cold seep fluids may be generated by the microbial transformation of organic deposits in shallow sediments (microbial) or by geological processes occurring at greater depths in the sediment (thermogenic) (Suess, 2010; 2020; Levin et al., 2016; Ceramicola et al., 2018). Both methane and the sulfide generated through its anaerobic oxidation can function as energy sources for chemosynthesis, however, sulfide is highly toxic. Therefore cold seeps usually host low-diversity, high-biomass communities, which stand in contrast to the high-diversity, low-biomass communities of the non-seep background seafloor (Sibuet and Olu, 1998; Levin, 2005).

High latitude (e.g., Arctic and subarctic) seeps have only recently been subject to detailed studies and these have revealed both higher biomass and diversity in comparison to the surrounding benthos, as well as a notable absence of typical seep associated chemosymbiotrophic species such as vestimentiferans and large bodied mollusks (Gebruk et al., 2003; Rybakova et al., 2013; Sen et al., 2018b; 2018a; 2019a; Åström et al., 2018; Vedenin et al., 2020). Instead, communities of northern latitude seeps are often dominated by extensive meadows of chemosymbiotic *Oligobrachia* frenulate siboglinids (Smirnov, 2000; 2014; Lösekann et al., 2008; Paull et al., 2015; Sen et al., 2018b; Åström et al., 2018; Vedenin et al., 2020) and moniliferans (*Sclerolinum contortum*) (Gebruk et al., 2003; Lösekann et al., 2008; Rybakova et al., 2013). These are also the only confirmed chemoautotrophic symbiont-bearing animals at all high latitude seeps and are therefore particularly important for the functioning of high latitude seep ecosystems (Sen et al., 2018b; 2018a; 2020). Factors determining their presence or absence are however still under debate. Shallow water seeps tend to host few, if any chemosymbiotrophic animals (Sibuet and Olu, 1998; Sibuet and Olu-Le Roy, 2002; Dando, 2010), however, shallow water depths are no clear indicator of whether high latitude seeps host siboglinids or not, since active seep sites in the Laptev Sea at depths as shallow as 63 m host *Oligobrachia* siboglinids, whereas active seeps of similar depths (88 m) on the Prins Karls Forland shelf (western Svalbard) do not (Åström et al., 2016; Savvichev et al., 2018; Vedenin et al., 2020). It has been hypothesized that in shallow water areas, hydrographic regimes and associated photosynthetically derived food availability plays a role; productive, Atlantic water, for example, might favor animals that feed on phytodetrital material and select against chemosymbiotic animals, whereas eutrophic, food poorer regions allow for successful colonization by the latter (Åström et al., 2022). Other than oceanographic factors, the presence or absence of siboglinids has been linked to bottom substrate (i.e., a preference for soft muddy sediments) and to the animals' need for high sulfide flux rates, and not simply high sulfide concentration (Åström et al., 2016; Sen et al., 2018a; 2019a; Vedenin et al., 2020). The interplay of oceanographic, geochemical and geophysical factors together likely determines the faunal inventories of high latitude seeps and whether or not chemosymbiotrophic animals are present.

Here, we address this question by analyzing a seep on the productive Mid-Norwegian continental shelf (63°28′N, 6°31′E), where the combined characteristics of relatively shallow water depth but yet beyond the photic zone (270 m) and high methane flux rates with free gas bubble emissions provide the perfect opportunity to explore these factors in relation to chemosymbiotrophic fauna and subsequent community composition of high latitude seeps. Due to the abundance of extensive methane-derived carbonate crusts at this site, close to the Vestbrona Volcanic province (Bugge et al., 1980), we refer to it as the Vestbrona Carbonate Field (VCF). We combined high-resolution imagery within a Geographic Information System (GIS) to characterize this newly discovered high latitude seep site. We additionally carried out free gas and porewater analyses to estimate the life stage and seepage regime of the site. Bulk stable carbon, nitrogen and sulfur isotope ratios measurements were made on opportunistically collected fauna, in order to gain insight into the role of chemosynthetically fixed carbon within the seep food web. We furthermore made semi-quantitative comparisons between the megafaunal community of the cold seep and the adjacent non-seep background area to assess the impact of the seep on local benthic community composition. The fundamental information reported here may be helpful for gaining new insights on seep ecosystems close to the photic zone in northern latitudes and generating new ecological perspectives in the context of marine conservation, sustainable management and exploration in the Norwegian Sea.

2 Methods and materials

2.1 Site location

The Vestbrona Carbonate Field (VCF) seep site is located on the mid-continental shelf of the Norwegian Sea, off the coast of Kristiansund, central Norway, at a water depth of about 270 m (63°28′N, 6°31′E; Figure 1A). In June 2020, we investigated the area with the remotely operated vehicle (ROV) Ægir 6,000 on board the R/V *G.O. Sars* (University of Bergen). Prior to seafloor inspection, free gas flares were mapped from the ship through acquisition of multibeam bathymetry and water column data using a Kongsberg EM302 system (Figure 1B). The site is characterized by massive carbonate precipitates in a generally hemipelagic environment with sediment largely composed of mud (Figure 2).

2.2 Video surveys and mosaicking of the VCF seep

A vertical, downward facing high-definition (HD) video camera mounted to the bottom of the ROV was used to map two locations

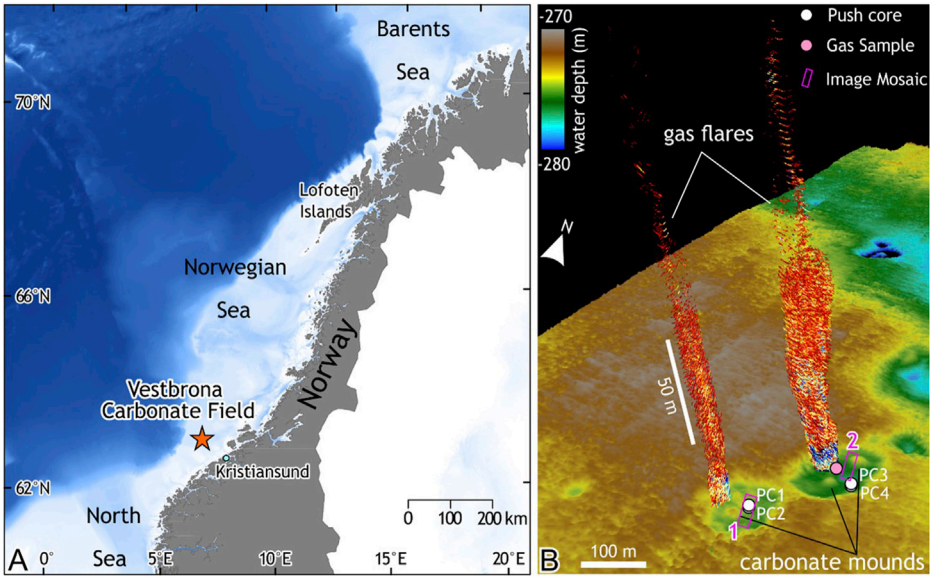

FIGURE 1
The studied Vestbrona Carbonate Field (VCF) seep site and its location. **(A)** Map of mainland Norway with the location of the VCF seep marked with a star. **(B)** Bathymetric map (in meters below sea surface) of the VCF and free gas escaping the seafloor into the water column (mapped with the ship based echosounder), ROV mosaicked areas and sampling locations are indicated. Note also carbonate mounds that are clearly visible in the bathymetric map.

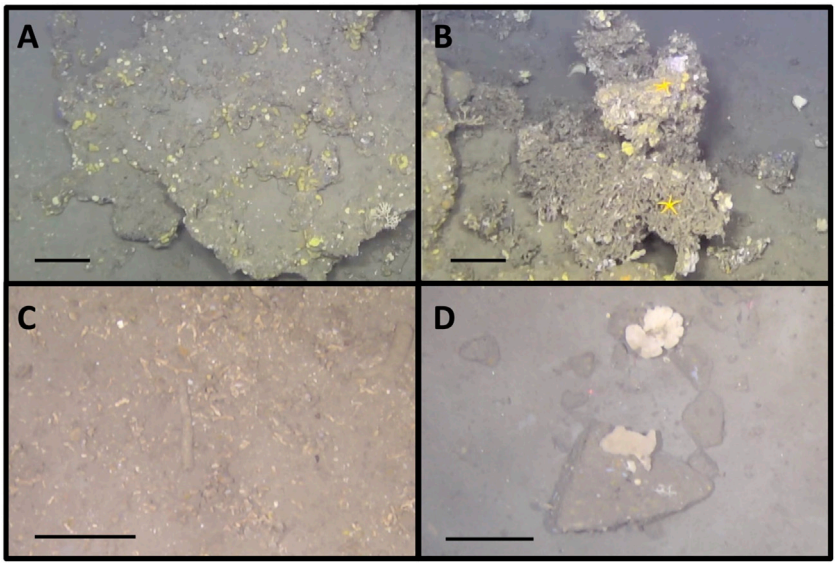

FIGURE 2
(A) Methane-derived carbonate crusts, **(B)** Dead *Desmophyllum pertusum* coral (formerly known as *Lophelia pertusa*), **(C)** Coral rubble, **(D)** Dropstones surrounded by soft sediment. Scale bars: 20 cm.

(Mosaic 1: 679 m^2 and Mosaic 2: 563 m^2) in the VCF where active seepage was observed in the form of small gas flares (bubbling) and microbial mats (Figure 1). The ROV was maintained at an altitude of 2 m above the seafloor and moved slowly at a speed of about 0.5 knots in a lawn mower fashion, to ensure overlap between video lines. Still images were extracted from the video every 2 seconds with the free software FFmpeg (http://ffmpeg.org/) and time stamps were used to obtain the corresponding navigation data from the ROV. Resulting images and navigation files were loaded into Agisoft's Metashape software (version 1.6.2 build 10247, 2020) to construct two georeferenced mosaics (Figure 3).

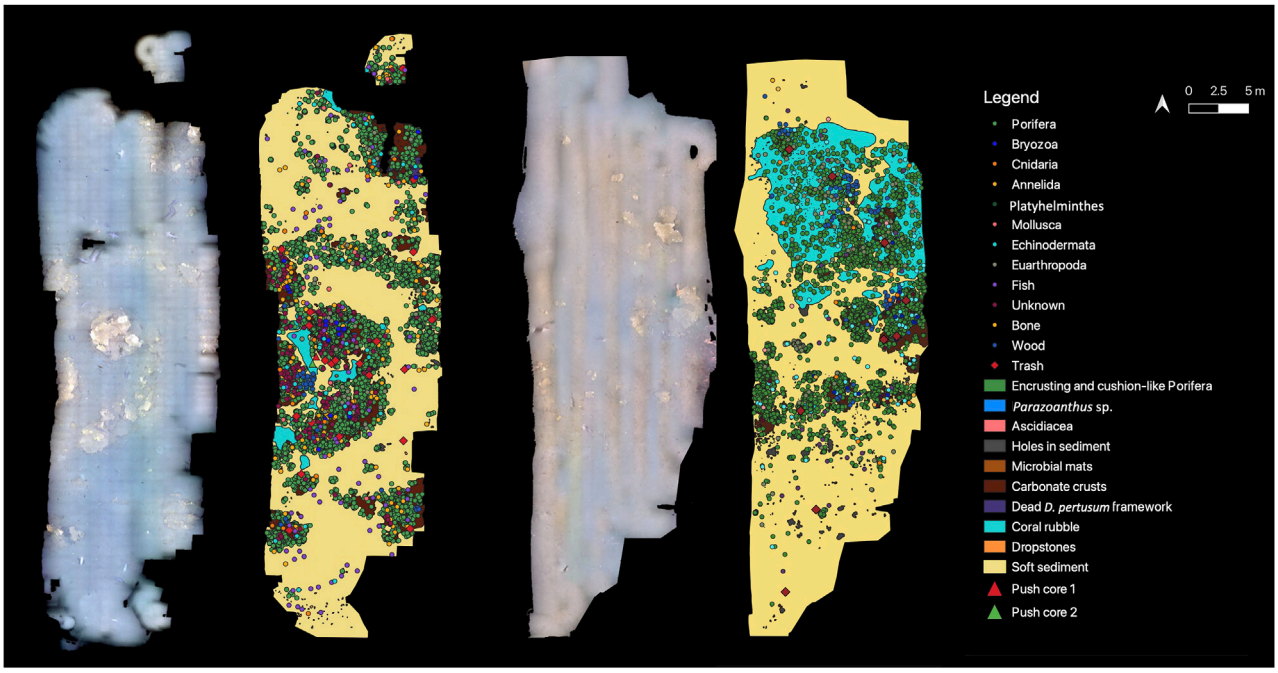

FIGURE 3
Georeferenced mosaics M1 and M2 with all visible features digitized. Note that taxa at the phylum level are presented here to enhance visualization, but numbers for individual taxa are in Table 1. Additionally all mosaic (and transect) data are published in GBIF (Sinner et al., 2023).

2.3 GIS based community characterization

All visible features (i.e., visible to the naked eye), such as animals (hereafter referred to as 'megafauna'), microbial mats, litter and substrates were manually marked in ArcGIS Pro 2.6.0 via the Editor tool in the two georeferenced mosaics (Figure 3). Individuals were marked as point feature classes, whereas colonial animals, encrusting sponges and substrates were outlined using the polygon feature class. Classification was based on visible morphology and made to the lowest possible taxonomic level. Both the size of megafauna and the resolution of seafloor images did not always allow for identification of taxa to species-level. Therefore, our faunal inventory consists of groups based on taxonomic ranks ranging from species to class. Biological features (e.g., sponges) that could not be assigned to any taxon due to high levels of morphological plasticity between and within species, were classified as "morphotypes", with some morphotypes possibly including several species. Some organisms could not be assigned to any specific phylum and were thus classified as 'Unknown'. A variety of fish were observed and marked in both mosaics. Most of them were clearly demersal and swimming rather slowly just above the seabed or appeared completely immobile which allowed for reliable quantification. However, Atlantic Cod (*Gadus morhua*) was seen swimming slightly higher in the water column and was highly motile, making it difficult to effectively enumerate. This species was thus only included in species counts, but not in the statistical analyses.

Similarly, the 5 different substrate types (carbonate crusts, soft sediment, dead *Desmophyllum pertusum*, coral rubble and dropstones; Figure 2) were at times difficult to differentiate either due to overlap (e.g., corals growing on hard substrates) or due to image quality. Identification was made as best as possible and for the most part, texture differences or angled corners were clearly visible enough to distinguish between the different substrates.

2.4 Data analyses

Densities for all taxa were calculated based on the spatial extents of the two mosaics. Colonies of individuals (i.e., Ascidiacea, small living *D. pertusum* colonies and *Parazoanthus* sp.) were considered as individuals to calculate densities. Average megafaunal density, taxa richness (S), Pielou's evenness (J), and Shannon's diversity (H) were calculated from density data for each substrate across both mosaics to obtain integral community characteristics. As the Shannon index (H) in itself does not give any information on true diversity of the community and as its entropy is highly nonlinear, the effective number of species (ENS) was additionally calculated from all Shannon indices (exp(H)) (Jost, 2006).

Density data was square root transformed to reduce the impact of highly abundant taxa (e.g., sponges) and the similarity between "hard" (i.e., carbonate crusts, dead *D. pertusum*, dropstones) and 'unconsolidated' (i.e., coral rubble, soft sediment) substrates was estimated using the Bray-Curtis index. Non-metric multidimensional scaling (nMDS) was used to reveal separate groups and results were verified through an analysis of similarity (ANOSIM). Finally, contributions of the different morphotaxa to the dissimilarity between substrates was investigated through a similarity percentage analysis (SIMPER). All data analyses and data visualizations were performed in R with the packages

"vegan" version 2.5–7 (Oksanen et al., 2022), "ggplot2" version 3.3.5 (Wickham et al., 2023), "ggpubr" version 0.4.0 (Kassambara, 2023) and "ggsci" version 2.9 (Xiao et al., 2023).

2.5 Gas and porewater analyses

Free gas was sampled with a gas sampler by the ROV near Mosaic 1. In addition, two push cores within Mosaic 1 (PC1-2) and two adjacent to Mosaic 2 (PC3-4) (see Figure 1 for locations), were taken and sampled immediately after recovery on deck. For methane (CH_4) headspace analyses in the pore water samples, holes with a diameter of 1.5 cm were drilled into the plastic liner at intervals up to 5 cm (2 cm–26 cm), starting at the sediment-water interface. It should be noted however, that only three samples could be taken for PC4 (at 2 cm and 5 cm depth) and one for PC1 (at 24 cm). Sediment plugs of 3 ml were taken using a 5 ml syringe with the luer tip removed. Each sediment sample was transferred to a 20 ml serum vial containing 2 glass beads and 6 ml NaOH (2.5%) to prevent microbial degradation. The vial was immediately closed with a septum and an aluminum crimp seal and stored at 4°C until further analyses.

Stable carbon isotopes of methane (C_1) and ethane (C_2), as well as hydrogen isotopes of methane were analysed at Hydroisotop GmbH, Germany. For the analyses an aliquot of the free and headspace gas was taken with a 10 ml gastight syringe and injected into 20 ml headspace vial filled with helium (He). In the purge&trap autosampler (MessTechnik GmbH) the content of the bottle is flushed with He and trapped 20 min on the absorption material at −120°C. After fast heating up to 200°C the gas mixture was transferred to the GC–MS – IRMS system (Thermo Fischer Scientific GmbH). The GC (Trace Ultra) separates C_1-C_4 gases from each other which were then transferred to the combustion/pyrolysis interface for conversion of hydrocarbons to CO_2 or H_2 for carbon and hydrogen stable isotope measurements using an isotope ratio mass-spectrometer (IRMS, DeltaV Advantage). The isotopic composition ($\delta^{13}C$ and $\delta^{2}H$) is reported in ‰ (δ-values) against the international standards Vienna Pee Dee Belemnite (VPDB) for carbon and Vienna Standard Mean Ocean Water (VSMOW) for hydrogen, according to the following equations:

$$\delta^{13}C_{VPDB} = \frac{(^{13}C/^{12}C)_{sample} - (^{13}C/^{12}C)_{VPDB}}{(^{13}C/^{12}C)_{VPDB}} \text{x1000 (‰)}$$

$$\delta^{2}H_{VSMOW} = \frac{(^{2}H/^{1}H)_{sample} - (^{2}H/^{1}H)_{VSMOW}}{(^{2}H/^{1}H)_{VSMOW}} \text{x1000 (‰)}$$

Porewater samples for sulfide ($\Sigma HS = H_2S + HS^- + S^{2}$) concentrations were taken at a ∿2-cm-depth resolution (2 cm–39 cm) along the length of PC1 and PC4, starting at the sediment-water interface. Porewater was extracted in a temperature-controlled room (4°C) with acid-washed rhizon samplers and syringes, and 0.5–2 ml of porewater was preserved with Zn(OAc)2 onboard (<30 min after rhizons were disconnected) for further analyses in the lab. Samples were kept frozen all the time until analyses were conducted. The concentrations of total dissolved sulfide ($\Sigma HS = H_2S + HS^- + S^{2}$) were determined by the iodometric method (US Environmental Protection Agency, method 9030 and Pawlak and Pawlak, 1999). Before the analyses, samples were centrifuged for 5–7 min at 2000 rpm to separate the ZnS precipitates from the residual porewater. The supernatant fluid was pipetted and discarded as it may contain other reductants (such as dissolved organic carbon species) that may react with I_2 and affect the results. The remaining ZnS precipitates were washed into a glass beaker with ca. 2 mL of 18Ω Milli-Q water for titration. Iodine (I_2) solution of ca. 14 mM was added (0.2 mL). Aliquots of starch solution (0.05 mL; prepared every other day) were added as an end-point indicator and 4M HCl was added to ensure a completed reduction of I_2 to $2I^-$ by lowering the sample pH with HCl (Pawlak and Pawlak, 1999). The ZnS in the sample then reduces I_2 when in contact ($ZnS + I_2 \rightarrow 2ZnI + S$). We then titrated the residual I_2 to calculate the amounts of total sulfide in the samples (i.e., $I_{2\text{-unreacted}} - I_{2\text{-residual}} = ZnS_{sample}$). Factory-made 0.00109N Na-thiosulfate (stabilized standard solution, Hach Lot# 2408949) was sequentially diluted 10 times and 100 times and used as titrants. Titrants were added to the sample with an automatic pipette under constant mixing in an open beaker until the purple color faded away as a result of complete I_2 reduction. The amounts of titrant were then recorded for the calculation of ZnS_{sample}. As I_2 is fairly unstable when exposed to light, its concentration was closely monitored every ca. 30 min during the titration to constrain $I_{2\text{-unreacted}}$. The uncertainty of the measurements was then determined from the two closest I_2 measurements before and after the titration of the actual sample. In general, the concentration of $I_{2\text{-unreacted}}$ decreased by 0.27 mM every hour. New I_2 was used during the same session of analyses if the $I_{2\text{-unreacted}}$ concentration was below 85% of its concentration earlier in the session. The Zn-acetate solution used to precipitate out total sulfide was also titrated following the identical protocol to ensure no measurable sulfide remained in it.

2.6 Animal bulk tissue and stable isotope ratio analyses

All attached fauna from two carbonate rocks collected from within Mosaic 1 were retrieved and all organisms, e.g., including sponge fragments, brittle stars, polychaete fragments (*Nephtys* sp.) and cnidarians were immediately frozen at −20°C after recovery on deck. In the lab, the recovered organisms were freeze-dried in a vacuum chamber for 24 h, then dissected to separate soft and non-metabolically active tissues (e.g., muscle, tegument) or, when body size was small, were used whole (Mateo et al., 2008). They were subsequently ground to a homogeneous powder using mortar and pestle. Samples containing hard inorganic carbon parts that could not be physically removed were acidified by exposing them to HCl vapors for 48 h in an airtight container (Hedges and Stern, 1984). Stable isotope ratio measurements were performed via continuous flow - elemental analysis - isotope ratio mass spectrometry (CF-EA-IRMS) at University of Liège (Belgium), using a vario MICRO cube C-N-S elemental analyzer (Elementar Analysensysteme GMBH, Hanau, Germany) coupled to an IsoPrime100 isotope ratio mass spectrometer (Isoprime, Cheadle, United Kingdom). Isotopic ratios were expressed using the widespread δ notation (Coplen, 2011), in ‰ and relative to the international references Vienna Pee Dee Belemnite (for carbon), atmospheric air (for nitrogen) and Vienna

TABLE 1 Community, substrate, and litter observed and marked in the two georeferenced mosaics of the VCF seep (M1 and M2) and transects of the surrounding background area (T1 and T2). For each mosaic/transect, total numbers of individuals/polygons, densities of individuals/polygons and percent cover of polygons with respect to the entire mosaic/transect are listed, first, at the phylum level (in bold), and then for each individual taxon. Density of individuals and polygons are calculated as per square meter, based on the total area of the mosaic/transects (see first entry in the table). Colonial taxa are marked with +. This data are also publicly available at GBIF (Sinner et al., 2023) https://doi.org/10.15468/5vrbbj.

	Number of individuals/polygons					Density of individuals/polygons					% Cover of polygons				
Phylum/Category															
Morphospecies	M1	M2	T1	T2	T3	M1	M2	T1	T2	T3	M1	M2	T1	T2	T3
Total area (m^2)	**679.09**	**562.97**	**129.87**	**58.06**	**87.36**										
Porifera	**19824**	**10897**	**5**	**2**	**4**	**29.19**	**19.36**	**0.04**	**0.04**	**0.05**	**1.00**	**0.54**	**0.00**	**0.00**	**0.00**
Foliaceous (white, cream) [*Phakellia* sp., *Axinella* sp.]	474	544	0	0	0	0.70	0.97	0.00	0.00	0.00	n/a	n/a	n/a	n/a	n/a
Branching foliaceous (white, cream)	144	21	0	0	0	0.21	0.04	0.00	0.00	0.00	n/a	n/a	n/a	n/a	n/a
Branching finger-shaped (white, cream) [*Antho dichotoma*]	0	1	0	0	0	0.00	0.00	0.00	0.00	0.00	n/a	n/a	n/a	n/a	n/a
Arborescent (white, cream)	7	6	0	0	0	0.01	0.01	0.00	0.00	0.00	n/a	n/a	n/a	n/a	n/a
Glass sponge	1	1	0	0	0	0.00	0.00	0.00	0.00	0.00	n/a	n/a	n/a	n/a	n/a
Spherical (white with brown hairy texture)	19	7	0	0	0	0.03	0.01	0.00	0.00	0.00	n/a	n/a	n/a	n/a	n/a
Globular/irregular (white, cream) [*Geodia* sp., *Mycale* sp.]	5784	3023	3	0	2	8.52	5.37	0.02	0.00	0.02	n/a	n/a	n/a	n/a	n/a
Large irregular (white and brown) [*Geodia* sp.]	22	2	0	0	0	0.03	0.00	0.00	0.00	0.00	n/a	n/a	n/a	n/a	n/a
Large bulby (white)	7	0	0	0	0	0.01	0.00	0.00	0.00	0.00	n/a	n/a	n/a	n/a	n/a
Globular (yellow)	0	0	2	0	2	0.00	0.00	0.02	0.00	0.02	n/a	n/a	n/a	n/a	n/a
Fistular (white, cream)	0	0	0	2	0	0.00	0.00	0.00	0.03	0.00	n/a	n/a	n/a	n/a	n/a
Encrusting (yellow/orange) [*Amphilectus* sp.]	756	1568	0	0	0	1.11	2.79	0.00	0.00	0.00	0.03	0.07	0.00	0.00	0.00
Encrusting (white) [*Stryphnus* sp.]	67	28	0	0	0	0.10	0.05	0.00	0.00	0.00	0.08	0.04	0.00	0.00	0.00
Encrusting (yellow) [*Aplysilla* sp.]	261	105	0	0	0	0.38	0.19	0.00	0.00	0.00	0.17	0.12	0.00	0.00	0.00
Encrusting (orange) [*Hymedesmia* sp.]	2064	1948	0	0	0	3.04	3.46	0.00	0.00	0.00	0.10	0.09	0.00	0.00	0.00
Encrusting (blue) [*Hymedesmia* sp.]	674	313	0	0	0	0.99	0.56	0.00	0.00	0.00	0.05	0.01	0.00	0.00	0.00
Cushion-like (orange) [*Suberites* sp.]	9544	3330	0	0	0	14.05	5.91	0.00	0.00	0.00	0.57	0.21	0.00	0.00	0.00
Bryozoa	**33**	**17**	**0**	**0**	**0**	**0.05**	**0.03**	**0.00**	**0.00**	**0.00**	**n/a**	**n/a**	**n/a**	**n/a**	**n/a**
Unknown species	33	17	0	0	0	0.05	0.03	0.00	0.00	0.00	n/a	n/a	n/a	n/a	n/a
Cnidaria	**76**	**57**	**3**	**0**	**2**	**0.11**	**0.10**	**0.02**	**0.00**	**0.02**	**0.18**	**0.21**	**0.00**	**0.00**	**0.00**
Bolocera sp.	4	2	0	0	0	0.01	0.00	0.00	0.00	0.00	n/a	n/a	n/a	n/a	n/a
Cerianthus sp.	10	9	3	0	2	0.01	0.02	0.02	0.00	0.02	n/a	n/a	n/a	n/a	n/a
Gorgonia sp.	2	0	0	0	0	0.00	0.00	0.00	0.00	0.00	n/a	n/a	n/a	n/a	n/a
Paragorgia arborea	3	1	0	0	0	0.00	0.00	0.00	0.00	0.00	n/a	n/a	n/a	n/a	n/a

(Continued on following page)

TABLE 1 (*Continued*) Community, substrate, and litter observed and marked in the two georeferenced mosaics of the VCF seep (M1 and M2) and transects of the surrounding background area (T1 and T2). For each mosaic/transect, total numbers of individuals/polygons, densities of individuals/polygons and percent cover of polygons with respect to the entire mosaic/transect are listed, first, at the phylum level (in bold), and then for each individual taxon. Density of individuals and polygons are calculated as per square meter, based on the total area of the mosaic/transects (see first entry in the table). Colonial taxa are marked with +. This data are also publicly available at GBIF (Sinner et al., 2023) https://doi.org/10.15468/5vrbbj.

	Number of individuals/polygons					Density of individuals/polygons					% Cover of polygons				
Paramuricea placomus	1	0	0	0	0	0.00	0.00	0.00	0.00	0.00	n/a	n/a	n/a	n/a	n/a
Primnoa resedaeformis	1	0	0	0	0	0.00	0.00	0.00	0.00	0.00	n/a	n/a	n/a	n/a	n/a
Parazoanthus sp. +	53	45	0	0	0	0.08	0.08	0.00	0.00	0.00	0.17	0.21	0.00	0.00	0.00
Desmophyllum pertusum	2	0	0	0	0	0.00	0.00	0.00	0.00	0.00	0.01	0.00	0.00	0.00	0.00
Annelida	**159**	**51**	**0**	**0**	**0**	**0.23**	**0.09**	**0.00**	**0.00**	**0.00**	**n/a**	**n/a**	**n/a**	**n/a**	**n/a**
Serpulidae	21	5	0	0	0	0.03	0.01	0.00	0.00	0.00	n/a	n/a	n/a	n/a	n/a
Sabellidae	15	2	0	0	0	0.02	0.00	0.00	0.00	0.00	n/a	n/a	n/a	n/a	n/a
Echiuridae	123	44	0	0	0	0.18	0.08	0.00	0.00	0.00	n/a	n/a	n/a	n/a	n/a
Platyhelminthes	**1**	**0**	**0**	**0**	**0**	**0.00**	**0.00**	**0.00**	**0.00**	**0.00**	**n/a**	**n/a**	**n/a**	**n/a**	**n/a**
Unknown species	1	0	0	0	0	0.00	0.00	0.00	0.00	0.00	n/a	n/a	n/a	n/a	n/a
Mollusca	**12**	**6**	**0**	**0**	**1**	**0.02**	**0.01**	**0.00**	**0.00**	**0.01**	**n/a**	**n/a**	**n/a**	**n/a**	**n/a**
Unknown species	12	6	0	0	1	0.02	0.01	0.00	0.00	0.01	n/a	n/a	n/a	n/a	n/a
Echinodermata	**49**	**23**	**5**	**6**	**6**	**0.07**	**0.04**	**0.04**	**0.10**	**0.07**	**n/a**	**n/a**	**n/a**	**n/a**	**n/a**
Ceramaster granularis	2	0	0	0	0	0.00	0.00	0.00	0.00	0.00	n/a	n/a	n/a	n/a	n/a
Henricia sp.	31	20	0	0	0	0.05	0.04	0.00	0.00	0.00	n/a	n/a	n/a	n/a	n/a
Cidaris cidaris	1	3	0	0	0	0.00	0.01	0.00	0.00	0.00	n/a	n/a	n/a	n/a	n/a
Echinus sp.	4	0	0	0	0	0.01	0.00	0.00	0.00	0.00	n/a	n/a	n/a	n/a	n/a
Spatangoida sp.	1	0	0	0	0	0.00	0.00	0.00	0.00	0.00	n/a	n/a	n/a	n/a	n/a
Crinoidea	2	0	0	0	0	0.00	0.00	0.00	0.00	0.00	n/a	n/a	n/a	n/a	n/a
Ophiuroidea	7	0	0	0	0	0.01	0.00	0.00	0.00	0.00	n/a	n/a	n/a	n/a	n/a
Stichopus tremulus	1	0	5	6	6	0.00	0.00	0.04	0.10	0.07	n/a	n/a	n/a	n/a	n/a
Euarthropoda	**52**	**142**	**2**	**0**	**0**	**0.08**	**0.25**	**0.02**	**0.00**	**0.00**	**n/a**	**n/a**	**n/a**	**n/a**	**n/a**
Paguridae	0	8	2	0	0	0.00	0.01	0.02	0.00	0.00	n/a	n/a	n/a	n/a	n/a
Munida sp.	52	134	0	0	0	0.08	0.24	0.00	0.00	0.00	n/a	n/a	n/a	n/a	n/a
Chordata	**119**	**49**	**2**	**2**	**0**	**0.18**	**0.09**	**0.02**	**0.03**	**0.00**	**0.01**	**0.01**	**0.00**	**0.00**	**0.00**
Unknown fish species	0	0	0	1	0	0.00	0.00	0.00	0.02	0.00	n/a	n/a	n/a	n/a	n/a
Gadus morhua	45	1	0	0	0	0.07	0.00	0.00	0.00	0.00	n/a	n/a	n/a	n/a	n/a
Brosme brosme	13	1	0	0	0	0.02	0.00	0.00	0.00	0.00	n/a	n/a	n/a	n/a	n/a
Molva molva	31	15	0	1	0	0.05	0.03	0.00	0.02	0.00	n/a	n/a	n/a	n/a	n/a
Helicolenus dactylopterus	4	7	0	0	0	0.01	0.01	0.00	0.00	0.00	n/a	n/a	n/a	n/a	n/a
Sebastes viviparus	0	1	0	0	0	0.00	0.00	0.00	0.00	0.00	n/a	n/a	n/a	n/a	n/a
Trisopterus esmarkii	0	0	1	0	0	0.00	0.00	0.01	0.00	0.00	n/a	n/a	n/a	n/a	n/a
Merluccius merluccius	0	0	1	0	0	0.00	0.00	0.01	0.00	0.00	n/a	n/a	n/a	n/a	n/a
Ascidiacea +	26	24	0	0	0	0.04	0.04	0.00	0.00	0.00	0.01	0.01	0.00	0.00	0.00
Unknown	**263**	**11**	**0**	**0**	**1**	**0.39**	**0.02**	**0.00**	**0.00**	**0.01**	**n/a**	**n/a**	**n/a**	**n/a**	**n/a**
Round blob (white/blue)	7	0	0	0	0	0.01	0.00	0.00	0.00	0.00	n/a	n/a	n/a	n/a	n/a
Fan animal	253	11	0	0	0	0.37	0.02	0.00	0.00	0.00	n/a	n/a	n/a	n/a	n/a

(Continued on following page)

TABLE 1 (*Continued*) Community, substrate, and litter observed and marked in the two georeferenced mosaics of the VCF seep (M1 and M2) and transects of the surrounding background area (T1 and T2). For each mosaic/transect, total numbers of individuals/polygons, densities of individuals/polygons and percent cover of polygons with respect to the entire mosaic/transect are listed, first, at the phylum level (in bold), and then for each individual taxon. Density of individuals and polygons are calculated as per square meter, based on the total area of the mosaic/transects (see first entry in the table). Colonial taxa are marked with +. This data are also publicly available at GBIF (Sinner et al., 2023) https://doi.org/10.15468/5vrbbj.

	Number of individuals/polygons					Density of individuals/polygons					% Cover of polygons				
Filter feeder	3	0	0	0	0	0.00	0.00	0.00	0.00	0.00	n/a	n/a	n/a	n/a	n/a
Circular structure	0	0	0	0	1	0.00	0.00	0.00	0.00	0.01	n/a	n/a	n/a	n/a	n/a
Archaea/Bacteria	**225**	**34**	**0**	**0**	**0**	**0.33**	**0.06**	**0.00**	**0.00**	**0.00**	**0.02**	**0.01**	**0.00**	**0.00**	**0.00**
Bacterial mats +	225	34	0	0	0	0.33	0.06	0.00	0.00	0.00	0.02	0.01	0.00	0.00	0.00
Total	**20,813**	**11,287**	**17**	**10**	**14**	**30.65**	**20.05**	**0.13**	**0.17**	**0.16**	**n/a**	**n/a**	**n/a**	**n/a**	**n/a**
Non-living															
Wood	40	81	0	0	0	0.06	0.14	0.00	0.00	0.00	n/a	n/a	n/a	n/a	n/a
Bone	0	1	0	0	0	0.00	0.00	0.00	0.00	0.00	n/a	n/a	n/a	n/a	n/a
Holes in sediment	14	29	1	1	1	0.02	0.05	0.01	0.02	0.01	0.22	0.67	0.00	0.00	0.00
Large burrows	0	0	6	2	2	0.00	0.00	0.05	0.03	0.02	n/a	n/a	n/a	n/a	n/a
Circular depression	0	0	6	1	4	0.00	0.00	0.05	0.02	0.05	n/a	n/a	n/a	n/a	n/a
Total	**54**	**111**	**13**	**4**	**7**	**0.08**	**0.20**	**0.10**	**0.07**	**0.08**	**n/a**	**n/a**	**n/a**	**n/a**	**n/a**
Trash															
Plastic	2	0	0	0	0	0.00	0.00	0.00	0.00	0.00	n/a	n/a	n/a	n/a	n/a
Fabric	2	0	0	0	0	0.00	0.00	0.00	0.00	0.00	n/a	n/a	n/a	n/a	n/a
Carton	1	0	0	1	0	0.00	0.00	0.00	0.02	0.00	n/a	n/a	n/a	n/a	n/a
Paper	0	0	0	0	1	0.00	0.00	0.00	0.00	0.01	n/a	n/a	n/a	n/a	n/a
Metal can	5	0	0	0	0	0.01	0.00	0.00	0.00	0.00	n/a	n/a	n/a	n/a	n/a
Glass bottle	0	1	0	0	0	0.00	0.00	0.00	0.00	0.00	n/a	n/a	n/a	n/a	n/a
Fishing net	7	5	0	0	0	0.01	0.01	0.00	0.00	0.00	n/a	n/a	n/a	n/a	n/a
Nylon fishing line	0	1	0	0	0	0.00	0.00	0.00	0.00	0.00	n/a	n/a	n/a	n/a	n/a
Anchor	0	1	0	0	0	0.00	0.00	0.00	0.00	0.00	n/a	n/a	n/a	n/a	n/a
Unidentifiable	18	1	0	0	0	0.03	0.00	0.00	0.00	0.00	n/a	n/a	n/a	n/a	n/a
Total	**35**	**9**	**0**	**1**	**1**	**0.05**	**0.02**	**0.00**	**0.02**	**0.01**	**n/a**	**n/a**	**n/a**	**n/a**	**n/a**
Substrates															
Carbonate crusts +	247	392	0	0	0	n/a	n/a	n/a	n/a	n/a	27.11	12.15	0.00	0.00	0.00
Dead *D. pertusum* +	9	0	0	0	0	n/a	n/a	n/a	n/a	n/a	0.63	0.00	0.00	0.00	0.00
Coral rubble +	10	11	0	0	0	n/a	n/a	n/a	n/a	n/a	2.55	21.61	0.00	0.00	0.00
Soft sediment +	22	10	0	0	0	n/a	n/a	n/a	n/a	n/a	69.39	65.50	0.00	0.00	0.00
Dropstones +	156	9	0	0	0	n/a	n/a	n/a	n/a	n/a	0.38	0.07	0.00	0.00	0.00
Total	**444**	**422**	**0**	**0**	**0**	**n/a**	**n/a**	**n/a**	**n/a**	**n/a**	**100.06**	**99.33**	**0.00**	**0.00**	**0.00**

Canyon Diablo Troilite (for sulfur). IAEA (International Atomic Energy Agency, Vienna, Austria) certified reference materials sucrose (IAEA-C-6; $\delta^{13}C$ = −10.8 ± 0.5‰; mean ± SD), ammonium sulfate (IAEA-N-2; $\delta^{15}N$ = 20.3 ± 0.2‰; mean ± SD) and silver sulfide (IAEA-S-1; $\delta^{34}S$ = −0.3‰) were used as primary analytical standards. Sulfanilic acid (Sigma-Aldrich; $\delta^{13}C$ = −25.6 ± 0.4‰; $\delta^{15}N$ = −0.13 ± 0.4‰; $\delta^{34}S$ = 5.9 ± 0.5‰; means ± SD) was used as secondary analytical standard. Standard deviations on multi-batch replicate measurements of secondary and internal lab standards (amphipod crustacean muscle) analyzed interspersed with samples (one replicate of each standard every 15 analyses) were 0.2‰ for both $\delta^{13}C$ and $\delta^{15}N$ and 0.3‰ for $\delta^{34}S$.

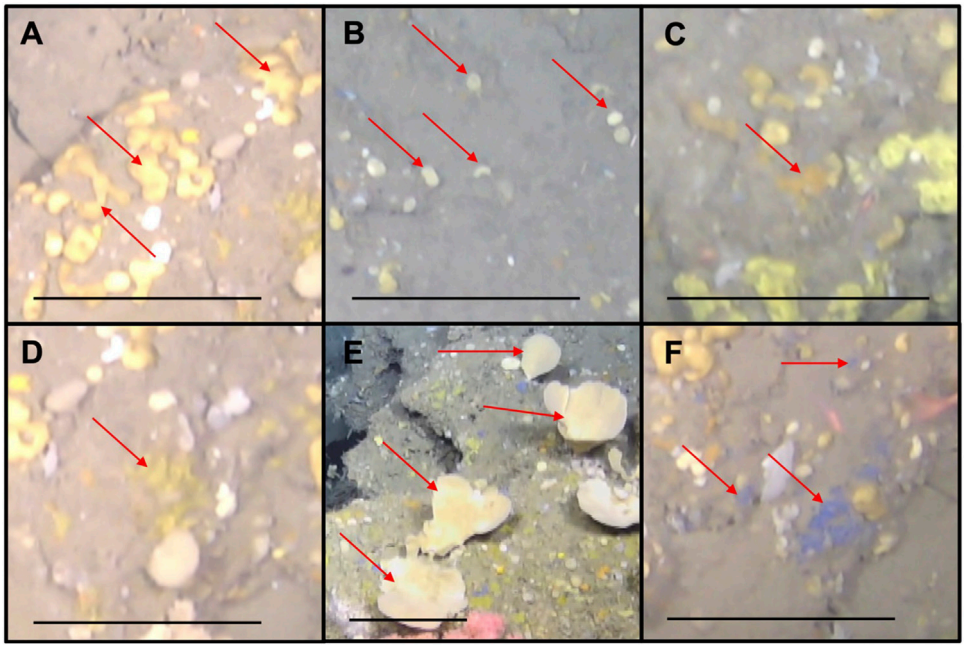

FIGURE 4
Porifera morphotaxa that constituted the majority of all marked individuals in both mosaics. **(A)** *Suberites* sp. (cushion-like orange sponge); **(B)** *Geodia* sp. and *Mycale* sp. (globular/irregular white/cream colored sponge); **(C)** *Hymedesmia* sp. (encrusting orange sponge); **(D)** *Amphilectus* sp. (encrusting yellow/orange sponge); **(E)** *Phakellia* sp. and *Axinella* sp. (foliaceous white/cream colored sponge); **(F)** *Amphilectus* sp. (encrusting blue sponge). Scale bars: 20 cm.

2.7 Background megabenthos community characterization

Three video transects of the non-seep background area were extracted from the ROV video surveys of the surrounding background area. These videos were taken with a forward-facing and slightly downward tilted camera and since this camera setup does not allow for precise areal measurements to be made, georeferenced mosaics could not be constructed in the same manner as within the seep area. Nonetheless, time stamps were used to obtain the corresponding navigation data from the ROV which allowed for approximate areas of the seafloor covered by the transects to be calculated. All visible features (biological and non-biological, as in the two georeferenced mosaics) were counted within each transect and converted to densities based on the approximate area calculations. Diversity indices were then calculated for comparisons with the seep mosaics.

3 Results

3.1 Overall seep community composition

In total, 20,813 individuals/colonies of individuals were enumerated in Mosaic 1 (30.65 ind./m^2) and 11,287 in Mosaic 2 (20.05 ind./m^2) (Table 1; Figure 3). Forty-nine taxa (i.e., species, genus, family, class, and 'morphotypes', including microbial mats) across 9 phyla were identified within the two mosaics: Porifera, Bryozoa, Cnidaria, Annelida, Platyhelminthes, Mollusca, Echinodermata, Arthropoda and Chordata. These, however, are likely underestimates due to the difficulty of identifying fauna from images, the possible presence of cryptic species and some morphotypes possibly including several species. Therefore, the total taxonomic richness of the mosaics is likely higher than the 49 taxa shown in Table 1. The majority of all marked individuals (M1: 95%; M2: 97%) belonged to the phylum Porifera and included most importantly cushion-like orange sponges (possibly of the genus *Suberites*), globular/irregular white/cream colored sponges (possibly of the genera *Geodia* and *Mycale*), encrusting orange sponges (possibly of the genus *Hymedesmia*), encrusting yellow/orange sponges (possibly of the genus *Amphilectus*) and foliaceous white/cream colored sponges (possibly of the genera *Phakellia* and *Axinella*) (Figure 4). All remaining morphotaxa (i.e., not belonging to the phylum Porifera) together, only accounted for 5% or less of all marked individuals in both mosaics. Sponges were thus by far the most dominant members of the megafaunal community at the VCF seep. Furthermore, besides being extremely abundant, many sponges also displayed considerable sizes and very diverse three-dimensional morphologies (e.g., *Phakellia* sp., *Axinella* sp., *Geodia* sp., glass sponge, Figure 5). Following sponges, the next most numerous taxa were unidentifiable 'fan' animals (possibly bryozoans), *Munida* squat lobsters, Echiurids and *Parazoanthus* polyps (Figure 6). Among the various taxa identified in the mosaicked area, several also hold commercial value, such as Atlantic cod (*G. morhua*), common ling (*Molva molva*) and tusk (*Brosme brosme*) (Kvangarsnes et al., 2012; Helle et al., 2015; Norwegian Directorate of Fisheries, 2020). Despite this being a seep site, microbial mats appeared rather small (in the range of

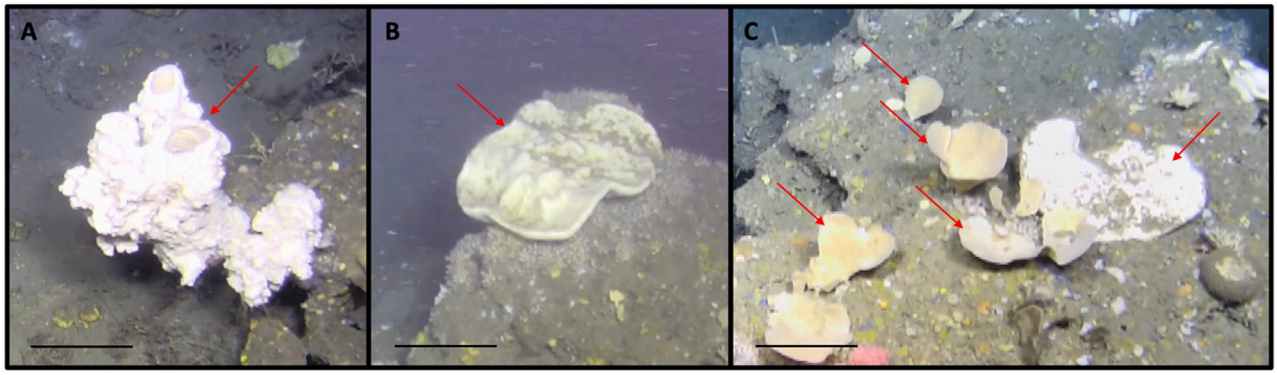

FIGURE 5
Porifera morphotaxa that displayed considerable sizes and diverse three-dimensional morphologies. **(A)** Glass sponge of unknown genus; **(B)** *Geodia* sp. (large irregular white and brown colored sponge); **(C)** arrows pointing towards the right: *Phakellia* sp. and *Axinella* sp. (foliaceous white/cream colored sponge), arrow pointing towards the left: *Geodia* sp. (large irregular white and brown colored sponge). Scale bars: 20 cm.

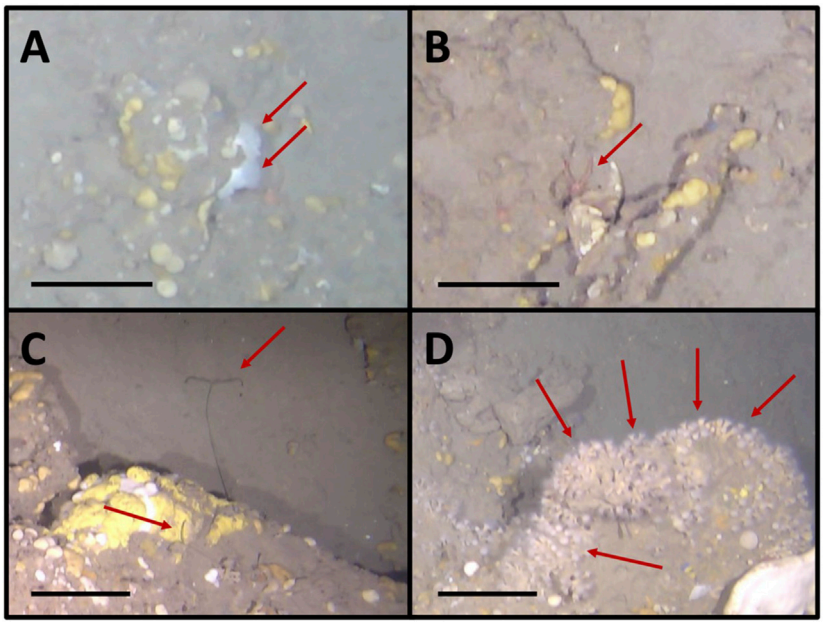

FIGURE 6
Examples of the most abundant taxa after sponges **(A)** 'fan' animals (possibly bryozoans), **(B)** *Munida* squat lobsters, **(C)** Echiurids and **(D)** *Parazoanthus* polyps. Scale bars: 20 cm.

several cm at the most) and no visible chemosynthesis-based animals such as siboglinid polychaete worms were seen.

3.2 Substrate types and associated communities

Five substrates were observed at the VCF: carbonate crusts, soft sediment, dead *D. pertusum*, coral rubble and dropstones. Of these, soft sediment made up the largest proportion of the surface area in both mosaics (M1: 69% and M2: 65%) (Table 1). Regarding hard substrata, M1 contained a large amount of carbonate crusts (27% of mosaicked area) but very little coral rubble (3% of mosaicked area), while M2 contained more coral rubble than carbonate crusts (22% and 12% of mosaicked area respectively). Dropstones and dead *D. pertusum* were less abundant and only accounted for less than 1% each of the total surface area in both mosaics (Table 1).

Based on the nMDS and ANOSIM, the fauna associated with the different substrates was significantly different (R: 0.67; $p = 0.03$). Faunal assemblages of 'hard' (i.e., carbonate crusts, dead *D. pertusum*, dropstones) were also significantly different from those on 'unconsolidated' (i.e., coral rubble, soft sediment) substrates (R: 0.91;

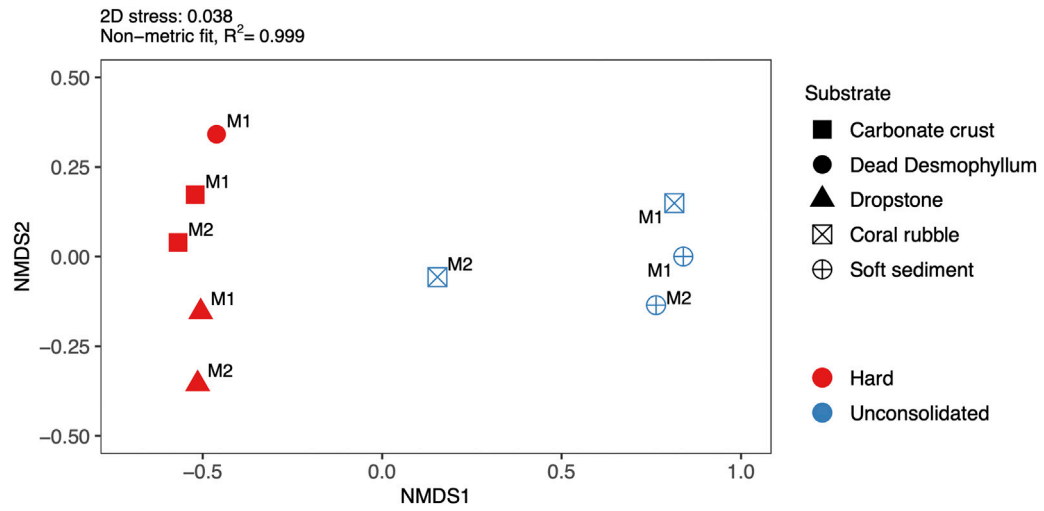

FIGURE 7
Non-metric multidimensional scaling (nMDS) plot of the communities associated with the different substrates (carbonate crust, coral rubble, dead *Desmophyllum pertusum*, dropstone and soft sediment) in the two mosaics (M1 and M2). 'Hard' substrates are indicated with red, filled icons and 'unconsolidated' substrates are indicated with blue unfilled icons.

TABLE 2 Total number of individuals, total megafaunal density, taxa richness (S), Shannon's diversity (H), Pielou's evenness (J) and effective number of species (ENS) for the different substrates within the two seep mosaics.

	Nb. of individuals		Density		Richness		Evenness		Diversity		ENS	
Substrate	M1	M2	M1	M2	M1	M2	M1	M2	M1	M2	M1	M2
Carbonate crusts	19,811	9262	108	135	42	31	0.4	0.5	1.6	1.7	4.9	5.7
Dead *D. pertusum*	250	n/a	58	n/a	17	n/a	0.5	n/a	1.5	n/a	4.4	n/a
Dropstones	143	32	55	80	14	5	0.6	0.8	1.5	1.3	4.6	3.5
Coral rubble	38	1,565	2	13	10	20	0.9	0.6	2.0	1.8	7.1	6.3
Soft sediment	524	428	2	3	27	21	0.6	0.6	2.1	1.7	8.5	5.4

$p < 0.01$) (Figure 7). In terms of megafaunal densities, carbonate crusts were the most highly populated substrate in both mosaics (M1: 108 ind./m^2; M2: 135 ind./m^2), dominated however, by extremely high numbers of sponges (e.g., the cushion-like orange sponge or the globular/irregular white/cream colored sponge) leading to low taxa evenness and thus only intermediate diversity values compared to the other substrates (Table 2). Nonetheless, carbonate crusts hosted the absolute majority of all marked individuals (M1: 95%; M2: 82%), as well as the majority (M1: 91%; M2:89%) of all morphotaxa identified in both mosaics. In contrast, soft sediment, which dominated both mosaics, hosted only 3%–4% of all marked individuals and 57%–60% of all morphotaxa identified. While the taxonomic composition on dead *D. pertusum* (M1: 58 ind./m^2) and dropstones (M1: 55 ind./m^2; M2: 80 ind./m^2) was similar to that on carbonate crusts (66% and 60% similarity respectively) (Table 3), megafauna was only about half as dense and diversity values were comparatively low. Megafaunal densities were the lowest on coral rubble (M1: 2; M2: 13 ind./m^2) and soft sediment (M1: 2; M2: 3 ind./m^2), while diversity values were the highest among these two substrates. Community composition was very similar between soft sediment and coral rubble (57%), while similarities in taxonomic composition between soft sediment and most other substrates (i.e., carbonate crusts, dead *D. pertusum* and dropstones) were very low, ranging from 23% to 27%.

3.3 Geochemical characteristics of the seep site

Stable carbon and hydrogen isotope analyses were conducted on the free gas samples to assess whether the underlying source of methane was microbial ($-110‰ \geq \delta^{13}C \geq -50‰$ and $-400‰ \geq \delta D \geq -150‰$) or thermogenic ($-50‰ \geq \delta^{13}C \geq -20‰$ and $-275‰ \geq \delta D \geq -100‰$) origin (Whiticar, 1999). Wetness was measured by the molar ratio of methane to the sum of ethane and propane (C1/(C2+C3)), with wetter gases containing higher amounts of C2+ gases and displaying a low C1/(C2+C3) ratio. Microbial methane tends to be light and dry, whereas thermogenic methane is usually rather heavy and wet (Milkov and Etiope, 2018). The free gas was nearly entirely composed of methane (99.97%) with $\delta^{13}C$-CH_4 and δD-CH_4 values of −74.4‰ and −194‰ respectively, and with a ratio of

TABLE 3 Similarity percentage (SIMPER) results for average overall dissimilarities in the community assemblages between different substrates. The column "Contributions (%)" contains the three species contributing the most (cut-off at 70% contribution) to the average overall Bray-Curtis dissimilarity between communities.

Substrate	Overall dissimilarity (%)	Most influential species	Cumulative contributions (%)	Contributions (%)	Respective taxa densities		
Carbonate crust - Dead *D. pertusum*	33.89	Encrusting yellow, orange sponge	13.83	13.83	10.84	-	0.23
		Encrusting orange sponge	27.29	13.46	17.18	-	2.32
		Cushion-like orange sponge	35.35	8.06	47.97	-	29.30
		Globular/irregular white, cream sponge	43.37	8.02	31.73	-	16.94
		Foliaceous white, cream sponge	49.08	5.71	3.86	-	0.70
		Fan animal	53.21	4.13	0.72	-	0.00
		Branching foliaceous white, cream sponge	56.88	3.67	0.48	-	1.86
		Echiuridae	60.45	3.57	0.45	-	0.00
		***Parazoanthus* sp.**	63.99	7.11	0.47	-	0.00
		Encrusting white sponge	67.26	3.27	0.38	-	0.00
		***Henricia* sp.**	69.85	2.59	0.12	-	0.70
		Platyhelminthe	72.41	2.56	0.00	-	0.23
Carbonate crust - Dropstone	40.32	Cushion-like orange sponge	23.75	23.75	47.97	-	3.47
		Encrusting blue sponge	32.42	8.67	3.50	-	0.00
		Encrusting yellow, orange sponge	40.23	7.81	10.84	-	10.50
		Encrusting orange sponge	47.69	7.46	17.18	-	6.02
		Microbial mats	51.99	4.29	0.76	-	1.72
		Encrusting yellow sponge	55.53	3.55	1.43	-	0.38
		***Munida* sp.**	58.78	3.25	0.55	-	0.00
		***Parazoanthus* sp.**	61.89	3.11	0.45	-	0.00
		Fan animal	64.98	3.09	0.47	-	0.00
		Globular/irregular white, cream sponge	67.64	2.66	0.72	-	0.38
		Foliaceous white, cream sponge	70.22	2.58	31.73	-	37.36
Carbonate crust - Coral rubble	66.81	Cushion-like orange sponge	21.88	21.88	47.97	-	0.94
		Globular/irregular white, cream sponge	37.24	15.36	31.73	-	2.36
		Encrusting orange sponge	48.56	11.32	17.18	-	1.35
		Encrusting yellow, orange sponge	57.01	8.45	10.84	-	1.29
		Encrusting blue sponge	62.46	5.46	3.50	-	0.31
		Foliaceous white, cream sponge	66.92	4.45	3.86	-	0.52
		Encrusting yellow sponge	70.62	3.70	1.43	-	0.03

(Continued on following page)

TABLE 3 (*Continued*) Similarity percentage (SIMPER) results for average overall dissimilarities in the community assemblages between different substrates. The column "Contributions (%)" contains the three species contributing the most (cut-off at 70% contribution) to the average overall Bray-Curtis dissimilarity between communities.

Substrate	Overall dissimilarity (%)	Most influential species	Cumulative contributions (%)	Contributions (%)	Respective taxa densities		
Carbonate crust - Soft sediment	76.92	Cushion-like orange sponge	21.37	21.37	47.97	-	0.28
		Globular/irregular white, cream sponge	36.79	15.41	31.73	-	1.02
		Encrusting orange sponge	49.06	12.27	17.18	-	0.14
		Encrusting yellow, orange sponge	58.34	9.29	10.84	-	0.12
		Encrusting blue sponge	64.18	5.84	3.50	-	0.02
		Foliaceous white, cream sponge	69.15	4.97	3.86	-	0.17
		Encrusting yellow sponge	72.80	3.64	1.43		0.02
Dead *D. pertusum* - Dropstone	48.72	Cushion-like orange sponge	18.11	18.11	29.30	-	3.47
		Encrusting yellow, orange sponge	29.85	11.73	0.23	-	10.50
		Globular/irregular white, cream sponge	39.87	10.03	16.94	-	37.36
		Encrusting blue sponge	47.90	8.03	2.55	-	0.00
		Foliaceous white, cream sponge	55.69	7.79	0.70	-	5.73
		Branching foliaceous white, cream sponge	60.41	4.72	1.86	-	0.38
		Encrusting orange sponge	65.04	4.63	2.32	-	6.02
		Microbial mats	69.66	4.62	0.46	-	1.72
		Encrusting yellow sponge	73.46	3.80	1.39	-	0.38
Dead *D. pertusum* - Coral rubble	61.55	Cushion-like orange sponge	25.79	25.79	29.30	-	0.94
		Globular/irregular white, cream sponge	41.45	15.65	16.94	-	2.36
		Branching foliaceous white, cream sponge	48.75	7.30	1.86	-	0.02
		Encrusting blue sponge	55.84	7.10	2.55	-	0.31
		Encrusting yellow sponge	61.58	5.73	1.39	-	0.03
		Encrusting yellow, orange sponge	65.94	4.37	0.23	-	1.29
		***Henricia* sp.**	70.01	4.06	0.70	-	0.04
Dead *D. pertusum* - Soft sediment	72.42	Cushion-like orange sponge	25.91	25.91	29.30	-	0.28
		Globular/irregular white, cream sponge	42.43	16.51	16.94	-	1.02
		Encrusting blue sponge	50.26	7.83	2.55	-	0.02
		Branching foliaceous white, cream sponge	57.33	7.07	1.86	-	0.00
		Encrusting orange sponge	63.45	6.12	2.32	-	0.14
		Encrusting yellow sponge	69.18	5.73	1.39	-	0.02
		***Henricia* sp.**	73.05	3.87	0.70	-	0.01

(Continued on following page)

TABLE 3 (*Continued*) Similarity percentage (SIMPER) results for average overall dissimilarities in the community assemblages between different substrates. The column "Contributions (%)" contains the three species contributing the most (cut-off at 70% contribution) to the average overall Bray-Curtis dissimilarity between communities.

Substrate	Overall dissimilarity (%)	Most influential species	Cumulative contributions (%)	Contributions (%)	Respective taxa densities		
Dropstone - Coral rubble	63.25	Globular/irregular white, cream sponge	28.34	28.34	37.36	-	2.36
		Encrusting yellow, orange sponge	42.43	14.09	10.50	-	1.29
		Foliaceous white, cream sponge	52.65	10.22	5.73	-	0.52
		Encrusting orange sponge	61.89	9.24	6.02	-	1.35
		Cushion-like orange sponge	67.45	5.57	3.47	-	0.94
		Microbial mats	72.80	5.34	1.72	-	0.09
Dropstone - Soft sediment	75.77	Globular/irregular white, cream sponge	27.75	27.75	37.36	-	1.02
		Encrusting yellow, orange sponge	41.66	13.91	10.50	-	0.12
		Encrusting orange sponge	52.94	11.28	6.02	-	0.14
		Foliaceous white, cream sponge	63.61	10.67	5.73	-	0.17
		Cushion-like orange sponge	70.63	7.01	3.47	-	0.28
Coral rubble - Soft sediment	43.03	Encrusting yellow, orange sponge	13.45	13.45	1.29	-	0.12
		Encrusting orange sponge	23.53	10.08	1.35	-	0.14
		Globular/irregular white, cream sponge	32.79	9.26	2.36	-	1.02
		Encrusting blue sponge	39.30	6.52	0.31	-	0.02
		Cushion-like orange sponge	45.62	6.31	0.94	-	0.28
		Fan animal	51.91	6.29	0.14	-	0.02
		***Munida* sp.**	57.45	5.55	0.29	-	0.04
		Foliaceous white, cream sponge	61.96	4.51	0.52	-	0.17
		Microbial mats	65.76	3.80	0.09	-	0.02
		Echiuridae	68.80	3.04	0.04	-	0.04
		Ophiuridae	71.47	5.71	0.03	-	0.01

*Morphotaxa not belonging to the phylum Porifera are marked in bold.

methane over ethane and propane of >4,000, appears to be of microbial origin (Figure 8) (Whiticar, 1999; Nicot et al., 2017). Similarly, headspace gas analysis from the push cores also revealed methane of microbial origin (δ^{13}C-CH_4: −79.1‰ – −91.7‰; δD-CH_4: −189‰ – −215‰ across all push cores). Note that while the δ^{13}C-CH_4 values clearly confirm the hydrogenotrophic methanogenesis (CO2-reduction), also in the revised genetic diagram by Milkov and Etiope (2018), the isotopic composition of ethane (d13C-C2H6)of −37.2‰ is well within the thermogenic range (Nakagawa et al., 2003). We suggest two possible pathways to explain this: 1) microbial methanogenesis in shallow sediment as a result of organic matter degradation fueled by methane-seep related biomass or 2) secondary methanogenesis as a result of thermogenic hydrocarbon biodegradation (Stagars et al., 2017) or a combination of both processes. At least, some admixture of thermogenic gas in our free gas sample is evident from the high ethane δ^{13}C value. In push cores PC2 and PC3, low concentrations of methane (3 and 10 μM respectively) were measured shallow in the sediment (2 cm), although concentrations increased downcore, but nonetheless remained below the millimolar range (Figure 9). On the other hand, in both push cores 1 and 4, millimolar concentrations (1.0 and 1.9 mM) of methane were measured at 24 and 2 cm depth respectively. Sulfide concentrations were in the low millimolar range (<0.6 mM) in the first sediment layers (0–3 cm), and rapidly increased downcore, with high millimolar

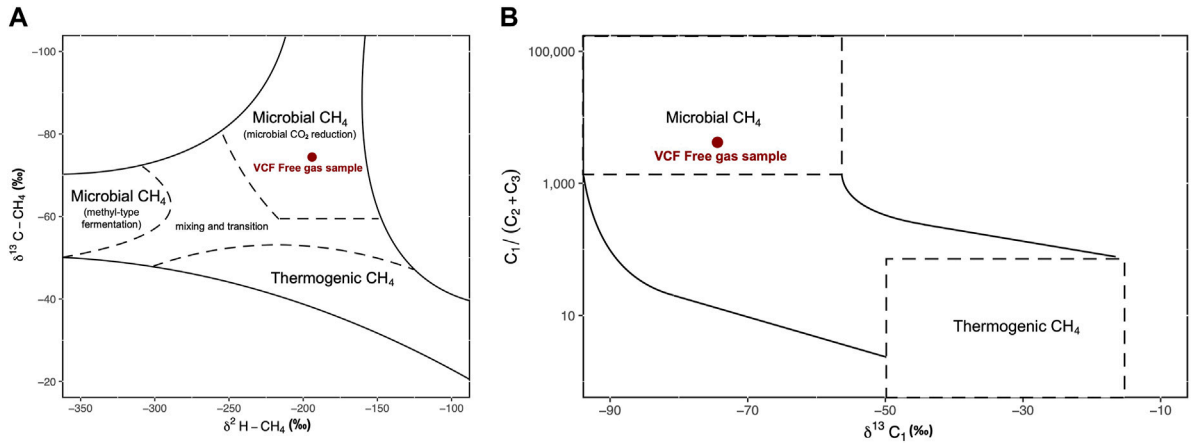

FIGURE 8
(A) Carbon and hydrogen isotopic composition of methane at the time of free gas sampling (adapted from Whiticar, 1999). **(B)** Ratio of methane (C_1) to the higher-chain hydrocarbons ethane (C_2) and propane (C_3) vs. the $\delta^{13}C$ of methane. Curves show mixing lines between thermogenic and microbial end members (dashed areas) (adapted from Sano et al., 2017).

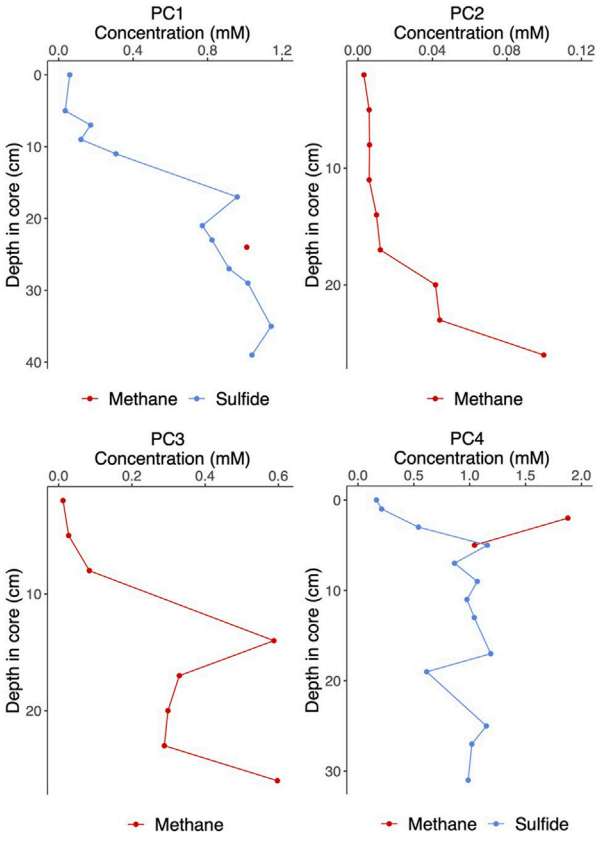

FIGURE 9
Sediment porewater methane and sulfide concentrations in push cores collected from the VCF study site. Push cores 1–2 (PC1 and PC2) were collected from within mosaic 1 (see Figures 1, 3 for locations) and push cores 3–4 (PC3 and PC4) were collected adjacent to mosaic 2 (Figure 1).

concentrations (max: 1.1 and 1.2 mM respectively) measured across both PC1 and PC4 (Figure 9).

3.4 Animal bulk stable isotopes

All $\delta^{34}S$ values ranged from 18.9 to 21.6‰ and were slightly lower or similar to ocean sulfate (MacAvoy et al., 2003) (Figure 10A). Bulk-tissue $\delta^{13}C$ values varied between −18.3 and −25.8‰, corresponding to the range typically associated with biomass produced through photosynthesis (Hobson et al., 1996; Søreide et al., 2006), while $\delta^{15}N$ values ranged between 7.7 and 8.2‰ for sponges, between 8.6 and 9.0‰ for cnidarians, between 9.3 and 9.7‰ for brittle stars and between 11.8 and 13.1‰ for polychaetes (Figure 10B) (All stable isotope data are published open access in SEANOE Sinner et al., 2020). These values are in line with samples belonging to different trophic levels, and food sources, e.g., filter feeding by sponges, deposit feeding by brittle stars and predation and deposit feeding by polychaetes (Fredriksen, 2003; Grall et al., 2006).

3.5 Background benthos community composition and comparison to the seep community

The three transects outside the seep area contained a total of 12 megafaunal taxa (Table 1) across 6 phyla (Porifera, Cnidaria, Mollusca, Echinodermata, Arthropoda and Chordata). Three phyla (Bryozoa, Annelida and Platyhelminthes), which were seen in the seep mosaics were absent from the background transects. On the other hand, two sponge morphotaxa (yellow globular and white/cream fistular sponges), as well as three fish species (*Trisopterus esmarkii*, *Merluccius merluccius* and one fish of unknown genus)

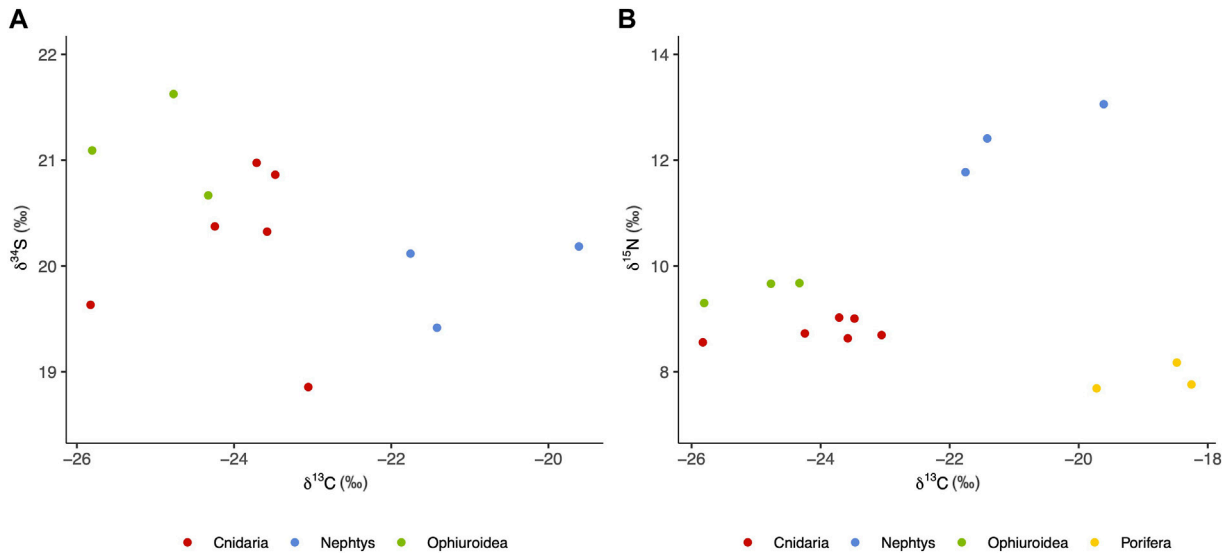

FIGURE 10
Scatterplot of $\delta^{34}S$ and $\delta^{13}C$ **(A)** and $\delta^{15}N$ and $\delta^{13}C$ **(B)** values of the fauna collected in the study. Porifera samples are not shown in the first plot because $\delta^{34}S$ values were below detectable range. Stable isotope data are published and publicly available in SEANOE: https://doi.org/10.17882/95359 (Sinner et al., 2020).

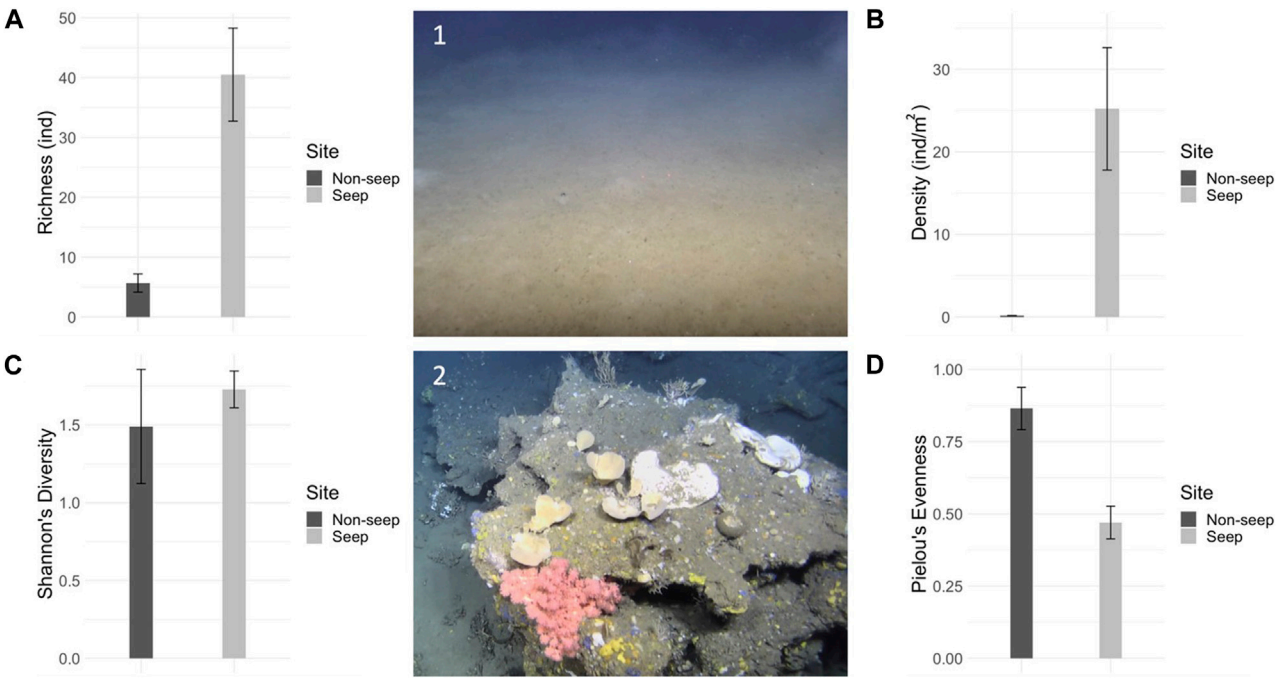

FIGURE 11
Richness and diversity of seep mosaics and non-seep background transects. **(A)** Taxa richness (S), mean (±s.d.), **(B)** megafaunal density (individuals/m²), **(C)** Pielou's evenness (J), **(D)** Shannon's diversity (H) for seep and non-seep (background) sites. 1: Representative image of the non-seep background area, 2: Representative image of the seep site.

were identified in the background area that were not seen in the seep areas. The holothuroid *Stichopus tremulus* accounted for the majority of all megafauna in the background transects, representing 44% of all marked individuals (T1 – T3 combined). Substrate features included large burrows or circular depressions in the soft sediment and small holes, the latter also being present in the seep mosaics. No hard substrata were recorded in the background transects. Mean megafaunal density as well as total taxa richness

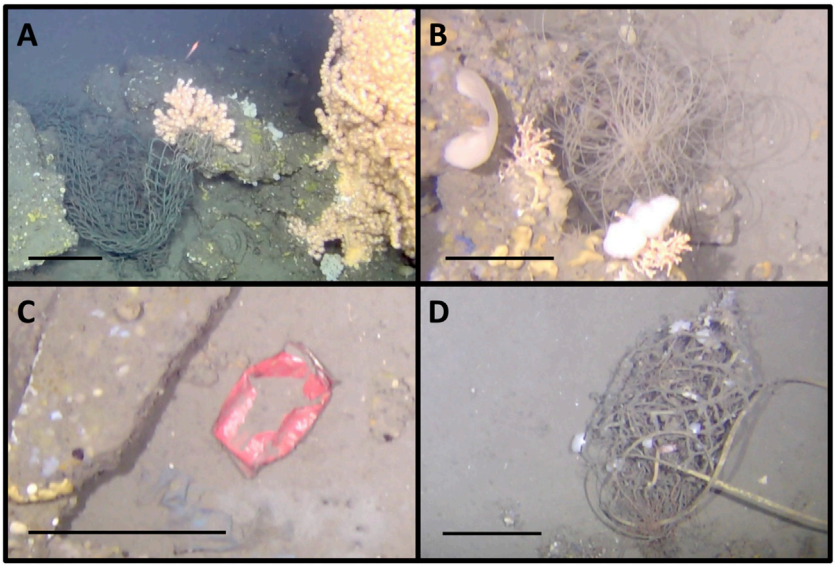

FIGURE 12
Examples of litter observed in the mosaicked areas. **(A)** Big fishing net entangled in a *Paragorgia arborea* soft coral; **(B)** Nylon fishing line entangled in carbonate seep crusts and its epifauna; **(C)** Soda can; **(D)** Fishing equipment. Scale bars: 20 cm.

were notably lower in the background non-seep transects compared to the seep mosaics (25 ± 7.4 ind./m^2 vs. 0.15 ± 0.0 ind./m^2 and 48 taxa vs. 12 taxa) (Figure 11). However, while evenness was high in the background area (J: 0.86 ± 0.1) and low in the seep area (J: 0.47 ± 0.1), diversity indices were similar in both areas (H': 1.73 ± 0.1 in the seep area vs. 1.49 ± 0.4 in the non-seep area), with the true diversity showing 6 ± 0.7 effective species in the seep area and 5 ± 1.6 effective species in the non-seep area.

3.6 Marine litter

Many instances of human-mediated litter were observed in the seep mosaics (Table 1; Figure 12). In total, 35 and 9 items were marked in M1 and M2 respectively, which consisted predominantly of fishing gear, but also glass, metals, paper, etc. (Figure 12). Fishing nets were the most abundant, with seven nets being marked in M1 and five in M2. Some reached sizes in the order of some square meters and many were entangled in soft corals and other benthic megafauna (Figure 12). Most of the litter did not appear to be particularly degraded, on the contrary, some bottles and cans were still perfectly intact. Considerably lower numbers of human litter items (2 in total) were observed in the transects of the background area outside the VCF seep.

4 Discussion

4.1 Chemosynthesis and nutrition at the VCF seep

Siboglinids dominate high latitude seeps and as chemosymbiotic fauna, they represent the base of the food chain and alter sediment geochemistry, functioning as ecosystem engineers (Levin, 2005; Cordes et al., 2010; Levin et al., 2016). Surprisingly, the VCF site did not contain any siboglinids at all. Low latitude shallow water cold seeps around the world tend to have a lower proportion of obligate taxa and a higher abundance of predators and other background taxa, than their deep water counterparts (Carney, 1994; Sahling et al., 2003; Tarasov et al., 2005; Vanreusel et al., 2009; Dando, 2010; Kiel, 2010). A possible hypothesis for this depth-related trend is that the increased input of photosynthetic organic matter from surface primary production at shallow depths mitigates the need for chemosynthesis as an energy source, even selecting against it and the energetically expensive adaptations it requires (Levin, 2005; Tarasov et al., 2005). Furthermore, shallow seeps are more prone to be invaded by higher levels of carnivorous predators from adjacent habitats, which would be able to efficiently prey on the largely sessile chemosynthesis-based (Carney, 1994; Sahling et al., 2003; Levin, 2005; Tarasov et al., 2005; Dando, 2010). Therefore, the relatively shallow water depth of the VCF site (270 m) could offer an explanation for the lack of siboglinids there. However, paradoxically, siboglinids have been recorded at Arctic seeps at considerably lower water depths (<80 m) (Savvichev et al., 2018; Vedenin et al., 2020). It has been hypothesized that among shallow water locations, the presence or absence of chemosymbiotic animals is linked to surface primary production, such that highly productive regions (with presumably considerable deposition of phytodetrital material to the seafloor) leads to the exclusion of chemosymbiotic animals, whereas more oligotrophic regions with lower levels of phytodetrital deposition favor them (Åström et al., 2022). Based on this, an explanation for the absence of siboglinids from the VCF site could be its location within the highly productive Norwegian Sea.

However, it can also be argued that the VCF site is simply beyond the photic zone where chemosynthesis-based symbioses

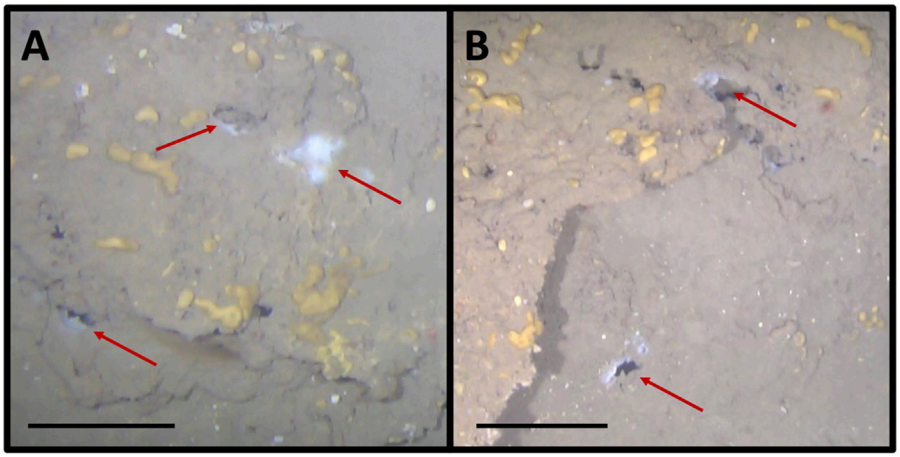

FIGURE 13
(A) and **(B)**: Microbial mats observed at the VCF seep site. Scale bars: 20 cm.

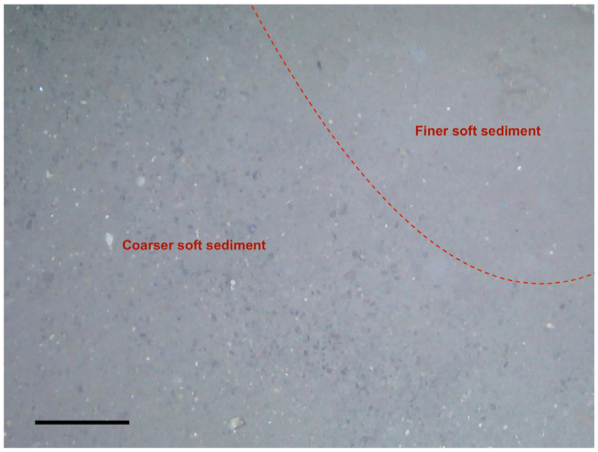

FIGURE 14
Coarser soft sediment compared to finer soft sediment observed within the mosaics. Scale bar: 20 cm.

would be selected against. In this case, other reasons need to be considered for the lack of chemosymbiotic animals at VCF. Since siboglinids are obligately symbiotic with chemosynthetic bacteria, the availability of chemosynthetic energy sources such as methane and sulfide represents a major limiting factor. We mapped two distinct gas flares in the multibeam survey (Figure 1B) and collected bubbling gas via the ROV close to the presence of carbonate crusts. This indicates that seepage is actively occurring at the VCF site. Indeed, we measured methane concentrations reaching up to 1.9 mM as shallow as 2 cm below the sediment-water interface and sulfide concentrations reaching up to 1.2 mM in only 5 cm of depth in the sediments. Therefore, it seems unlikely that sulfide (and methane) concentrations are insufficient to support siboglinids at the VCF site. However, despite sulfide and methane concentrations reaching millimolar concentrations at shallow depths in the sediment, we did observe considerable variation across different push cores. Thus, fluid release and sediment concentrations could be highly heterogeneous over very short lateral distances. Microbial mats were very patchy and small (Figure 13), which further supports the idea of the fluid regime at VCF being characterized by point sources with little lateral diffusion. Sediment heterogeneity (e.g., grain size) can lead to small-scale flow channelization, creating preferential rapid flow channels for methane, decreasing its residence time in the sediment and thus bypassing AOM by methane-consuming microbial communities (Torres et al., 2002; Luff et al., 2004; Mahadevan et al., 2012; Wankel et al., 2012). We did, in fact, observe patches of coarse sediment in the mosaics (Figure 14). The highly localized point sources of methane emission, which can act as a "bypass shunt" of AOM (Wankel et al., 2012) and by extension sulfide generation, may thus be a possible explanation for the absence of siboglinid polychaetes at the VCF seep.

Cold seep sabellids have recently been found to host methane oxidizing bacteria on their crowns and a nutritional symbiotic association has been suggested (Goffredi et al., 2020). We observed sabellids and sabellid-like animals at the VCF seep, including, in some instances, directly above microbial mats (Figure 15). Therefore, it is conceivable that methane-based chemosynthetic associations occur at the VCF seep, even if sulfide-based siboglinid chemosynthetic symbioses are absent. Nonetheless, the possible instances of methanotrophy-based sabellids at VCF are scarce overall in the community, in contrast with the extremely high densities and abundances exhibited by siboglinids when they are present at high latitude seeps (Åström et al., 2016; 2019; Sen et al., 2018b; 2018a; 2019b; Vedenin et al., 2020).

A lack, or paucity of chemosymbiotic animals would subsequently suggest that chemosynthetically fixed carbon does not constitute a major part of the food web at the VCF seep. We opportunistically sampled megabenthic fauna from two carbonate rocks retrieved from the VCF seep and conducted stable isotope analyses on them in order to assess the role of, and to track

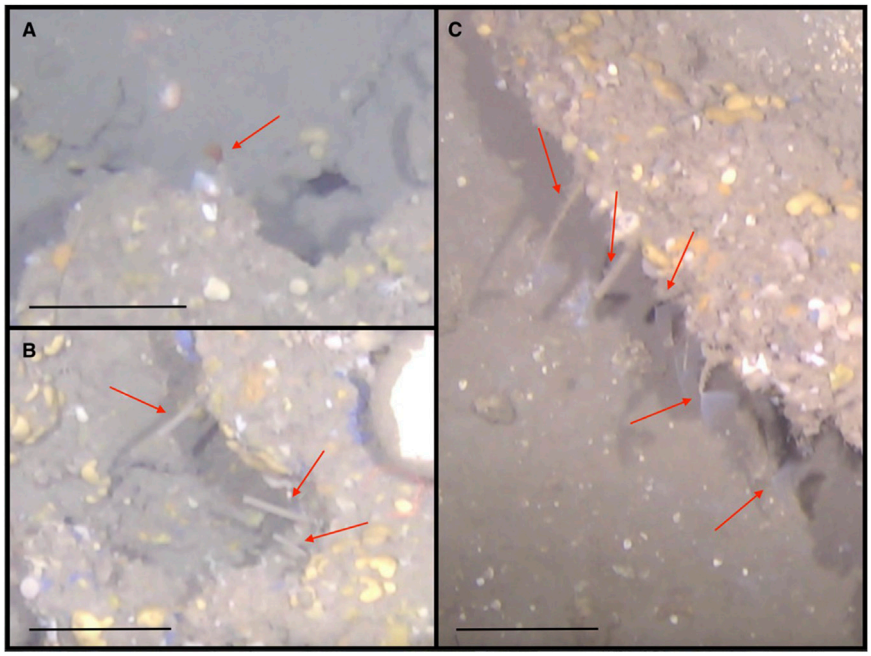

FIGURE 15
(A) Sabellids with protruding red feathery branchiae; **(B)** Sabellids with retracted branchiae; **(C)** Sabellids with protruding white feathery branchiae. Scale bars: 20 cm.

chemosynthetically fixed carbon through the food chain. Photosynthesis and chemosynthesis favor the two stable isotopes of carbon (^{12}C and ^{13}C) differently, therefore the ratio of the two constitutes a record of the carbon source at the base of the food web (DeNiro and Epstein, 1978; Fry, 2006). Specifically, biomass produced through chemosynthesis is depleted in the heavy isotopes of carbon (^{13}C), and thus result in lower $\delta^{13}C$ values, in comparison to biomass derived from photosynthesis (Kennicutt et al., 1992; MacAvoy et al., 2003). Methane seep organisms relying on chemosynthesis-derived organic matter have $\delta^{13}C$ values typically lower than −30‰ when this matter is synthesized through sulfide oxidation, and even lower (sometimes as low as −60‰) when synthesized through methane oxidation (Demopoulos et al., 2010; Yamanaka et al., 2015). All of the sampled taxa of the VCF seeps displayed $\delta^{13}C$ values between −25.8 and −19.6‰, suggesting a predominantly photosynthetic source of carbon (Hobson et al., 1996; Søreide et al., 2006) (Figure 10). Similarly, $\delta^{34}S$ values were typical for ocean sulfate (19–21‰), further suggesting a lack of sulfide based chemosynthetic pathways (MacAvoy et al., 2003; Grey and Deines, 2005; Yamanaka et al., 2015) (Figure 10A). $\delta^{15}N$ values display a notable tissue-diet shift, increasing by 2–4‰ with each trophic level (Minagawa and Wada, 1984; McCutchan Jr et al., 2003). The lowest values we found were 7.69 and 8.18‰ but given that those individuals also had the highest $\delta^{13}C$ values, it is unlikely that they represent low level consumers feeding on chemosynthetic microbes. Chemosynthetic signatures have even been observed in higher trophic level organisms at Arctic seeps. For example, $\delta^{13}C$ values as low as −31‰ have been recorded in predatory *Nepthys* worms at the Bjørnøyrenna crater field (Åström et al., 2019). We also sampled *Nepthys* worms, and they displayed the highest $\delta^{15}N$ values (11.8–13.1‰, Figure 10B), which indicates that they are predatory at VCF as well. However, $\delta^{13}C$ values among these worms were between −21.7 and −19.6‰ implying a photosynthetic origin of the ingested carbon.

Therefore, the combined results of our stable carbon, sulfur and nitrogen stable isotope analyses suggest that chemosynthesis does not play a major role in the benthic food web at the VCF seep, and that taxa primarily obtain their nutrition from phytodetrital material. It should be kept in mind however, that only a small fraction of the local fauna was subjected to stable isotope analyses, and that taxa with the highest potential for being chemosymbiotrophic, such as the previously mentioned sabellids were not analyzed. Additionally, we observed high numbers of echiurans (M1: 123 individuals; M2: 44 individuals), probably *Bonellia viridis*, a species that has previously been suggested to feed on microbial mats at the periphery of the Milos vent fields (Dando et al., 1995). Therefore, despite a lack or paucity of chemosymbiotic fauna, it is possible that chemosynthesis nonetheless plays a role in the food web and nutrition of the benthic community at the VCF site, and we simply could not detect it based on our sampling efforts. Furthermore, no sampling was done on sediment infauna and we thus cannot exclude the possibility of chemosymbiotrophic infauna (e.g., thyasirid bivalves), commonly seen at Arctic and subarctic seeps (Åström et al., 2017; Sen et al., 2018a), from being present at the VCF seep. Nonetheless, a lack of extensive microbial mat cover and the absence of siboglinid worms in combination with our isotope results together strongly suggest a minor role, if any, of chemosynthesis and chemosynthetically

fixed carbon in the local food web and nutrition of the resident fauna of the VCF seeps. This is despite high sediment sulfide concentrations and free gas methane emissions. Therefore, the VCF represents an active seep within what is generally considered the deep sea with a predominantly background community. This implies that direct evidence of active seepage does not necessarily result in chemosynthesis-based seep communities in high latitude locations. If fluid flow pathways are highly localized and restricted to point sources, background communities can develop, supported through conventional phytodetrital nutritional pathways, even at water depths below the photic zone.

4.2 Impacts of seep substrates on the local benthos

Low latitude cold seeps around the world have been seen to host high biomass but low diversity communities compared to the surrounding non-seep seafloor, while seeps in higher latitudes appear to host both high abundance and high diversity communities in comparison to surrounding non-seep areas (Fisher et al., 2007; Levin et al., 2016; Sen et al., 2018a; 2019a; Åström et al., 2020). Our results seem to fall in between both trends with the VCF seeps hosting high biomass communities, compared to the background area (25 ind./m^2 versus 0.15 ind./m^2) with however probably similar diversity (Figure 11). Similar to other methane seep studies (Levin et al., 2016; Sen et al., 2018a; 2019a; Åström et al., 2018; 2020), we link the presence of most benthic community members and their high abundances to heightened habitat heterogeneity and the occurrence of hard substrates, especially carbonate crusts, which are absent from the surrounding non-seep background area (Figure 11). Carbonate crusts are formed due to an increased carbonate alkalinity in the seep sediment, mediated through microbial activity, specifically, through the anaerobic oxidation of methane (AOM) coupled to the reduction of sulfate, a highly localized process which can continue at seep locations over hundreds to thousands of years (Boetius et al., 2000; Joye et al., 2004; Bayon et al., 2009; Sen et al., 2019b).

Despite carbonate crusts not representing the most abundant substrate within the seep area, they hosted nearly all morphotaxa identified, as well as the majority of all marked individuals. In contrast, soft sediment, which dominated both mosaics, only hosted about half of the morphotaxa identified and less than a tenth of all marked individuals. Thus, even compared to other hard substrates, such as dead *D. pertusum* and dropstones, the latter also being found in the non-seep background area (in some supplementary video material, but not in the video transects), carbonate crusts seem to play a particularly important role in structuring the local benthos. This may be explained by methane-derived authigenic carbonate crusts having higher three-dimensional complexity, offering more nooks and crannies for different kinds of animals to find fixation points (e.g., *Parazoanthus* sp.) and shelter in (e.g., *Munida* sp.); higher elevation from the seafloor, giving heightened access to organic material from the water column (e.g., Sabellidae); and sheer volume/size compared to the other hard substrates such as dropstones or dead *D. pertusum* corals, offering more space for animals to grow in large numbers (e.g., cushion-like orange sponge) and to grow in size (e.g., *Paragorgia arborea*) (Gutt and Schickan, 1998; Meyer et al., 2016; Sedano et al., 2020). Moreover, while dropstones constitute island-like habitats for hardbottom-dwelling fauna at high latitudes, increasing taxa richness of the region overall, they are limited by their small size and consequently mechanisms such as hydrodynamics, affecting food supply, larval dispersal and recruitment (Meyer et al., 2016; Ziegler et al., 2017). Seep carbonate crusts on the other hand are much bigger and may thus function more like archipelagos (Sen et al., 2019a), where the previously mentioned limitations may not apply in the same manner. Instead, faunal recruitment on these substrates may be linked to the presence or absence of interacting species or their channelization of seeping fluids that could enhance or aggregate particular species (Grupe, 2014).

Though carbonates had the highest abundances and numbers of taxa overall, other substrates, and most importantly the two unconsolidated substrates (i.e., soft sediment and coral rubble) showed higher taxa evenness and diversity. In addition, community composition on these substrates highly differed from all other substrates through the absence or low abundance of hard-substrate dwelling suspension-feeding animals, such as sponges, sabellids, 'fan animals' or soft corals. Only one single taxon was unique to these substrates, *S. tremulus*, a soft-bottom dwelling sea cucumber commonly found on soft sediments along the Norwegian coast (Schagerström and Sundell, 2021). Differences between the two unconsolidated substrates were also observed, primarily the presence of a few more hard-substrate-dwelling animals, such as sponges and 'fan animals' and mobile animals such as *Munida* sp. and ophiuroids on coral rubble compared to soft sediment. Indeed, *D. pertusum* rubble has been linked to an increased abundance of predators, in contrast to soft sediment and increased diversity compared to hard substrates covered in microbial mats, sponges, or corals (Jonsson et al., 2004; Lessard-Pilon et al., 2010). Moreover, the diversity of microhabitats found on coral rubble has been found to provide perfect conditions for the settlement of juveniles and to protect them until adulthood (Jensen and Frederiksen, 1992). It is thus the multitude of different substrates, that makes the VCF different from the background seafloor, by offering a variety of colonization surfaces for the background taxa, supporting them from larval settlement to their adult life, and thereby functioning as an important megafaunal oasis and 'ecological stepping stone' that would not be possible if only soft sediment and dropstones would be present (Jensen and Frederiksen, 1992; Gutt and Schickan, 1998; Kiel, 2016; Meyer et al., 2016; Sedano et al., 2020).

4.3 Implications for marine management

Norway is the seventh biggest oil producer, the third largest net oil exporter, as well as the world's second largest exporter of fish and seafood in the world (Mohn and Osmundsen, 2008; Lipková and Hovorková, 2018; Johansen et al., 2019). In order to limit the significant detrimental impacts these activities have on benthic communities, Norway has created its 'Integrated Ocean Management Plans', restricting the use of bottom trawls in areas with coral reefs (i.e., *D. pertusum*) and at depths exceeding 1,000 m and managing seismic surveying and exploration drilling in oil-

bearing formations through seasonal permits (ICES, 2019; Norvegian Ministry of Climate and Environment, 2020). However, no targeted measures exist to protect sponge aggregations in water depths less than 1,000 m and/or coral garden habitats from human stressors unless they occur in conjunction with *D. pertusum* reefs in the closed areas (OSPAR, 2010). As a consequence, hard-bottom coral gardens, dominated by vulnerable and very fragile soft corals are still under high fishing pressure and their total area has considerably declined in the last decades (Norvegian Ministry of Climate and Environment, 2020).

The VCF seep, with its multitude of hard substrates, hosts a high diversity and high abundance faunal community that is distinct from the surrounding seafloor community. Based on OSPAR (The Convention for the Protection of the Marine Environment of the North-East Atlantic) descriptions, the VCF seep ought to be categorized as a threatened and/or declining habitat, as they not only feature *D. pertusum* colonies and soft corals, such as *P. arborea*, *Paramuricea placomus* and *Primnoa resedaeformis*, but also deep-sea sponge aggregations, including some which have reached very large sizes. All these taxa are extremely slow-growing and are therefore particularly vulnerable to disturbances, such as oil drilling, bottom trawling and other fisheries related activities (Clark et al., 2016; Sundahl et al., 2020). Deep-water coral and sponge habitats often have high levels of endemism, host the early life-stages of many deep-sea animals including juvenile fish of commercial value, act as substrate and shelter for many other species, and play a major role in marine biogeochemical cycles, acting as hotspots of carbon processing in the food devoid deep ocean (Jensen and Frederiksen, 1992; Buhl-Mortensen and Mortensen, 2004; Buhl-Mortensen and Mortensen, 2005; Rogers, 2004; Hogg, M.M. et al., 2010; Beazley et al., 2013; Kenchington et al., 2013; Cathalot et al., 2015; Maldonado et al., 2017; De Clippele et al., 2019; D'Onghia, 2019). Furthermore, sponges in conjunction with corals seem to be particularly important, as they have a huge pallet of functional roles within coral ecosystems (Wulff, 2001; McLean and Yoshioka, 2007; Bell, 2008; De Goeij et al., 2013). Destructive relationships range from boring sponges infesting the tissue-barren portions of coral skeletons, to sponges outcompeting corals for space and overgrowing them (Beuck et al., 2007; McLean and Yoshioka, 2007; Bell, 2008). Many sponge species, however, have a beneficial, rather than destructive, relationship with corals. Sponges are known to increase coral survival by binding live corals to the substrate and preventing access to their skeletons, to mediate the regeneration of physically damaged corals and to return dissolved organic carbon (DOC) from the water column to the coral reef ecosystem as detritus, while producing detrital particulate organic Nitrate (PON), which may act as high-quality food source for corals and other detritivores and suspension feeders (Wulff, 2001; McLean and Yoshioka, 2007; Bell, 2008; De Goeij et al., 2013; Pawlik and McMurray, 2020). In addition to functioning as a biogenic habitat and controlling coral populations, sponges are also highly effective filter-feeders and play an important role in denitrification, carbon sequestration and benthic–pelagic coupling (Pham et al., 2019; Rooks et al., 2020). The presence and activity of sponges and corals therefore likely enhances settlement of other animals at the VCF site, making it a high abundance and biomass location, despite a lack of typical seep ecosystem engineering taxa. Furthermore, cold water corals on the Norwegian shelf have been hypothesized to be linked to seeps (Hovland and Risk, 2003), and the VCF site represents a location where cold water corals are directly associated with seeps.

In the VCF seep mosaics we observed a considerable amount of marine litter (on average 0.03 items/m^2), the majority of which was fishing gear (Table 1). Seven fishing nets were seen in M1 and five in M2, with one of the bigger fishing nets in M1 being completely entangled in a large *P. arborea* soft coral (Figure 12A). Demersal fishing such as bottom gillnetting or bottom trawling (De Juan and Lleonart, 2010) has thus taken place at the VCF at some point. Importantly as well, we observed much more fishing gear in the mosaics in comparison to the background areas (Table 1), even with differences in areas being accounted for. This could be due to the abundance of large carbonate slabs at the VCF seep, as well as associated large, three-dimensional structure-forming taxa, which stand in the way of nets that are towed along the ocean floor, leading to fragments of the nets being ripped off. Therefore, the seep itself could be more susceptible to being affected by fishing from a purely physical perspective.

Recovery time after damaging impacts (e.g., physical damage through fishing nets) in coral habitats may take decades and even though recovery time appears to be shorter for deep-sea sponge aggregations, they have been found to suffer from lingering damage and experience delayed mortality over the course of many years or even decades (Rogers, 2004; Althaus et al., 2009; Rooper et al., 2011; Clark et al., 2016; Malecha and Heifetz, 2017). Our results indicate that, in clear contrast with the surrounding non-seep background area, the VCF seeps with their multitude of substrates act as biomass hotspots, hosting a wide array of animals, including not only species of commercial interest but also large sponge aggregations and a variety of soft and hard corals. The VCF thus not only increases the diversity of the region overall, but also acts as a habitat for various species considered priorities for protection under the OSPAR convention, while possibly playing an important role in nitrogen cycling, carbon retention and benthic–pelagic coupling. Therefore, persistent fishing pressures, or the commencement of oil drilling could put animals that have lived there for decades, maybe centuries at risk, which would additionally affect associated benthic and epibenthic fauna. Our results therefore highlight why seeps should be maintained as particularly valuable and vulnerable habitats and protection efforts need to be implemented in order to achieve adequate protection and prevent significant adverse impacts, compromising ecosystem integrity.

5 Conclusion

Despite active seepage and high sediment methane and sulfide concentrations, the megafaunal communities of the Vestbrona Carbonate Field (VCF) on the Mid-Norwegian continental shelf lacked chemosymbiotrophic animals, which generally tend to dominate seep ecosystems. Instead, the VCF was dominated by dense sponge aggregations and was composed of heterotrophic background taxa. Our results emphasize however, that despite a lack of ecosystem engineering chemosymbiotrophic animals, seeps and their multitude of different substrates can play significant roles in benthic ecosystems by functioning as density hotspots and increasing the regional diversity. Our study shows that although

the observed taxa are considered priorities for protection under the OSPAR convention and partly protected under national legislation, they are still subject to multiple human stressors, including highly destructive fishing activities. Informed and effective conservation measures will be needed to protect the VCF seeps and the unique biodiversity hotspot they represent.

Data availability statement

All data used in this study are presented in the tables. Data generated from the mosaics and transects 689 are published in GBIF (Sinner et al., 2020): https://doi.org/10.15468/5vrbbj. Stable isotope data 690 generated and used in this study are published in SEANOE (Sinner et al., 2020): 691 https://doi.org/10.17882/95359.

Author contributions

AS, MS, and JK contributed to the conception and design of the study. AS and JK were responsible for sample collections. WH conducted porewater chemistry measurements, LM conducted animal stable isotope measurements and SV conducted acoustic measurements. JK was responsible for the free gas analyses. AS and MS constructed the georeferenced seep mosaics and MS extracted the background transects. MS digitized and enumerated all features in the mosaics and transects and conducted all statistical analyses. MS wrote the main text of the manuscript under the supervision of AS with contributions from all authors. All authors contributed to the article and approved the submitted version.

Funding

We sincerely thank Spirit Energy Ltd. (now: Sval Energy AS) for supporting the ROV expedition onboard R/V *G.O. Sars*. The research was supported by the Research Council of Norway (RCN) (project numbers 223259, and 332635). The funder was not involved in the study design, collection, analysis, interpretation of data, the writing of this article or the decision to submit it for publication.

Acknowledgments

We would like to thank the captain and crew of the R/V *G. O. Sars* (University of Bergen), the ROV Ægir team, and the scientific team of the 20-0 CAGE cruise from which data for this project was gathered. We thank Henning Reiss and Morten Krogstad for helping with organization and logistics and Nord University for hosting the first author and providing office space and technical equipment. We thank the MER Consortium and Erasmus+ for funding the first author's stay at Nord University and Brian Sevin for providing guidance and suggestions. We are grateful to Henning Reiss, Sabine Cochrane, Paul Renaud and Bodil Bluhm for help with identifying animals such as the "fan animal."

Conflict of interest

LM was employed by the company Ifremer.

The remaining authors declare that the research was conducted in the absence of any commercial or financial relationships that could be construed as a potential conflict of interest.

Publisher's note

References

Althaus, F., Williams, A., Schlacher, T. A., Kloser, R. J., Green, M. A., Barker, B. A., et al. (2009). Impacts of bottom trawling on deep-coral ecosystems of seamounts are long-lasting. *Mar. Ecol. Prog. Ser.* 397, 279–294. doi:10.3354/meps08248

Åström, E. K. L., Bluhm, B. A., and Rasmussen, T. L. (2022). Chemosynthetic and photosynthetic trophic support from cold seeps in Arctic benthic communities. *Front. Mar. Sci.* 9, 910558. doi:10.3389/fmars.2022.910558

Åström, E. K. L., Carroll, M. L., Ambrose, W. G., Sen, A., Silyakova, A., and Carroll, J. (2018). Methane cold seeps as biological oases in the high-Arctic deep sea. *Limnol. Oceanogr.* 63, S209–S231. doi:10.1002/lno.10732

Åström, E. K. L., Carroll, M. L., Jr, W. G. A., and Carroll, J. (2016). Arctic cold seeps in marine methane hydrate environments: Impacts on shelf macrobenthic community structure offshore svalbard. *Mar. Ecol. Prog. Ser.* 552, 1–18. doi:10.3354/meps11773

Astrom, E., Carroll, M., Sen, A., Niemann, H., Ambrose, W., Lehmann, M., et al. (2019). Chemosynthesis influences food web and community structure in high-Arctic benthos. *Mar. Ecol. Prog. Ser.* 629, 19–42. doi:10.3354/meps13101

Åström, E. K. L., Oliver, P. G., and Carroll, M. L. (2017). A new genus and two new species of Thyasiridae associated with methane seeps off Svalbard, Arctic Ocean. *Mar. Biol. Res.* 13, 402–416. doi:10.1080/17451000.2016.1272699

Åström, E. K. L., Sen, A., Carroll, M. L., and Carroll, J. (2020). Cold seeps in a warming arctic: Insights for benthic ecology. *Front. Mar. Sci.* 7, 244. doi:10.3389/fmars.2020.00244

Bayon, G., Henderson, G. M., and Bohn, M. (2009). U–Th stratigraphy of a cold seep carbonate crust. *Chem. Geol.* 260, 47–56. doi:10.1016/j.chemgeo.2008.11.020

Beazley, L. I., Kenchington, E. L., Murillo, F. J., Sacau, M., and del, M. (2013). Deep-sea sponge grounds enhance diversity and abundance of epibenthic megafauna in the Northwest Atlantic. *ICES J. Mar. Sci.* 70, 1471–1490. doi:10.1093/icesjms/fst124

Bell, J. J. (2008). The functional roles of marine sponges. *Estuar. Coast. Shelf Sci.* 79, 341–353. doi:10.1016/j.ecss.2008.05.002

Beuck, L., Vertino, A., Stepina, E., Karolczak, M., and Pfannkuche, O. (2007). Skeletal response of Lophelia pertusa (Scleractinia) to bioeroding sponge infestation visualised with micro-computed tomography. *Facies* 53, 157–176. doi:10.1007/s10347-006-0094-9

Boetius, A., Ravenschlag, K., Schubert, C. J., Rickert, D., Widdel, F., Gieseke, A., et al. (2000). A marine microbial consortium apparently mediating anaerobic oxidation of methane. *Nature* 407, 623–626. doi:10.1038/35036572

Bugge, T., Prestvik, T., and Rokoengen, K. (1980). Lower tertiary volcanic rocks off Kristiansund — mid Norway. *Mar. Geol.* 35, 277–286. doi:10.1016/0025-3227(80)90121-8

Buhl-Mortensen, L., and Mortensen, P. B. (2004). Crustaceans associated with the deep-water gorgonian corals Paragorgia arborea (L., 1758) and Primnoa resedaeformis (Gunn., 1763). *J. Nat. Hist.* 38, 1233–1247. doi:10.1080/00222930310001555205

Buhl-Mortensen, L., and Mortensen, P. B. (2005). "Distribution and diversity of species associated with deep-sea gorgonian corals off Atlantic Canada," in *Cold-water corals and ecosystems erlangen Earth conference series*. Editors A. Freiwald and J. M. Roberts (Berlin, Heidelberg: Springer), 849–879. doi:10.1007/3-540-27673-4_44

Carney, R. S. (1994). Consideration of the oasis analogy for chemosynthetic communities at Gulf of Mexico hydrocarbon vents. *Geo-Marine Lett.* 14, 149–159. doi:10.1007/BF01203726

Cathalot, C., Van Oevelen, D., Cox, T. J. S., Kutti, T., Lavaleye, M., Duineveld, G., et al. (2015). Cold-water coral reefs and adjacent sponge grounds: Hotspots of benthic respiration and organic carbon cycling in the deep sea. *Front. Mar. Sci.* 2, 37. doi:10.3389/fmars.2015.00037

Ceramicola, S., Dupré, S., Somoza, L., and Woodside, J. (2018). "Cold seep systems," in *Submarine geomorphology springer geology*. Editors A. Micallef, S. Krastel, and A. Savini (Cham: Springer International Publishing), 367–387. doi:10.1007/978-3-319-57852-1_19

Clark, M. R., Althaus, F., Schlacher, T. A., Williams, A., Bowden, D. A., and Rowden, A. A. (2016). The impacts of deep-sea fisheries on benthic communities: A review. *ICES J. Mar. Sci.* 73, i51–i69. doi:10.1093/icesjms/fsv123

Coplen, T. B. (2011). Guidelines and recommended terms for expression of stable-isotope-ratio and gas-ratio measurement results: Guidelines and recommended terms for expressing stable isotope results. *Rapid Commun. Mass Spectrom.* 25, 2538–2560. doi:10.1002/rcm.5129

Cordes, E. E., Cunha, M. R., Galéron, J., Mora, C., Roy, K. O.-L., Sibuet, M., et al. (2010). The influence of geological, geochemical, and biogenic habitat heterogeneity on seep biodiversity. *Mar. Ecol.* 31, 51–65. doi:10.1111/j.1439-0485.2009.00334.x

Dando, P. R. (2010). "Biological communities at marine shallow-water vent and seep sites," in *The vent and seep biota: Aspects from microbes to ecosystems topics in geobiology*. Editor S. Kiel (Dordrecht: Springer Netherlands), 333–378. doi:10.1007/978-90-481-9572-5_11

Dando, P. R., Hughes, J. A., and Thiermann, F. (1995). Preliminary observations on biological communities at shallow hydrothermal vents in the Aegean Sea. *Geol. Soc. Lond. Spec. Publ.* 87, 303–317. doi:10.1144/GSL.SP.1995.087.01.23

De Clippele, L. H., Huvenne, V. A. I., Molodtsova, T. N., and Roberts, J. M. (2019). The diversity and ecological role of non-scleractinian corals (antipatharia and alcyonacea) on scleractinian cold-water coral mounds. *Front. Mar. Sci.* 6, 184. doi:10.3389/fmars.2019.00184

De Goeij, J. M., Van Oevelen, D., Vermeij, M. J. A., Osinga, R., Middelburg, J. J., De Goeij, A. F. P. M., et al. (2013). Surviving in a marine desert: The sponge loop retains resources within coral reefs. *Science* 342, 108–110. doi:10.1126/science.1241981

De Juan, S., and Lleonart, J. (2010). *Fisheries conservation management and vulnerable ecosystems in the Mediterranean open seas, including the deep sea*. Tunis: UNEP-MAP-RAC/SPA.

Demopoulos, A. W. J., Gualtieri, D., and Kovacs, K. (2010). Food-web structure of seep sediment macrobenthos from the Gulf of Mexico. *Deep Sea Res. Part II Top. Stud. Oceanogr.* 57, 1972–1981. doi:10.1016/j.dsr2.2010.05.011

DeNiro, M. J., and Epstein, S. (1978). Influence of diet on the distribution of carbon isotopes in animals. *Geochimica Cosmochimica Acta* 42, 495–506. doi:10.1016/0016-7037(78)90199-0

D'Onghia, G. (2019). "30 cold-water corals as shelter, feeding and life-history critical habitats for fish species: Ecological interactions and fishing impact," in *Mediterranean cold-water corals: Past, present and future: Understanding the deep-sea realms of coral coral reefs of the world*. Editors C. Orejas and C. Jiménez (Cham: Springer International Publishing), 335–356. doi:10.1007/978-3-319-91608-8_30

Fisher, C., Roberts, H., Cordes, E., and Bernard, B. (2007). Cold seeps and associated communities of the gulf of Mexico. *Oceanog* 20, 118–129. doi:10.5670/oceanog.2007.12

Fredriksen, S. (2003). Food web studies in a Norwegian kelp forest based on stable isotope (δ13C and δ15N) analysis. *Mar. Ecol. Prog. Ser.* 260, 71–81. doi:10.3354/meps260071

Fry, B. (2006). *Stable isotope ecology*. New York, NY: Springer. doi:10.1007/0-387-33745-8

Gebruk, A. V., Krylova, E. M., Lein, A. Y., Vinogradov, G. M., Anderson, E., Pimenov, V., et al. (2003). Methane seep community of the Ha˚kon mosby mud volcano (the Norwegian sea): Composition and trophic aspects. *Sarsia N. Atl. Mar. Sci.* 88, 394–403. doi:10.1080/00364820310003190

Goffredi, S. K., Tilic, E., Mullin, S. W., Dawson, K. S., Keller, A., Lee, R. W., et al. (2020). Methanotrophic bacterial symbionts fuel dense populations of deep-sea feather duster worms (Sabellida, Annelida) and extend the spatial influence of methane seepage. *Sci. Adv.* 6, eaay8562. doi:10.1126/sciadv.aay8562

Grall, J., Le Loc'h, F., Guyonnet, B., and Riera, P. (2006). Community structure and food web based on stable isotopes (δ15N and δ13C) analysis of a North Eastern Atlantic maerl bed. *J. Exp. Mar. Biol. Ecol.* 338, 1–15. doi:10.1016/j.jembe.2006.06.013

Grey, J., and Deines, P. (2005). Differential assimilation of methanotrophic and chemoautotrophic bacteria by lake chironomid larvae. *Aquat. Microb. Ecol.* 40, 61–66. doi:10.3354/ame040061

Grupe, B. M. (2014). Implications of environmental heterogeneity for community structure, colonization, and trophic dynamics at eastern pacific methane seeps. Available at: https://escholarship.org/uc/item/3r68b6pz (Accessed November 8, 2022).

Gutt, J., and Schickan, T. (1998). Epibiotic relationships in the Antarctic benthos. *Antarct. Sci.* 10, 398–405. doi:10.1017/S0954102098000480

Hedges, J. I., and Stern, J. H. (1984). Carbon and nitrogen determinations of carbonate-containing solids1. *Limnol. Oceanogr.* 29, 657–663. doi:10.4319/lo.1984.29.3.0657

Helle, K., Pennington, M., Hareide, N.-R., and Fossen, I. (2015). Selecting a subset of the commercial catch data for estimating catch per unit effort series for ling (Molva molva L). *Fish. Res.* 165, 115–120. doi:10.1016/j.fishres.2014.12.015

Hobson, K. A., Ambrose, W. G., and Renaud, P. R. (1996). Sources of primary production, benthicpelagic coupling, and trophic relationships within the northeast water polynya: Insights from δ 1 3 C and δ 1 5 N analysis. *Oceanogr. Lit. Rev.* 7, 689.

Hogg, M. M., Tendal, O. S., Conway, K. W., Pomponi, S. A., van Soest, R. W. M., Gutt, J., et al. (2010). Deep-sea sponge grounds: Reservoirs of biodiversity. UNEP-WCMC Available at: https://dare.uva.nl/personal/pure/en/publications/deepsea-sponge-grounds-reservoirs-of-biodiversity(c0c920a3-4208-4d3c-b55d-1a1b09aced52).html (Accessed July 6, 2021).

Hovland, M., and Risk, M. (2003). Do Norwegian deep-water coral reefs rely on seeping fluids? *Mar. Geol.* 198, 83–96. doi:10.1016/S0025-3227(03)00096-3

ICES (2019). *Norwegian Sea Ecoregion—Ecosystem overview. In Report of the ICES Advisory Committee*. ICES Advice 2019, Section 12.1. doi:10.17895/ices.advice.5748

Jensen, A., and Frederiksen, R. (1992). The fauna associated with the bank-forming deepwater coral Lophelia pertusa (Scleractinaria) on the Faroe shelf. *Sarsia* 77, 53–69. doi:10.1080/00364827.1992.10413492

Johansen, U., Bull-Berg, H., Vik, L. H., Stokka, A. M., Richardsen, R., and Winther, U. (2019). The Norwegian seafood industry – importance for the national economy. *Mar. Policy* 110, 103561. doi:10.1016/j.marpol.2019.103561

Jonsson, L. G., Nilsson, P. G., Floruta, F., and Lundälv, T. (2004). Distributional patterns of macro- and megafauna associated with a reef of the cold-water coral Lophelia pertusa on the Swedish west coast. *Marine Ecology Progress Series* 284, 163–171. doi:10.3354/meps284163

Jost, L. (2006). Entropy and diversity. *Oikos* 113, 363–375. doi:10.1111/j.2006.0030-1299.14714.x

Joye, S. B., Boetius, A., Orcutt, B. N., Montoya, J. P., Schulz, H. N., Erickson, M. J., et al. (2004). The anaerobic oxidation of methane and sulfate reduction in sediments from Gulf of Mexico cold seeps. *Chem. Geol.* 205, 219–238. doi:10.1016/j.chemgeo.2003.12.019

Kassambara, A. (2023). Ggpubr: "ggplot2" based publication ready plots. Available at: https://CRAN.R-project.org/package=ggpubr (Accessed March 29, 2023).

Kenchington, E., Power, D., and Koen-Alonso, M. (2013). Associations of demersal fish with sponge grounds on the continental slopes of the northwest Atlantic. *Mar. Ecol. Prog. Ser.* 477, 217–230. doi:10.3354/meps10127

Kennicutt, M. C., Burke, R. A., MacDonald, I. R., Brooks, J. M., Denoux, G. J., and Macko, S. A. (1992). Stable isotope partitioning in seep and vent organisms: Chemical and ecological significance. *Chem. Geol. Isot. Geosci. Sect.* 101, 293–310. doi:10.1016/0009-2541(92)90009-T

Kiel, S. (2016). A biogeographic network reveals evolutionary links between deep-sea hydrothermal vent and methane seep faunas. *Proc. R. Soc. B Biol. Sci.* 283, 20162337. doi:10.1098/rspb.2016.2337

Kiel, S. (2010). On the potential generality of depth-related ecologic structure in cold-seep communities: Evidence from Cenozoic and Mesozoic examples. *Palaeogeogr. Palaeoclimatol. Palaeoecol.* 295, 245–257. doi:10.1016/j.palaeo.2010.05.042

Kvangarsnes, K., Frantzen, S., Julshamn, K., Sætre, L. J., Nedreaas, K., and Maage, A. (2012). Distribution of mercury in a gadoid fish species, tusk (brosme brosme), and its implication for food safety. *J. Food Sci. Eng.* 2, 603–615. doi:10.17265/2159-5828/2012.11.001

Lessard-Pilon, S. A., Podowski, E. L., Cordes, E. E., and Fisher, C. R. (2010). Megafauna community composition associated with Lophelia pertusa colonies in the Gulf of Mexico. *Deep Sea Res.* 57, 1882–1890. doi:10.1016/j.dsr2.2010.05.013

Levin, L. A., Baco, A. R., Bowden, D. A., Colaco, A., Cordes, E. E., Cunha, M. R., et al. (2016). Hydrothermal vents and methane seeps: Rethinking the sphere of influence. *Front. Mar. Sci.* 3, 72. doi:10.3389/fmars.2016.00072

Levin, L. A. (2005). "Ecology of cold seep sediments: Interactions of fauna with flow, chemistry and microbes," in *Oceanography and Marine Biology: An Annual Review* (Boca Raton: CRC Press), 1–46. doi:10.1201/9781420037449

Levin, L. A., and Michener, R. H. (2002). Isotopic evidence for chemosynthesis-based nutrition of macrobenthos: The lightness of being at Pacific methane seeps. *Limnol. Oceanogr.* 47, 1336–1345. doi:10.4319/lo.2002.47.5.1336

Lipková, L., and Hovorková, K. (2018). Economic situation in Norway after the outbreak of the global financial and oil crises in the context of EU integration trends. *EA-XXI* 169, 12–14. doi:10.21003/ea.V169-02

Lösekann, T., Robador, A., Niemann, H., Knittel, K., Boetius, A., and Dubilier, N. (2008). Endosymbioses between bacteria and deep-sea siboglinid tubeworms from an arctic cold seep (haakon mosby mud volcano, barents sea). *Environ. Microbiol.* 10, 3237–3254. doi:10.1111/j.1462-2920.2008.01712.x

Luff, R., Wallmann, K., and Aloisi, G. (2004). Numerical modeling of carbonate crust formation at cold vent sites: Significance for fluid and methane budgets and chemosynthetic biological communities. *Earth Planet. Sci. Lett.* 221, 337–353. doi:10.1016/S0012-821X(04)00107-4

MacAvoy, S. E., Macko, S. A., and Carney, R. S. (2003). Links between chemosynthetic production and mobile predators on the Louisiana continental slope: Stable carbon

isotopes of specific fatty acids. *Chem. Geol.* 201, 229–237. doi:10.1016/S0009-2541(03)00204-3

Mahadevan, A., Orpe, A. V., Kudrolli, A., and Mahadevan, L. (2012). Flow-induced channelization in a porous medium. *EPL* 98, 58003. doi:10.1209/0295-5075/98/58003

Maldonado, M., Aguilar, R., Bannister, R. J., Bell, J. J., Conway, K. W., Dayton, P. K., et al. (2017). "Sponge Grounds as Key Marine Habitats: A Synthetic Review of Types, Structure, Functional Roles, and Conservation Concerns," in *Marine Animal Forests: The Ecology of Benthic Biodiversity Hotspots*. Editor S. Rossi, L. Bramanti, A. Gori, and C. Orejas Saco del Valle (Cham: Springer International Publishing), 1–39. doi:10.1007/978-3-319-17001-5_24-1

Malecha, P., and Heifetz, J. (2017). Long-term effects of bottom trawling on large sponges in the Gulf of Alaska. *Cont. Shelf Res.* 150, 18–26. doi:10.1016/j.csr.2017.09.003

Mateo, M. A., Serrano, O., Serrano, L., and Michener, R. H. (2008). Effects of sample preparation on stable isotope ratios of carbon and nitrogen in marine invertebrates: Implications for food web studies using stable isotopes. *Oecologia* 157, 105–115. doi:10.1007/s00442-008-1052-8

McCutchan, J. H., Jr, Lewis, W. M., Jr, Kendall, C., and McGrath, C. C. (2003). Variation in trophic shift for stable isotope ratios of carbon, nitrogen, and sulfur. *Oikos* 102, 378–390. doi:10.1034/j.1600-0706.2003.12098.x

McLean, E. L., and Yoshioka, P. M. (2007). "Associations and interactions between gorgonians and sponges," in *Porifera research: Biodiversity, innovation and sustainability série livros* (Rio de Janeiro: Museu Nacional), 139–145.

Meyer, K. S., Young, C. M., Sweetman, A. K., Taylor, J., Soltwedel, T., and Bergmann, M. (2016). Rocky islands in a sea of mud: Biotic and abiotic factors structuring deep-sea dropstone communities. *Mar. Ecol. Prog. Ser.* 556, 45–57. doi:10.3354/meps11822

Milkov, A. V., and Etiope, G. (2018). Revised genetic diagrams for natural gases based on a global dataset of >20,000 samples. *Org. Geochem.* 125, 109–120. doi:10.1016/j.orggeochem.2018.09.002

Minagawa, M., and Wada, E. (1984). Stepwise enrichment of 15N along food chains: Further evidence and the relation between δ15N and animal age. *Geochimica Cosmochimica Acta* 48, 1135–1140. doi:10.1016/0016-7037(84)90204-7

Mohn, K., and Osmundsen, P. (2008). Exploration economics in a regulated petroleum province: The case of the Norwegian Continental Shelf. *Energy Econ.* 30, 303–320. doi:10.1016/j.eneco.2006.10.011

Nakagawa, F., Tsunogai, U., Yoshida, N., and Adams, D. D. (2003). "Stable isotopic compositions of bacterial light hydrocarbons in marginal marine sediments," in *Land and marine hydrogeology*. Editors M. Taniguchi, K. Wang, and T. Gamo (Amsterdam: Elsevier), 141–150. doi:10.1016/B978-044451479-0/50021-2

Nicot, J.-P., Mickler, P., Larson, T., Castro, M. C., Darvari, R., Uhlman, K., et al. (2017). Methane occurrences in aquifers overlying the barnett shale play with a focus on parker county, Texas. *Groundwater* 55, 469–481. doi:10.1111/gwat.12508

Norvegian Ministry of Climate and Environment (2020). Norway's integrated Ocean Management plans — barents sea–lofoten area; the Norwegian sea; and the North sea and skagerrak— report to the storting (white paper). regjeringen.no Available at: https://www.regjeringen.no/en/dokumenter/meld.-st.-20-20192020/id2699370/ (Accessed June 13, 2021).

Norwegian Directorate of Fisheries (2020). *Economic and biological figures from Norwegian fisheries – 2020.*

Oksanen, J., Simpson, G. L., Blanchet, F. G., Kindt, R., Legendre, P., Minchin, P. R., et al. (2022). vegan: Community ecology package. Available at: https://CRAN.R-project.org/package=vegan (Accessed March 29, 2023).

OSPAR (2010). *Background document for coral gardens*. London: OSPAR Commission.

Paull, C. K., Dallimore, S. R., Caress, D. W., Gwiazda, R., Melling, H., Riedel, M., et al. (2015). Active mud volcanoes on the continental slope of the Canadian Beaufort Sea. *Geochem. Geophys. Geosystems* 16, 3160–3181. doi:10.1002/2015GC005928

Pawlik, J. R., and McMurray, S. E. (2020). The emerging ecological and biogeochemical importance of sponges on coral reefs. *Annu. Rev. Mar. Sci.* 12, 315–337. doi:10.1146/annurev-marine-010419-010807

Pham, C. K., Murillo, F. J., Lirette, C., Maldonado, M., Colaço, A., Ottaviani, D., et al. (2019). Removal of deep-sea sponges by bottom trawling in the flemish cap area: Conservation, ecology and economic assessment. *Sci. Rep.* 9, 15843. doi:10.1038/s41598-019-52250-1

Rogers, A., Kennedy, A., Nelson, E., and Robinson, A. (2004). Patients' experiences of an open access follow up arrangement in managing inflammatory bowel disease. *Qual. Saf. Health Care* 13, 374–378. doi:10.1136/qhc.13.5.374

Rooks, C., Fang, J. K.-H., Mørkved, P. T., Zhao, R., Rapp, H. T., Xavier, J. R., et al. (2020). Deep-sea sponge grounds as nutrient sinks: Denitrification is common in boreo-arctic sponges. *Biogeosciences* 17, 1231–1245. doi:10.5194/bg-17-1231-2020

Rooper, C. N., Wilkins, M. E., Rose, C. S., and Coon, C. (2011). Modeling the impacts of bottom trawling and the subsequent recovery rates of sponges and corals in the Aleutian Islands, Alaska. *Cont. Shelf Res.* 31, 1827–1834. doi:10.1016/j.csr.2011.08.003

Rybakova (Goroslavskaya), E., Galkin, S., Bergmann, M., Soltwedel, T., and Gebruk, A. (2013). Density and distribution of megafauna at the Håkon Mosby mud volcano (the Barents Sea) based on image analysis. *Biogeosciences* 10, 3359–3374. doi:10.5194/bg-10-3359-2013

Sahling, H., Galkin, S. V., Salyuk, A., Greinert, J., Foerstel, H., Piepenburg, D., et al. (2003). Depth-related structure and ecological significance of cold-seep communities—A case study from the sea of Okhotsk. *Deep Sea Res. Part I Oceanogr. Res. Pap.* 50, 1391–1409. doi:10.1016/j.dsr.2003.08.004

Sano, Y., Kinoshita, N., Kagoshima, T., Takahata, N., Sakata, S., Toki, T., et al. (2017). Origin of methane-rich natural gas at the West Pacific convergent plate boundary. *Sci. Rep.* 7, 15646. doi:10.1038/s41598-017-15959-5

Savvichev, A. S., Kadnikov, V. V., Kravchishina, M. D., Galkin, S. V., Novigatskii, A. N., Sigalevich, P. A., et al. (2018). Methane as an organic matter source and the trophic basis of a Laptev Sea cold seep microbial community. *Geomicrobiol. J.* 35, 411–423. doi:10.1080/01490451.2017.1382612

Schagerström, E., and Sundell, K. S. (2021). Parastichopus tremulus (Gunnerus, 1767) red sea cucumber, red signal sea cucumber (Sweden), rødpølse (Norway and Denmark), Aspidochirotida, Stichopodidae. *BECHE-DE-MER Inf. Bull.* 3, 22–24.

Sedano, F., Navarro-Barranco, C., Guerra-García, J. M., and Espinosa, F. (2020). Understanding the effects of coastal defence structures on marine biota: The role of substrate composition and roughness in structuring sessile, macro- and meiofaunal communities. *Mar. Pollut. Bull.* 157, 111334. doi:10.1016/j.marpolbul.2020.111334

Sen, A., Åström, E. K. L., Hong, W.-L., Portnov, A., Waage, M., Serov, P., et al. (2018a). Geophysical and geochemical controls on the megafaunal community of a high Arctic cold seep. *Biogeosciences* 15, 4533–4559. doi:10.5194/bg-15-4533-2018

Sen, A., Chitkara, C., Hong, W.-L., Lepland, A., Cochrane, S., Primio, R., et al. (2019a). Image based quantitative comparisons indicate heightened megabenthos diversity and abundance at a site of weak hydrocarbon seepage in the southwestern Barents Sea. *PeerJ* 7, e7398. doi:10.7717/peerj.7398

Sen, A., Didriksen, A., Hourdez, S., Svenning, M. M., and Rasmussen, T. L. (2020). Frenulate siboglinids at high Arctic methane seeps and insight into high latitude frenulate distribution. *Ecol. Evol.* 10, 1339–1351. doi:10.1002/ece3.5988

Sen, A., Duperron, S., Hourdez, S., Piquet, B., Léger, N., Gebruk, A., et al. (2018b). Cryptic frenulates are the dominant chemosymbiotrophic fauna at Arctic and high latitude Atlantic cold seeps. *PLOS ONE* 13, e0209273. doi:10.1371/journal.pone.0209273

Sen, A., Himmler, T., Hong, W. L., Chitkara, C., Lee, R. W., Ferré, B., et al. (2019b). Atypical biological features of a new cold seep site on the Lofoten-Vesterålen continental margin (northern Norway). *Sci. Rep.* 9, 1762. doi:10.1038/s41598-018-38070-9

Sibuet, M., and Olu, K. (1998). Biogeography, biodiversity and fluid dependence of deep-sea cold-seep communities at active and passive margins. *Deep Sea Res. Part II Top. Stud. Oceanogr.* 45, 517–567. doi:10.1016/S0967-0645(97)00074-X

Sibuet, M., and Olu-Le Roy, K. (2002). "Cold seep communities on continental margins: Structure and quantitative distribution relative to geological and fluid venting patterns," in *Ocean margin systems*. Editors P. D. G. Wefer, D. D. Billett, D. D. Hebbeln, P. D. B. B. Jørgensen, P. D. M. Schlüter, and D. T. C. E. van Weering (Berlin Heidelberg: Springer), 235–251. doi:10.1007/978-3-662-05127-6_15

Sinner, M., Hong, W., Michel, L., Vadakkepuliyambatta, S., Knies, J., and Sen, A. (2020). *Stable isotope ratios of C, N and S in fauna sampled at the Vestbrona Carbonate Field (Norway)*. doi:10.17882/95359

Sinner, M., Sen, A., Hong, W. L., Michel, L. N., Vadakkepuliyambatta, S., and Knies, J. (2023). *Megafauna of Vestbrona Carbonate Field and surrounding benthos from seafloor mosaics*. doi:10.15468/5vrbbj

Smirnov, R. V. (2014). A revision of the Oligobrachiidae (Annelida: Pogonophora), with notes on the morphology and distribution of Oligobrachia haakonmosbiensis Smirnov. *Mar. Biol. Res.* 10, 972–982. doi:10.1080/17451000.2013.872799

Smirnov, R. V. (2000). Two new species of Pogonophora from the arctic mud volcano off northwestern Norway. *null* 85, 141–150. doi:10.1080/00364827.2000.10414563

Søreide, J. E., Hop, H., Carroll, M. L., Falk-Petersen, S., and Hegseth, E. N. (2006). Seasonal food web structures and sympagic–pelagic coupling in the European Arctic revealed by stable isotopes and a two-source food web model. *Prog. Oceanogr.* 71, 59–87. doi:10.1016/j.pocean.2006.06.001

Stagars, M. H., Mishra, S., Treude, T., Amann, R., and Knittel, K. (2017). Microbial community response to simulated petroleum seepage in caspian sea sediments. *Front. Microbiol.* 8, 764. Available at:. doi:10.3389/fmicb.2017.00764Accessed June 12, 2023)

Suess, E. (2010). "Marine cold seeps," in *Handbook of hydrocarbon and lipid microbiology*. Editor K. N. Timmis (Berlin, Heidelberg: Springer), 185–203. doi:10.1007/978-3-540-77587-4_12

Suess, E. (2020). "Marine cold seeps: Background and recent advances," in *Hydrocarbons, oils and lipids: Diversity, origin, chemistry and fate*. Editor H. Wilkes (Cham: Springer International Publishing), 747–767. doi:10.1007/978-3-319-90569-3_27

Sundahl, H., Buhl-Mortensen, P., and Buhl-Mortensen, L. (2020). Distribution and suitable habitat of the cold-water corals Lophelia pertusa, Paragorgia arborea, and

Primnoa resedaeformis on the Norwegian continental shelf. *Front. Mar. Sci.* 7, 213. doi:10.3389/fmars.2020.00213

Tarasov, V. G., Gebruk, A. V., Mironov, A. N., and Moskalev, L. I. (2005). Deep-sea and shallow-water hydrothermal vent communities: Two different phenomena? *Chem. Geol.* 224, 5–39. doi:10.1016/j.chemgeo.2005.07.021

Torres, M. E., McManus, J., Hammond, D. E., de Angelis, M. A., Heeschen, K. U., Colbert, S. L., et al. (2002). Fluid and chemical fluxes in and out of sediments hosting methane hydrate deposits on Hydrate Ridge, OR, I: Hydrological provinces. *Earth Planet. Sci. Lett.* 201, 525–540. doi:10.1016/S0012-821X(02)00733-1

Vanreusel, A., Andersen, A., Boetius, A., Connelly, D., Cunha, M., Decker, C., et al. (2009). Biodiversity of cold seep ecosystems along the European margins. *Oceanog* 22, 110–127. doi:10.5670/oceanog.2009.12

Vedenin, A. A., Kokarev, V. N., Chikina, M. V., Basin, A. B., Galkin, S. V., and Gebruk, A. V. (2020). Fauna associated with shallow-water methane seeps in the Laptev Sea. *PeerJ* 8, e9018. doi:10.7717/peerj.9018

Wankel, S. D., Adams, M. M., Johnston, D. T., Hansel, C. M., Joye, S. B., and Girguis, P. R. (2012). Anaerobic methane oxidation in metalliferous hydrothermal sediments: Influence on carbon flux and decoupling from sulfate reduction. *Environ. Microbiol.* 14, 2726–2740. doi:10.1111/j.1462-2920.2012.02825.x

Whiticar, M. J. (1999). Carbon and hydrogen isotope systematics of bacterial formation and oxidation of methane. *Chem. Geol.* 161, 291–314. doi:10.1016/S0009-2541(99)00092-3

Wickham, H., Chang, W., Henry, L., Pedersen, T. L., Takahashi, K., Wilke, C., et al. (2023). ggplot2: Create elegant data visualisations using the grammar of graphics. Available at: https://CRAN.R-project.org/package=ggplot2 (Accessed March 29, 2023).

Wulff, J. (2001). Assessing and monitoring coral reef sponges: Why and how? *Bull. Mar. Sci.* 69, 831–846. Available at: http://pascalfrancis.inist.frvibadindex.phpaction=getRecordDetail&idt=13403160 (Accessed July 12, 2023).

Xiao, N., Cook, J., Jégousse, C., and Li, M. (2023). ggsci: Scientific journal and sci-fi themed color palettes for ggplot2. Available at: https://CRAN.R-project.org/package=ggsci (Accessed March 29, 2023).

Yamanaka, T., Shimamura, S., Nagashio, H., Yamagami, S., Onishi, Y., Hyodo, A., et al. (2015). "A compilation of the stable isotopic compositions of carbon, nitrogen, and sulfur in soft body parts of animals collected from deep-sea hydrothermal vent and methane seep fields: Variations in energy source and importance of subsurface microbial processes in the sediment-hosted systems," in *Subseafloor biosphere linked to hydrothermal systems: TAIGA concept*. Editors J. Ishibashi, K. Okino, and M. Sunamura (Tokyo: Springer Japan), 105–129. doi:10.1007/978-4-431-54865-2_10

Ziegler, A. F., Smith, C. R., Edwards, K. F., and Vernet, M. (2017). Glacial dropstones: Islands enhancing seafloor species richness of benthic megafauna in west antarctic peninsula fjords. *Mar. Ecol. Prog. Ser.* 583, 1–14. doi:10.3354/meps12363

frontiers | Frontiers in Earth Science

TYPE Original Research
PUBLISHED 13 December 2023
DOI 10.3389/feart.2023.1277027

OPEN ACCESS

EDITED BY
Jochen Knies,
Geological Survey of Norway, Norway

REVIEWED BY
Sunil Vadakkepuliyambatta,
National Centre for Polar and Ocean Research (NCPOR), India
Wolfram Geissler,
Alfred Wegener Institute Helmholtz Centre for Polar and Marine Research (AWI), Germany

*CORRESPONDENCE
Thomas Birchall,
tom@geobirch.com

RECEIVED 13 August 2023
ACCEPTED 30 October 2023
PUBLISHED 13 December 2023

CITATION
Birchall T, Jochmann M, Betlem P, Senger K, Hodson A and Olaussen S (2023), Permafrost trapped natural gas in Svalbard, Norway.
Front. Earth Sci. 11:1277027.
doi: 10.3389/feart.2023.1277027

Permafrost trapped natural gas in Svalbard, Norway

Thomas Birchall[1]*, Malte Jochmann[1,2], Peter Betlem[1,3], Kim Senger[1], Andrew Hodson[1,4] and Snorre Olaussen[1]

[1]Department of Arctic Geology, The University Centre in Svalbard, Longyearbyen, Norway, [2]Store Norske Spitsbergen Kulkompani AS, Longyearbyen, Norway, [3]Department of Geosciences, University of Oslo, Oslo, Norway, [4]Department of Environmental Science, Western Norway University of Applied Science, Sogndal, Norway

Permafrost is widespread in the High Arctic, including the Norwegian archipelago of Svalbard. The uppermost permafrost intervals have been well studied, but the processes at its base and the impacts of the underlying geology have been largely overlooked. More than a century of coal, hydrocarbon, and scientific drilling through the permafrost in Svalbard shows that accumulations of natural gas trapped at the base of permafrost are common. These accumulations exist in several stratigraphic intervals throughout Svalbard and show both thermogenic and biogenic origins. The gas, combined with the relatively young permafrost age, is evidence of ongoing gas migration throughout Svalbard. The accumulation sizes are uncertain, but one case demonstrably produced several million cubic metres of gas over 8 years. Heavier gas encountered in two boreholes on Hopen may be situated in the gas hydrate stability zone. While permafrost is demonstrably ice-saturated and acting as seal to gas in lowland areas, in the highlands permafrost is more complex and often dry and permeable. Svalbard shares a similar geological and glacial history with much of the Circum-Arctic, suggesting that sub-permafrost gas accumulations are regionally common. With permafrost thawing in the Arctic, there is a risk that the impacts of releasing of methane trapped beneath permafrost will lead to positive climatic feedback effects.

KEYWORDS

permafrost, natural gas, cryosphere, greenhouse gas, methane, Arctic

1 Introduction

Thawing permafrost results in the release of methane gas to the atmosphere (Knoblauch et al., 2018). Methane is a potent greenhouse gas and its release from permafrost acts as a positive climatic feedback loop (Lashof and Ahuja, 1990; Boucher et al., 2009; Howarth et al., 2011). The Arctic is particularly sensitive to climatic changes due to the polar amplification effect and Svalbard is one of the most rapidly warming places today (Aagaard et al., 1987; Divine and Dick, 2006; Van Pelt et al., 2016). Svalbard is, therefore, a critical site for studying the evolution of permafrost and sub-permafrost processes (Isaksen et al., 2000; Christiansen et al., 2010; Hodson et al., 2019; Hornum et al., 2020).

While methane emissions from thawing of the permafrost's uppermost surface, i.e., the active layer, is relatively well understood (Vonk and Gustafsson, 2013; Knoblauch et al., 2018), the prevalence and volumes of gas accumulations trapped beneath the permafrost, i.e., the "cryospheric cap" (Anthony et al., 2012), have been much less studied. Here we present evidence of such gas accumulations in Svalbard, where the relatively young (e.g., 2–4 kyr in Adventdalen) permafrost (Gilbert et al., 2018) appears to be sealing significant gas accumulations. The gas here may originate from biogenic or thermogenic processes (Hodson

et al., 2019; Ohm et al., 2019) and may be in free-gas form or, under the right compositional and thermobaric conditions, in the form of natural gas hydrates (Sloan et al., 2007; Betlem et al., 2019).

Occurrences of gas originating from within or below intervals of permafrost are typically identified in studies on natural gas hydrates and have been documented in both the Russian (Chuvilin et al., 2000; Yakushev and Chuvilin, 2000; Skorobogatov et al., 2007; Makogon and Omelchenko, 2013; Chuvilin et al., 2020) and North American Arctic (Bily and Dick, 1974; Kamath et al., 1987; Majorowicz and Hannigan, 2000; Collett et al., 2011; Nielsen et al., 2014).

Permafrost is defined as ground that remains at <0°C for more than two consecutive years, regardless of fluid content. Physically speaking, ice-saturated permafrost possesses extremely good sealing properties (Keating et al., 2018). However, its effectiveness it is as a long-lived and laterally continuous seal is uncertain. In Svalbard this is reflected by methane emissions at pingos (Hodson et al., 2019) where permafrost demonstrates its local sealing ability but also the prevalence of migration pathways through it. Abrupt changes in hydrogeological flow conditions at the base of the permafrost also indicate the permeability-reducing nature of the permafrost interval (Hornum et al., 2020). In geological terms, permafrost is very short-lived which, in addition to being very shallow and potentially patchy, would typically preclude it from being regarded as a feasible seal for conventional hydrocarbon accumulations at geological timescales of millions of years.

In Svalbard, methane migrating through near-coastal pingos shows characteristics of a biogenic origin (Hodson et al., 2019). Approximately 3 km inland, analysis of gas encountered at the base of permafrost during research drilling indicated a further contribution from thermogenic origins (Ohm et al., 2019). Several hydrocarbon source rocks are encountered in Svalbard, so traces of thermogenic gas are not particularly surprising. What is surprising, and the focus of this study, is the widespread occurrence, both spatial and stratigraphic, of gas accumulations at the base of permafrost in Svalbard.

In this contribution, we provide previously unpublished data from 41 boreholes to systematically review the occurrence of sub-permafrost gas accumulations from Svalbard. We also analyse data from these boreholes to attempt to characterise the permafrost, its thickness and sealing properties.

2 Geological and physiographic setting

The Svalbard archipelago is situated in the High Arctic between 74° and 81°N and 15° to 35°E with sub-zero average air temperatures for 8 months of the year. Permafrost in Svalbard is typically thinner than the other pan-Arctic landmasses at the same latitude due to the warming effects of the West Spitsbergen Currentand the effects of glaciers and their erosion (Humlum, 2005).

Permafrost in Svalbard ranges in thickness from more than 500 m in mountainous areas inland to less than 100 m near the coastlines (Humlum, 2005). Continuous sub-sea permafrost is absent offshore Spitsbergen's west coast (Christiansen et al., 2005), and is not believed to be present offshore elsewhere around Svalbard (Landvik et al., 1988; Humlum et al., 2003), although these areas have been little studied in this respect and may feature locally discontinuous permafrost. Because of the West Spitsbergen Current, air temperatures are several degrees warmer in the west than they are in the east (Przybylak et al., 2014). Although poorly studied in eastern parts, one can reasonably anticipate thicker permafrost due to colder temperatures, as is also shown by numerical modelling of the permafrost-associated gas hydrate stability zone (Betlem et al., 2019). However, thicker insulating snow coverage in coastal settings can also help in preventing winter heat loss from the ground and limit permafrost growth (Humlum et al., 2003). In a more local context, permafrost in the major valley of Adventdalen has been relatively well studied and comprises a thin permafrost interval of 20–30 m (though containing liquid water due to salinity) on the coast, that rapidly thickens to approximately 150 m thick 3 km inland at the Longyearbyen CO_2 site, and approximately 220 m thick in the valley at Janssonhaugen, some 15 km from the coast (Figure 1; Isaksen et al., 2000; Harada and Yoshikawa, 1996; Gilbert et al., 2018).

Permafrost evolution in Svalbard is largely driven by glacial settings rather than temperature changes. During the Weichselian glacial stage (115 kya to 11.7 kya) Svalbard was covered by thick glacial ice, although the extent and thickness of this ice cover is still debated (e.g., Gataullin et al., 2001; Lambeck, 1996: Winsborrow et al., 2010). Glacial striations in several locations suggest that these glaciers were warm-based for at least parts of the Weichselian glaciation (Humlum et al., 2003; Humlum, 2005). The frictional heat generated from the sliding of warm-based glaciers likely thawed permafrost in major valleys (Humlum et al., 2003). Sedimentological and cryostratigraphic analysis of boreholes in Adventdalen support this (Gilbert et al., 2018), suggesting that the permafrost in Adventdalen formed in the past few thousand years following the dynamic retreat of these warm-based glaciers and ice streams. Whether permafrost survived the Weichselian glaciations is dependent on the persistence of ice-free zones and/or cold based glaciers. Because of this, permafrost in highland areas was more likely to have survived, possibly for several hundred thousand years, through multiple glacial events (Humlum et al., 2003). There is also strong evidence of lowland areas in north-western Svalbard being ice-free at this time which may have enabled the persistence of much older permafrost (Landvik et al., 2003). Valley settings are pertinent to this study as the majority of wellbores have been drilled in valleys or near to the coast for logistical reasons.

Permafrost often poses a challenge to geologists, particularly during drilling (Vrielink et al., 2010), and in the acquisition and processing of seismic data (Johansen et al., 2003; Schmitt et al., 2005). This is because permafrost changes the properties of shallow unlithified sediments to become much more rigid if cemented by ice. Therefore, the permafrost interval in these sedimentary rocks has much faster seismic velocities and can lose mechanical competence as it is drilled through with heated or saline fluids. The near-surface rocks in Svalbard are typically well cemented due to mechanical and chemical compact and very rigid due to deep burial and subsequent uplift (Henriksen et al., 2011).

In a tectonic context, Svalbard represents the exposed north-western part of the Barents Shelf. With the exception of the late Cretaceous and parts of the Neogene, Svalbard exhibits a nearly continuous stratigraphic record from the Devonian to present (Steel and Worsley, 1984; Olaussen et al., 2022). Figure 1 shows the distribution and ages of outcrops in Svalbard and the key

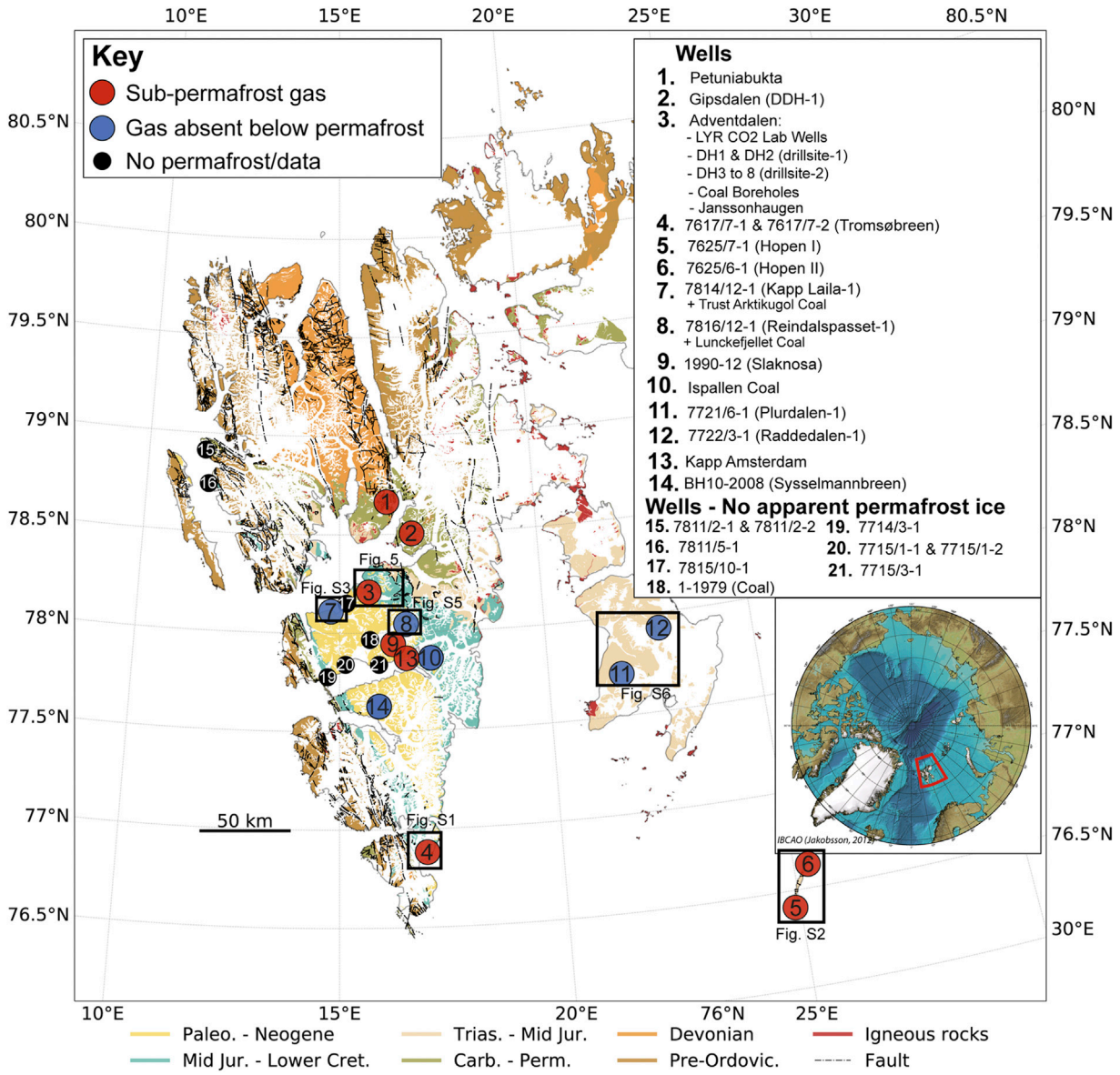

FIGURE 1
Geological map of Svalbard with boreholes and areas of interest investigated in this study. Geological data is courtesy of Norwegian Polar Institute (Dallmann et al., 2015). The locations of detailed maps shown in later figures are highlighted.

wellbore sites for this study. Palaeozoic events from the Caledonian (Gasser, 2014) and Ellesmerian-Svalbardian (Piepjohn, 2000) orogenies are predominantly recorded in the northern parts of Svalbard. From the late Carboniferous to Permian, mixed shallow marine rocks were deposited in localised half-grabens (Bælum and Braathen, 2012; Smyrak-Sikora et al., 2019). From the Triassic to early Cretaceous, clastic deposition occurred in regional-scale basins (Steel and Worsley, 1984). The drainage pattern changed from the west in the early Triassic to the east from the middle Triassic. During this time Svalbard was situated on the northwestern periphery of the largest recorded delta system in Earth's history (Mørk, 2013; Anell et al., 2014; Klausen et al., 2019). The latest Triassic to middle Jurassic saw much less sedimentation with numerous hiatuses and changes in drainage patterns (Olaussen et al., 2018; Rismyhr et al., 2019). The late Jurassic to early Cretaceous saw greater deposition, including regionally important source rock intervals, and change in drainage due to the opening of the Amerasian Basin (Dypvik and Zakharov, 2012; Koevoets et al., 2018). During the early Cretaceous the development of the High Arctic Large Igneous Province is evident from predominantly mafic dykes and sills in Svalbard (Senger et al., 2014). This likely resulted in major erosion during the late Cretaceous and early Palaeocene (Jochmann et al., 2019).

In Svalbard and the rest of the Barents Shelf, the Cenozoic geological history is the most important to understand subsurface fluid flow. Maximum burial of the rocks exposed in Svalbard occurred during the Eocene (Dörr et al., 2018)

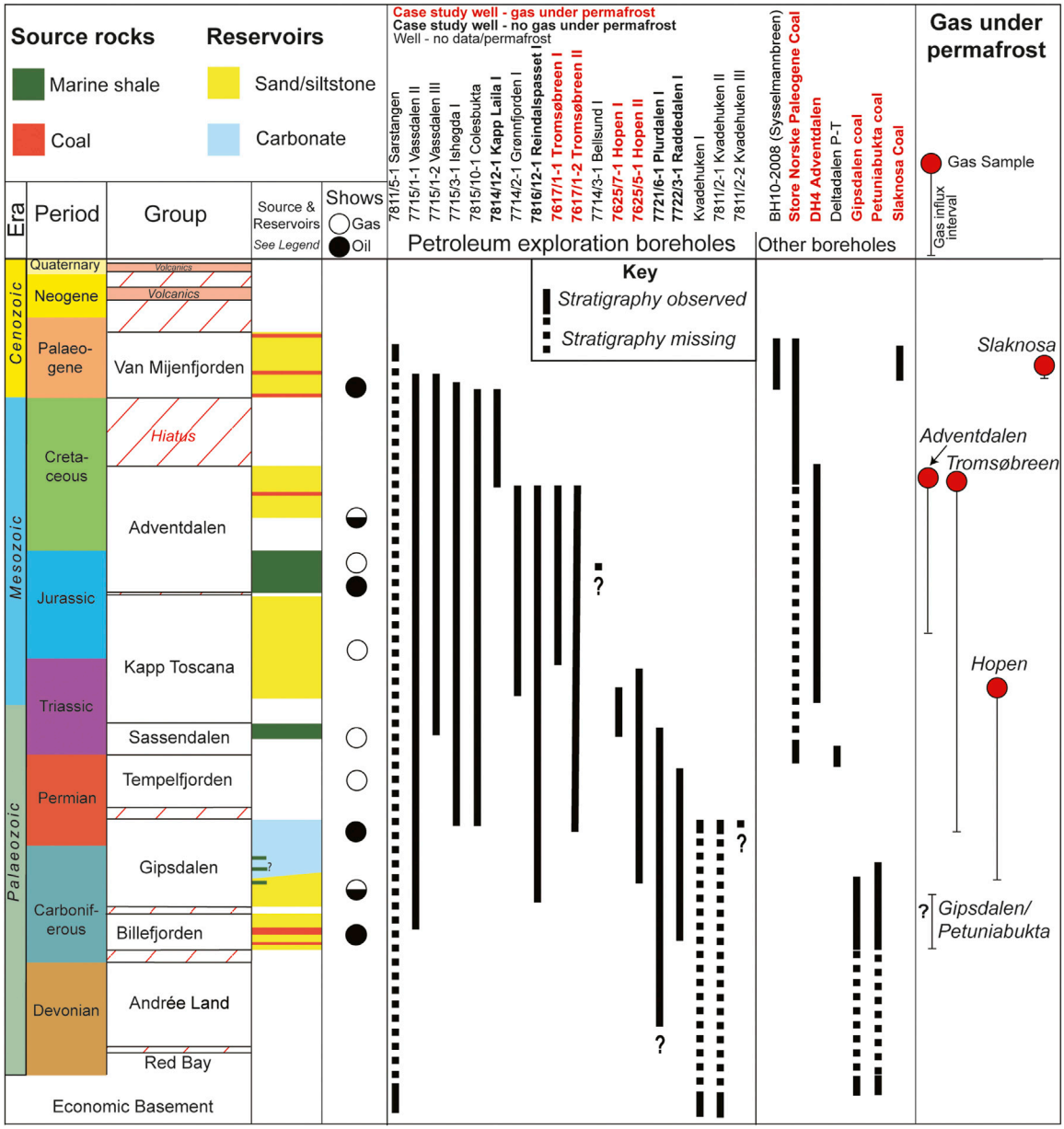

FIGURE 2
The hydrocarbon exploration wells of Svalbard and key coal and scientific boreholes showing the stratigraphy they penetrated, modified from Senger et al. (2019). The base-permafrost, gas-bearing stratigraphy is shown in the right hand column.

whereas the stratigraphy of the Barents Sea experienced maximum burial and hydrocarbon generation during the late Oligocene to early Miocene (Faleide et al., 1996; Henriksen et al., 2011). From the Eocene to present, major regional events resulted in the cumulative uplift of 1–3 km and is ongoing at present. The Svalbard region experienced the greatest uplift magnitudes, resulting in it being subaerially exposed as an archipelago today (Dimakis et al., 1998; Lasabuda et al., 2018). For this study, the most pertinent geological events are the widespread uplift and erosion due to repeated glacial-interglacial cycles during the past few million years (Dimakis et al., 1998; Landvik et al., 1998). These recent events are still ongoing (Kierulf et al., 2022) and are the most important with respect to the migration and leakage of hydrocarbons from deeper traps to the shallow subsurface (Ohm et al., 2008; Abay et al., 2017).

The prevalence of hydrocarbon shows and gas influxes throughout the stratigraphy can be attributed to the presence of multiple mature source rocks (Figure 2; Ohm et al., 2008). The marine shales of the late Jurassic-early Cretaceous Agardhfjellet Formation and the mid-Triassic Botneheia Formation are both regionally extensive and prolific source rocks, responsible for charging most of the oil and gas discoveries in the Norwegian Barents Sea. In addition, Permian organic-rich shales in the Gipsdalen Group (Braathen et al., 2012) probably represent laterally restricted source rocks. Carboniferous, Cretaceous and

Paleogene coal seams have been exploited in Svalbard's past, with the latter still under production in the Central Tertiary Basin in Adventdalen and Barentsburg. These coal seams are widespread and typically form gas-prone and oil-prone source rocks (Marshall et al., 2015; Uguna et al., 2017).

Numerous sandstones and karstified carbonates provide potential reservoirs throughout Svalbard's stratigraphy (Figure 2), many of which are direct analogues to proven hydrocarbon reservoirs in the Barents Sea (Nøttvedt et al., 1993; Olaussen et al., 2022). For this study the most notable reservoirs are the shallow marine sandstone-dominated Lower Cretaceous Helvetiafjellet and Carolinefjellet formations (Steel et al., 1981; Grundvåg et al., 2019), and the Triassic-Jurassic Kapp Toscana Group deltaic to shoreline deposited siltstone and sandstones (Mørk, 1999; Rismyhr et al., 2019).

The above-mentioned source rocks are also the best candidates for sealing intervals due to their extremely low permeability and high ductility due to high organic content. In addition, the mudstones of the late Palaeocene Basilika Formation and Palaeocene-Eocene Frysjaodden Formation also possess potential sealing properties (Steel et al., 1981). The numerous source rocks, technical oil and gas discoveries, bitumen-stained strata and surface seeps suggest that Svalbard possesses working petroleum systems (Olaussen et al., 2022 and references therein). Nonetheless, none of the eighteen exploration wells drilled onshore Svalbard from 1961 to 1994 resulted in commercially viable discoveries (Senger et al., 2019). Although hydrocarbon accumulations likely first formed tens of millions of years ago when source rocks were at maximum burial (Magoon and Dow, 2000), subsequent tectonic events have undoubtedly caused tertiary fluid migration (Ohm et al., 2008; Abay et al., 2017).

Repeated glaciation and deglaciation of the Barents region through the Quaternary has caused tilting and hydrocarbon spillage and remigration from existing traps (Lasabuda et al., 2018 and references therein: Lerche et al., 1997).Gas, particularly methane, is the dominant hydrocarbon found in Svalbard due to the prevalence of over-mature or gas-prone source rocks (Michelsen and Khorasani, 1991; Ohm et al., 2019; Senger et al., 2019) and active methanogenesis (Hodson et al., 2019). Deglaciation and uplift has reduced confining pressure on subsurface fluids and led to gas exsolution and expansion. Therefore, the subsurface fluid systems in Svalbard are in a state of disequilibrium and widespread hydrocarbon migration is likely ongoing at present (Abay et al., 2017). Evidence of this is manifested as out-of-equilibrium pore pressures (Birchall et al., 2020) and the previously mentioned surface seeps across Spitsbergen.

In Svalbard, the timing of hydrocarbon migration and permafrost formation overlap, meaning there is potential for accumulations to develop beneath the impermeable permafrost. Although numerous hydrocarbon and coal exploration wellbores penetrate the entire permafrost interval, it has rarely been of interest to the operators. However, on detailed inspection of well data, reports, and anecdotal evidence, it is clear that sub-permafrost gas accumulations have been frequently encountered throughout the archipelago (Figure 2). In Adventdalen, sub-permafrost free-gas was first documented in 1967 during coal exploration and encountered again in 1979 (SNSK, 1981). This accumulation was further confirmed and sampled during scientific drilling of the Longyearbyen CO_2 Lab between 2008 and 2012 (Huq et al., 2017; Ohm et al., 2019).

3 Materials and methods

Several decades of coal and petroleum exploration as well as research drilling in Svalbard has led to much anecdotal evidence of gas accumulations beneath permafrost. We have attempted to verify this by analysing data from boreholes that have penetrated through the permafrost in Svalbard. These boreholes include eighteen hydrocarbon exploration wells, approximately five hundred coal exploration bores, and ten scientific boreholes, eight of which are from the Longyearbyen CO_2 Lab (Olaussen et al., 2019). Coal exploration drilling data are integral to this study and come from some five hundred coal exploration boreholes that were drilled over the course of nearly a century by Store Norske Spitsbergen Kullkompani (SNSK, 1979), although are more fragmentary and proprietary. We identify where gas accumulations occur and where these coincide with the base of permafrost, or the first permeable interval below it. The available well data used in this study are presented in Table 1. Despite good spatial and stratigraphic wellbore coverage in Svalbard (Figures 1, 2), there are still some significant challenges in identifying the presence of sub-permafrost gas accumulations, most of which relate to identifying permafrost and its base in the available data, and eliminating other potential causes of gas influxes.

The most obvious evidence of permafrost comes from reliable downhole temperature measurements. However, in industrial boreholes, downhole temperature data are typically obtained during wireline logging and are highly unreliable. This is due to wellbores rarely being allowed to reach thermal equilibrium with the surrounding formations following drilling and fluid circulation. Heating drilling mud was also required to be circulated in these wellbores to prevent them from freezing, making direct temperature measurements of the formations impossible. Therefore, accurate absolute temperature measurements are rare, though temperature trends can be used more qualitatively to estimate the approximate base permafrost position. Wells monitored over longer time periods, such as the scientific boreholes in Adventdalen and at Sysselmannbreen (Juliussen et al., 2010; Olaussen et al., 2019) are relatively rare, but provide much more reliable and precise temperature data.

The uppermost active layer of permafrost (down to ca. 2 m) is well-studied in Svalbard (Rachlewicz and Szczuciński, 2008; Westermann et al., 2010; Strand et al., 2021). Conversely, the base permafrost is rarely the focus of academic study due to its inaccessible nature and, thus, the overwhelming majority of data come from industrial boreholes. The base permafrost has been of little industrial interest resulting in limited data acquisition over the permafrost interval. Downhole logging data over the interval typically comprises only of gamma ray data. Additionally, the very low porosity of Svalbard's highly compacted rocks (Henriksen et al., 2011) means that the effect of any pore fluid change such as the contrast of ice and water at the base of permafrost, is impossible to identify in petrophysical data alone. However, drilling data, such as fluid influxes into the wellbore do provide reliable evidence as to where impermeable permafrost ice is absent. Table 2 shows the ideal responses of petrophysical and drilling data at the base permafrost boundary and the challenges posed to each method in Svalbard. Further uncertainties as to the precise location of the base of permafrost arise from the fact that

TABLE 1 Data availability and intervals recorded for the permafrost penetrating boreholes. BHT = bottom hole temperature. For petrophysical data, the start of data refers to the shallowest extent of each well log, with coverage extending from that point to the bottom of the wellbore.

Well	Petrophysics – Start of data (measured depth)						Gas Data		Well Report
	Gamma Ray	Resistivity	Acoustic	Density	Temperature	Cuttings	Gas Shows (Chromatograph)	Depth of Fluid Sample	
Hydrocarbon Exploration									
7617/7-1 Tromsøbreen-1	(Drilling parameters only)				BHT	Entire well	Entire well	768 m	Y
7617/7-2 Tromsøbreen-2	17 m	350 m	350 m	330 m	BHT	Entire well	Entire well	-	Y
7625/7-1 Hopen-1	3.5 m	Spontaneous potential	-	-	BHT	Entire well	Entire well	c. 150 m	Y
7625/6-2 Hopen-2	Entire well	349 m	349 m	638 m	Entire well	Entire well	Entire well	-	Y
7714/2-1 Grønnfjorden	not logged					Cored	-	-	Y
7714/3-1 Bellsund	?								N
7715/1-1 Vassdalen-2	Entire well	17	-	-	-	-	-	-	N
7715/1-2 Vassdalen-3	-	-	-	-	-	-	-	-	N
7715/3-1 Ishøgda	Entire well	Entire well	Entire well	Entire well	Entire well	Entire well	-	-	N
7721/6-1 Plurdalen	5 m	83 m	5 m	83 m	Entire well	Entire well	Entire well	Water at 500 m	Y
7722/3-1 Raddedalen	Entire well	5 m	591 m	593 m	5 m	Entire well	Entire well	-	Y
7811/2-1 Kvadehuken-1	not logged					Cored	-	-	N
7811/2-2 Kvadehuken-2	not logged					Cored	-	-	N
-Kvadehuken-0	Shallow, no data								
7811/5-1 Sarstangen	30 m	615 m			BHT	Entire well	260m	-	Y
7814/12-1 Kapp Laila	Entire well	- (SP logged)				24 m (partial recovery)			Y
7815/10-1 Colesbukta	Entire well	41 m	1467 m	-	-	-	-	-	N
7816/12-1 Reindalspasset	Entire well	22 m (induction)	22 m	22 m	17.4 m	Entire well	20 m	-	Y
Selected Coal Boreholes									
1967-1 Adventdalen	Cored (not logged)						Y	-	Y
1979-10 Adventdalen							-	-	Y
1979-11 Adventdalen							-	-	Y
DDH1B Gippsdalen							-	-	Y

(Continued on following page)

TABLE 1 (*Continued*) Data availability and intervals recorded for the permafrost penetrating boreholes. BHT = bottom hole temperature. For petrophysical data, the start of data refers to the shallowest extent of each well log, with coverage extending from that point to the bottom of the wellbore.

Well	Petrophysics – Start of data (measured depth)						Gas Data		
	Gamma Ray	Resistivity	Acoustic	Density	Temperature	Cuttings	Gas Shows (Chromatograph)	Depth of Fluid Sample	Well Report
1982-20	No data						-	-	1982 drilling summary
Gruve 7 - H1							Y	-	1979 drilling summary
1981-02							-	-	1981 drilling summary
1981 (Platåberget)							-	-	1981 drilling summary
1981-05 Breinosa	Cored (not logged)						-	-	1981 drilling summary
1981-06 Breinosa							-	-	1981 drilling summary
1979-1 Reindalen							-	-	Y
1990-12 Slaknosa							-	-	Y
Scientific Boreholes									
DH1	3 m	3 m	9 m	-	Entire well	Cored	-		Y
DH2	10 m	10 m	10 m	-	Entire well	Cored	-	-	Y
DH3	Cored: not logged					Cored	-	-	Y
DH4	Entire well	440 m	440 m	-	Entire well	Cored	-	Entire well	Y
DH5r	3 m	-	100 m	-	Entire well	Cored	-	Below 645 m	Y
DH6	Cored: not logged					Cored	-		Y
DH7a	Cored: not logged					Cored	-	Below 645 m	Y
DH8 (Shallow)	Cored: not logged					Cored	-	-	Y
BH10-2008	Entire well	67 m	48 m	Entire well	-	-	-	-	Y
Janssonhaugen (temperature)	-	-	-		Entire well	-	-	-	N

the drilling fluid used in the wellbores is typically heated and hypersaline. The final challenge is that the characteristics of the base permafrost boundary is poorly understood. Factors such as water presence, chemistry, heterogenous geology, thermal conductivity and associated dynamic processes make predicting the base permafrost properties challenging It is a reasonable assumption that it is likely a diffuse boundary which adds further uncertainty in identifying it. Nevertheless, the combination of drilling data for identifying formation fluids (e.g., fluid influxes into the wellbore) and petrophysical data for lithological interpretation (e.g., sandstone vs. shale) can indicate where the transition from permafrost ice to liquid water occurs. Fluid influxes with no discernible change in lithology or other trapping features (e.g., faulting) can be found in porous and permeable strata in Adventdalen, Hopen, Tromsøbreen, Gipsdalen, and Petuniabukta (Figure 1). Other indicators that can help identify the position of permafrost include the formation of ice within the wellbore (often referred to as ice-

TABLE 2 Petrophysical and drilling parameters that may identify permafrost and its base. Idealised responses are shown and typically identify the transition from ice to water. The final column shows the complicating factors, all of which are applicable to Svalbard. Perhaps the most pertinent complication to Svalbard is that the geology is comprised of well cemented, compacted, hard rocks.

Log type	Property measured (Units)	Idealised permafrost response	Complicated by
Petrophysical Data			
Gamma ray	Radioactivity of rocks (API)	No Response but useful in determining lithology	N/A
Acoustic (Sonic)	Seismic velocity of rocks and fluids within. Measured in slowness (microsecond per foot)	Faster velocities (lower slowness) in icebound intervals	Overcompacted, dense and rigid rocks
			Low porosity and heterolithic rocks
Resistivity	Resistivity of rocks and fluids within	High resistivity in permafrost becoming low in water bearing interval	Resistive hydrocarbons below permafrost
			Fresh water below
			Low porosity rocks
			Clay rich and heterolithic rocks
Density	Density of rocks and fluids within	Decreased density in ice-bearing intervals	Low porosity
			Heterolithic rocks (fluid response is generally overwhelmed by lithological response)
Temperature	Temperature of fluid in borehole at a given depth	0°C or lower in permafrost interval	Measures wellbore fluid, not fluid within formation
			Drilling fluid circulates and is often heated
			Requires a long time to equilibrate to formation
Fluid Sampling	Pressure and fluid properties	Qualitative - shows fluid phase and type	Low permeability (including permafrost ice)
		Abnormal pressures indicate a vertical barrier or seal	Limited to few points in well
			Shallow samples rarely of interest
Drilling Parameters			
Fluid influx	Fluid entering wellbore (often flowing to surface)	Indicates transition from impermeable to permeable zone	Exact depth of influx is uncertain
Background gas	Measures levels and composition of gas returned with drilling fluid at the surface. Does not measure dissolved gas. (Percentage or parts per x)	Indicates transition from impermeable to permeable zone	Varies depending on drilling rate, permeability, drilling mud type
			Exact depth/formation of gas origin is uncertain
Rate of penetration (ROP)	The rate the drill bit penetrates the ground (ft. or m per hour)	A rapid rise in rate of penetration when transitioning from ice-bound to unbound rock	Well-cemented, compacted and hard rocks
		Best used with Weight-on-bit (1000 lbs) measurement	Rate can depend on external factors including drill bit condition
D-exponent	Extrapolation of numerous drilling parameters to estimate pore-pressure	May identify anomalously high drilling rate (or pressure) at base permafrost	Well cemented, compacted and hard rocks
			Heterolithic rocks
			Largely qualitative

plugging), sudden changes in the character or quantity of drill cuttings, and increases in background gas measurements. The presence of overpressures at the base of permafrost is commonly reported in drilling reports, which, in the absence of lithological boundaries, is strong evidence that permafrost is acting as an impermeable seal.

Similarly, the presence of trapped gas at the base of permafrost (Figure 2) is also testament to its sealing potential. Identifying the presence of gas is relatively simple with evidence in the form of gas influxes into the wellbore. In some cases, such as Adventdalen, Tromsøbreen and Hopen, shallow gas from the base of the permafrost was collected for hydrocarbon analysis. Elevated free gas levels (but not gas dissolved in fluids) recorded in the returning drilling fluid is another good indicator of gas entering the wellbore from the formation, and is measured in drilling fluids returning to the surface and extracted by a gas

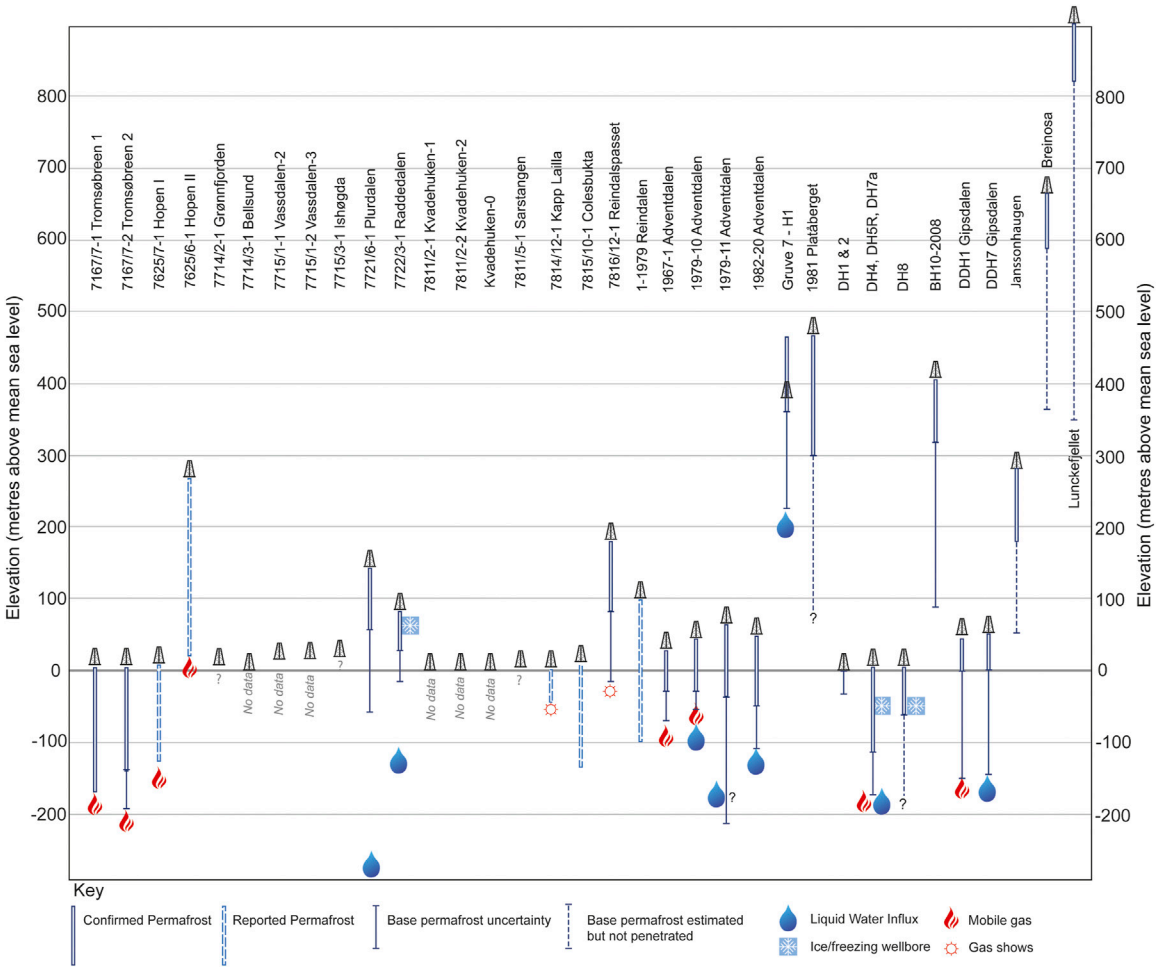

FIGURE 3
A plot of the wellbores in this study showing their elevation and the depth to the base of permafrost seal. Solid well path outlines show where data analysed in this study confirms the presence of permafrost while dashed outlines represent where base permafrost has been reported but data is not available. For the Breinosa wellbore, which shows −7.8° at its coldest point at 78 m (and a TD at 90 m) (Juliussen et al., 2010), we extrapolated the base permafrost the local geothermal gradient of 35°/km (Isaksen et al., 2000; Betlem et al., 2018; Senger et al., 2023). Borehole locations are shown in Figure 1.

trap. A variety of factors, including drilling rate, drilling mud type and temperature; lower temperatures can result in lower gas influx detection rates, also due to greater levels of condensation and viscosity (Marum et al., 2019).

In addition to well reports and wireline log data, we also include data from published studies including isotope (Huq et al., 2017), thermobaric (Isaksen et al., 2000; Betlem et al., 2018; Betlem et al., 2019), geophysical (Johansen et al., 2003; Beka et al., 2017) and geochemical (Leythaeuser et al., 1984; Ohm et al., 2008) analyses. We also analysed Russian published literature for areas operated by Trust Arktikugol (Lyutkevich, 1937; Verba, 2013).

For Adventdalen, Tromsøbreen and Hopen (with the latter two found in the appendices) we performed simple modelling to estimate the permafrost thickness in addition to the gas hydrate stability zone using the workflow outlined in Betlem et al. (2019) and further refined in Betlem et al. (2021). The modelling implements gas hydrate phase boundary curves relevant to each location, generated through the HWHYD modelling software (Masoudi and Tohidi, 2005). The model utilises spatial mean annual air temperature after Pryzbylak et al. (2014) and a vertical lapse rate of −6°C per km of elevation and geothermal gradient of 33°C per km of increasing depth. The model assumes steady state conditions and a hydrostatic fluid pressure gradient from the land surface.

4 Results

4.1 Evidence of permafrost

Integrating all data provides good evidence as to the presence of ice-bearing permafrost in different geographical settings. From the perspective of permafrost as an impermeable seal we have observed differences in three geographical settings: coastal areas, valleys, and highlands. Figure 3 shows the estimated permafrost thicknesses from all relevant wellbores in this study (see Figure 1 for well locations).

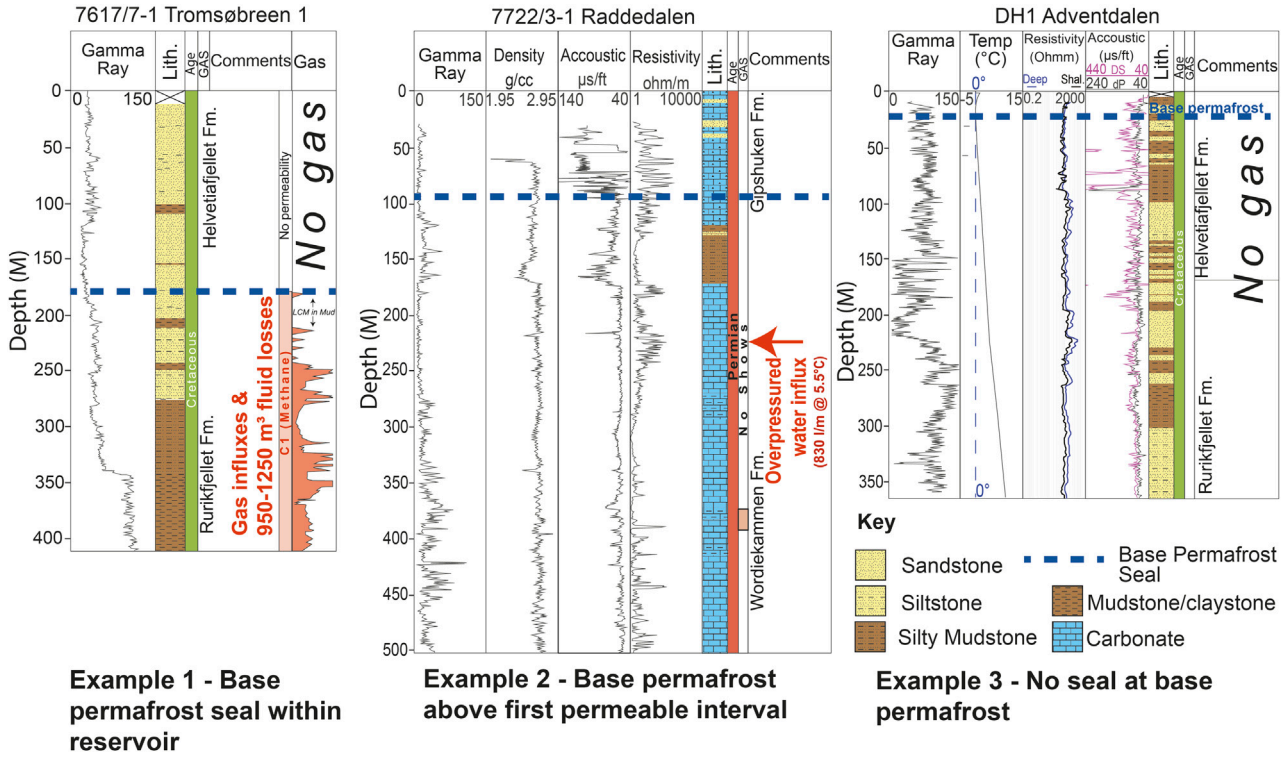

FIGURE 4
Examples of different types of base permafrost. Example 1 is the most commonly encountered and shows where permafrost within a normally permeable interval transforms it into a seal. In this Tromsøbreen example, methane influxed the wellbore at this base permafrost seal in addition to drilling fluid being lost into the formation which is further evidence of the change in permeability. Example 2 is where permafrost ice exists but the base is above the first impermeable interval. The Raddedalen well on the island of Edgeøya is a rare example of where evidence of the base permafrost exists in the petrophysical data, as shown by the acoustic log skipping and resistivity drop. Example 3 is a case where a permafrost interval demonstrably exists by definition (below 0°C) but apparently lacks any seal, in this case by the coast in Adventdalen, the lack of seal is probably due to fluid salinity.

In coastal areas in the west, evidence is mixed for the presence of ice-bearing permafrost (Figure 1). Hydrocarbon exploration wells on the west coast acquired limited data over shallow parts but provide no evidence of a sealing permafrost interval. However, wellbore temperature data from the western fjord of Isfjorden shows the evidence of a thin permafrost interval (UNIS CO_2 Lab AS, 2015; SNSK, 1994). At Kapp Laila, on the southern Isfjorden coast, the permafrost interval is apparently ice-bearing, while around the town of Longyearbyen the permafrost interval is not, likely due to the presence of saline fluids. At Kapp Amsterdam, near the coal mining settlement of Svea, thin sealing permafrost interval (SNSK, 1986). In the east, where air temperatures are cooler (Pryzbylak et al., 2014), observations indicate thicker ice-bearing permafrost intervals.

Data from valleys show the strongest evidence of sealing permafrost throughout Svalbard. Wellbores in valleys (Figure 1). Wellbores in five valleys in Central Spitsbergen and two on Edgeøya demonstrate this and are discussed in more details in later sections. The majority of these cases are based on the occurrence of overpressure or free gas accumulations in reservoirs without an overlying conventional seal.

In colder highland areas the permafrost interval (by temperature definition) is thicker than adjacent valleys. However, different plateau areas appear to possess differing degrees of sealing ice-bound permafrost. In the Adventdalen area and at Ispallen the permafrost zone is permeable as evident by complete drilling fluid losses into the wellbore wile drilling. Converseley at Slaknosa a gas accumulation, without a conventional top seal was encountered.

We have observed that where permafrost can be identified within wellbores, the sealing characteristics can be classed into three types, shown in Figure 4. In much of central Spitsbergen, where the geology is relatively flat-lying and the permafrost interval is often sandstone dominated, the base permafrost can be directly observed to seal by sudden fluid influx into the wellbore despite no apparent downward change in lithology (Figure 3, example 1). Well data can also give evidence that permafrost is acting as a seal laterally away from a wellbore. Figure 4, example 2 may be representative of Edgeøya where the abnormally pressured reservoir was encountered well below the permafrost interval, but because that reservoir outcrops to the east. The latter example of evidence of permafrost sealing is much less certain because of inherent subsurface uncertainties and the transient nature of subsurface fluid flow. Finally, permafrost may be identifiable but is demonstrably not forming a good seal (Figure 4, example 3), which is the case for some highland areas and possibly the coast near Longyearbyen. Table 3 shows these different sealing types for each borehole in this study.

TABLE 3 Wells showing where gas is and is not present at the base of permafrost. Wells without a bullet either contain no permafrost or no relevant data. Base permafrost type: 1) Sealing within reservoir 2) Lateral seal 3) No seal within permafrost (by temperature definition) interval. n/a = no data or no evidence of permafrost.

Well	Evidence for gas under permafrost	Tentative/shows	Permafrost but no gas	Base permafrost type
Hydrocarbon exploration				
7617/7-1 Tromsøbreen-1	•			1
7617/7-2 Tromsøbreen-2	•			1
7625/7-1 Hopen I	•			1
7625/6-1 Hopen II	•			1
7714/2-1 Grønnfjorden				n/a
7714/3-1 Bellsund				n/a
7715/1-1 Vassdalen-2				n/a
7715/1-2 Vassdalen-3				n/a
7715/3-1 Ishøgda				n/a
7721/6-1 Plurdalen			•	2
7722/3-1 Raddedalen			•	2
7811/2-1 Kvadehuken-1				n/a
7811/2-2 Kvadehuken-2				n/a
Kvadehuken-0				n/a
7811/5-1 Sarstangen				n/a
7814/12-1 Kapp Laila		•		1
7815/10-1 Colesbukta				n/a
7816/12-1 Reindalspasset			•	1 or 2
Coal				
1967-1 Adventdalen	•			1
1979-10 Adventdalen	•			1
1979-11 Adventdalen			•	1
1982-20 Adventdalen			•	1
Gruve 7 - H1 Adventdalen			•	1
DDH1B Gippsdalen	•			1 or 2
1979-1 Reindalen		•		1 or 2
1981 Platåberget	TD above base permafrost			3
1981-Breinosa				3
Lunckefjellet				3
Ispallen				3
1990-12 Slaknosa	•			1 or 2
Kapp Amsterdam	•			1
Petuniabukta	•			1
Scientific wellbores				
DH1				3

(Continued on following page)

TABLE 3 (*Continued*) Wells showing where gas is and is not present at the base of permafrost. Wells without a bullet either contain no permafrost or no relevant data. Base permafrost type: 1) Sealing within reservoir 2) Lateral seal 3) No seal within permafrost (by temperature definition) interval. n/a = no data or no evidence of permafrost.

Well	Evidence for gas under permafrost	Tentative/shows	Permafrost but no gas	Base permafrost type
DH2				n/a
DH3				n/a
DH4	•			1
DH5r	•			1
DH6				1
DH7a				
DH8 (Shallow)				1 or 2
BH10-2008			•	1
Janssonhaugen	TD above base permafrost			1 or 2

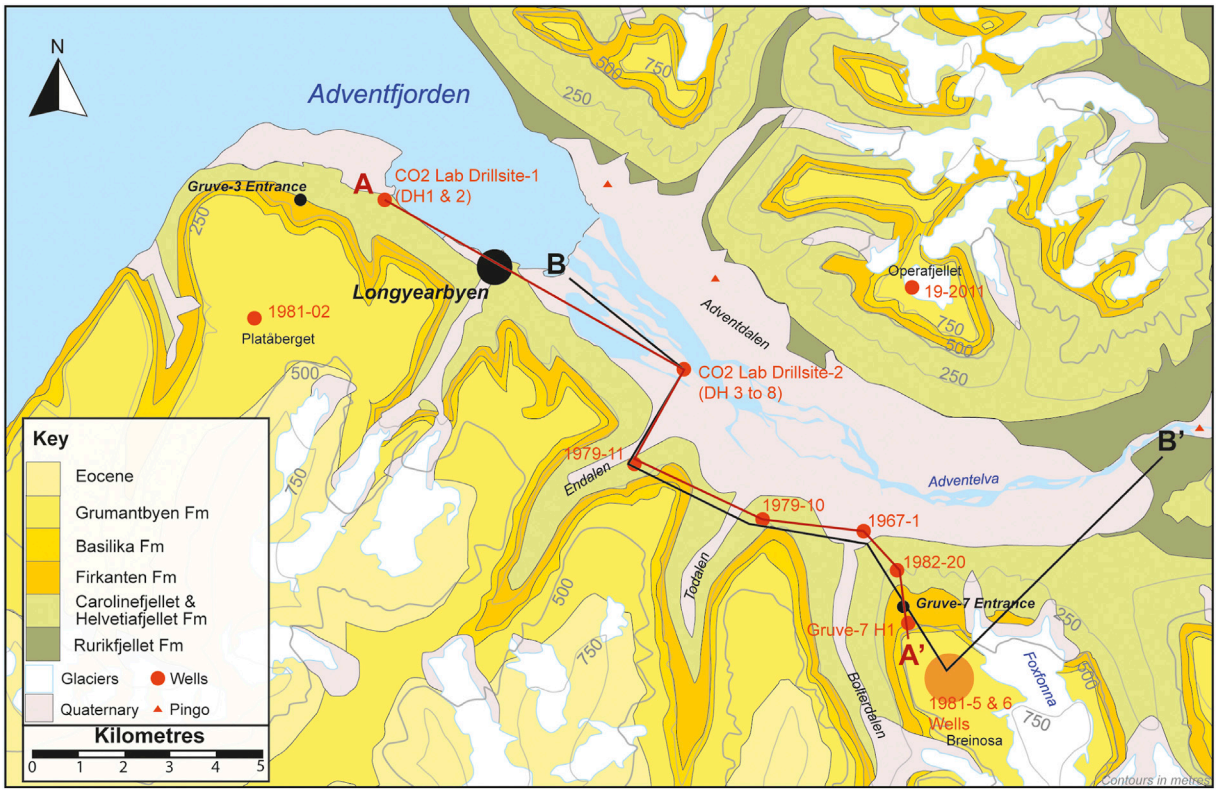

FIGURE 5
A Geological Map of Adventdalen showing some of the youngest stratigraphy exposed in Svalbard. The profile A to A′ represents the well correlation in Figure 6 B to B′ the modelled permafrost profile in Figure 7.

4.2 Permafrost trapped gas

Table 3 shows occurrences of where gas has and has not been encountered at the base of the permafrost. The wells in Adventdalen, Tromsøbreen, Hopen and Gipsdalen all indicate gas accumulation at the base of permafrost despite being geologically distinct (detailed case studies from Tromsøbreen and Hopen can be found in the additional material). The case in Adventdalen comes from multiple wellbores drilled by different operators for different research and economic reasons and is discussed in more detail in this section. The cases from Reindalen, Kapp Laila and the Plurdalen and Raddedalen wells on Edgeøya all demonstrate good evidence of sealing permafrost but lack trapped gas (detailed case studies of these can be found in the Supplementary Material).

Despite the frequency of gas being encountered at the base of permafrost, it should be noted that none of the wellbores were

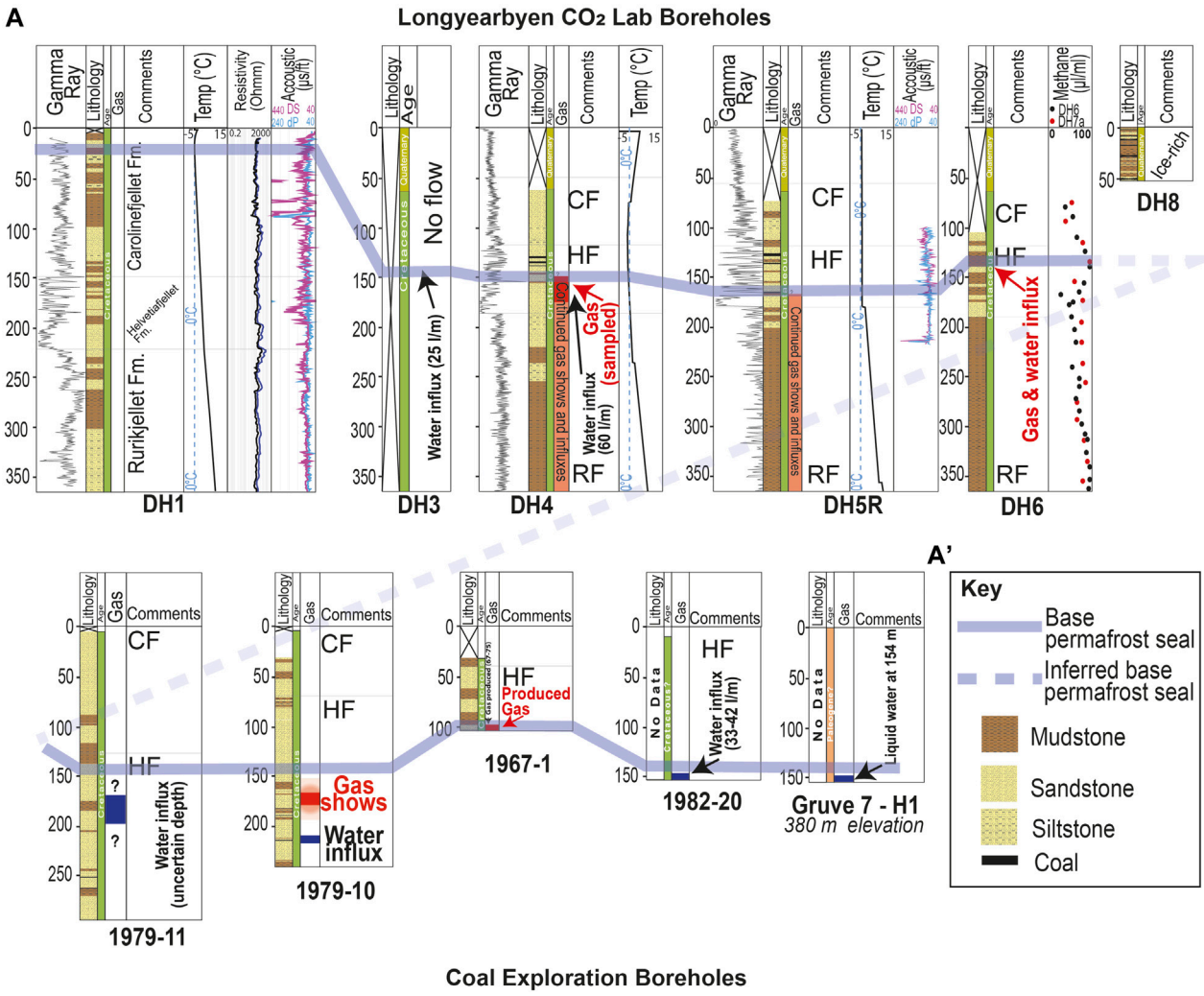

FIGURE 6
A Well correlation of base permafrost with all available geological, drilling and petrophysical data. The location of the correlation is shown in Figure 5. The wells in this section highlight the somewhat sporadic nature of data availability over the shallow, permafrost bearing intervals.

attempting to find it, which suggests that the phenomenon is extremely common in the archipelago. Permafrost trapped gas appears to show no particular stratigraphic or spatial prevalence. In Adventdalen and at Tromsøbreen the base of permafrost and underlying methane are situated within Cretaceous sandstones. On the island of Hopen in the southeasternmost part of Svalbard, the gas was encountered in the heterolithic sandstone, siltstone and shales of the Triassic De Geerdalen Formation. In Gipsdalen and at Petuniabukta, gas was encountered in Carboniferous or Permian carbonates.

Shallow gas is typically considered a hazard to drilling and this is exemplified by two SNSK wellbores, one on the plateau of Slaknosa on the southern edge of Reindalen (SNSK, 1991), and one at Kapp Amsterdam near Svea (SNSK, 1986). Both wells encountered blowouts that occurred with enough pressure to eject rock and material from the wellbores and lasted for several hours (until the following day in the Kapp Amsterdam case). The Kapp Amsterdam case is particularly intriguing as the gas came from 33.5 m depth at the base of permafrost (thermistors in the wellbore confirmed this) from glacial moraine sediments deposited some 600 years ago (Kristensen et al., 2009), meaning that the gas had accumulated quickly and recently.

There are numerous wellbores that demonstrate the presence of permafrost without an underlying gas accumulation. At Kapp Laila, Colesbukta and Reindalen no free gas was encountered below the Paleogene and Cretaceous situated base-permafrost intervals. The Carboniferous to Permian carbonates of Edgeøya demonstrate the same.

4.2.1 Adventdalen case study

Svalbard's largest settlement, Longyearbyen, is located in Adventdalen (Figure 5), and the best studied area of Svalbard in the context of this article (Hodson et al., 2020; Hornum et al., 2020; Johansen et al., 2003; Beka et al., 2017; Betlem et al., 2019; Olaussen et al., 2019 and references therein). The high number and density of scientific and industry data sets provide the most comprehensive data on the base of permafrost seal and underlying fluids. The wells of the Longyearbyen CO_2 Lab and coal exploration boreholes of SNSK both show the presence of gas trapped beneath the permafrost

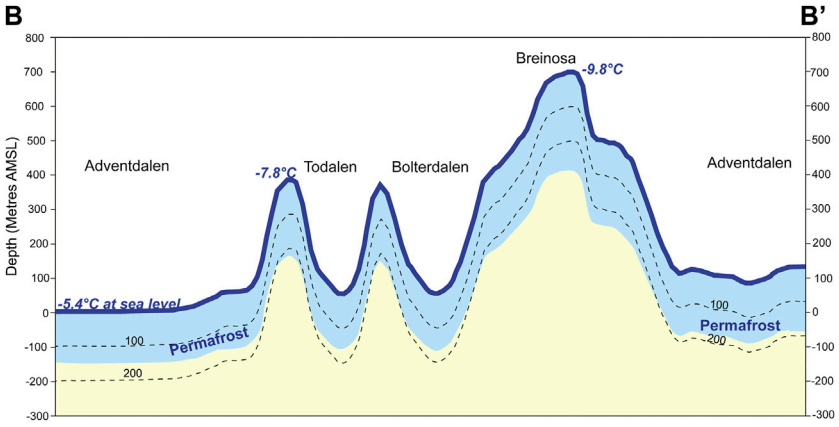

FIGURE 7
Modelled permafrost thickness through Adventdalen with the profile shown in Figure 5. The model parameters are discussed in the methods section but note that the permafrost interval is entirely based on temperature rather than ice thickness or presence. Modelling suggests that gas hydrates are not stable at this location based on a methane composition and hydrostatic pressures, at higher fluid pressures or heavier gas compositions gas hydrates be stable at the base of permafrost here. Modelled mean annual air temperatures are shown for reference in the highland areas and at sea level. Dashed lines represent contours of depth below land surface.

in Adventdalen. Figure 6 provides a correlation panel of these wellbores.

At the near-coast drillsite-1 of the Longyearbyen CO_2 Lab wells temperature data from DH1 (Figure 4 example 3) and DH2 indicate a thin permafrost interval with the base at approximately 20–30 m (Beka et al., 2017). Although sub-zero temperatures were recorded at this site, the presence of ice is strongly dependent on the pore-fluid salinity. At drillsite-2, wellbores DH3 and DH4 encountered overpressured water at the base permafrost. DH4 and DH5R also encountered significant natural gas together with the water influx that was collected in gas bags for sampling (Huq et al., 2017; Ohm et al., 2019). Temperature logs from DH4 suggest base permafrost from 150 to 200 m depth, but the best evidence of a base permafrost seal comes from the sudden influx of water and gas at approximately 150 m. Cores from nearby wells DH6 and DH7A also show elevated methane levels at this depth. The water and gas influxes occur somewhere towards the middle (i.e., not top of the reservoir) of the sandstone dominated Helvetiafjellet Formation.

In the same area, several hundred coal boreholes, drilled by SNSK over the past century, have penetrated the permafrost interval, although data for these is fragmented (see Figure 5 for well locations). Well 1979-11 was drilled approximately 2 km south of Longyearbyen CO_2 Lab drillsite-2 in Endalen. This well encountered water influxes with no mention of gas, although no depths are stated in the report (SNSK, 1980; 1981). Well 1979-10, in the valley of Todalen, encountered methane-rich gas overlying inflowing water at the base of permafrost at a depth between 150 and 200 m (SNSK, 1981; 1982b; Leythaeuser et al., 1984). Well 1967-1, approximately 3 km east of, and geologically updip of 1979-10, reached a depth of 106 m where a gas accumulation was encountered (SNSK, 1981). This well was also the subject of considerable interest by SNSK who investigated the potential of producing the gas commercially. Well 1982-20, at the base of Breinosa and the coal mine Gruve-7, did not encounter gas and took water influxes of 33-42 L per minute at approximately 150 m at the base of permafrost (SNSK, 1982a). Another reported well, named only "first water well" (SNSK, 1982a), in the same area flowed from the same interval at 40–50 L per minute. Water from these two wells had a measured chloride concentration of 1,500 ppm (SNSK, 1982a). A well drilled inside Gruve-7 at approximately 380 m above mean sea level (AMSL) encountered liquid water at 154 m depth.

The observed base permafrost in the coal and scientific wellbores show broad agreement with the modelled permafrost, by temperature definition (Figure 7). However, on the plateaus in this area, drilling mud losses into permeable strata in the permafrost interval indicate that a permafrost seal is absent. On Platåberget, the permafrost base is well defined due to its presence in the Gruve-3 coal mine (location in Figure 5); a drilling summary report (SNSK, 1982a) documents two wells drilled at approximately 400 m AMSL total drilling fluid losses at 160–170 m MD. This is within the permafrost interval based on the presence of permafrost in the coal mine. Similarly, on Breinosa, where the Gruve-7 coal mine is situated some 15 km to the east, wells 81-05 and 81-06 both encountered total fluid losses at a similar depth of 170 m (SNSK, 1982a), within the permafrost interval (Juliussen et al., 2010). Similar losses occurred in several intervals between 106 and 196 m in well 19-2011 on Operafjellet, a plateau on the northern side of Adventdalen (SNSK, 2011a; SNSK, 2011b; SNSK, 2011c; SNSK, 2011d), also well within the permafrost interval as freezing was encountered within the wellbore at 132 m depth.

Five pingos are situated along the northern edge of Adventdalen. Four of them provide active migration pathways through the permafrost leading to the discharge of brackish springs and high concentrations of methane (up to and marginally exceeding the solubility limit of 41 mg L-1) (Hodson et al., 2020). At the easternmost pingos, the chloride concentrations and the $d^{13}C$ isotopic composition of both the methane and dissolved CO_2 are similar to those described in the wellbore records above.

4.2.2 Gas production—Adventdalen

SNSK commissioned flow analysis work to be carried out on the 1967-1 well in July 1975 and the results of these two test runs are shown in Supplementary Figure S1B. Here it is clear the well

10.3389/feart.2023.1277027

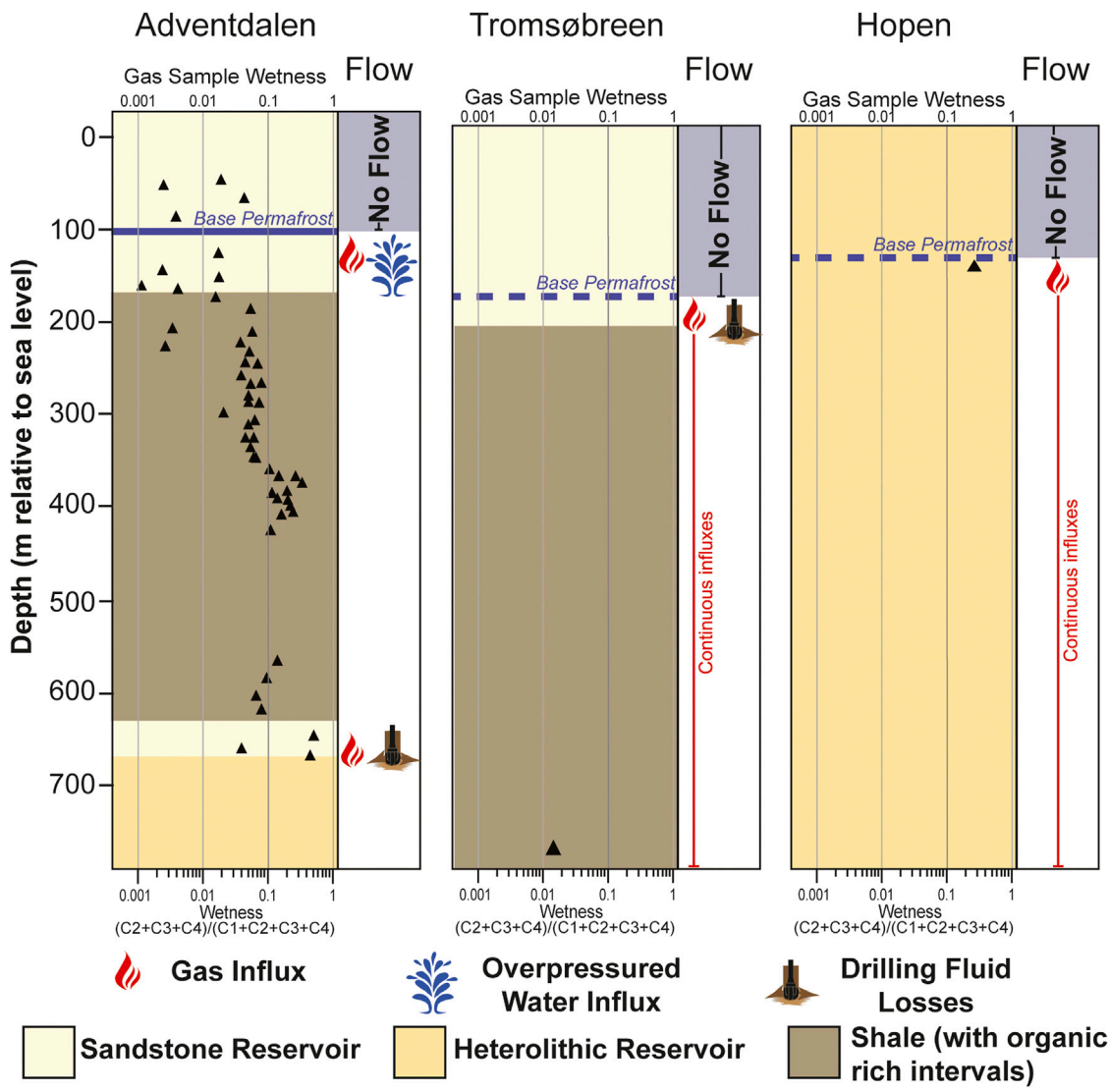

FIGURE 8
Gas wetness from samples taken in wells from Adventdalen (Ohm et al., 2019), Tromsøbreen (Norsk Polar Navigasjon A/S, 1977b) and Hopen (Norske Fina, 1972a). The Hopen gas is much heavier and thus more prone to form hydrates at lower pressures and higher temperatures than methane.

responded to pressure drawdown. However, flow rates were still significantly lower than those recorded over the first year. Supplementary Figure S1C shows the pressure build-up when the well was shut in (effectively closed from the atmosphere) between the two test runs. The quick return to pre-drawdown pressures indicates, somewhat unsurprisingly, a good natural pressure support in the well. Ultimately the gas here was deemed by Statoil, and consequently SNSK, to be an uneconomic accumulation locally trapped by permafrost (SNSK, 1981).

Well 1967-1 and 1979-10 also encountered gas, likely the same gas accumulation, while well 1982-20 encountered permafrost over the same stratigraphic interval and well 1979-11 is probably down-dip of the gas-water interface. Intermittent flow from the 1967-1 well was monitored between October 1967 and July 1975 (SNSK, 1981). The first year of this production was continuous and monitored as shown in Supplementary Figure S1C. An initial wellhead gas pressure of 14 bar was recorded (SNSK, 1981) with relatively slow pressure and production decline over time. This indicates that the gas accumulation is in the order of millions of cubic-metres and has well connected pressure support. If the aquifer pressure is known then the length of the methane gas column can be calculated from this pressure. It is clear the aquifer is not at hydrostatic pressure from the surface due to the repeated influxes and water flow from wells 1979-10, 1979-11 and in the CO_2 lab research boreholes. Unfortunately, these pressures were not measured.

4.3 Sampled gas

Gas samples were taken by hydrocarbon exploration wells at Tromsøbreen and Hopen, and from the Longyearbyen CO_2 Lab wellbores in Adventdalen (Figure 8). Three samples each were

TABLE 4 Geochemical data from samples taken at the hydrocarbon exploration wells at Tromsøbreen-1 and Hopen-1. A comprehensive analysis of gas from the Longyearbyen CO_2 Lab Ohm et al. (2019) demonstrates gas at the base of permafrost in Adventdalen is almost entirely methane (>99%).

Sample number	Sample run 1	Sample run 2	Sample run 3	Sample run 1	Sample run 2	Sample run 3
Hydrocarbons	7617/7-1 (Hopen I)—from c. 150 m depth			**7625/7-1 (Troms**øbreen I)—from 768 m depth		
C1	64.79–70.81	68.57	63.84	92.35	94.97	97.24
C2	20.23–18.67	18.20	20.21	0.11	0.05	0.49
C3	10.97–7.76	9.26	11.10	0.09	0.01	0.16
C4	3.51–2.46	3.39	4.08	0.18	0.06	0.20
C5+	0.58–1.32	1.22	0.79	0.97	1.03	0.96
Nitrogen	Abnormally high (not quantified)			6.26	3.86	0.91
CO2	-			0.04	0.02	0.04
Gravity	-			0.609	0.600	0.591

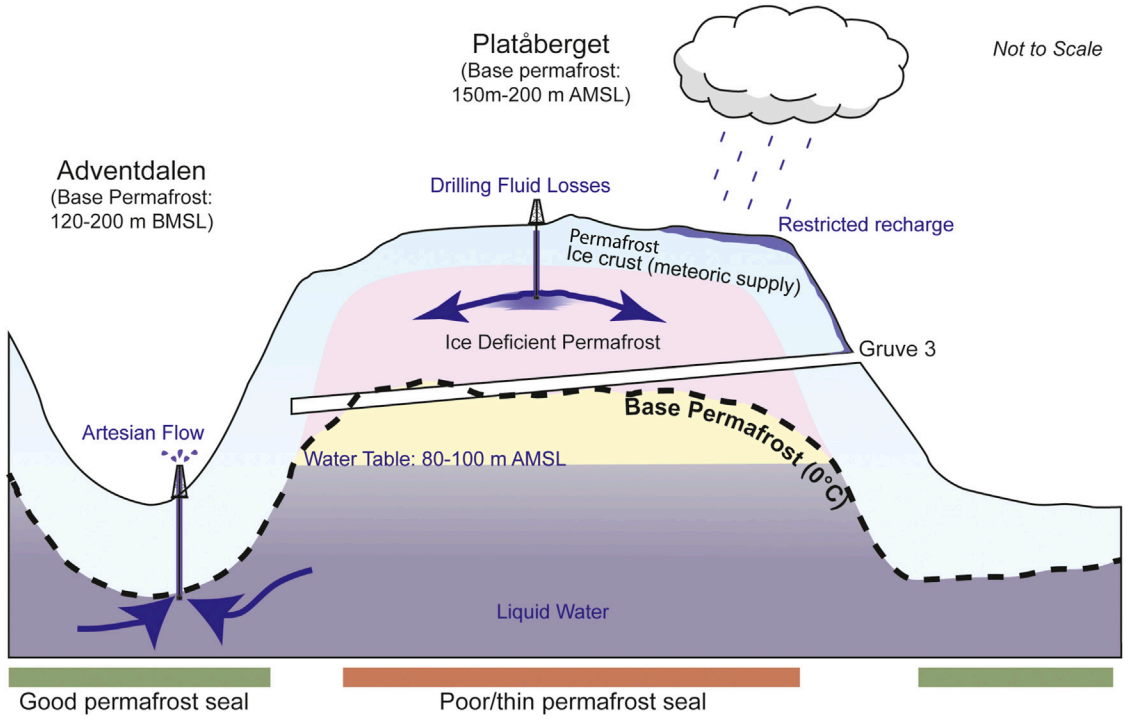

FIGURE 9
Schematic cross section of the permafrost interval at Platåberget and Adventdalen showing the potentially contrasting seal effectiveness. Artesian pressures in the valley wellbore 1967-1 suggest an elevated water table (Table 5) which still sits below the base of permafrost in the mountain. The lack of water supply from below during permafrost formation leads to a dry and permeable permafrost interval and subsequent drilling losses. Similar drilling fluid losses appear common in the permafrost interval in several plateau areas in Svalbard. In the valleys the permafrost interval forms through the water table and results in a thick impermeable ice seal. Coal gas was a common hazard in mine 3 and it is plausible that the lack of a permafrost seal is why wellbores on Platåberget did not encounter gas.

taken at Tromsøbreen and Hopen and their compositions were analysed and are shown in Table 4. A comprehensive analysis of the gas at the Longyearbyen CO_2 was carried out by Ohm et al. (2019), Huq et al. (2017), and a rudimentary analysis of the 1967-1 Adventdalen coal exploration gas discovery was carried out by SNSK (1981). These analyses of the gas accumulations and analysis of seeps of the pingo systems in Adventdalen (Hodson et al., 2019) show that these base-permafrost accumulations are methane dominated. The more extensive analysis of the Longyearbyen CO_2 Lab gas provides a more complex story throughout the entire stratigraphy with contributions from biogenic and thermogenic sources (Huq et al., 2017; Ohm et al., 2019). Analysis at Tromsøbreen was taken from gas much deeper than that encountered at base permafrost but also suggests the gas is comprised of methane. However, it shows this

TABLE 5 Aquifer pressure calculation from a known virgin wellhead pressure of 14 bar (Supplementary Figure S1A) in well 1967-1 and the possible range of a gas-water contact from wellbore 1971-10 (Figure 6). The low case uses a saline water pressure gradient of 0.10067 bar/m while high case uses freshwater gradient of 0.09795 bar/m.

Case	High	Low
Contact	160 m	210 m
Buoyancy pressure (gas SG = 0.5537)	7.1 bar	9.3 bar
Aquifer overpressure	6.9 bar	4.7 bar
Hydraulic head Elevation (well: 32.5 m)	103 m AMSL	79.2 m AMSL

gas is relatively dry although still likely to be thermogenic due to the sample depth of 768 m and its extraction directly from the Agardhfjellet Formation source rock (Norsk Polar Navigasjon a/S, 1977b; Norsk Polar Navigasjon a/S, 1977a). However, on Hopen the gas, sampled from approximately 150 m depth, is much wetter and clearly of a thermogenic origin. Figure 8 shows the wetness of gas from the three locations: wetter gas means it has a greater component of heavier hydrocarbon molecules such as ethane or propane.

The composition of the gas is important in understanding its potential phase in the subsurface. Phase diagrams for the gas compositions and thermobaric conditions at Hopen, and at Adventdalen and Tromsøbreen are shown in Supplementary Figure S2. While the dry gas at Tromsøbreen and Adventdalen is unlikely to be in hydrate form at their points of discovery, the gas at Hopen is much wetter. As a consequence, it is more susceptible to be thermodynamically stable as gas hydrates (Betlem et al., 2019).

5 Discussion

5.1 Permafrost seals and traps

Theoretically, the permafrost interval should form an extremely effective seal or "cryogenic cap." If ice-bound it is highly impermeable, often thick, and can self-heal. The story is a little more complex and the permafrost seal-forming process is poorly understood. An effective permafrost seal is demonstrable in various locations in Svalbard by the presence of gas and abnormally pressured water at the base of permafrost. In the most data rich area of Svalbard, Adventdalen, it appears that the permafrost zone is ice-saturated in valleys and forms an effective seal. By contrast, the plateau settings show a permeable permafrost interval. The previously described drilling losses in wells on the plateaus of Platåberget, Breinosa, Operafjellet, Lunckefjellet and Ispallen (SNSK, 2013c; SNSK, 2013a; SNSK, 2013b; SNSK, 2014) occurred in known permafrost intervals (Juliussen et al., 2010). The lack of impermeable permafrost in the highlands is probably simply due to being situated far above the water table (Figure 9). Pressures from the 1967-1 wellbore indicate a hydraulic head between 80 and 100 m above sea level (Table 5) while the base permafrost is considerably higher in the pleateau. Therefore valleys have an ample supply of pore-water in the permafrost interval as it forms downwards in time, while the plateaus do not. Conversely, the gas blowout of the 1990-12 well on Slaknosa plateau, 25 km to the southeast, demonstrates that a permafrost seal is still possible in plateau settings and the story is far from simple. Although data from the Slaknosa blowout is limited to drilling reports (SNSK, 1991), the geological setting of relatively flat and unfaulted sandstones, and their up-dip outcropping in steep cliffs to the north, and high enough gas flow rates into the wellbore at depth to cause a blowout all suggest a permafrost sealed (both vertically and laterally) free gas accumulation in a high permeability reservoir.

Gas accumulations beneath the permafrost are common and widespread regardless of stratigraphy (Figures 2, 4; Table 3) which demonstrates the good sealing potential. Abnormal pressures are common at the base of permafrost in several locations in Svalbard which demonstrates the sealing properties of the overlying permafrost. The best data is in Adventdalen where sudden, slightly saline, water influxes occur at the base of permafrost in the Helvetiafjellet Formation. The strong and sustained flow rates indicate appreciable lateral connectivity within the aquifer, indicating an artesian origin of overpressure. The current view of this overpressure is attributed to the formation of permafrost (Hornum et al., 2020) but the high flow rates (Magnabosco et al., 2014), reservoir connectivity and its outcropping beneath the fjord to the west (Blinova et al., 2012) discount this. The effectiveness of a permafrost seal is demonstrated by the high overpressures that have been encountered and it is reasonable to consider that a permafrost

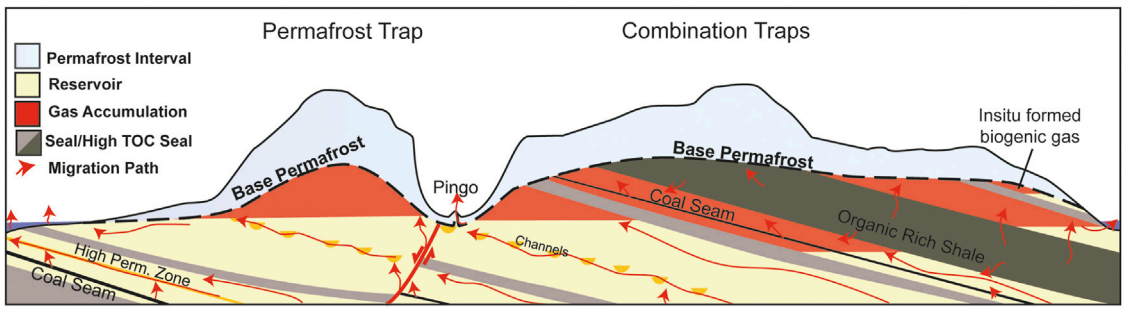

FIGURE 10
The different trapping mechanisms permafrost can provide. Undulations in the base permafrost alone may form traps, which may be large under mountains if the permafrost seal is effective. Combination traps require permafrost to contribute a lesser sealing surface area and appears to be the mechanism for trapping gas in Adventdalen (Figure 11).

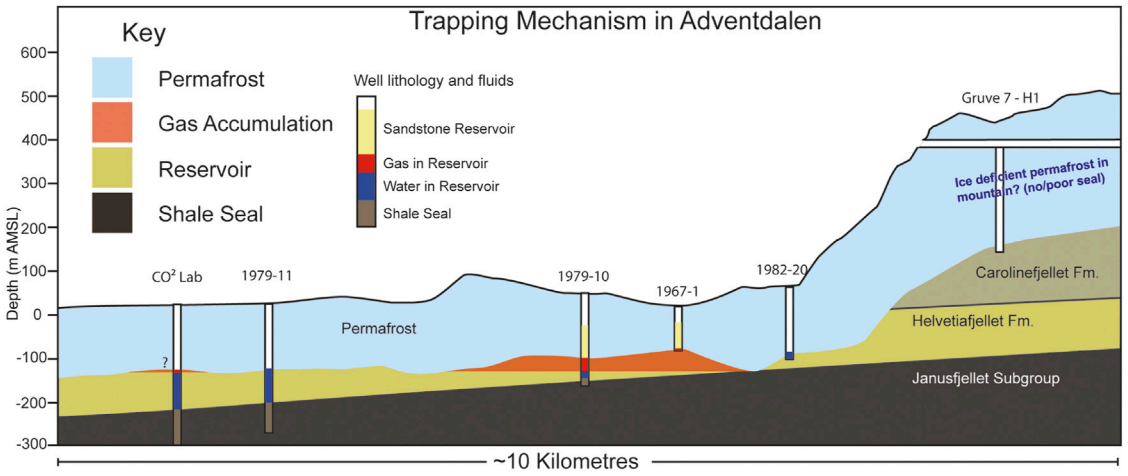

FIGURE 11
The potential combination-trapping style of the Adventdalen gas accumulation based on well observations.

seal can withstand significant buoyancy pressures to withhold large gas columns. It seems more likely that the accumulations are regulated laterally by natural pathways through the permafrost at pingos, fjords, or glaciers.

Natural pathways through the cryospheric cap, even in areas of thick permafrost, are present in the form of pingos, springs, warm-based glaciers, and beneath the fjords. At the Reindalen petroleum exploration borehole, elevated gas readings and shows were encountered at 120 m in the wellbore (Supplementary Figure S8) and may represent a migration pathway at the base of permafrost where no trap exists.

For gas to accumulate beneath the permafrost a trap must be present. The undulating base of permafrost can form a trap and seal itself, or it may act as the top seal in combination with the underlying geology, these examples are shown in Figure 10. In valley settings where the base permafrost forms a synclinal structure it is more likely that accumulations are situated within combination traps. This is further supported by the fact the regional and local geology in Svalbard is rarely flat and contains multiple lithological seals and reservoirs. In these traps a combination of structural geology, lithology and permafrost properties contribute to developing hydrocarbon accumulations. This mechanism can be attributed to the gas accumulation in Adventdalen (Figure 11). The combination of this combination trap type and the ice-saturated seals may explain why gas accumulations have been frequently encountered in valleys rather than migrating and accumulating beneath shallower permafrost in highlands. Smaller accumulations, such as the one encountered in Gipsdalen, may be restricted to localised undulations in the base-permafrost.

Gas trapped in hydrate form under the right thermobaric conditions is the exception to the previously discussed trapping mechanisms. The gas sampled at Hopen is a strong candidate to originate from hydrates. The heavier gas composition (Table 4) means it has a greater propensity to form hydrates at a given depth and temperature. Though it should be noted many regional hydrate stability zone models assume a hydrostatic fluid pressure from the land surface, while our observations of water-free intervals in highlands suggest this is unlikely to be the case.

In some cases, a permafrost seal is present but lacks an underlying gas accumulation. This can be explained by either a lack of charge or the lack of trap. Given the numerous thermogenic (Abay et al., 2017; Senger et al., 2019; Olaussen et al., 2022) and biogenic (Hodson et al., 2020) hydrocarbon seeps, flares, and sheer prevalence of shallow gas accumulations throughout the sedimentary outcrops of Svalbard, it is unlikely that these result from a lack of charge, with the exception of locations where there are no source rocks (e.g., Edgeøya and northern Svalbard). Where accumulations do not exist beneath sealing permafrost it is highly likely due to the lack of a trapping geometry (e.g., Figure 10).

5.2 Origins of gas

Gas originating from permafrost is typically attributed to a biogenic origin, primarily because thermogenic gas is generated and migrates on much longer timescales. While biogenic gas is undoubtedly a contributor to sub-permafrost gas in Svalbard (Hodson et al., 2019), thermogenic gas is also clearly a major contributor in several locations (Ohm et al., 2019). Considering this, the lack of any accumulations or significant shows in the wells on Edgeøya is probably due to the lack of any significant source rock.

Approximately 60% of wells in the Barents Shelf offer hydrocarbon shows (Senger et al., 2020), indicating that the basin has at one point in the past been almost saturated with hydrocarbons. The large ultra-shallow discoveries like Wisting, containing relatively non-biodegraded oil, are evidence of more geologically recent hydrocarbon migration. This recent migration is almost certainly driven by major recent uplift over the past thousands to hundreds-of-thousands of years (Henriksen et al., 2011).

Svalbard itself has undergone the greatest uplift of anywhere in the Barents region in the geologically recent past. Recent uplift has enabled gas to escape directly from the source rocks from fracturing and unloading, and from deeper accumulations due to tilting and changes in pressure-volume-temperature (PVT)

conditions. The formation of permafrost has effectively added an additional sealing interval for migrating gas before reaching the atmosphere.

5.3 Timing and migration

Supplementary Figure S11 is a petroleum systems chart with a focus on sub-permafrost accumulations in Svalbard. Clearly, all other elements of the petroleum system must be present prior to migration taking place. Here the timescales are binary with source, reservoirs and lithological seals forming tens or hundreds of millions of years ago. Conversely, permafrost stability in Svalbard is on much shorter timescales and location dependent; permafrost in valleys likely thawed beneath warm-based glaciers, with most permafrost growth occurring over the last 4,000 years, though localised permafrost in high mountains may have survived for as much as 700,000 years (Humlum, 2005; Gilbert et al., 2018). The most critical elements in this petroleum system are undoubtedly the most recent: permafrost seal formation and gas migration.

The geologically recent and severe uplift means that present-day depths of source rocks is not representative of their maturity or gas generating potential. Indeed, uplift has almost certainly driven migration from deeper pre-existing structures (Cavannah et al., 2006; Ohm et al., 2008; Henriksen et al., 2011; Chand et al., 2012) and from the numerous source rocks (Ohm et al., 2018; Birchall et al., 2020). This has been ongoing throughout the Pleistocene and predates permafrost formation. Therefore, the critical moment for most sub-permafrost gas accumulations in Svalbard is the timing of permafrost formation itself. The exception to this is the case of Kapp Amsterdam, where the formation of reservoir, seal, and migration have all occurred within the last 600 years.

Gas migration will occur through permeable intervals, typically at the crest of structures. Faults may aid the movement of gas from deeper structures, particularly during uplift and fault reactivation as appears to be the case at Reindalen which sits on the Billefjorden Fault Zone (Bælum and Braathen, 2012). The discovery of shale gas in Adventdalen (Ohm et al., 2019) also shows that source rocks still internally trap large amounts of gas. This gas will have migrated directly out of source rocks during uplift due to gas expansion and rock fracturing.

5.4 Size, frequency and regional implications

While gas accumulations beneath permafrost have been frequently encountered in wellbores, it is important to remember that none of these were actually looking for it, indeed most hydrocarbon exploration wells aim to avoid such shallow gas accumulations (Ronen et al., 2012). In this study, of eighteen hydrocarbon wells in Svalbard, eight show good evidence of permafrost (44%). Four of these permafrost bearing wells show free gas accumulations at the base of permafrost (22% of all wells or 50% of permafrost bearing wells), three clearly show no presence of an accumulation while one contains gas shows. Expanding this to all wells in this study, 18 show evidence of permafrost and 9 of these show evidence of a gas accumulation (50%), though the coal wells for this study were obviously biased to areas of interest. This is an extremely high success rate for something that was not being targeted, and thus highlights the likelihood that these gas accumulations are very common. For reference, the Barents Shelf has one of the highest technical success rates in the world at just below 50% (Norskpetroleum, 2020) for prospects that have been specifically targeted using advanced geological and geophysical methods.

As with conventional hydrocarbon accumulations, the size of sub-permafrost accumulations probably varies significantly. The accumulation in Adventdalen is relatively significant, but also of little economic interest; the 1967-1 well produced in excess of 2.5 million cubic metres of gas between 1967 and 1975 (SNSK, 1981). Despite this, these accumulations may still provide an alternative and cleaner energy source than coal, which is presently used to generate power in Svalbard. Unfortunately, the data are quite poor because the well was also periodically shut in over this time. The use of geophysical methods in assessing accumulations is challenged; high seismic velocities of rigid, compacted rocks results in low acoustic impedance and imaging the base of permafrost or fluid escape features has been impossible in Svalbard. This is highlighted by the mapping of flares and pockmarks in Isfjorden, which show a clear link with underlying faults, but no manifestation in good seismic data (Roy et al., 2015; Rodes et al., 2023).

Because the sub-permafrost accumulations are relatively shallow and under lower pressure, the gas will be much less dense, and thus voluminous, than conventional deeper accumulations. The exception to this is if the gas is in hydrate form where methane concentrations are 160 times higher than in free gas form (Majorowicz and Hannigan, 2000).

Given the sparse data and a sampling bias due to exploration boreholes typically targeting specific intervals or structures, it is difficult to be quantitative with respect to the size and frequency of these accumulations. What is evident is that permafrost is acting as an ultimate seal to these accumulations, that they are numerous, and, based on the only occurrence where flow was recorded, on the orders of million cubic metres.

Based on the occurrences in Svalbard, the prerequisites for sub-permafrost gas to accumulate are, firstly, an impermeable (ice-saturated) permafrost layer, secondly, a source of gas and, finally, gas migration at a time after permafrost formation. Much of the Circum-Arctic shares a similar geological history with Svalbard. A major source of migrating gas in Svalbard is likely from the Mesozoic source rocks (Ohm et al., 2019), which can also be found in the Russian and North American Arctic (Leith et al., 1993; Polyakova, 2015). Recent uplift caused by isostatic rebound has left fluids in the subsurface on the Barents and Svalbard out of pressure equilibrium and driving present-day migration (Birchall et al., 2020). Svalbard shares its Pleistocene glacial history with the Circum-Arctic (Batchelor et al., 2019) so it is not unreasonable to expect sub-permafrost gas accumulations to be regionally widespread. Indeed, gas emanating from zones of permafrost is well-documented onshore and offshore in the Russian Arctic, particularly in hydrocarbon provinces (Chuvilin et al., 2020 and references therein) and as natural gas hydrates (Yakushev and Chuvilin, 2000).

Because methane is a potent greenhouse gas and the Arctic is warming faster than anywhere else on Earth (Lind et al., 2018), the release of sub-permafrost gas accumulations in Svalbard may contribute a positive climatic feedback effect. Strand et al. (2021) show the active layer is thickening at approximately 1.6 cm/year in Adventdalen. Assuming permafrost continues to thaw at this rate then most permafrost trapped gas should remain relatively stable. However, permafrost will not simply thaw from above, but also laterally from the coastlines, in addition to having complex mechanical implications in the strata overlying these accumulations.

6 Conclusion

Although gas at the base of permafrost has been encountered frequently during more than 50 years of drilling in Svalbard, it has not been systematically studied or widely recognised until now. In this study we have provided a synthesis of historical and modern observations and their implications. Our key findings are:

- Gas accumulations trapped at the base of permafrost occur throughout the archipelago in several stratigraphic intervals.
- The gas accumulations provide evidence for ongoing hydrocarbon migration
- Gas encountered in wellbores on Hopen is compositionally heavier and likely within the gas hydrate stability zone
- Permafrost is a good seal in valleys but appears to possess permeable intervals in highland areas
- Groundwater flow below permafrost is much greater than previously documented
- There is evidence of relatively thick coastal permafrost, particularly in eastern Svalbard

Shallow gas associated with permafrost has been documented throughout much of the Circum-Arctic (Nielsen et al., 2014; Chuvilin et al., 2020; Hodson et al., 2020; Minshull et al., 2020). Given the shared geological and glacial history, it is very likely that the gas accumulations we document in Svalbard are more widespread.

Data availability statement

The historical nature of the data and reports means they are available in hard-copy only. Reports referenced in this article are proprietary to their respective companies. Requests to access these datasets should be directed to kims@unis.no. For an overview of historical reports used in this study see: https://zenodo.org/records/5919082.

Author contributions

TB: Conceptualization, Data curation, Investigation, Methodology, Project administration, Visualization, Writing–original draft, Writing–review and editing. MJ: Conceptualization, Data curation, Investigation, Resources, Validation, Writing–review and editing. PB: Methodology, Software, Validation, Writing–review and editing. KS: Conceptualization, Methodology, Supervision, Validation, Writing–review and editing. AH: Supervision, Validation, Writing–review and editing. SO: Supervision, Validation, Writing–review and editing.

Funding

The author(s) declare financial support was received for the research, authorship, and/or publication of this article. This research is funded by the Research Centre for Arctic Petroleum Exploration (ARCEx) partners and the Research Council of Norway (grant number: 228107), CLIMAGAS (grant number: 284764) and the Norwegian CCS Research Centre (grant number: 257579). Data mining was supported by the Svalbard Rock Vault project financed through a Svalbard Strategic Grant from the Research Council of Norway (#295781).

Acknowledgments

We sincerely appreciate access to Store Norske Spitsbergen Kulkompani's vast internal archives and to the data from the Longyearbyen CO_2 lab project (http://co2-ccs.unis.no). We also thank Sarah Strand for fruitful discussions on permafrost dynamics. We are very grateful for the very constructive feedback from two reviewers who have undoubtedly improved the quality of this article.

Conflict of interest

Author MJ was employed by Store Norske Spitsbergen Kulkompani AS.

The remaining authors declare that the research was conducted in the absence of any commercial or financial relationships that could be construed as a potential conflict of interest.

Publisher's note

Supplementary material

The Supplementary Material for this article can be found online at: https://www.frontiersin.org/articles/10.3389/feart.2023.1277027/full#supplementary-material

References

Aagaard, K., Foldvik, A., and Hillman, S. (1987). The West Spitsbergen Current: disposition and water mass transformation. *J. Geophys. Res. Oceans* 92, 3778–3784. doi:10.1029/JC092iC04p03778

Abay, T., Karlsen, D., Lerch, B., Olaussen, S., Pedersen, J., and Backer-Owe, K. (2017). Migrated petroleum in outcropping Mesozoic sedimentary rocks in Spitsbergen: organic geochemical characterization and implications for regional exploration. *J. Petroleum Geol.* 40, 5–36. doi:10.1111/jpg.12662

Anell, I. M., Braathen, A., and Olaussen, S. (2014). The triassic–early jurassic of the northern Barents shelf: a regional understanding of the longyearbyen CO2 reservoir. *Nor. Geol. Tidsskr.* 94, 83–98.

Anthony, K. M. W., Anthony, P., Grosse, G., and Chanton, J. (2012). Geologic methane seeps along boundaries of Arctic permafrost thaw and melting glaciers. *Nat. Geosci.* 5, 419–426. doi:10.1038/ngeo1480

Bælum, K., and Braathen, A. (2012). Along-strike changes in fault array and rift basin geometry of the Carboniferous Billefjorden Trough. *Svalbard, Nor. Tectonophys.* 546, 38–55. doi:10.1016/j.tecto.2012.04.009

Batchelor, C. L., Margold, M., Krapp, M., Murton, D. K., Dalton, A. S., Gibbard, P. L., et al. (2019). The configuration of Northern Hemisphere ice sheets through the Quaternary. *Nat. Commun.* 10, 3713–3810. doi:10.1038/s41467-019-11601-2

Beka, T. I., Senger, K., Autio, U. A., Smirnov, M., and Birkelund, Y. (2017). Integrated electromagnetic data investigation of a Mesozoic CO2 storage target reservoir-cap-rock succession, Svalbard. *J. Appl. Geophys.* 136, 417–430. doi:10.1016/j.jappgeo.2016.11.021

Betlem, P., Midttømme, K., Jochmann, M., Senger, K., and Olaussen, S. (2018). "Geothermal gradients on svalbard," in First EAGE/IGA/DGMK Joint Workshop on Deep Geothermal Energy, Arctic, Norway, November 2018.

Betlem, P., Roy, s., Birchall, T., Hodson, A., Noormets, R., Römer, M., et al. (2021). Modelling of the gas hydrate potential in Svalbard's fjords. *J. Nat. Gas Sci. Eng.* 94, 104127. doi:10.1016/j.jngse.2021.104127

Betlem, P., Senger, K., and Hodson, A. (2019). 3D thermobaric modelling of the gas hydrate stability zone onshore central Spitsbergen, Arctic Norway. *Mar. Petroleum Geol.* 100, 246–262. doi:10.1016/j.marpetgeo.2018.10.050

Bily, C., and Dick, J. (1974). Naturally occurring gas hydrates in the Mackenzie Delta, NWT. *Bull. Can. Petroleum Geol.* 22, 340–352. doi:10.35767/gscpgbull.22.3.340

Birchall, T., Senger, K., Hornum, M., Olaussen, S., and Braathen, A. (2020). Underpressure in the northern Barents shelf: causes and implications for hydrocarbon exploration. *AAPG Bull.* 38, 2267–2295. doi:10.1306/02272019146

Birkenmajer, K., Nagy, J., and Dallmann, W. K. (1992). *Markhambreen, spitsbergen.* Tromsø: Norsk Polarinstitutt.Geological map svalbard 1:100,000

Blinova, M., Inge Faleide, J., Gabrielsen, R. H., and Mjelde, R. (2012). Seafloor expression and shallow structure of a fold-and-thrust system, Isfjorden, west Spitsbergen. *Polar Res.* 31, 11209. doi:10.3402/polar.v31i0.11209

Boucher, O., Friedlingstein, P., Collins, B., and Shine, K. P. (2009). The indirect global warming potential and global temperature change potential due to methane oxidation. *Environ. Res. Lett.* 4, 044007. doi:10.1088/1748-9326/4/4/044007

Braathen, A., Bælum, K., Maher, H., Jr, and Buckley, S. J. (2012). Growth of extensional faults and folds during deposition of an evaporite-dominated half-graben basin; the Carboniferous Billefjorden Trough. *Svalbard, Nor. J. Geol.* 91, 137.

Cavanagh, A. J., Primio, R. D., Scheck-Wenderoth, M., and Horsfield, B. (2006). Severity and timing of cenozoic exhumation in the southwestern Barents Sea. *J. Geol. Soc.* 163, 761–774. doi:10.1144/0016-76492005-146

Chand, S., Thorsnes, T., Rise, L., Brunstad, H., Stoddart, D., Bøe, R., et al. (2012). Multiple episodes of fluid flow in the SW Barents Sea (Loppa High) evidenced by gas flares, pockmarks and gas hydrate accumulation. *Earth Planet. Sci. Lett.* 331-332, 305–314. doi:10.1016/j.epsl.2012.03.021

Christiansen, H. H., Etzelmüller, B., Isaksen, K., Juliussen, H., Farbrot, H., Humlum, O., et al. (2010). The thermal state of permafrost in the Nordic area during the International Polar Year 2007–2009. *Permafr. Periglac. Process.* 21, 156–181. doi:10.1002/ppp.687

Christiansen, H. H., French, H. M., and Humlum, O. (2005). Permafrost in the Gruve-7 mine, adventdalen, svalbard. *Norsk Geografisk Tidsskrift-Norwegian J. Geogr.* 59, 109–115. doi:10.1080/00291950510020592

Chuvilin, E., Ekimova, V., Davletshina, D., Sokolova, N., and Bukhanov, B. (2020). Evidence of gas emissions from permafrost in the Russian arctic. *Geosciences* 10, 383. doi:10.3390/geosciences10100383

Chuvilin, E., Yakushev, V. S., and Perlova, E. (2000). Gas and possible gas hydrates in the permafrost of bovanenkovo gas field, yamal peninsula, west siberia. *Polarforschung* 68, 215–219.

Collett, T. S., Lee, M. W., Agena, W. F., Miller, J. J., Lewis, K. A., Zyrianova, M. V., et al. (2011). Permafrost-associated natural gas hydrate occurrences on the Alaska North Slope. *Mar. Petroleum Geol.* 28, 279–294. doi:10.1016/j.marpetgeo.2009.12.001

Dallmann, W. K., Elvevold, S., Gerland, S., Hormes, A., Majka, J., Ottemöller, L., et al. (2015). *Geoscience atlas of svalbard.* Tromsø, Norway: Norsk Polarinstitutt.

Dimakis, P., Braathen, B. I., Faleide, J. I., Elverhøi, A., and Gudlaugsson, S. T. (1998). Cenozoic erosion and the preglacial uplift of the Svalbard–Barents Sea region. *Tectonophysics* 300, 311–327. doi:10.1016/S0040-1951(98)00245-5

Divine, D. V., and Dick, C. (2006). Historical variability of sea ice edge position in the Nordic Seas. *J. Geophys. Res. Oceans* 111. doi:10.1029/2004JC002851

Dörr, N., Lisker, F., Jochmann, M., Rainer, T., Schlegel, A., Schubert, K., et al. (2018). "Subsidence, rapid inversion, and slow erosion of the Central Tertiary Basin of Svalbard: evidence from the thermal evolution and basin modeling," in *Circum-arctic structural events: tectonic evolution of the arctic margins and trans-arctic links with adjacent orogens*. Editors K. Piepjohn, J. V. Strauss, R. Lutz, and W. C. McClelland (Boulder, Colorado: The Geological Society of America), 169–188.

Dypvik, H., and Zakharov, V. (2012). Fine-grained epicontinental Arctic sedimentation–mineralogy and geochemistry of shales from the Late Jurassic-Early Cretaceous transition. *Nor. J. Geology/Norsk Geol. Forening* 92, 65–87.

Faleide, J. I., Solheim, A., Fiedler, A., Hjelstuen, B. O., Andersen, E. S., and Vanneste, K. (1996). Late Cenozoic evolution of the western Barents Sea-Svalbard continental margin. *Glob. Planet. Change* 12, 53–74. doi:10.1016/0921-8181(95)00012-7

Gasser, D. (2014). The Caledonides of Greenland, Svalbard and other Arctic areas: status of research and open questions. *Geol. Soc. Lond. Spec. Publ.* 390, 93–129. doi:10.1144/SP390.17

Gilbert, G. L., O'Neill, H. B., Nemec, W., Thiel, C., Christiansen, H. H., and Buylaert, J. P. (2018). Late Quaternary sedimentation and permafrost development in a Svalbard fjord-valley, Norwegian high Arctic. *Sedimentology* 65, 2531–2558. doi:10.1111/sed.12476

Grundvåg, S.-A., Jelby, M. E., Śliwińska, K. K., Nøhr-Hansen, H., Aadland, T., Sandvik, S. E., et al. (2019). Sedimentology and palynology of the Lower Cretaceous succession of central Spitsbergen: integration of subsurface and outcrop data. *Nor. J. Geol.* 99, 253–284. doi:10.17850/njg006

Harada, K., and Yoshikawa, K. (1996). Permafrost age and thickness near Adventfjorden, Spitsbergen. *Polar Geogr.* 20, 267–281. doi:10.1080/10889379609377607

Henriksen, E., Bjørnseth, H., Hals, T., Heide, T., Kiryukhina, T., Kløvjan, O., et al. (2011). Chapter 17 Uplift and erosion of the greater Barents Sea: impact on prospectivity and petroleum systems. *Geol. Soc. Lond. Memoirs* 35, 271–281. doi:10.1144/M35.17

Hodson, A. J., Nowak, A., Holmlund, E., Redeker, K. R., Turchyn, A. V., and Christiansen, H. H. (2019). Seasonal dynamics of methane and carbon dioxide evasion from an open system pingo: lagoon pingo, svalbard. *Front. Earth Sci.* 30, 1–12. doi:10.3389/feart.2019.00030

Hodson, A. J., Nowak, A., Senger, K., Redeker, K., Christiansen, H. H., Jessen, S., et al. (2020). Open system pingos as hotspots for sub-permafrost methane emission in Svalbard. *Cryosphere Discuss.*, 1–21.

Hornum, M. T., Hodson, A. J., Jessen, S., Bense, V., and Senger, K. (2020). Numerical modelling of permafrost spring discharge and open-system pingo formation induced by basal permafrost aggradation. *Cryosphere Discuss.* 14, 4627–4651. doi:10.5194/tc-14-4627-2020

Howarth, R. W., Santoro, R., and Ingraffea, A. (2011). Methane and the greenhouse-gas footprint of natural gas from shale formations. *Clim. change* 106, 679–690. doi:10.1007/s10584-011-0061-5

Humlum, O. (2005). *Holocene permafrost aggradation in Svalbard.* London: Geological Society. doi:10.1144/GSL.SP.2005.242.01.11

Humlum, O., Instanes, A., and Sollid, J. L. (2003). Permafrost in Svalbard: a review of research history, climatic background and engineering challenges. *Polar Res.* 22, 191–215. doi:10.3402/polar.v22i2.6455

Huq, F., Smalley, P. C., Mørkved, P. T., Johansen, I., Yarushina, V., and Johansen, H. (2017). The Longyearbyen CO2 Lab: fluid communication in reservoir and caprock. *Int. J. Greenh. Gas Control* 63, 59–76. doi:10.1016/j.ijggc.2017.05.005

Hynne, I. B. (2010). *Depositional environment on eastern svalbard and central spitsbergen during carnian time (late triassic): a sedimentological investigation of the De Geerdalen Formation, Institutt for geovitenskap og petroleum.* Trondheim: Norwegian University of Science and Technology.

Isaksen, K., Mühll, D. V., Gubler, H., Kohl, T., and Sollid, J. L. (2000). Ground surface-temperature reconstruction based on data from a deep borehole in permafrost at Janssonhaugen, Svalbard. *Ann. Glaciol.* 31, 287–294. doi:10.3189/172756400781820291

Jochmann, M. M., Augland, L. E., Lenz, O., Bieg, G., Haugen, T., Grundvåg, S. A., et al. (2019). Sylfjellet: a new outcrop of the Paleogene van mijenfjorden Group in svalbard. *arktos* 1-22. doi:10.1007/s41063-019-00072-w

Johansen, T. A., Digranes, P., van Schaack, M., and Lønne, I. (2003). Seismic mapping and modeling of near-surface sediments in polar areas. *Geophysics* 68, 566–573. doi:10.1190/1.1567226

Juliussen, H., Jochmann, M., and Christiansen, H. H. (2010). "High-mountain permafrost temperature monitoring in central Svalbard; implications for Arctic coal mining," in Third European Confreence on Permafrost; EUCOP III, Svalbard, June 2010.

Kamath, A., Godbole, S., Ostermann, R., and Collett, T. (1987). Evaluation of the stability of gas hydrates in northern Alaska. *Cold Regions Sci. Technol.* 14, 107–119. doi:10.1016/0165-232X(87)90026-7

Keating, K., Binley, A., Bense, V., Van Dam, R. L., and Christiansen, H. H. (2018). Combined geophysical measurements provide evidence for unfrozen water in permafrost in the adventdalen valley in Svalbard. *Geophys. Res. Lett.* 45, 7606–7614. doi:10.1029/2017GL076508

Kierulf, H. P., Kohler, J., Boy, J.-P., Geyman, E. C., Mémin, A., Omang, O. C. D., et al. (2022). Time-varying uplift in Svalbard—an effect of glacial changes. *Geophys. J. Int.* 231, 1518–1534. doi:10.1093/gji/ggac264

Klausen, T. G., Nyberg, B., and Helland-Hansen, W. (2019). The largest delta plain in Earth's history. *Geology* 47, 470–474. doi:10.1130/G45507.1

Knoblauch, C., Beer, C., Liebner, S., Grigoriev, M. N., and Pfeiffer, E.-M. (2018). Methane production as key to the greenhouse gas budget of thawing permafrost. *Nat. Clim. Change* 8, 309–312. doi:10.1038/s41558-018-0095-z

Koevoets, M. J., Hammer, Ø., Olaussen, S., Senger, K., and Smelror, M. (2018). Integrating subsurface and outcrop data of the middle Jurassic to Lower Cretaceous Agardhfjellet formation in central Spitsbergen. *Nor. J. Geol.* 98, 1–34. doi:10.17850/njg98-4-01

Kristensen, L., Benn, D. I., Hormes, A., and Ottesen, D. (2009). Mud aprons in front of Svalbard surge moraines: evidence of subglacial deforming layers or proglacial glaciotectonics? *Geomorphology* 111, 206–221. doi:10.1016/j.geomorph.2009.04.022

Landvik, J., Mangerud, J., and Salvigsen, O. (1988). "Glacial history and permafrost in the Svalbard area," in Proceedings of the 5th International Conference on Permafrost, Trondheim, Norway, August 1988.

Landvik, J. Y., Bondevik, S., Elverhøi, A., Fjeldskaar, W., Mangerud, J., Salvigsen, O., et al. (1998). The last glacial maximum of Svalbard and the Barents Sea area: ice sheet extent and configuration. *Quat. Sci. Rev.* 17, 43–75. doi:10.1016/S0277-3791(97)00066-8

Landvik, J. Y., Brook, E. J., Gualtieri, L., Raisbeck, G., Salvigsen, O., and Yiou, F. o. (2003). Northwest Svalbard during the last glaciation: ice-free areas existed. *Geology* 31, 905–908. doi:10.1130/g19703.1

Lasabuda, A., Laberg, J. S., Knutsen, S.-M., and Safronova, P. (2018). Cenozoic tectonostratigraphy and pre-glacial erosion: a mass-balance study of the northwestern Barents Sea margin, Norwegian Arctic. *J. Geodyn.* 119, 149–166. doi:10.1016/j.jog.2018.03.004

Lashof, D. A., and Ahuja, D. R. (1990). Relative contributions of greenhouse gas emissions to global warming. *Nature* 344, 529–531. doi:10.1038/344529a0

Leith, T., Weiss, H., Mørk, A., Elvebakk, G., Embry, A., Brooks, P., et al. (1993). "Mesozoic hydrocarbon source-rocks of the Arctic region," in *Norwegian petroleum society special publications* (Amsterdam, Netherlands: Elsevier), 1–25. doi:10.1016/B978-0-444-88943-0.50006-X

Lerche, I., Yu, Z., Tørudbakken, B., and Thomsen, R. O. (1997). Ice loading effects in sedimentary basins with reference to the Barents Sea. *Mar. Petroleum Geol.* 14, 277–338. doi:10.1016/s0264-8172(96)00059-1

Leythaeuser, D., Mackenzie, A., Schaefer, R. G., and BjorØy, M. (1984). A novel approach for recognition and quantification of hydrocarbon migration effects in shale-sandstone sequences. *AAPG Bull.* 68, 196–219. doi:10.1306/AD4609FE-16F7-11D7-8645000102C1865D

Lind, S., Ingvaldsen, R. B., and Furevik, T. (2018). Arctic warming hotspot in the northern Barents Sea linked to declining sea-ice import. *Nat. Clim. change* 8, 634–639. doi:10.1038/s41558-018-0205-y

Lord, G. S., Solvi, K. H., Ask, M., Mørk, A., Hounslow, M. W., and Paterson, N. W. (2014). The hopen member: a new member of the Triassic De Geerdalen Formation. *Svalbard, Nor. Pet. Dir. Bull.* 11, 81–96.

Lyutkevich, E. M. (1937). Geology of tertiary coals of spitzbergen, Isfjord region. *Tr. Arkticheskogo Instituta* 76, 7–24.

Magnabosco, C., Braathen, A., and Ogata, K. (2014). Permeability model of tight reservoir sandstones combining core-plug and Miniperm analysis of drillcore. *Longyearbyen CO2 Lab, Svalbard, Nor. J. Geol.* 94, 189–200.

Magoon, L., and Dow, W. (2000). Mapping the petroleum system-an investigative technique to explore the hydrocarbon fluid system. *AAPG Mem.* 73, 53–68.

Majewski, W., and Zajaczkowski, M. (2007). Benthic foraminifera in Adventfjorden, Svalbard: last 50 years of local hydrographic changes. *J. Foraminifer. Res.* 37, 107–124. doi:10.2113/gsjfr.37.2.107

Majorowicz, J., and Hannigan, P. (2000). Stability zone of natural gas hydrates in a permafrost-bearing region of the Beaufort—mackenzie Basin: study of a feasible energy Source1 (geological Survey of Canada contribution No. 1999275). *Nat. Resour. Res.* 9, 3–26. doi:10.1023/A:1010105628952

Makogon, Y., and Omelchenko, R. (2013). Commercial gas production from Messoyakha deposit in hydrate conditions. *J. Nat. Gas Sci. Eng.* 11, 1–6. doi:10.1016/j.jngse.2012.08.002

Marshall, C., Large, D. J., Meredith, W., Snape, C. E., Uguna, C., Spiro, B. F., et al. (2015). Geochemistry and petrology of Palaeocene coals from Spitsbergen—Part 1: oil potential and depositional environment. *Int. J. Coal Geol.* 143, 22–33. doi:10.1016/j.coal.2015.03.006

Marum, D. M., Afonso, M. D., and Ochoa, B. B. (2019). Optimization of the gas-extraction process in a new mud-logging system. *SPE Drill. Complet.* 35, 001–013. doi:10.2118/198909-PA

Masoudi, R., and Tohidi, B. (2005). Estimating the hydrate stability zone in the presence of salts and/or organic inhibitors using water partial pressure. *J. Petroleum Sci. Eng.* 46, 23–36. doi:10.1016/j.petrol.2004.10.002

Michelsen, J. K., and Khorasani, G. K. (1991). A regional study on coals from Svalbard; organic facies, maturity and thermal history. *Bull. Société Géologique Fr.* 162, 385–397.

Minshull, T. A., Marín-Moreno, H., Betlem, P., Bialas, J., Buenz, S., Burwicz, E., et al. (2020). Hydrate occurrence in Europe: a review of available evidence. *Mar. Petroleum Geol.* 111, 735–764. doi:10.1016/j.marpetgeo.2019.08.014

Mørk, M. B. E. (1999). Compositional variations and provenance of triassic sandstones from the Barents shelf. *J. Sediment. Res.* 69, 690–710. doi:10.2110/jsr.69.690

Mørk, M. B. E. (2013). Diagenesis and quartz cement distribution of low-permeability Upper Triassic–Middle Jurassic reservoir sandstones, Longyearbyen CO2 lab well site in Svalbard, Norway. *AAPG Bull.* 97, 577–596. doi:10.1306/10031211193

Nielsen, T., Laier, T., Kuijpers, A., Rasmussen, T. L., Mikkelsen, N. E., and Nørgård-Pedersen, N. (2014). Fluid flow and methane occurrences in the Disko Bugt area offshore West Greenland: indications for gas hydrates? *Geo-Marine Lett.* 34, 511–523. doi:10.1007/s00367-014-0382-2

Norsk Hydro, (1991). *Final well report - 7816/12-1, HarstadSVA021, 122*. Oslo, Norway: Norsk Hydro.

Norsk Polar Navigasjon A/S, (1977a). *Geological report - tromsøbreen No. 1*. Stabekk, Norway: Norsk Polar Navigasjon.

Norsk Polar Navigasjon A/S, (1977b). *Final drilling report - tromsøbreen No. 1*. Stabekk, Norway: Norsk Polar Navigasjon.

Norsk Polarinstitutt: Svalbardkartet, (2015).*Norsk Polarinstitutt*, Tromsø: Norsk Polarinstitutt WebGIS.

Norske Fina, A./S. (1971a). *Geological report - well hopen No. 1*. Stabekk, Norway.

Norske Fina, A./S. (1971b). *Final drilling report - well hopen No. 1*. Stabekk, Norway.

Norske Fina, A./S. (1972a). *Geological report - well: plurdalen No. 1*. Stabekk, Norway: Norske Fina.

Norske Fina, A./S. (1972b). *Final drilling report - well: plurdalen No.1*, 71. Stabekk, Norway: Norske Fina.

Norske Fina, A./S. (1973a). *Geological report - well hopen No. 2*. Oslo, Norway: Stabekk.

Norske Fina, A./S. (1973b). *Final drilling report - well hopen No. 2*. Stabekk, Norway: Norske Fina.

Norskpetroleum, (2020). Exploration activity. https://www.norskpetroleum.no/en/exploration/exploration-activity/.

Nøttvedt, A., Cecchi, M., Gjelberg, J., Kristensen, S., Lønøy, A., Rasmussen, A., et al. (1993). "Svalbard-Barents Sea correlation: a short review," in *Norwegian petroleum society special publications* (Amsterdam, Netherlands: Elsevier), 363–375.

Ohm, S., Larsen, L., Olaussen, S., Senger, K., Birchall, T., Demchuk, T., et al. (2019). Discovery of shale gas in organic-rich jurassic successions, adventdalen, central spitsbergen, Norway. *Nor. J. Geol.* 99, 28. doi:10.17850/njg007

Ohm, S. E., Karlsen, D. A., and Austin, T. (2008). Geochemically driven exploration models in uplifted areas: examples from the Norwegian Barents Sea. *AAPG Bull.* 92, 1191–1223. doi:10.1306/06180808028

Olaussen, S., Grundvåg, S.-A., Senger, K., Anell, I., Betlem, P., Birchall, T., et al. (2022). *The svalbard carboniferous to cenozoic composite tectono-stratigraphic element*. London, Memoirs: Geological Society. doi:10.1144/M57-2021-36

Olaussen, S., Larssen, G. B., Helland-Hansen, W., Johannessen, E. P., Nøttvedt, A., Riis, F., et al. (2018). Mesozoic strata of kong karls land, svalbard, Norway; a link to the northern Barents Sea basins and platforms. *Nor. J. Geol.* 98, 1–69. doi:10.17850/njg98-4-06

Olaussen, S., Senger, K., Braathen, A., Grundvåg, S. A., and Mørk, A. (2019). You learn as long as you drill; research synthesis from the Longyearbyen CO2 Laboratory, Svalbard, Norway. *Nor. J. Geol.* 99, 157–187. doi:10.17850/njg008

Osterkamp, T., and Payne, M. (1981). Estimates of permafrost thickness from well logs in northern Alaska. *Cold Regions Sci. Technol.* 5, 13–27. doi:10.1016/0165-232X(81)90037-9

Piepjohn, K. (2000). *The svalbardian-ellesmerian deformation of the old red sandstone and the pre-devonian basement in NW spitsbergen (svalbard)*. London: Geological Society. doi:10.1144/GSL.SP.2000.180.01.31

Polargas Prospektering, K. B. (1988). *Geological report - tromsøbreen No. 2*. Oslo, Norway: Polargas Prospektering.

Polyakova, I. (2015). Petroleum source rocks of the Arctic region. *Lithology Mineral Resour.* 50, 26–49. doi:10.1134/S002449021406008X

Przybylak, R., Arazny, A., Nordli, O., Finkelnburg, R., Kejna, M., Budzik, T., et al. (2014). Spatial distribution of air temperature on Svalbard during 1 year with campaign measurements. *Int. J. Climatol.* 34, 3702–3719. doi:10.1002/joc.3937

Rachlewicz, G., and Szczuciński, W. (2008). Changes in thermal structure of permafrost active layer in a dry polar climate. *Petuniabukta, Svalbard, Pol. Polar Res.* 29, 261–278.

Rismyhr, B., Bjærke, T., Olaussen, S., Mulrooney, M., and Senger, K. (2019). Facies, palynostratigraphy and sequence stratigraphy of the wilhelmøya subgroup (upper triassic–middle jurassic) in western central spitsbergen, svalbard. *Nor. J. Geol.* 99, 35–64. doi:10.17850/njg001

Rodes, N., Betlem, P., Senger, K., Römer, M., Hodson, A., Liira, M., et al. (2023). Active gas seepage in western Spitsbergen fjords, Svalbard archipelago: spatial extent and geological controls. *Front. Earth Sci.* 11, 2023. doi:10.3389/feart.2023.1173477

Ronen, S., Rokkan, A., Bouraly, R., Valsvik, G., Larson, L., Ostensvig, E., et al. (2012). Imaging shallow gas drilling hazards under three Forties oil field platforms using ocean-bottom nodes. *Lead. Edge* 31, 465–469. doi:10.1190/tle31040465.1

Roy, S., Hovland, M., Noormets, R., and Olaussen, S. (2015). Seepage in isfjorden and its tributary fjords, West Spitsbergen. *Mar. Geol.* 363, 146–159. doi:10.1016/j.margeo.2015.02.003

Schmitt, D., Welz, M., and Rokosh, C. (2005). High-resolution seismic imaging over thick permafrost at the 2002 Mallik drill site. *Geol. Surv. Can. Bull.* 585, 125.

Schulson, E. M. (2001). Brittle failure of ice. *Eng. Fract. Mech.* 68, 1839–1887. doi:10.1016/S0013-7944(01)00037-6

Senger, K., Birchall, T., Betlem, P., Ogata, K., Ohm, S., Olaussen, S., et al. (2020). Resistivity of reservoir sandstones and organic rich shales on the Barents Shelf: implications for interpreting CSEM data. *Geosci. Front.* 64, 101063. doi:10.1016/j.gsf.2020.08.007

Senger, K., Brugmans, P., Grundvåg, S.-A., Jochmann, M. M., Nøttvedt, A., Olaussen, S., et al. (2019). Petroleum, coal and research drilling onshore Svalbard: a historical perspective. *Nor. J. Geol.* 99, 30. doi:10.17850/njg99-3-1

Senger, K., Nuus, M., Balling, N., Betlem, P., Birchall, T., Christiansen, H. H., et al. (2023). The subsurface thermal state of Svalbard and implications for geothermal potential. *Geothermics* 111, 102702. doi:10.1016/j.geothermics.2023.102702

Senger, K., Tveranger, J., Ogata, K., Braathen, A., and Planke, S. (2014). Late mesozoic magmatism in svalbard: a review. *Earth-Science Rev.* 139, 123–144. doi:10.1016/j.earscirev.2014.09.002

Skorobogatov, V. A., Yakushev, V. S., and Chuvilin, E. M. (2007). "Sources of natural gas within permafrost; North-West, Siberia," in Permafrost Proceedings Seventh International Conference, Collection Nordicana, Canada, June 2007.

Sloan, E. D., Jr, Koh, C. A., and Koh, C. (2007). *Clathrate hydrates of natural gases*. Boca Raton, Florida, United States: CRC Press.

Smyrak-Sikora, A., Johannessen, E. P., Olaussen, S., Sandal, G., and Braathen, A. (2019). Sedimentary architecture during Carboniferous rift initiation–the arid billefjorden trough, svalbard. *J. Geol. Soc.* 176, 225–252. doi:10.1144/jgs2018-100

SNSK (1979). *Report SN1979_002*. Longyearbyen: SNSK.

SNSK (1980). *Drawing nr. 14204-3; borhullslogg 79/11*. Endalen, Longyearbyen: SNSK.

SNSK (1981). *Report SN1981_008*. Longyearbyen: SNSK.

SNSK (1982a). *Report SN1982_004*. Longyearbyen: SNSK.

SNSK (1982b). *Report SN1982_005*. Longyearbyen: SNSK.

SNSK (1986). *Report SN1986_001*. Longyearbyen: SNSK.

SNSK (1991). *Report SN1991.04*. Longyearbyen: SNSK.

SNSK (1994). *Report - Kapp Laila - 1*. Longyearbyen: SNSK.

SNSK (2011a). *BH 14-2011 drilling report*. Longyearbyen: SNSK.

SNSK (2011b). *BH 16-2011 drilling report*. Longyearbyen: SNSK.

SNSK (2011c). *BH 18-2011 drilling report*. Longyearbyen: SNSK.

SNSK (2011d). *BH 19-2011 drilling report*. Longyearbyen: SNSK.

SNSK (2013a). *BH 10-2013 drilling report*. Longyearbyen: SNSK.

SNSK (2013b). *BH 6-2013 drilling report*. Longyearbyen: SNSK.

SNSK (2013c). *BH 7-2013 drilling report*. Longyearbyen: SNSK.

SNSK (2014). *BH 8-2014 drilling report*. Longyearbyen: SNSK.

Steel, R., Dalland, A., Kalgraff, K., and Larsen, V. (1981). The Central Tertiary Basin of Spitsbergen: sedimentary development of a sheared-margin basin. *AAPG Mem.* 7, 647–664.

Steel, R. J., and Worsley, D. (1984). "Svalbard's post-Caledonian strata - an atlas of sedimentational patterns and paleogeographic evolution," in *Petroleum geology of the north European margin*. Editor A. M. Spencer (London: Graham & Trotman), 109–135. doi:10.1007/978-94-009-5626-1_9

Strand, S. M., Christiansen, H. H., Johansson, M., Åkerman, J., and Humlum, O. (2021). Active layer thickening and controls on interannual variability in the Nordic Arctic compared to the circum-Arctic. *Permafr. Periglac. Process.* 32 (1), 47–58. doi:10.1002/ppp.2088

Total Marine Norsk (1972). *Final well report - raddedalen I*. Norway: Total Marine Norsk.

Uguna, J. O., Carr, A. D., Marshall, C., Large, D. J., Meredith, W., Jochmann, M., et al. (2017). Improving spatial predictability of petroleum resources within the Central Tertiary Basin, Spitsbergen: a geochemical and petrographic study of coals from the eastern and western coalfields. *Int. J. Coal Geol.* 179, 278–294. doi:10.1016/j.coal.2017.06.007

UNIS CO2 Lab AS (UNIS – The University Centre in Svalbard) (2015). *The longyearbyen CO2 lab - phase 2 final report*. Longyearbyen, Svalbard: The University Centre in Svalbard, 2015.

van Pelt, W. J., Kohler, J., Liston, G., Hagen, J. O., Luks, B., Reijmer, C., et al. (2016). Multidecadal climate and seasonal snow conditions in Svalbard. *J. Geophys. Res. Earth Surf.* 121, 2100–2117. doi:10.1002/2016JF003999

Verba, M. (2013). Sedimentary cover reservoir of Svalbard archipelago. *Neftegazov. Geol. Teor. I Prakt.* 8, 1–45. doi:10.17353/2070-5379/5_2013

Vonk, J. E., and Gustafsson, Ö. (2013). Permafrost-carbon complexities. *Nat. Geosci.* 6, 675–676. doi:10.1038/ngeo1937

Vrielink, H. J., Bradford, J. S., Basarab, L., and Ubaru, C. C. (2010). "Successful application of casing-while-drilling technology in a Canadian arctic permafrost application," in IADC/SPE Drilling Conference, Orlando, Florida, USA, March 2010. doi:10.2118/111806-MS

Westermann, S., Wollschläger, U., and Boike, J. (2010). Monitoring of active layer dynamics at a permafrost site on Svalbard using multi-channel ground-penetrating radar. *Cryosphere* 4, 475–487. doi:10.5194/tc-4-475-2010

Yakushev, V., and Chuvilin, E. (2000). Natural gas and gas hydrate accumulations within permafrost in Russia. *Cold regions Sci. Technol.* 31, 189–197. doi:10.1016/S0165-232X(00)00012-4

frontiers | Frontiers in Earth Science

TYPE Original Research
PUBLISHED 15 December 2023
DOI 10.3389/feart.2023.1290882

OPEN ACCESS

EDITED BY
Andrew Jonathan Hodson,
The University Centre in Svalbard, Norway

REVIEWED BY
Xiyang Dong,
Third Institute of Oceanography of the Ministry of Natural Resources, China
Qianyong Liang,
Guangzhou Marine Geological Survey, China

*CORRESPONDENCE
Muhammed Fatih Sert,
muhammed.f.sert@uit.no

RECEIVED 08 September 2023
ACCEPTED 04 December 2023
PUBLISHED 15 December 2023

CITATION
Sert MF, Schweitzer HD, de Groot TR, Kekäläinen T, Jänis J, Bernstein HC, Ferré B, Gründger F, Kalenitchenko D and Niemann H (2023), Elevated methane alters dissolved organic matter composition in the Arctic Ocean cold seeps.
Front. Earth Sci. 11:1290882.
doi: 10.3389/feart.2023.1290882

Elevated methane alters dissolved organic matter composition in the Arctic Ocean cold seeps

Muhammed Fatih Sert[1]*, Hannah D. Schweitzer[2,3], Tim R. de Groot[4], Timo Kekäläinen[5], Janne Jänis[5], Hans C. Bernstein[2,3], Bénédicte Ferré[1], Friederike Gründger[6], Dimitri Kalenitchenko[1,7] and Helge Niemann[1,4,8]

[1]Centre for Arctic Gas Hydrate, Environment and Climate, UiT-The Arctic University of Norway, Tromsø, Norway, [2]Faculty of Biosciences, Fisheries, and Economics, UiT-The Arctic University of Norway, Tromsø, Norway, [3]The Arctic Centre for Sustainable Energy, UiT-The Arctic University of Norway, Tromsø, Norway, [4]Department of Marine Microbiology and Biogeochemistry, NIOZ Royal Institute for Sea Research, Texel, Netherlands, [5]Department of Chemistry, University of Eastern Finland, Joensuu, Finland, [6]Arctic Research Centre, Department of Biology, Aarhus University, Aarhus, Denmark, [7]Littoral Environnement et Sociétés (LIENSs), UMR 7266, CNRS-La Rochelle Université, La Rochelle, France, [8]Department of Earth Sciences, Faculty of Geosciences, Utrecht University, Utrecht, Netherlands

Cold seeps release methane (CH_4) from the seafloor to the water column, which fuels microbially mediated aerobic methane oxidation (MOx). Methane-oxidising bacteria (MOB) utilise excess methane, and the MOB biomass serves as a carbon source in the food web. Yet, it remains unclear if and how MOx modifies the composition of dissolved organic matter (DOM) in cold seeps. We investigated MOx rates, DOM compositions and the microbial community during *ex-situ* incubations of seawater collected from a cold seep site at Norskebanken (north of the Svalbard archipelago) in the Arctic Ocean. Samples were incubated with and without methane amendments. Samples amended with methane (~1 µM final concentration) showed elevated rates of MOx in both seep and non-seep incubations. Fourier transform ion cyclotron resonance mass spectrometry (FT-ICR MS) analyses showed that the number of DOM formulas (i.e., molecular diversity) increased by up to 39% in these incubations. In contrast, the number of formulas decreased by 20% in samples not amended with methane, both from non-seep and seep locations. DOM composition was thus altered towards a more diverse and heterogeneous composition along with elevated methanotrophic activity in methane-amended conditions. In addition to microbial DOM production, abating microbial diversity indicates that elevated DOM diversity was potentially related to grazing pressure on bacteria. The diversity of DOM constituents, therefore, likely increased with the variety of decaying cells contributing to DOM production. Furthermore, based on a principal coordinate analysis, we show that the final DOM composition of non-seep samples amended with methane became more resemblant to that of seep samples. This suggests that methane intrusions will affect water column DOM dynamics similarly, irrespective of the water column's methane history.

KEYWORDS

dissolved organic matter, methane, cold seeps, Arctic Ocean, methane oxidation, methanotrophs, FT-ICR MS

1 Introduction

Dissolved organic matter (DOM) in the open ocean is a heterogeneous mixture of organic compounds. DOM originates predominantly from marine primary production and further modification through a plethora of microbial and abiotic processes (Sjöstedt et al., 2021). The main microbial control on the marine DOM cycle is that primary producers transform inorganic nutrients into organic matter (dissolved and particulate) in the epipelagic ocean, and heterotrophic microbes decompose DOM to inorganic nutrients, which may then again fuel primary producers (Amon and Benner, 1996; Kujawinski, 2011; Carlson and Hansell, 2015). In addition to these two key players, protozoa, zooplankton, and viruses are also taking part in DOM cycling as they are involved in various production and decomposition mechanisms (Carlson and Hansell, 2015).

Despite the increasing number of studies addressing the interaction of microbes with DOM, pathways that generate functional and chemical diversity of DOM are poorly identified (Lau and del Giorgio, 2020). This is mainly caused by the complexity, variety and interactions of microbial processes that cannot be constrained to single mechanisms in environmental samples. Nevertheless, monoculture and co-culture experiments point out that microbes can control DOM composition by releasing unique characteristics of metabolites depending on isolation or grazing factors/conditions (Kujawinski et al., 2004; Rosselló-Mora et al., 2008; Kujawinski et al., 2016). Closely related species may produce similar suites of DOM (Becker et al., 2014; Lian et al., 2021) by producing chemically diverse and mostly persistent exometabolites from simple substrates (Lechtenfeld et al., 2015; Osterholz et al., 2015; Noriega-Ortega et al., 2019).

One important microbial process in the ocean water column that may affect DOM composition is the aerobic oxidation of methane (MOx) (Pohlman et al., 2011; Kalyuzhnaya et al., 2013; Sert et al., 2020). MOx is mediated by aerobic methane-oxidising bacteria (MOB) for energy gain and growth (Hanson and Hanson, 1996):

$$CH_4 + O_2 \rightarrow CO_2 + 2H_2O$$

It is the final sink for methane in the ocean water column before reaching the atmosphere, where it contributes to global warming (Reeburgh, 2007; Graves et al., 2015; Steinle et al., 2015). In the ocean, methane is often released from sea floor point sources, so called cold seeps, where methane bubbles emanating from the sea floor are a commonly observed feature (James et al., 2016). Various geological and geochemical mechanisms and processes have been suggested as a source of seeping methane from the arctic continental shelf (Bünz et al., 2012; Berndt et al., 2014; Serov et al., 2015; James et al., 2016; Andreassen et al., 2017). Regardless of the methane source, a substantial part of the seeping methane is utilised by MOBs (Boetius and Wenzhöfer, 2013; James et al., 2016). It has been suggested that seep-derived biogeochemical processes also modify the water column DOM composition towards a more bioavailable and heterogeneous composition at Arctic Ocean cold seeps (Sert et al., 2020). MOBs are known to produce a number of organic compounds as part of their metabolism, including small molecules such as methanol (Hanson and Hanson, 1996) that are more accessible to a broader range of microbes. MOBs also produce microbial biomass comprised of e.g., lipids, fatty acids, hopanoids and steroids (Elvert and Niemann, 2008) as well as proteins (Kerckhof et al., 2021). Some strains of MOBs can also utilise carbon substrates other than methane, such as acetate, pyruvate and succinate (Dedysh et al., 2005; Theisen and Murrell, 2005; Murrell, 2010). However, the influence of MOx on water column DOM systematics on short-time scales remains mostly unresolved.

In highly complex environmental systems (e.g., cold seeps), tracing the unique signatures of a particular type of microorganism is challenging. We used an *ex-situ* incubation approach to (in part) constrain this complexity. Our objective was to control the temperature, light conditions and methane concentrations and provide an opportunity to elevate the activity of MOBs, which are ubiquitous organisms that are capable of utilising methane in the oxic marine water column (Hanson and Hanson, 1996; Lidstrom, 2006; Kalyuzhnaya et al., 2019). In a closed, partially controlled medium, MOx can thus be stimulated by elevating methane concentration, and all the organisms that can benefit from methane could contribute to the composition of DOM. Despite the growing interest in assessing the interactions of microbes with marine DOM, biochemical mechanisms are too versatile and complex to be fully resolved. This study provides a basis for assessing the impact of methanotrophy on DOM compositions in cold seep environments.

2 Materials and methods

2.1 Incubation setup

Seawater for the incubation medium was collected in the framework of cruise CAGE 20-7 (Ferré et al., 2020b) with R/V Kronprins Haakon at Norskebanken (ca. 80° 37′N, 14° 20′E), which is located on the continental shelf north of the Svalbard archipelago in the Arctic Ocean (Figure 1). Methane seepage was discovered at this location in 2013 (Geissler et al., 2016). We sampled two stations: one within a cluster of methane release sites (seep station) and a second one outside the methane seepage area ~4 km to the West of the seep station (non-seep station). Water samples were collected ~3 m above the seafloor with Niskin bottles mounted on a rosette sampler equipped with a Sea-Bird 911 plus CTD (Conductivity Temperature Depth) profiler and an SBE 43 oxygen sensor.

The following sampling procedure and incubation protocols were carried out at both stations: immediately after recovery of the rosette sampler, we subsampled the Niskin bottles for methane concentration and MOx measurements (methods described below) to characterise the initial conditions of the incubation medium. Then, 12 muffled glass bottles of 1,135 mL (total volume) were filled with 1,000 mL of bottom water as incubation medium (Figure 2). The bottles were sealed with airtight stoppers made of bromobutyl rubber (SCHOTT DURAN). Four out of these twelve bottles were amended with 100 µL of pure methane (≥99.0% purity, Sigma-Aldrich) with an airtight syringe immediately after capping, while the remaining eight bottles were not amended. All twelve bottles were placed horizontally in a dark, temperature-controlled incubator at 4°C. Four unamended bottles were processed within 6 h to characterise initial incubation conditions. The remaining eight bottles (four amended and four unamended) were incubated for approximately 3 days until final sampling and characterisation.

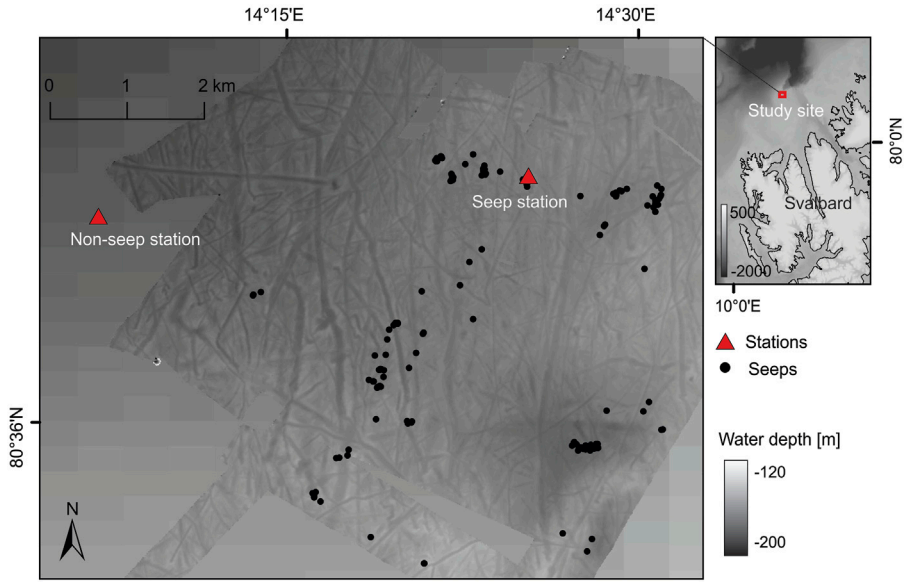

FIGURE 1
Bathymetric map of the study site showing the stations where water samples were taken for the incubation experiments (red triangles). Methane flares detected using the ship's multibeam echosounder are indicated (black dots).

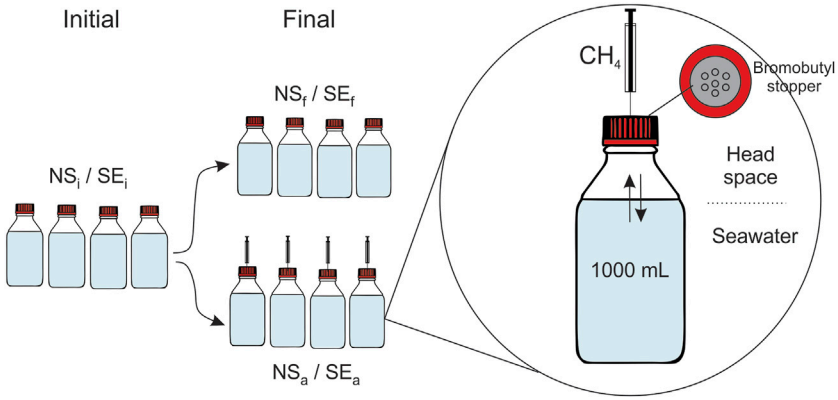

FIGURE 2
Schematic of experimental design of seawater incubations from non-seep (NS) and seep stations (SE) for either initial ($_i$), final ($_f$) or methane-amended final ($_a$) conditions.

The same procedure was carried out at both seep and non-seep stations, resulting in a total of 24 bottles of six different incubation conditions with four replicates: non-seep initial (NS_i), non-seep final (NS_f) and non-seep amended final (NS_a) from the non-seep station and seep initial (SE_i), seep final (SE_f), and seep amended final (SE_a) from the seep station (see Figure 2; Table 1).

2.2 Subsampling and storage

Samples for methane concentration measurements for the initial characterisation of the incubation samples (NS_i and SE_i) were collected headspace free from Niskin bottles into 120 mL serum vials, fixed with 1 mL of NaOH solution (1 M) and crimp top sealed with bromobutyl septa. For methane concentration measurements from the incubation bottles (NS_f, NS_a, SE_f and SE_a), a 1 mL aliquot of headspace gas was sampled with a gas-tight syringe through the bromobutyl septa of the bottle caps at the end of the incubation. The 1 mL aliquot of headspace was then injected into 20 mL crimp top vials (Thermo) filled bubble-free with 0.1 M sodium hydroxide solution by replacing the same amount of solution with the help of a second syringe. Samples were stored at 4°C until analysis in the laboratory on land.

For MOx measurements, quadruplicates of 20 mL crimp top vials were filled from the Niskin bottles (initial conditions: NS_i and SE_i). Similarly, aliquots were subsampled from the incubation bottles after incubation (final conditions, NS_f, NS_a, SE_f and SE_a). All vials for MOx measurements were sealed bubble-free with grey-

TABLE 1 Overview of the experimental conditions during incubation of water column samples from non-seep and seep locations. Abbreviations indicated here also used in the text.

Station	Incubation condition	Abbrevia-tion	Incubation time (h)	Methane concentrations (nM)	
				Initial	Final
Non-seep (NS)	Initial	NS_i	6	5.8	-
	Unamended final	NS_f	75	-	4.5
	Amended final	NS_a	75	1032.5[a]	737.9
Seep (SE)	Initial	SE_i	6	83.1	-
	Unamended final	SE_f	84	-	35.0
	Amended final	SE_a	84	1109.9[a]	846.2

[a]Calculated from initial concentration and added methane.

bromobutyl stoppers that are known not to hamper methanotrophic activity (Niemann et al., 2015).

Sampling for the remaining analyses was carried out as follows: four replicates of each incubation condition were filtered separately through a 0.22 µm polyether sulfone membrane filter (Millipore Sterivex) with a peristaltic pump. Filters were stored at −80°C for DNA extraction. Filtration effluent from one bottle was used for nutrients and dissolved organic carbon (DOC); i.e., 50 mL aliquots were collected into 60 mL high-density polyethylene containers and stored at −20°C until analysis of nitrate, phosphate, silicate, and DOC concentration. The remaining three bottles were used for DOM characterisation; for solid-phase extraction (SPE) of DOM, 3 × 1 L of the filtrate was acidified to pH 2 with HCl (37% v/v, Merck) and extracted with preconditioned (6 mL methanol +12 mL pH 2 water) 500 mg PPL cartridges (BondElut, Agilent Technologies) (Dittmar et al., 2008). Following the sample extraction, the cartridges were dried under an air vacuum for about 30 min, and concentrated SPE-DOM samples were eluted into pre-combusted, amber glass vials with 2 mL methanol and stored at −20°C until FT-ICR MS analysis.

2.3 Biochemical analyses

Methane samples were analysed within a week after the cruise using a gas chromatography (GC) system in our home laboratory (Thermo Scientific, GC Trace 1,310, FID detector, MSieve 5A column), as explained previously (Sert et al., 2020).

Dissolved oxygen was measured directly in the incubation media with a needle-type oxygen probe (Unisense fx-6 UniAmp, OPTO-50) at the beginning and the end of the incubations. For this, we pierced through the rubber septa of the bottle caps.

MOx rates were determined by *ex-situ* incubations with trace amounts of ^{3}H-labelled CH_4, as described previously (Niemann et al., 2015; Steinle et al., 2015). Briefly, each sample was amended with 5 µL of ^{3}H-CH_4/N_2 (18.5 kBq, American Radiolabelled Chemicals, United States of America) and incubated for 48 h in the dark at *in situ* temperatures. Activities of residual C^3H_4 and the MOx product ^3H_2O were measured by liquid scintillation counting. First-order rate constants (k_{MOx}) were determined from fractional tracer turnover:

$$k_{MOx} = ({}^3H_2O)/({}^3H_2O + C^3H_4) \times t^{-1}$$

where t is the incubation time in days. k_{MOx} was corrected for tracer turnover in killed controls (k_{KC} <0.003 days $^{-1}$; fixed with 50 µL $HgCl_2$) and multiplied with methane concentrations [CH_4], yielding MOx:

$$MOx = (k_{MOx} - k_{KC}) \times [CH_4]$$

Nitrate, silicate, and phosphate concentrations were measured colourimetrically with a segmented flow nutrient analyser (ALPKEM Flow Solution IV, OI Analytical) with detection limits of 0.5 µM for nitrate, 0.06 µM for phosphate and 0.4 µM for silicate (Grasshoff et al., 1999). The precisions for the measurements were 0.1 µM for nitrate and silicate and 0.01 µM for phosphate (Sert et al., 2022). Dissolved organic carbon (DOC) and total dissolved nitrogen (TDN) concentrations were measured by a high-temperature combustion method (MQ Scientific MQ-1001) against in-house calibration standards and reference deep ocean samples (Qian and Mopper, 1996).

2.4 Fourier transform ion cyclotron resonance mass spectrometry analysis

All FT-ICR MS measurements were carried out with a 12-T Bruker SolariX FT-ICR mass spectrometer (Bruker Daltonics, Bremen, Germany) equipped with a dynamically harmonised ICR cell (ParaCell) and an Apollo-II electrospray ionisation (ESI) source. DOM samples, diluted 1:10 (v/v) with HPLC-grade methanol, were directly infused into the ion source with a syringe pump, operating at a flow rate of 2 µL min^{-1}. Nitrogen was used as the drying and nebulising gas. The ESI-generated ions were accumulated in the hexapole ion trap and transferred into the ICR cell for trapping, excitation, and detection. For each spectrum, 100 scans were co-added over a mass/charge ratio (m/z) range of 150–2000. Bruker Compass ftmsControl 2.1 software was used for instrument control and data acquisition. The initial spectral post-processing was done

with the Bruker DataAnalysis 5.0 SR1 software package, including an internal mass re-calibration with an in-house calibration list for DOM samples. Molecular formula assignments were done with the PetroOrg IS-18.0.3 software (Omics LLC, Tallahassee, FL, United States of America) for the peaks observed at a signal-to-noise ratio (S/N) ≥ 5. Monoisotopic compositions were limited to $^{12}C_{1-100}{}^{1}H_{1-200}{}^{14}N_{0-4}{}^{16}O_{0-30}{}^{32}S_{0-2}$, with a double bond equivalent (DBE) of 0–50, homologous series inclusion (minimum of 3) and a mass error of ≤1.0 ppm. However, much lower mass errors (ca <0.2 ppm) have been achieved by visual inspection of the spectra for average mass error and by removing formulas with systematically high errors. Sodium (Na) and chlorine adducts (Cl) were also considered for positive and negative ion modes.

2.5 DOM formula assignments

Molecular formulas were assigned for 18 samples (3 replicates of 6 treatments) in negative-ion ESI following the subtraction of formulas compiled from four method blanks. The replicate with the highest ionisation efficiency from each treatment (based on maximum signal intensity and the number of detected peaks) was also analysed with positive-ion ESI. Analysis performance varied considerably between replicates; we, therefore, chose the least conservative approach, and all unique formulas were considered from the replicate samples (see Supplementary Section S1 and Supplementary Table S1 for details). Then, the obtained molecular formula lists from one positive and three negative mode replicates were pooled and merged to obtain a single molecular formula list for each treatment. The intensity of negative ion replicate (with the highest number of formulas) was considered in the case of duplicate formulas from the merging lists.

Chemical characterisation of DOM compositions was conducted to obtain four different heteroatomic classes: CHO, CHON, CHOS and CHONS. Additionally, DOM compositions were classified by H:C and O:C atomic ratios using van Krevelen diagrams (Kim et al., 2003). Considering the H:C and O:C atomic ratios of major biochemical compounds, ranges of H:C and O:C were related to four distinct compound classes: 1) lipid & protein-like (LPD: H:C ≥1.5 & O:C ≤0.7), 2) carbohydrates and amino-sugar-like (CAR: H:C ≥1.5 & O:C >0.7), 3) unsaturated hydrocarbons & condensed aromatics (UHC: H:C ≤0.7 & O:C ≤0.7) and 4) lignin and tannin-like (LGN: 0.7< H:C <1.5 and H:C >0.7 & O:C >0.7). Boundaries for these classes were modified from Hockaday et al. (2009) and Hodgkins et al. (2016), as explained previously (Sert et al., 2020).

2.6 Ordination analysis of DOM data

Principal coordinate analysis (PCoA) was applied to the combined molecular formula lists to depict compositional variation between incubation samples on an ordination plot in R (R Core Team, 2022). Briefly, a dissimilarity (distance) matrix was constructed based on Bray-Curtis indices (Bray and Curtis, 1957) using the 'vegdist' function and sum-normalised relative intensities of pooled DOM data. Then, the PCoA was conducted on the dissimilarity matrix using the 'cmdscale' function in Vegan (Oksanen et al., 2020). Ordination plots were constructed based on the first two principal axes, which explain the highest variations between samples. The explained variances for these two main coordination axes were calculated by determining the percentages of the first two eigenvalues relative to the sum of all eigenvalues.

2.7 Amplicon sequencing

Genomic DNA was extracted from the 0.22 µm filters using the DNeasy PowerWater Kit (Qiagen, Carlsbad, CA). DNA concentration was checked with Qubit 4 Fluorometer dsDNA HS assay (ThermoFisher Scientific), and quality checks were performed using the DNA 12000 assay with the Agilent Bioanalyzer (Agilent Technologies, Germany). PCR amplification and amplicon sequencing was performed at Novogene Company Limited (Cambridge, United Kingdom) using the V4 forward primer (515F) and reverse primer (806R) which targets a hypervariable region that amplifies both bacterial and archaeal 16S rRNA (Caporaso et al., 2010). In order to identify background sequences, PCR template-free negative controls were also amplified and sequenced.

2.8 Amplicon sequence analysis

Amplicon sequences were analysed in accordance with the Earth Microbiome Project (EMP) protocols (Gilbert et al., 2010) with minor modifications in quality checks. Briefly, the forward and reverse Illumina reads were joined using QIIME2 paired end flags. The reads were further denoised using DADA2 v2021.2.0 package, which pooled, filtered, de-replicated, and chimera-checked sequences (Callahan et al., 2016). After denoising, DADA2 further processes data by determining the amplicon sequence variants (ASVs). The ASVs were classified using the SILVA database v138.1 (Quast et al., 2013; Yilmaz et al., 2014).

2.9 Microbial community analysis

Downstream analysis was completed in R (R Core Team, 2022), using primarily the 'microeco' (Liu et al., 2021) and 'vegan' packages (Oksanen et al., 2020). The 16S data reads assigned Mitochondria and Chloroplast (at any taxonomic level) were removed. Alpha diversity was quantified using counts of observed unique ASVs (species richness). The target taxa for methane-associated bacteria were selected from Knief (2015), and relative abundances were averaged from four replicates for incubation conditions.

3 Results

3.1 Hydrography at the study site

The primary current system of the study site is the Svalbard branch of the West Spitsbergen current, which carries warmer Atlantic waters to the Arctic Ocean (Menze et al., 2020). Incoming Atlantic waters mix with the local surface water, forming Polar surface waters down to ~100 m depth. CTD

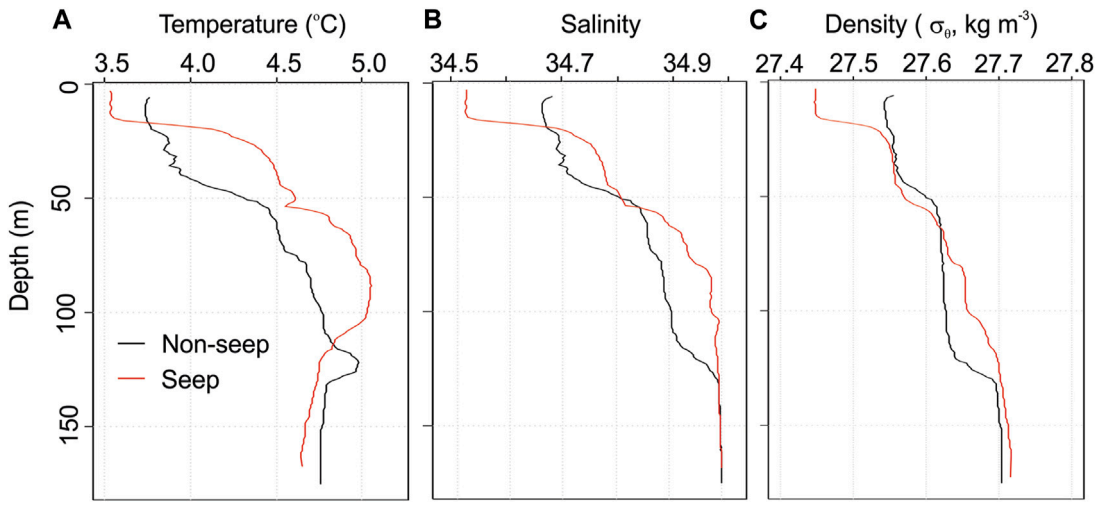

FIGURE 3
Depth profiles of **(A)** temperature, **(B)** salinity, and **(C)** density at both stations.

profiles at both stations revealed these two water masses as indicated by a temperature increase from ~3.5°C at the surface to 5°C at ~100 m water depth, followed by a relatively uniform temperature of ~4.7°C down below (Figure 3A). Similarly, salinity was low at the surface (34.5 psu at seep and 34.7 psu at non-seep) and reached 35 psu at ~100 m from whereon it remained constant until the bottom (Figure 3B). Compatible with the temperature and salinity, the vertical density profile of the stations implies several stratification layers separated by isoclines at 25 and 50 m in seep station and 50 and 125 m in the non-seep station (Figure 3C). Below 125 m, both stations indicate a uniform temperature, salinity, and density until the bottom including the layers that the incubation waters were taken.

3.2 Biochemical parameters

The dissolved methane concentrations were 5.8 nM for NS_i and 83.1 nM for SE_i, decreasing to final concentrations of 4.5 nM in NS_f and 35.0 nM in SE_f (Table 1). The amount of added methane corresponded to 1,026 nM in the water phase in methane-amended incubations with 1,000 mL of water and 135 mL of headspace. Therefore, the initial methane concentrations in NS_a and SE_a were calculated as 1032.5 and 1109.9 nM, respectively. After the incubation, the final methane concentrations were measured as 737.9 nM in NS_a and 846.2 nM in SE_a.

The reaction rate constants for MOx (k_{MOx}) varied in a narrow range from 0.019 to 0.027 $days^{-1}$ in all incubation setups without showing a clear pattern (Figure 4A). With respect to the higher methane concentrations in the seep stations and the amended incubations, MOx activities were markedly higher in these incubations, too (Figure 4B). Overall, MOx was low in NS_i and NS_f samples (0.09–0.16 nM day^{-1}), slightly elevated by ~20% in SE_i (0.97 nM day^{-1}) *versus* SE_f (1.15 nM day^{-1}) samples. MOx activities were high (up to 12 nm day^{-1}) in methane-amended samples, irrespective of whether the sample originated from a seep or non-seep station.

Dissolved oxygen concentrations decreased in all incubation bottles from 0.25 mM initial concentration to 0.19 mM final concentration (Figure 4C). Concentrations of nitrate and phosphate remained nearly constant during the incubations with average concentrations of 12.2 and 0.8 μM, respectively (Figure 4D,E). Despite a slight increase in seep incubation, silicate concentrations only varied from 5.1 to 5.8 μM in all incubation bottles (Figure 4F). DOC concentrations increased in all incubations from 55.3 μM to 56.8 and 57.9 μM in non-seep and from 47.5 μM to 55.6, and 56.8 μM seep conditions (Figure 4G). TDN concentrations were 13.6 μM in NS_i and increased to 16.3 and 16.8 μM in NS_f and NS_a, respectively. On the contrary, TDN decreased from a maximum concentration in SE_i with 18.0 μM to 16.0 and 16.8 μM in SE_f and SE_a, respectively (Figure 4H).

3.3 DOM molecular compositions

DOM comprised 3,671 and 5,137 unique molecular formulas in NS_i and SE_i, respectively (Figure 5A). The numbers of formulas were lower in both unamended final conditions compared to the initial values (2,837 in NS_f and 4,014 in SE_f). In methane-amended incubations, in stark contrast, the number of formulas increased to 5,105 and 5,551 for NS_a and SE_a (Figure 5A). Similar trends were observed in the numbers of formulas in biochemical class categories (CAR, LGN, LPD, see Section 2.5 for acronym description) and atomic content categories (CHO, CHON, CHOS), except for UHC and CHONS. For UHC, the number of formulas was higher in NS_f compared to NS_i and NS_a and in SE_i compared to SE_a. CHONS formulas were only detected in NS_a with 37 assigned peaks. Percentages of subcategories differed slightly without any particular trend between treatments (Figure 5B).

The average molecular weights (*m/z*) and average peak intensities displayed a similar trend with the number of molecular formulas (Figure 5C,D). The average MW decreased from 458 in NS_i and 464 in SE_i to 439 in NS_f and 451 in SE_f. In

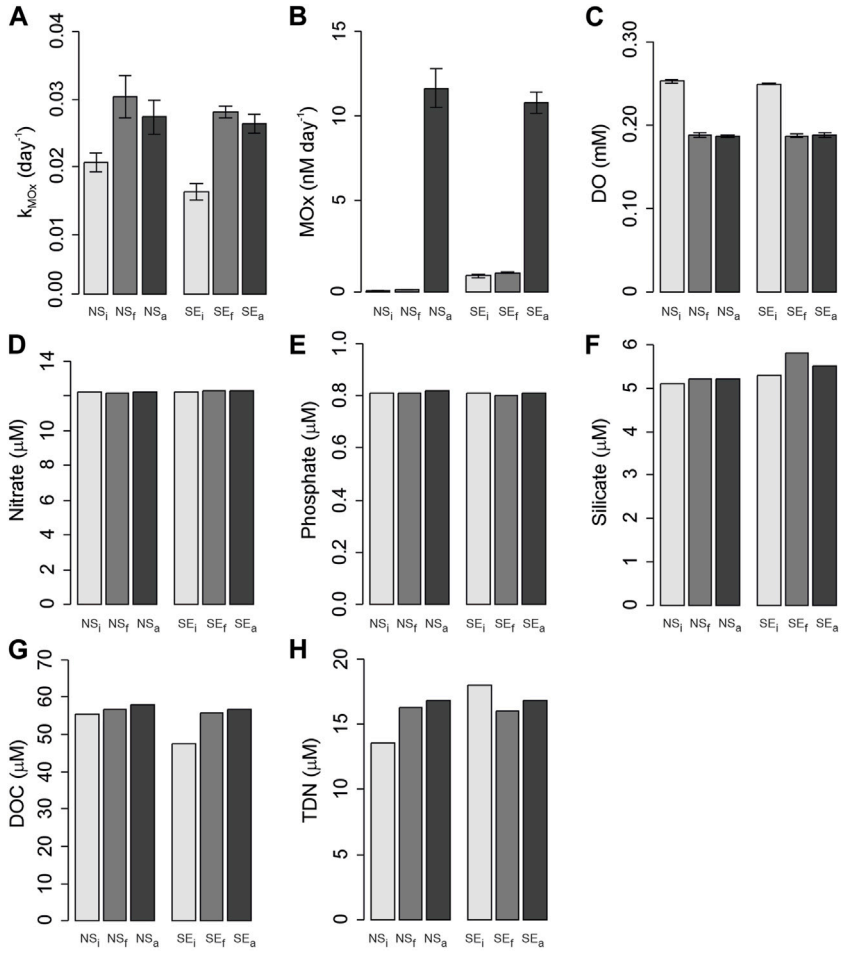

FIGURE 4
Changes in biochemical parameters before and after incubations from non-seep (NS) and seep stations (SE) for initial ($_i$), final ($_f$), and methane-amended final ($_a$) conditions. **(A)** k_{MOx}, first order rate constant; **(B)** MOx, methane oxidation rate; **(C)** DO, dissolved oxygen; **(D)** Nitrate; **(E)** Phosphate; **(F)** Silicate; **(G)** DOC, dissolved organic carbon; **(H)** TDN, total dissolved nitrogen.

NS_a and SE_a, the average MW were 486 and 470, respectively (Figure 5C). Similarly, average intensities in NS_i and SE_i were higher compared to NS_f and SE_f. However, it decreased slightly at SE_a compared to SE_i as opposed to NS_i *versus* NS_a (Figure 5D). Numbers of formulas obtained from the three ESI- and one ESI+ replicates varied noticeably (Figure 5E, Supplementary Table S1) yet without a significant statistical difference in the mean number of formulas between the incubation conditions (ANOVA, p=0.7).

The molecular compositions of SPE-DOM were similarly distributed on van Krevelen diagrams in all incubation conditions (Figure 6). The majority of mass peaks were identified in the central region of the van Krevelen diagrams from H:C atomic ratios of 1–2 and O:C atomic ratios of 0.25–0.50. Relative abundances (sum-normalised) were larger in the LPD region, with mainly CHO molecular series in NS_i, NS_f, NS_a and SE_i. However, the highest relative abundances were obtained in NS_i with N-containing formulas in the LPD region (Figure 6A). With increasing molecular diversity (i.e., number of formulas), relative abundances were lower for NS_a and SE_a in the LPD region compared to the initial conditions. Relative abundances of CHON and CHOS formulas were higher in SE_a compared to SE_i in the lower half of the van Krevelen diagram.

Compositional changes in DOM were evident in both non-seep and seep incubations, as depicted in PCoA (Figure 7). The composition shifts from NS_i to NS_a were evident in the first principal coordination axis (35.3% of the variation). On the other hand, compositional changes from NS_i to NS_f and SE_i to SE_f or SE_a were more pronounced on the second (vertical) coordination axis, explaining 22.1% of the variation. Overall, the compositional change from NS_i to NS_a was the strongest, with NSa becoming more similar to the SE_i and SE_a composition (Figure 7).

The 2055 formulas were common in all incubation conditions. In order to determine molecular trends between these common formulas, changes in the intensities were calculated and interpreted as presumably decreasing or increasing during the incubation, or initial seep and non-seep conditions (Figure 8). Accordingly, the number of compounds with increasing intensity were distinctly high in NS_i - SE_i (1,652) and NS_a -NSi (1,576). Proportionally, compounds with decreasing intensities were notably lower NS_i -SE_i (403) and NS_a – NS_i (639) compared to NS_i - NS_f (1,416), SE_i - SE_f (1,383) and SE_i - SE_a (1,358).

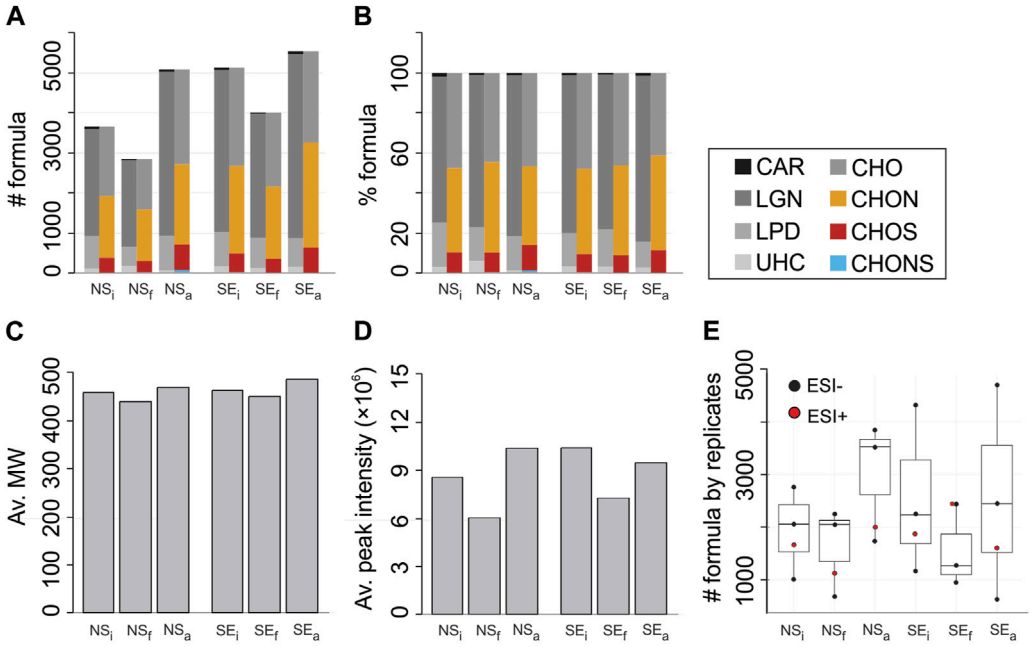

FIGURE 5
(A) Number of molecular formulas, **(B)** percentages of formulas, **(C)** average molecular weights, **(D)** average peak intensities and **(E)** number of molecular formulas by replicates obtained from non-seep (NS) and seep stations (SE) for either initial ($_i$), final ($_f$) or methane-amended final ($_a$) conditions. Number of formulas in biochemical compound groups defined by H:C and O:C ratios and heteroatomic contents are given in colors. Abbreviations are LPD, lipid- and protein-like; CAR, carbohydrate-like; LGN, lignin- andtannin-like; UHC, unsaturated hydrocarbon- & condensed aromatic-like; Av., average.

3.4 Microbial community

Sequences classified within the Bacterial kingdom were more abundant than Archaeal sequences across all samples regardless of location or incubation conditions (Figure 9A). As the most abundant Phylum, Proteobacteria accounted for 34.2%–82.0% of the total community in each sample, with NS_a featuring the lowest relative abundance and NS_i the highest one.

The sequences were further classified and filtered to reveal five different genus-level organisms: *Methylocella* (1 ASV), OM43 clade (10 ASVs), *Methyloprofundus* (1 ASV), Milano WF1B-03 (1 ASV) and *Methylophagaceae* (2 ASVs), i.e., methanotrophic bacteria that were previously found in Arctic cold seeps (Gründger et al., 2021). Total relative abundances of these sequences accounted for 2.0% and 1.5% in NS_i and SE_i and decreased slightly in all four cases up to 1.1% in SE_a (Figure 9B). The most apparent decreases in relative abundance were found in clades *Methylocella* and *Methylophagaceae*. However, in all methane-replate conditions (NS_a, SE_f and SE_a), two MOB clades, Milano-WF 1B-03 and *Methyloprofundus*, increased relative abundance compared to NS_i and SEi, respectively.

The alpha diversity (Figure 9C) increased in both methane-amended and unamended samples compared to the initial samples from both locations (seep and non-seep). The highest difference in alpha diversity was between non-seep amended (NS_a) conditions compared to the initial one (NS_i).

4 Discussion

4.1 Evaluation of incubation parameters and dominant microbial processes

All incubations were performed under dark and oxic conditions (Figure 4C). Decreasing oxygen and elevated MOx rates indicate microbial respiration, and MOx would be the dominant process during incubations. MOx of a few nM d^{-1} (Figure 4B) can only explain <0.1% of the total oxygen decrease (~0.06 mM), considering the 1:1 stoichiometry of CH_4 to O_2. Accordingly, 16S rRNA gene analyses indicated that non-methanotrophic, bacteria were very abundant (<98%) and the heterotrophs amongst them were the primary consumer of dissolved oxygen during the incubation. This was in line with previous observations at Arctic cold seeps, where the abundance of MOB accounts for only a small portion of the microbial community, even with high MOx and methane concentrations (Steinle et al., 2015; Gründger et al., 2021).

MOx was low at the non-seep station and in incubations without methane amendment, as expected. However, a similar range of k_{MOx} implies the existence of an active MOB community in all samples. Based on 16S data, the most dominant member of the methane-associated bacterial community was the OM43 clade of the family *Methylophilaceae*, irrespective of sample and with low variation in abundance. These organisms are affiliated to Type I methylotrophs, which do not oxidise methane directly but use C1 compounds (Chistoserdova et al.,

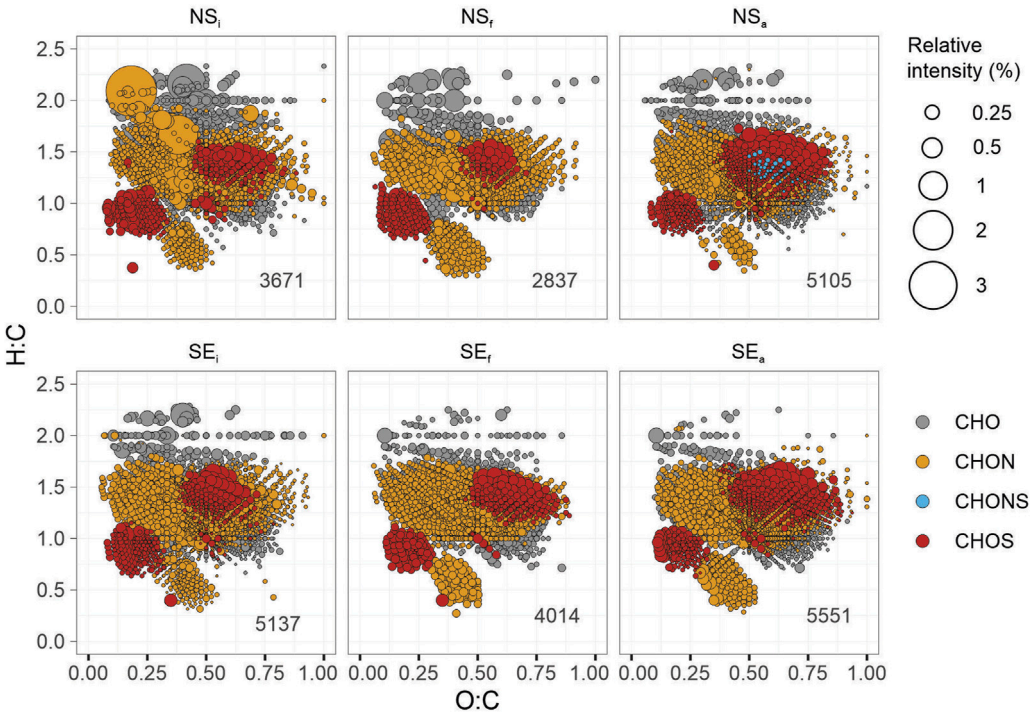

FIGURE 6
Molecular compositions of pooled DOM formulas on the van Krevelen diagrams for non-seep (NS) and seep (SE) incubations representing initial ($_i$), final ($_f$), or methane-amended final ($_a$) conditions. Each symbol represents a molecular formula colored according to the heteroatomic composition: CHO (grey), CHON (yellow), CHONS (blue), and CHOS (red). Symbol sizes represent the sum-normalised relative intensity of the formulas from pooled DOM molecular lists (e.g., the sum of all relative intensities corresponds to 100% for each treatment). The total number of formulas is given on the lower right for each plot.

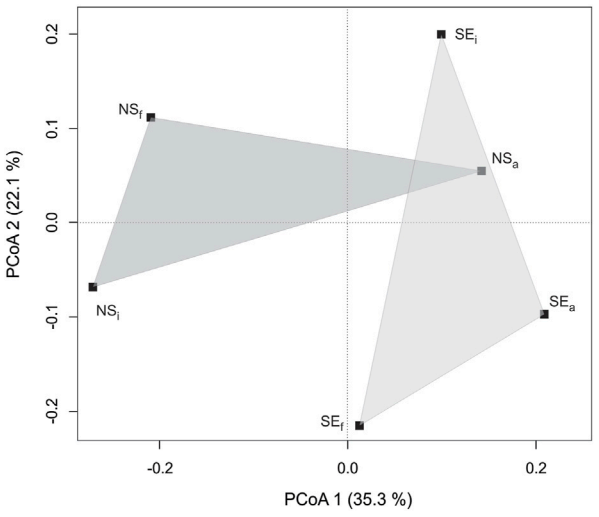

FIGURE 7
Graphical representation of principal coordinate analysis based on Bray-Curtis indices of DOM molecular compositions from non-seep (NS) and seep stations (SE) for either initial ($_i$), final ($_f$), or methane-amended final ($_a$) conditions. Shaded triangles are used to illustrate non-seep and seep incubations.

2009) and are commonly associated with coastal diatom bloom (Morris et al., 2006). Therefore, its constant abundance in all samples may be associated with typical spring-to-summer Arctic diatom successions (Tremblay et al., 2006; Croteau et al., 2022). Milano-WF1B-03 and *Methyloprofundus* are two known MOB species that increased in abundance in methane-replete conditions, and *Methylocella* and *Methylophagacea* decreased in all conditions (Figure 9B). However, the overall change of MOB species was considerably low, and they occurred at abundances in sub-percent range. Taken together with microbial data, we observed that a small but active MOB community was present in all samples, irrespective of the origin of the source water masses. Due to low variance in abundances, however, we suggest that MOx was not a dominant microbial process, yet it might have initiated a microbial growth.

Our measurements are the first MOx data available from the Norskebanken seep site and were in the same order of magnitude as those reported from the western and southern sections of the Svalbard continental shelve (Steinle et al., 2015; Mau et al., 2017; Gründger et al., 2021) and in other coastal margins with seep activity (Mau et al., 2012; Steinle et al., 2017) (see Supplementary Table S2). Since the variations in k_{MOx} were relatively small compared to methane concentrations, MOx rates were higher in samples containing high amounts of methane, either naturally

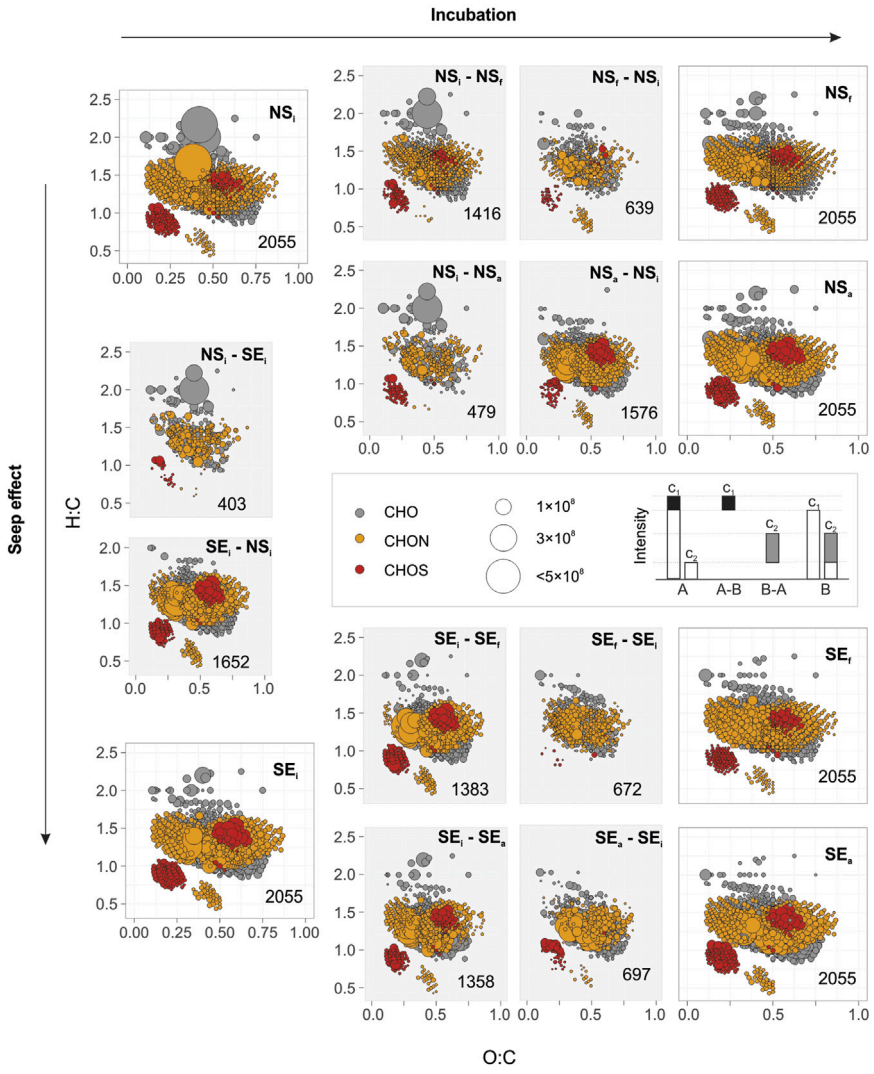

FIGURE 8
Molecular compositions of common DOM formulas on the van Krevelen diagrams for non-seep (NS) and seep (SE) incubations representing initial ($_i$), final ($_f$), or methane-amended final ($_a$) conditions. Each symbol represents a molecular formula coloured according to heteroatomic composition: CHO (grey), CHON (yellow), and CHOS (red). Plots on the corners indicate 2055 DOM formulas commonly found in all six conditions whose intensities are denoted by the size of the symbols. Pale grey background plots indicate compounds with changing intensities towards the direction of the arrows so that their intensities either decreased or increased during the incubation E.g., NS$_i$ - NS$_f$ indicates compounds that declined during non-seep unamended incubation, whereas NS$_f$- NS$_i$ shows compounds with elevated intensities (see figure caption). Differences in molecular compositions between NS$_i$ and SE$_i$ are also plotted over the vertical axis on the left (seep effect). The numbers of formulas in each plot are given in the lower right.

(SE$_i$ and SE$_f$) or amended (NS$_a$ and SE$_a$). The efficiency of MOx and turnover of methane increase with increasing methane concentration in various marine settings (James et al., 2016). In nature, this relationship is strongly influenced by hydrography and MOB community size, as previously observed at the southern and western shelves off the Svalbard archipelago (Mau et al., 2012; Steinle et al., 2015; Gründger et al., 2021). There, the prevalent current systems were found to transport open ocean waters with a low-standing stock of MOBs to the seep systems at times when the water column MOx was low (Steinle et al., 2015). Elevated MOx, in contrast, was found when shelf waters with a methane history and higher standing stock of MOBs were present at the seep location (Mau et al., 2012; Steinle et al., 2015; Gründger et al., 2021). The origin of potential MOBs at Norskebanken needs to be tested in future studies; it seems nevertheless possible that MOBs were transported from the western shelf towards the reference and then Norskebanken station along with a branch of the West Spitsbergen current that flows North of Svalbard eastwards.

DOC and nutrients concentrations were in line with the previous observations in the study area (e.g., Owrid et al., 2000; Renner et al., 2020; Zabłocka et al., 2020). Dissolved inorganic nutrients (phosphate, nitrate, and silicate) concentrations did not change considerably during incubations. On the other hand, there was a marked increase in DOC concentrations in all incubations and TDN concentration in non-seep incubations. Taking these together with the absence of phototrophic primary

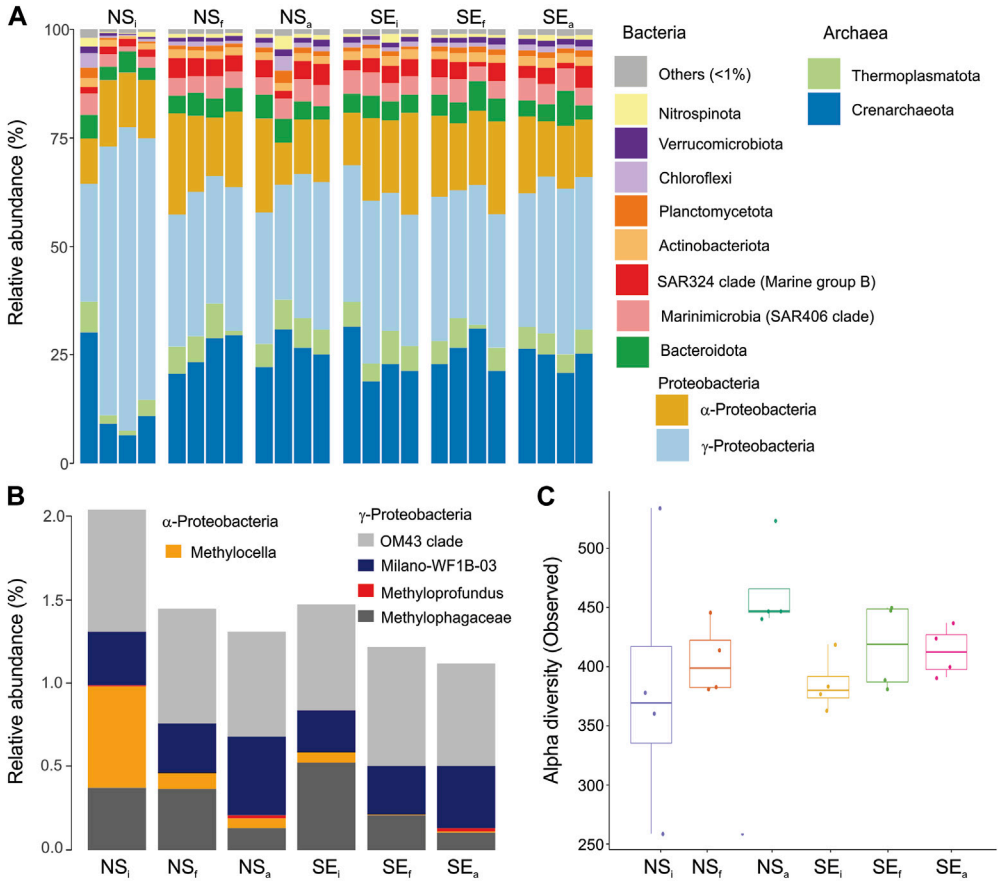

FIGURE 9
Prokaryotic community composition based on 16S rRNA gene sequences. **(A)** Relative abundance at Phylum level for six conditions with four replicates. All taxa that were below 1% relative abundance were grouped as Other. **(B)** Relative abundances of 16S rRNA sequences grouped in genus level from six conditions associated with methane oxidation. **(C)** Boxplots of alpha diversity based on the number of ASVs observed in each treatment that are grouped for 6 conditions.

production due to dark conditions and declining dissolved oxygen concentration, we conclude that respiration was the dominant microbial process during the incubation. We suggest that DOC concentrations increased by recycling planktonic biomass via respiration. Cell deaths, viral lysis, bacterial exudates, or sloppy feeding of zooplankton and protists can all contribute to the DOC budget (Van den Meersche et al., 2011; Fouilland et al., 2014). DOC released by the cell lysis differ in biolability and include intact cellular components, metabolic products and viruses (Wilhelm and Suttle, 1999) that do not retain on the filter. DOC components stoichiometrically include organic nitrogen and phosphorus atoms that are also being part of the organic nitrogen (DON) and phosphorus (DOP) pools. Although some of the organic matter would have been rapidly incorporated by heterotrophic bacteria based on their cellular needs, the rest elevate the DOC, DON, DOP concentrations without contributing to the inorganic nutrient concentrations in the short term. Therefore, while the concentrations of DOC and TDN increased, inorganic nutrient concentrations did not change during our incubations.

4.2 Bacterial reworking affecting DOM molecular compositions

Apparent modifications in DOM compositions occurred in all incubations. DOM molecular diversity and atomic heterogeneity (N and S content) increased in methane-amended incubations in both seep and non-seep treatments (Figures 5, 6). Yet, these values decreased in unamended incubations (greater extent in non-seep treatment), revealing that the availability of methane and the related activity of MOB would be the main factor for the changes in DOM molecular compositions. While the microbial role in DOM modifications was consistent with increased microbial diversity, the total relative abundance of MOB decreased in all treatments. Nevertheless, it has to be noted that we did not determine absolute cell numbers of MOBs. We can thus not fully determine if the other microbial clades became more abundant, which might have led to a decrease in the relative abundance of MOBs even if MOB biomass was constant (or even increased). Furthermore, the abundance of two MOB clades (Milano-WF 1B03 and *Methyloprofundus*; (Knief, 2015); increased in methane-replete incubations (NS_a, SE_f and SE_a), indicating a positive association

with elevated methane levels. Besides, our PCoA analysis indicated that DOM converges towards similar compositions in methane-rich samples (Figure 7). These observations imply an interaction between microbial composition and molecular DOM turnover. Modifications on DOM compositions were likely accomplished by microbes that were initially fuelled by methane, and their exudates and necromass were then reworked by other microbial consortia that are in competition or syntropy with MOBs (e.g., Vekeman et al., 2016).

Similar opposite trends were observed in the average molecular weights (Figure 5C) for amended and unamended incubations. Decreasing molecular weights (unamended incubations) were consistent with the bacterial reworking on DOM based on the size-reactivity continuum model stating that the degradation of DOM occurs from larger reactive molecules to smaller unreactive moieties (Benner and Amon, 2015). Based on molecular lability on the other hand, it is likely that low molecular weight DOM compounds (e.g., glucose and amino acids) are quickly assimilated by many groups of bacteria, as opposed to high molecular weight DOM (Elifantz et al., 2005; Alonso-Sáez et al., 2009). In our data, the number of compounds associated with LPD and CAR classes and corresponding percentages decreased in NS_f and yet increased in NS_a. Compounds in LPD and CAR molecular classes are usually interpreted as labile DOM having atomic H:C ratios larger than 1.5 (D'Andrilli et al., 2015) and are likely to indicate more recent production with lower molecular masses (Flerus et al., 2012). Therefore, we suggest that changes in molecular DOM compositions occur in connection with a higher degree of DOM production in methane-amended incubations, whereas microbial DOM assimilation was favoured in unamended incubations.

In addition to active molecular synthesis and extracellular release, cell lysis, viral infections, and sloppy feeding are also the main production routes of DOM. Therefore, if microbial network favour DOM production, this may also in connection with the pressure from upper trophic organisms or viral lysis. When methane is available, MOBs have an advantage (energy metabolism and growth) over other organisms with a limited substrate supply. MOB growth initiates microbial competition, possibly because MOBs consume micronutrients (e.g., Fe, Cu) so that other organisms are impaired or starve and die. Dead cells may then get lysed and contribute to DOM production. Alternatively, methane intrusion may cause stress in the initial microbial system altogether and elevate viral density and DOM production through viral shunt (Wilhelm and Suttle, 1999; Middelboe and Lyck, 2002; Vincent and Vardi, 2023). As opposed to an increase in microbial diversity, quantitative PCR data indicated a marked decrease in the 16S copy gene numbers in all incubation conditions compared to initial values (Supplementary Figure S1). This indicates that some portions of the DOM modifications are closely related to declining microbial activity rather than active microbial production, and the versatility of the DOM constituents increased with the variety of bacteria that have a role in DOM production.

The composition of bacteria-derived DOM is relatively unknown since they are considered to be a consumer rather than a producer of DOM (Kujawinski, 2011). Also, their ecological role in the microbial loop is defined as a facilitator for transforming DOM to particulate organic matter or from DOM to inorganic constituents (Carlson and Hansell, 2015). However, investigations on bacteria-derived DOM across various monoculture, multiculture and environmental consortia imply that bacteria may release unique characteristics of metabolites in relation to the location of isolation and grazing factors (Kujawinski et al., 2004; Rosselló-Mora et al., 2008; Kujawinski et al., 2016). For instance, recent studies showed that virus-induced DOM release is complex but features a unique metabolic footprint representative of viral infection (Zhao et al., 2019; Kuhlisch et al., 2021). Halogenation with chlorine and iodine was found to be a hallmark of virus-induced DOM of a very common coccolithophore *Emiliana huxleyi* (Kuhlisch et al., 2021). Our method was not optimised for detecting halogenated exometabolites, yet we confirmed that the percentage of the chlorine adducts was more than 10% in all samples. Therefore, if the abundance of chlorine adducts is a proxy for these metabolites, viral lysis could have contributed to DOM production during our incubations. Consequently, we suggest that similar DOM compositions in methane-replete samples are likely to indicate a similar microbial progression.

Another indication of microbial modification of DOM was observed in compositional characteristics. Such as the majority of DOM formulas, both in pooled and common DOM data (73%–83%), had a range of H:C ratio from 1.0 to 1.5 and O:C ratio from 0.10 to 0.75 and corresponded to the central region of van Krevelen diagram. Compounds in this range are rather unsaturated, with high abundances of oxygen atoms attached to the carbon backbone and associated with several molecular classes like lignins, tannins, (Kim et al., 2003; Rivas-Ubach et al., 2018; D'Andrilli et al., 2019), carboxylic-rich alicyclic molecules (Hertkorn et al., 2006) and to a lesser degree proteins and carbohydrates (Hockaday et al., 2009). These compounds are usually associated to a terrestrial origin (Bianchi, 2011). The ones that are stable enough to escape complete mineralisation are modified through time by diagenetic processes (Valle et al., 2018), photochemical reactions (Gonsior et al., 2009) and microbial modifications (Jiao et al., 2010). Therefore, changing compositions in these ranges are more likely linked to old DOM rather than recent production and more likely commenced by microbial mechanisms as by-products rather than fresh input of algal synthesis.

4.3 Extensive DOM production in cold seeps

We hypothesise that the varying methane concentrations in our incubation media represent a typical cold seep environment and its surroundings in the Arctic Ocean's continental shelf. Our seep incubations (unamended/amended) simulated the water column above typical hydrate-controlled arctic seeps at the Svalbard shelf (Berndt et al., 2014; Ferré et al., 2020a). Non-seep amended incubation, on the other hand, was designed to mimic the water column further away from cold seeps but which receive sporadic methane intrusions due to geospatial variation and dynamic hydrography (Steinle et al., 2015; Dølven et al., 2022). The observed molecular and microbial trends in these treatments suggest that methane intrusion from cold seeps may affect microbial communities and consequently alter DOM towards chemically more diverse compositions (also see Sert et al., 2020). This effect was also unambiguous in common DOM formulas (Figure 8). Analysis of these formulas on the van Krevelen diagrams showed that spectral features of changing intensities of non-seep amended incubation (NS_i - NS_a and NS_a - NS_i) were more similar to the initial composition at both sites (NS_i - SE_i and SE_i - NS_i) than to non-seep unamended incubation (NS_i - NS_a and NS_a - NS_i). Likewise, compounds with changing intensities in non-seep unamended incubation (NS_i - NS_f and NS_f - NS_i) were

compositionally more similar to amended non-seep incubation (NS_i - NS_a and NS_a - NS_i) than to seep amended and unamended incubations. The number of compounds within these categories also points towards a similar trend. For instance, the number of compounds with decreasing intensity during non-seep amended incubation (NS_i - NS_a; n = 479) was almost equal to the number of compounds that have higher intensity in NS_i compared to SE_i (NS_i - SE_i; n=403).

Such trends in shared formulas match with the trends obtained in pooled-DOM data in terms of seep *versus* non-seep comparisons. First, the numbers of formulas in subcategories agree with the idea of methane limitation. Such as, the number of formulas with increasing intensity was markedly higher from methane-poor initials to methane-replete endpoints. In contrast, other treatments had higher numbers of formulas with decreasing intensities and were likely to favour DOM consumption. This indicates that DOM production was elevated when excess methane was introduced in a methane-limited environment, and in contrast, DOM was not similarly affected by new methane inclusion in already methane-replete conditions. Secondly, the compounds with increasing intensity from non-seep unamended incubation (NS_a – NS_i) were already high in seep samples (SE_i) compared to non-seep samples (NS_i). In other words, compounds with increasing intensities in NS_i escalated considerably up to the level of SE_i when methane was excessively available, as is the case in NS_a (seep effect). This indicates that a greater extent of DOM production occurs in the seep areas compared to non-seep conditions (e.g., Sert et al., 2020).

5 Conclusion

Our main conclusion is that the changing microbial composition, activity, and grazing pressure modify DOM molecular formula compositions in seep environments. While observed trends did not entirely warrant whether active MOB cause a shift in the DOM features and/or produce specific compounds, it seems very likely that the DOM features detected in methane-replate incubations are associated with MOBs and other microbes affected by the activity of MOBs. That includes potential scavengers feeding on exudates/(necro)mass of MOB, microbes that are in competition or syntropy with MOBs and viruses that induce various biomass into DOM through viral shunt. We showed that elevated methane concentrations and methanotrophy influence both the production and consumption of DOM, converging to similar compositions despite different initial conditions (i.e., non-seep vs. seep). In addition, heterotrophic bacteria other than MOB contribute to the DOM modification in the incubation media, conceding with the production of DOM rather than the consumption, as indicated by the increasing number of molecular formulas in methane-amended incubations.

To our knowledge, this is the first incubation experiment investigating changes in DOM composition as a function of methanotrophy in microcosms with seep and non-seep waters. Our results also imply that the DOM composition in waters from non-seep locations converges to a DOM signature from seep location upon methane admixture to these waters. How far the change of DOM is directly determined by methanotrophs or indirectly by other microbes that profit from methanotrophy needs to be investigated in future studies. Ecological links (e.g., microbial community structure and activity vs. metabolic DOM profiles) consequently need to be better constrained in future studies, for example, by investigating MOB-DOM interactions with environmental stressors such as grazing pressure, community competition or hydrographic conditions.

Data availability statement

Biochemical data and R code for statistical analyses are stored in the UiT Open Research Data Repository (https://doi.org/10.18710/U3YMFQ). Sequencing data, along with R scripts used for analysis and graphing of microbial compositions are stored in the Open Science Framework (https://doi.org/10.17605/OSF.IO/5E36J).

Author contributions

MS: Conceptualization, Data curation, Methodology, Project administration, Visualization, Writing–original draft, Writing–review and editing. HS: Methodology, Writing–original draft, Writing–review and editing. TG: Methodology, Writing–original draft, Writing–review and editing. TK: Methodology, Writing–original draft, Writing–review and editing. JJ: Methodology, Supervision, Writing–review and editing. HB: Methodology, Supervision, Writing–review and editing. BF: Funding acquisition, Project administration, Resources, Writing–review and editing. FG: Supervision, Writing–review and editing. DK: Methodology, Supervision, Writing–review and editing. HN: Conceptualization, Methodology, Supervision, Writing–review and editing.

Funding

The author(s) declare financial support was received for the research, authorship, and/or publication of this article. This study is funded by the Research Council of Norway through CAGE (Centre for Gas Hydrate, Environment and Climate) project number 223259 and EMAN7 (Environmental impact of Methane seepage and sub-seabed characterisation at LoVe-Node 7) project number 320100. This project was supported by the European Union's Horizon 2020 Research and Innovation Programme (EU FT-ICR MS project; grant agreement 731077). The FT-ICR MS facility is also supported by Biocenter Finland, Biocenter Kuopio and the European Regional Development Fund (grant A70135). Authors HS and HB are grateful for funding from ABSORB–Arctic Carbon Storage from Biomes (https://site.uit.no/absorb/), a strategic funding initiative from UiT–The Arctic University of Norway.

Acknowledgments

We would like to acknowledge the crew of R/V Kronprins Haakon and the shipboard scientific party during cruise CAGE 20-7. We would like to thank Colin A. Stedmon for DOC and TDN measurements, Linda Fondes Lunde for nutrient analyses, Matteus Lindgren for methane measurements. We would like to acknowledge Anna Silyakova for discussions on the project design and earlier drafts of the manuscript.

Conflict of interest

The authors declare that the research was conducted in the absence of any commercial or financial relationships that could be construed as a potential conflict of interest.

Publisher's note

All claims expressed in this article are solely those of the authors and do not necessarily represent those of their affiliated organizations, or those of the publisher, the editors and the reviewers. Any product that may be evaluated in this article, or claim that may be made by its manufacturer, is not guaranteed or endorsed by the publisher.

Supplementary material

The Supplementary Material for this article can be found online at: https://www.frontiersin.org/articles/10.3389/feart.2023.1290882/full#supplementary-material

References

Alonso-Sáez, L., Unanue, M., Latatu, A., Azua, I., Ayo, B., Artolozaga, I., et al. (2009). Changes in marine prokaryotic community induced by varying types of dissolved organic matter and subsequent grazing pressure. *J. Plankton Res.* 31, 1373–1383. doi:10.1093/plankt/fbp081

Amon, R. M. W., and Benner, R. (1996). Bacterial utilization of different size classes of dissolved organic matter. *Limnol. Oceanogr.* 41, 41–51. doi:10.4319/lo.1996.41.1.0041

Andreassen, K., Hubbard, A., Winsborrow, M., Patton, H., Vadakkepuliyambatta, S., Plaza-Faverola, A., et al. (2017). Massive blow-out craters formed by hydrate-controlled methane expulsion from the Arctic seafloor. *Science* 356, 948–953. doi:10.1126/science.aal4500

Becker, J., Berube, P., Follett, C., Waterbury, J., Chisholm, S., DeLong, E., et al. (2014). Closely related phytoplankton species produce similar suites of dissolved organic matter. *Front. Microbiol.* 5, 111. doi:10.3389/fmicb.2014.00111

Benner, R., and Amon, R. M. W. (2015). The size-reactivity continuum of major bioelements in the ocean. *Annu. Rev. Mar. Sci.* 7, 185–205. doi:10.1146/annurev-marine-010213-135126

Berndt, C., Feseker, T., Treude, T., Krastel, S., Liebetrau, V., Niemann, H., et al. (2014). Temporal constraints on hydrate-controlled methane seepage off Svalbard. *Science* 343, 284–287. doi:10.1126/science.1246298

Bianchi, T. S. (2011). The role of terrestrially derived organic carbon in the coastal ocean: a changing paradigm and the priming effect. *Proc. Natl. Acad. Sci.* 108, 19473–19481. doi:10.1073/pnas.1017982108

Boetius, A., and Wenzhöfer, F. (2013). Seafloor oxygen consumption fuelled by methane from cold seeps. *Nat. Geosci.* 6, 725–734. doi:10.1038/ngeo1926

Bray, J. R., and Curtis, J. T. (1957). An ordination of the upland forest communities of southern Wisconsin. *Ecol. Monogr.* 27, 325–349. doi:10.2307/1942268

Bünz, S., Polyanov, S., Vadakkepuliyambatta, S., Consolaro, C., and Mienert, J. (2012). Active gas venting through hydrate-bearing sediments on the Vestnesa Ridge, offshore W-Svalbard. *offshore w-svalbard. Mar. Geol.* 334, 189–197. doi:10.1016/j.margeo.2012.09.012

Callahan, B. J., McMurdie, P. J., Rosen, M. J., Han, A. W., Johnson, A. J. A., and Holmes, S. P. (2016). DADA2: high-resolution sample inference from Illumina amplicon data. *Nat. Methods* 13, 581–583. doi:10.1038/nmeth.3869

Caporaso, J. G., Kuczynski, J., Stombaugh, J., Bittinger, K., Bushman, F. D., Costello, E. K., et al. (2010). QIIME allows analysis of high-throughput community sequencing data. *Nat. Methods* 7, 335–336. doi:10.1038/nmeth.f.303

Carlson, C. A., and Hansell, D. A. (2015). "Chapter 3 - DOM sources, sinks, reactivity, and budgets," in *Biogeochemistry of marine dissolved organic matter*. Second Edition (Boston: Academic Press), 65–126. doi:10.1016/B978-0-12-405940-5.00003-0

Chistoserdova, L., Kalyuzhnaya, M. G., and Lidstrom, M. E. (2009). The expanding world of methylotrophic metabolism. *Annu. Rev. Microbiol.* 63, 477–499. doi:10.1146/annurev.micro.091208.073600

Croteau, D., Lacour, T., Schiffrine, N., Morin, P.-I., Forget, M.-H., Bruyant, F., et al. (2022). Shifts in growth light optima among diatom species support their succession during the spring bloom in the Arctic. *J. Ecol.* 110, 1356–1375. doi:10.1111/1365-2745.13874

D'Andrilli, J., Cooper, W. T., Foreman, C. M., and Marshall, A. G. (2015). An ultrahigh-resolution mass spectrometry index to estimate natural organic matter lability: FTICRMS organic matter molecular lability index. *Rapid Commun. Mass Spectrom.* 29, 2385–2401. doi:10.1002/rcm.7400

D'Andrilli, J., Junker, J. R., Smith, H. J., Scholl, E. A., and Foreman, C. M. (2019). DOM composition alters ecosystem function during microbial processing of isolated sources. *Biogeochemistry* 142, 281–298. doi:10.1007/s10533-018-00534-5

Dedysh, S. N., Knief, C., and Dunfield, P. F. (2005). *Methylocella* species are facultatively methanotrophic. *J. Bacteriol.* 187, 4665–4670. doi:10.1128/JB.187.13.4665-4670.2005

Dittmar, T., Koch, B., Hertkorn, N., and Kattner, G. (2008). A simple and efficient method for the solid-phase extraction of dissolved organic matter (SPE-DOM) from seawater. *Limnol. Oceanogr. Methods* 6, 230–235. doi:10.4319/lom.2008.6.230

Dølven, K. O., Ferré, B., Silyakova, A., Jansson, P., Linke, P., and Moser, M. (2022). Autonomous methane seep site monitoring offshore western Svalbard: hourly to seasonal variability and associated oceanographic parameters. *Ocean. Sci.* 18, 233–254. doi:10.5194/os-18-233-2022

Elifantz, H., Malmstrom, R. R., Cottrell, M. T., and Kirchman, D. L. (2005). Assimilation of polysaccharides and glucose by major bacterial groups in the Delaware Estuary. *Appl. Environ. Microbiol.* 71, 7799–7805. doi:10.1128/AEM.71.12.7799-7805.2005

Elvert, M., and Niemann, H. (2008). Occurrence of unusual steroids and hopanoids derived from aerobic methanotrophs at an active marine mud volcano. *Org. Geochem.* 39, 167–177. doi:10.1016/j.orggeochem.2007.11.006

Ferré, B., Jansson, P. G., Moser, M., Serov, P., Portnov, A., Graves, C. A., et al. (2020a). Reduced methane seepage from Arctic sediments during cold bottom-water conditions. *Nat. Geosci.* 13, 144–148. doi:10.1038/s41561-019-0515-3

Ferré, B., Moser, M., Dølven, K. O., Sert, F., Stetzler, M., Savini, A., et al. (2020b). *CAGE 20-7 Cruise report: sediment and water column analyses around flares at Norskebanken, Hinlopen and offshore Prins Karls Forland.*

Flerus, R., Lechtenfeld, O. J., Koch, B. P., McCallister, S. L., Schmitt-Kopplin, P., Benner, R., et al. (2012). A molecular perspective on the ageing of marine dissolved organic matter. *Biogeosciences* 9, 1935–1955. doi:10.5194/bg-9-1935-2012

Fouilland, E., Tolosa, I., Bonnet, D., Bouvier, C., Bouvier, T., Bouvy, M., et al. (2014). Bacterial carbon dependence on freshly produced phytoplankton exudates under different nutrient availability and grazing pressure conditions in coastal marine waters. *FEMS Microbiol. Ecol.* 87, 757–769. doi:10.1111/1574-6941.12262

Geissler, W. H., Gebhardt, A. C., Gross, F., Wollenburg, J., Jensen, L., Schmidt-Aursch, M. C., et al. (2016). Arctic megaslide at presumed rest. *Sci. Rep.* 6, 38529. doi:10.1038/srep38529

Gilbert, J. A., Meyer, F., Jansson, J., Gordon, J., Pace, N., Tiedje, J., et al. (2010). The Earth Microbiome project: meeting report of the "1st EMP meeting on sample selection and acquisition" at argonne national laboratory october 6th 2010. *Stand. Genomic Sci.* 3, 249–253. doi:10.4056/aigs.1443528

Gonsior, M., Peake, B. M., Cooper, W. T., Podgorski, D., D'Andrilli, J., and Cooper, W. J. (2009). Photochemically induced changes in dissolved organic matter identified by ultrahigh resolution Fourier transform ion cyclotron resonance mass spectrometry. *Environ. Sci. Technol.* 43, 698–703. doi:10.1021/es8022804

Grasshoff, K., Ehrhardt, M., Kremling, K., and Anderson, L. G. (Editors) (1999). Methods of seawater analysis. *3rd, completely rev.* extended ed ed. (Weinheim ; New York: Wiley VCH).

Graves, C. A., Steinle, L., Rehder, G., Niemann, H., Connelly, D. P., Lowry, D., et al. (2015). Fluxes and fate of dissolved methane released at the seafloor at the landward limit of the gas hydrate stability zone offshore western Svalbard: dissolved methane off western Svalbard. *J. Geophys. Res. Oceans* 120, 6185–6201. doi:10.1002/2015JC011084

Gründger, F., Probandt, D., Knittel, K., Carrier, V., Kalenitchenko, D., Silyakova, A., et al. (2021). Seasonal shifts of microbial methane oxidation in Arctic shelf waters above gas seeps. Limnol. Oceanogr. *N/a.* 66, 1896–1914. doi:10.1002/lno.11731

Hanson, R. S., and Hanson, T. E. (1996). Methanotrophic bacteria. *Microbiol. Rev.* 60, 439–471. doi:10.1128/mr.60.2.439-471.1996

Hertkorn, N., Benner, R., Frommberger, M., Schmitt-Kopplin, P., Witt, M., Kaiser, K., et al. (2006). Characterization of a Major Refractory Component of Marine Dissolved Organic Matter. *Geochimica et Cosmochimica Acta* 70 (12), 2990–3010. doi:10.1016/j.gca.2006.03.021

Hockaday, W. C., Purcell, J. M., Marshall, A. G., Baldock, J. A., and Hatcher, P. G. (2009). Electrospray and photoionization mass spectrometry for the characterization of organic matter in natural waters: a qualitative assessment. *Limnol. Oceanogr. Methods* 7, 81–95. doi:10.4319/lom.2009.7.81

Hodgkins, S. B., Tfaily, M. M., Podgorski, D. C., McCalley, C. K., Saleska, S. R., Crill, P. M., et al. (2016). Elemental composition and optical properties reveal changes in dissolved organic matter along a permafrost thaw chronosequence in a subarctic peatland. *Geochim. Cosmochim. Acta* 187, 123–140. doi:10.1016/j.gca.2016.05.015

James, R. H., Bousquet, P., Bussmann, I., Haeckel, M., Kipfer, R., Leifer, I., et al. (2016). Effects of climate change on methane emissions from seafloor sediments in the Arctic Ocean: a review. *Limnol. Oceanogr.* 61, S283–S299. doi:10.1002/lno.10307

Jiao, N., Herndl, G. J., Hansell, D. A., Benner, R., Kattner, G., Wilhelm, S. W., et al. (2010). Microbial production of recalcitrant dissolved organic matter: long-term carbon storage in the global ocean. *Nat. Rev. Microbiol.* 8, 593–599. doi:10.1038/nrmicro2386

Kalyuzhnaya, M. G., Gomez, O. A., and Murrell, J. C. (2019). "The methane-oxidizing bacteria (methanotrophs)," in *Taxonomy, genomics and ecophysiology of hydrocarbon-degrading microbes*. Editor T. J. McGenity (Cham: Springer International Publishing), 245–278. doi:10.1007/978-3-030-14796-9_10

Kalyuzhnaya, M. G., Yang, S., Rozova, O. N., Smalley, N. E., Clubb, J., Lamb, A., et al. (2013). Highly efficient methane biocatalysis revealed in a methanotrophic bacterium. *Nat. Commun.* 4, 2785. doi:10.1038/ncomms3785

Kerckhof, F.-M., Sakarika, M., Van Giel, M., Muys, M., Vermeir, P., De Vrieze, J., et al. (2021). From biogas and hydrogen to microbial protein through co-cultivation of methane and hydrogen oxidizing bacteria. *Front. Bioeng. Biotechnol.* 9, 733753. Available at:. doi:10.3389/fbioe.2021.733753

Kim, S., Kramer, R. W., and Hatcher, P. G. (2003). Graphical method for analysis of ultrahigh-resolution broadband mass spectra of natural organic matter, the van Krevelen Diagram. *Anal. Chem.* 75, 5336–5344. doi:10.1021/ac034415p

Knief, C. (2015). Diversity and habitat preferences of cultivated and uncultivated aerobic methanotrophic bacteria evaluated based on pmoA as molecular marker. *Front. Microbiol.* 6. 1346, doi:10.3389/fmicb.2015.01346

Kuhlisch, C., Schleyer, G., Shahaf, N., Vincent, F., Schatz, D., and Vardi, A. (2021). Viral infection of algal blooms leaves a unique metabolic footprint on the dissolved organic matter in the ocean. *Sci. Adv.* 7, eabf4680. doi:10.1126/sciadv.abf4680

Kujawinski, E. B. (2011). The impact of microbial metabolism on marine dissolved organic matter. *Annu. Rev. Mar. Sci.* 3, 567–599. doi:10.1146/annurev-marine-120308-081003

Kujawinski, E. B., Del Vecchio, R., Blough, N. V., Klein, G. C., and Marshall, A. G. (2004). Probing molecular-level transformations of dissolved organic matter: insights on photochemical degradation and protozoan modification of DOM from electrospray ionization Fourier transform ion cyclotron resonance mass spectrometry. *Mar. Chem.* 92, 23–37. doi:10.1016/j.marchem.2004.06.038

Kujawinski, E. B., Longnecker, K., Barott, K. L., Weber, R. J. M., and Kido Soule, M. C. (2016). Microbial community structure affects marine dissolved organic matter composition. *Front. Mar. Sci.* 3. doi:10.3389/fmars.2016.00045

Lau, M. P., and del Giorgio, P. (2020). Reactivity, fate and functional roles of dissolved organic matter in anoxic inland waters. *Biol. Lett.* 16, 20190694. doi:10.1098/rsbl.2019.0694

Lechtenfeld, O. J., Hertkorn, N., Shen, Y., Witt, M., and Benner, R. (2015). Marine sequestration of carbon in bacterial metabolites. *Nat. Commun.* 6, 6711–6718. doi:10.1038/ncomms7711

Lian, J., Zheng, X., Zhuo, X., Chen, Y.-L., He, C., Zheng, Q., et al. (2021). Microbial transformation of distinct exogenous substrates into analogous composition of recalcitrant dissolved organic matter. *Environ. Microbiol.* 23, 2389–2403. doi:10.1111/1462-2920.15426

Lidstrom, M. E. (2006). "Aerobic methylotrophic prokaryotes," in *The prokaryotes: volume 2: ecophysiology and biochemistry*. Editors M. Dworkin, S. Falkow, E. Rosenberg, K.-H. Schleifer, and E. Stackebrandt (New York, NY: Springer), 618–634. doi:10.1007/0-387-30742-7_20

Liu, C., Cui, Y., Li, X., and Yao, M. (2021). microeco: an R package for data mining in microbial community ecology. *FEMS Microbiol. Ecol.* 97, fiaa255. fiaa255. doi:10.1093/femsec/fiaa255

Mau, S., Heintz, M. B., and Valentine, D. L. (2012). Quantification of CH4 loss and transport in dissolved plumes of the Santa Barbara Channel, California. *Cont. Shelf Res.* 32, 110–120. doi:10.1016/j.csr.2011.10.016

Mau, S., Römer, M., Torres, M. E., Bussmann, I., Pape, T., Damm, E., et al. (2017). Widespread methane seepage along the continental margin off Svalbard - from Bjørnøya to Kongsfjorden. *Sci. Rep.* 7, 42997. doi:10.1038/srep42997

Menze, S., Ingvaldsen, R. B., Nikolopoulos, A., Hattermann, T., Albretsen, J., and Gjøsæter, H. (2020). Productive detours – Atlantic water inflow and acoustic backscatter in the major troughs along the Svalbard shelf. *Prog. Oceanogr.* 188, 102447. doi:10.1016/j.pocean.2020.102447

Middelboe, M., and Lyck, P. G. (2002). Regeneration of dissolved organic matter by viral lysis in marine microbial communities. *Aquat. Microb. Ecol.* 27, 187–194. doi:10.3354/ame027187

Morris, R. M., Longnecker, K., and Giovannoni, S. J. (2006). Pirellula and OM43 are among the dominant lineages identified in an Oregon coast diatom bloom. *Environ. Microbiol.* 8, 1361–1370. doi:10.1111/j.1462-2920.2006.01029.x

Murrell, J. C. (2010). "The aerobic methane oxidizing bacteria (methanotrophs)," in *Handbook of hydrocarbon and lipid microbiology*. Editor K. N. Timmis Germany, (Springer Berlin Heidelberg), 1953–1966. doi:10.1007/978-3-540-77587-4_143

Niemann, H., Steinle, L., Blees, J., Bussmann, I., Treude, T., Krause, S., et al. (2015). Toxic effects of lab-grade butyl rubber stoppers on aerobic methane oxidation. *Limnol. Oceanogr. Methods* 13, 40–52. doi:10.1002/lom3.10005

Noriega-Ortega, B. E., Wienhausen, G., Mentges, A., Dittmar, T., Simon, M., and Niggemann, J. (2019). Does the chemodiversity of bacterial exometabolomes sustain the chemodiversity of marine dissolved organic matter? *Front. Microbiol.* 10, 215. doi:10.3389/fmicb.2019.00215

Oksanen, J., Blanchet, F. G., Friendly, M., Kindt, R., Legendre, P., McGlinn, D., et al. (2020). Vegan: community ecology package. Available at: https://CRAN.R-project.org/package=vegan.

Osterholz, H., Niggemann, J., Giebel, H.-A., Simon, M., and Dittmar, T. (2015). Inefficient microbial production of refractory dissolved organic matter in the ocean. *Nat. Commun.* 6, 7422. doi:10.1038/ncomms8422

Owrid, G., Socal, G., Civitarese, G., Luchetta, A., Wiktor, J., Nöthig, E.-M., et al. (2000). Spatial variability of phytoplankton, nutrients and new production estimates in the waters around Svalbard. *Polar Res.* 19, 155–171. doi:10.3402/polar.v19i2.6542

Pohlman, J. W., Bauer, J. E., Waite, W. F., Osburn, C. L., and Chapman, N. R. (2011). Methane hydrate-bearing seeps as a source of aged dissolved organic carbon to the oceans. *Nat. Geosci.* 4, 37–41. doi:10.1038/ngeo1016

Qian, J., and Mopper, K. (1996). Automated high-performance, high-temperature combustion total organic carbon analyzer. *Anal. Chem.* 68, 3090–3097. doi:10.1021/ac960370z

Quast, C., Pruesse, E., Yilmaz, P., Gerken, J., Schweer, T., Yarza, P., et al. (2013). The SILVA ribosomal RNA gene database project: improved data processing and web-based tools. *Nucleic Acids Res.* 41, D590–D596. doi:10.1093/nar/gks1219

R Core Team (2022). R: a language and environment for statistical computing. Available at: https://www.R-project.org/.

Reeburgh, W. S. (2007). Oceanic methane biogeochemistry. *Chem. Rev.* 107, 486–513. doi:10.1021/cr050362v

Renner, A., Bailey, A., Reigstad, M., Sundfjord, A., and Øygarden, S. (2020). Hydrography and nutrient concentrations in years of contrasting sea ice conditions in the Atlantic inflow region north of Svalbard. *Copernicus Meetings*. doi:10.5194/egusphere-egu2020-1606

Rivas-Ubach, A., Liu, Y., Bianchi, T. S., Tolić, N., Jansson, C., and Paša-Tolić, L. (2018). Moving beyond the van Krevelen diagram: a new stoichiometric approach for compound classification in organisms. *Anal. Chem.* 90, 6152–6160. doi:10.1021/acs.analchem.8b00529

Rosselló-Mora, R., Lucio, M., Peña, A., Brito-Echeverría, J., López-López, A., Valens-Vadell, M., et al. (2008). Metabolic evidence for biogeographic isolation of the extremophilic bacterium Salinibacter ruber. *ISME J.* 2, 242–253. doi:10.1038/ismej.2007.93

Serov, P., Portnov, A., Mienert, J., Semenov, P., and Ilatovskaya, P. (2015). Methane release from pingo-like features across the South Kara Sea shelf, an area of thawing offshore permafrost. *J. Geophys. Res. Earth Surf.* 120, 1515–1529. doi:10.1002/2015JF003467

Sert, M. F., D'Andrilli, J., Gründger, F., Niemann, H., Granskog, M. A., Pavlov, A. K., et al. (2020). Compositional differences in dissolved organic matter between arctic cold seeps versus non-seep sites at the Svalbard continental margin and the Barents Sea. *Front. Earth Sci.* 8, 552731. doi:10.3389/feart.2020.552731

Sert, M. F., Niemann, H., Reeves, E. P., Granskog, M. A., Hand, K. P., Kekäläinen, T., et al. (2022). Compositions of dissolved organic matter in the ice-covered waters above the Aurora hydrothermal vent system, Gakkel Ridge, Arctic Ocean. *Biogeosciences* 19, 2101–2120. doi:10.5194/bg-19-2101-2022

Sjöstedt, J., Lapierre, J.-F., Yamashita, Y., and Baltar, F. (2021). Editorial: microbial utilization and transformation of dissolved organic matter in aquatic environments–from streams to the deep ocean. *Front. Microbiol.* 12, 668560. Available at:. doi:10.3389/fmicb.2021.668560

Steinle, L., Graves, C. A., Treude, T., Ferré, B., Biastoch, A., Bussmann, I., et al. (2015). Water column methanotrophy controlled by a rapid oceanographic switch. *Nat. Geosci.* 8, 378–382. doi:10.1038/ngeo2420

Steinle, L., Maltby, J., Treude, T., Kock, A., Bange, H. W., Engbersen, N., et al. (2017). Effects of low oxygen concentrations on aerobic methane oxidation in seasonally hypoxic coastal waters. *Biogeosciences* 14, 1631–1645. doi:10.5194/bg-14-1631-2017

Theisen, A. R., and Murrell, J. C. (2005). Facultative methanotrophs revisited. *J. Bacteriol.* 187, 4303–4305. doi:10.1128/JB.187.13.4303-4305.2005

Tremblay, J.-É., Michel, C., Hobson, K. A., Gosselin, M., and Price, N. M. (2006). Bloom dynamics in early opening waters of the Arctic Ocean. *Limnol. Oceanogr.* 51, 900–912. doi:10.4319/lo.2006.51.2.0900

Valle, J., Gonsior, M., Harir, M., Enrich-Prast, A., Schmitt-Kopplin, P., Bastviken, D., et al. (2018). Extensive processing of sediment pore water dissolved organic matter during anoxic incubation as observed by high-field mass spectrometry (FTICR-MS). *Water Res.* 129, 252–263. doi:10.1016/j.watres.2017.11.015

Van den Meersche, K., Soetaert, K., and Middelburg, J. J. (2011). Plankton dynamics in an estuarine plume: a mesocosm 13C and 15N tracer study. *Mar. Ecol. Prog. Ser.* 429, 29–43. doi:10.3354/meps09097

Vekeman, B., Kerckhof, F.-M., Cremers, G., de Vos, P., Vandamme, P., Boon, N., et al. (2016). New Methyloceanibacter diversity from North Sea sediments includes methanotroph containing solely the soluble methane monooxygenase. *Environ. Microbiol.* 18, 4523–4536. doi:10.1111/1462-2920.13485

Vincent, F., and Vardi, A. (2023). Viral infection in the ocean—a journey across scales. *PLOS Biol.* 21, e3001966. doi:10.1371/journal.pbio.3001966

Wilhelm, S. W., and Suttle, C. A. (1999). Viruses and Nutrient Cycles in the Sea: viruses play critical roles in the structure and function of aquatic food webs. *BioScience* 49, 781–788. doi:10.2307/1313569

Yilmaz, P., Parfrey, L. W., Yarza, P., Gerken, J., Pruesse, E., Quast, C., et al. (2014). The SILVA and "all-species living tree project (LTP)" taxonomic frameworks. *Nucleic Acids Res.* 42, D643–D648. doi:10.1093/nar/gkt1209

Zabłocka, M., Kowalczuk, P., Meler, J., Peeken, I., Dragańska-Deja, K., and Winogradow, A. (2020). Compositional differences of fluorescent dissolved organic matter in Arctic Ocean spring sea ice and surface waters north of Svalbard. *Mar. Chem.* 227, 103893. doi:10.1016/j.marchem.2020.103893

Zhao, Z., Gonsior, M., Schmitt-Kopplin, P., Zhan, Y., Zhang, R., Jiao, N., et al. (2019). Microbial transformation of virus-induced dissolved organic matter from picocyanobacteria: coupling of bacterial diversity and DOM chemodiversity. *ISME J.* 13, 2551–2565. doi:10.1038/s41396-019-0449-1

frontiers | Frontiers in Earth Science

TYPE Original Research
PUBLISHED 07 February 2024
DOI 10.3389/feart.2024.1340399

OPEN ACCESS

EDITED BY
Patrick G Hatcher,
Old Dominion University, United States

REVIEWED BY
Jan Kavan,
Masaryk University, Czechia
Chunlin Song,
Sichuan University, China

*CORRESPONDENCE
Gabrielle E. Kleber,
gakle2914@uit.no

RECEIVED 17 November 2023
ACCEPTED 23 January 2024
PUBLISHED 07 February 2024

CITATION
Kleber GE, Magerl L, Turchyn AV, Redeker K, Thiele S, Liira M, Herodes K, Øvreås L and Hodson A (2024), Shallow and deep groundwater moderate methane dynamics in a high Arctic glacial catchment.
Front. Earth Sci. 12:1340399.
doi: 10.3389/feart.2024.1340399

Shallow and deep groundwater moderate methane dynamics in a high Arctic glacial catchment

Gabrielle E. Kleber[1,2,3]*, Leonard Magerl[3], Alexandra V. Turchyn[1], Kelly Redeker[4], Stefan Thiele[5], Martin Liira[6,7], Koit Herodes[8], Lise Øvreås[5] and Andrew Hodson[2,9]

[1]Department of Earth Sciences, University of Cambridge, Cambridge, United Kingdom, [2]Arctic Geology, University Centre in Svalbard (UNIS), Longyearbyen, Norway, [3]Department of Geology, UiT the Arctic University of Norway, Tromsø, Norway, [4]Department of Biology, University of York, York, United Kingdom, [5]Department of Biological Sciences, University of Bergen, Bergen, Norway, [6]Department of Geology, University of Tartu, Tartu, Estonia, [7]The Geological Survey of Estonia, Rakvere, Estonia, [8]Institute of Chemistry, University of Tartu, Tartu, Estonia, [9]Department of Environmental Sciences, Western Norway University of Applied Sciences, Sogndal, Norway

Glacial groundwater can mobilize deep-seated methane from beneath glaciers and permafrost in the Arctic, leading to atmospheric emissions of this greenhouse gas. We present a temporal, hydro-chemical dataset of methane-rich groundwater collected during two melt seasons from a high Arctic glacial forefield to explore the seasonal dynamics of methane emissions. We use methane and ion concentrations and the isotopic composition of water and methane to investigate the sources of groundwater and the origin of the methane that the groundwater transports to the surface. Our results suggest two sources of groundwater, one shallow and one deep, which mix, and moderate methane dynamics. During summer, deep methane-rich groundwater is diluted by shallow oxygenated groundwater, leading to some microbial methane oxidation prior to its emergence at the surface. Characterization of the microbial compositions in the groundwater shows that microbial activity is an important seasonal methane sink along this flow-path. In the groundwater pool studied, we found that potential methane emissions were reduced by an average of 29% (±14%) throughout the summer due to microbial oxidation. During winter, deep groundwater remains active while many shallow systems shut down due to freezing, reducing subsurface methane oxidation, and potentially permitting larger methane emissions. Our results suggest that ratios of the different groundwater sources will change in the future as aquifer capacities and recharge volumes increase in a warming climate.

KEYWORDS

methane, groundwater, Svalbard, glacier, biogeochemistry, cryosphere, hydrology

1 Introduction

Groundwater systems within glaciated catchments play a significant role in proglacial hydrology, often modulating the timing and magnitude of bulk runoff (Andermann et al., 2012; Liljedahl et al., 2017; Ó Dochartaigh et al., 2019), and controlling winter baseflow (Chesnokova et al., 2020a). A complex hydrological system contributes to groundwater aquifers in periglacial environments, which can be recharged by subglacial meltwater, snow

melt, buried ice formations, moraine lakes, summer precipitation and hillslope groundwater (Chesnokova et al., 2020b; Hodson et al., 2023).

In the high Arctic, the presence of permafrost and buried glacier ice in the proglacial environment dramatically limits the hydraulic conductivity of moraine and talus (Williams and Smith, 1989). Near-surface groundwater flow in permafrost regions can be seasonal and dependent on the thawing of the active layer during summer (Cooper et al., 2011). Alternatively, perennial, intra-permafrost groundwater flow requires the maintenance of a zone of unfrozen ground that penetrates the permafrost, known as a talik. In this case, the talik is maintained by the constant, year-round flow of water, which transfers sufficient advective heat to prevent freeze-back during winter (Hodson et al., 2023).

Winter baseflows, which are related to hydrologic systems that are active year-round, are increasing in response to climactic changes in glacierized (Walvoord and Striegl, 2007; Liljedahl et al., 2017; Chesnokova et al., 2020a) and non-glacierized (Lammers et al., 2001; Smith et al., 2007; St. Jacques and Sauchyn, 2009; Danilovich et al., 2019; Makarieva et al., 2019) catchments across the Arctic and subarctic. Larger groundwater storage capacities and increased summer recharge of deeper groundwater aquifers are responsible for this increased discharge during the freezing season (Liljedahl et al., 2017). The capacity of aquifer storage is increasing as a result of the deepening of the permafrost active layer and taliks with increased summer temperatures and longer melt seasons (Liljedahl et al., 2017). Larger inputs of water sources such as precipitation, permafrost thaw and glacier melt collectively contribute to increased groundwater recharge (Liljedahl et al., 2017).

At high latitudes, cold conditions mean that the thermal regime of valley glaciers is primarily polythermal (i.e., only a small portion of basal ice is at the pressure-melting point) or cold-based (i.e., the ice is completely frozen to the glacier bed) (Hodgkins, 1997). In addition, the thinning of previously polythermal glaciers due to a warming climate is leading to an increased proportion of cold-based glaciers in the high Arctic (Hambrey et al., 2005; Lovell et al., 2015). The predominance of cold ice suggests that groundwater recharge due to subglacial melt and hydraulic connectivity is limited in the subglacial environment. However, large icings, which are stratified layers of ice formed by the freezing of continuous outflows of groundwater during winter (Carey, 1973), are commonly observed in proglacial plains of the high Arctic. These icings provide evidence for year-round groundwater systems that are active in both polythermal and cold-based catchments (Moorman and Michel, 2000; Hodgkins et al., 2004; Bukowska-Jania and Szafraniec, 2005; Pollard, 2005; Bælum and Benn, 2011; Mallinson et al., 2019; Chesnokova et al., 2020b; Kleber et al., 2023). Hydrological observations suggest that taliks formed beneath glaciers can extend beyond the glacial margin, providing a conduit for the groundwater flow (Moorman, 2003). The source of this groundwater, however, is less understood, particularly in high Arctic glaciers where subglacial meltwaters can be limited.

A recent study identified over 100 groundwater springs present in the forefields of glaciers across central Svalbard in the Norwegian high Arctic (Kleber et al., 2023). The study found that each of these springs was super-saturated with methane and, consequently, a source of this greenhouse gas to the Arctic atmosphere. The methane concentrations were correlated with the local geology, with higher concentrations occurring more frequently in regions with outcrops of Jurassic and Triassic shale. Our current study aims to investigate the primary sources of this methane-rich groundwater to gain a better understanding of the origin of the methane and the chemical and biological reactions that occur along the groundwater flowpaths.

Over a spring and summer season, we collect a high-resolution, temporal dataset of biogeochemical parameters of the river water and groundwater from one glacial catchment in central Svalbard. We perform an in-depth analysis, or inverse deduction, of this biogeochemical data to identify the primary sources of the groundwater and its flowpaths. Furthermore, we determine the source of methane in the proglacial groundwater and consider its seasonal modifications, which ultimately govern its potential emissions. We explore the relationships between groundwater, glacial meltwater, snow melt, weather conditions and mineral weathering to unravel a complex, interconnected hydrological system that moderates methane dynamics in a high Arctic glacial catchment.

2 Materials and methods

2.1 Site description

Svalbard is a Norwegian archipelago located in the Arctic Ocean between 76 and 81°N. The majority of its landmass (57%) is covered by glacier (Nuth et al., 2013) and permafrost is continuous throughout the islands, reaching up to 500 m in thickness (Humlum et al., 2003). Our study focuses on the Vallåkrabreen catchment in central Svalbard (Figure 1). This catchment contains a ~20 km^2 valley glacier, Vallåkrabreen, that has likely been receding since the start of the 20th century—which represents the onset of significant glacial retreat on Svalbard (Svendsen and Mangerud, 1997). The thermal regime of Vallåkrabreen is presumed to be polythermal based on published thermal regimes of similarly sized glaciers on Svalbard (Macheret et al., 2019).

The forefield of Vallåkrabreen is ~3.5 km long, from the glacier terminus to the fjord, and 1 km across, flanked by mountains with ~750 m elevation on either side. Aerial images of the region taken by the Norwegian Polar Institute in 1936 show that Vallåkrabreen terminated in the fjord at the time, and thus the forefield has been exposed within the last 85 years. The moraine is largely ice-cored and dominated by a glaciofluvial outwash plain and till plain with buried ice. The forefield is dotted with many small ponds and has little-to-no vegetation. During the winter and spring, a large icing forms in the proglacial plain and extends with some discontinuities along the river plain to the fjord. During summer, groundwater springs form pools and small streams throughout the proglacial plain, with bubbling often observed.

The geology of central Svalbard is dominated by the Central Palaeogene Basin, a 3,000–4,000 m thick succession of sandstone, siltstone and shale that accumulated during the Paleocene and Eocene. Vallåkrabreen sits primarily within the Carolinefjellet geological formation, a shale-dominated formation which is composed of Lower Cretaceous successions of fine-to medium-grained sandstones and shales deposited in pro-delta to distal marine conditions (Dallmann, 2015). The members of the

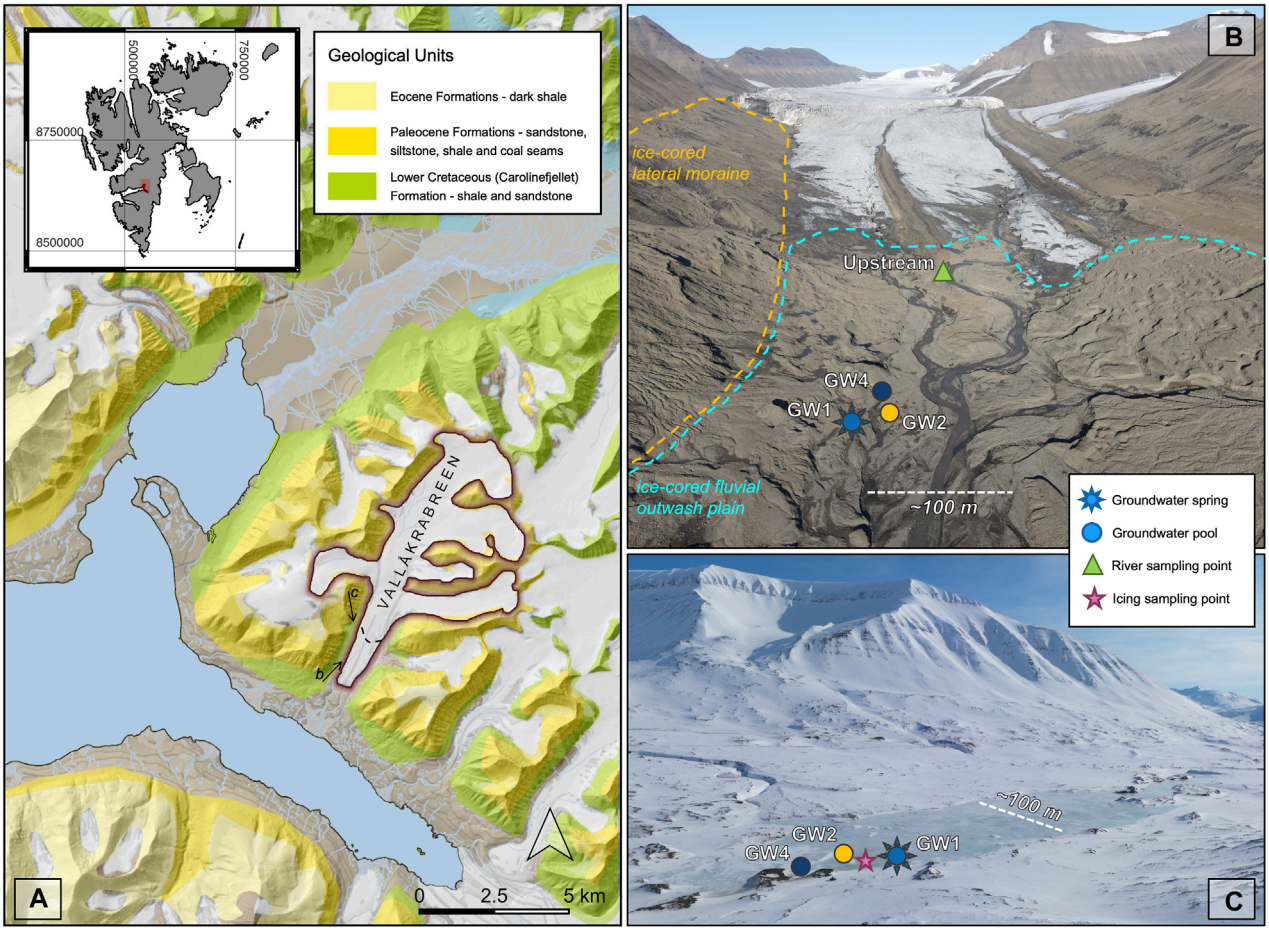

FIGURE 1
Overview of the Vallåkrabreen catchment: **(A)** geological map of the study region with inset map of Svalbard, arrows mark the approximate locations and angles that drone images in **b** and **c** were taken (base map provided by the Norwegian Polar Institute and created with data from 2011—dotted line represents 2021 glacier margin, maps displayed in WGS84 UTM Zone 33 coordinates (EPSG:25833)); **(B)** overview of summertime sampling locations (photograph taken in summer 2022); **(C)** image of the winter icing with summer and springtime sampling locations marked (photo credit: Erik Schytt Mannerfelt, taken in spring 2022).

Carolinefjellet formation are dominated by silicate minerals with quartz and feldspars (plagioclase and alkali) making up 74%–100% of the grain composition (Maher et al., 2004). Other silicate minerals such as micas (muscovite, biotite, glauconite), chlorite and, to a lesser degree, andalusite and hornblende are present throughout the members (Maher et al., 2004). Micrite beds and coquina horizons bearing carbonate minerals such as siderite, calcite and glendonite are found in the upper part of the formation, as well as large "cannon ball" carbonate concretions (Maher et al., 2004). Pyrite is present throughout the shale as well as within a distinctive horizon of iron ooids found in the lower part of the formation (Mutrux et al., 2008).

2.2 Water sampling

During the summer of 2021, we focused primarily on sampling a groundwater spring called 'GW2' which formed a small (~7 x 2 m) pool in the forefield of Vallåkrabreen, about 250 m from the glacier terminus. Water samples were collected from the pool every 2–5 days between 03 July (day of year, DOY = 184) and 24 September (DOY = 267), alongside *in situ* measurements of electrical conductivity (EC) and dissolved oxygen (DO) taken with a Hach HQ40d meter and electrodes. Less frequent sampling and *in situ* measurements of two other groundwater springs were also undertaken: GW1 ($n = 6$), a spring that flowed from an ice-cored hummock in the moraine and GW4 ($n = 2$), a spring that formed a larger (~6 x 8 m) pool nearby. Water was also collected and *in situ* measurements taken every 2–5 days from the main melt river at an upstream location, as close to the glacier terminus as possible. The sampling location was approximately 50 m downstream of the confluence of the main subglacial river and a supraglacial river. It was assumed that the much larger size of the subglacial river meant that the degree of mixing between these two sources would have minimal impacts on sample chemistry, although discrete discharge measurements of each river were not taken.

During the summer of 2022, more frequent sampling of the GW1 spring was completed to gain a more comprehensive understanding of the dynamics of the spring throughout the melt

season, which was not fully captured by the irregular sampling in 2021. Water samples and *in situ* measurements of the GW1 spring were taken every 3–9 days between 12 July (DOY = 193) and 18 September 2022 (DOY = 261).

Springtime sampling of the Vallåkrabreen groundwaters also occurred three times throughout April and May 2021, while the winter icing still covered the proglacial floodplain. Samples were collected by drilling into the icing with a 7 cm diameter auger until pressurized water was released. The springtime sampling location was close to the locations of the GW1 spring and GW2 pool. Six water samples were also collected during summer for profiling the microbial community composition with specific emphasis on known methanogenic and methanotrophic microorganisms within the GW1, GW2 and GW4 groundwaters. Springtime and summer sampling locations are marked on Figure 1.

2.3 Analysis of water samples

The following method was used for samples collected in both spring and summer. Water samples for the analyses of the oxygen and hydrogen isotopic composition of water, the carbon isotopic composition of dissolved inorganic carbon (DIC), alkalinity and anion concentrations (SO_4^{2-} and Cl^-) were pressed through a 0.45 µm Whatman cellulose acetate syringe filter. The filtrate was collected in a 50 mL falcon tube with no headspace. Samples for the analyses of cation concentrations (Ca^{2+}, K^+, Mg^{2+}, Na^+, Si) were also filtered and 10 mL filtrate was collected in 15 mL falcon tubes that were pre-acidified with 0.1 mL 69% nitric acid. Unfiltered samples for the analysis of methane (CH_4) concentration, the stable carbon isotopic composition of methane (δ^{13}C-CH_4), and ethane (C_2H_6) and propane (C_3H_8) concentrations were sealed in 22 mL gas-tight serum vials with no headspace. Samples for the analyses of methane concentration and the isotopic composition of methane were spiked within 12 h with 1 mL of 1 M NaOH while concurrently removing 1 mL of sample to stop microbial activity. All samples were stored at ~4°C in the dark until analysis.

The oxygen and hydrogen isotopic composition of the waters (δ^2H-H_2O and δ^{18}O-H_2O) were measured using a Picarro Cavity Ringdown Spectrometer. Average values of six repeat measurements are reported with reference to the international standard VSMOW. Analytical precision was better than 1.0‰ for δ^2H and 0.1‰ for δ^{18}O. Measurements of the carbon isotopic composition of DIC (δ^{13}C-DIC) were made using a Thermo Gas Bench attached to a Delta V Mass Spectrometer. Approximately 1.5 mL of sample water was injected into a helium-flushed vial pre-acidified with four drops of orthophosphoric acid (100%) and left to react for 1 hour. The resulting CO_2 in the headspace was analyzed alongside a series of standards and reference samples used to calibrate to the international standard VPDB. Analytical precision was better than 0.1‰. The above isotopic analyses were completed in the Godwin Laboratory of Paleoclimate Research at the University of Cambridge, United Kingdom.

Major anion (SO_4^{2-} and Cl^-) concentrations were measured by ion chromatography on a Thermo Scientific Dionex ICS5000+ at the University of Cambridge, with an error of ±2%. Alkalinity, presumed to be predominantly HCO_3^-, was determined with the inflection point method by titrating 1–10 mL aliquots of samples with 0.0166 M analytical grade hydrochloric acid. Major and minor cation concentrations of all 2021 water samples (Ca^{2+}, K^+, Mg^{2+}, Na^+, Si) were measured by an Agilent 5,100 Inductively-Coupled Plasma Optical Emission Spectrometer (ICP-OES) at the University of Cambridge, United Kingdom, with an error of ±10%. Major and minor cation concentrations of the 2022 GW1 samples were also determined using ICP-OES (iCAP-7400, Thermo Scientific, United Kingdom) at the University of York, United Kingdom, with an error of ±10%.

The concentration of methane was measured by the headspace method described in Kleber et al. (2023), using a gas chromatograph fitted with a flame ionization detector (GC/FID, Agilent Technologies United Kingdom Ltd.) at Queen Mary University of London, United Kingdom. Measurements have an error of ±5%. The carbon isotopic composition of methane was measured using a Picarro G2201-I cavity ringdown spectrometer at the University of Cambridge, United Kingdom in the LASER-ENVI gas isotope facility and were reported with an error of ±1‰ and with reference to the international standard VPDB.

The concentrations of ethane and propane were measured using an Agilent Technologies 7890A GC System equipped with a 30 m x 530 µm x 1.5 µm DB-5MS column (Agilent J&W GC columns) and flame ionization detector (FID) at the University of Tartu, Estonia. The carrier gas was high purity helium with a flow rate of 6 mL min^{-1}. The oven was programmed with an initial temperature of −30°C (using liquid N_2) for 1.7 min, increasing at 30°C min^{-1}–60°C with run time 4.7 min. The inlet was set at 40°C and flow split ratio 10:1. The FID was set at 300°C. The FID hydrogen flow rate was 30 mL min^{-1}, the air flow rate was 400 mL min^{-1}, and nitrogen makeup gas flow rate was 25 mL min^{-1}. Identification and quantification were done using external alkane standard gas mixtures. A 5 mL helium headspace was added to the samples and equilibrated by vigorously shaking for >10 min before 50 µL of the sample was injected manually to the GC system.

2.4 DNA extraction and sequencing

Water samples used to profile the microbial community composition were taken by pushing 250–1,000 mL of water through a sterile 0.22 µm Sterivex filter unit using a sterile 50 mL syringe. Filters were stabilized with RNA*later* (Thermo Fisher) in the field and stored in the dark at 4°C until access to a −80°C freezer was available up to 2 months later.

Extractions for DNA and RNA were done using the AllPrep DNA/RNA kit (QIAGEN, Hilden, Germany) according to the manual. From the RNA, DNA was removed using the DNA-free DNA Removal kit (Invitrogen, Waltham, US) and subsequently cDNA was synthesized using the SuperScript III First-strand synthesis system (Invitrogen, Waltham, US). The DNA and cDNA was send for sequencing using primers 515F–5′- GTGYCAGCMGCCGCGGTAA-3′ and 806R–5′-GGACTACNVGGGTWTCTAAT-3’ (Apprill et al., 2015; Parada et al., 2016). The libraries were sequenced using Illumina NextSeq technology with paired-end reads of 2x250 bp length at Novogene Co., Cambridge, United Kingdom. The raw reads were deposited in the European Nucleotide Archive as project PRJEB60294.

The DADA2 pipeline was used in R to generate Amplicon sequence variants (ASVs) (Callahan et al., 2016). For this, primers were removed, the quality of the sequences checked, and trimmed according to sequence quality. The final ASVs were then generated after dereplication. Subsequently, the complementary reads were merged, chimeras were removed, and the taxonomy was assigned to the ASVs using a trained Silva database, based on the Silva release SSU Ref NR v138 (Quast et al., 2013). Thereafter, ASVs identified as mitochondria, chloroplasts, Eukaryotes, <4 sequences or <1 x 10^{-5}% of relative abundance, as well as samples with <10.000 reads were removed. The samples are presented relative abundances with standard errors if applicable. The analyses were done using R and the "vegan", "tidyverse", "phyloseq", "ggplot2", "forcats", "patchwork", "scales", and "ape" packages (Mazerolle, 2020; McMurdie and Holmes, 2013; Oksanen et al., 2022; Paradis and Schliep, 2019; Pedersen, 2022; R Core Team, 2023; Wickham et al., 2022; Wickham et al., 2019; Wickham, 2023). Using PiCRUST2 with standard parameters in bioconda, the metabolic potential of the different ASVs was inferred based on their location in a phylogenetic tree of fully sequenced organisms and the genomic assets of the closest relative in this tree (Grüning et al., 2018; Douglas et al., 2020). Enzyme commission (EC)-numbers marker genes, namely, *pmoA* and *mmoX* (methanotrophy) and *mcrA* (methanogenesis), were extracted and used to identify methanogens and methanotrophs. Due to the uncertainty in PiCRUST analyses, known methanotrophs and methanogens were found manually and added to the analyses.

2.5 Weather Station

A Hobo U30 USB Weather Station was erected in the forefield of Vallåkrabreen, approximately 900 m from the glacier front and 650 m from the groundwater station. Hourly average measurements of temperature, incident radiation, relative humidity, wind and gust speed and wind direction were taken at an elevation of ~2 m throughout the melt season.

3 Results

3.1 Water geochemistry

The geochemical composition of waters collected from the GW1 spring remained relatively constant throughout the 2021 and 2022 summers, with very little variation among the measured samples. The GW2 pool, on the other hand, showed considerable variation throughout the 2021 summer. The geochemical compositions of the GW1 and GW2 groundwaters are shown in Figure 2–5, along with the upstream melt river, and estimates of the average composition of the GW4 pool (n = 2) and the water sampled from the winter icing during April and May 2021 (n = 3).

The hydrogen and oxygen isotopic composition of the waters lie between the Global Meteoric Water Line (GMWL) and the Local Meteoric Water Line (LMWL), which is based on precipitation at Isfjord Radio, a location 85 km northwest of Vallåkrabreen (Figure 2). Throughout both summers, the GW1 spring maintained a lower hydrogen and oxygen isotopic composition between −109.7‰ and −107.3‰ for δ^2H and between −15.5‰ and −15.1‰ for δ^{18}O, consistently plotting close to the winter average (δ^2H = −108.6‰, δ^{18}O = −15.3‰). The GW2 pool varied considerably and ranged within the bounds of the winter average and the average of the GW4 pool (δ^2H = −94.7‰, δ^{18}O = −13.3‰). The upstream melt river maintained a higher hydrogen and oxygen isotopic composition, ranging between −97.9‰ and −92.6‰ for δ^2H and between −13.8‰ and −13.1‰ for δ^{18}O, consistently plotting close to the GW4 average.

The electrical conductivity (EC) of the GW1 spring was stable throughout both summers, ranging from 450 to 493 µS cm^{-1}, which was close to the winter average of 489 µS cm^{-1} (Figure 3). The EC of the GW2 pool was higher and more variable, fluctuating between 436 and 643 µS cm^{-1}. The GW4 pool average was 574 µS cm^{-1}. The EC of the upstream melt river was much lower than the groundwaters, staying below 100 µS cm^{-1} for most of the summer but rising up to a maximum of 133 µS cm^{-1} towards the end of the summer. The dissolved oxygen (DO) of the GW1 spring was consistently low at the beginning of the 2021 summer and throughout the 2022 summer (between 0.65 and 1.28 ppm) but rose to higher levels at the end of the 2021 summer with a maximum of 4.05 ppm (Figure 3). The winter average had even lower DO levels, at 0.28 ppm. The DO of the GW2 pool fluctuated throughout the summer between 0.52 and 9.20 ppm and the GW4 pool average was 6.13 ppm. The DO of the upstream melt river was high (between 12.4 and 15.4 ppm), often exceeding the atmospheric equilibrium concentration in freshwater at 0°C, which is 14.6 ppm.

The concentrations of all ions (Ca^{2+}, K^+, Mg^{2+}, Na^+, SO_4^{2-}, Cl^-, and HCO_3^-) within the GW1 spring remained relatively stable throughout both summers and consistently plot close to the winter average concentrations (Figure 4). Ionic concentrations of the GW2 pool fluctuated throughout the summer between the bounds of the winter and GW4 average concentrations. Concentrations of the various ions within the upstream melt river were generally lower than or similar to concentrations in the groundwaters. The carbon isotopic composition of DIC was variable for all water types, although its values were generally more positive in the GW2 pool (Figure 4).

The methane concentrations of the GW1 spring have two distinctly different trends between the two summers sampling seasons (Figure 5). The groundwater spring started each summer with similar concentrations (roughly 950,000 nM), but the concentrations in 2021 dropped considerably at the end of the summer to less than half the initial concentrations. The carbon isotopic composition of the methane, which started the summer at an average of −45‰, correspondingly showed a slight enrichment in ^{13}C at the end of the 2021 summer with an average composition of −44‰. In 2022, the methane concentration of the GW1 spring remained relatively stable (ranging from 956,000 nM to 11,650,000 nM) and likewise, the carbon isotopic composition varied little (ranging from −44.3‰ to −43.9‰). Like the geochemistry of the GW2 spring, the methane concentration and the isotopic composition of the methane varied significantly throughout the summer. The concentration ranged from 122,000 nM to 945,000 nM and the isotopic composition ranged from −45‰ to −41‰. Both the GW1 and GW2 springs started each summer with methane concentrations similar to the winter average (808,000 nM).

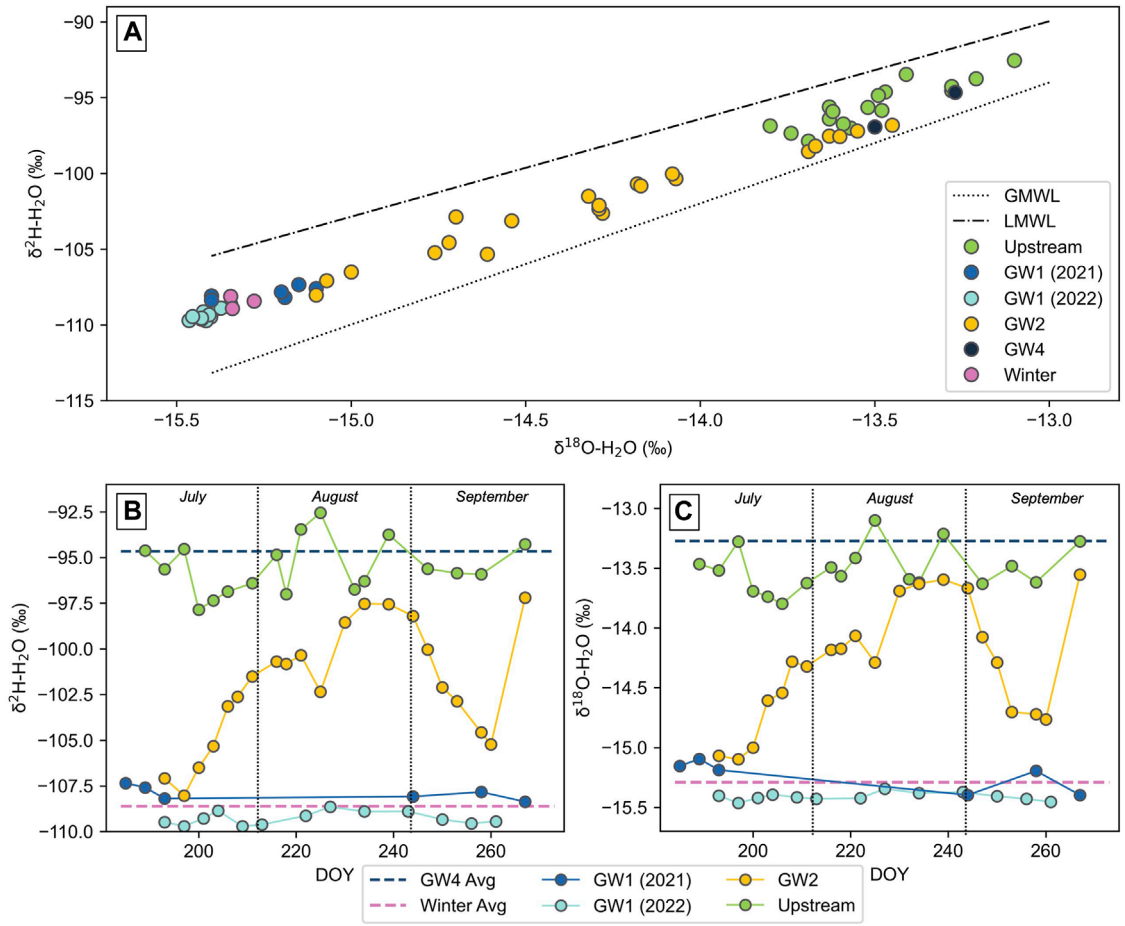

FIGURE 2
Oxygen and hydrogen isotopic composition of water collected during summer from the GW1 spring, GW2 pool, GW4 pool, the upstream melt river and the winter icing (taken during springtime): **(A)** plotted with the global meteoric water line (GMWL) and the local meteoric water line (LMWL, based on precipitation at Isfjord Radio), Svalbard and **(B)**, **(C)** plotted temporally across the summer. DOY represents the day number of the year.

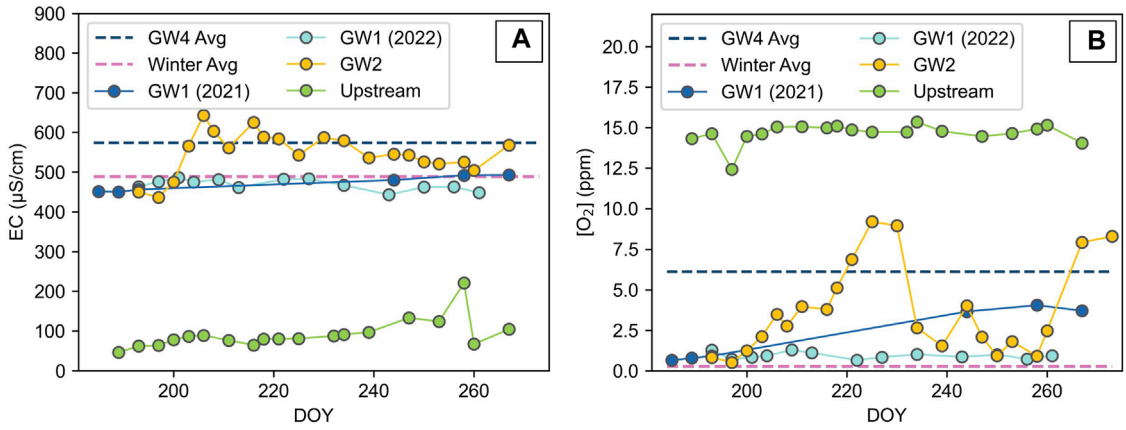

FIGURE 3
Temporal variation of *in situ* measurements **(A)** electrical conductivity (EC) and **(B)** dissolved oxygen of the GW1 spring, GW2 pool and the upstream melt river. Average values of the GW4 pool (n=2, taken during the summer) and the samples taken from the winter icing (denoted 'Winter Avg', n = 3) are plotted as endmember lines. DOY represents the day number of the year.

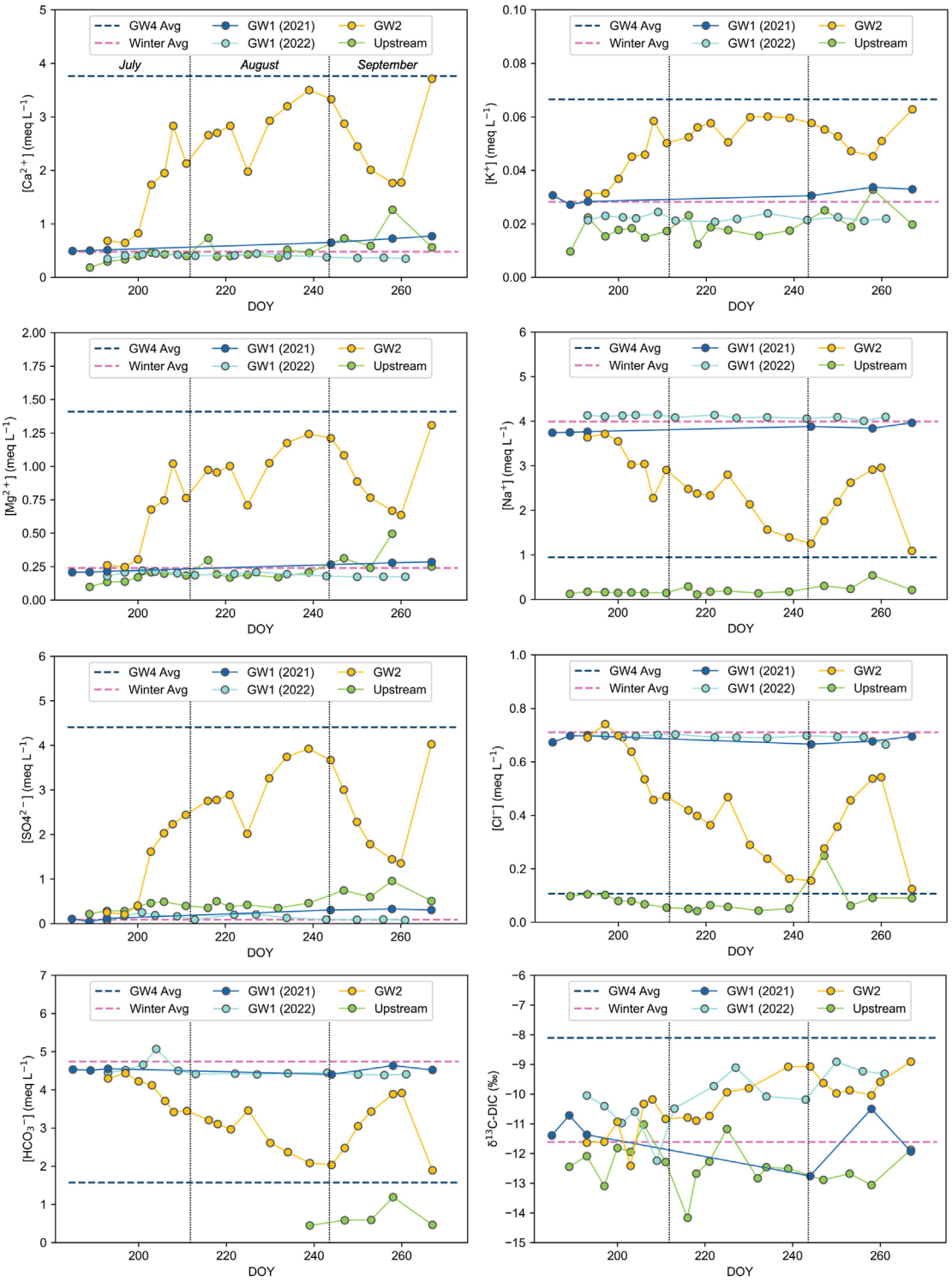

FIGURE 4
Temporal variation of major ion concentrations and carbon isotopes of DIC (δ^{13}C-DIC) in the GW1 spring, GW2 pool and the upstream melt river. Average values of the GW4 pool (n = 2, taken during the summer) and the springtime samples taken from the winter icing (denoted 'Winter Avg,' n = 3) are plotted as endmember lines. HCO_3^- concentrations are based on alkalinity measurements; early summer measurements of the upstream melt river were below the detection limit. DOY represents the day number of the year.

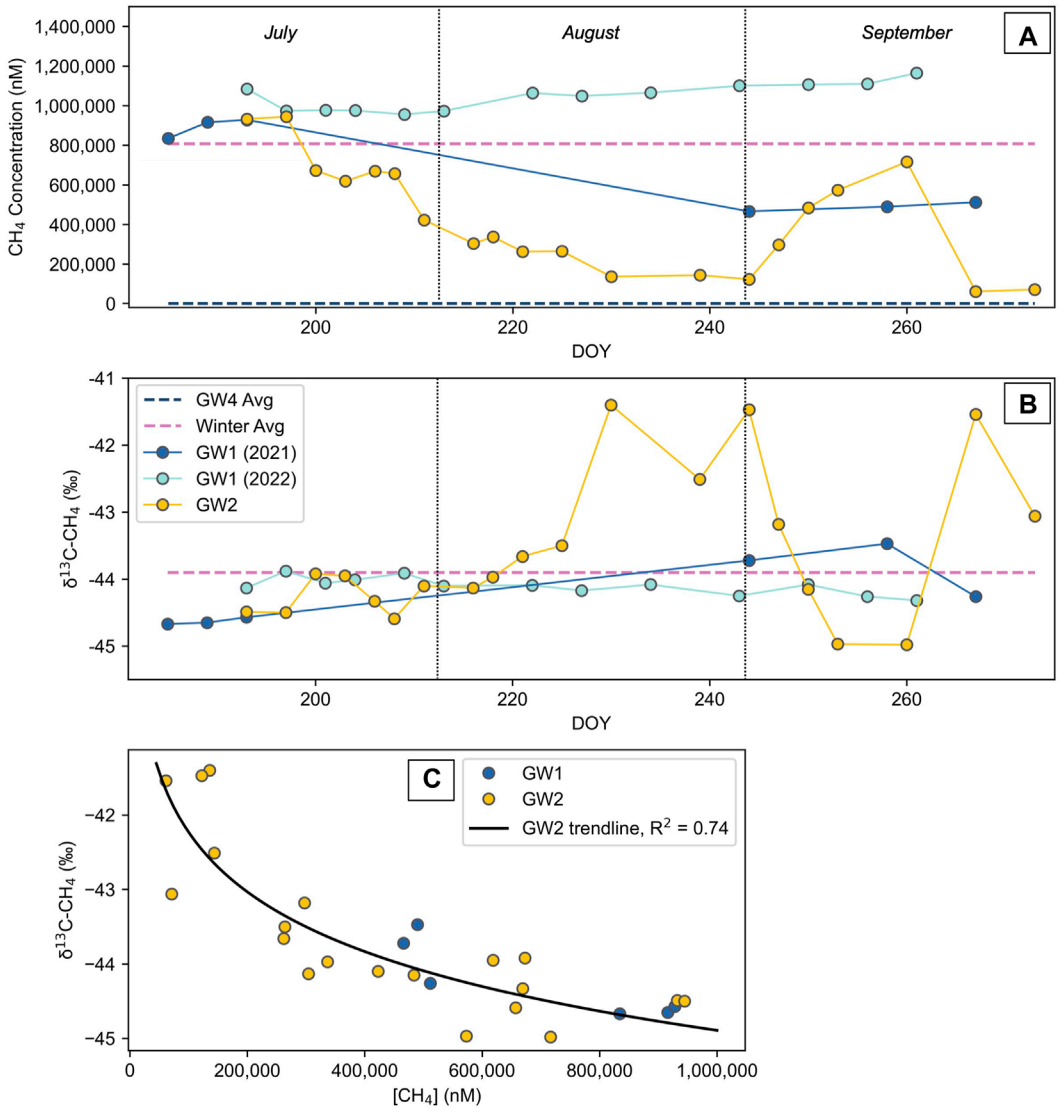

FIGURE 5
(A) Methane concentrations of the GW1 spring during summer 2021 and summer 2022 and the GW2 pool during summer 2021. Winter average concentrations (n=3) and the average of the GW4 pool during summer 2021 (n=2) are included. **(B)** The stable carbon isotopic compositions of the same sites listed above, except the GW4 pool. The legend in **(B)** applies to both plots. **(C)** Methane concentrations of the GW1 spring in 2021 and the GW2 pool plotted against the corresponding isotopic composition of carbon in methane.

One water sample taken from the winter icing during springtime and three samples taken during summer (including one from the GW1 spring and two from the GW2 pool) were analyzed for the concentration of ethane and propane to aid in the identification of a thermogenic gas source. The results are displayed in Table 1. Ethane was present in both the winter sample as well as the GW1 spring. Propane was only present in the winter sample. Neither gas was detected in the samples from the GW2 pool.

3.2 Microbial composition

Hight throughput sequencing of DNA of the 16S ribosomal RNA gene provide information on all sequences in the samples analyzed and might also originate from dead and inactive cells, or from extracellular DNA captured in the water. The direct examination of rRNA through RNA isolation has been found, in general, to be a more reliable indicator of cellular viability than rRNA gene targets. In an environment with low biological activity and has many dead and metabolically inactive cells, the rRNA fraction can provide a more ecologically relevant insight into the factors that drive microbial community dynamics (Gomez-Silvan et al., 2018). Here we refer to the DNA based sequences as the relative abundance of microorganisms and the RNA based sequences as the relatively active part of the community.

Methanogens were found with very low or no relative abundance in all groundwater samples taken apart from the GW1 spring,

10.3389/feart.2024.1340399

TABLE 1 Methane, ethane (C_2H_6) and propane (C_3H_8) concentrations of a selection of water samples.

	Date	[CH_4] (ppm)	[C_2H_6] (ppm)	[C_3H_8] (ppm)
Winter icing	21-Apr-21	11.8	52	44
GW1 spring	15-Sep-21	7.86	35	n.d
GW2 pool	12-Jul-21	15.0	n.d	n.d
GW2 pool	04-Sep-21	4.77	n.d	n.d

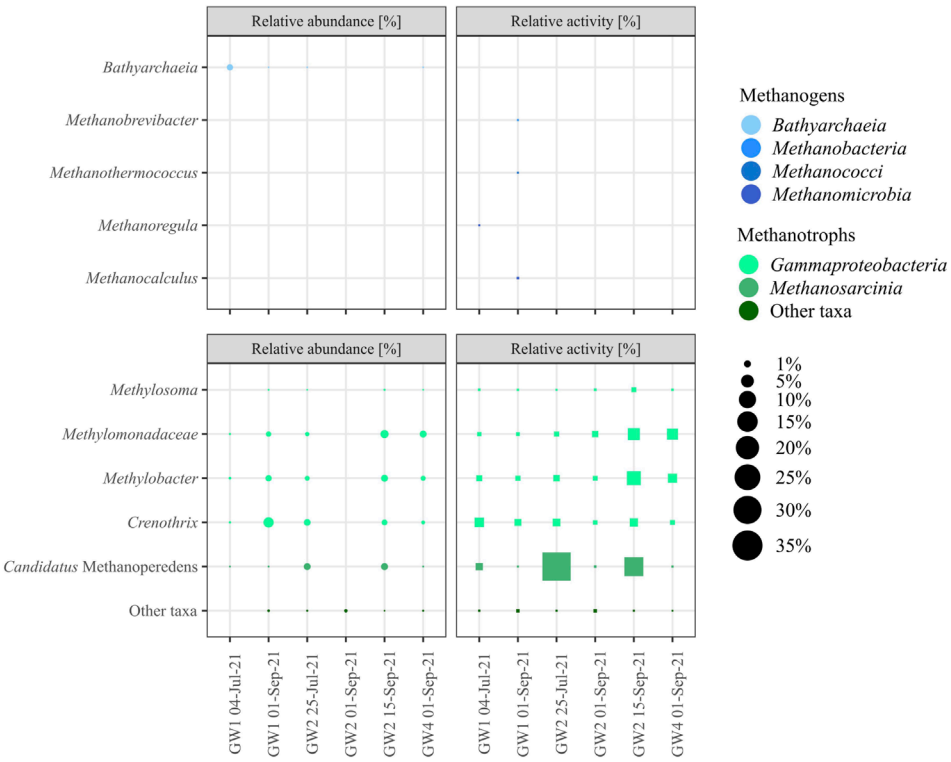

FIGURE 6
Relative abundance (●) and relative activity (■) of taxa associated with methanogenesis (blue, top two boxes) and methanotrophy (green, lower two boxes). Taxa with an average of relative abundance and activity <0.1% are summed as Other taxa.

which showed 1.2% relative abundance of *Bathyarchaeia* in early summer but just 0.01% later in the season (Figure 6). Similarly, the relative activity of methanogens was very low in all samples throughout the season, with no activity in the GW2 or GW4 pool and less than 0.1% relative rRNA sequence abundance in the GW1 spring. The community of methanotrophic bacteria and archaea was more abundant in the groundwater samples and was dominated by *Candidatus* Methanoperedens, *Crenothrix*, *Methylobacter*, and *Methylomonadaceae*. The highest relative abundance was found in GW1 in September (6.1%) and GW2 in mid-September (5.0%), whereas the highest relative activity was found with *Candidatus* Methanoperedens in the GW2 pool in late-July (33.2%) and mid-September (14.4%).

4 Discussion

4.1 Projected geochemistry of two discrete groundwater sources

Changes in the geochemistry of the GW2 pool throughout the summer suggest mixing of two discrete groundwater sources. The average composition of the GW4 groundwater pool and the groundwater sampled from the winter icing are shown as approximate endmember compositions of the two groundwater sources in Figures 2–5. Although these average compositions are based on few samples (GW4: $n = 2$, winter: $n = 3$), the geochemistry of the GW2 pool consistently fluctuated within the bounds of

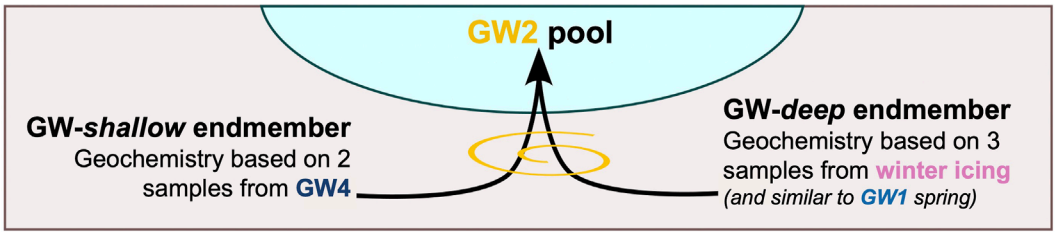

FIGURE 7
Mixing of the groundwater endmembers to form the GW2 pool.

these two average compositions and thus they represent a good approximation for projected endmembers. In addition, the notable similarity between the GW1 spring and the winter samples suggest the same source, which appears to maintain consistent geochemistry year-round, making it a likely primary groundwater source. Thus, the projected chemistry of the two groundwater sources that feed into the GW2 pool, hereafter referred to as "GW-*shallow*" and "GW-*deep*" and depicted in Figure 7, are represented by the GW4 pool and the groundwater that forms the winter icing, respectively.

Considering these endmembers, GW-*shallow* is characterized by a higher δ^2H and $\delta^{18}O$ (Figure 2), a slightly higher EC (Figure 3) and higher concentrations of Ca^{2+}, Mg^{2+}, K^+, and SO_4^{2-} (Figure 4). It is also more oxygenated (Figure 3), with DIC that is less enriched with ^{13}C (Figure 4) and relatively low levels of methane (~10^2–10^3 nM range, Figure 5). In contrast, GW-*deep* is characterized by distinctly different geochemistry: nearly anoxic water with higher concentrations of Na^+, Si, Cl^-, and HCO_3^-. It is also much more concentrated with aqueous methane (~10^6 nM). A summary of the average projected water chemistries of these two endmembers (Table 2) can be used to establish the provenance of their hydrological sources throughout the rest of this paper.

4.2 Origin of the GW-*shallow* endmember

The oxygen and hydrogen isotopic composition of the GW-*shallow* endmember lies within the range of isotopic composition measured in the main glacial melt river (Figure 2), suggesting the water is sourced by melting glacier ice. A lack of Cl^- in the GW-*shallow* endmember further hints that the water is not of recent meteoric origin where it would contain marine aerosols. The conservative behaviour of Cl^- within the glacial drainage system has meant that it is commonly used as a tracer for snowmelt (Tranter et al., 1993; Wadham et al., 1998; Hodson, 2006; Hodson and Yde, 2022). Chloride is released from the snow through snowpack elution while transforming into glacier ice, producing glacier ice with very little Cl^- to mobilize upon melting. A low Cl^- concentration is therefore further evidence supporting the notion that GW-*shallow* originates from melting glacier ice.

Rather than subglacial melt supplying the GW-*shallow* water, we suggest that it is sourced seasonally from buried glacier ice within the moraine. The groundwater springs are located approximately 250 m from the 2021 glacier margin at the edge of the floodplain formed by the main glacial melt river. In this area, the floodplain is bordered by moraine that was uncovered by the retreating glacier within the last 10 years and further bound by a lateral moraine flanking the neighbouring mountain (see Figure 1). The moraine is largely ice-cored, evident by patches of exposed, melting ice throughout the proglacial area and the flank of the mountain during summer. Observations in the field showed that many springs have formed beneath patches of buried ice, disappearing into moraine and resurfacing several times as the water flows towards the GW2 pool. Buried glacier ice within the active layer is recognized as a common contributor to groundwater systems in proglacial environments (Cooper et al., 2002; Levy et al., 2015).

Melting of buried ice is a seasonal phenomenon, requiring the active layer to thaw before heat can penetrate to melt the ice. This can delay the contribution of shallow groundwater sources such as buried ice, which then increase as the melt season proceeds and the active layer progressively deepens (Cooper et al., 2011). As such, a seasonal change should be observed in the contribution from GW-*shallow* to the GW2 pool. Using Cl^- (which is present in much higher concentrations in GW-*deep* than GW-*shallow*) as an indicator of the degree of mixing within the GW2 pool, we can assess the impact of seasonal air temperature changes on the proportion of GW2 that is sourced from GW-*shallow*. Figure 8 shows the variation of Cl^- concentrations in the GW2 pool throughout the summer plotted with average hourly air temperatures. High concentrations of Cl^- at the start of the melt season (~25 mg L^{-1}), similar to the GW-*deep* endmember value, indicate little to no contribution from GW-*shallow*. The delayed contribution from GW-*shallow*, followed by a progressive increase in the contribution from GW-*shallow*, is due to the thawing and gradual deepening of the active layer, which can begin after the recession of the snowpack at the start of the summer. This delay is later than would be expected if subglacial meltwaters were the source, as the isotopic composition of the water and low Cl^- concentrations in the melt river at this time indicate that glacier ice melt is already active and the primary contributor to the melt river. Later in the melt season, temperatures were near freezing during a cold period at the start of September, which coincided with a decrease in contribution from GW-*shallow* to GW2, likely due to a recess of moraine ice melt. This reverted when the temperatures began to increase again.

4.3 Geochemistry of the GW-*shallow* endmember

The short distance between the buried ice along the edge of the moraine and the GW2 pool (<500 m) limits the time available

TABLE 2 Average water chemistries of the GW-*shallow* and GW-*deep* endmembers. GW-*shallow* is based on average values of samples taken at GW4 during summer (n = 2). GW-*deep* is based on average values of samples taken from the winter icing (n = 3). Error ranges are based on two-times the standard deviation of n measurements and include analytical error.

	GW-*shallow*	GW-*deep*
EC (µS cm^{-1})	**574** (*517–631*)	**489** (*483–495*)
O_2 (mg L^{-1})	**6.1** (*2.3–9.9*)	**0.28** (*0.09–0.48*)
pH	**7.65** (*7.39–7.69*)	**8.50** (*8.15–8.85*)
$\delta^{18}O$-H_2O (‰)	**−13.3** (*−13.7–12.9*)	**−15.3** (*−15.5–15.1*)
$\delta^{2}H$-H_2O (‰)	**−94.7** (*-98.9–90.4*)	**−108.5** (*−110.3–106.7*)
$\delta^{13}C$-DIC (‰)	**−8.10** (*-8.20–8.00*)	**−11.61** (*−13.5–9.72*)
Ca^{2+} (ppm)	**75.3** (*56.9–93.7*)	**9.56** (*8.16–11.0*)
Ca^{2+} (meq L^{-1})	**3.76** (*2.84–4.69*)	**0.478** (*0.408–0.584*)
K^{+} (ppm)	**2.60** (*1.93–3.26*)	**1.10** (*0.818–1.38*)
K^{+} (meq L^{-1})	**0.067** (*0.050–0.084*)	**0.028** (*0.021–0.035*)
Mg^{2+} (ppm)	**16.9** (*13.1–20.7*)	**2.88** (*2.38–3.38*)
Mg^{2+} (meq L^{-1})	**1.41** (*1.09–1.72*)	**0.240** (*0.198–0.282*)
Na^{+} (ppm)	**21.8** (*18.5–25.2*)	**91.8** (*78.4–105*)
Na^{+} (meq L^{-1})	**0.948** (*0.803–1.09*)	**3.99** (*3.41–4.58*)
Si (ppm)	**1.33** (*1.17–1.49*)	**2.27** (*1.70–2.85*)
Si (mM)	**0.048** (*0.042–0.053*)	**0.081** (*0.061–0.10*)
Cl^{-} (ppm)	**3.78** (*2.43–5.13*)	**25.2** (*21.6–28.7*)
Cl^{-} (meq L^{-1})	**0.107** (*0.069–0.145*)	**0.710** (*0.610–0.810*)
SO_4^{2-} (ppm)	**212** (*160–263*)	**4.42** (*3.74–5.11*)
SO_4^{2-} (meq L^{-1})	**4.41** (*3.31–5.50*)	**0.092** (*0.078–0.11*)
HCO_3^{-} (ppm)	**87.5** (*63.2–112*)	**289** (*285–293*)
HCO_3^{-} (meq L^{-1})	**1.43** (*1.04–1.83*)	**4.74** (*4.68–4.81*)
CH_4 (nM)	**480** (*0–990*)	**808,000** (*615,000–1,000,000*)
$\delta^{13}C$-CH_4 (‰)		**−44** (*-45–43*)

for chemical weathering reactions to occur along the flowpath. However, the relatively high EC of the GW-*shallow* endmember (~575 µS cm^{-1}) suggests that the water must acquire ions rapidly by flowing through a highly reactive substrate such as glacial till. This near-surface, high rock-water contact environment facilitates efficient chemical weathering, including aerobic oxidation reactions that utilize oxygen readily acquired from the atmosphere.

Geochemical modelling by WEB-PHREEQ suggests that the GW-*shallow* endmember is undersaturated with respect to all minerals except iron-hydroxides, thus it is not expected that its major ion chemistry would be altered by mineral precipitation along its flowpath, but more by mineral dissolution. Among other ions, the GW-*shallow* endmember is characterized by high levels of Ca^{2+} (75.3 mg L^{-1}) and SO_4^{2-} (212 mg L^{-1}). While this could suggest the dissolution of an evaporite mineral such as gypsum, there is no known source of evaporite minerals in the local bedrock. Instead, the presence of Ca^{2+} and SO_4^{2-} in such high concentrations likely results from a shallow flowpath where secondary, or efflorescent, gypsum that has precipitated on the surface of the moraine dissolves into the groundwater. White, efflorescent salts were observed on the surface of the Vallåkrabreen moraine during the melt season, presumably formed by evaporative concentration of groundwater during summer or cryoconcentration during winter. Similar observations are common in proglacial water and moraines of other Arctic and Antarctic glaciers (Cooper et al., 2002; Bisson et al., 2015; Stachnik et al., 2016; Lehn et al., 2017; Puigdomenech et al., 2017; Deuerling et al., 2018). The molar ratio of SO_4^{2-}/Ca^{2+} (1.17) in GW-*shallow* suggests an excess of SO_4^{2-} above the 1:1 ratio that would be expected from the simple dissolution of gypsum, hinting that there is an additional source of SO_4^{2-}, or a reaction that is consuming calcium, such as carbonate mineral precipitation. We favor the former given the undersaturation of the groundwater with respect to carbonate mineral precipitation, although ion exchange reactions cannot be ruled out, which may remove calcium from the groundwater flow.

Pyrite (FeS_2) oxidation, a key weathering mechanism in many glacial environments, produces SO_4^{2-}. It also produces acidity which aids in the dissolution of carbonate and silicate minerals. The high concentration of SO_4^{2-} and the low concentration of HCO_3^{-} in the GW-*shallow* endmember suggests that pyrite oxidation is the prevailing producer of acidity. The sulfate mass fraction (SMF), can be calculated:

$$SMF = \frac{[SO_4^{2-}]}{[SO_4^{2-}] + [HCO_3^{-}]} \quad (1)$$

Equation 1 uses concentrations in molar equivalents. The SMF provides insights into chemical weathering reactions in a catchment. An SMF ratio of 0.5 suggests that sulfide oxidation coupled with carbonate dissolution is most prevalent (Tranter et al., 2002). Values <0.5 are associated with reactions driven by the dissolution of CO_2 with rock consisting of few sulfide minerals, or anoxic environments where microbial sulfide reduction consumes SO_4^{2-} and yields HCO_3^{-} (Wadham et al., 1998). In the case of the GW-*shallow* endmember, the SMF is >0.5 (at 0.75) which suggests that the dominant weathering reaction is sulfide oxidation coupled to silicate mineral dissolution. While both carbonate (siderite, calcite) and silicate (quartz, albite, microcline, chlorite, micas) minerals are present in the Carolinefjellet formation (Dixon, 2019), the HCO_3^{-} concentration is much too low for extensive carbonate mineral dissolution to be occurring and thus silicate mineral dissolution is expected to dominate the supply of cations to the GW-*shallow* endmember. This is not surprising considering that silicate minerals make up at least three-quarters of the grains within the Carolinefjellet formation (Maher et al., 2004). In addition, the carbon isotopic composition of DIC ($\delta^{13}C$-DIC, −8.1‰) is lower than what would be expected for carbonate mineral weathering, which typically yields isotopic ratios closer to 0‰, which is closer

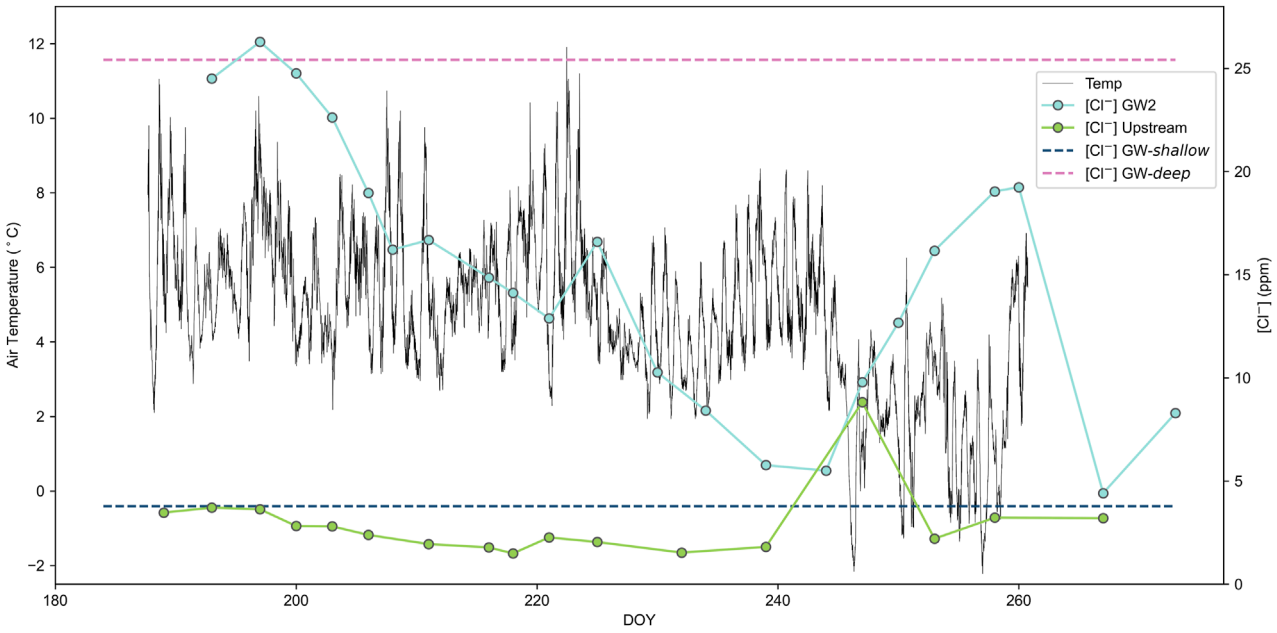

FIGURE 8
Cl-concentrations of the upstream river and GW2 pool throughout the summer with GW-*shallow* and GW-*deep* endmember concentrations plotted over the hourly air temperature.

to the 'average' $\delta^{13}C$ of carbonate minerals (Darling et al., 2006). The DIC is likely derived from a mix of processes, mainly the dissolution of atmospheric CO_2 due to the near-surface flowpath, with some carbonate mineral dissolution and the oxidation of organic carbon, which would produce DIC with a lower carbon isotopic composition.

There is very little methane present in the GW-*shallow* endmember (~477 nM) compared to concentrations measured in GW-*deep* (~808,000 nM). At such low methane concentrations and with trivial levels of methanogenic activity detected in the GW4 pool by 16S analysis (Figure 6) (GW4 is the groundwater that the GW-*shallow* endmember is founded on), it does not appear that methane is acquired or produced along the GW-*shallow* flowpath. Any methane that is present in the GW4 pool is likely introduced by minor mixing of groundwaters or nearby degassing of methane from the methane-rich groundwaters, as the groundwater springs and pools are in close proximity to each other.

In summary, the GW-*shallow* endmember is a seasonal, shallow, oxygenated groundwater system that is sourced from the melt of buried glacial ice within the moraine and is active only during the melt season. It flows through highly reactive glacial till where it weathers mostly silicate minerals, driven predominantly by sulfide mineral oxidation which depletes the water of some of its oxygen, presumably before consuming other electron acceptors. It exhibits open-system behavior due to its shallow flowpath that allows for some interaction and exchange with atmospheric gases, notably O_2 and CO_2. Methane is not expected to be acquired or produced in significant amounts along the flowpath of GW-*shallow*.

4.4 Origin of the GW-*deep* endmember

The GW-*deep* endmember is represented by the average chemistry of samples taken from the groundwater that forms the winter icing (n = 3). It is important to note that the chemistry of the GW1 spring throughout the summer is remarkably similar to the projected chemistry of the GW-*deep* endmember. Thus, it is assumed that the GW1 spring runs year-round and contributes substantially to the formation of the proglacial icing throughout the winter. This is also supported by the observation that the GW1 spring discharge did not appear to fluctuate with weather, precipitation or temperature throughout the summer, but rather its flow remained more or less constant.

The chemistry of the GW-*deep* endmember is distinct to that of GW-*shallow*, first evident by the isotopic composition of the water (Figure 2). The water is much more negative in its hydrogen and oxygen isotopic composition and closer to what would be expected from high-elevation snowmelt. Progressive isotopic fractionation during precipitation in mountainous regions, in which molecules containing heavier isotopes of hydrogen and oxygen preferentially partition from atmospheric water vapor, leads to snowpack that is more depleted in heavy isotopes with increasing altitude (Siegenthaler and Oeschger, 1980). Therefore, the isotopic composition of high-elevation snow tends to be more negative than snowpack at lower elevations, with $\delta^{18}O$-H_2O ratios found to decrease by about 0.48‰ per 100 m of increasing altitude in other regions of Svalbard (Pohjola et al., 2002).

The GW-*deep* endmember therefore likely originates from upper-catchment and high mountain snowmelt that enters storage in the sub-permafrost or sub-glacial environment through

discontinuities such as bergschrunds, crevasses, or fractures in the bedrock. Surprisingly, the water isotopic composition of the GW1 spring remained stable throughout the summer, with $\delta^{18}O$-H_2O only fluctuating between −15.10 and −15.40‰ and $\delta^{2}H$-H_2O between −107.3 and −108.4‰ (n=6). This suggests that the reservoir of snowmelt is large enough to supply the spring year-round and is not recharged by glacial melt during summer.

4.5 Geochemistry of the GW-*deep* endmember

Closed-system leaching experiments carried out on crushed rock samples from glacial catchments in Svalbard by Dixon (2019) suggest a larger degree of HCO_3^-, Na^+ and silica released from the upper Carolinefjellet formation and the overlying Eocene formations compared to the lower Carolinefjellet formation. In 6°C leaching experiments, HCO_3^- concentrations were up to 5.4-times higher after 11 days using rock powders from the upper Carolinefjellet formation than from the lower. Sodium concentrations were up to 20-times higher and silica up to 3.5-times higher. The dominance of HCO_3^-, Na^+ and silica in the GW-*deep* endmember is likely the result of a flowpath through the upper catchment within the upper Carolinefjellet formation and the overlying Eocene formations. Conversely, the other cations (Ca^{2+}, K^+ and Mg^{2+}) were leached at higher concentrations in the lower part of the Carolinefjellet formation, aligning more closely with the GW-*shallow* endmember.

A high concentration of Cl^- (25.2 mg L^{-1}) further supports that the GW-*deep* endmember is snowmelt-derived and indicates a significant contribution of major ions from marine aerosols. The Cl^- concentration is in a similar range to that of some glacial melt rivers on Svalbard during the early melt-season, when the river is predominantly snowmelt (Hodson and Yde, 2022). Sampling for this study did not begin until after the initial snowmelt had passed through the drainage system and so it is not possible to compare to the early melt-season discharge of Vallåkrabreen. Due to the high contribution from sea salt to the chemistry of the GW-*deep* endmember, standard marine ratios-to-chloride are used to remove the major ion contribution from seasalt aerosols and thus reveal the major ion concentrations of crustal provenance (denoted hereafter by '*').

The lack of oxygen in the GW-*deep* endmember requires a closed system with no interaction with the atmosphere. Any oxygen present in the snowmelt when it initially entered the groundwater system would have been depleted within the flowpath, probably due to a combination of the oxidation of sulfide minerals, such as pyrite, and methane oxidation. Weathering of pyrite produces sulfuric acid which lowers the pH of the water. With a pH of 8.30, as well as notably low concentrations of $^*SO_4^{2-}$ (the calculated contribution of sulfate from rock weathering), the GW-*deep* flowpath most likely runs through rocks that contain low abundances of pyrite, such that carbonic-acid weathering and hydrolysis reactions dominate.

Sodium is typically sourced from weathering of silicate minerals (Hodson et al., 2023) and thus high $^*Na^+$ concentrations (70.5 ppm) in the GW-*deep* endmember imply weathering of silicate minerals such as albite. Low concentrations of Ca^{2+} and Mg^{2+} suggest minimal carbonate mineral weathering; although cation exchange reactions, in which divalent cations are preferentially substituted for monovalent cations on exchange sites (Stumm and Morgan, 2012), may also account for the lack of Ca^{2+} and Mg^{2+} relative to HCO_3^-. While carbonic-acid weathering of both silicate and carbonate minerals may be occurring, the dominance of Na^+ suggests a greater occurrence of silicate mineral weathering.

Carbonic and sulfuric acid drives the weathering of carbonate and silicate minerals to produce distinctive ratios of cations to SO_4^{2-} and HCO_3^-. The molar equivalence ratio of the total sum of cations to HCO_3^- (*catsum/HCO_3^-), which should be unity or greater according to the idealized weathering products of these reactions, is 0.77 in the GW-*deep* endmember. This suggests a source of HCO_3^- in addition to any supplied by carbonate mineral dissolution. Additional sources of DIC can be derived from dissolved atmospheric CO_2 or DIC produced from aerobic bacterial respiration, however low oxygen levels in the GW-*deep* endmember suggest that the flowpath has little-to-no interaction with the atmosphere and thus neither CO_2 nor O_2 are readily available. Evidence for microbial sulfate reduction (MSR), a microbially-mediated process that occurs in anoxic environments, consuming sulfate and producing HCO_3^{2-} and HS^-, has been found in the subglacial environment of glaciers in Svalbard and Greenland (Lauritzen and Bottrell, 1994; Skidmore et al., 2000; Wadham et al., 2004; Hodson et al., 2023). Considering the notably low $^*SO_4^{2-}$ concentration (0.95 mg L^{-1}, SMF = 0.004) and lack of oxygen in GW-*deep*, the additional source of HCO_3^- could rather be from microbial sulfate reduction. It is worth noting that a strong smell of HS^- was observed at the GW1 site as well as at the winter icing.

There are several potential sources of organic carbon that can be used as the electron donor in microbial sulfate reduction, including hydrocarbons, kerogen in the bedrock and microbial necromass (Wadham et al., 2004). Due to the high concentration of methane present in the GW-*deep* endmember (>800,000 nM), we surmise that the anaerobic oxidation of methane (AOM) coupled to sulfate reduction (sulfate-driven AOM) is occurring. This process should result in a DIC pool that is depleted in ^{13}C because methane is exceptionally depleted in ^{13}C and when it is oxidized, it adds its highly negative $\delta^{13}C$ to the DIC pool. The $\delta^{13}C$ of the methane in the GW-*deep* endmember is −43.9‰, thus the $\delta^{13}C$-DIC (−11.6‰) of the GW-*deep* endmember suggests that the DIC is sourced from a mixture of sulfate-driven AOM and some dissolution of carbonate minerals. Measurements of the sulfur and oxygen isotopic composition of the sulfate would be useful to substantiate if sulfate-driven AOM is occurring in the GW-*deep* endmember.

An upper catchment or high mountain source suggests a much longer flowpath and travel time for the GW-*deep* endmember than the GW-*shallow* endmember, however the EC of GW-*deep* is consistently within a narrow range that is slightly lower than the EC of GW-*shallow*. This is likely due to a flowpath through fractured bedrock with less surface area for rock-water interaction, as opposed to comminuted glacial till. It is expected that within this bedrock, geologic methane is introduced to the groundwater. The $\delta^{13}C$-CH_4 of the GW-*deep* endmember (−43.9‰ on average, n=3), the presence of ethane (C_2H_6) and propane (C_3H_8) gases in the formation water of the winter icing and the GW1 spring (Table 1), and a lack of active methanogenic microbial communities in all groundwaters (Figure 6) suggest a thermogenic source of the methane. The methane is thus introduced in a pressurized

environment, allowing the concentrations to reach extreme levels of supersaturation, up to 275,000 times the concentration at equilibrium with the atmosphere. As the groundwater reaches the surface and the pressure reduces, the methane begins to rapidly degas from solution and causes ebullition, which was observed at the site in both summer and winter.

The methane gas is presumed to originate in the Agardhfjellet formation, a Middle Jurassic geologic formation containing organic-rich black shale that lies beneath the Carolinefjellet formation. The Agardhfjellet formation is a well-known source rock for petroleum on Svalbard (Leith et al., 1993) and is also known to contain C_1-C_4 gaseous hydrocarbons within fluid inclusions (Abay et al., 2017). Abay et al. (2017) determined that petroleum and thermogenic gaseous hydrocarbons (67.8% C_1 and 32.1% C_{2-4}) identified in outcrop samples of the Carolinefjellet formation had originated and migrated upward from the Agardhfjellet formation. It is expected that the gases introduced to the GW-*deep* groundwater are also derived from the Jurassic shales of the Agardhfjellet formation and have migrated upwards to the Carolinefjellet formation, where they became trapped beneath glacier ice and permafrost.

In summary, the GW-*deep* endmember is a deeper, anoxic groundwater that is sourced from high-elevation snowmelt. It is stored in a fracture-dominated hard rock aquifer that is likely present within the upper Carolinefjellet formation, where it acquires substantial amounts of thermogenic methane. The GW-*deep* groundwater system is perennial, and thus continues to flow throughout the winter, bringing methane gas to the surface year-round. Its residence time within the aquifer must be greater than 1 year, allowing for a steady state system that yields a groundwater with water chemistry and a flow rate that is constant year-round. It exhibits a more closed-system behavior due to its lack of interaction with the atmosphere, as is expected with a deep groundwater flowpath. A conceptual model of groundwater flow in the Vallåkrabreen catchment is presented in Figure 9.

4.6 Methanotrophy in GW1

The drop in methane concentration in GW1 observed at the end of summer 2021 (Figure 5) is likely due to an introduction of oxygen to the groundwater flowpath. The oxygen is potentially introduced through mixing with another groundwater source or subglacial melt water, although the degree of mixing is likely to be minor considering that the geochemistry of the GW1 spring exhibited very little change (Figure 4). The measured oxygen concentration changed from approximately 0.65 mg L^{-1} at the start of the summer to 4.0 mg L^{-1} at the end. While much of the measured geochemistry showed only slight changes, such as the isotopic composition of the water and most ion concentrations, the introduction of oxygen will have changed the redox environment of the system. It is likely that this inhibited microbial sulfate reduction, leading to higher concentrations of sulfate, and likely caused more efficient aerobic methane oxidation (MOx), leading to lower concentrations of methane.

Methylobacter is a prevalent, abundant and environmentally important methanotroph found in the high Arctic wetland soil of Svalbard (Wartiainen et al., 2003) and is known to oxidize methane under aerobic conditions in freshwater environments (Pester et al., 2004). *Methylobacter* has been identified in all sampled groundwaters from the Vallåkrabreen forefield (Figure 6). These methanotrophs can be stimulated by the addition of oxygen (Rothfuss et al., 1997) and thus may have become more active in the GW1 spring later in the 2021 season when oxygen was introduced to the system. This is also reflected in a slight enrichment of ^{13}C in the residual methane (Figure 5).

4.7 Methanotrophy in GW2

While the variation in methane concentrations of the GW2 pool is driven partly by the degree of mixing between GW-*shallow* and GW-*deep*, there is evidence that methanotrophy along the groundwater flowpath is also influencing these values. The isotopic composition of the methane becomes more enriched in ^{13}C in GW2 samples with lower methane concentrations (Figure 5), which may be the result of methanotrophic microbes preferentially oxidizing molecules with the lighter ^{12}C. Methanotropic bacteria and archaea were found to be abundant and active in all groundwaters (Figure 6), with a high relative activity of *Candidatus* Methanoperedens (33.2% relative 16S rRNA sequence abundance in the sample of the GW2 pool taken on 25 July 2021), hinting that methanotrophic communities act as a methane sink along the flowpath of each endmember.

To determine the extent of methanotrophy that may be occurring, a methane deficit was calculated for each GW2 sample. First, the impact upon the methane concentrations due to mixing was considered. The δ^2H of water was used as a tracer for the GW-*deep* endmember to determine the fraction of each GW2 sample that is likely sourced from GW-*deep*. Assuming all methane is sourced from GW-*deep*, an expected methane concentration was calculated, removing the impact of mixing. This expected methane concentration was then compared to the measured concentrations to determine a deficit.

A linear regression between the δ^2H-H_2O and the methane concentration of the two endmembers, plotted as a line in Figure 10, is used to determine the contribution from GW-*deep* and thus the expected methane concentration. All samples that plot below the trendline in Figure 10 suggest a quantifiable methane deficit, while all samples that plot above the trendline suggest a methane surplus. Most samples exhibit a methane deficit.

The methane deficits are plotted against the corresponding $\delta^{13}C$ of methane in Figure 11A, and shaded according to their dissolved oxygen content. Figure 11A suggests that the deficits of methane are due to methanotrophy along the GW2 flowpath. As expected, larger methane deficits correspond with methane more enriched in the heavier carbon isotope (R^2 = 0.69). This is likely the result of the preferential uptake of the lighter isotope during methanotrophy, leaving behind a methane pool that's more enriched in the heavier isotope. Larger methane deficits are also found to correspond with more oxygenated water (Figure 11A), likely due to stimulated aerobic methane oxidation (MOx) in the presence of oxygen.

Temporally examining the extent of methane deficiency throughout the melt season in Figure 11C suggests that the methane deficiency and the corresponding enrichment of ^{13}C in the methane are driven by the extent of oxygenation in the water. The level of

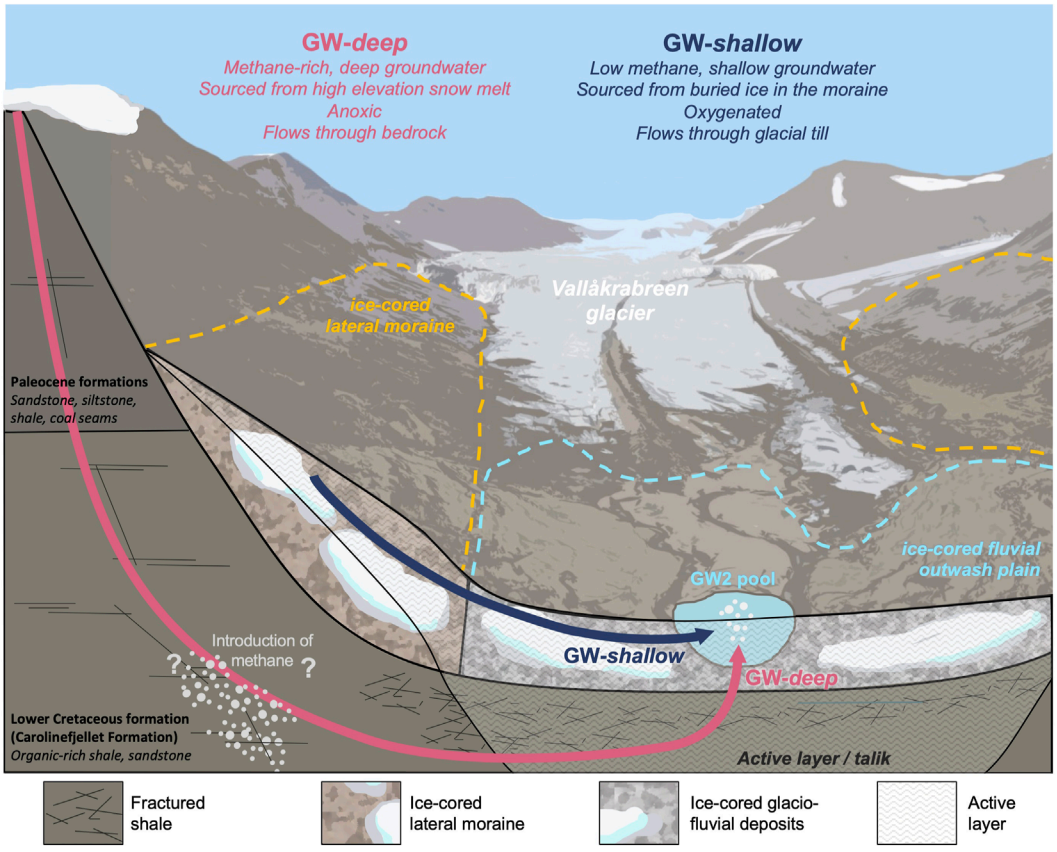

FIGURE 9
Conceptual model of groundwater flow in the Vallåkrabreen catchment.

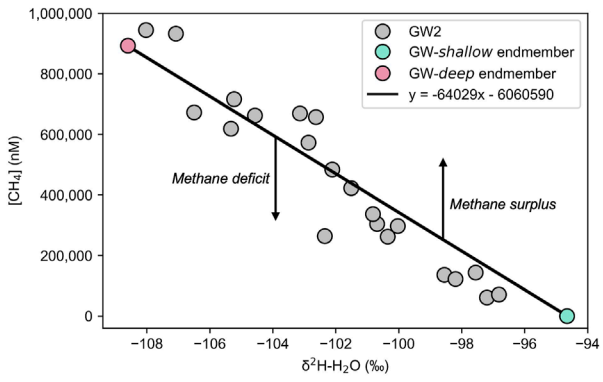

FIGURE 10
Linear regression for methane deficit calculation. Measured methane concentrations and δ^2H of sample water are plotted for each GW2 sample taken throughout the 2021 summer. The GW-*shallow* and GW-*deep* endmembers are plotted with a linear regression line between.

oxygen in the GW2 pool is regulated by its relative contribution of the GW-*shallow* endmember, which slowly increases at the start of the melt season as the active layer progressively thaws and releases more melt from buried ice in the moraine. The system reverts to low oxygen and thus low methane deficits when the air temperatures decrease in mid-September and the melt of buried ice is reduced.

The methane deficit calculations suggest that microbial activity is likely a significant methane sink within the GW2 flowpath, especially when oxygen is available for more efficient oxidation. The deficit calculations suggest that this oxygenation has led to variable consumption of the methane within the GW2 flowpath—reducing an average of 29% (±14%) of the methane throughout the summer and up to 62% (±14%) when the water was most oxygenated in mid-summer. This implies that the melt season methane emissions from groundwater within the Vallåkrabreen catchment are likely to be lower than the emissions occurring throughout the rest of the year due to the mixing of oxygen-rich waters that are active during summer.

4.8 Methane surplus in GW2

The methane deficit calculations in the previous subsection suggest that the GW2 pool exhibits a surplus of methane in some cases, up to 29% (±14%) above what would be expected from a GW-*deep* contribution alone. The presence of thermogenic methane, which may lead to the system being depleted of its

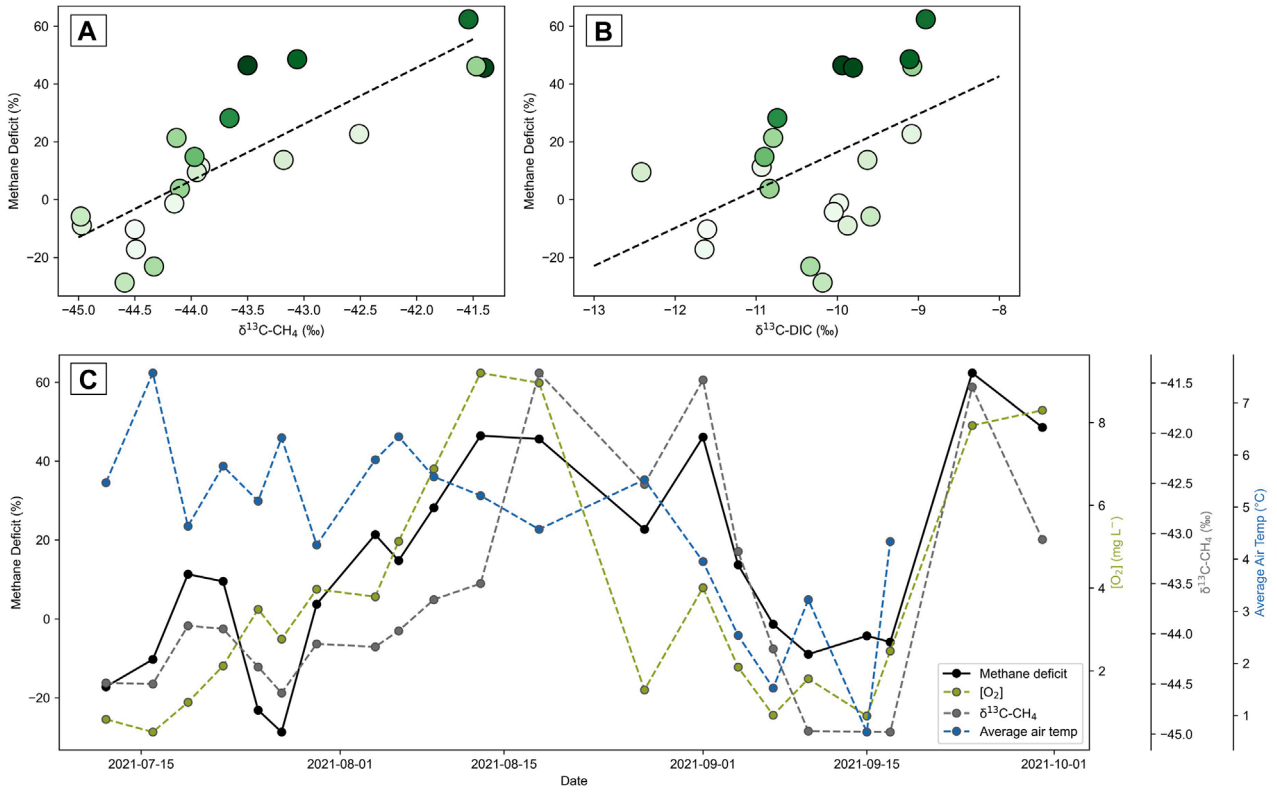

FIGURE 11
Methane deficit (%) of the GW2 pool, determined by the δ2H of water, plotted against the corresponding **(A)** $\delta^{13}C$ of methane and **(B)** $\delta^{13}C$ of DIC. Positive values represent a deficit of methane and negative values represent a surplus of methane, above the expected amount. Markers are colored on a linear scale according to dissolved oxygen (DO) content. Lighter greens represent lower DO, down to 0.52 mg L^{-1}, while darker greens represent higher DO, up to 9.2 mg L^{-1}. The trendline plotted in **(A)** has R^2 = 0.69 and **(B)** has R^2 = 0.23. **(C)** Methane deficit of the GW2 pool is plotted temporally with DO, the $\delta^{13}C$ of methane and the average air temperature of the sampling day.

oxygen through methane oxidation, can generate a low redox environment that is conducive for methanogenesis. This has been observed beneath the Icelandic glacier, Sólheimajökull, where the introduction of reduced volcanic gases lowers the redox status of the subglacial environment, facilitating the production of methane and preventing its consumption (Burns et al., 2018). In the case of the GW2 pool however, no activity of microbial methanogenic communities was found (Figure 6). One might also hypothesize that additional microbial methanogenesis would change both the $\delta^{13}C$ of the methane and the residual DIC, which is not observed (Figure 11B) (Whiticar, 1999). Thus, we conclude that microbial methane production is not a significant contributor to the methane levels in the GW2 pool.

Instead, the surplus methane is likely due to accumulation and freeze-concentration of methane beneath ice. Samples that show a methane surplus occur within two time periods: the start of the summer season and a cold period during mid-September (Figure 11C). At the start of the summer, methane that has accumulated beneath the winter icing may still be flushed out of the groundwater system, as there were still remnants of the winter icing in the flood plain. During mid-September, low air temperatures led to a thin layer of ice forming on the surface of the GW2 pool which could have trapped methane and elevated concentrations within the water. A reduced contribution from GW-*shallow* due to a reduction in the rate of buried ice ablation means that less oxygen was available in the groundwater mixture to promote methane oxidation, allowing for the methane to accumulate. In addition, partial freezing of the pool may have led to some freeze-concentration of methane in the water. Neither of these processes are related to any significant kinetic isotopic fractionation and thus they are more likely to explain the methane surpluses observed.

In summary, the thermogenic methane present in the groundwater springs within the Vallåkrabreen catchment does not appear to be supplemented by the microbial production of methane.

4.9 Implications

Our findings demonstrate how shallow and deeper groundwaters interact to control methane dynamics in glacierized environments within permafrost regions. However, ratios of the differing groundwater sources will change markedly in years to come. Climatic changes are leading to larger storage capacities of aquifers and increased summer recharge of groundwater aquifers in glacierized catchments across the Arctic (Liljedahl et al., 2017). Such changes are likely to expand aquifers that store methane-super-saturated groundwaters and increase the recharge of aquifers supplied by upper-catchment precipitation. Therefore, the contribution of deep groundwaters to total runoff may increase.

Conversely, as the summer melt season is prolonged due to rising air temperatures, the period in which shallow, oxygenated groundwater is available to oxidise methane may increase, thus reducing yearly emissions. However, as glaciers are reduced in size and more buried ice has melted out of the moraine, less glacier ice will be available to produce shallow, oxygenated groundwaters during summer. These changes may ultimately lead to less oxidation of methane in the future and, in turn, larger overall methane emissions. Deep, methane-rich groundwaters will become increasingly important to catchment runoff chemistry and methane dynamics.

4.10 Conclusion

The objectives of this study were to identify and characterize the active groundwater in the Vallåkrabreen catchment, while also establishing their provenance and their role in methane dynamics. This study concludes that two dominant groundwater sources interact within the Vallåkrabreen catchment to moderate methane emissions during the melt season. One is a seasonal, shallow oxygenated groundwater system that is sourced from the melt of buried glacial ice within the moraine and is active only during the melt season. The other is a deeper, anoxic groundwater that is sourced from high-elevation snowmelt and acquires substantial amounts of geologic methane along its flowpath. This deep groundwater system is perennial, and thus it continues to flow throughout the winter, bringing methane gas to the surface year-round.

During summer, methane-rich deep groundwaters are diluted and oxidized by shallow groundwaters, invoking more efficient methanotrophic communities and tempering the release of methane to the Arctic atmosphere. This has led to an average reduction of 29% (±14%) of potential emissions from the GW2 spring. Given that the oxygenated shallow groundwaters are not expected to be as active outside of the melt season, it is likely that these oxygenation processes are less efficient throughout the rest of the year. A reduction in the efficiency of the microbial methane sink within the groundwater flowpaths may lead to higher net methane release to the atmosphere. Therefore, the melt season methane emissions from groundwater in the Vallåkrabreen catchment are likely to be lower than the emissions occurring throughout the rest of the year.

In summary, this study has demonstrated that during the Arctic summer, methane emissions from proglacial groundwaters are regulated by subsurface oxidation. Oxygenated groundwater that is only active during the melt season is mixed with anoxic, methane-rich groundwater that flows year-round. The introduction of oxygen induces more efficient microbial consumption of methane and thereby reduces potential methane emissions. Microbial activity is an important moderator of methane emissions from proglacial groundwaters during the Arctic summer.

Data availability statement

The datasets presented in this study can be found in online repositories. The names of the repository/repositories and accession number(s) can be found below: https://zenodo.org/records/10600361, PRJEB60294.

Author contributions

GEK: Conceptualization, Data curation, Formal Analysis, Funding acquisition, Investigation, Methodology, Project administration, Visualization, Writing–original draft. LM: Investigation, Visualization, Writing–review and editing. AVT: Supervision, Resources, Writing–review and editing. KR: Formal Analysis, Writing–review and editing. ST: Data curation, Formal Analysis, Writing–review and editing. ML: Formal Analysis, Writing–review and editing. KH: Formal Analysis, Methodology, Writing–review and editing. LØ: Writing–review and editing. AH: Conceptualization, Funding acquisition, Investigation, Project administration, Resources, Supervision, Writing–review and editing.

Funding

The author(s) declare financial support was received for the research, authorship, and/or publication of this article. This research was supported by grants awarded by The Research Council of Norway to GEK (RCN project no. 329174) and AH (RCN project no. 294764).

Acknowledgments

We thank Yizhu Zhu and Mark Trimmer for their support with the methane analysis at the School of Biological and Behavioural Sciences, Queen Mary University of London. We thank the governor of Svalbard for granting us access to restricted zones to conduct fieldwork, as well as Sara Mollie Cohen and the rest of the UNIS Logistics team for their field support. We are grateful to Marjolein Gevers for her help in the field.

Conflict of interest

The authors declare that the research was conducted in the absence of any commercial or financial relationships that could be construed as a potential conflict of interest.

Publisher's note

References

Abay, T. b., Karlsen, D. a., Lerch, B., Olaussen, S., Pedersen, J. h., and Backer-Owe, K. (2017). Migrated petroleum in outcropping mesozoic sedimentary rocks in spitsbergen: organic geochemical characterization and implications for regional exploration. *J. Petroleum Geol.* 40, 5–36. doi:10.1111/jpg.12662

Andermann, C., Longuevergne, L., Bonnet, S., Crave, A., Davy, P., and Gloaguen, R. (2012). Impact of transient groundwater storage on the discharge of Himalayan rivers. *Nat. Geosci.* 5, 127–132. doi:10.1038/ngeo1356

Apprill, A., McNally, S., Parsons, R., and Weber, L. (2015). Minor revision to V4 region SSU rRNA 806R gene primer greatly increases detection of SAR11 bacterioplankton. *Aquat. Microb. Ecol.* 75, 129–137. doi:10.3354/ame01753

Bælum, K., and Benn, D. I. (2011). Thermal structure and drainage system of a small valley glacier (Tellbreen, Svalbard), investigated by ground penetrating radar. *Cryosphere* 5, 139–149. doi:10.5194/tc-5-139-2011

Bisson, K. M., Welch, K. A., Welch, S. A., Sheets, J. M., Lyons, W. B., Levy, J. S., et al. (2015). Patterns and processes of salt efflorescences in the McMurdo region, Antarctica. *Arct. Antarct. Alp. Res.* 47, 407–425. doi:10.1657/AAAR0014-024

Bukowska-Jania, E., and Szafraniec, J. (2005). Distribution and morphometric characteristics of icing fields in Svalbard. *Polar Res.* 24, 41–53. doi:10.3402/polar.v24i1.6252

Burns, R., Wynn, P. M., Barker, P., McNamara, N., Oakley, S., Ostle, N., et al. (2018). Direct isotopic evidence of biogenic methane production and efflux from beneath a temperate glacier. *Sci. Rep.* 8, 17118. doi:10.1038/s41598-018-35253-2

Callahan, B. J., McMurdie, P. J., Rosen, M. J., Han, A. W., Johnson, A. J. A., and Holmes, S. P. (2016). DADA2: high-resolution sample inference from Illumina amplicon data. *Nat. Methods* 13, 581–583. doi:10.1038/nmeth.3869

Carey, K. L. (1973). *Icings developed from surface water and ground water 73*.

Chesnokova, A., Baraër, M., and Bouchard, É. (2020a). Proglacial icings as records of winter hydrological processes. *Cryosphere* 14, 4145–4164. doi:10.5194/tc-14-4145-2020

Chesnokova, A., Baraër, M., Laperrière-Robillard, T., and Huh, K. (2020b). Linking Mountain glacier retreat and hydrological changes in southwestern yukon. *Water Resour. Res.* 56, e2019WR025706. doi:10.1029/2019WR025706

Cooper, R., Hodgkins, R., Wadham, J., and Tranter, M. (2011). The hydrology of the proglacial zone of a high-Arctic glacier(Finsterwalderbreen, Svalbard): sub-surface water fluxes and complete water budget. *J. Hydrology* 406, 88–96. doi:10.1016/j.jhydrol.2011.06.008

Cooper, R. J., Wadham, J. L., Tranter, M., Hodgkins, R., and Peters, N. E. (2002). Groundwater hydrochemistry in the active layer of the proglacial zone, Finsterwalderbreen, Svalbard. *J. Hydrology* 269, 208–223. doi:10.1016/S0022-1694(02)00279-2

Dallmann, W. K. (2015). *Geoscience atlas of svalbard*. Tromsø, Norway: Norsk Polarinstitutt.

Danilovich, I., Zhuravlev, S., Kurochkina, L., and Groisman, P. (2019). The past and future estimates of climate and streamflow changes in the western dvina river basin. *Front. Earth Sci.* 7. doi:10.3389/feart.2019.00204

Darling, W. G., Bath, A. H., Gibson, J. J., and Rozanski, K. (2006). "ISOTOPES IN WATER," in *Isotopes in palaeoenvironmental research, developments in paleoenvironmental research*. Editor M. J. Leng (Netherlands, Dordrecht: Springer), 1–66. doi:10.1007/1-4020-2504-1_01

Deuerling, K. M., Martin, J. B., Martin, E. E., and Scribner, C. A. (2018). Hydrologic exchange and chemical weathering in a proglacial watershed near Kangerlussuaq, west Greenland. *J. Hydrology* 556, 220–232. doi:10.1016/j.jhydrol.2017.11.002

Dixon, T. J. (2019). *Geogenic nitrogen as a nutrient source to subglacial microbial ecosystems 365*.

Douglas, G. M., Maffei, V. J., Zaneveld, J. R., Yurgel, S. N., Brown, J. R., Taylor, C. M., et al. (2020). PICRUSt2 for prediction of metagenome functions. *Nat. Biotechnol.* 38, 685–688. doi:10.1038/s41587-020-0548-6

Gomez-Silvan, C., Leung, M. H. Y., Grue, K. A., Kaur, R., Tong, X., Lee, P. K. H., et al. (2018). A comparison of methods used to unveil the genetic and metabolic pool in the built environment. *Microbiome* 6, 71. doi:10.1186/s40168-018-0453-0

Grüning, B., Dale, R., Sjödin, A., Chapman, B. A., Rowe, J., Tomkins-Tinch, C. H., et al. (2018). Bioconda: sustainable and comprehensive software distribution for the life sciences. *Nat. Methods* 15, 475–476. doi:10.1038/s41592-018-0046-7

Hambrey, M. J., Murray, T., Glasser, N. F., Hubbard, A., Hubbard, B., Stuart, G., et al. (2005). Structure and changing dynamics of a polythermal valley glacier on a centennial timescale: midre Lovénbreen, Svalbard. *J. Geophys. Res. Earth Surf.* 110. doi:10.1029/2004JF000128

Hodgkins, R. (1997). GLACIER HYDROLOGY IN SVALBARD, NORWEGIAN HIGH ARCTIC. *Quat. Sci. Rev.* 16, 957–973. doi:10.1016/s0277-3791(97)00032-2

Hodgkins, R., Tranter, M., and Dowdeswell, J. A. (2004). The characteristics and formation of a high-arctic proglacial icing. *Geogr. Ann. Ser. A, Phys. Geogr.* 86, 265–275. doi:10.1111/j.0435-3676.2004.00230.x

Hodson, A. (2006). Biogeochemistry of snowmelt in an Antarctic glacial ecosystem. *Water Resour. Res.* 42. doi:10.1029/2005WR004311

Hodson, A., Kleber, G., Johnson, J., Lonardi, M., Petroselli, C., Dixon, T., et al. (2023). Effects of glacier retreat upon glacier-groundwater coupling and biogeochemistry in Central Svalbard. *J. Hydrology* 624, 129894. doi:10.1016/j.jhydrol.2023.129894

Hodson, A. J., and Yde, J. C. (2022). "4.15 - the geochemistry of glacial meltwaters," in *Treatise on geomorphology* J. Shroder, and F. Jack 2 (Oxford: Academic Press), 290–304. doi:10.1016/B978-0-12-818234-5.00145-0

Humlum, O., Instanes, A., and Sollid, J. L. (2003). Permafrost in Svalbard: a review of research history, climatic background and engineering challenges. *Polar Res.* 22, 191–215. doi:10.1111/j.1751-8369.2003.tb00107.x

Kleber, G. E., Hodson, A. J., Magerl, L., Mannerfelt, E. S., Bradbury, H. J., Zhu, Y., et al. (2023). Groundwater springs formed during glacial retreat are a large source of methane in the high Arctic. *Nat. Geosci.* 16, 597–604. doi:10.1038/s41561-023-01210-6

Lammers, R. B., Shiklomanov, A. I., Vörösmarty, C. J., Fekete, B. M., and Peterson, B. J. (2001). Assessment of contemporary Arctic river runoff based on observational discharge records. *J. Geophys. Res. Atmos.* 106, 3321–3334. doi:10.1029/2000JD900444

Lauritzen, S., and Bottrell, S. (1994). Microbiological activity in thermoglacial karst springs, south spitsbergen. *Geomicrobiol. J.* 12, 161–173. doi:10.1080/01490459409377983

Lehn, G. O., Jacobson, A. D., Douglas, T. A., McClelland, J. W., Barker, A. J., and Khosh, M. S. (2017). Constraining seasonal active layer dynamics and chemical weathering reactions occurring in North Slope Alaskan watersheds with major ion and isotope (δ34SSO4, δ13CDIC, 87Sr/86Sr, δ44/40Ca, and δ44/42Ca) measurements. *Geochimica Cosmochimica Acta* 217, 399–420. doi:10.1016/j.gca.2017.07.042

Leith, T. L., Weiss, H. M., Mørk, A., århus, N., Elvebakk, G., Embry, A. F., et al. (1993). "Mesozoic hydrocarbon source-rocks of the Arctic region," in *Norwegian petroleum society special publications*. Editors T. O. Vorren, E. Bergsager, Ø. A. Dahl-Stamnes, E. Holter, B. Johansen, E. Lie, et al. (Amsterdam, Netherlands: Elsevier), 1–25. doi:10.1016/B978-0-444-88943-0.50006-X

Levy, A., Robinson, Z., Krause, S., Waller, R., and Weatherill, J. (2015). Long-term variability of proglacial groundwater-fed hydrological systems in an area of glacier retreat, Skeiðarársandur, Iceland. *Earth Surf. Process. Landforms* 40, 981–994. doi:10.1002/esp.3696

Liljedahl, A. K., Gädeke, A., O'Neel, S., Gatesman, T. A., and Douglas, T. A. (2017). Glacierized headwater streams as aquifer recharge corridors, subarctic Alaska. *Geophys. Res. Lett.* 44, 6876–6885. doi:10.1002/2017GL073834

Lovell, H., Fleming, E. J., Benn, D. I., Hubbard, B., Lukas, S., and Naegeli, K. (2015). Former dynamic behaviour of a cold-based valley glacier on Svalbard revealed by basal ice and structural glaciology investigations. *J. Glaciol.* 61, 309–328. doi:10.3189/2015JoG14J120

Macheret, Y., Glazovsky, A., and Lavrentiev, I. (2019). Distribution of cold and temperate ice and water in glaciers at Nordenskiöld Land, Svalbard, according to data on ground-based radio-echo sounding. *Bull. Geogr. Phys. Geogr. Ser.* 17, 77–90. doi:10.2478/bgeo-2019-0016

Maher, Jr., Hays, T., Shuster, R., and Mutrux, J. (2004). Petrography of lower cretaceous sandstones on spitsbergen. *Polar Res.* 23, 147–165. doi:10.3402/polar.v23i2.6276

Makarieva, O., Nesterova, N., Post, D. A., Sherstyukov, A., and Lebedeva, L. (2019). Warming temperatures are impacting the hydrometeorological regime of Russian rivers in the zone of continuous permafrost. *Cryosphere* 13, 1635–1659. doi:10.5194/tc-13-1635-2019

Mallinson, L., Swift, D. A., and Sole, A. (2019). Proglacial icings as indicators of glacier thermal regime: ice thickness changes and icing occurrence in Svalbard. *Geogr. Ann. Ser. A, Phys. Geogr.* 101, 334–349. doi:10.1080/04353676.2019.1670952

Mazerolle, M. J. (2020). *AICcmodavg: model selection and multimodel inference based on (Q)AIC(c)*.

McMurdie, P. J., and Holmes, S. (2013). Phyloseq: an R package for reproducible interactive analysis and graphics of microbiome census data. *PLOS ONE* 8, e61217. doi:10.1371/journal.pone.0061217

Moorman, B. J. (2003). *Glacier-Permafrost hydrology interactions, bylot island, Canada 6*.

Moorman, B. J., and Michel, F. A. (2000). Glacial hydrological system characterization using ground-penetrating radar. *Hydrol. Process.* 14, 2645–2667. doi:10.1002/1099-1085(20001030)14:15<2645::AID-HYP84>3.0.CO;2-2

Mutrux, J., Maher, H., Shuster, R., and Hays, T. (2008). Iron ooid beds of the Carolinefjellet formation, spitsbergen, Norway. *Polar Res.* 27, 28–43. doi:10.1111/j.1751-8369.2007.00039.x

Nuth, C., Kohler, J., König, M., von Deschwanden, A., Hagen, J. O., Kääb, A., et al. (2013). Decadal changes from a multi-temporal glacier inventory of Svalbard. *Cryosphere* 7, 1603–1621. doi:10.5194/tc-7-1603-2013

Ó Dochartaigh, B. É., MacDonald, A. M., Black, A. R., Everest, J., Wilson, P., Darling, W. G., et al. (2019). Groundwater–glacier meltwater interaction in proglacial aquifers. *Hydrology Earth Syst. Sci.* 23, 4527–4539. doi:10.5194/hess-23-4527-2019

Oksanen, J., Simpson, G. L., Blanchet, F. G., Kindt, R., Legendre, P., Minchin, P. R., et al. (2022). *Vegan: community ecology package*.

Parada, A. E., Needham, D. M., and Fuhrman, J. A. (2016). Every base matters: assessing small subunit rRNA primers for marine microbiomes with mock communities, time series and global field samples. *Environ. Microbiol.* 18, 1403–1414. doi:10.1111/1462-2920.13023

Paradis, E., and Schliep, K. (2019). Ape 5.0: an environment for modern phylogenetics and evolutionary analyses in R. *Bioinformatics* 35, 526–528. doi:10.1093/bioinformatics/bty633

Pedersen, T. L. (2022). *Patchwork: the composer of plots*.

Pester, M., Friedrich, M. W., Schink, B., and Brune, A. (2004). pmoA-based analysis of methanotrophs in a littoral lake sediment reveals a diverse and stable community in a dynamic environment. *Appl. Environ. Microbiol.* 70, 3138–3142. doi:10.1128/AEM.70.5.3138-3142.2004

Pohjola, V. A., Moore, J. C., Isaksson, E., Jauhiainen, T., van de Wal, R. S. W., Martma, T., et al. (2002). Effect of periodic melting on geochemical and isotopic signals in an ice core from Lomonosovfonna, Svalbard. *J. Geophys. Res. Atmos.* 107. ACL 1-1-ACL 1-14. doi:10.1029/2000JD000149

Pollard, W. H. (2005). Icing processes associated with high arctic perennial springs, axel heiberg island, nunavut, Canada. *Permafr. Periglac. Process.* 16, 51–68. doi:10.1002/ppp.515

Puigdomenech, I., Tullborg, E.-L., Kontula, A., and Lamminmäki, T. (2017). Glacial meltwater and moraine interaction: evolution of near-surface waters at kangerlussuaq, western Greenland. *Procedia Earth Planet. Sci.* 17, 778–781. doi:10.1016/j.proeps.2017.01.027

Quast, C., Pruesse, E., Yilmaz, P., Gerken, J., Schweer, T., Yarza, P., et al. (2013). The SILVA ribosomal RNA gene database project: improved data processing and web-based tools. *Nucleic Acids Res.* 41, D590–D596. doi:10.1093/nar/gks1219

R Core Team (2023). The R project for statistical computing. [WWW Document]. URL Available at: https://www.r-project.org/ (Accessed February 19, 23).

Rothfuss, F., Bender, M., and Conrad, R. (1997). Survival and activity of bacteria in a deep, aged lake sediment (lake constance). *Microb. Ecol.* 33, 69–77. doi:10.1007/s002489900009

Siegenthaler, U., and Oeschger, H. (1980). Correlation of 18O in precipitation with temperature and altitude. *Nature* 285, 314–317. doi:10.1038/285314a0

Skidmore, M. L., Foght, J. M., and Sharp, M. J. (2000). Microbial life beneath a high arctic glacier. *Appl. Environ. Microbiol.* 66, 3214–3220. doi:10.1128/AEM.66.8.3214-3220.2000

Smith, L. C., Pavelsky, T. M., MacDonald, G. M., Shiklomanov, A. I., and Lammers, R. B. (2007). Rising minimum daily flows in northern Eurasian rivers: a growing influence of groundwater in the high-latitude hydrologic cycle. *J. Geophys. Res. Biogeosciences* 112. doi:10.1029/2006JG000327

Stachnik, Ł., Majchrowska, E., Yde, J. C., Nawrot, A. P., Cichała-Kamrowska, K., Ignatiuk, D., et al. (2016). Chemical denudation and the role of sulfide oxidation at Werenskioldbreen, Svalbard. *J. Hydrology* 538, 177–193. doi:10.1016/j.jhydrol.2016.03.059

St. Jacques, J.-M., and Sauchyn, D. J. (2009). Increasing winter baseflow and mean annual streamflow from possible permafrost thawing in the Northwest Territories, Canada. *Geophys. Res. Lett.* 36. doi:10.1029/2008GL035822

Stumm, W., and Morgan, J. J. (2012). *Aquatic chemistry: chemical equilibria and rates in natural waters*. New Jersey, United States: John Wiley & Sons.

Svendsen, J. I., and Mangerud, J. (1997). Holocene glacial and climatic variations on Spitsbergen, Svalbard. *Holocene* 7, 45–57. doi:10.1177/095968369700700105

Tranter, M., Brown, G., Raiswell, R., Sharp, M., and Gurnell, A. (1993). A conceptual model of solute acquisition by Alpine glacial meltwaters. *J. Glaciol.* 39, 573–581. doi:10.3189/S0022143000016464

Tranter, M., Sharp, M. J., Lamb, H. R., Brown, G. H., Hubbard, B. P., and Willis, I. C. (2002). Geochemical weathering at the bed of Haut Glacier d'Arolla, Switzerland—a new model. *Hydrol. Process.* 16, 959–993. doi:10.1002/hyp.309

Wadham, J. L., Bottrell, S., Tranter, M., and Raiswell, R. (2004). Stable isotope evidence for microbial sulphate reduction at the bed of a polythermal high Arctic glacier. *Earth Planet. Sci. Lett.* 219, 341–355. doi:10.1016/S0012-821X(03)00683-6

Wadham, J. L., Hodson, A. J., Tranter, M., and Dowdeswell, J. A. (1998). The hydrochemistry of meltwaters draining a polythermal-based, high Arctic glacier, south Svalbard: I. The ablation season. *Hydrol. Process.* 12, 1825–1849. doi:10.1002/(sici)1099-1085(19981015)12:12<1825::aid-hyp669>3.3.co;2-i

Walvoord, M. A., and Striegl, R. G. (2007). Increased groundwater to stream discharge from permafrost thawing in the Yukon River basin: potential impacts on lateral export of carbon and nitrogen. *Geophys. Res. Lett.* 34. doi:10.1029/2007GL030216

Wartiainen, I., Hestnes, A. G., and Svenning, M. M. (2003). Methanotrophic diversity in high arctic wetlands on the islands of Svalbard (Norway) - denaturing gradient gel electrophoresis analysis of soil DNA and enrichment cultures. *Can. J. Microbiol.* 49, 602–612. doi:10.1139/w03-080

Whiticar, M. J. (1999). Carbon and hydrogen isotope systematics of bacterial formation and oxidation of methane. *Chem. Geol.* 161, 291–314. doi:10.1016/S0009-2541(99)00092-3

Wickham, H. (2023). *RStudio, forcats: tools for working with categorical variables (factors)*.

Wickham, H., Averick, M., Bryan, J., Chang, W., McGowan, L., François, R., et al. (2019). Welcome to the tidyverse. *JOSS* 4, 1686. doi:10.21105/joss.01686

Wickham, H., and Seidel, D. (2022). *RStudio, scales: scale functions for visualization*.

Williams, P. J., and Smith, M. W. (1989). *The frozen Earth: fundamentals of geocryology, studies in polar research*. Cambridge: Cambridge University Press. doi:10.1017/CBO9780511564437

frontiers | Frontiers in Earth Science

TYPE Original Research
PUBLISHED 01 March 2024
DOI 10.3389/feart.2024.1355621

OPEN ACCESS

EDITED BY
Moritz Felix Lehmann,
University of Basel, Switzerland

REVIEWED BY
Mark Alexander Lever,
The University of Texas at Austin, United States
Martin Blumenberg,
Federal Institute For Geosciences and Natural Resources, Germany

*CORRESPONDENCE
Tobias Himmler,
himmler@uni-bremen.de

RECEIVED 14 December 2023
ACCEPTED 15 February 2024
PUBLISHED 01 March 2024

CITATION
Himmler T, Wagner D, Sahy D, Vadakkepuliyambatta S, Chand S, Martma T, Kirsimäe K, Mattingsdal R, Panieri G, Bünz S, Condon DJ, Knies J and Lepland A (2024), Protracted post-glacial hydrocarbon seepage in the Barents Sea revealed by U–Th dating of seep carbonates.
Front. Earth Sci. 12:1355621.
doi: 10.3389/feart.2024.1355621

Protracted post-glacial hydrocarbon seepage in the Barents Sea revealed by U–Th dating of seep carbonates

Tobias Himmler[1,2,3]*, Doris Wagner[4], Diana Sahy[4], Sunil Vadakkepuliyambatta[2,5], Shyam Chand[1,2], Tõnu Martma[6], Kalle Kirsimäe[7], Rune Mattingsdal[8], Giuliana Panieri[2], Stefan Bünz[2], Daniel J. Condon[4], Jochen Knies[1,2] and Aivo Lepland[1,2,6]

[1]Geological Survey of Norway, Trondheim, Norway, [2]Department of Geosciences, Centre for Arctic Gas Hydrate, Environment and Climate, UiT-The Arctic University of Norway, Tromsø, Norway, [3]Fachbereich Geowissenschaften, Universität Bremen, Bremen, Germany, [4]British Geological Survey, Keyworth, United Kingdom, [5]National Centre for Polar and Ocean Research, Ministry of Earth Sciences, Vasco da Gama, India, [6]Department of Geology, Tallinn University of Technology, Tallinn, Estonia, [7]Department of Geology, Tartu University, Tartu, Estonia, [8]Norwegian Petroleum Directorate, Harstad, Norway

The hydrocarbon seepage chronology during deglaciation across the formerly glaciated Barents Sea was established using uranium-thorium (U–Th) dating of seep carbonates. Seep carbonates were sampled with remotely operated vehicles (ROV) from the seafloor at three active hydrocarbon seeps (water depth 156–383 m), located in the north-west (Storfjordrenna), north-central (Storbanken High), and south-west (Loppa High) Barents Sea. Overall, the U–Th dates range from 13.5 to 1.2 thousand years (ka) before present, indicating episodic seep carbonate formation since the late Pleistocene throughout the Holocene. The new U–Th dates indicate protracted post-glacial gas seepage, congruent with previously published seep carbonate ages from the south-west Barents Sea. Gas hydrate dissociation and associated seep carbonate formation occurred at Storfjordrenna between ≈6 and 1.2 ka, and around 13.5 and 6 ka at Storbanken. Early and late Holocene seep carbonate ages from Loppa High support post-glacial seismic activity as potential seepage trigger mechanism.

KEYWORDS

methane, glacial, carbonates, seeps, Barents Sea, U-Th dating

1 Introduction

Hydrocarbon seeps occur on the seafloor where upward migrating hydrocarbon-rich fluids emanate, delivering dissolved and free gas by diffusion and ebullition from the sediment into the seawater (e.g., Suess, 2014). The seeping hydrocarbon fluids can contain methane from various sources, including hydrocarbon reservoirs, free gas accumulations underneath gas hydrate layers, dissociating gas hydrates, or from microbial processes in the shallow subsurface (e.g., Judd et al., 2002; Pohlmann et al., 2009). Before escaping at the seafloor, most of the dissolved methane is typically consumed below the sediment–water interface *via* microbial mediated sulfate-driven anaerobic oxidation of methane (AOM: CH_4

+ SO_4^{2-} → HCO_3^- + HS^- + H_2O) (Boetius et al., 2000; Reeburgh, 2007; and references therein). AOM can also be coupled to the reduction of iron and manganese oxides, making it an effective microbial barrier in marine sediments for upward migrating dissolved methane (Beal et al., 2009; Egger et al., 2018). A consequence of sulfate- and metal-driven AOM is increased pore water carbonate alkalinity through the production of bicarbonate (HCO_3^-), which induces the precipitation of authigenic seep carbonates (e.g., Ritger et al., 1987; Aloisi et al., 2002; Luff et al., 2004; Leefmann et al., 2008). Seep carbonates comprise authigenic carbonate phases including mainly aragonite and minor calcite and dolomite cements. The authigenic carbonate minerals cement seafloor sediments, ranging from cm-sized cemented nodules to meter-sized mounds and exhaustive seafloor pavements (e.g., Greinert et al., 2001; Teichert et al., 2003; Naehr et al., 2007; Himmler et al., 2015; Sauer et al., 2017; Crémière et al., 2018). By using uranium–thorium (U–Th) radioisotopic dating of seep carbonates, the chronology of methane flux episodes can be reconstructed, which plausibly reflects the timing of various environmental and geological mechanisms triggering past methane release (e.g., Teichert et al., 2003; Feng et al., 2010; Crémiere et al., 2016; Himmler et al., 2019).

On the formerly glaciated Barents Sea shelf more than 7000 active hydrocarbon seeps have been discovered, originating from Palaeozoic through Cenozoic petroleum systems (e.g., Serov et al., 2023; Thorsnes et al., 2023). Upward gas migration is controlled by multiple geological mechanisms, including faults/fractures connecting reservoirs to the seafloor, reservoir rocks structurally exposed at the seafloor, and repeated glacial erosion of cap rocks (e.g., Andreassen et al., 2017; Serov et al., 2023). Depending on the ambient pressure–temperature conditions, rising methane may be sequestered as or released from gas hydrate in the shallow sub-seafloor gas hydrate stability zone (GHSZ; e.g., Chand et al., 2008; Andreassen et al., 2017). While the GHSZ was relatively thicker when grounded ice sheets covered the Barents Sea during the Last Glacial Maximum (LGM; ≈20,000 ka), oceanographic and environmental changes in concert with post–LGM ice retreat caused thinning of the hydrate stability zone, resulting in enhanced gas efflux (e.g., Andreassen et al., 2017; Serov et al., 2023). Indeed, hydrate-related enhanced post–LGM methane seepage has been suggested for various Barents Sea sites. It was previously put forward that increased bottom water temperatures in concert with depressurization and isostatic adjustment following the ice retreat has induced gas hydrate dissociation, resulting in strong episodic methane seepage in the south-west Barents Sea (Crémière et al., 2016). Likewise, ice-sheet and GHSZ modeling implies that the gradual changes in oceanographic conditions and isostatic adjustment following ice retreat promoted rapid gas hydrate dissociation and enhanced gas seepage in the north-west and central Barents Sea (Andreassen et al., 2017; Waage et al., 2019; Waage et al., 2020; Serov, et al., 2023). Regardless of the more than 7000 currently active hydrocarbon seeps mapped in the Barents Sea, seepage histories based on U–Th dates of seep carbonates corroborating enhanced post-glacial methane seepage have only been reported from the south-west Barents Sea (Crémière et al., 2016; Crémière et al., 2018; Argentino et al., 2022). Reconstruction of the post-glacial gas efflux chronology in the north-west and central areas of the Barents Sea has remained model-based to date.

Here we report petrographic and geochemical data including new U–Th dates of 17 seep carbonates collected from three active methane seeps located in the north-west (Storfjordrenna), central-north (Storbanken High), and south-west (Loppa High) Barents Sea (Figure 1). The U–Th dates reveal multiple episodes of seep carbonate precipitation and enhanced methane release since the late Pleistocene through the Holocene. The new carbonate ages are in agreement with strong episodic gas efflux in the Barents Sea following ice-retreat, and allow us to reconstruct the seepage chronology and associated carbonate formation after deglaciation.

2 Materials and methods

Seep carbonates were sampled from the seabed using remotely operated vehicles (ROVs) during four expeditions (Table 1; Figure 1); samples HH1029 and HH1077 were collected using the ROV 30K (Centre for Autonomous Marine Operations and Systems AMOS, Norwegian University of Science and Technology) during expedition CAGE16–5 with R/V Helmer Hanssen in 2016; the other samples were retrieved with the ROV Ægir 6000 (University of Bergen) during R/V Kronprins Haakon expedition CAGE18–5 in 2018 (Bünz et al., 2022); the PR1810 and PL954 samples were collected using a work class ROV (FMC Technologies) during two expeditions with M/S Bourbon Arctic in 2018.

2.1 XRD analyses

Quantitative mineralogical compositions were determined by powder X-ray diffraction and are reported in weight-% (wt%; Table 2). Powders were produced by pulverizing broken chunks (i.e., bulk-rock) and micro-drilling of cut slabs using a hand-held micro-drill. The powders were analysed with a Bruker D8 Advance diffractometer using Cu K α radiation at a 2Θ scanning angle of 3°–75° (step size of 0.02°, 1 s per step). Minerals were identified by automatic and manual peak search using the Bruker DIFFRAC EVA3.1 software; quantification was performed applying Rietveld refinement with the TOPAS 5 software. Repeated internal standard measurements yielded a detection limit and uncertainty of ±2 wt%.

2.2 Petrography and carbonate $\delta^{13}C$ and $\delta^{18}O$ analyses

Thin sections (6.5 x 5 cm) were prepared from ca. 1.5 cm thick cut slabs that were embedded in epoxy resin. The thin sections were examined using standard petrographic microscopy (Figure 2). Samples for stable carbon and oxygen isotopes ($\delta^{13}C$ and $\delta^{18}O$) were drilled from the surface of cut slabs with a hand-held micro-drill. Approximately 200 µg of the obtained powders were reacted with anhydrous phosphoric acid in a GasBench II preparation line; released CO_2 gas was analysed with a ThermoScientific Delta V Advantage isotope ratio mass spectrometer. The $\delta^{13}C$ and $\delta^{18}O$ values are reported in per mill (‰) relative to the Vienna–Pee Dee Belemnite standard (V–PDB). The data were calibrated against standard materials and the uncertainties for $\delta^{13}C$ and $\delta^{18}O$ were not higher than ± 0.2‰.

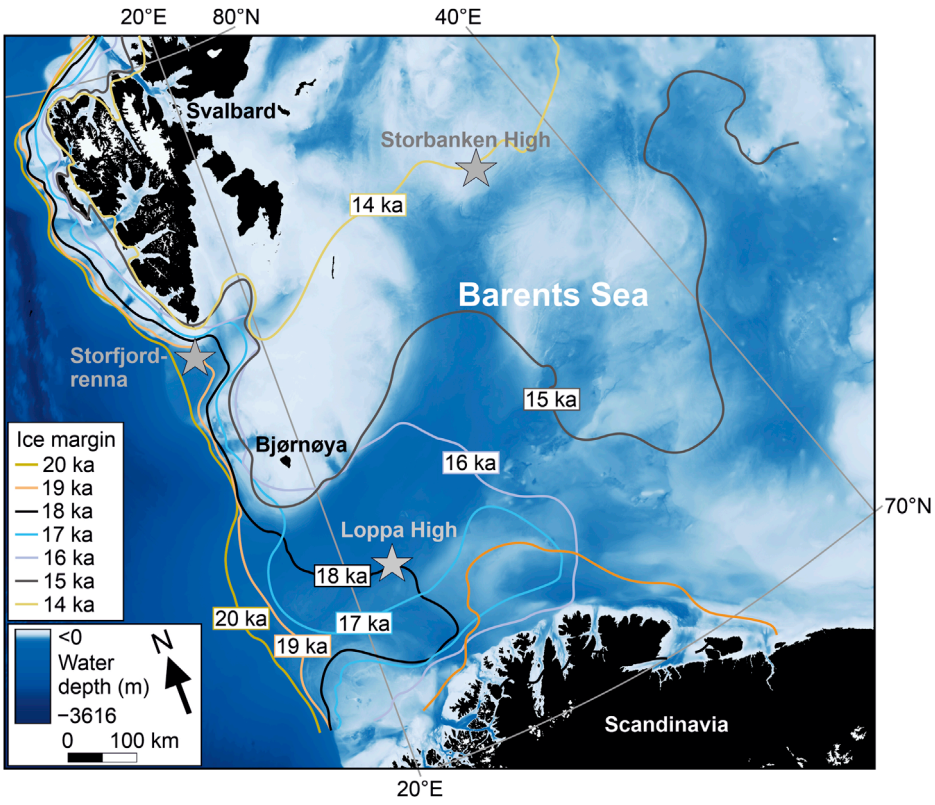

FIGURE 1
Sampling locations (stars) in the north-west (Storfjordrenna), central-north (Storbanken High), and south-west (Loppa High) Barents Sea, relative to reconstructed marine-based ice margin positions during deglaciation (redrawn after Sejrup et al., 2022; bathymetry data from Jakobsson et al., 2012).

2.3 Uranium–thorium dating

From 17 seep carbonates the U–Th ages of 55 fibrous cement samples were determined. Sample powders between 0.2 and 9.3 mg were obtained from polished cut slabs using a hand-held micro-drill. After powder digestion in 8 M HNO_3 U and Th were separated, concentrated, and analysed as described previously (Crémière et al., 2016). In brief, after digestion, centrifuging, and detritus dissolution, U and Th were pre-concentrated by iron co-precipitation and separated via column ion chromatography (Edwards et al., 1987). Isotope ratios were measured with a Neptune Plus multicollector inductively coupled plasma mass spectrometer. Argon and nitrogen were used as carrying gases to minimize oxide formation. Uranium–Th ages were calculated using an in-house spreadsheet, applying the ^{230}Th and ^{234}U decay constants of Cheng et al. (2013). Initial ^{230}Th correction was based on mean continental crust values. Sample ages are given in thousand years before present (ka BP; BP = before 1950). Samples with ^{230}Th/^{232}Th activity ratios ≤2 were rejected for data interpretation. The initial U isotope signature of seep carbonate tends to reflect seawater values or slight enrichment in ^{234}U relative to seawater if precipitation occurs under more restrictive conditions from pore fluids (Teichert et al., 2003). Therefore, analyses where $(^{234}U/^{238}U)_i$ sample <1.14 or $(^{234}U/^{238}U)_i$ sample >1.18 were assumed to represent an open-system behaviour with respect to U and/or Th, and were rejected for interpretation, too (see Supplementary Figure S1).

3 Results

3.1 Mineralogy, petrography, and carbonate $\delta^{13}C$ and $\delta^{18}O$ values

Aragonite is the main carbonate mineral (22–90 wt%), followed by moderate to low contents in magnesium-calcite (Mg-calcite; 3 to 63 wt%) and calcite (up to 22 wt%; Table 2). Quartz, feldspar, and clay minerals are the major non-carbonate components, ranging between 3 and 17 wt%. Micro-drilled fibrous aragonite in samples HH1029 and HH1077 is completely devoid of non-carbonate components (Table 2). Micrite in sample HH1029 has more Mg-calcite (63 wt%) than aragonite (22 wt%), whereas micrite in HH1077 is mainly aragonite (77 wt%) with only trace Mg-calcite content (below 2 wt%).

The carbonates comprise porous intraformational breccias of micrite-cemented sediment clasts, cemented by fibrous aragonite crusts (Figure 2; Supplementary Figures S1–S6). Relatively earlier formed micrite cemented clasts and subsequently formed fibrous aragonite cement comprise the volumetric dominant microfacies. The micrite cements hemipelagic sediment rich in silt-sized quartz and feldspar grains (Figures 2A,D). Fibrous aragonite forms mm-to cm-thick cement crusts, partly surrounding clasts and filling the pore space between micrite-cemented sediment and bioclasts (Figures 2B, C; Supplementary Figures S1–S6). Samples from Storfjordrenna show abundant tube-worm fossils in

TABLE 1 Overview of sampling sites and locations; GHP = gas hydrate pingo; mbsl = meters below sea level.

Sample	Location	Site	Latitude [N]	Longitude [E]	Water depth (mbsl)
HH1029	NW Barents Sea	Storfjordrenna, GHP 3	76°6′24.804″	15°58′4.728″	378
HH1077	NW Barents Sea	Storfjordrenna, GHP 3	76°6′25.2″	15°58′9.876″	378
CAGE18–5–C1	NW Barents Sea	Storfjordrenna, GHP 3	76°6′25.204″	15°58′4.195″'	377
CAGE18–5–C2	NW Barents Sea	Storfjordrenna, GHP 3	76°6′25.628″	15°58′7.372″	378
CAGE18–5–C3	NW Barents Sea	Storfjordrenna, GHP 3	76°6′25.585″	15°58′7.813″	379
CAGE18–5–C4	NW Barents Sea	Storfjordrenna, GHP 3	76°6′25.799″	15°58′7.79″	379
CAGE18–5–C5	NW Barents Sea	Storfjordrenna, GHP 3	76°6′25.75″	15°58′7.669″	379
CAGE18–5–C6	NW Barents Sea	Storfjordrenna, GHP 3	76°6′25.198″	15°58′0.101″	379
CAGE18–5–C7	NW Barents Sea	Storfjordrenna, GHP 3	76°6′25.297″	15°57′59.961″	379
CAGE18–5–C11	Central-north Barents Sea	Storbanken High	76°46′49.007″	35°9′45.99″	156
CAGE18–5–C14	Central-north Barents Sea	Storbanken High	76°46′56.926″	35°13′51.4″	158
PR 1810–001	SW Barents Sea	Loppa High	72°4′2.442″	21°48′19.3356″	383
PR 1810–002	SW Barents Sea	Loppa High	72°4′2.365″	21°48′19.3608″	382
PR 1810–003	SW Barents Sea	Loppa High	72°4′2.481″	21°48′19.4832″	383
PR 1810–051	SW Barents Sea	Loppa High	72°4′2.524″	21°48′20.1024″	383
PL954–C1	SW Barents Sea	Loppa High	71°57′58.104″	21°35′11.256″	354
PL954–C2	SW Barents Sea	Loppa High	71°57′58.104″	21°35′11.256″	354

both, micrite and fibrous cement (Figures 2A, B), relatively few articulated bivalve shells, and centimetre-sized grains of ice-rafted debris (IRD; Supplementary Figures S1–S3). Likewise, the Storbanken High samples display some bivalve shells and IRD grains (Supplementary Figures S3D, E). Samples from the Loppa High contain many articulated bivalves with abundant inter- and intraparticle fibrous cement (Supplementary Figure S5). Macroscopically, fibrous cement in the Loppa High samples can be distinguished into whitish and grey aragonite. Whitish aragonite appears as incoherent layer of inclusion-rich, cryptocrystalline cement between micrite and fibrous aragonite (Figure 2E; Supplementary Figures S6). Under UV light cryptocrystalline aragonite exhibits intense fluorescence, whereas subsequent clear fibrous aragonite is non-fluorescent. Likewise, dark inclusion-rich clotted aragonite and brownish botryoidal aragonite display strong fluorescence (Figure 2F). Occasionally, pockets of a few square centimetre size containing cemented IRD are intercalated within cemented clasts and bivalves (Supplementary Figures S6).

Carbonate $\delta^{13}C$ and $\delta^{18}O$ values were analysed for micrite (n = 47) and fibrous cement (n = 47; Figure 3; Supplementary Figures S1). Overall, $\delta^{13}C$ values range from −43.3 to −18.4‰ while the $\delta^{18}O$ values range from 3.1‰ to 5.6‰. Micrite yielded slightly lower $\delta^{13}C$ (median ±SD: −32.2‰ ± 4.8‰) and slightly higher $\delta^{18}O$ (4.8‰ ± 0.5‰) values than fibrous cement ($\delta^{13}C$ = −31.2‰ ± 5.1‰; $\delta^{18}O$ = 4.6‰ ± 0.5‰). Samples from Storbanken High exhibit relatively lower $\delta^{13}C$ values (−37.8‰ ± 3.7‰; n = 19) than the Loppa High (−31.9‰ ± 3.6‰; n = 51) and Storfjordrenna (−27.0‰ ± 2.5‰; n= 30) samples. Storfjordrenna samples show relatively higher $\delta^{18}O$ values (5.0‰ ± 0.3‰) than the samples from Storbanken (4.9‰ ± 0.2‰) and Loppa High (4.3‰ ± 0.5‰).

3.2 Carbonate U–Th ages

From the 55 micro-drilled U–Th samples, four have been discarded for interpretation due to relatively low data quality and resulting high uncertainty, and three are coral skeleton material (Figure 4; Supplementary Figure S1–S6; Supplementary Figure S1). Samples C1 through C7, HH1029, and HH1077, were collected from the gas hydrate pingo mound 3 (GHP 3; Serov et al., 2017) at Storfjordrenna and yielded exclusively mid to late Holocene ages, ranging from 6.3 ± 2.3 (ka ± 2σ) to 1.2 ± 0.1 ka. The two samples from the Storbanken High area yielded one late Pleistocene 13.5 ± 2.4 ka (one subsample from C11) and three mid-Holocene ages from 6.6 ± 0.3 to 5.4 ± 0.1 ka (three subsamples, C14). Samples PR1810 and PL954 from the Loppa High area exhibit late Pleistocene and early to mid Holocene ages, ranging from 13.4 ± 0.7 to 4.1 ± 1.3 ka. The three coral samples exhibit Holocene ages from 10.4 ± 1.3 to 4.2 ± 1.3 ka.

TABLE 2 Mineralogical compositions (weight−%). Arag = aragonite; Cc = calcite Mg-Cc = magnesium calcite; Qtz = quartz; K-fsp = potassium feldspar; Plc = plagioclase; Clays = illite, muscovite, smectite, and chlorite; tr. = trace; n.d. = not detected.

Sample	Site	Sampling method	Microfacies	Arag	Cc	Mg-Cc	Qtz	K-fsp	Plc	Clays
HH1029	Storfjordrenna, GHP 3	micro-drill	micrite	22	n.d	63	10	n.d	tr	5
HH1029	Storfjordrenna, GHP 3	micro-drill	fibrous cement	78	22	n.d	n.d	n.d	n.d	n.d
HH1077	Storfjordrenna, GHP 3	micro-drill	fibrous cement	90	10	n.d	n.d	n.d	n.d	n.d
HH1077	Storfjordrenna, GHP 3	micro-drill	micrite	77	tr.	3	11	n.d	4	4
CAGE18–5–C1	Storfjordrenna, GHP 3	broken chunk	bulk-rock	43	n.d	31	10	n.d	4	12
CAGE18–5–C2	Storfjordrenna, GHP 3	broken chunk	bulk-rock	55	n.d	15	11	n.d	4	14
CAGE18–5–C3	Storfjordrenna, GHP 3	broken chunk	bulk-rock	68	n.d	8	10	n.d	4	10
CAGE18–5–C4	Storfjordrenna, GHP 3	broken chunk	bulk-rock	71	n.d	7	9	n.d	3	10
CAGE18–5–C5	Storfjordrenna, GHP 3	broken chunk	bulk-rock	65	n.d	10	9	n.d	4	12
CAGE18–5–C6	Storfjordrenna, GHP 3	broken chunk	bulk-rock	80	n.d	5	4	n.d	3	8
CAGE18–5–C7	Storfjordrenna, GHP 3	broken chunk	bulk-rock	61	n.d	17	8	n.d	3	11
CAGE18–5–C11	Storbanken High	broken chunk	bulk-rock	40	n.d	28	11	3	6	12
CAGE18–5–C14	Storbanken High	broken chunk	bulk-rock	61	n.d	7	17	3	4	8
P1810–001–5	Loppa High	broken chunk	bulk-rock	68	n.d	9	8	n.d	4	11
P1810–002–2	Loppa High	broken chunk	bulk-rock	61	n.d	23	5	n.d	3	8
P1810–003–2	Loppa High	broken chunk	bulk-rock	70	n.d	3	8	n.d	5	14
P1810–051–2	Loppa High	broken chunk	bulk-rock	66	n.d	4	14	3	5	8

4 Discussion

4.1 Carbonate precipitation induced by anaerobic oxidation of methane and non-methane hydrocarbons

The carbonate $\delta^{13}C$ values are as low as previously reported values of seep carbonates sampled from the south-west and north-west Barents Sea (Crémière et al., 2016; Crémière et al., 2018; Yao et al., 2021; Argentino et al., 2022), and indicate a predominantly hydrocarbon-derived carbon source. Seepage gas samples from Storfjordrenna and Loppa High show a thermogenic composition and yielded $\delta^{13}C_{methane}$ values of −47‰ and−48% V–PDB, respectively (Crémière et al., 2016; Serov et al., 2017). Weniger et al. (2019) extracted gas from surface sediments at Storfjordrenna and report a thermogenic composition with slightly higher average $\delta^{13}C_{methane}$ of −41.3‰ ± 2.7‰ V–PDB (n=4). In the same study, Weniger et al. (2019) show a thermogenic gas composition with average $\delta^{13}C_{methane}$ of −50.8‰ ± 5.2‰ V–PDB (n=18) for surface sediment bound gas from the Olga Basin, which borders along the southern flank of the Storbanken High. To the best of the authors' knowledge there are no published methane $\delta^{13}C$ values for seepage or bound gas from the Storbanken High seeps. Given that the Storbanken High and the Olga Basin share the same reservoir rocks (Lundschien et al., 2023; Serov et al., 2023), a thermogenic origin for the gas seeping at Storbanken High is assumed.

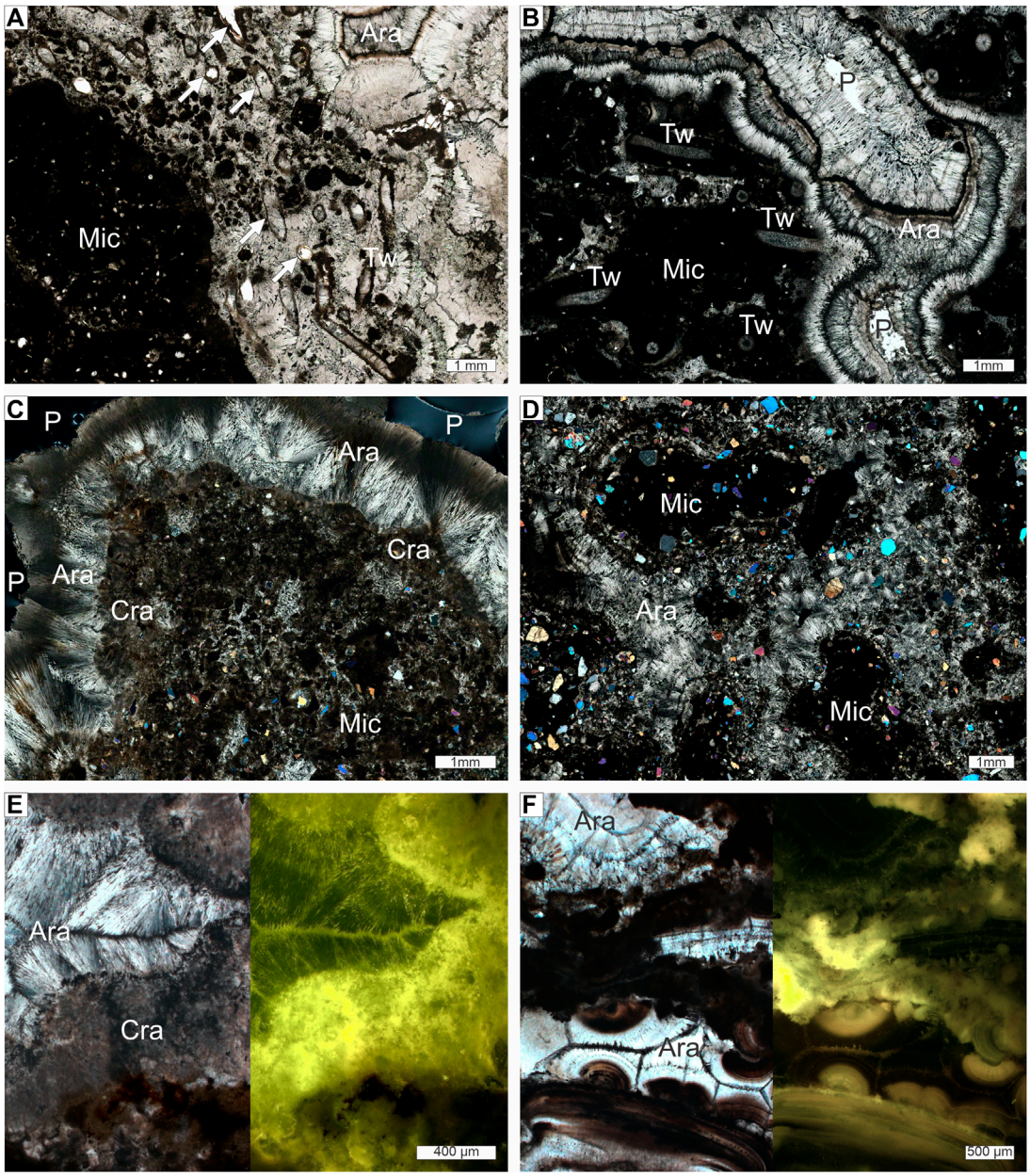

FIGURE 2
Thin section micrographs of representative seep carbonates from Storfjordrenna **(A,B)**, Storbanken High **(C,D)**, and Loppa High **(E,F)**; PPL = parallel-polarized light, XPL = cross-polarized light; P = pore space. **(A)** Sample CAGE18-5-C1, showing micrite-cemented sediment (Mic) with abundant silt-sized quartz grains, surrounded by radial and botryoidal aragonite (Ara) cement; please note the abundant dark layered, and clotted and peloidal inclusions; note also the longitudinal/oblique and perpendicular cut tube worm walls (Tw; arrows) which are open or completely cemented; Tw are likely fossils of siboglinid *Oligobrachia* sp. (Sen et al., 2018); PPL, open pore space appears white. **(B)** Sample CAGE18-5-C4 with abundant cemented tubes in micritic sediment (Mic), cross-cut by multiple layers of dark inclusion rich, mm-thick radial and botryoidal aragonite (Ara); PPL. **(C)** XPL view (pore space appears black) of sample CAGE18-5-C11, showing micrite-cemented sediment with silt-sized quartz and some areas with clotted micrite, surrounded by botryoidal aragonite (Ara); note that the aragonite fans originate from a layer of inclusion-rich cryptocrystalline aragonite (Cra). **(D)** Sample CAGE18-5-C14 exhibiting rounded clasts of micrite-cemented sediment (Mic), cemented by radial fibrous aragonite (Ara); note abundant siliciclastic grains cemented fibrous aragonite (XPL). **(E)** and **(F)** show transmitted light (left panels, XPL) and UV epifluorescence images (right panels) of samples PR 1810–002 and PL954-02, respectively; inclusion-rich cryptocrystalline aragonite (Cra) and clotted and botryoidal aragonite in sample P1810-002; note the stronger fluorescence of Cra compared to clear non-fluorescent aragonite; inclusion-rich clotted and botryoidal aragonite (Ara) in sample PL954-02 exhibits strong fluorescence whereas clear aragonite is non-fluorescent.

The seep carbonates are relatively ^{13}C-enriched compared to the methane. This is interpreted as the result of mixing ^{13}C-depleted dissolved inorganic carbon (DIC) with ^{13}C-rich DIC during carbonate precipitation, yielding higher carbonate δ^{13}C values relative to the parent methane (Formolo et al., 2004; Peckmann and Thiel, 2004; Roberts et al., 2010; Himmler et al., 2015). Seep carbonate δ^{13}C values represent a DIC mixture of seawater (δ^{13}C ≈ 0‰), DIC produced during organiclastic sulfate

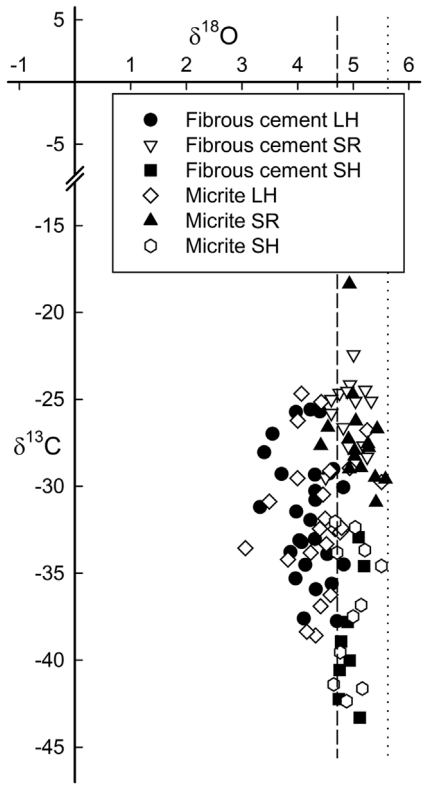

FIGURE 3
Seep carbonate $\delta^{13}C$ and $\delta^{18}O$ values (‰ V–PDB); LH = Loppa High, SR = Storfjordrenna; SH = Storbanken High. The dashed and stippled lines mark theoretical $\delta^{18}O$ values for aragonite (4.7‰) and magnesium-calcite (5.6‰) precipitated in equilibrium with bottom water at 1°C temperature and $\delta^{18}O$ = 1‰ (Vienna–Standard Mean Ocean Water) assumed for ≈15 ka (see Crémière et al., 2016).

reduction (≈ −25‰), and DIC produced by AOM/or and oxidation of higher hydrocarbons ($\delta^{13}C$ below −20‰; e.g., Irwin, et al., 1977; Formolo et al., 2004; Sassen et al., 2004; Smrzka et al., 2019). Whereas the highest $\delta^{13}C_{carbonate}$ value of −18‰ (Figure 3; Supplementary Figure S1) can be explained by a DIC mixture of seawater and organiclastic sulfate-reduction, the rest of the $\delta^{13}C_{carbonate}$ values between −43‰ and −24‰ point to a DIC mixture produced by the anaerobic oxidation of the thermogenic methane and/or non-methane hydrocarbons (Formolo et al., 2004; Sassen et al., 2004; Smrzka et al., 2019). The relatively lower values indicate a higher contribution of AOM-derived DIC, whereas the relatively higher values indicate significant contribution DIC resulting from the anaerobic oxidation non-methane hydrocarbons (Formolo et al., 2004).

Aragonite is the dominant carbonate phase, except for the magnesium-calcite rich micrite in sample HH1029 (Table 2). It is not unusual for seep carbonates to mainly comprise aragonite and partly include Mg-calcite (e.g., Greinert et al., 2001; Crémière et al., 2018; Lu et al., 2021). At hydrocarbon seeps aragonite formation is likely favoured over calcite by relatively high sulfate concentrations (Burton, 1993). Bioturbation of the sediment by bivalves and bubble ebullition during episodes of strong gas efflux likely eased entrainment of sulfate-rich seawater into the shallow subsurface, supporting sulfate-driven AOM near the sediment–water interface (e.g., Borowski et al., 1999; Aloisi et al., 2002; Luff et al., 2004). In contrast, during episodes of weak seepage with low gas flux, AOM was likely mediated deeper in the sediment at relatively lower pore water sulfate concentrations, and Mg-calcite precipitation was favoured (e.g., Greinert et al., 2001). Increased magnesium incorporation into the calcite lattice is plausible under low flux conditions, when abundant AOM-produced hydrogen sulfide (HS^-) supports de-hydration of Mg^{2+} ions, thus increasing the pore fluid Mg^{2+}/Ca^{2+} ratio (Zhang et al., 2012; Lu et al., 2021). At the same time, the increased alkalinity resulting from AOM-produced bicarbonate (HCO_3^-) also supports carbonate precipitation.

Overall, the aragonite-dominated mineralogy is congruent with carbonate precipitation near the sediment–water interface. This is also supported by the macrofossil content, including the chemosynthesis-based siboglinid tube worms *Oligobrachia* sp. (Sen et al., 2018; Åström et al., 2018), unidentified articulated bivalves, and a presumably cool water coral (Figure 2, Supplementary Figures S1–S6). Moreover, molecular fossils including ^{13}C-depleted lipid biomarkers diagnostic of AOM-mediating methanotrophic archaea and sulfate-reducing bacteria have been found in Storfjordrenna samples HH1029 and HH1077, corroborating that microbial-mediated sulfate-driven AOM induced carbonate precipitation (Yao et al., 2021). Although no lipid biomarker data are available for the Storbanken High and Loppa High samples, they contain abundant microbial textures, including clotted micrite and cryptocrystalline aragonite (Figures 2C–F; Riding, 2000; Zwicker et al., 2018). Both textures exhibit strong fluorescence under UV radiation, indicative of high organic matter content resulting from *in situ* organomineralization (Neuweiler et al., 2000). Given that increased carbonate alkalinity at methane seeps supports the lithification of microbial biofilms, it is feasible that the fluorescent textures observed in the Storbanken High and Loppa High samples represent mineralized AOM hotspots (Himmler et al., 2018; Zwicker et al., 2018). Remarkably, the strong fluorescent textures in samples PR1810-002 and PL945-C2 (Figures 2E,F) correspond macroscopically to whitish aragonite, similar to whitish and cryptorcrystalline aragonite with high AOM-biomarker contents described in modern and ancient seep carbonates (Leefmann et al., 2008; Hagemann et al., 2013).

4.2 Timing of seep-carbonate formation relative to the palaeoenvironment

Regarding the reconstructed ice margins, all U–Th dates are consistent with carbonate formation after local ice retreat and protracted methane flux (e.g., Crémière et al., 2016; Serov et al., 2023). The oldest samples C11 (Storbanken High; SH) and PR1810-001C (Loppa High; LH) yielded similar ages of 13.5 (SH) and 13.4 (LH) ka. The ages indicate relatively high gas flux and associated seep carbonate formation at these two distant sites during the Bølling–Allerød interstadial. At this time, influx of relatively warmer Atlantic seawater promoted rapid disintegration of the grounded Barents Sea ice sheet, leaving large areas in the west and south-west Barents Sea ice free (e.g., Rasmussen and Thomsen, 2021; Sejrup et al., 2022). The influx of warm water likely accelerated the dissociation of shallow subsurface gas hydrates, resulting in

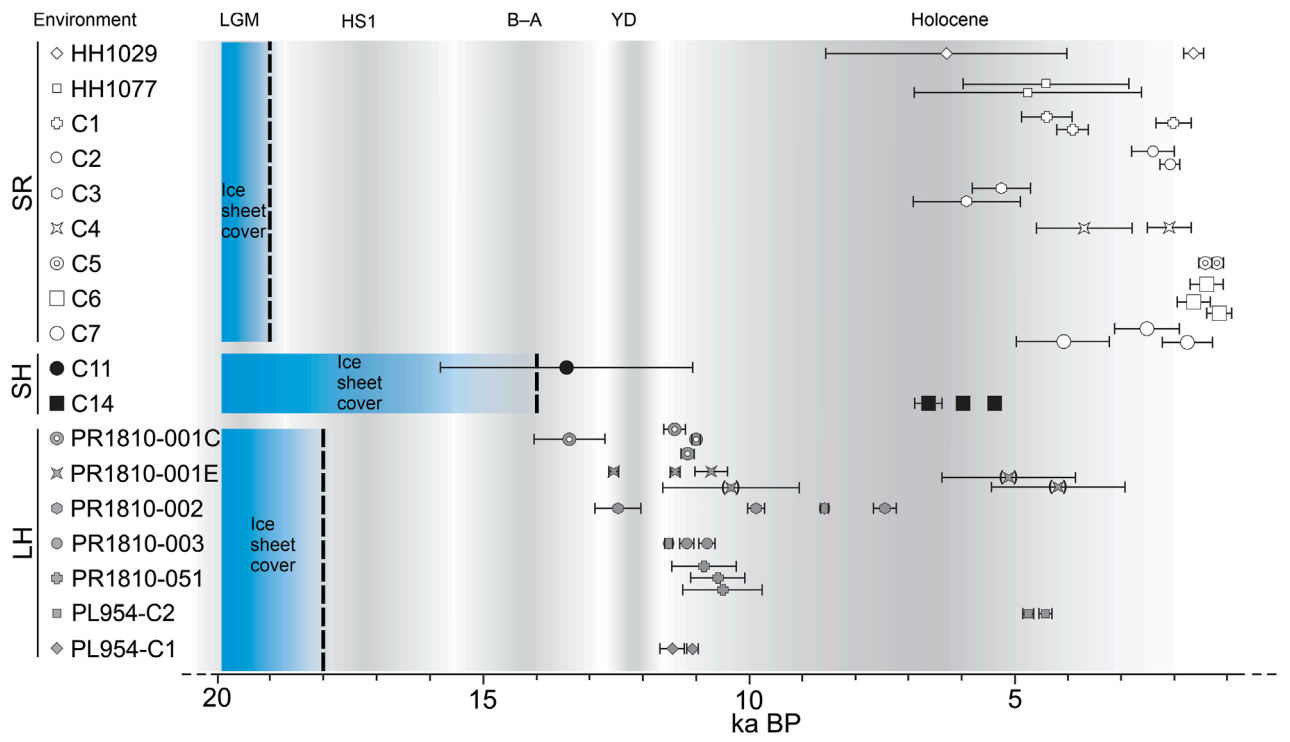

FIGURE 4
Seep carbonate U–Th ages (±2σ) from Storfjordrenna (SR), Storbanken High (SH) and Loppa High (LH), relative to reconstructed regional ice cover and palaeoenvironment (vertical shaded bars). Symbols in brackets indicate coral skeleton ages (seep carbonate sample PR 1810–001E; note that the oldest coral date is likely a mixture of skeleton and seep carbonate cement); HS1 = Heinrich stadial 1 (cool); B–A = Bølling–Allerød interstadial (warm); YD, Younger Dryas (cool); palaeoenvironment timing after Rasmussen and Thomsen (2021); ice-sheet cover after Sejrup et al. (2022).

increased methane emissions at the seafloor (Crémière et al., 2016; Andreassen, et al., 2017). This is congruent with the SH carbonate $\delta^{18}O$ values, indicating a contribution of hydrate-derived ^{18}O-enriched water during carbonate precipitation (Figure 3).

Except for sample PL954–C2 (≈4.7 and 4.4 ka), the rest of the non-coral LH samples have late Pleistocene and early Holocene U–Th ages between ≈12.6 and 7.5 ka. Overall, the LH dates are in agreement with previously reported seep carbonate U–Th dates from the south-west Barents Sea and northern Norwegian Sea, together indicating episodic post–LGM hydrocarbon gas release and seep carbonate formation between 17.5 and 1.6 ka (Crémière et al., 2016; Sauer et al., 2017; Crémière et al., 2018; Argentino et al., 2022). Sauer et al. (2017) suggested that in northern Scandinavia, seismic activities and resulting fault reactivation and changes in reservoirs pore pressure could have triggered gas seepage around ≈11 and 4 ka. Remarkably, the majority of the new LH U–Th ages between 12 and 10 ka plus the two ages of sample PL954–C2 (≈4.7 and 4.4 ka), are in agreement with this scenario.

The carbonate ages reveal lag times between local ice retreat and distinct episodes of enhanced gas efflux. It needs to be stressed that the reported ages were exclusively derived from relatively late-stage fibrous aragonite cement and do not constrain the initial seepage stage (see also Crémière et al., 2016; Crémière et al., 2018). In particular at Storfjordrenna, seep carbonate formation occurred ≈13 ka after the grounded ice has had retreated after ≈19 ka (Rasmussen and Thomsen, 2021; Sejrup et al., 2022). The long lag time at Storfjordrenna is surprising, considering that abundant gas hydrates (and probably free gas) had accumulated in the subsurface during the LGM in an approximately 200 m thick GHSZ (Serov et al., 2017). After glacial retreat, the GHSZ totally diminished by ≈13 ka and must have released significant gas amounts from the seabed due to gas hydrate dissociation (Serov et al., 2017). Yet, the carbonate ages do not indicate carbonate formation before 6.3 ka. It could be that the U–Th ages of seafloor-sampled seep carbonates do not reflect the entire post–LGM seepage history, and large ice bergs from the disintegrating ice sheet might have eroded any older seep carbonates from the seafloor (Rasmussen and Thomsen, 2021). El bani Altuna et al. (2021) showed that the average bottom water temperature at Storfjordrenna increased from 2.5°C ± 1°C to 4.3°C ± 1°C between ≈13 and 5 ka, followed by cooling down to down 2.8°C ± 1°C after 4 ka. In addition, their gas hydrate model suggests that a fluctuating GHSZ existed between 13 and 9 ka (i.e., variable thickness of 0 to ca. 100 m below seafloor), but was absent between 9 and 5 ka, resulting in liberation of gas and hydrate-derived water. Remarkably, the gas hydrate modeling also shows a stable GHSZ since 5 ka, which would sequester most of the upward migrating gas. Yet, our U–Th ages show constant seep carbonate formation near the sediment–water interface since 6.3 ka. Regardless of the existence of the GHSZ, the carbonate dates support the notion that the underlying hydrocarbon reservoir actively injects thermogenic methane into the shallow subsurface sediments at this site, probably since the mid to late Holocene until modern times, as put forward by Waage et al. (2019). Given constant gas supply from below and the resulting high methane concentrations, free methane likely

bypasses the GHSZ through cracks and faults, eventually escaping at the seafloor.

Seep carbonate $\delta^{18}O$ values depend on the mineralogy, the ambient temperature and the $\delta^{18}O$ of the carbonate-precipitating fluid, and serve as proxy for possible gas hydrate dissociation during carbonate formation (e.g., Aloisi et al., 2000; Greinert et al., 2001; Crémière et al., 2016; Crémière et al., 2018). Assuming seep carbonate formation under post-glacial conditions, i.e., bottom water temperature 1°C and seawater $\delta^{18}O$ = 1‰ V–SMOW (Duplessy et al., 2002), carbonate $\delta^{18}O$ values of 4.7‰ for aragonite and 5.6‰ for magnesium–calcite would be expected (Kim et al., 2007; Crémière et al., 2016). Samples from Storfjordrenna (median $\delta^{18}O$ = 5.0) and Storbanken High (median $\delta^{18}O$ = 4.9) show carbonate $\delta^{18}O$ values slightly higher than 4.7‰, while the Loppa High samples are mostly (but not exclusively) below 4.7‰ (median $\delta^{18}O$ = 4.3; Figure 3). Values above 4.7‰ would indicate either precipitation from fluids below 1°C temperature or relatively enriched in ^{18}O, while lower values point to precipitation at slightly higher temperatures or fluids depleted in ^{18}O. Given that the reconstructed bottom water temperature was above 2°C in the Storfjordrenna since the early Holocene (El bani Altuna et al., 2021; Rasmussen and Thomsen, 2021), the seep carbonates most likely precipitated from ^{18}O-enriched fluids. It is feasible that the ^{18}O-rich fluids originated from extensive post–LGM gas hydrate dissociation, since hydrate incorporates preferentially ^{18}O (Davidson et al., 1983; Serov et al., 2023). Considering that warm water influx has triggered abrupt gas hydrate dissociation to form large craters on the seafloor between 15 and 12 ka ago (Andreassen et al., 2017), a similar formation scenario for the ≈6 ka old Storbanken High sample C14 is suggested. Influx of warmer bottom water around 6 ka, as shown by El bani Altuna et al. (2021), likely accelerated gas hydrate dissociation in the shallow subsurface, which would explain the relatively ^{18}O-erniched carbonates. For the Loppa High samples, most of the carbonate $\delta^{18}O$ values can be explained by precipitation in equilibrium with ambient post–LGM bottom water temperatures. However, as pointed out by Crémière et al. (2018), a contribution of ^{18}O-rich fluids from the relatively deeper reservoir and/or from gas hydrate dissociation can not be ruled out, considering the complex tectono–sedimentary history and possible fluid dilution effects during carbonate precipitation.

5 Conclusions

1) Carbonates sampled from active gas seeps at Storfjordrenna, Storbanken High, and Loppa High areas in the Barents Sea formed as a result of the anaerobic oxidation of methane and higher hydrocarbons. New U–Th ages overlap with previously published ages for seep carbonates from the south-west Barents Sea, corroborating episodic gas release and carbonate precipitation in the aftermath of the retreat of the Barents Sea–Svalbard Ice Sheet since the Last Glacial Maximum.
2) Major carbonate formation periods occurred after the Bølling–Allerød interstadial, during the Younger Dryas stadial, and at the beginning of and throughout the mid to late Holocene.
3) The U–Th ages from Storfjordrenna, where gas hydrates are present today, indicate seep carbonate precipitation resulting from gas hydrate dissociation-related methane release ca.13 ka after the marine-based ice sheet had retreated. The new U–Th ages indicate that carbonate formation continued between 6.3 and 1.2 ka.
4) At gas seeps which are structurally connected to deep-seated hydrocarbon reservoirs at Storbanken High and Loppa High, seep carbonates formed relatively early after the local ice retreat, indicating episodic gas release from ca.13.5 to 4.4 ka. It is speculated that seismic activity resulting from post-glacial isostatic adjustment reactivated faults and triggered episodic gas seepage.
5) Relatively ^{18}O-enriched seep carbonates indicate gas hydrate dissociation related seepage due to relative warmer bottom waters since the mid Holocene at Storfjordrenna and Storbanken High.

Data availability statement

The original contributions presented in the study are included in the article/Supplementary Material, further inquiries can be directed to the corresponding author.

Author contributions

TH: Conceptualization, Writing–original draft, Investigation. DW: Investigation, Writing–review and editing. DS: Investigation, Methodology, Writing–review and editing. SV: Investigation, Writing–review and editing. SC: Investigation, Writing–review and editing. TM: Investigation, Writing–review and editing. KK: Investigation, Writing–review and editing. RM: Investigation, Writing–review and editing. GP: Investigation, Writing–review and editing. SB: Funding acquisition, Writing–review and editing. DC: Investigation, Writing–review and editing. JK: Funding acquisition, Writing–review and editing. AL: Funding acquisition, Investigation, Writing–review and editing.

Funding

The author(s) declare financial support was received for the research, authorship, and/or publication of this article. This study was supported by CAGE and the Research Council of Norway through its Centres of Excellence scheme (Grant No. 223259) and the Petromaks2 NORCRUST project (Grant No. 255150).

Acknowledgments

Professional support by the masters and the crews during seagoing expeditions on R/V Helmer Hannsen (CAGE16–5), R/V Kronprins Haakon (CAGE18–5), and M/S Bourbon Arctic, as well as the skilled work of the respective ROV teams, are greatly acknowledged. We thank J. Schönenberger (Geological Survey of Norway) for the XRD measurements. Thoughtful comments by the Editor and the two reviewers helped to improve the manuscript.

Conflict of interest

The authors declare that the research was conducted in the absence of any commercial or financial relationships that could be construed as a potential conflict of interest.

Publisher's note

All claims expressed in this article are solely those of the authors and do not necessarily represent those of their affiliated organizations, or those of the publisher, the editors and the reviewers. Any product that may be evaluated in this article, or claim that may be made by its manufacturer, is not guaranteed or endorsed by the publisher.

Supplementary material

The Supplementary Material for this article can be found online at: https://www.frontiersin.org/articles/10.3389/feart.2024.1355621/full#supplementary-material

References

Aloisi, G., Bouloubassi, I., Heijs, S. K., Pancost, R., Pierre, C., Sinninghe Damsté, J. S., et al. (2002). CH4-consuming microorganisms and the formation of carbonate crusts at cold seeps. *Earth Planet. Sci. Lett.* 203, 195–203. doi:10.1016/s0012-821x(02)00878-6

Aloisi, G., Pierre, C., Rouchy, J.-M., Foucher, J.-P., and Woodside, J. (2000). Methane-related authigenic carbonates of eastern Mediterranean Sea mud volcanoes and their possible relation to gas hydrate destabilisation. *Earth Planet Sci. Lett.* 184, 321–338. doi:10.1016/S0012-821X(00)00322-8

Andreassen, K., Hubbard, A., Winsborrow, M., Patton, H., Vadakkepuliyambatta, S., Plaza-Faverola, A., et al. (2017). Massive blow-out craters formed by hydrate controlled methane expulsion from the Arctic seafloor. *Science* 356 (80), 948–953. doi:10.1126/science.aal4500

Argentino, C., Lee, A., Fallati, L., Sahy, D., Birgel, D., Peckmann, J., et al. (2022). Biogeochemistry and timing of methane-derived carbonate formation at Leirdjupet fault complex, SW Barents sea. *Front. Earth Sci.* 10, 1029471. doi:10.3389/feart.2022.1029471

Åström, E. K. L., Carroll, M. L., Ambrose, W. G., Sen, A., Silyakova, A., and Carroll, J. (2018). Methane cold seeps as biological oases in the high-Arctic deep sea. *Limnol. Oceanogr.* 63, S209–S231. doi:10.1002/lno.10732

Beal, E. M., House, C. H., and Orphan, V. J. (2009). Manganese- and iron-dependent marine methane oxidation. *Science* 325, 184–187. doi:10.1126/science.1169984

Boetius, A., Ravenschlag, K., Schubert, C., Rickert, D., Widdel, F., Gieseke, A., et al. (2000). A marine microbial consortium apparently mediating anaerobic oxidation of methane. *Nature* 407, 623–626. doi:10.1038/35036572

Borowski, W. S., Paull, C. K., and Ussler, W. (1999). Global and local variations of interstitial sulfate gradients in deep-water, continental margin sediments: sensitivity to underlying methane and gas hydrates. *Mar. Geol.* 159, 131–154. doi:10.1016/S0025-3227(99)00004-3

Bünz, S., Vadakkepuliyambatta, S., Serov, P., Lepland, A., Himmler, T., Hong, W.-L., et al. (2022). CAGE18-5 Cruise report: remotely-operated vehicle (ROV) investigations of active gas seepage sites in the Barents Sea. *CAGE–Centre Arct. Gas Hydrate, Environ. Clim. Rep. Ser.* 6. doi:10.7557/cage.6853

Burton, E. A. (1993). Controls on marine carbonate cement mineralogy: review and reassessment. *Chem. Geol.* 105, 163–179. doi:10.1016/0009-2541(93)90124-2

Chand, S., Mienert, J., Andreassen, K., Knies, J., Plassen, L., and Fotland, B. (2008). Gas hydrate stability zone modelling in areas of salt tectonics and pockmarks of the Barents Sea suggests an active hydrocarbon venting system. *Mar. Petroleum Geol.* 25, 625–636. doi:10.1016/j.marpetgeo.2007.10.006

Cheng, H., Edwards, R. L., Shen, C.-C., Polyak, V. J., Asmerom, Y., Woodhead, J., et al. (2013). Improvements in 230Th dating, 230Th and 234U half-life values, and U–Th isotopic measurements by multi-collector inductively coupled plasma mass spectrometry. *Earth Planet. Sci. Lett.* 371, 82–91. doi:10.1016/j.epsl.2013.04.006

Crémière, A., Chand, S., Sahy, D., Thorsnes, T., Martma, T., Noble, S. R., et al. (2018). Structural controls on seepage of thermogenic and microbial methane since the last glacial maximum in the Harstad Basin, southwest Barents Sea. *Mar. Petroleum Geol.* 98, 569–581. doi:10.1016/j.marpetgeo.2018.07.010

Crémière, A., Lepland, A., Chand, S., Sahy, D., Condon, D. J., Noble, S. R., et al. (2016). Timescales of methane seepage on the Norwegian margin following collapse of the Scandinavian Ice Sheet. *Nat. Commun.* 7, 11509. doi:10.1038/ncomms11509

Davidson, D. W., Leaist, D. G., and Hesse, R. (1983). Oxygen-18 enrichment in the water of a clathrate hydrate. *Geochem. Cosmochim. Acta* 47, 2293–2295. doi:10.1016/0016-7037(83)90053-4

Duplessy, J.-C., Labeyrie, L., and Waelbroeck, C. (2002). Constraints on the ocean oxygen isotopic enrichment between the last glacial maximum and the Holocene: paleoceanographic implications. *Quat. Sci. Rev.* 21, 315–330. doi:10.1016/S0277-3791(01)00107-X

Edwards, R. L., Chen, J. H., and Wasserburg, G. J. (1987). 238U–234U–230Th–232Th systematics and the precise measurement of time over the past 500,000 years. *Earth Planet. Sci. Lett.* 81, 175–192. doi:10.1016/0012-821x(87)90154-3

Egger, M., Riedinger, N., Mogollón, J. M., and Jørgensen, B. B. (2018). Global diffusive fluxes of methane in marine sediments. *Nat. Geosci.* 11, 421–425. doi:10.1038/s41561-018-0122-8

El bani Altuna, N., Rasmussen, T. L., Ezat, M. M., Vadakkepuliyambatta, S., Groeneveld, J., and Greaves, M. (2021). Deglacial bottom water warming intensified Arctic methane seepage in the NW Barents Sea. *Commun. Earth Environ.* 2, 188. doi:10.1038/s43247-021-00264-x

Feng, D., Roberts, H. H., Cheng, H., Peckmann, J., Bohrmann, G., Edwards, R. L., et al. (2010). U/Th dating of cold-seep carbonates: an initial comparison. *Deep Sea Res. Part II* 57, 2055–2060. doi:10.1016/j.dsr2.2010.09.004

Formolo, H., Lyons, T. W., Zhang, C., Kelley, C., Sassen, R., Horita, J., et al. (2004). Quantifying carbon sources in the formation of authigenic carbonates at gas hydrate sites in the Gulf of Mexico. *Chem. Geol.* 205, 253–264. doi:10.1016/j.chemgeo.2003.12.021

Greinert, J., Bohrmann, G., and Suess, E. (2001). "Gas hydrate-associated carbonates and methane-venting at Hydrate Ridge: classification, distribution, and origin of authigenic lithologies," in *Natural gas hydrates: occurrence, distribution, and detection*. Editors C. K. Paull, and W. P. Dillon (Washington, DC, USA: American Geophysical Union).

Hagemann, A., Leefmann, T., Peckmann, J., Hoffmann, V.-E., and Thiel, V. (2013). Biomarkers from individual carbonate phases of an Oligocene cold-seep deposit, Washington State, USA. *Lethaia* 46, 7–18. doi:10.1111/j.1502-3931.2012.00316.x

Himmler, T., Birgel, D., Bayon, G., Pape, T., Ge, L., Bohrmann, G., et al. (2015). Formation of seep carbonates along the Makran convergent margin, northern Arabian Sea and a molecular and isotopic approach to constrain the carbon isotopic composition of parent methane. *Chem. Geol.* 415, 102–117. doi:10.1016/j.chemgeo.2015.09.016

Himmler, T., Sahy, D., Martma, T., Bohrmann, G., Plaza–Faverola, A., Bünz, S., et al. (2019). A 160,000-year-old history of tectonically controlled methane seepage in the Arctic. *Sci. Adv.* 5, eaaw1450. doi:10.1126/sciadv.aaw1450

Himmler, T., Smrzka, D., Zwicker, J., Kasten, S., Shapiro, R. S., Bohrmann, G., et al. (2018). Stromatolites below the photic zone in the northern Arabian Sea formed by calcifying chemotrophic microbial mats. *Geology* 46 (4), 339–342. doi:10.1130/G39890.1

Irwin, H., Curtis, C., and Coleman, M. (1977). Isotopic evidence for source of diagenetic carbonates formed during burial of organic-rich sediments. *Nature* 269, 209–213. doi:10.1038/269209a0

Jakobsson, M., Mayer, L., Coakley, B., Dowdeswell, J. A., Forbes, S., Fridman, B., et al. (2012). The international bathymetric chart of the arctic ocean (IBCAO) version 3.0. *Res. Lett.* 39, L12609. doi:10.1029/2012GL052219

Judd, A. G., Hovland, M., Dimitrov, L. I., Garcia, G. S., and Jukes, V. (2002). The geological methane budget at continental margins and its influence on climate change. *Geofluids* 2, 109–126. doi:10.1046/j.1468-8123.2002.00027.x

Kim, S.-T., O'Neil, J. R., Hillaire-Marcel, C., and Mucci, A. (2007). Oxygen isotope fractionation between synthetic aragonite and water: influence of temperature and Mg2+ concentration. *Geochem. Cosmochim. Acta* 71, 4704–4715. doi:10.1016/j.gca.2007.04.019

Leefmann, T., Bauermeister, J., Kronz, A., Liebetrau, V., Reitner, J., and Thiel, V. (2008). Miniaturized biosignature analysis reveals implications for the formation of cold seep carbonates at Hydrate Ridge (off Oregon, USA). *Biogeosciences* 5, 731–738. doi:10.5194/bg-5-731-2008

Lu, Y., Yang, X., Lin, Z., Sun, X., Yang, Y., and Peckmann, J. (2021). Reducing microenvironments promote incorporation of magnesium ions into authigenic carbonate forming at methane seeps: constraints for dolomite formation. *Sedimentology* 68, 2945–2964. doi:10.1111/sed.12919

Luff, R., Wallmann, K., and Aloisi, G. (2004). Numerical modeling of carbonate crust formation at cold vent sites: significance for fluid and methane budgets and chemosynthetic biological communities. *Earth Planet. Sci. Lett.* 221, 337–353. doi:10.1016/S0012-821X(04)00107-4

Lundschien, B. A., Mattingsdal, R., Johansen, S. K., and Knutsen, S.-M. (2023). "North Barents composite tectono-sedimentary element," in *Sedimentary successions of the arctic region and their hydrocarbon prospectivity*. Editors S. S. Drachev, H. Brekke, E. Henriksen, and T. Moore (London, Memoirs: Geological Society), 57. doi:10.1144/M57-2021-39

Naehr, T. H., Eichhubl, P., Orphan, V. J., Hovland, M., Paull, C. K., Ussler, W., III., et al. (2007). Authigenic carbonate formation at hydrocarbon seeps in continental margin sediments: a comparative study. *Deep-Sea Res. II Top. Stud. Oceanogr.* 54 (11–13), 1268–1291. doi:10.1016/j.dsr2.2007.04.010

Neuweiler, F., Rutsch, M., Geipel, G., Reimer, A., and Heise, K.-H. (2000). Soluble humic substances from *in situ* precipitated microcrystalline calcium carbonate, internal sediment, and spar cement in a Cretaceous carbonate mud-mound. *Geology* 28, 851–854. doi:10.1130/0091-7613(2000)28<851:shsfis>2.0.co;2

Peckmann, J., and Thiel, V. (2004). Carbon cycling at ancient methane–seeps. *Chem. Geol.* 205, 443–467. doi:10.1016/j.chemgeo.2003.12.025

Pohlman, J. W., Bauer, J. E., Canuel, E. A., Grabowski, K. S., Knies, D. L., Mitchell, C. S., et al. (2009). Methane sources in gas hydrate-bearing cold seeps: evidence from radiocarbon and stable isotopes. *Mar. Chem.* 115, 102–109. doi:10.1016/j.marchem.2009.07.001

Rasmussen, T. L., and Thomsen, E. (2021). Climate and ocean forcing of ice-sheet dynamics along the Svalbard-Barents Sea ice sheet during the deglaciation ~20,000–10,000 years BP. *Quat. Sci. Adv.* 3, 100019. doi:10.1016/j.qsa.2020.100019

Reeburgh, W. S. (2007). Oceanic methane biogeochemistry. *Chem. Rev.* 107 (2), 486–513. doi:10.1021/cr050362v

Riding, R. (2000). Microbial carbonates: the geological record of calcified bacterial–algal mats and biofilms. *Sedimentology* 47, 179–214. doi:10.1046/j.1365-3091.2000.00003.x

Ritger, S., Carson, B., and Suess, E. (1987). Methane-derived authigenic carbonates formed by subduction-induced pore-water expulsion along the Oregon/Washington margin. *Geol. Soc. Am. Bull.* 98, 147–156. doi:10.1130/0016-7606(1987)98<147:macfbs>2.0.co;2

Roberts, H. H., Feng, D., and Joye, S. B. (2010). Cold-seep carbonates of the middle and lower continental slope, northern Gulf of Mexico. *Deep-Sea Res. II* 57, 2040–2054. doi:10.1016/j.dsr2.2010.09.003

Sassen, R., Roberts, H. H., Carney, R., Milkov, A. V., DeFreitas, D. A., Lanoil, B., et al. (2004). Free hydrocarbon gas, gas hydrate, and authigenic minerals in chemosynthetic communities of the northern Gulf of Mexico continental slope: relation to microbial processes. *Chem. Geol.* 205, 195–217. doi:10.1016/j.chemgeo.2003.12.032

Sauer, S., Crémière, A., Knies, J., Lepland, A., Sahy, D., Martma, T., et al. (2017). U-Th chronology and formation controls of methane-derived authigenic carbonates from the Hola trough seep area, northern Norway. *Chem. Geol.* 470, 164–179. doi:10.1016/j.chemgeo.2017.09.004

Sejrup, H. P., Hjelstuen, B. O., Patton, H., Esteves, M., Winsborrow, M., Rasmussen, T. L., et al. (2022). The role of ocean and atmospheric dynamics in the marine-based collapse of the last Eurasian Ice Sheet. *Commun. Earth Environ.* 3, 119. doi:10.1038/s43247-022-00447-0

Sen, A., Åström, E. K. L., Hong, W.-L., Portnov, A., Waage, M., Serov, P., et al. (2018). Geophysical and geochemical controls on the megafaunal community of a high Arctic cold seep. *Biogeosciences* 15, 4533–4559. doi:10.5194/bg-15-4533-2018

Serov, P., Vadakkepuliyambatta, S., Mienert, J., Patton, H., Portnov, A., Silyakova, A., et al. (2017). Postglacial response of Arctic Ocean gas hydrates to climatic amelioration. *Proc. Natl. Acad. Sci. USA* 114 (24), 6215–6220. doi:10.1073/pnas.1619288114

Serov, P., Mattingsdal, R., Winsborrow, M., Patton, H., and Andreassen, K. (2023). Widespread natural methane and oil leakage from sub-marine Arctic reservoirs. *Nat. Commun.* 14, 1782. doi:10.1038/s41467-023-37514-9

Smrzka, D., Zwicker, J., Misch, D., Walkner, C., Gier, S., Monien, P., et al. (2019). Oil seepage and carbonate formation: a case study from the southern Gulf of Mexico. *Sedimentology* 66, 2318–2353. doi:10.1111/sed.12593

Suess, E. (2014). Marine cold seeps and their manifestations: geological control, biogeochemical criteria and environmental conditions. *Int. J. Earth Sci. Geol. Rundsch* 103, 1889–1916. doi:10.1007/s00531-014-1010-0

Teichert, B. M. A., Eisenhauer, A., Bohrmann, G., Haase-Schramm, A., Bock, B., and Linke, P. (2003). U/Th systematics and ages of authigenic carbonates from Hydrate Ridge, Cascadia Margin: recorders of fluid flow variations. *Geochim. Cosmochim. Acta* 67, 3845–3857. doi:10.1016/s0016-7037(03)00128-5

Thorsnes, T., Chand, S., Bellec, V., Nixon, F. C., Brunstad, H., Lepland, A., et al. (2023). Gas seeps in Norwegian waters – distribution and mechanisms. *Nor. J. Geol.* 103, 2. doi:10.17850/njg103-2-4

Waage, M., Portnov, A., Serov, P., Bünz, S., Waghorn, K. A., Vadakkepuliyambatta, S., et al. (2019). Geological controls on fluid flow and gas hydrate pingo development on the Barents Sea margin. *Geochem. Geophysics,Geosystems* 20, 630–650. doi:10.1029/2018GC007930

Waage, M., Serov, P., Andreassen, K., Waghorn, K. A., and Bünz, S. (2020). Geological controls of giant crater development on the Arctic seafloor. *Sci. Rep.* 10, 8450. doi:10.1038/s41598-020-65018-9

Weniger, P., Blumenberg, M., Berglar, K., Ehrhardt, A., Klitzke, P., Krüger, M., et al. (2019). Origin of near-surface hydrocarbon gases bound in northern Barents Sea sediments. *Mar. Petroleum Geology* 102, 455–476. doi:10.1016/j.marpetgeo.2018.12.036

Yao, H., Panieri, G., Lehmann, M. F., Himmler, T., and Niemann, H. (2021). Biomarker and isotopic composition of seep carbonates record environmental conditions in two arctic methane seeps. *Front. Earth Sci.* 8, 570742. doi:10.3389/feart.2020.570742

Zhang, F., Xu, H., Konishi, H., Kemp, J. M., Roden, E. E., and Shen, Z. (2012). Dissolved sulfide-catalyzed precipitation of disordered dolomite: implications for the formation mechanism of sedimentary dolomite. *Geochim. Cosmochim. Acta* 97, 148–165. doi:10.1016/j.gca.2012.09.008

Zwicker, J., Smrzka, D., Himmler, T., Monien, P., Gier, S., Goedert, J. L., et al. (2018). Rare earth elements as tracers for microbial activity and early diagenesis: a new perspective from carbonate cements of ancient methane-seep deposits. *Chem. Geol.* 501, 77–85. doi:10.1016/j.chemgeo.2018.10.010

frontiers | Frontiers in Earth Science

TYPE Original Research
PUBLISHED 08 April 2024
DOI 10.3389/feart.2024.1356341

OPEN ACCESS

EDITED BY
Jacek Raddatz,
Helmholtz Association of German Research Centres (HZ), Germany

REVIEWED BY
André Bahr,
Heidelberg University, Germany
Wolfram Geissler,
Alfred Wegener Institute Helmholtz Centre for Polar and Marine Research (AWI), Germany

*CORRESPONDENCE
Tine L. Rasmussen,
tine.rasmussen@uit.no

RECEIVED 15 December 2023
ACCEPTED 21 March 2024
PUBLISHED 08 April 2024

CITATION
Rasmussen TL and Nielsen T (2024), Glacial-interglacial sedimentation control on gas seepage exemplified by Vestnesa Ridge off NW Svalbard margin.
Front. Earth Sci. 12:1356341.
doi: 10.3389/feart.2024.1356341

Glacial-interglacial sedimentation control on gas seepage exemplified by Vestnesa Ridge off NW Svalbard margin

Tine L. Rasmussen[1]* and Tove Nielsen[2]

[1]Department of Geosciences, UiT the Arctic University of Norway, Tromsø, Norway, [2]Geological Survey of Denmark and Greenland (GEUS), Copenhagen, Denmark

Vestnesa Ridge is built-up of thick contourites mainly deposited during the last ~5 million years. Methane leaks from deep gas reservoirs creating pockmarks on its crest, and which have been the focus of numerous studies. Sedimentation patterns in relation to the pronounced changes in oceanography and climate of the last glacial-interglacial cycles and its possible impact of seepage of gas have rarely been studied. Here, we present a detailed history of contourite development covering the last ~130,000 years with most details for the last 60,000 years. The study is based on 43 marine sediment cores and 1,430 km of shallow seismic lines covering the ridge including methane seep sites, with the purpose of reconstructing changes in depositional patterns in relation to paleoceanographical changes on glacial, interglacial, and millennial time scale in relation to activity of seepage of gas. The results show that thick Holocene deposits occurred below ~1,250 m water depth in the western part of the ridge. Both in pockmarks at western and eastern Vestnesa Ridge, seepage decreased at ~10–9 ka in the early Holocene. The fine Holocene mud likely reduced seepage to a slow diffusion of gas and microbial oxidation probably prevented escape from the seafloor. Results also showed that seepage of gas was highly variable during the glacial, and low to moderate during the cold Heinrich stadial H1 (19–15 ka) and Younger Dryas stadial (13–12 ka). Seepage reached a maximum during the deglaciation in the Bølling and Allerød interstadials 15–13 ka and early Holocene 12–10 ka. The deglaciation was a period of rapid climatic, oceanographic, and environmental changes. Seepage of gas varied closely with these events indicating that slower tectonic/isostatic movements probably played a minor role in these millennial scale rapid fluctuations in gas emission.

KEYWORDS

gas hydrates, contourite deposition, deep-sea cores, shallow seismic mapping, carbon isotopes, deglaciation, Fram Strait

1 Introduction

Vestnesa Ridge is located in the Arctic off the northwestern Svalbard margin in eastern Fram Strait just north of the Molloy Transform Fault (Figure 1A). The 100-km long ridge is a southeast-northwest stretching elongated contourite drift at 79°N, 05–07°E, its crest spanning a water depth of ~1,200 m towards east and >1,300 m towards west. Intensive seepage of methane occurs from a series of pockmarks on the crest of the ridge (Vogt et al., 1994; Hustoft et al., 2009; Plaza-Faverola et al., 2015). The gas migrates upwards from a deep

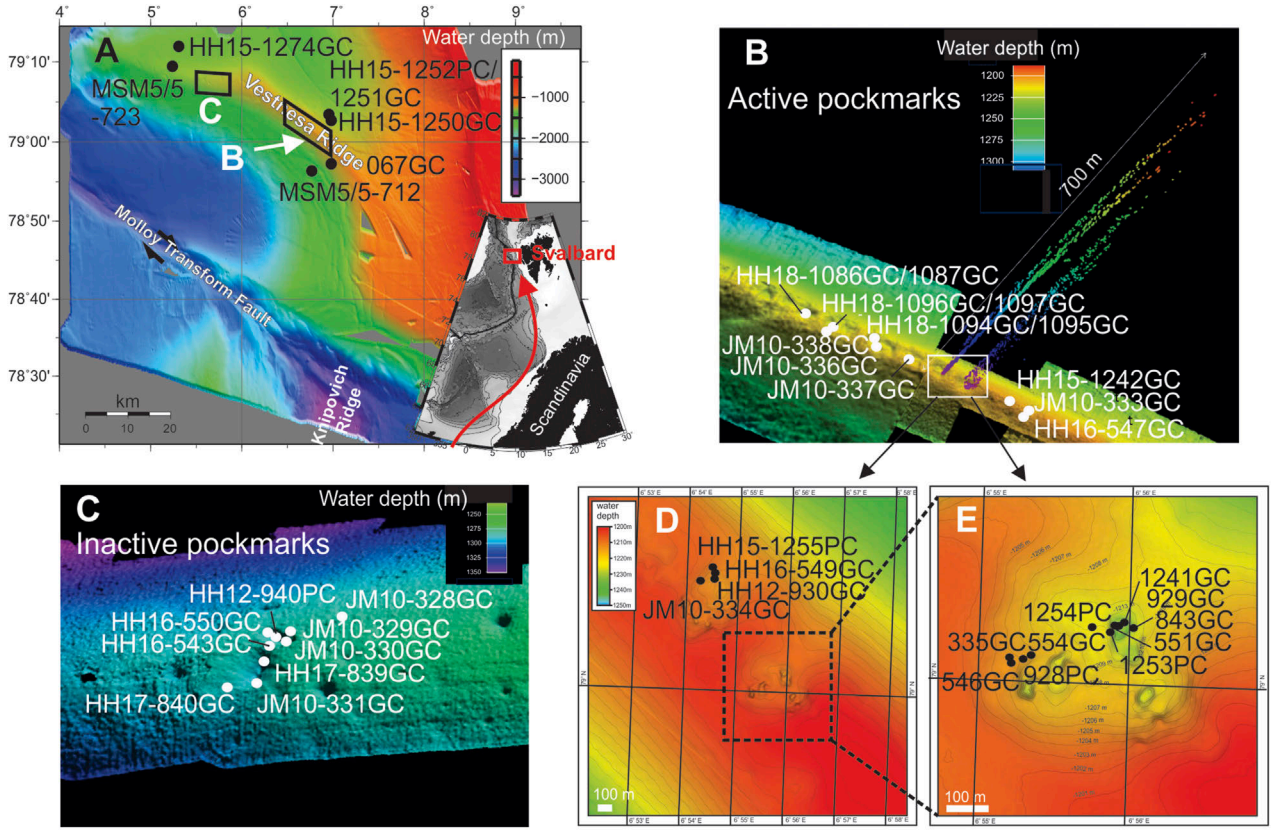

FIGURE 1
Overview maps and detail maps of study area. **(A)**: Map of Vestnesa Ridge with eastern active **(B)** and western inactive **(C)** pockmark areas marked. Core location of published records discussed in the text are also indicated. Insert show the Nordic Seas and location of Svalbard and Vestnesa Ridge with red arrow indicating the West Spitsbergen Current. **(B)**: Detail of eastern active pockmark area showing location of core sites outside of 'Lunde' and 'Lomvi' pockmarks (the latter two marked by white frame). **(C)**: Detail of western Vestnesa pockmark area showing location of core sites. **(D)**: Detail of 'Lunde' pockmark showing core sites. **(E)** Detail of 'Lomvi' pockmark showing core sites (core names abbreviated). See Supplementary Table S1 for details and references to previously published records and Supplementary Figure S1.

thermogenic reservoir through faulted chimneys penetrating the gas hydrate stability zone (GHSZ). The GHSZ is several hundred of meters thick on the ridge extending from ~160 m below the seafloor and well into the water column (Bünz et al., 2012; Plaza-Faverola et al., 2017). Patchy deposits of gas hydrates have been found close to the sediment surface (Sztybor and Rasmussen, 2017a; Laier et al., 2017; Hong et al., 2021).

The thermohaline ocean circulation in the Nordic Seas intensified about 5 million years ago and deposits from the Pliocene onwards are up to ~5 km thick on the ridge (Knies et al., 2014). Increased glaciation regimes during the Quaternary led to increased sedimentation rates from 2.7 Ma (Gebhardt et al., 2014) and seepage of methane intensified from that time (Knies et al., 2018). Modeling studies indicated that the strength of seepage is influenced by offshore isostatic adjustments during glacial periods (Daszinnies et al., 2021). Also, tectonic movements of the Molloy Transform Fault and Knipovich spreading zone have been interpreted to cause fracturing and increase in seepage (Plaza-Faverola et al., 2015; 2023).

Pockmarks are seen along the entire ridge crest (e.g., Hustoft et al., 2009). Presently, seepage of methane gas is only active on the eastern part of the ridge at ~1,200 m water depth where acoustic flares are rising from the seafloor up to 800 m into the water column (Hustoft et al., 2009) (Figure 1B). On the central and western part of the ridge down to >~1,300 m water depth the pockmarks are inactive and without detectable acoustic flares (Bünz et al., 2012) (Figure 1C). In recent years, most studies from the ridge have focused on release of methane, its history, causes of variability and patterns of release (e.g., Plaza-Faverola et al., 2015; 2023; Sztybor and Rasmussen, 2017a; b; Himmler et al., 2018; Schneider et al., 2018) as well as its present seep related environments and associated faunas (e.g., Åström et al., 2018; Yasuhara et al., 2018; Sen et al., 2020; Melaniuk et al., 2022a; b). Little attention has been given to the depositional patterns on the ridge and its variability and potential impact on seepage of methane. Thus, there is a need to better understand the implication of changes in depocenters of the contourite on the degree of seepage of methane in relation to the large glacial-interglacial and millennial climatic and oceanographic changes through time (e.g., Bailey et al., 2021; Hornbach, 2022).

The contourite on Vestnesa Ridge is deposited by the strong currents of the northward flowing West Spitsbergen Current (WSC) before entering the Arctic Ocean via the eastern Fram Strait (Figures 1A,B, 2A). The WSC is a continuation of the Norwegian

Atlantic Current (NAC) comprising warm, saline Atlantic Water (AW) flowing between ~50 and 600 m water depth (Figures 2A–D). The NAC originates from the North Atlantic Drift (derived from the Gulf Stream system) flowing northeastward across the North Atlantic and into the Nordic Seas. Below the AW cold Intermediate and Deep Waters generated by convection in the Nordic Seas flow northward into the Arctic Ocean (e.g., Aagaard et al., 1987; Hopkins, 1991; Schlichtholz and Houssais, 1999a; b; Fer et al., 2023) (Figures 2A–D). The intermediate water also overflows the Greenland-Scotland Ridge in the southern Nordic Seas and continues into the North Atlantic contributing to the North Atlantic Deep Water (NADW) and forms an important part of the Atlantic Meridional Ocean Circulation (AMOC) (Broecker et al., 1991) (Figure 2A).

During the last glacial period the northern hemisphere experienced profound millennial scale changes (termed Dansgaard-Oeschger (DO) events) of warm interstadials and cold stadials (Dansgaard et al., 1993). Particularly cold and long lasting stadials correlated with release of icebergs from continents and are termed Heinrich stadials (Bond et al., 1993). Abrupt atmospheric warmings of up to 8°C–16°C occurred over Greenland (e.g., Kindler et al., 2014). A total of 25 warming events took place during the Weichselian glaciation within the period ~115–12 ka. Studies of paleoceanographic changes over the western and northwestern Svalbard margin and in the Nordic Seas have indicated profound changes in convection strength and water mass properties on DO time scales (e.g., Rasmussen and Thomsen, 2004; Rasmussen et al., 2007). During cold stadials convection slowed or stopped because of presence of the melting icebergs at the surface causing stratification of the upper water column (Figure 2E). The Atlantic Water continued its flow below the low-saline surface meltwater as an intermediate water mass and bottom water warmed up >5.5°C during the latest Heinrich Stadial H1 (19–15 ka) (Ezat et al., 2014; El bani Altuna et al., 2021a) (Figure 2E). During interstadials the Atlantic Water flowed again at the surface and strong convection resumed, briefly cooling the bottom water masses similar to today (Figures 2C,D).

The $\delta^{13}C$ values in benthic and planktic foraminiferal shells reflect ventilation in the deep sea but also the presence of seepage of methane. Methane has very low $\delta^{13}C$ values (<-60‰ for biogenic and ~-40 to −50‰ for thermogenic gas (Whiticar, 1999)). Thus, low $\delta^{13}C$ in foraminifera are taken as a sign of influence of methane (e.g., Wefer et al., 1994; Kenneth et al., 2003; Cook et al., 2011). However, it has been a matter of debate whether benthic foraminifera incorporate the low $\delta^{13}C$ from methane, either through precipitation of their shells from porewater and/or metabolic processes (Smith et al., 2001; Torres et al., 2003; Mackensen et al., 2006; Martin et al., 2010; Wollenburg et al., 2015; Melaniuk et al., 2022a). Values as low as −6‰ in live benthic foraminifera have been reported from the Håkon Mosby Mud Volcano (Mackensen et al., 2006) and lately −5 to <-6‰ in live foraminifera from active seeps from eastern Vestnesa Ridge (Melaniuk et al., 2022a). In areas of low to moderate seepage as for example, in Siboglinid worm fields, the benthic foraminifera appear to be able to live and incorporate methane-derived ^{12}C, while in areas of strong seepage with bacterial mats and low oxygen only dead specimens were found (Melaniuk et al., 2022a; b). After death of a foraminifera the shell can be covered by methane-derived authigenic carbonate from anaerobic oxidation of methane (AOM) (e.g., Boetius et al., 2000; Schneider et al., 2018 and references therein), which can lead to even lower measured values of <-20‰ to −10‰ (e.g., Martin et al., 2010). The precipitation of the authigenic carbonate occurs in the sulfate-methane transition zone (SMTZ) i.e., the transition zone of anaerobic oxidation of methane by archaea and sulfate-reducing bacteria, which depending on strength of seepage can be found at various depths in the sediments (e.g., Boetius et al., 2000). Under conditions of strong seepage, the precipitation occurs close to the sediment surface or at the surface and at high rates (e.g., Borowski et al., 1996; Melaniuk et al., 2022a). Under weak seepage, the formation of authigenic carbonates is slow and occurs deep in the sediment and can take thousands of years (e.g., Snyder et al., 2007).

Here we study the contourite sedimentation patterns and impact on seepage of methane on glacial, interglacial, and millennial DO time scales based on a suite of 43 sediment cores and a grid of shallow seismic lines (Figures 1, 3A). The cores are taken both at the crest and northern flank of Vestnesa Ridge, spanning a water depth of ~1,200–1767 m covering both active pockmarks and sites without seepage of methane (Figure 1). The core study is primarily based on the distribution patterns in magnetic susceptibility, lithology, benthic and planktic $\delta^{18}O$ and $\delta^{13}C$ values, organic and inorganic carbon, and detailed AMS-^{14}C datings. The shallow seismic lines are passing over or close to the core sites and covering crest and flanks of the ridge (Figure 3). The aim of the study is to correlate core records with a known stratigraphy to the seismic data to obtain a more comprehensive overview of the age of sediments on the ridge for a better understanding of the depositional patterns through time in relation to past climatic and oceanographic fluctuations and the effects on the strength of seepage of methane. The results are also compared and correlated with earlier published marine core records from the western and northern Svalbard margin.

2 Material and methods

The study is built on a large database consisting of published and new data from sediment cores and 1,430 km of shallow seismic profiles, all acquired during six successive cruises to Vestnesa Ridge with R/V *Helmer Hanssen* (HH) in 2010 (then named R/V *Jan Mayen* (JM)), in 2012, 2015, 2016, 2017 and 2018 (Figure 1; Supplementary Table S1; see references to cruise reports in Supplementary Material). In addition, core KH19-09GPC is included and tied to the main study area on Vestnesa Ridge by shallow seismic line GAGE-19-3-KH-018 (Knies and Vadakkepuliyambatta, 2023).

2.1 Sediment cores

A total of 8 piston and 35 gravity cores are included in the study (Supplementary Table S1). Both active pockmarks from eastern Vestnesa Ridge and inactive/weakly active pockmarks from western Vestnesa Ridge, sites away from gas seepage fields but near the top of the ridge plus sites from the northern flank of the ridge were targeted (Figure 1). From eastern Vestnesa Ridge the most active and very heterogenous pockmark informally known as 'Lomvi' (Eng.: 'Guillemot') and the more 'quiet' and more homogenous

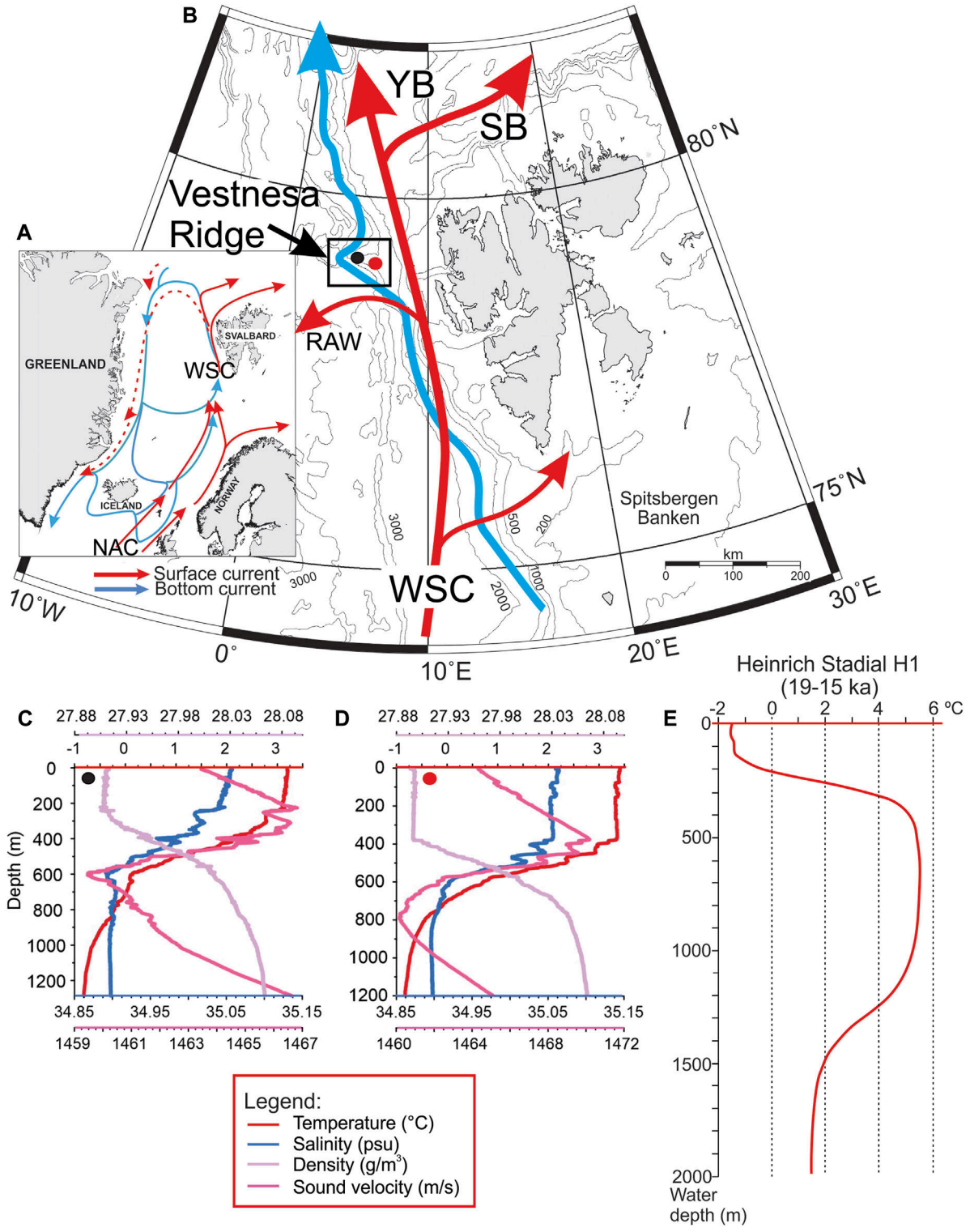

FIGURE 2
Map of major ocean currents, CTD stations, and paleo-CTD of present and past water mass characteristics. **(A)** Overview map of Nordic Seas with major surface (red arrows) and bottom water (blue arrows) currents indicated. **(B)** Detail of same parameters as in **(A)** for the western Svalbard margin and Vestnesa Ridge (black frame). CTD-sites for western (black dot) and eastern (red dot) pockmark areas are marked. Abbreviations: NAC; North Atlantic Current, WSC; West Spitsbergen Current, RAW; Return Atlantic Current, YB; Yermak Branch, SB; Svalbard Branch. Maps modified from Jessen and Rasmussen (2019). **(C)** CTD-station HH16-541CTD from western pockmark area showing temperature (°C), conductivity salinity, (psu), density (g/m^3) and sound velocity (m/s). **(D)** Same parameters as in **(C)** for CTD-station HH16-548CTD from eastern pockmark area. See insert for legend. **(E)** Paleo-CTD showing temperature in the water column for Heinrich stadial H1. Modified from Rasmussen et al. (2007) and based on Mg/Ca bottom water temperature reconstructions for core HH15-1252PC from north of Vestnesa ridge El bani Altuna et al. (2021a).

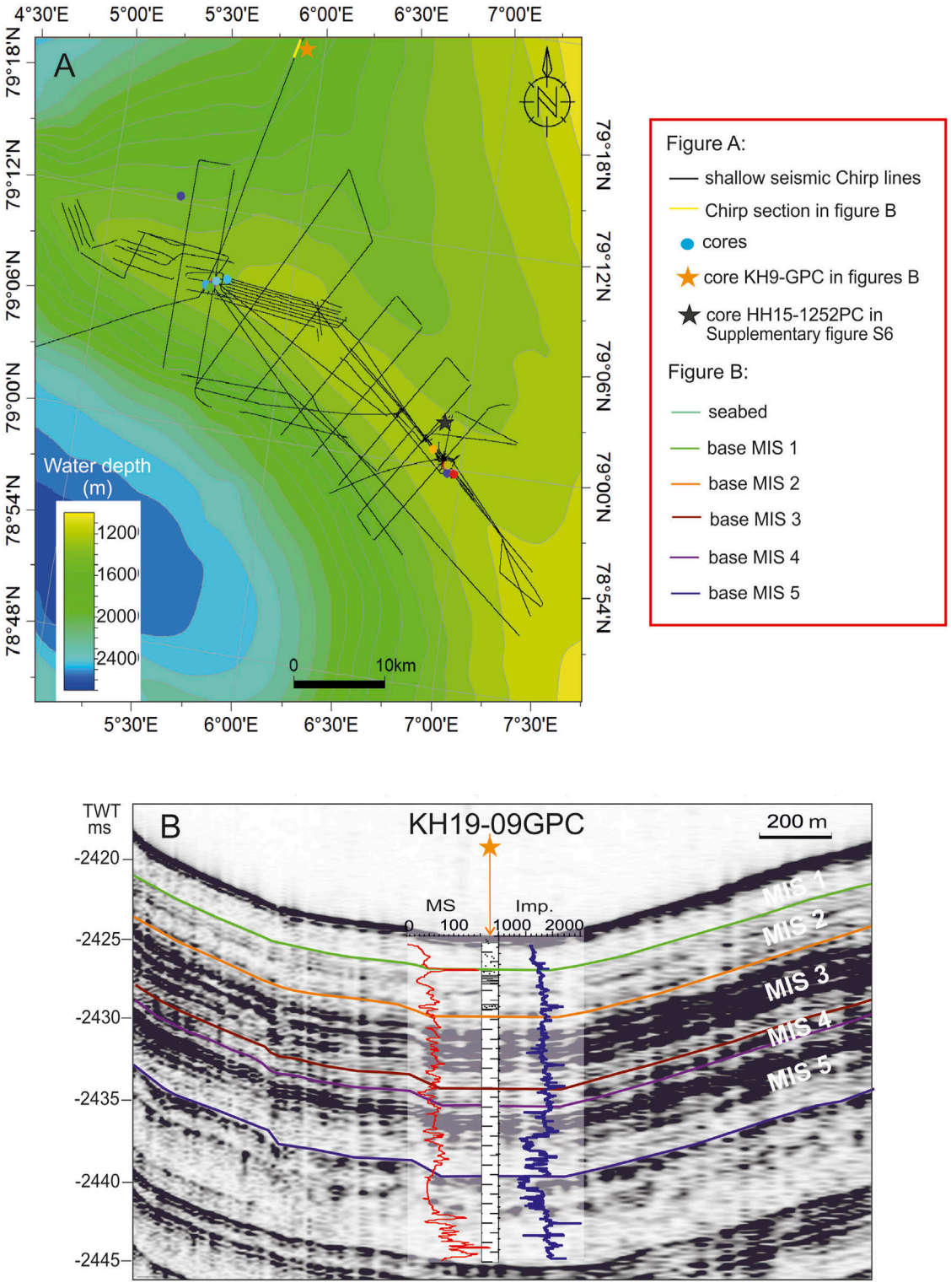

FIGURE 3
Database for shallow seismic interpretation. **(A)**: Database of shallow seismic Chirp lines together with position of sediment cores used to tie marine isotope stage (MIS) boundaries to the seismic data. Bathymetry illustrating the outline of Vestnesa Ridge from IBCAO (Jakobsson et al., 2020). **(B)**: Core-to-seismic tie of marine isotope stage (MIS) boundaries exemplified by core KH19-09GPC using the lithological log with marked MIS boundaries together with magnetic susceptibility (10^{-5} SI) and Impedance data from GEOTEK logging (Supplementary Figure S6, column C, D). An average sound velocity of 1,500 m/s is used for converting core data to time domain - see section 2.2 for additional information. See Figure 3A for location of core and Chirp line.

pockmark 'Lunde' (Eng.: 'Puffin') with irregular seepage of gas (Bünz et al., 2012) were sampled along active pockmarks slightly further to the west (Figures 1B,D,E). The majority of cores were taken from 'Lomvi' in two distinct areas with four cores taken from a southern elevated part with hard carbonate pavement in some parts and with fine-grained deposits in other parts (Figure 1E). From the elevated area, core HH12-928PC sampled hard pavement and contained numerous chemosymbiotic bivalves encrusted by authigenic carbonates and little sediment (Sztybor and Rasmussen, 2017a; Thomsen et al., 2019). Several cores were taken in an area to the northeast comprising the deepest depression within the 'pockmark (Figure 1E). Core HH12-929GC contained gas hydrates in the lower part (Sztybor and Rasmussen, 2017a) while two other cores taken from the same deep depression contained no gas hydrates (cores HH16-551GC and HH15-1241GC; 16 m and 38 m from site HH12-929GC) (Figure 1E). Nearby piston cores HH15-1253PC and HH15-1254PC, distanced 0.11 m and 29 m from site HH12-929GC, respectively had hit large chunks of gas hydrate probably preventing deeper penetration (Figure 1E; Supplementary Figure S1I,J). Core HH17-843GC from the same depression also hit gas hydrates (Figure 1E). Four cores from 'Lunde' pockmark were all taken near the edge of the pockmark in a relatively smooth area with no apparent disturbances (Figure 1D). Cores taken in active pockmarks further to the west contained large chunks of gas hydrates (Figure 1B; see references to cruise reports in Supplementary Material). The latter cores were logged onboard for magnetic susceptibility, but not opened (Supplementary Table S1; Supplementary Figure S1A–C,D–G). Three cores were taken away from the active pockmarks (JM10-333GC, HH15-1242GC and HH16-547GC) (Figure 1B; Supplementary Table S1). Cores from the inactive western Vestnesa pockmark field were taken in two different pockmarks (Figure 1C; Supplementary Table S1). In the northern sites three cores were taken from inside the pockmark (JM10-330GC, HH12-940PC, and HH16-550GC) and three taken outside, with two cores taken in the southern elongated pockmark (JM10-331GC and HH17-839GC) and one core HH17-840GC from outside of the pockmark.

The 14.81 m long giant piston ('Calypso') core KH19-09GPC was taken with RV *Kronprins Haakon* (KH) north of Vestnesa Ridge in 2019 (Supplementary Table S1). Several of the core records from Vestnesa Ridge have been previously published and is included, all with detailed stratigraphy from stable isotope-, grain size- (including counts of ice rafted debris (IRD)), foraminiferal faunal records and AMS-^{14}C datings (Supplementary Table S1). Published records from the western Svalbard margin are also included for comparison (Figure 1A; Supplementary Table S1).

Most cores were logged with a GEOTEK 7.9 Multi Sensor Core Logger at UiT the Arctic University of Norway before opening i.e., split in two-halves by cutting along the liners. Magnetic susceptibility (MS) was measured with a mounted loop sensor for 10 s in 1-cm steps along with wet bulk density, impedance, and P-wave velocity. Subsequently the cores were X-rayed on a GEOTEK Standard X-ray CT System. Not all cores were split, in particular cores that hit chunks of gas hydrates and were considered too disturbed, and some cores taken in 2017 and 2018 that were sampled for porewater onboard. Some split cores sampled for porewater were instead logged with GEOTEK for point-sensor magnetic susceptibility and color spectrophotometry. Also, split cores taken in 2016 and later were color imaged with a Jai L-107CC 3 CCD RGB line scan camera installed on an Avaatech XRF core scanner. All split cores were visually described, and color determined with a Munsell chart. Most cores were sampled by cutting the sediment into 1-cm thick slices. These were wet weighed, freeze dried and weighed again for water content. Samples were chosen from various intervals (from every 1 cm, 2.5 cm, or 5 cm intervals) according to lithology. Samples were sieved over sieves with mesh-sizes 0.063, 0.1 and 0.5 mm.

Selected cores taken in 2016, 2017 and 2018 were drilled for porewater sampling with holes of 2.5 cm diameter at either 10 or 20 cm intervals. After porewater extraction (10 mL) the cores were sampled with 20-mL syringes through the drilled holes for measurements of various parameters; here %TOC (total organic carbon) and %$CaCO_3$, grain size distributions and stable isotopes ($\delta^{18}O$ and $\delta^{13}C$).

Total carbon (TC) and total organic carbon (TOC) were measured in freeze dried samples in 10 or 20 cm intervals. Powdered bulk samples of 2–3 g each were measured using a Leco CS-200 induction furnace instrument. The weight percentages of TC and TOC were calculated and the %$CaCO_3$ was calculated using the equation of Espitalié et al. (1977).

The $\delta^{18}O$ and $\delta^{13}C$ values were measured in 10–20 specimens of the planktic foraminiferal species *Neogloboquadrina pachyderma* and/or benthic foraminiferal species *Cibicidoides wuellerstorfi* (two to five specimens), and/or *Melonis barleeanus*, (5–10 specimens) and/or *Cassidulina neoteretis* (20–30 specimens). The samples were analyzed on a ThermoScientific Gasbench II, MAT253 IRMS at the Department of Geosciences, UiT the Arctic University of Norway, Tromsø, Norway with a precision of the instrument of <0.1‰ on both $\delta^{18}O$ and $\delta^{13}C$. The results are reported on the VPDB (Vienna Pee Dee Belemnite) scale relative to NBS-18, NBS-19 and LSVEC.

New Accelerator Mass Spectrometry (AMS) ^{14}C datings for this study were performed at the 14Chrono Centre, Queen's University, Belfast, Northern Ireland, United Kingdom (Table 1). Samples of the planktic foraminiferal species *N. pachyderma* and bivalves were dated (Table 1). To be comparable to the previously published dates, the new ^{14}C dates for this study were calibrated using the Calib 7.04, Marine13 program (Reimer et al., 2013) with a reservoir age correction of −405 years and 1-σ error.

2.2 Shallow seismic data

A hull-mounted EdgeTech 3300-HM chirp sonar ('Chirp') with a frequency range of 2–16 kHz was used to collect high-resolution seismic profiles. Pulse mode and shot rate were varied, depending on the water depth and weather conditions. The maximum penetration of the Chirp data in the study area is ~60–70 ms two-way-time (TWT). A total of 1,430 km lines was used in the study. The Chirp data were stored in segy format and loaded onto a Petrel@ interpretation workstation in time domain (Figure 3A).

The seismic interpretation and stratigraphic breakdown of the contourite depositional system was based on identification of seismic horizons tying to marine isotope stage (MIS) boundaries defined in the sediment cores (Figures 3B,C). Only cores taken outside of pockmarks were included. The longest core KH19-09PGC was tied to the contourite system using seismic line

TABLE 1 AMS-^{14}C dates and calibrated ages for cores from Vestnesa Ridge.

Core (GC)	Depth cm	^{14}C -age	Calibrated age	Lab. Code	Species
HH16-543	432	25,789 ± 181	29,447 ± 250	UB36057	*N. pachyderma*
HH16-546	180	13,440 ± 51	15,617 ± 124	UB34706	*Nucula* sp.
HH16-547	156	Failed		UB35513	*N. pachyderma*
	308	Failed		UB35514	*N. pachyderma*
HH16-551	135	13,161 ± 55	15,199 ± 80	UB34711	*Nucula* sp.
	145	14,794 ± 57	17,593 ± 94	UB35149	*N. pachyderma*
	234	18,825 ± 84	22,317 ± 107	UB35150	*N. pachyderma*
	274	21,020 ± 106	24,809 ± 208	UB35151	*N. pachyderma*
HH16-554	156	Failed		UB35512	*N. pachyderma*

CAGE-19-3-KH-018 (Knies and Vadakkepuliyambatta, 2023) (Figures 3A,B). To tie the metric core records to the time records of the Chirp data, the core records were converted to time using an average seismic velocity of 1,500 m/s, which was found suitable based on the sediment content and GEOTEK measurements (Magnetic susceptibility, wet bulk density, P-wave velocity and impedance; Supplementary Figure S6). The same average seismic velocity for the upper sediment column at Vestnesa Ridge was observed by other studies (e.g., Plaza-Faverola et al., 2023). CTD measurements have shown that sound velocity in the water column is on average 1,465 m/s in our study area (Figures 2A,C,D).

Isochore maps of the individual MIS units were created by subtracting their corresponding upper and lower bounding reflectors in time domain and subsequently converted to metric scale using an average seismic velocity of 1,500 m/s. This velocity may be a little too high in areas with some free gas content or a little too low for areas with a patchy content of gas hydrate. However, dealing with the shallow sediment column, these minor variations will not significantly change the greater perspective of erosional and depositional areas which the main purpose of the mapping. The maps were produced using the Convergent interpolation algorithm with input data as boundary and grid increment set to 1,200.

3 Results

3.1 Sediment cores

3.1.1 Correlation to the general stratigraphy of the Svalbard margin

The stratigraphy of cores is based primarily on patterns of variability in magnetic susceptibility (MS) values in combination with lithology, sediment color, grain size, $\delta^{18}O$, %TOC, %$CaCO_3$ and AMS ^{14}C dates and by correlation to the magnetic susceptibility stack of Jessen et al. (2010) that are based on 11 cores from the western Svalbard margin. The pattern of variation in MS values is linked to characteristic sediment marker horizons: a dark grey-brown, coarse, unsorted layer of low magnetic susceptibility dating ~24 ka (marked by a brown bar in Figures 4–6; Supplementary Figure S2–S5), a dark bluish-grey laminated clay deposit also of low magnetic susceptibility dating ~15 ka (grey bar). A diatom layer deposited in the lower Holocene dates ~10 ka (Jessen et al., 2010) (yellow bar).

The MS stratigraphy and age model of Jessen et al. (2010) cover the last 30 ka (Figure 4A). The stratigraphy has since been extended into MIS 4 (Rasmussen et al., 2014; Jessen and Rasmussen, 2015; El bani Altuna et al., 2021a) and through MIS 5 into MIS 6 (Michel et al., 1999; Risebrobakken et al., 2005). Most cores from western Vestnesa Ridge only reach into late MIS 3 (Figures 4I–L) while cores from off the crest and eastern Vestnesa Ridge reach into early or mid-MIS 3 or MIS 4 (Figures 4B–F; Supplementary Figure S2D). Only one record, the giant piston core KH19-09GPC reach into MIS 6 (Supplementary Figure S2E).

Deposits of MIS 6 (>130 ka) are predominantly of dark grey color, while MIS 5, MIS 4 and MIS 3 130–75 ka (75–60 ka, and 60–29 ka, respectively) are composed of layers of light greyish sediment and darker grey layers with a varying content of IRD and highly variable MS and $\delta^{18}O$ values reflecting the DO millennial scale events (Michel et al., 1999; Rasmussen et al., 2014; Jessen and Rasmussen, 2015; 2019; Caricchi et al., 2019) (Figures 5A,C,E). The sediments of MIS 2 (28–12 ka) has layers of both light grey, and dark grey color. The last glacial maximum (LGM) is defined as the period of maximum oxygen isotope values dating 24–19 ka (Lisiecki and Raymo, 2005) (Figure 5; Supplementary Figure S4). The start of the LGM is marked by the coarse dark grey-brown layer.

The Heinrich stadial H1 of the early deglaciation on the western and northwestern Svalbard margin is generally marked by a thin light-grey horizon dating ~19–15 ka and is characterized by very low sedimentation rates and a characteristic spike of low $\delta^{18}O$ values (e.g., Birgel and Hass, 2004; Jessen et al., 2010; Jessen and Rasmussen, 2019) (Figure 5; Supplementary Figure S4). The Bølling

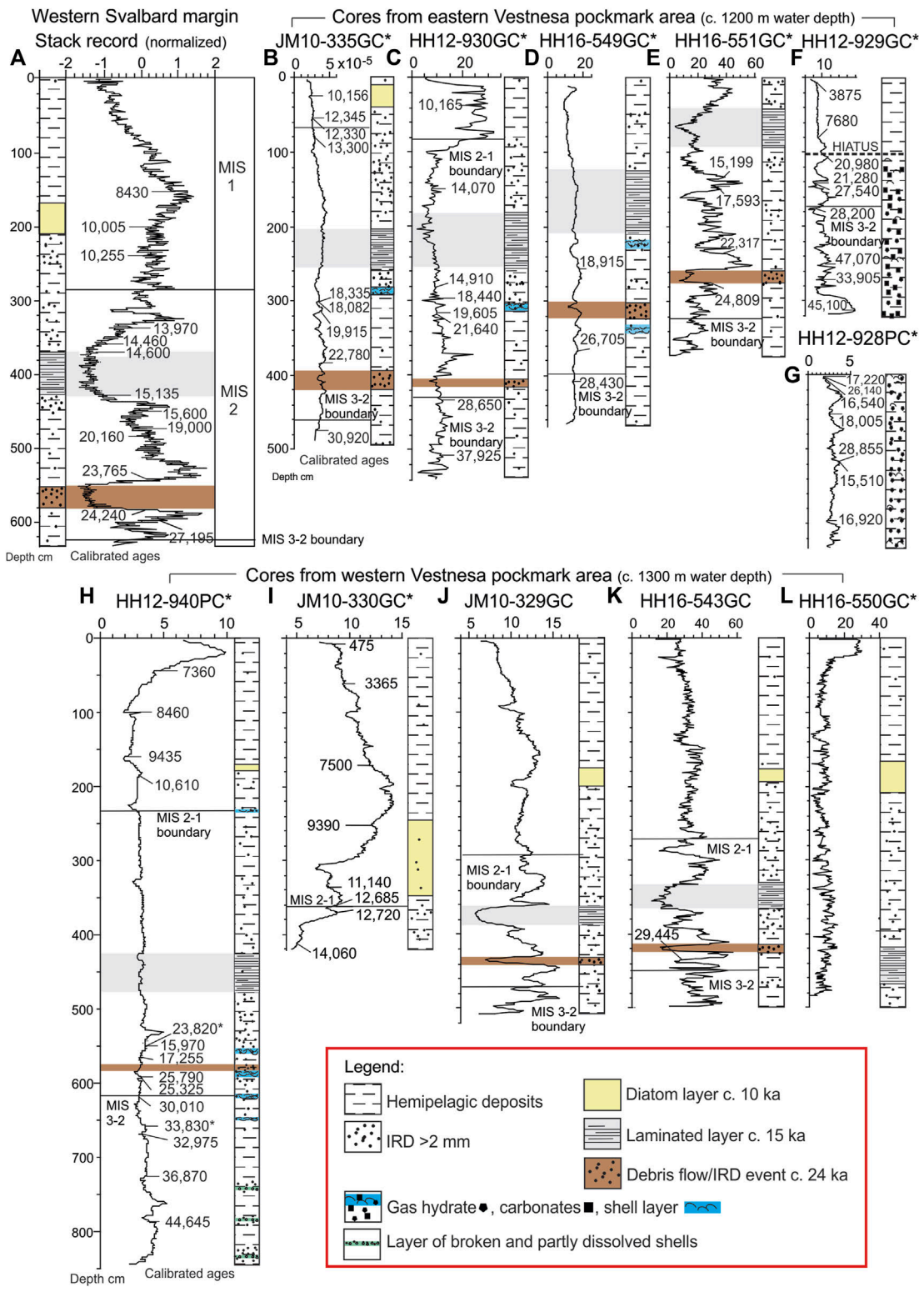

FIGURE 4
Magnetic susceptibility (10^{-5} SI) and lithological logs with marine isotope stage (MIS) boundaries marked. **(A)** Stack records of magnetic susceptibility for the western Svalbard margin from Jessen et al. (2010). **(B–G)**. Cores from the eastern active pockmark area. **(H–L)**: Cores from the western inactive pockmark area. See insert for legend. AMS-^{14}C dates are indicated; see also Table 1 for new dates for this study. Abbreviations: IRD; ice rafted debris. Asterisks mark cores taken from within pockmarks. See also Supplementary Table S1 for details and references to previously published records.

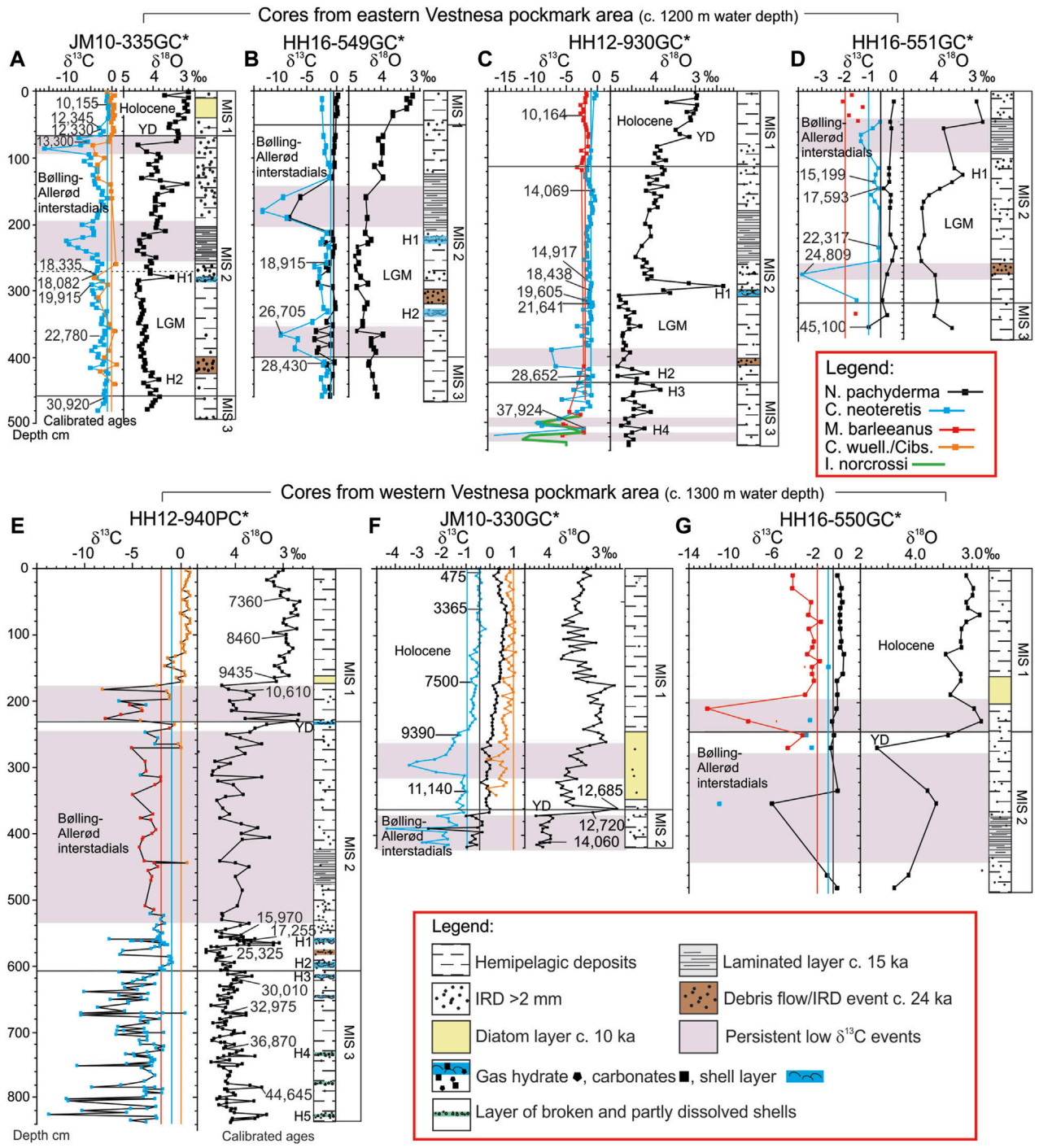

FIGURE 5
Stable isotope records (‰) ($\delta^{13}C$ and $\delta^{18}O$) for cores from the eastern active **(A–D)** and western inactive **(E–G)** pockmark areas along lithological logs. Purplish bars mark event of low $\delta^{13}C$ mainly focusing on MIS 2 and MIS 1. Vertical colored lines mark average minimum glacial $\delta^{13}C$ values of the measured benthic and planktic foraminiferal species. See insert for legend. AMS-^{14}C dates are indicated. Marine isotope stage (MIS) boundaries are marked, and specific stratigraphic horizons indicated (LGM; last glacial maximum, Heinrich stadials; H1–H5, Bølling and Allerød interstadials, YD; Younger Dryas, and Holocene. Abbreviations: IRD; ice rafted debris, C. wuell.; *Cibicidoides wuellerstorfi*, Cibs.; *Cibicides lobatulus*. Asterisks mark cores taken from within pockmarks. See also Supplementary Table S1 for details and references to previously published records.

interstadial of the deglaciation (~15–14 ka) is marked by the dark-grey, bluish laminated layer of low MS seen in all records (Figures 4–6; Supplementary Figure S2–S5). The sediments of the following Allerød interstadial 14–13 ka contain a high concentration of IRD, while the Younger Dryas stadial (13–12 (11.7) ka) appears as a light grey layer with low $\delta^{18}O$ (Figure 5A, C–G).

The Holocene interglacial is characterized by light brownish sediments. The cores show a typical Holocene MS signal of

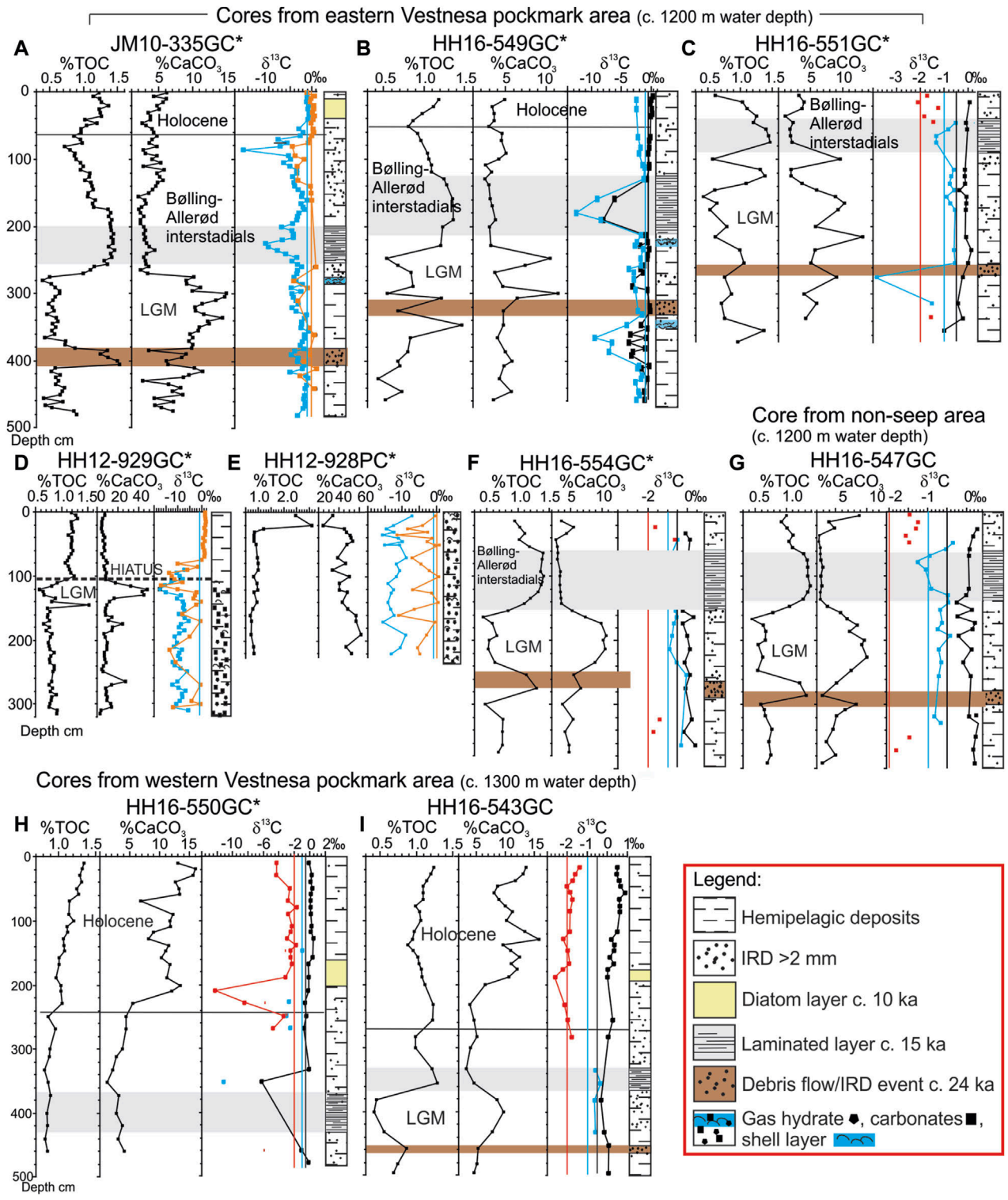

FIGURE 6
Percent total organic carbon (%TOC), percent calcium carbonate (%$CaCO_3$), and $\delta^{13}C$ (‰) for cores from the eastern active **(A–G)** and western inactive **(H, I)** pockmark areas along lithological logs. See insert for legend. Holocene, Bølling and Allerød interstadials, and LGM (last glacial maximum) are marked where present. Asterisks mark cores taken from within pockmarks. Abbreviations: IRD; ice rafted debris. See also Supplementary Table S1 for details and references to previously published records.

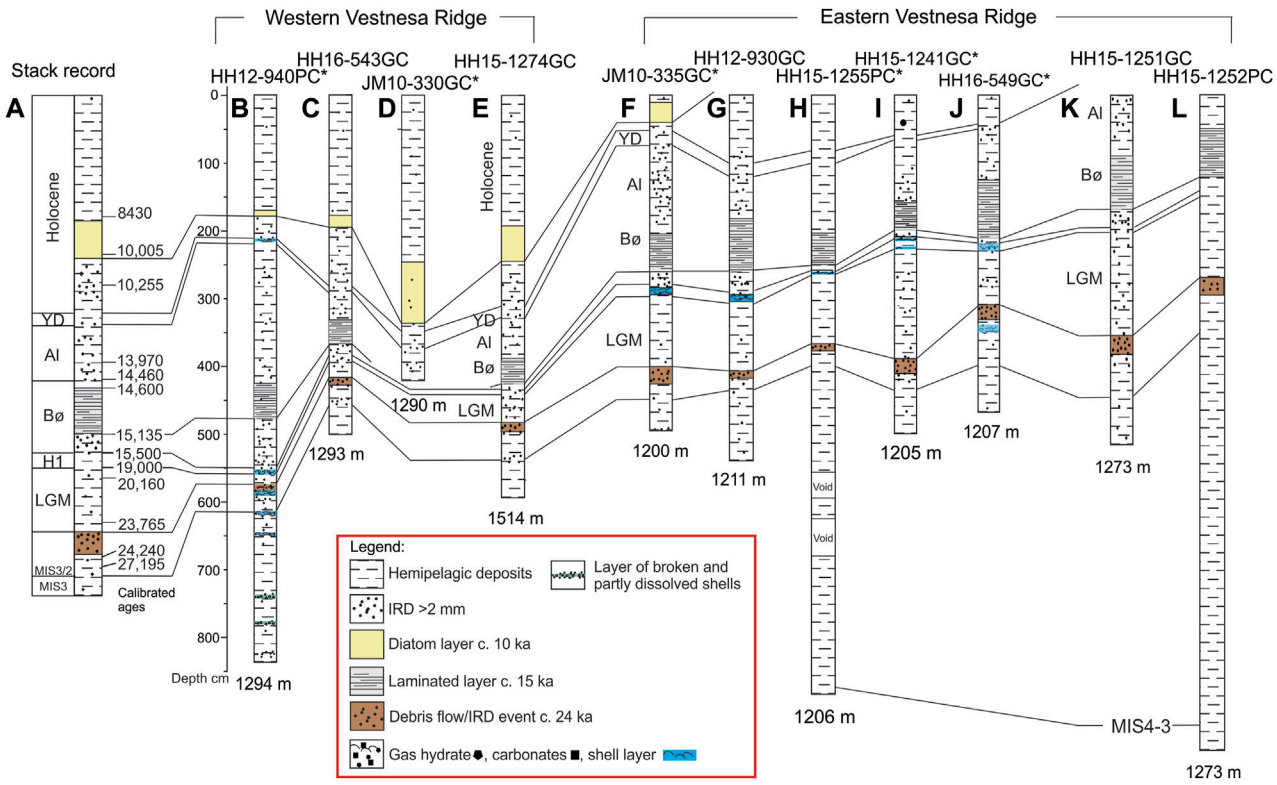

FIGURE 7
Correlation between the stack lithological record **(A)** with selected core records from western **(B–E)** to eastern Vestnesa Ridge **(F–J)** and to cores north of eastern Vestnesa Ridge **(K, L)**. The stack record from the western Svalbard margin in **(A)** is modified from Jessen et al. (2010). See insert for legend. The sediments dating from the last glacial maximum (LGM) thickens, while Holocene sediments thins and disappears towards the east. In general (with the exception of **(B)**), the Bølling and Allerød (abbreviated Bø, Al) thickens towards east. Other abbreviations: H1; Heinrich stadial 1, YD; Younger Dryas stadial, IRD; ice rafted debris. Water depths are marked below each core record.

slowly increasing values to a peak dating ~8.2 ka followed by gradually decreasing values (Jessen et al., 2010) (Figure 4A, H–K). The $\delta^{18}O$ values are low characteristic for interglacial conditions (Figures 5A–C, E–G; Supplementary Figure S5C,F,G). The diatomite of whitish or yellowish color deposited at ~10 ka in the early Holocene is present in most records from western Vestnesa Ridge areas, but has only been observed in a few cores from the eastern part as Holocene deposits are either thin or lacking here (Sztybor and Rasmussen, 2017a; b; Thomsen et al., 2019; El bani Altuna et al., 2021a) (Figures 4, 7; Supplementary Figure S2, S3).

3.1.2 Magnetic susceptibility patterns in pockmark records

Several cores from within pockmarks on Vestnesa Ridge has low, and sometimes nearly constant MS values (Figure 4; Supplementary Figure S1, S3). This is due to disturbance by strong seepage of methane or presence of gas hydrates (e.g., Novosel et al., 2005). However, in most cases the records display an undisturbed lithology (e.g., Myrvang, 2015; Sztybor and Rasmussen, 2017a; Åsheim, 2017; Matteis, 2018; Hansen et al., 2020) (Figure 4; Supplementary Figure S2, S3). Other cores from pockmarks can show the typical pattern and values of MS as found elsewhere on the western and northern Svalbard margin (e.g., Elverhøi et al., 1995; Knies et al., 1999; Birgel and Hass, 2004; Jessen et al., 2010; Chauhan et al., 2016a) (Figure 4E; Supplementary Figure S3B). Note that some records with low MS values but plotted on an expanded x-axis scale in fact do display the typical MS pattern (Figures 4I,J; Supplementary Figure S3A,C,F–H).

3.1.3 Distribution of %TOC and %$CaCO_3$ and correlation to known stratigraphy

Cores from Vestnesa Ridge and outside of pockmark areas and published cores JM10-335GC, JM10-333GC (Sztybor, 2016), HH16-549GC (Åsheim, 2017), and cores from 2016 with a known stratigraphy from oxygen isotopes and/or AMS-^{14}C dates, all show a clear correlation between %TOC and %$CaCO_3$ data with lithology (Figures 6A–C, F–H; Supplementary Figure S5C). The coarse unsorted dark layer and the laminated horizon show high %TOC and low %CaCO3, while the LGM have low %TOC and high %$CaCO_3$. Some cores show some deviating peaks in % $CaCO_3$ (Figures 6D,E; Supplementary Figure S5D,F).

The same pattern in distribution of %TOC and %$CaCO_3$ is seen in cores from the inactive western pockmark sites (Figures 6G,H; Supplementary Figure S5G, H). Here, the Holocene sediments show high %TOC >1%, and high %$CaCO_3$ >10%. Four cores sampled for pore water, %TOC and %$CaCO_3$ and presumably containing gas hydrates were not logged for magnetic

susceptibility or opened for description. Based on the %TOC and $\%CaCO_3$ records the stratigraphic marker horizons and Holocene deposits could be identified for three of the cores (Supplementary Figure S5A, B, F).

3.1.4 Variations in benthic $\delta^{13}C$ values

The $\delta^{13}C$ records show generally high $\delta^{13}C$ values in cores taken outside of pockmarks and highly variable values in records from inside of pockmarks. In environments unaffected by methane seepage $\delta^{13}C$ values in the species measured in this study range −2 to 0‰ for the infaunal benthic foraminiferal species *M. barleeanus* and *C. neoteretis* on glacial and interglacial time scale (McCorkle et al., 1990; El bani Altuna et al., 2021a) and 0 to >+1‰ for the epifaunal species *C. wuellerstorfi* (e.g., McCorkle et al., 1990; 1997). In cores taken from pockmarks many have intervals of values <-10‰ (Figures 5A–C,E,G; Supplementary Figure S4C–E), a sign that the measured foraminiferal specimens have had coatings with authigenic carbonate, although not visible in the binocular microscope. Other cores have slightly lower $\delta^{13}C$ than the typical range of the species (Figures 5D,F; Supplementary Figure S4A,B,E). The low $\delta^{13}C$ intervals correlate with the glacial period and the deglaciation with peak low values in the Bølling and Allerød interstadials and lower Holocene until ~10–9 ka (Figures 5A,B, D–G; Supplementary Figure S4A–C,E).

3.2 Depositional patterns and sedimentation rates

3.2.1 Eastern Vestnesa Ridge, ~1,200 m water depth, ~60–14 (10) ka

Cores taken on the crest outside of pockmarks on eastern Vestnesa Ridge contain no Holocene sediments but show a coarse sandy, gravelly lag deposit at the top dating ~14 ka right below the sediment surface (Sztybor and Rasmussen, 2017a) (Supplementary Figure S2C,D,F–I). The cores taken from inside of pockmarks at the very active pockmark field of seepage of methane at ~1,200 m water depth (Figures 1B,D,E) cover MIS 4–2, ~60–14 ka (except for some cores that may contain sediments of lower Holocene age dating <10 ka near the core top) (Figures 4B–G, Figure 5A–C). Sediments dating from the LGM (not including the coarse dark deposit dating ~24 ka) are around 1–2 m thick, giving an average sedimentation rate for the period 24–19 ka of 23 cm/ka (range 19–34 cm/ka) (Table 2). Sediments from the deglaciation including the laminated horizon are thick with an average sedimentation rate of 91 cm/ka (range 38–140 cm/ka) (ignoring H1 of very low sedimentation rates of average ~3 cm/ka (range 1.6–4.4 cm/ka)) (Table 2). Thus, in most cores from ~1,200 m water depth, the laminated layer occurs close to the seafloor at about 20–100 cm down core depending on presence of sediments dating from the Early Holocene (Figures 4B,C,F). The longest record core HH15-1255PC reaches back to ~60 ka and has an average depositional rate for MIS 3 of ~10 cm/ka with variable MS values indicating millennial scale oscillations (Matteis, 2018) (Supplementary Figure S3F).

3.2.2 Southern flank of Vestnesa Ridge

The southern ridge flank is relatively steep and affected by faulting and slumping, but not affected by seepage of gas and represented by cores 067GC and MSM5/5-712 (Figure 1A; Supplementary Table S1). These cores show the same characteristic MS signal for the time interval 30–14 ka (Howe et al., 2008; Zamelczyk et al., 2014). The shallow core 067 is very similar to the records from the eastern pockmark area with no Holocene and dating approximately 14 ka at the top. The record has similarly high sedimentation rates of 113 cm/ka for the deglaciation and 20 cm/ka for the LGM interval (Table 2). Core MSM5/5-712 (Müller et al., 2012; Zamelczyk et al., 2014; Falardeau et al., 2018; 2019) has 3.5 m of Holocene sediments (average Holocene sedimentation rates ~30 cm/ka), deglaciation ~87 cm/ka and 22 cm/ka for the LGM (Table 2).

3.2.3 Western Vestnesa Ridge pockmark area, ~1,300 m water depth

We note that both the coarse dark, grey-brown layer and the laminated layer are thinner than in the records from eastern Vestnesa Ridge (Figures 4, 7; Supplementary Figure S3). The deposits dating from the LGM are also much thinner. The average sedimentation rates for the LGM are thus 10 cm/ka (range 2–22 cm/ka) at 1,300 m water depth compared to 23 cm/ka at ~1,200 m water depth (Table 2). The sedimentation rates for the deglaciation (ignoring H1; see Table 2) are also lower than at eastern Vestnesa Ridge and is of 39 cm/ka (range 22–86 cm/ka) compared to almost 1 m/ka on the inner part at 1,200 m water depth.

In contrast to the records from the eastern part, western records show presence of >2.5 to >3 m thick Holocene deposits (Figures 4H–L, 7; Supplementary Figure S3G–J). The well-dated record of core JM10-330GC (Consolaro et al., 2015) confirms that the entire Holocene probably is preserved in all records except core HH12-940PC. The diatomite is prominent and located ~2 m to >3 m below the seafloor. The Holocene sediments at western Vestnesa Ridge are generally deposited at high average sedimentation rates of 26 cm/ka (range 19–32 cm/ka) (Table 2).

The longest record HH12-940PC dates ~50 ka at the bottom (calculated by extrapolation from the two lowermost dates in the core; Figure 4H). Thus, the average sedimentation rate for the mid-late MIS 3 at 28–50 ka is calculated to ~13 cm/ka (Table 2).

3.2.4 Northern flank of Vestnesa Ridge, 0–>150 ka

Cores HH15-1250GC, HH15-1251GC and HH15-1252PC are all taken on the northern flank of Vestnesa Ridge off the active pockmarks at the eastern part of the ridge (Figure 1A; Supplementary Figure S2C,D,H; Supplementary Table S1). They are taken at similar water depths (1,265 m, 1,273 m, and 1,273 m, respectively). All three cores possess the typical lithological features and patterns of MS and shows a lag deposit at the core top dating ~14 ka and thus no Holocene deposits as for records on the eastern crest of the ridge. The average sedimentation rate for the LGM in the three records is 30 cm/ka (Table 2). In core HH15-1252PC which reach into MIS 4 (El bani Altuna et al., 2021a) (Figure 7L; Supplementary Figure S2D), the average sedimentation rate for MIS 3 is 19 cm/ka, the highest so far compared to sedimentation rates on the crest of the ridge.

TABLE 2 Average sedimentation rates for Vestnesa Ridge core records in cm/ka ∗ .

Area/period	Inner Vestnesa ~1,200 m water depth	Outer Vestnesa ~1,300 m water depth	Outer northern flank HH15-1274GC	Northern flank HH15-1250GC, –1251GC, –1252PC	KH19-09GPC	Northern flank MSM5/5-723	Southern flank MSM5/5-712	Sourthern flank 067GC
Holocene 11.7-0 ka		26	24			40	30	
Deglaciation 15.5-11.7 ka	91	39	41	111	133		87	113
H1 19–15.5 ka	3	3	2	3			3	3
LGM 24-19 ka	23	10	11	30	16		22	20
MIS 3	9	13		19	12			
MIS 4					9			
MIS 5					8			

∗ See Supplementary Table S1 for core locations and references.

Core HH15-1274GC taken on the northern flank of western Vestnesa Ridge at 1,514 m water depth is very comparable to the cores from the western crest of Vestnesa with ~3 m of sediments of Holocene age (Figure 7E; Supplementary Figure S2B). For this site the average sedimentation rate is 24 cm/ka for the Holocene, 41 cm/ka for the deglaciation and 11 cm/ka for the LGM (Table 2). Core MSM5/5-723 from 1,350 m water depth shows >4 m of Holocene sediments with an average sedimentation rate exceeding 40 cm/ka (Werner et al., 2015) (Figure 1A).

Giant piston core KH19-09GPC of high resolution from 1767 m water depth north of Vestnesa Ridge and north of site HH15-1274GC shows an MS pattern with the characteristic intervals of low values marking the laminated and coarse grey-brown horizons and indicating that ~1 m of Holocene sediments is present at this location (Supplementary Figure S2E). From comparison and correlation with the MS records of cores MD99-2303 and MD99-2304 from the western Svalbard margin (Michel et al., 1999) and age models by Risebrobakken et al. (2005), it becomes evident that core KH19-09GPC probably reach well into MIS 6 and possibly MIS 7 at the bottom dating >150 ka. In core KH19-09GPC, MIS 3 has an average sedimentation rate of 12 cm/ka; low rates deeper in the core are probably due to some level of compaction (Table 2).

3.3 Shallow seismic mapping

A gross breakdown of Vestnesa Ridge into three large seismic units (YP-1, YP-2 and YP-3 from below) was first described by Eiken and Hinz (1993). Subsequently, the youngest YP-3 unit has been dated to span the last ~2.7 Ma (e.g., Mattingsdal et al., 2014). The shallow penetrating Chirp data cover the uppermost and youngest sub-units of the YP-3 unit.

The reflection patterns of the Chirp lines show strong parallel to sub-parallel reflections occurring as stacked, close-lying reflectors separated by sections with no or only faint internal reflectors as illustrated in Supplementary Figure S3B. This reflection pattern is seen throughout most of the study area apart from the lower southern ridge flank where it become dense and tapes out to below the Chirp data resolution, and where also faults and slides displace or destroy the reflections. Passing over pockmarks, the overall reflection patterns is also disturbed and often bended downwards. At some places the bended reflectors can be traced underneath the pockmark, at other places the reflection patterns are strongly disturbed or completely wiped out. The latter phenomenon is most pronounced in the eastern pockmark area. The stratigraphic breakdown of the Chirp data into MIS units are illustrated by the ties to core KH19-09GPC in Figure 3B and creation of isochore maps (Figures 8B–F). The isochore map of MIS 1 (Figure 8B) shows a marked depocenter up to 4 m thick on the northwestern Vestnesa Ridge at 1,300–1,600 m present water depth and displays an overall absence of the MIS 1 unit on the eastern crest and flanks, as well as a thinning of the unit to below seismic resolution approximately halfway down the southwestern ridge flank where also faulting and sliding prevent further downslope interpretation.

The MIS 2 unit was mapped throughout the study area (Figure 8C). The isochore map of this unit demonstrates a somewhat chaotic distribution of the up to 3–4 m thick sediment column with no clear depocenter, yet with some thinning of the unit at the lower southwestern ridge flank. Also, some thinning is seen in places along the ridge crest which, however, could be connected to presence of pockmark fields.

More than 6 m of sediments has been deposited during MIS 3 as illustrated in Figure 8D. This unit is also mapped throughout the study area and shows a clear depocenter within the same area, yet a little further east compared to the MIS 1 depocenter. But in contrast to MIS 1, deposition during MIS 3 also took place along the ridge crest and northeastern ridge flank, while the sediment thickness thins to ~2 m at the lower southwestern ridge flank. This deposition pattern is taken as evidence of the action

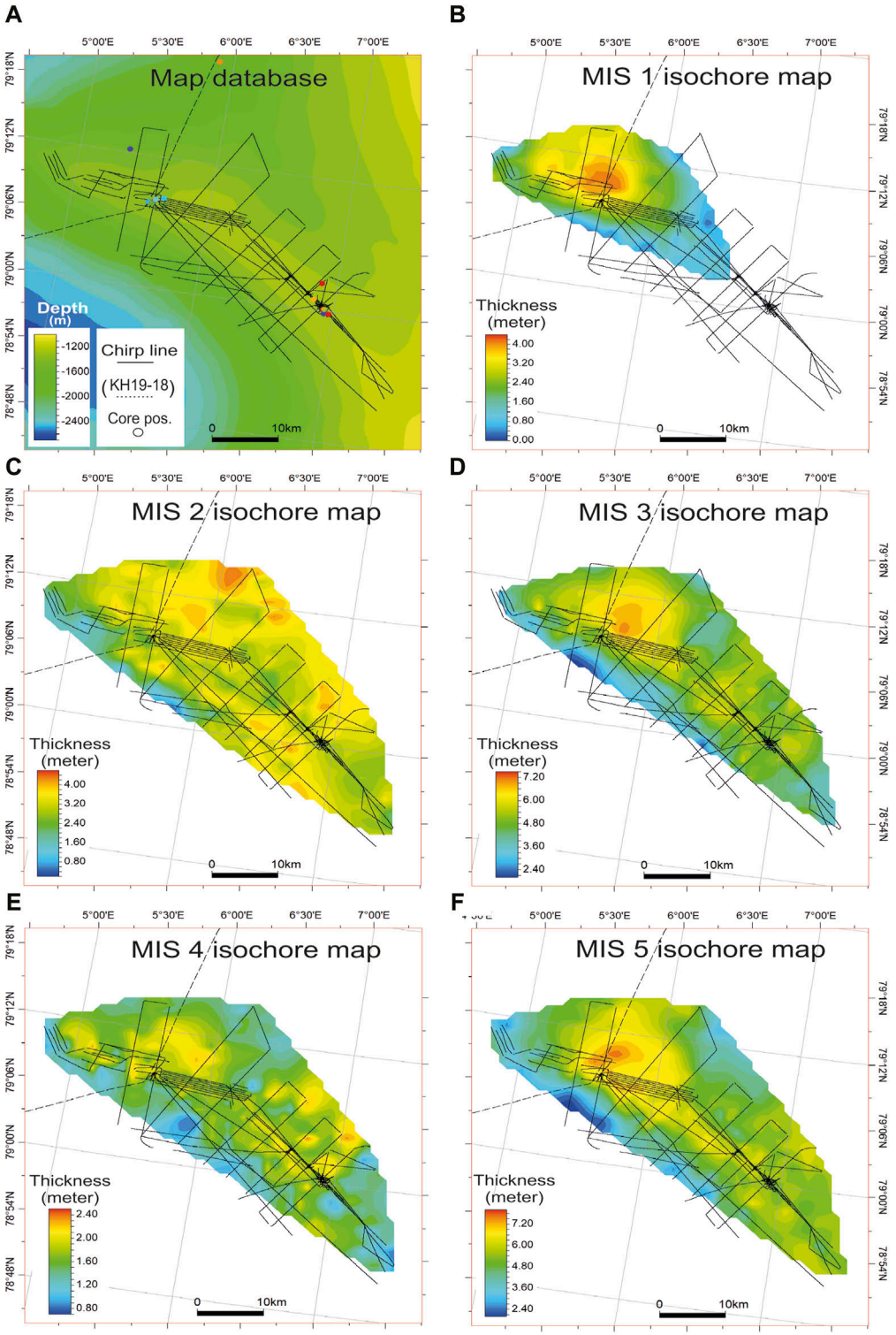

FIGURE 8
Seismic isochore maps of marine isotope stage (MIS) units 1 to 5. **(A)**: Database of shallow seismic Chip lines (black lines) and location of sediment cores (various colored dots) used for creation of the various marine isotope stage (MIS) isochore maps. **(B–F)**: Isochore maps (in meters) illustrating the thickness of MIS units 1 to 5 (see section 2.2 for details on construction of the maps). Note the color ranges are scaled to sediment thickness for each map.

of a current flowing northward following the depth contours of Vestnesa Ridge, and with a current core lying close to the then ridge crest.

The MIS 4 isochore map (Figure 8E) reveals that sediments deposited during this period are relatively thin and amounts to little more than 2 m. The depositional pattern across the ridge appears chaotic and resembles that of MIS 2 (Figure 8C), though with lesser deposition on the ridge flanks.

MIS 5 is the oldest period mapped and the thickest unit with more than 7 m of sediments as revealed by the MIS 5 isochore map (Figure 8F). The depositional pattern of this unit resembles remarkedly that of MIS 3, suggesting an overall similar sedimentation environment for the two periods.

4 Discussion

4.1 Spatial-temporal distribution of depocenters at Vestnesa Ridge: combining cores and seismic mapping

While the shallow seismic mapping provides an overview of the gross depositional environment on Vestnesa Ridge on isotope stage levels of MIS 5–1 using cores from outside of pockmarks (Figures 8A–E), the core records from both inside and outside of pockmarks offer more details on millennial-scale changes in sedimentation patterns, bottom current speed, and sediment source. Most cores taken in pockmarks have a solid stratigraphy from both AMS-^{14}C dates, lithology, and magnetic susceptibility, stable isotope records, organic and inorganic carbon records that allow for identifying events on suborbital scale (Figures 4–6; Supplementary Figure S2–S5). Most core records from Vestnesa Ridge from both inside and outside of pockmarks contain MIS 3 to MIS 1 (including the LGM, deglaciation, and Holocene), which represent the clearest contrasting changes in sedimentation patterns (Figures 4–7; Table 2).

MIS 1: The gross distribution of Holocene interglacial (MIS 1) sediments, as seen in the seismic isochore map (Figure 8B), indicates that the bottom currents during MIS 1 flowed northwards following the seabed contours around the tip of Vestnesa Ridge, and that the strongest currents were focused around 1,200 m present water depth similar to today (e.g., Fer et al., 2023), causing non-deposition or erosion over the eastern crest and upper flanks of Vestnesa Ridge. The core records show the same pattern of sedimentation (Figures 2, 4 –7, Figure 8B; Table 2). The maximum sedimentation rates are found north of the ridge tip, where core MSM5/5-723-2 at 1,350 m water depth with >4 m of Holocene deposits (Werner et al., 2015) and core HH15-1274GC are located (Figure 1A). On the lower southern flank, a maximum thickness recorded by sediment cores was found at 1,500 m water depth in core MSM5/5-712-2 (Müller et al., 2012), while erosion took place on the upper southern flank at 1,226 m water depth (Howe et al., 2008) (Figure 1A). In general, on the western Svalbard slope, Holocene deposits are found deeper than ~1,300 m water depth (e.g., Ebbesen et al., 2007; Jessen et al., 2010; Lucchi et al., 2013; Rebesco et al., 2013). Our results are in accordance with modern ocean current patterns where strongest currents over the western Svalbard margin occur around ~1,200 m water depth (e.g., Hopkins, 1991; Schlichtholz and Houssais, 1999a; Fer et al., 2023). Erosion or non-deposition usually occur at <1,200 m water depth (Howe et al., 2008; Jessen et al., 2010; Rebesco et al., 2013) (Figure 7). The 1,500 m depth contours along the western Svalbard margin form the main depocenters of contourites on the margin (e.g., Jessen et al., 2010; Müller et al., 2012; Rebesco et al., 2013; Caricchi et al., 2019). On Vestnesa Ridge, the depocenters appears to be slightly shallower located at 1,300–1,400 m over the western and northwestern part (Figures 7, 8B), indicating that the tip of the protruding ridge has caused the currents to slack.

MIS 2: The chaotic sediment distribution and lack of a marked depocenter seen in the seismic isochore map (Figure 8C) suggests a slowdown of the current strength during MIS 2 causing a change in the depositional environment to be less current dominated. In the seismic mapping however, MIS 2 comprises both the LGM and the deglaciation. The core records can refine MIS 2 by distinguishing the glacial maximum and the deglaciation. In the core records, we observe the highest sedimentation rates and thus thickest deposits for the LGM on the eastern part at ~1,200 m water depth and often with >2 m of sediments excluding the dark coarse layer (Figures 4B–G, 7; Table 2; Supplementary Figure S3A–F). Deeper than ~1,250 m at western Vestnesa Ridge deposits from the LGM thins to <1–~1 m of thickness (Figures 4H–L, 7; Supplementary Figure S3G–J). The coarse layer is interpreted as part debris flow event and an event of intense deposition of local IRD from the Barents Sea and Svalbard margin consisting of grey, brown, and black shales of very low MS (e.g., Jessen et al., 2010; Jessen and Rasmussen, 2019). The event occurred when the Svalbard-Barents Sea Ice Sheet reached the shelf edge at ~24 ka (e.g., Elverhøi et al., 1995; 1998; Jessen et al., 2010) (Figures 4–6; Supplementary Figure S2–S5).

During the deglaciation (late MIS 2) sedimentation rates were at a maximum over the entire Vestnesa Ridge (Table 2). The laminated layer dating from the Bølling interstadial is interpreted as a plumite deposited at very high sedimentation rates from sediment-laden meltwater plumes from the Barents Sea when the Barents Sea Ice Sheet melted back at the beginning of the warming of the Bølling interstadial (e.g., Birgel and Hass, 2004; Jessen et al., 2010; Junttila et al., 2010; Lucchi et al., 2013; 2015). The layer is found along the entire western Svalbard margin (e.g., Elverhøi et al., 1998; Jessen et al., 2010; Lucchi et al., 2013; Caricchi et al., 2019) being thickest off Storfjorden Trough and south of the Storfjorden Fan and thins with water depth on the slope and northward (Knies et al., 1999; Jessen et al., 2010; Lucchi et al., 2013; 2015; Chauhan et al., 2016a). In general, on Vestnesa Ridge the laminated layer and deglacial sediments thins from southeast to northwest with depth (Figures 4–7; Table 2; Supplementary Figure S2–S5). This points to that bottom currents must have been relatively weak and that distance to the source (Barents Sea) was the overruling factor (e.g., Elverhøi et al., 1998; Jessen et al., 2010; Jessen and Rasmussen, 2019).

Sortable silt records from 1880 m water depth on the western Svalbard slope show generally strong bottom currents during the Holocene and weaker (but variable) currents during the LGM and minimum strength during the Bølling interstadial (Jessen and Rasmussen, 2015). Also, currents were reduced and sedimentation rates low during Heinrich event H1 and the Younger Dryas, as we also record at Vestnesa Ridge (Table 2). Results from the western

Svalbard margin and Nordic Seas show that the H1 event was deposited under very cold conditions with almost permanent sea ice cover (Müller and Stein, 2014; Hoff et al., 2016; El bani Altuna et al., 2024). The cold Younger Dryas event was also characterized by dense sea-ice cover and generally low sedimentation rates (Müller et al., 2009; Jessen et al., 2010; Müller and Stein, 2014; Jessen and Rasmussen, 2019).

The sedimentation pattern of the contourite on Vestnesa Ridge on a glacial-interglacial scale mimic patterns of sedimentation in other contourites from the western Svalbard margin indicating a large change in strength of the deeper water flow (Figures 7, 8C; Table 2). The contourites were building up during glacial times shallower than ~1,200 m, and deeper than 1,300 m during interglacial times on Vestnesa Ridge and generally deeper than ~1,500 m on the western slope of Svalbard (e.g., Eiken and Hinz, 1993; Jessen et al., 2010; Rebesco et al., 2013; Caricchi et al., 2019). This points to weaker currents during glacials allowing deposition higher on the slope, while strong currents led to deposition at depth during the Holocene (Figures 7, 8B). Similar changes on glacial-interglacial scale were found on the northern Faroe margin and the Faroe-Shetland Channel. Here, Holocene deposits were found deeper on the slope from ~1,000 m and deeper while erosion and non-deposition took place shallower than ~900 m water depth (Nielsen et al., 2007). The similarity in sedimentation patterns and bottom water flow at both the Faroe and Svalbard margin thus indicates pronounced changes in strength of deep convection in the Nordic Seas.

MIS 3: The overall depositional pattern observed in the MIS 3 isochore map (Figure 8D), and its resemblance with that of MIS 1 (Figure 8B), likely evidence a similar depositional environment of the two interglacial periods, i.e., the bottom current flowed northward following the depth contours of Vestnesa Ridge with a current core lying close to the depth of the then ridge crest.

Sediments covering most or all of MIS 3 are represented by four records from Vestnesa Ridge. During MIS 3 deposition over the ridge shows lowest average sedimentation rates at 1,200 m water depth in accordance with sediment thicknesses from the seismic compilation. On the western ridge from ~1,250 m deposits were thicker and depositional rates higher (Figures 7, 8D; Table 2). Also, north of the eastern part of Vestnesa Ridge average rates for MIS 3 were high (El bani Altuna et al., 2021b) (Figure 7L; Table 2) in accordance with the seismic observations.

Sortable silt measurements on DO millennial scale for MIS 3 have indicated stronger currents during the warm interstadials than during the cold stadials from many locations in the Nordic Seas (Gabrielsen (2016) - East Greenland slope, 1,616 m water depth; Solheim (2018) - northern Faroe Islands margin, 1,179 m water depth; Chauhan et al. (2016b) - northern Svalbard margin, 501 m water depth; Jessen and Rasmussen (2015) - western Svalbard margin, 1880 m water depth. In general, investigated long records from the western Svalbard margin also show higher sedimentation rates for interstadial periods than for stadials (Rasmussen and Thomsen, 2013; Rasmussen et al., 2014; Jessen and Rasmussen, 2019; El bani Altuna et al., 2021a) (here exemplified by the very low rates during Heinrich stadial H1 and the high rates during the Bølling and Allerød interstadials) (Figures 4–7; Table 2; Supplementary Figure S2–S5). Rates on DO time scale thus mimics rates on a glacial-interglacial time scale, most likely of lower magnitude given the thinner deposits (Figure 8D) but indicating convection changes on millennial time scale.

MIS 4: Our seismic isochore mapping revealed that the depositional environment during MIS 4 has several similarities with that of MIS 2 by demonstrating a chaotic distribution pattern (Figures 8C,E). The smaller thickness of the MIS 2 layer may be due to the shorter timeframe for this period compared to MIS 4. As for the MIS 2 period, the MIS 4 depositional pattern likely indicate a slowdown of the current strength leading to less current-dominated sedimentation environment. MIS 4 includes the transition to MIS 3, where a similar sequence of sedimentary horizons occur over the northern and western Svalbard margin with a laminated horizon followed by deposition of IRD at high sedimentation rates (e.g., Vogt et al., 2001; Rasmussen et al., 2014; Jessen and Rasmussen, 2015; 2019; Chauhan et al., 2016a).

MIS 5: Only few core records from the western Svalbard margin covering MIS 5 exists (e.g., Risebrobakken et al., 2005). The depositional pattern seen in the MIS 5 isochore map. resembles that of the MIS 1 and MIS 3 maps (Figures 8B,D,F), indicating a similar depositional environment for these three interglacial periods, i.e., the action of a bottom current flowing northward following the depth contours around the ridge, and with a current core lying close to the then ridge crest. The KH19-09GPC record covering MIS 5 show a lower average depositional rate compared to that of MIS 1 and MIS 3, which could be due to compaction (Figure 8F; Table 2).

4.2 Depositional patterns and seepage of gas

4.2.1 Organic and inorganic carbon records from active and inactive pockmark areas

The distribution of %TOC and %$CaCO_3$ appears very consistent between seep- and non-seep records and between the western and eastern pockmark fields regardless of time resolution (Figure 6; Supplementary Figure S5). Similar distribution patterns of %TOC and %$CaCO_3$ have also been recorded elsewhere from the Svalbard margin (e.g., Vogt et al., 2001). This indicates that these two parameters together form a good correlation tool for both seep- and non-seep sites. However, at the eastern active pockmark field at Vestnesa Ridge some calcium carbonate records show very high values and peaks in $CaCO_3$ that do not correlate with the general pattern (Figures 6D,E; Supplementary Figure S5A,F). This we attribute to precipitation of authigenic carbonate in these apparently most active core sites. For example, the carbonate peak in core HH12-929GC correlates with a layer of high concentrations of calcareous nodules of authigenic carbonate (Thomsen et al., 2019) (Figure 6D).

The high %TOC for the dark coarse layer (part debris flow, part IRD layer) and for the laminated layer (deposited by meltwater plumes) is probably mainly a cause of deposition of terrestrial carbon transported out to sea (e.g., Vogt et al., 2001) (Figure 6; Supplementary Figure S5). The Holocene sediments younger than

~10 ka differs from the earlier periods by being characterized by both high %TOC and %$CaCO_3$ and deposition of fine muds. The high organic content during the Holocene is mainly of marine origin (e.g., Vogt et al., 2001).

4.2.2 Benthic and planktic $\delta^{13}C$ records, chemosymbiotic bivalves and seepage of methane

Events of low $\delta^{13}C$ are found in MIS 3, and MIS 2, including parts of the LGM (Figure 5; Supplementary Figure S4; note MIS 3 events are not highlighted). In pockmark cores, the debris flow/IRD event dating ~24 ka generally show low values (Figures 5A,C–E; note no data points for this event in Figures 5B,G–I). The best resolved $\delta^{13}C$ variations occurs during the deglaciation; therefore, we focus the discussion on these millennial scale events.

Records from both the presently apparently inactive pockmarks at western Vestnesa and the eastern active pockmarks tend to show recurrent patterns and timings in low $\delta^{13}C$ values, while records unaffected by seepage show comparatively high $\delta^{13}C$ throughout and within the typical range of the measured species (Figure 5; Supplementary Figure S4). The records affected by seepage thus show low values in the laminated horizon dating ~15 ka correlating with the Bølling interstadial, in the Allerød interstadial and early Holocene indicating strong seepage of gas (note that H1 and Younger Dryas intervals generally have comparatively higher $\delta^{13}C$ values of −3 to −2‰ just below the typical range of the measured species and indicating low to moderate seepage during these events). In addition, records from the SW Svalbard shelf at 76 °N also show this pattern with the same timing as on Vestnesa Ridge indicating that a large geographical area was affected by seepage at the same time (El bani Altuna et al., 2021b and references therein). Three records with the typical configuration of high MS values all show low $\delta^{13}C$ in the laminated horizon, one core being from outside of pockmarks, the other two from inside the 'Lomvi' pockmark (Figure 5D; Supplementary Figure S4A,B). This indicates a particularly strong seepage event at that time. Holocene deposits younger than ~9–10 ka BP in all studied cores affected by seepage have typical $\delta^{13}C$ values for the measured benthic foraminiferal species indicating a reduction in gas seepage (Figures 5A–C,E–G).

Even if these low $\delta^{13}C$ events (often <-10‰) are due to coating of the foraminiferal shells with authigenic carbonate, it would be difficult to reconcile that these recurrent patterns in low $\delta^{13}C$ with similar timing and over a large geographical area, in particular in MIS 2 to lower MIS 1, is a random distribution (Figure 5; Supplementary Figure S4). The four lithological units of low $\delta^{13}C$ are sedimentologically very different (the unsorted dark layer deposited from debris flow evens, the laminated horizon from turbid meltwater plumes, the Allerød period from intense ice rafting, and the early Holocene, with decreasing ice rafting). Therefore, similarity in timing indicates that the events must have a forcing in the pace of the DO millennial scale events. Bottom water temperature increased by up to 6 °C during Heinrich stadial H1 as shown by nearby core record HH15-1252PC from the northern flank of Vestnesa Ridge. The BWT reached a maximum of 5.5 °C before the start of the Bølling interstadial (El bani Altuna et al., 2021a) (Figure 1A; Figure 2E). The temperature rise is probably the likely cause of dissociation of gas hydrates (e.g., Buffet and Archer, 2004; Ketzer et al., 2020) as also shown by modeling of the thickness of the GHSZ at the shelf of southwestern Svalbard (El bani Altuna et al., 2021b). The presence of chemosymbiotic bivalves in H1 in many pockmark records from both the western and eastern part of Vestnesa Ridge points to low to moderate seepage during most of the event (Figures 4A–C,H; Supplementary Figure S3A). Seep-associated- or chemosymbiotic macrofaunas tend to avoid areas of very strong seepage that causes toxic levels of H_2S (e.g., Sahling et al., 2002; Levin et al., 2003). We note that seepage in older Heinrich stadials also was low to moderate where many also are marked by layers of chemosymbiotic bivalves (Figures 5B,H).

There is an apparent time lag from the peak warm bottom water conditions during H1 until gas seepage intensified during the Bølling and Allerød interstadials. Thus, downward diffusion of heat took time to reach substantial layers of gas hydrates. Several modeling studies have shown that in the deep sea, the time from bottom water warming to increased emission of gas can take a thousand to several thousands of years (e.g., Phrampus and Hornbach, 2012; Karstens et al., 2018). Other studies have invoked active faulting from tectonism due to the proximity of Vestnesa Ridge to active spreading zones, the Molloy Transform Fault, and/or offshore glacial isostatic rebound (e.g., Plaza-Faverola et al., 2015; Dazcinnies et al., 2021; Vachon et al., 2022). However, these slower processes alone cannot explain the rapid millennial DO-scale fluctuations in gas emissions that aligns with climatic and oceanographic changes. Another possible forcing factor is the high sediment loading during the deglaciation (Bølling and Allerød interstadials and lower Holocene) (Figure 7; Table 2). High sedimentation rates at the Vøring Plateau caused an increase in temperature in the sediments eventually destabilizing gas hydrates with a time delay of 1,000 years (e.g., Karstens et al., 2018). However, the high sedimentation rates we record at Vestnesa Ridge is an order of magnitude lower than at the Vøring Plateau (~1 m/ka *versus* >10 m/ka) (Table 2) but could have added to the effect from the bottom water warming. Hydrostatic pressure would have counteracted the effect of temperature rise due to the rapidly increasing sea level during the deglaciation (e.g., Fairbanks, 1989). Then again, the effects of sea level changes are small in deep water and much smaller than the effect of a 3 °C temperature increase that would thin the GHSZ by 85% (e.g., Buffett and Archer, 2004).

Core HH12-930GC differs by having only slightly decreased $\delta^{13}C$ values in the Bølling-Allerød interstadials and early Holocene compared to nearby core HH16-549GC just 11 m away. In older sediments of mid-late MIS 3 and early MIS 2, HH12-930GC shows a pattern in $\delta^{13}C$ similar to the other cores (Myrvang, 2015; Chu et al., 2023) (Figures 5C,E). The reason for this deviation for the deglaciation interval is unknown but taken as a signal of heterogeneity in the 'Lunde' pockmark.

Since the $\delta^{13}C$ patterns and timing of low values are similar between western and eastern records there is clear evidence of periodical intensification of seepage in the western part of the ridge and that the area was as active as the eastern part during MIS 3, 2 and lower MIS 1 until ~10–9 ka and with high $\delta^{13}C$ from that time onwards (Figures 4, 5; Supplementary Figure S3, S4). The time of decrease in gas emission correlates approximately

with the time when ice rafting ceased or decreased over the Svalbard margin and the Svalbard-Barents Sea Ice Sheet had retreated into fjord heads or further inland (e.g., Ślubowska et al., 2005; Ślubowska-Woldengen et al., 2007; Forwick and Vorren, 2009). The rapidly settled fine-grained Holocene mud deposited from the contour currents and with its high content of TOC and $CaCO_3$ (Figures 5H,I; Supplementary Figure S5F,G) probably reduced seepage to a slow diffusion of gas through the sediments. We suggest that this slow diffusion formed a basis for efficient oxidation by the microbial consortia (and that little if any gas would escape because of the 'microbial filter' or 'methanotrophic sink'; e.g., James et al., 2016). The SMTZ at western Vestnesa Ridge is found >2 m in the pockmark of core site HH16-550GC and >10 m outside of the pockmark at site HH16-543GC (Laier et al., 2017) (Figure 1C; Figure 4K,L). Results from studies combining seismic data and pore pressure data from Vestnesa Ridge have indicated that the western part at present mostly experience gas seepage as slow and diffusive, while in the eastern part numerous faults and fractures from sediment deformation also allow gas to escape in the gas phase, i.e., termed advective seepage (Plaza-Faverola et al., 2015; 2023; Cooke et al., 2023). At Vestnesa Ridge the thick Holocene deposits in the western part effectively filled the pockmarks and slowed the seepage of methane. According to our results the change from advective to diffusive seepage probably occurred at ~10 ka. Nevertheless, active tectonism and onshore and offshore isostatic rebound continued after ~10 ka and until today (e.g., Forman et al., 2004; Vachon et al., 2022; Domel et al., 2023). Fine-grained drift sediments can often seal fractured or coarse, porous glacial sediments in contourites exampled by studies of the very seismically active Hikurangi Margin, New Zealand (Bailey et al., 2021).

In the eastern part of Vestnesa Ridge, Holocene sediments are generally absent but occurs locally within some pockmarks (Figures 5A–D; Supplementary Figure S4C). Here, even a thin cover of fine Holocene sediments apparently caused reduced seepage at ~10–9 ka as seen in high $\delta^{13}C$ values as in for example, core JM10-335GC. Nearby core HH12-928PC, has no Holocene sediments and low $\delta^{13}C$ throughout and contain large amounts of authigenic carbonates indicate strong seepage (Figures 6A,E; Supplementary Figure S4D). The two cores were taken about 40 m apart in the elevated area at the rim of 'Lomvi' pockmark (Figure 1E). Likely the upward migrating gas found other escape routes (e.g., Treude et al., 2020), which may have focused seepage to sites with no Holocene sediments younger than ~10 ka, or strong seepage could have prevented settling at some of these sites. In the deep depression in 'Lomvi' pockmark core HH12-929GC and nearby core HH15-1293PC contained gas hydrates from ~125 cm below the seafloor. Both shows the low and constant MS patterns. Core HH16-551GC taken 16 m away shows the typical MS signal for the western Svalbard margin, and contained no gas hydrate (Figure 1E; Figure 4E,F; Supplementary Figure S1I), The SMTZ was located >4 m in core 551GC (Laier, 2017). We have no porewater data for core HH12-929GC, but likely the SMTZ here was much shallower. A hiatus occurs from the top of the layer of authigenic nodules at 110 cm downcore covering the time interval 20–8 ka in the early Holocene probably indicating strong seepage in combination with bottom current activity and that nodules formed at the sediment surface (Thomsen et al., 2019) (Figure 6D). In core HH16-549GC from 'Lunde' pockmark (Figure 1D), the SMTZ was located ~1.5 m below the seafloor (Laier, 2017; Åsheim, 2017). In the central part of the pockmark in bacterial mats the SMTZ was at the seafloor (Melaniuk et al., 2022a). Thus, the sedimentary and seep environments and the depth of the SMTZ are very variable within both the 'Lomvi' and 'Lunde' pockmarks and within short distances. At western Vestnesa Ridge in the southern pockmark, core JM10-331GC show low magnetic susceptibility while core HH17-839GC shows typical MS values indicating some heterogeneity here (Figure 1C; Supplementary Figure S3H,I) and likely in other pockmarks as well.

4.2.3 Shallow seismic evidence of free gas and gas seepage

The pockmarks and gas seepage on Vestnesa Ridge have primarily been investigated by 2D reflection seismic data (e.g., Hustoft et al., 2009; Bünz et al., 2012). Using high-resolution Chirp data as in the present study provides means for more detailed observations of gas seepages and free gas in the shallow subsurface.

Several of gas-related acoustic phenomena have been observed on Chirp lines passing along the crest of Vestnesa Ridge, i.e., partly or completely wipeout of the signal (known as acoustic blanking), chaotic reflection patterns and lack of penetration, downwards bending seismic reflectors caused by reduced seismic velocity, and high-amplitude reflections (known as bright spots) caused by high gas and/or hydrate content.

Chirp lines crossing active pockmarks in the eastern active pockmark area mostly shows a completely chaotic seismic signal with no reflections from neither the mapped MIS 5–2 units or any older depositional units (Figure 9A). This seismic pattern confirms that sediment deformation caused by active seepage of gas occurs on the eastern Vestnesa Ridge. Further, regular occurrences of acoustic blanking signify that free gas also exists outside the pockmarks in this area, as also evidenced by sediment cores (Figure 6G; Supplementary Figure S4A, S5C).

Chirp lines from the western Vestnesa Ridge also display existence of pockmarks and several acoustic phenomena evidencing presence of free gas and gas hydrates in the sediment column despite the lack of acoustic flare observations in this part of the ridge area (Figure 9B). This is taken as evidence that gas seepages in the western ridge area have either slowed down or are prevented in reaching to the seafloor.

A notable difference between the eastern and western pockmark areas are the presence of the MIS 1 unit in the latter area, while this unit is missing in the eastern area (Figures 9A,B). This could hint that presence or lack of MIS 1 sediments may play a role in gas seepage activity at Vestnesa Ridge. This is also supported by core data from both eastern and western pockmarks (Figures 1C–E; Figures 5A–C, E–G; Supplementary Figure S3H,I). In addition, Chirp data crossing some of the pockmarks in the western area show that a disturbed and chaotic pattern characterize the MIS 5–3 units and deeper layers, while the overlaying MIS 1 and partly MIS 2 units appear relatively undisturbed. This suggest that similar to that of the present eastern pockmark area, some heterogeneity in the seepage patterns existed in the western pockmark area, as also evidenced by the core study.

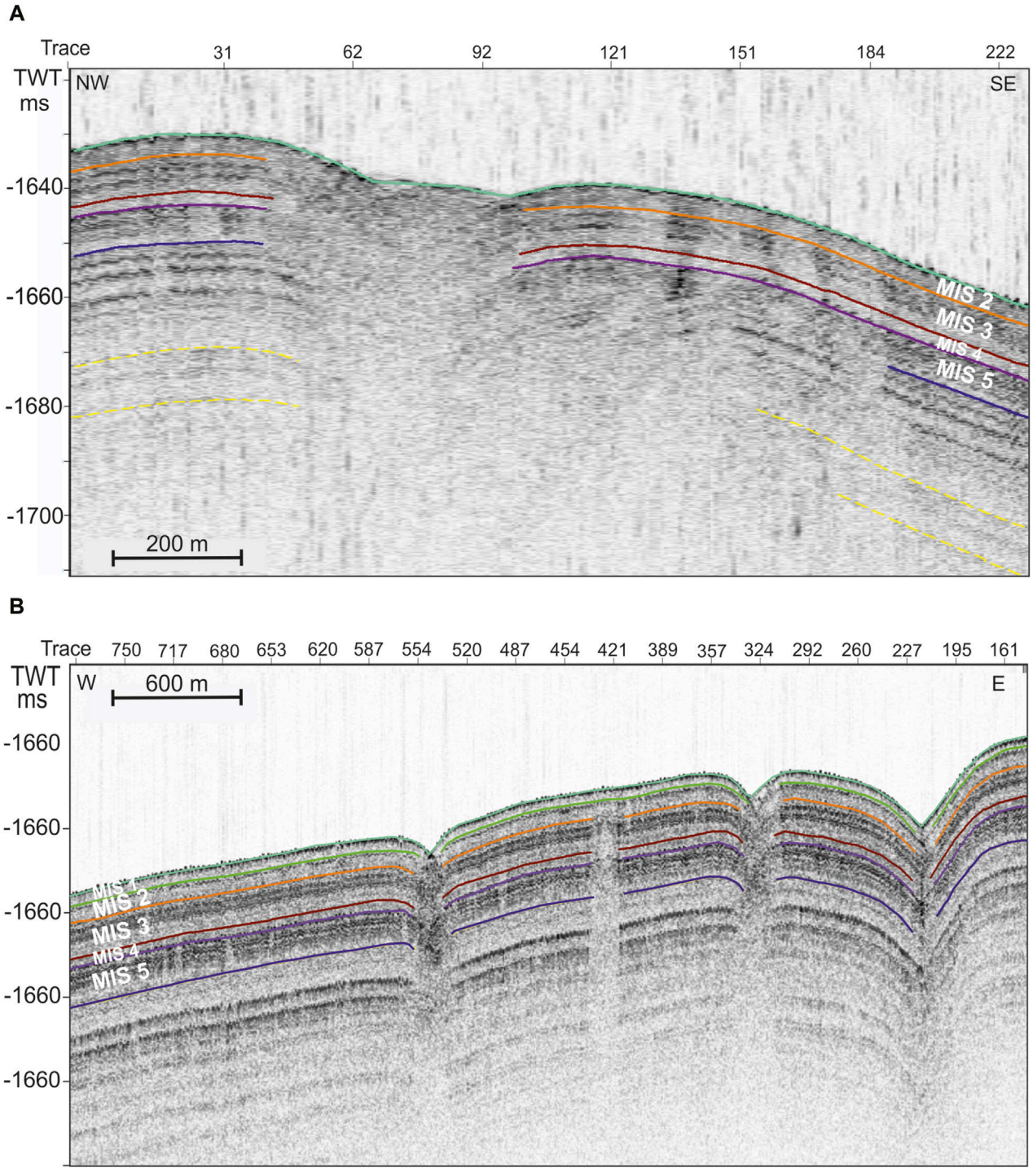

FIGURE 9
Shallow seismic illustration of gas content and seepage. **(A)**: Shallow seismic Chirp line crossing an active pockmark in the eastern Vestnesa Ridge pockmark area illustrating the complete disturbance of the underlying seismic reflections within the MIS 5–2 units, as well as deeper lying reflectors (some marked with dotted yellow lines) caused by gas seepages. Note the many acoustic blanking areas to the right of the pockmark evidencing presence of free gas in the sediment column. Also note the lack of the MIS 1 unit. **(B)**: Shallow seismic Chirp line along the crest of the western Vestnesa Ridge. Several acoustic phenomena, e.g., acoustic blanking (i.e.,~ trace 750-620 and 421), bright spots (i.e.,~ trace 554) and disturbed reflections, evidencing the presence of free gas and gas hydrates in the sediment column despite the lack of acoustic flare observations in the western ridge area. Note the presence of MIS 1 sediments in this area.

5 Conclusion

Based on our study of 43 sediment core records and 1,430 km of shallow seismic lines we can conclude the following:

- The depositional patterns of the Vestnesa Ridge drift changed on a glacial-interglacial time scale. During interglacial times (Holocene; marine isotope stage (MIS) 1, MIS 3 and MIS 5) a strong current flow resulted in build-up of thick, focused depocenters on the northwestern Vestnesa Ridge while decreased deposition or erosion occurred in other parts of the ridge. During glacial times (MIS 2 and MIS 4) a weakened current lead to thinner, more chaotic deposition covering the greater central part of the ridge
- During the last glacial maximum (LGM) 24–19 ka, the depocenter shifted upslope to 1,200 m water depth and shallower due to the weaker current activity
- The sedimentation patterns on millennial scale mimics those of the glacial-interglacial time scale, though likely of lower magnitude, but indicating current changes on millennial time scale with stronger currents during warm interstadials and weaker currents during cold stadials
- The depositional patterns, the magnetic susceptibility records, and ages of typical sediment marker horizons from Vestnesa Ridge entirely match records from elsewhere over the western Svalbard margin for the last 30 ka
- Gas seepage from the western inactive pockmark area was as strong as in the eastern active pockmark area during MIS 3, MIS 2 into early MIS 1. Seepage in both areas was particularly strong during the deglaciation (Bølling-Allerød interstadials 15–13 ka and lower Holocene ~12–~10 ka)
- The increase in seepage of gas during the deglaciation was likely primarily driven by temperature rise in the bottom water destabilizing deep reservoirs of gas hydrates. Tectonism/glacial isostatic rebound, and sediment loading probably played a secondary role in these rapid fluctuations in gas seepage
- At Vestnesa Ridge the thick Holocene deposits in the western part effectively filled pockmarks and probably slowed seepage of gas, while in the eastern active part Holocene deposits only occur locally within some pockmarks. Seepage through Holocene muds with high %TOC and %$CaCO_3$ became reduced to a slow diffusion. Efficient oxidation by microbial communities probably prevented gas escape from the seafloor

Data availability statement

The original contributions presented in the study are included in the article/Supplementary Material, further inquiries can be directed to the corresponding author.

Author contributions

TR: Conceptualization, Investigation, Methodology, Writing–original draft, Writing–review and editing. TN: Investigation, Writing–original draft, Writing–review and editing.

Funding

The author(s) declare that financial support was received for the research, authorship, and/or publication of this article. The study before 2013 was part of the Paleo-CIRCUS project, funded by TFS, UiT the Arctic University of Norway. From 2013 the study was funded by the Norwegian Research Council through its Centers of Excellence funding scheme, grant number 223259. The 2012 and 2015 cruises were funded by the Research School in Arctic Marine Geology and Geophysics (AMGG, Department of Geosciences, UiT the Arctic University of Norway, Tromsø).

Acknowledgments

We thank the captain and crew of RV *Jan Mayen* and RV *Helmer Hansen* and cruise participants during cruises 2010, 2012, 2015, 2016, 2017 and 2018 and captain, crew, cruise leaders Jochen Knies and Monica Winsborrow and cruise participants on RV *Kronprins Haakon* in 2019 for their assistance in core retrieval and handling. We also thank cruise participants during CAGE cruises in 2016, 2017 and 2018 for porewater and sediment sampling. We especially thank cruise participants of cruises GEO-8144/3144 in 2012 and 2015 for their assistance in core retrieval and onboard data measurements. Naima El bani Altuna, Kamila Sztybor, and Chiara Consolaro are thanked for GEOTEK-MSCL data (HH15- and JM10-cruises). Andreia Plaza-Faverola (UiT) is thanked for providing the seismic line KH19-018 data (KH19 cruise). The laboratory staff at the Department of Geosciences, UiT is thanked for endless GEOTEK measurements, XRF-image scans, and numerous Leco measurements over the last 10 years. Matteus Lindgren, Department of Geosciences, UiT supervised the stable isotope measurements. We thank Pavel Serov for the maps in Figures 1D,E. We also thank Naima El bani Altuna and Erik Thomsen for help with making Figure 2. The Geological Survey of Denmark and Greenland (GEUS) is thanked for providing TN time for interpretation and paper writing. We also thank Lars J. Kjaergaard and Shahjahan Laghari, GEUS, for loading seismic data and core locations into @Petrel. Finally, we thank the two reviewers for their very helpful and constructive comments and suggestions.

Conflict of interest

The authors declare that the research was conducted in the absence of any commercial or financial relationships that could be construed as a potential conflict of interest.

Publisher's note

All claims expressed in this article are solely those of the authors and do not necessarily represent those of

Supplementary material

The Supplementary Material for this article can be found online at: https://www.frontiersin.org/articles/10.3389/feart.2024.1356341/full#supplementary-material

References

Aagaard, K., Foldvik, A., and Hillman, S. R. (1987). The West spitsbergen current: disposition and water mass transformation. *J. Geophys. Res.* 92, 3778–3784. doi:10.1029/JC092iC04p03778

Åsheim, J.-E. F. (2017). Changes in paleoceanography and methane release in relation to past climatic variability at Vestnesa Ridge. Available at: http://hdl.handle.net/10037/11621.

Åström, E. K. L., Carroll, M. L., Ambrose, W. G., Sen, A., Silyakova, A., and Carroll, J. (2018). Methane cold seeps as biological oases in the high-Arctic deep sea. *Limnol. Oceanogr.* 63, S209–S231. doi:10.1002/lno.10732

Bailey, W., McArthur, A., and McCaffrey, W. (2021). Sealing potential of contourite drifts in deep-water fold and thrust belts: examples from the Hikurangi Margin, New Zealand. *Mar. Petrol. Geol.* 123, 104776. doi:10.1016/j.marpetgeo.2020.104776

Birgel, D., and Hass, H. C. (2004). Oceanic and atmospheric variations during the last deglaciation in the Fram Strait (Arctic Ocean): a coupled high-resolution organic-geochemical and sedimentological study. *Quat. Sci. Rev.* 23, 29–47. doi:10.1016/j.quascirev.2003.10.001

Boetius, A., Ravenschlag, K., Schubert, C. J., Rickert, D., Widdel, F., Gieseke, A., et al. (2000). A marine microbial consortium apparently mediating anaerobic oxidation of methane. *Nature* 407, 623–626. doi:10.1038/35036572

Bond, G., Broecker, W., Johnsen, S., McManus, J., Labeyrie, L., Jouzel, J., et al. (1993). Correlations between climate records from North Atlantic and Greenland ice. *Nature* 365, 343–347. doi:10.1038/365143a0

Borowski, W. S., Paull, C. K., and Ussler, W. (1996). Marine pore-water sulfate profiles indicate *in situ* methane flux from underlying gas hydrate. *Geology* 24, 655–658. doi:10.1130/0091-7613(1996)024<0655:mpwspi>2.3.co;2

Broecker, W. S. (1991). The great ocean conveyor. *Ocenography* 4, 79–89. doi:10.5670/oceanog.1991.07

Buffett, B., and Archer, D. (2004). Global inventory of methane clathrate: sensitivity to changes in the deep ocean. *Earth Planet. Sci. Lett.* 227, 185–199. doi:10.1016/j.epsl.2004.09.005

Bünz, S., Polyanov, S., Vadakkepuliyambatta, S., Consolaro, C., and Mienert, J. (2012). Active gas venting through hydrate-bearing sediments on the Vestnesa Ridge, offshore W-Svalbard. *Mar. Geol.* 332–334, 189–197. doi:10.1016/j.margeo.2012.09.012

Caricchi, C., Lucchi, R. G., Sagnotti, L., Macri, P., Di Roberto, A., Del Carlo, P., et al. (2019). A high-resolution geomagnetic relative paleointensity record from the Arctic Ocean deep-water gateway deposits during the last 60 kyr. *Geochem., Geophys., Geosys.* 20, 2355–2377. doi:10.1029/2018GC007955

Chauhan, T., Noormets, R., and Rasmussen, T. L. (2016b). Glaciomarine sedimentation and bottom current activity on the north-western and northern continental margins of Svalbard during the late Quaternary. *Geo-Mar. Lett.* 36, 81–99. doi:10.1007/s00367-015-0430-6

Chauhan, T., Rasmussen, T. L., and Noormets, R. (2016a). Palaeoceanography of the Barents Sea continental margin, north of Nordaustlandet, Svalbard, during the last 74 ka. *Boreas* 45, 76–99. doi:10.1111/bor.12135

Chu, R. W. C., Yasuhara, M., Myrvang Riise, K., Asahi, H., Huang, H.-H. M., Cotton, L. J., et al. (2023). Late Quaternary paleoceanography of Vestnesa Ridge, Fram Strait: ostracode species as a potential indicator of cold seep activity. *Geology* 51, 758–762. doi:10.1130/G51237.1

Consolaro, C., Rasmussen, T. L., Panieri, G., Mienert, J., Buenz, S., and Sztybor, K. (2015). Carbon isotope (δ¹³C) excursions suggest times of major methane release during the last 14 kyr in Fram Strait, the deep-water gateway to the Arctic. *Clim. Past.* 11, 669–685. doi:10.5194/cp-11-669-2015

Cook, M. S., Keigwin, L. D., Birgel, D., and Hinrichs, K.-U. (2011). Repeated pulses of vertical methane flux recorded in glacial sediments from the southeast Bering Sea. *Paleoceanography* 26, PA2210. doi:10.1029/2010PA001993

Cooke, F., Plaza-Faverola, A., Bünz, S., Sultan, N., Ramachandran, H., Bedle, H., et al. (2023). Sedimentary deformation relating to episodic seepage in the last 1.2 million years: a multi-scale seismic study from the Vestnesa Ridge, eastern Fram Strait. *Front. Earth Sci.* 11. doi:10.3389/feart.2023.1188737

Dansgaard, W., Johnsen, S., Clausen, H., Dahl-Jensen, D., Gundestrup, N., Hammer, C., et al. (1993). Evidence for general instability of past climate from a 250-kyr ice-core record. *Nature* 364, 218–220. doi:10.1038/364218a0

Daszinnies, M., Plaza-Faverola, A., Sylta, Ø., Bünz, S., Mattingsdal, R., Tømmerås, A., et al. (2021). The Plio-Pleistocene seepage history off western Svalbard inferred from 3D petroleum systems modelling. *Mar. Petrol. Geol.* 128, 105023. doi:10.1016/j.marpetgeo.2021.105023

Domel, P., Plaza-Faverola, A., Schlindwein, V., and Bünz, S. (2023). Local seismicity and sediment deformation in the west Svalbard margin: implications of neotectonics for seafloor seepage. *Geochem., Geophys., Geosys.* 24. doi:10.1029/2023GC011174

Ebbesen, H., Hald, M., and Eplet, T. H. (2007). Lateglacial and early Holocene climatic oscillations on the western Svalbard margin, European Arctic oscillations on the western Svalbard margin, European Arctic. *Quat. Sci. Rev.* 26, 1999–2011. doi:10.1016/j.quascirev.2006.07.020

Eiken, O., and Hinz, K. (1993). Contourites in the Fram Strait. *Sediment. Geol.* 82, 15–32. doi:10.1016/0037-0738(93)90110-q

El bani Altuna, N., Ezat, M. M., Greaves, M., and Rasmussen, T. L. (2021a). Millennial-scale changes in bottom water temperature and water mass exchange through the Fram Strait 79°N, 63-13 ka. *Paleoceanogr. Paleoclimatol.* 36. doi:10.1029/2020PA004061

El bani Altuna, N., Ezat, M. M., Smik, L., Muschitiello, F., Belt, S. T., Knies, J., et al. (2024). Sea ice-ocean coupling during Heinrich stadials in the atlantic-arctic gateway. *Sci. Rep.* 14, 1065. doi:10.1038/s41598-024-51532-7

El bani Altuna, N., Rasmussen, T. L., Ezat, M. M., Vadakkepuliyambatta, S., Groeneveld, J., and Greaves, M. (2021b). Deglacial bottom water warming intensified Arctic methane seepage in the NW Barents Sea. *Comm. Earth. Environ.* 2, 188. doi:10.1038/s43247-021-00264-x

Elverhoi, A., Andersen, E. S., Dokken, T., Hebbeln, D., Spielhagen, R., Svendsen, J. I., et al. (1995). The growth and decay of the Late Weichselian Ice Sheet in western Svalbard and adjacent areas based on provenance studies of marine sediments. *Quat. Res.* 44, 303–316. doi:10.1006/qres.1995.1076

Elverhøi, A., Hooke, R. L. E. B., and Solheim, A. (1998). Late Cenozoic erosion and sediment yield from the Svalbard-Barents Sea region: implications for understanding erosion of glacierized basins. *Quat. Sci. Rev.* 17, 209–241. doi:10.1016/s0277-3791(97)00070-x

Espitalié, J., Laporte, J. L., Madec, M., Marquis, F., Leplat, P., Paulet, J., et al. (1977). Méthode rapide de caractérisation des roches mètres, de leur potentiel pétrolier et de leur degré d'évolution. *Rev. L'inst. Francais Du. Pet.* 32, 23–42. doi:10.2516/ogst:1977002

Ezat, M., Rasmussen, T. L., and Groeneveld, J. (2014). Persistent intermediate water warming during cold stadials in the southeastern Nordic seas during the past 65 k.y. *Geology* 42, 663–666. doi:10.1130/g35579.1

Fairbanks, R. G. (1989). A 17,000-year glacio-eustatic sea level record: influence of glacial melting rates on the Younger Dryas event and deep-ocean circulation. *Nature* 342, 637–642. doi:10.1038/342637a0

Falardeau, J., de Vernal, A., and Spielhagen, R. F. (2018). Paleoceanography of northeastern Fram Strait since the last glacial maximum: palynological evidence of large amplitude changes. *Quat. Sci. Rev.* 195, 133–152. doi:10.1016/j.quascirev.2018.06.030

Falardeau, J., de Vernal, A., and Spielhagen, R. F. (2019). Palynological data of cores MSM5/5-712-2 and PS2863/1-2 from northeastern Fram Strait spanning the last glacial maximum to present. *Data Brief* 24, 103899. doi:10.1016/j.dib.2019.103899

Fer, I., Peterson, A. K., and Nilsen, F. (2023). Atlantic water boundary current along the southern Yermak plateau, Arctic Ocean. *JGR Oceans* 128. doi:10.1029/2023JC019645

Forman, S. L., Lubinski, D. J., Ingólfsson, Ó., Zeeberg, J. J., Snyder, J. A., Siegert, M. J., et al. (2004). A review of postglacial emergence on svalbard, franz josef land and novaya zemlya, northern eurasia. *Quat. Sci. Rev.* 23, 1391–1434. doi:10.1016/j.quascirev.2003.12.007

Forwick, M., and Vorren, T. O. (2009). Late weichselian and Holocene sedimentary environments and ice rafting in isfjorden, spitsbergen. *Spitsb. Palaeogeogr. Palaeoclimatol. Palaeoecol.* 280, 258–274. doi:10.1016/j.palaeo.2009.06.026

Gabrielsen, L. (2016). Study of millennial scale paleoclimatic and paleoceanographic changes in conjunction with variations in the East Greenland Current during the late Quaternary. Available at: https://munin.uit.no/handle/10037/11141.

Gebhardt, A. C., Geissler, W. H., Matthiessen, J., and Jokat, W. (2014). Changes in current patterns in the Fram Strait at the pliocene/pleistocene boundary. *Quat. Sci. Rev.* 92, 179–189. doi:10.1016/j.quascirev.2013.07.015

Hansen, J., Ezat, M. M., Åström, E. K. L., and Rasmussen, T. L. (2020). New late pleistocene species of *acharax* from arctic methane seeps off svalbard. *J. Syst. Palaeontol.* 18, 197–212. doi:10.1080/14772019.2019.1594420

Himmler, T., Sahy, D., Martma, T., Bohrmann, G., Plaza-Faverola, A., Bünz, S., et al. (2019). A 160,000-year-old history of tectonically controlled methane seepage in the Arctic. *Sci. Adv.* 5, eaaw1450. doi:10.1126/sciadv.aaw1450

Hoff, U., Rasmussen, T. L., Stein, R., Ezat, M., and Fahl, K. (2016). Sea ice and millennial-scale climate variability in the Nordic seas 90 kyr ago to present. *Nat. Comm.* 7, 12247. doi:10.1038/ncomms12247

Hong, W.-L., Pape, T., Schmidt, C., Yao, H., Wallmann, K., Plaza-Faverola, A., et al. (2021). Interactions between deep formation fluid and gas hydrate dynamics inferred from pore fluid geochemistry at active pockmarks of the Vestnesa Ridge, west Svalbard margin. *Mar. Petrol. Geol.* 127, 104957. doi:10.1016/j.marpetgeo.2021.104957

Hopkins, T. S. (1991). The GIN Sea - a synthesis of its physical oceanography and literature review 1972–1985. *Earth-Sci. Rev.* 30, 175–318. doi:10.1016/0012-8252(91)90001-v

Hornbach, M. J. (2022). "Bottom simulating reflectors below the blake ridge, western North Atlantic margin," in *World atlas of submarine gas hydrates in continental margins*. Editors J. Mienert, C. Berndt, A. M. Tréhu, A. Camerlenghi, and C.-S. Liu (Cham, Switzerland: Springer Nature), 131–138.

Howe, J. A., Shimmels, T. M., Harland, R., and Eyles, N. (2008). Late quaternary contourites and glaciomarine sedimentation in the Fram Strait. *Sedimentology* 55, 179–200. doi:10.1111/j.1365-3091.2007.00897.x

Hustoft, S., Bünz, S., Mienert, J., and Chand, S. (2009). Gas hydrate reservoir and active methane-venting province in sediments on <20 Ma young oceanic crust in the Fram Strait, offshore NWSvalbard. *Earth Planet. Sci. Lett.* 284, 12–24. doi:10.1016/j.epsl.2009.03.038

Jakobsson, M., Mayer, L. A., Bringensparr, C., Castro, C. F., Mohammad, R., Johnson, P., et al. (2020). The international bathymetric chart of the Arctic Ocean version 4.0. *Sci. Data* 7, 176. doi:10.1038/s41597-020-0520-9

James, R. H., Bousquet, P., Bussmann, I., Haeckel, M., Kipfer, R., Leifer, I., et al. (2016). Effects of climate change on methane emissions from seafloor sediments in the Arctic Ocean: a review. *Limnol. Oceanogr.* 61, 283–299. doi:10.1002/lno.10307

Jessen, S. P., and Rasmussen, T. L. (2015). Sortable silt cycles in svalbard slope sediments 74–0 ka. *J. Quat. Sci.* 30, 743–753. doi:10.1002/jqs.2807

Jessen, S. P., and Rasmussen, T. L. (2019). Ice rafting patterns on the western Svalbard slope 74–0 ka: interplay between ice-sheet activity, climate and ocean circulation. *Boreas* 48, 236–256. doi:10.1111/bor.12358

Jessen, S. P., Rasmussen, T. L., Nielsen, T., and Solheim, A. (2010). A new Late Weichselian and Holocene marine chronology for the western Svalbard slope 30,000 – 0 cal years BP. *Quat. Sci. Rev.* 29, 1301–1312. doi:10.1016/j.quascirev.2010.02.020

Junttila, J., Aagaard-Sørensen, S., Husum, K., and Hald, M. (2010). Late Glacial-Holocene clay minerals elucidating glacial history in the SW Barents Sea. *Mar. Geol.* 276, 71–85. doi:10.1016/j.margeo.2010.07.009

Karstens, J., Haflidason, H., Becker, L. W. M., Berndt, C., Rüpke, L., Planke, S., et al. (2018). Glacigenic sedimentation pulses triggered post-glacial gas hydrate dissociation. *Nat. Comm.* 9, 635. doi:10.1038/s41467-018-03043-z

Kennett, J. P., Cannariato, K. G., Hendy, I. L., and Behl, R. J. (2003). Methane hydrates in quaternary climate change: the clathrate gun hypothesis. *Am. Geophys. Union Spec. Publ. Ser.* 5. doi:10.1029/054SP

Ketzer, M., Praeg, D., Rodrigues, L. F., Augustin, A., Pivel, M. A. G., Rahmati-Abkenar, M., et al. (2020). Gas hydrate dissociation linked to contemporary ocean warming in the southern hemisphere. *Nat. Comm.* 11, 3788. doi:10.1038/s41467-020-17289-z

Kindler, P., Guillevic, M., Baumgartner, M., Schwander, J., Landais, A., and Leuenberger, M. (2014). Temperature reconstruction from 10 to 120 kyr b2k from the NGRIP ice core. *Clim. Past.* 10, 887–902. doi:10.5194/cp-10-887-2014

Knies, J., Daszinnies, M., Plaza-Faverola, A., Chand, S., Sylta, Ø., Bünz, S., et al. (2018). Modelling persistent methane seepage offshore western Svalbard since early Pleistocene. *Mar. Petrol. Geol.* 91, 800–811. doi:10.1016/j.marpetgeo.2018.01.020

Knies, J., Mattingsdal, R., Fabian, K., Grøsfjeld, K., Baranwal, S., Husum, K., et al. (2014). Effect of early Pliocene uplift on late Pliocene cooling in the Arctic-Atlantic gateway. *Earth Planet Sci. Lett.* 387, 132–144. doi:10.1016/j.epsl.2013.11.007

Knies, J., and Vadakkepuliyambatta, S. (2023). CAGE19-3 Cruise Report: calypso giant piston coring in the Atlantic-Arctic gateway – Investigation of continental margin development and effect of tectonic stress on methane release. *CAGE – Centre Arct. Gas Hydrate, Environ. Clim. Rep. Ser.* 7, 1–127. doi:10.7557/cage.6911

Knies, J., Vogt, C., and Stein, R. (1999). Late Quaternary growth and decay of the Svalbard/Barents Sea ice sheet and paleoceanographic evolution in the adjacent Arctic Ocean. *Geo-Mar. Lett.* 18, 195–202. doi:10.1007/s003670050068

Laier, T., Rasmussen, T. L., Sztybor, K., and Nielsen, T. (2017). "Gas migration through a 150 m hydrate stability zone off Svalbard results in local shallow 'secondary' hydrate formation," in Proceedings of the 9th International Conference on Gas Hydrates, Denver, Colorado, USA.

Levin, L. A., Ziebis, W., Mendoza, G. F., Growney, V. A., Tryons, M. D., Brown, K. M., et al. (2003). Spatial heterogeneity of macrofauna at northern California methane seeps: influence of sulfide concentration and fluid flow. *Mar. Ecol. Progr. Ser.* 265, 123–139. doi:10.3354/meps265123

Lisiecki, L. E., and Raymo, M. E. (2005). A Pliocene-Pleistocene stack of 57 globally distributed benthic $\delta^{18}O$ records. *Paleoceanography* 20, PA1003. doi:10.1029/2004PA001071

Lucchi, R. G., Camerlenghi, A., Rebesco, M., Colmenero-Hidalgo, E., Sierro, F. J., Sagnotti, L., et al. (2013). Postglacial sedimentary processes on the Storfjorden and Kveithola trough mouth fans: significance of extreme glacimarine sedimentation. *Glob. Planet. Change* 111, 309–326. doi:10.1016/j.gloplacha.2013.10.008

Lucchi, R. G., Sagnotti, L., Camerlenghi, A., Macri, P., Rebesco, M., Pedrosa, M. T., et al. (2015). Marine sedimentary record of meltwater pulse 1a along the NW Barents Sea continental margin. *Arktos* 1, 7. doi:10.1007/s41063-015-0008-6

Mackensen, A., Wollenburg, J., and Licari, L. (2006). Low $\delta^{13}C$ in tests of live epibenthic and endobenthic foraminifera at a site of active methane seepage. *Paleoceanography* 15. doi:10.1029/2005pa001196

Martin, R. A., Nesbitt, E. A., and Campbell, K. A. (2010). The effects of anaerobic methane oxidation on benthic foraminiferal assemblages and stable isotopes on the Hikurangi Margin of eastern New Zealand. *Mar. Geol.* 272, 270–284. doi:10.1016/j.margeo.2009.03.024

Matteis, F. (2018). Climate reconstruction during the Last Glacial Maximum based on a marine sediment core. Available in: https://munin.uit.no/handle/10037/13459.

Mattingsdal, R., Knies, J., Andreassen, K., Fabian, K., Husum, K., Grøsfjeld, K., et al. (2014). A new 6 Myr stratigraphic framework for the Atlantic–Arctic Gateway. *Quat.Sci. Rev.* 92, 170–178. doi:10.1016/j.quascirev.2013.08.022

McCorkle, D. C., Corliss, B. H., and Farnham, C. A. (1997). Vertical distributions and stable isotopic compositions of live (stained) benthic foraminifera from the North Carolina and California continental margins. *Deep-Sea Res.* 44, 983–1024. doi:10.1016/s0967-0637(97)00004-6

McCorkle, D. C., Keigwin, L. D., Corliss, B. H., and Emerson, S. R. (1990). The influence of microhabitats on the carbon isotopic composition of deep-sea benthic foraminifera. *Paleoceanography* 5, 161–185. doi:10.1029/pa005i002p00161

Melaniuk, K., Sztybor, K., Treude, T., Sommer, St., and Rasmussen, T. L. (2022a). Influence of methane seepage on isotopic signatures in living deep-sea benthic foraminifera, 79° N. *Sci. Rep.* 12, 1169–2022. doi:10.1038/s41598-022-05175-1

Melaniuk, K., Sztybor, K., Treude, T., Sommer, S., Zajaczkowski, M., and Rasmussen, T. L. (2022b). Response of benthic foraminifera to environmental successions of cold seeps from Vestnesa Ridge, Svalbard: implications for interpretations of paleo-seepage environments. *Front. Mar. Sci.* 9. doi:10.3389/fmars.2022.999902

Michel, E., Turon, J.-C., Labeyrie, L., Thouveny, N., Zahn, R., Hillaire-Marcel, C., et al. (1999). *MD 114 Campagne Interpole IMAGES V à bord du Marion-Dufresne du 13 juin 1999 au 20 septembre 1999*. Paris, France: L'Institut Français pour la Recherche et la Technologie Polaires.

Müller, J., Massé, G., Stein, R., and Belt, S. T. (2009). Variability of sea-ice conditions in the Fram Strait over the past 30,000 years Fram Strait over the past 30,000 years. *Nat. Geosci.* 2, 772–776. doi:10.1038/NGEO665

Müller, J., and Stein, R. (2014). High-resolution record of late glacial and deglacial sea ice changes in Fram Strait corroborates ice-ocean interactions during abrupt climate shifts. *Earth Planet. Sci. Lett.* 403, 446–455. doi:10.1016/j.epsl.2014.07.016

Müller, J., Werner, K., Stein, R., Fahl, K., Moros, M., and Jansen, E. (2012). Holocene cooling culminates in sea ice oscillations in Fram Strait. *Quat. Sci. Rev.* 47, 1–14. doi:10.1016/j.quascirev.2012.04.024

Myrvang, K. (2015). Correlation between changes in paleoceanography, paleoclimate and methane seepage on Vestnesa Ridge, eastern Fram Strait. Available in: http://hdl.handle.net/10037/8402.

Nielsen, T., Rasmussen, T. L., Ceramicola, S., and Kuijpers, A. (2007). Quaternary sedimentation, margin architecture and ocean circulation variability around the Faroe Islands, North Atlantic. *North Atl. Quat. Sci. Rev.* 26, 1016–1036. doi:10.1016/j.quascirev.2006.12.005

Novosel, I., Spence, G. D., and Hyndman, R. D. (2005). Reduced magnetization produced by increased methane flux at a gas hydrate vent. *Mar. Geol.* 216, 265–274. doi:10.1016/j.margeo.2005.02.027

Phrampus, B. J., and Hornbach, M. J. (2012). Recent changes to the Gulf Stream causing widespread gas hydrate destabilization. *Nature* 490, 527–530. doi:10.1038/nature11528

Plaza-Faverola, A., Bünz, S., Johnson, J. E., Chand, S., Knies, J., Mienert, J., et al. (2015). Role of tectonic stress in seepage evolution along the gas hydrate-charged Vestnesa Ridge, Fram Strait. *Geophys. Res. Lett.* 42, 733–742. doi:10.1002/2014GL062474

Plaza-Faverola, A., Sultan, N., Lucchi, R. G., El bani Altuna, N., Ramachandran, H., Singhroha, S., et al. (2023). Spatial changes in gas transport and sediment stiffness influenced by regional stress: observations from piezometer data along Vestnesa Ridge, eastern Fram Strait. *JGR Solid Earth* 128. doi:10.1029/2022JB025868

Plaza-Faverola, A., Vadakkepuliyambatta, S., Hong, W. L., Mienert, J., Bünz, S., Chand, S., et al. (2017). Bottom-simulating reflector dynamics at Arctic thermogenic gas provinces: an example from Vestnesa Ridge, offshore west Svalbard. *JGR Solid Earth* 122, 4089–4105. doi:10.1002/2016JB013761

Rasmussen, T. L., and Thomsen, E. (2004). The role of the North Atlantic Drift in the millennial timescale glacial climate fluctuations glacial climate fluctuations. *Palaeogeogr. Palaeoclim. Palaeoecol.* 210, 101–116. doi:10.1016/j.palaeo.2004.04.005

Rasmussen, T. L., and Thomsen, E. (2013). Pink marine sediments reveal rapid ice melt and Arctic meltwater discharge during Dansgaard-Oeschger warmings. *Nat. Comm.* 4, 2849. doi:10.1038/ncomms3849

Rasmussen, T. L., Thomsen, E., and Nielsen, T. (2014). Water mass exchange between the nordic seas and the Arctic Ocean on millennial timescale during MIS 4–MIS 2. *Geochem. Geophys. Geosys.* 15, 530–544. doi:10.1002/2013GC005020

Rasmussen, T. L., Thomsen, E., Ślubowska, M. A., Jessen, S., Solheim, A., and Koç, N. (2007). Paleoceanographic evolution of the SW Svalbard margin (76°N) since 20,000 ^{14}C yr BP. *Quat. Res.* 67, 100–114. doi:10.1016/j.yqres.2006.07.002

Rebesco, M., Wählin, A., Laberg, J. S., Schauer, U., Beszczynska-Möller, A., Lucchi, R. G., et al. (2013). Quaternary contourite drifts of the western Spitsbergen margin. *Deep-Sea Res. I* 79, 156–168. doi:10.1016/j.dsr.2013.05.013

Reimer, P. J., Edouard, B., Bayliss, A., Beck, J. W., Blackwell, P. G., Ramsey, C. B., et al. (2013). IntCal13 and Marine13 radiocarbon age calibration curves, 0–50,000 years cal BP. *Radiocarbon* 55, 1869–1887. doi:10.2458/azu_js_rc.55.16947

Risebrobakken, B., Dokken, T., and Jansen, E. (2005). Extent and variability of the Meridional Atlantic circulation in the Eastern Nordic Seas during marine isotope stage 5 and its influence on the inception of the last glacial. *Geophys. Monogr. Ser.* 158, 323–339. doi:10.1029/158GM20

Sahling, H., Rickert, D., Lee, R. W., Linke, P., and Suess, E. (2002). Macrofaunal community structure and sulfide flux at gas hydrate deposits from the Cascadia convergent margin, NE Pacific. *Mar. Ecol. Progr. Ser.* 231, 121–138. doi:10.3354/meps231121

Schlichtholz, P., and Houssais, M.-N. (1999a). An inverse modeling study in Fram Strait. Part I: dynamics and circulation. *Deep-Sea Res. II* 46, 1083–1135. doi:10.1016/s0967-0645(99)00018-1

Schlichtholz, P., and Houssais, M.-N. (1999b). An inverse modeling study in Fram Strait. Part II: water mass distribution and transports. *Deep-Sea Res. II* 46, 1137–1168. doi:10.1016/s0967-0645(99)00017-x

Schneider, A., Panieri, G., Lepland, A., Consolaro, C., Crèmière, A., Forwick, M., et al. (2018). Methane seepage at Vestnesa Ridge (NW svalbard) since the last glacial maximum. *Quat. Sci. Rev.* 193, 98–117. doi:10.1016/j.quascirev.2018.06.006

Sen, A., Didriksen, A., Hourdez, A., Svenning, M. M., and Rasmussen, T. L. (2020). Frenulate siboglinids at high Arctic methane seeps and insight into high latitude frenulate distribution. *Ecol. Evol.* 10, 1339–1351. doi:10.1002/ece3.5988

Ślubowska, M., Koç, N., Rasmussen, T. L., and Klitgaard-Kristensen, D. (2005). Changes in the flow of Atlantic water into the Arctic Ocean since the last deglaciation: evidence from the northern Svalbard continental margin, 80°N. *Paleoceanography* 20, PA4014. doi:10.1029/2005PA001141

Ślubowska-Woldengen, M., Rasmussen, T. L., Koç, N., Klitgaard-Kristensen, D., Nilsen, F., and Solheim, A. (2007). Advection of atlantic water to the western and northern svalbard shelf since 17,500calyr BP. *Quat. Sci. Rev.* 26, 463–478. doi:10.1016/j.quascirev.2006.09.009

Smith, L. M., Sachs, J. P., Jennings, A. E., Anderson, D. M., and de Vernal, A. (2001). Light δ^{13}C events during deglaciation of the East Greenland continental shelf attributed to methane release from gas hydrates. *Geophys. Res. Lett.* 28, 2217–2220. doi:10.1029/2000gl012627

Snyder, G. T., Hiruta, A., Matsumoto, R., Dickens, G. R., Tomaru, H., Takeuchi, R., et al. (2007). Pore water profiles and authigenic mineralization in shallow marine sediments above the methane-charged system on Umitaka Spur, Japan Sea. *Deep-Sea Res. II* 54, 1216–1239. doi:10.1016/j.dsr2.2007.04.001

Solheim, M. (2018). Reconstruction of the bottom current strength of overflow water through the Faroe-Shetland Channel in relation to climate change during the last 135,000 years. Available in: https://hdl.handle.net/10037/12857.

Sztybor, K. (2016). Late glacial and deglacial paleoceanographic and environmental changes at Vestnesa Ridge, Fram Strait: challenges in reading methane-influenced sedimentary records. Available at https://hdl.handle.net/10037/24978.

Sztybor, K., and Rasmussen, T. L. (2017a). Diagenetic disturbances of marine sedimentary records from methane-influenced environments in the Fram Strait as indications of variation in seep intensity during the last 35 000 years. *Boreas* 46, 212–228. doi:10.1111/bor.12202

Sztybor, K., and Rasmussen, T. L. (2017b). Late glacial and deglacial palaeoceanographic changes at Vestnesa Ridge, Fram Strait: methane seep versus non-seep environments. *Palaeogeogr. Palaeoclimatol. Palaeoecol.* 476, 77–89. doi:10.1016/j.palaeo.2017.04.001

Thomsen, E., Rasmussen, T. L., Sztybor, K., Hanken, N.-M., Tendal, O. S., and Uchman, A. (2019). Cold-seep fossil macrofaunal assemblages from Vestnesa Ridge, eastern Fram Strait during the past 45 000 years. *Polar Res.* 38. doi:10.33265/polar.v38.3310

Torres, M. E., Mix, A. C., Kinports, K., Haley, B., Klinkhammer, G. P., McManus, J., et al. (2003). Is methane venting at the seafloor recorded by δ^{13}C of benthonic foraminifera shells? *Paleoceanography* 18, 1062. doi:10.1029/2002PA000824

Treude, T., Krause, S., Steinle, L., Burwicz, E., Hamdan, L. J., Niemann, H., et al. (2020). Biogeochemical consequences of nonvertical methane transport in sediment offshore northwestern svalbard. *JGR Biogeosciences* 125, e2019JG005371. doi:10.1029/2019jg005371

Treude, T., Krüger, M., Boetius, A., and Jørgensen, B. B. (2005). Environmental control on anaerobic oxidation of methane in the gassy sediments of Eckernförde Bay (German Baltic). *Limnol. Oceanogr.* 50, 1771–1786. doi:10.4319/lo.2005.50.6.1771

Vachon, R., Schmidt, P., Lund, B., Plaza-Faverola, A., Patton, H., and Hubbard, A. (2022). Glacially induced stress across the Arctic from the Eemian interglacial to the present – implications for faulting and methane seepage. *JGR Solid Earth* 127. doi:10.1029/2022jb024272

Vogt, C., Knies, J., Spielhagen, R. F., and Stein, R. (2001). Detailed mineralogical evidence for two nearly identical glacial/deglacial cycles and Atlantic water advection to the Arctic Ocean during the last 90,000 years. *Glob. Planet. Change* 31, 23–44. doi:10.1016/s0921-8181(01)00111-4

Vogt, P. R., Crane, K., Sundvor, E., Max, M. D., and Pfirman, S. L. (1994). Methane-generated (?) pockmarks on young, thickly sedimented oceanic crust in the Arctic: Vestnesa ridge, Fram strait. *Geology* 22, 255–258. doi:10.1130/0091-7613(1994)022<0255:mgpoyt>2.3.co;2

Wefer, G., Heinze, P.-M., and Berger, W. H. (1994). Clues to ancient methane release. *Nature* 369, 282. doi:10.1038/369282a0

Werner, K., Müller, J., Husum, K., Spielhagen, R. F., Kandiano, E. S., and Polyak, L. (2015). Holocene sea subsurface and surface water masses in the Fram Strait – Comparisons of temperature and sea-ice reconstructions. *Quat. Sci. Rev.* 147, 194–209. doi:10.1016/j.quascirev.2015.09.007

Whiticar, M. J. (1999). Carbon and hydrogen isotope systematics of bacterial formation and oxidation of methane. *Chem. Geol.* 161, 291–314. doi:10.1016/s0009-2541(99)00092-3

Wollenburg, J. E., Raitzsch, M., and Tiedemann, R. (2015). Novel high-pressure culture experiments on deep-sea benthic foraminifera - evidence for methane seepage-related δ^{13}C of *Cibicides wuellerstorfi*. *Mar. Micropaleontol.* 117, 47–64. doi:10.1016/j.marmicro.2015.04.003

Yasuhara, M., Sztybor, K., Rasmussen, T. L., Okahashi, H., Sato, R., and Tanaka, H. (2018). Cold-seep ostracods from the western Svalbard margin: direct palaeo-indicator for methane seepage? *J. Micropaleontol.* 37, 139–148. doi:10.5194/jm-37-139-2018

Zamelczyk, K., Rasmussen, T. L., Husum, K., Godtliebsen, F., and Hald, M. (2014). Surface water conditions and calcium carbonate preservation in the Fram Strait during marine isotope stage 2, 28.8-15.4 kyr: PALEOCEANOGRAPHY AND $CACO_3$PRESERVATION. *Paleoceanography* 29, 1–12. doi:10.1002/2012PA002448

frontiers | Frontiers in Earth Science

TYPE Original Research
PUBLISHED 09 April 2024
DOI 10.3389/feart.2024.1328357

OPEN ACCESS

EDITED BY
Dongliang Luo,
Chinese Academy of Sciences (CAS), China

REVIEWED BY
Marcelo Ketzer,
Linnaeus University, Sweden
Jiapeng Jin,
Pilot National Laboratory for Marine Science and Technology, China
Jinxiu Yang,
China University of Petroleum, China

*CORRESPONDENCE
V. K. Bellec,
valerie.bellec@ngu.no

RECEIVED 26 October 2023
ACCEPTED 08 March 2024
PUBLISHED 09 April 2024

CITATION
Bellec VK, Chand S, Knies J, Bjarnadóttir LR, Lepland A, Sen A and Thorsnes T (2024), New cold seep sites on the continental slope southwest to Svalbard.
Front. Earth Sci. 12:1328357.
doi: 10.3389/feart.2024.1328357

New cold seep sites on the continental slope southwest to Svalbard

V. K. Bellec[1]*, S. Chand[1], J. Knies[1,2], L. R. Bjarnadóttir[1], A. Lepland[1], A. Sen[3,4] and T. Thorsnes[1]

[1]Geological Survey of Norway (NGU), Trondheim, Norway, [2]iC3: Centre for ice, Cryosphere, Carbon and Climate, Department of Geosciences, UiT The Arctic University of Norway, Tromsø, Norway, [3]Arctic Biology, The University Centre in Svalbard (UNIS), Longyearbyen, Norway, [4]Faculty of Biosciences and Aquaculture, Nord University, Bodø, Norway

We discovered seafloor features such as bacterial mats and carbonate crusts typical for active methane seeps on the continental slope southwest of Svalbard. These features are associated with two main northwest-southeast trending morphological structures that are oriented parallel to the regional continental slope. Both structures occur at c. 800 m water depth, at the boundary between the Storfjorden trough mouth fan to the south and the Hornsund trough mouth fan to the north, which suggests a loading related fluid seepage. The main structure displays depressions and ridges forming a crater in its center. Other occurring features include small sediment mounds, domes often covered by bacterial mats, and hummocky seafloor colonized by siboglinid tubeworms. Free gas bubbles were spotted close to the centre and plumes along the rims of the structure. Thick carbonate crusts indicate a long seepage history in the center of the structure and on top of the ridges. The sources of the seeps are likely to be Miocene old organic-rich deposits, or Paleocene hydrocarbon reservoirs.

KEYWORDS

cold seeps, Barents Sea, Svalbard margin, continental slope, Storfjorden trough mouth fan

1 Introduction

Cold seeps correspond to areas of gas or fluid venting from the seafloor at passive and active oceanic margins. They are characterized by different seafloor morphologies like pockmarks, mud volcanoes and mounds or just include gas seeps and/or chemosynthetic biological communities without prominent structures (see Talukder, 2012, for review) and are observed on bathymetry data and videos or photos around the world (e.g., Orange et al., 2002; Somoza et al., 2003; Paull et al., 2008a; Jones et a., 2010; Hart et al., 2011; Feng et al., 2018; Kim et al., 2020). In Norwegian waters, from south Norway to the Svalbard margins, more than 5,000 gas seeps were reported by Thorsnes et al. (2023) and a thousand more by Mau et al. (2017). Moreover, new seeps are continually discovered, like the new mud volcano southwest of the Bear Island found in May 2023 [University of Tromsø, 2023, https://uit.no/nyheter/artikkel?p_document_id=811650 (Accessed 9 May 2023)]. In the Barents Sea and the western Svalbard margin, cold seeps create structures like pockmarks (Vogt et al., 1994; Vogt et al., 1999; Bünz et al., 2012), mud volcanoes (Håkon Mosby mud volcano; Vogt et al., 1991), or gas-hydrate pingos and craters (e.g., Andreassen et al., 2017; Serov et al., 2017; Nixon et al., 2019). They can also occur without

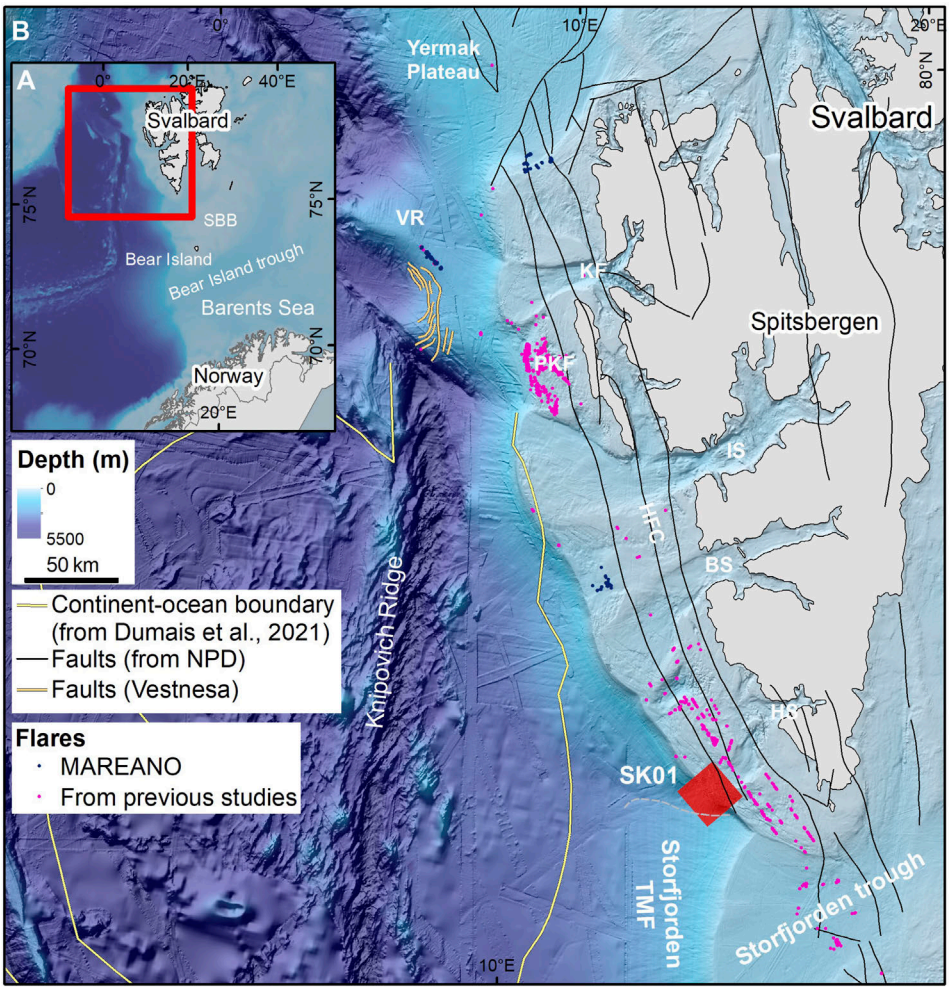

FIGURE 1
(A) Inset map and **(B)** Study location (SK01 in red) as well as the faults (from the Norwegian Petroleum Directorate–NPD), the continent-ocean boundary (Dumais et al., 2021) and gas flares found west to Svalbard. BS, Bellsund; HFC, Hornsund Fault Complex; HS, Hornsund; IS, Isjorden; KF, Kongsfjordrenna; PKF, Prins Karls Forland; SBB, Spitsbergen bank; TMF, trough mouth fan; VR, Vestnesa Ridge. Background bathymetry: IBCAO (Jakobsson et al., 2020). Flares from previous studies extracted from Knies et al., 2018; Mau et al., 2017; Myhre et al., 2016; Panieri, 2015; Sahling et al., 2014.

any seafloor expressions such as in the flare areas off Prins Karls Forland, western Svalbard (Westbrook et al., 2009; Ferré et al., 2020). Gas seeps are commonly associated with carbonate crusts, showing evidence of both past and present gas emissions (Crémière et al., 2016; Himmler et al., 2019; Thorsnes et al., 2019).

Along the western Norwegian continental slope, cold seeps are often associated to mass-movement structures (e.g., Bryn et al., 2005; Solheim et al., 2005). Striking examples of these are the Håkon Mosby mud volcano located in the middle of the Late Pleistocene Bear Island trough slide scar (Laberg and Vorren, 1993), gas-hydrates stored within the headwall side of the Storegga slide (e.g., Mienert et al., 2005) with cold seeps and pockmarks found on its northern rim at Nyegga (Bünz and Mienert, 2004; Bünz et al., 2005), and Sklinnadjupet slide and associated mud flows (Riis et al., 2005; Rise et al., 2006). Gas and fluids from subsurface reservoirs move up through open conduits such as faults becoming focussed zones of fluid escape locations like the large concentration of gas flares observed along the Hornsund fault complex (Mau et al., 2017; Figure 1). Fluids with or without sediments can also move vertically upward by loading of high-water content ooze and mud as observed in the cases of Sklinnadjupet slide (Riis et al., 2005), Håkon Mosby mud volcano (Vogt et al., 1991) and the Nyegga area (Hustoft et al., 2009).

Methane brought by cold seeps is consumed by microbes in the water column. Indeed chemical reactions (anaerobic oxidation of methane and sulphate reduction) occur in the upper part of the sediment layer when methane meets sulphate held in seawater in presence of methanotrophic archaea and sulphate-reducing bacteria (Boetius et al., 2000; Boetius and Wenzhöfer, 2013). These processes lead to the formation of hydrogen sulphide, bicarbonate, and also to CO_2 which impacts oceanic pH (e.g., Biastoch et al., 2011). Even if limited amounts of greenhouse gases escape to the atmosphere from these seeps, knowing their extents and possible origins give more information on their possible impact

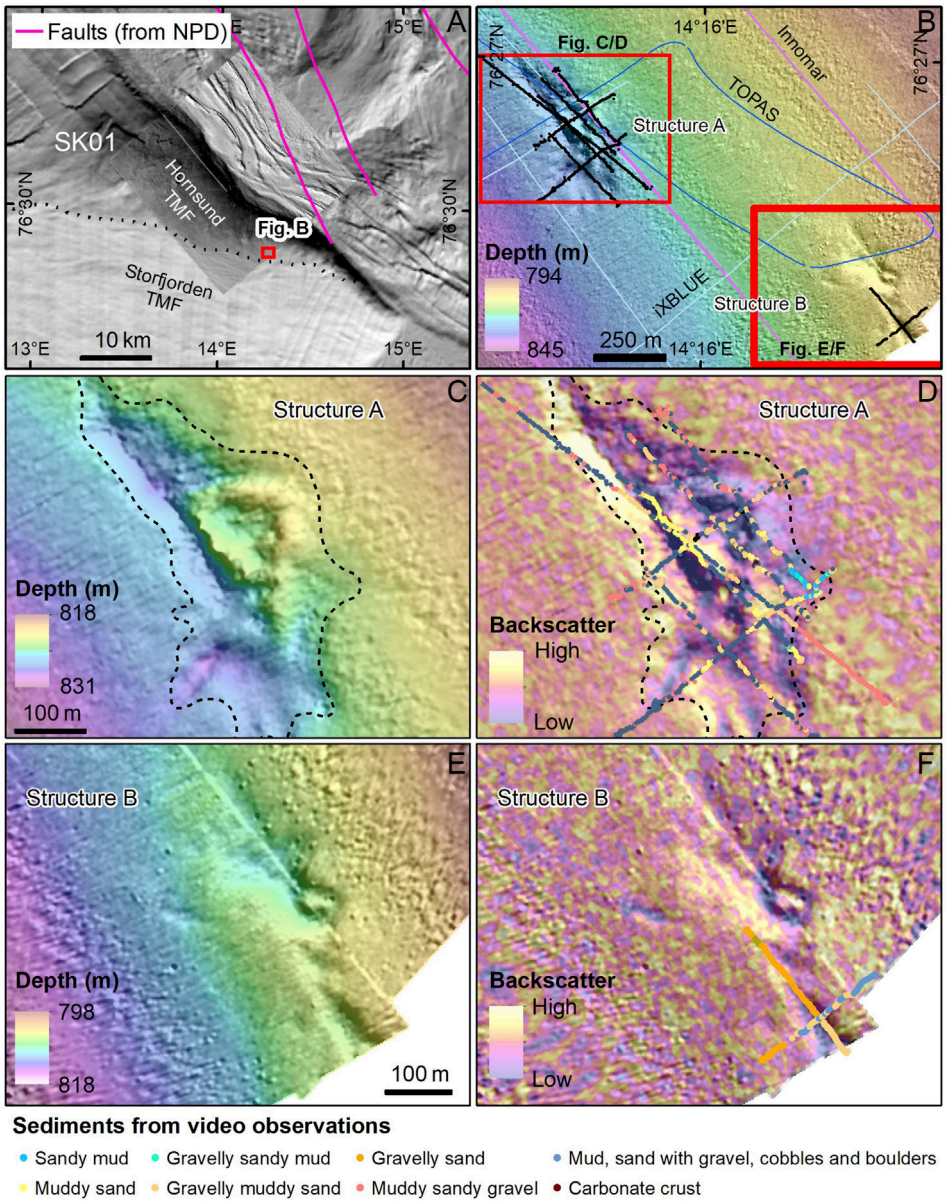

FIGURE 2
(A) Overview of SK01 (see Figure 1 for location, NPD: Norwegian Petroleum Directorate), **(B)** overview of the seep structures, **(C–F)** detailed maps of the two structures A and B. The limit of the structure A is highlighted by a black dotted line. Sediment observations from videos are on top of the backscatter maps. **(C, D)** display the structure A, while **(E, F)** show the structure B. Background map: IBCAO. Detailed bathymetry data supplied by MAREANO/Norwegian Hydrographic Survey.

on oceanic chemistry, biological habitat, and their contribution to greenhouse gases.

In this study, we will focus on the southwestern Svalbard margin at about 76° 30′ (Figure 1). This area forms part of a regional network of study areas in the MAREANO programme (www.mareano.no), where the goal is to describe seabed nature types, including assessment of the impact of previous and future fishing activity (bottom trawling). Here a new cold seep area has been discovered on the continental slope, thereby representing a different environment than the three main known Svalbard seep sites, Vestnesa Ridge (deepwater contourite), Prins Karls Forland (continental shelf), and Storfjorden gas-hydrate pingos (glacial trough). The aim of this study is to characterize this new seep discovery and assess its formation controls.

2 Study area

The Svalbard continental shelf is quite narrow, 50–60 km wide, and is crossed by glacial troughs formed during the Plio-Pleistocene glaciations by the efficient erosion of fast flowing ice streams (e.g., Ottesen et al., 2005). At the mouth of major troughs, glacially eroded materials were deposited in large fans (e.g., Vorren and Laberg, 1997) forming the trough mouth

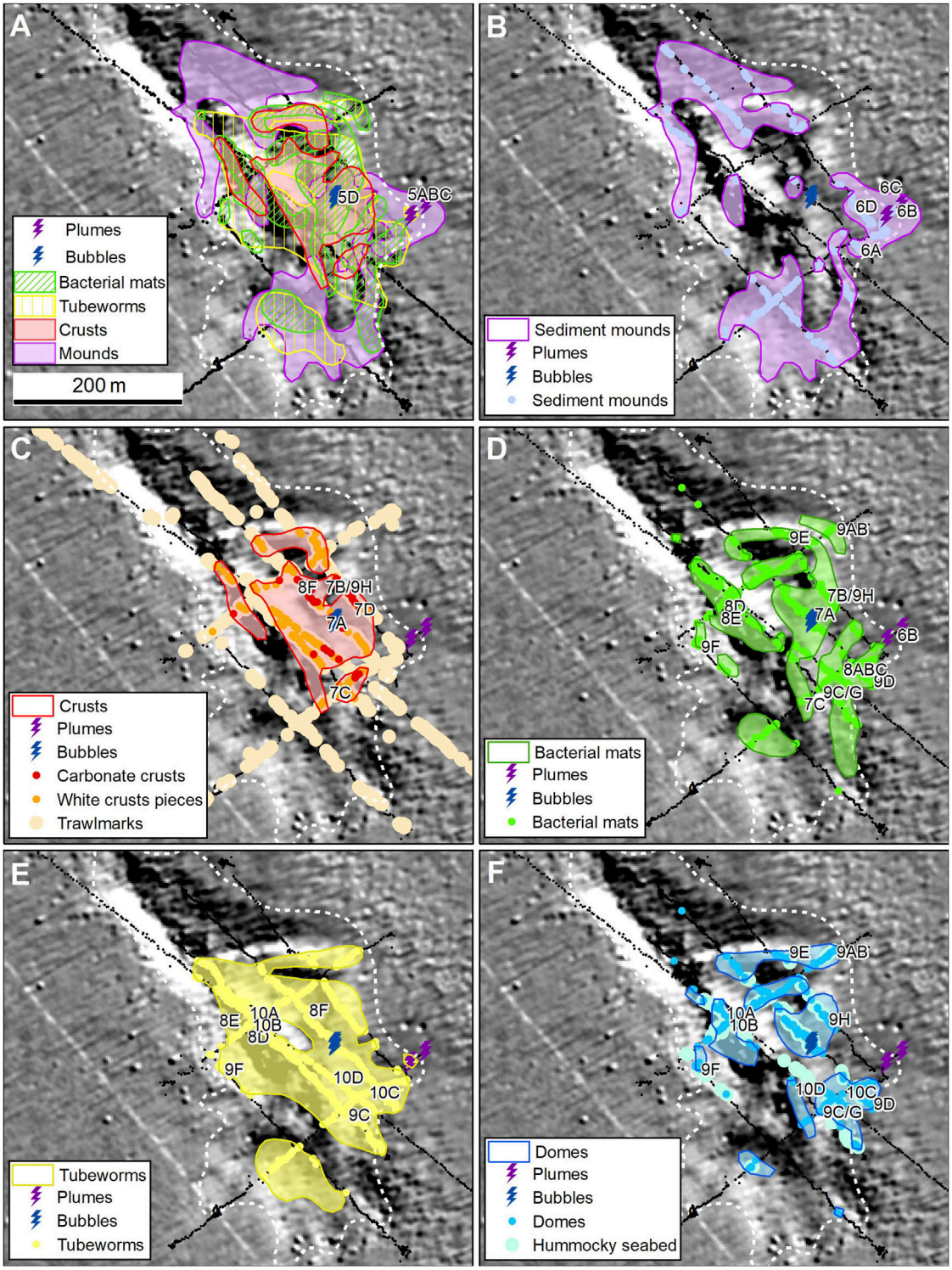

FIGURE 3
Mapping of the different features on the structure A. **(A)** summarizes the different features, while **(B–F)** show respectively the location of the sediment mounds, the crusts, the bacterial mats, the tubeworms, the domes and the hummocky seabed areas. Locations of bubbles and plumes have been added on all panels. The structure limit is highlighted by a white dotted line. Location of Figures 5–10 are indicated on the different panels. Bathymetry data supplied by MAREANO/Norwegian Hydrographic Survey.

fans we can observe today on the bathymetry (Figure 1). Two fan deposits cover the study area, the large Storfjorden trough mouth fan in the south and the smaller partly covered Hornsund trough mouth fan in the north (Figures 1, 2A). During the last glaciation, the ice sheet reached the western Svalbard continental shelf break and might have covered the seabed in

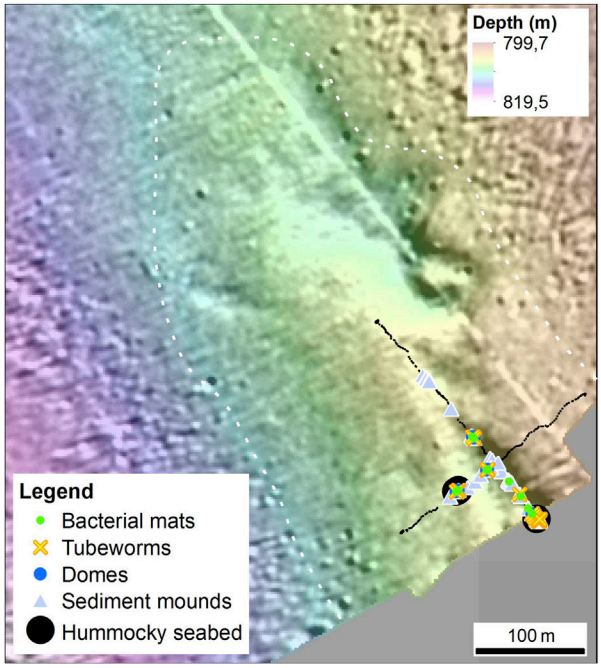

FIGURE 4
Mapping of the features on the structure B. See Figure 2 for location of this structure. Detailed bathymetry data supplied by MAREANO/Norwegian Hydrographic Survey.

the study area (SK01) (Hughes et al., 2016). Nowadays, the area is free of sea ice.

The northwest Barents Sea and the Svalbard areas are under the influence of two main water masses. The warm and saline Atlantic Water comes from the south and flows along the western Barents Sea margin, forming the West Spitsbergen Current, and into the Storfjorden trough. The cold Arctic Water forms a clockwise gyre around Svalbard, mostly along the Svalbard coastline (East and West Spitsbergen Currents) and on the Spitsbergen bank (Loeng, 1989).

3 Data and methods

The study area, named SK01 (Figure 1), has been mapped by the MAREANO programme in 2017 using EM710 Kongsberg multibeam echosounder. The Norwegian Hydrographic Service (NHS) quality checked and processed the multibeam bathymetry using Teledyne CARIS. Cleaned XYZ points and grids were then supplied to the Geological Survey of Norway (NGU). NGU processed the backscatter data using QPS FMGT software. Water column data were processed and interpreted using QPS Fledermaus Midwater software.

Multibeam data were gridded with 5 m resolution shallower than 1,000 m, and with 10 m–25 m resolution below this depth. However, the high density of points allowed some higher resolution gridding up to 2 m on the shelf and the upper slope. Smoothing and filtering with Esri ArcGIS low filter have been applied to reduce the artifacts while regridding data at 2 m resolution. Water column data were also acquired in the western part of the SK01 box (covering about 50% of the box). However, the data were very noisy (a lot of artifacts) above the continental slope, making difficult a fine-scale interpretation of the gas flares.

Innomar SES 2000 Medium 70 sub bottom profiler lines were acquired simultaneously with multibeam data by FUGRO which delivered them as seismic SEG-Y files to NGU. Lines from Kongsberg TOPAS PS18 parametric sonar data were acquired during MAREANO cruises in October 2017 and 2019 (both with R/V G.O. Sars), while lines from iXBLUE Echoes 3500 T7 sub bottom profiler data were acquired during a third cruise in September 2022 (R/V Celtic Explorer) and were delivered as SEG-Y files. Filter and gain were applied on the TOPAS lines by using the TOPAS software.

Video lines of the seafloor were acquired during two MAREANO cruises. In October 2019, a 700 m long video line was acquired using a towed video platform dragged close to the seafloor and stationery at the start of the line. In September 2022, 8 video lines with a total length of about 2,650 m were acquired using the ROV Holland 1 (ROV: remotely operated vehicle). Positions were recorded every 10 s.

A carbonate crust sample (10 cm in diameter) was collected in 2022 at 76.4477° N/14.2522° E using the manipulator arm of the ROV. Eight micro drilled subsamples from the crust were analysed for stable carbon and oxygen isotope composition ($\delta^{13}C$ and $\delta^{18}O$) and for mineral composition. Both analyses were conducted at the University of Tartu, Estonia. Stable isotope analyses were conducted using a GasBench II sample preparation device coupled to a Thermo Scientific Delta V Advantage isotope ratio mass spectrometer (IRMS). Samples were dissolved in >99% phosphoric acid with a reaction time of >8 h to ensure complete dissolution of carbonate minerals. Analyses were calibrated against the standard reference materials NBS 18, IAEA 603, LSVEC, and IAEA 611, with 1σ uncertainties smaller than ±0.2‰. Mineral composition analyses were conducted by X-ray diffraction (XRD) on a Bruker D8 Advance instrument using CuKα radiation and LynxEye positive sensitive detector. Mineral composition qualifications (relative error <20%) of the samples were interpreted and modelled using the Rietveld algorithm-based code Topaz by Bruker.

4 Results

4.1 Morphology of the cold seeps

Two conspicuous protruding structures (A and B) occurs at about 810–820 m water depth at SK01, where the seabed is otherwise flat (Figures 2A, B). The structure B is located at the edge of our dataset, 750 m southeast from the structure A. These two structures are located right at the border between Hornsund and Storfjorden trough mouth fans.

The structures A and B have a northwest-southeast orientation, more or less perpendicular to the regional slope. The structure A forms an elongated depression (about 600 m long, 250 m wide and up to 4 m deep) with two ridges inside (Figures 2C, D). The deeper ridge rises about 8 m up from the seafloor and follows part of the depression, while the shallowest ridge is about 4 m high and is not bounded by a trench upslope. The two ridges join to form a crater-like depression (about 2 m deep and 100 m wide). The southernmost structure B (Figures 2E, F) forms a large dome which is more than

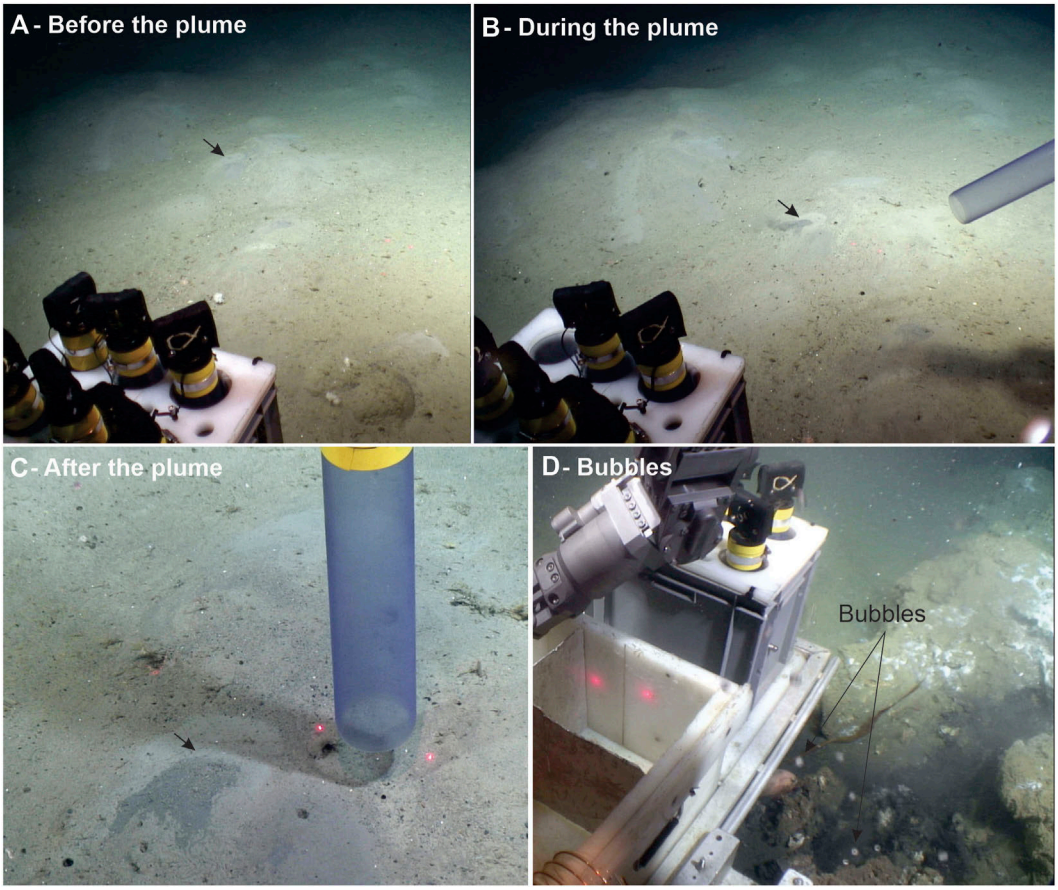

FIGURE 5
During a still **(A)**, a plume appeared several times a little bit further from the ROV **(B)**. It deposited a dark grey sediment lobe which was not there before the plume **(C)**. Similar dark grey lobes have been observed in several places (see Figure 6 mounds). Black arrows in **(A–C)** indicate the location of the plume. Bubbles were observed in one location where carbonate crusts were present **(D)**. They appeared after the ROV moved a piece of carbonate crust and were constant the 2′30′ the ROV stayed there. 10 cm between the red laser dots. Video data supplied by MAREANO/Institute of Marine Research.

480 m long, at least 2–3 m high and crossed by short depressions, an elongated one at the top of the structure, and more curved ones on the side of the structure. No flares were observed from the multibeam water column data at the cold seep area around and above the structures A and B.

4.2 Video observations

The sediments covering the seafloor outside the structure A, characterized by high backscatter (Figures 2D, F), comprise mixed grain sizes ranging from mud to cobbles and boulders. Inside the structure, this type of sediments is also present, especially on top of the ridges. Large areas with softer and muddier/sandier sediments, however, occur mainly on the flanks of the ridges and in depressions. These areas are marked by lower backscatter values (Figures 2D, F).

Carbonate crusts, crust fragments, bacterial mats, chemosynthetic tubeworms and different kinds of seabed deformation (sediment mounds, small domes and hummocky seafloor) are visible at the surface of the structures A and B (Figures 3, 4). Video observations on top of the structure A are described in more details below.

Signs of active seepage were observed in two different places on the structure A (Figures 3A, 5). A stream of gas bubbles started when the ROV's arm sampled a piece of carbonate crust located inside the crater in the middle of the structure A. In this area, the carbonate crust was covered by bacterial mats (Figure 5D). When the ROV was lifted about 2′30′ after the sampling, the bubble stream was still active. Several plumes were also observed at the southeast corner of the structure, where a large area is covered by small sediment mounds of different colours (Figures 5A–C); their accumulation forming larger hummocky features. A dark grey plume started on top of one of these small mounds at about 1–2 m from the ROV. The plume was intermittent and was active 6 times in about 3.5 min and was a few centimetres high. Before the plume, the seafloor was covered by light coloured sediment (Figure 5A), while once the plume stopped, a thin layer of dark grey coloured sediment had been deposited (Figure 5C).

Small bluish sediment mounds (Figure 6), some covered with dark grey lobes (Figures 6B–D), others with lighter coloured lobes (Figures 6A–D), are mostly found in the outer parts of the structure A (Figure 3B) and occur in both gravelly and muddy sediments. A similar light bluish colour is often found in the underlying

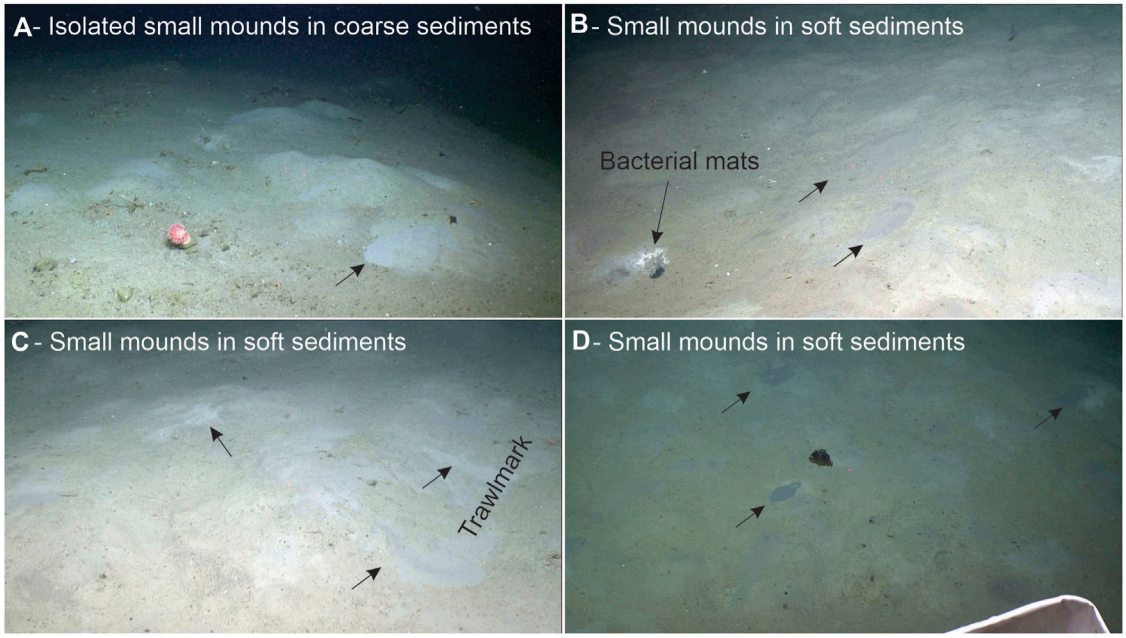

FIGURE 6
Sediment mounds which disturbed the seafloor. They occur in coarse sediment bottom **(A)** or in softer sediments **(B–D)**. They show different colours which do not correspond to the brownish surface sediment colours. Soft sediment lobes occur around these mounds (indicated by small black arrows). These mounds often occur without visible bacterial mats. However, some localized spots of mats can occur **(B)**. 10 cm between red laser dots. Video data supplied by MAREANO/Institute of Marine Research.

sediments, below a few centimetres of brownish sediments. They are up to 20 cm high and a few decimetres wide and can display sediment lobes originating from their top showing colours like light grey or dark grey (showing by small dark arrows in Figure 6). No chemosynthetic tubeworms or bacterial mats occur on top of these mounds, even if they occur between the mounds at a few locations (Figure 6B).

Carbonate crusts rising up to 80 cm above the seafloor were observed at several places, on and around the ridges and in the center of the structure A (Figures 3C, 7). Some crusts are covered by bacterial mats (Figure 7A, bubble stream site). Smaller crust fragments were observed on top of the ridges where they are often crushed and redistributed to a large area by trawling (Figures 7B–D). In fact, as shown by Figure 3A, the area has been intensively trawled and most of the higher areas are completely disturbed (Figures 7C, D).

Bacterial mats are present both over the ridges and in depressions (Figures 3D, 8). However, as for the carbonate crusts, very few bacterial mats occur in the northern depression. Bacterial mats can cover large areas, like along the southern ridge where mats are found continuously on an 18 m long transect, or just be tiny millimetre white spots. They can occur in rounded shapes (Figure 8C), form lines or nets of lines (Figure 8D), be present under stones (Figures 8A, B) or on top of domes (Figure 9). They are also present in areas recently disturbed by trawling (Figure 7B). They are often, but not always, associated with chemosynthetic tubeworms.

Possible chemosynthetic tubeworms are present on most of the structure A (Figures 3E, 8D–F, 9F, 10). They often form patches on top of highs of different sizes (Figures 10A–D). They also occur in a few decimetres long lines together with the bacterial mats (Figures 8D, E) or form more scattered patches (Figure 8F). However, they rarely occur on domes (Figure 9, one exception is the Figure 9C), even if they can be largely present between them (Figure 9F). The tubeworms are most likely *Oligograchia* frenulate siboglinids and more specifically either *Oligobrachia webbi* or *Oligobrachia* sp. CPL-clade, but a genetic study is necessary to differentiate them (Sen et al., 2018; Sen et al., 2023). The moniliferan siboglinid, *Sclerolinum contortum* might also be present (Lösekenn et al., 2008).

Domes are small highs up to 20 cm high and from a few centimetres to several metres long (Figure 9). Their shape is generally rounded (Figures 9C–E), but metre long ridges also occur (Figures 9A, B) as well as more complex shapes, like the q shape in the Figure 9D or the irregular dome of the Figure 9F. Gravelly sediments occur in some places in the middle of some domes (Figure 9A). They appear to be slightly harder than the surrounding sediment, even if they can also be damaged and destroyed by trawling (Figures 9G, H), letting their internal structure to be apparent. Their body are formed by layered sediments which show empty spaces between the layers. Bacterial mats are generally present on their top, where craters of different sizes might occur. Their occurrences are very similar to the bacterial mat locations (Figures 3D, F). Domes are often associated with a pinkish coloured surface (Figure 9F).

Hills forming hummocky surfaces are one the largest features observed on the structure A (Figures 3F, 10), aside from the ridges forming the structure A. They are often covered by chemosynthetic tubeworms which highlight highs and lows as they tend to settle on highs. They can also be covered by small sediment mounds (Figures 10E, F). They seem to be mostly restricted to the central and

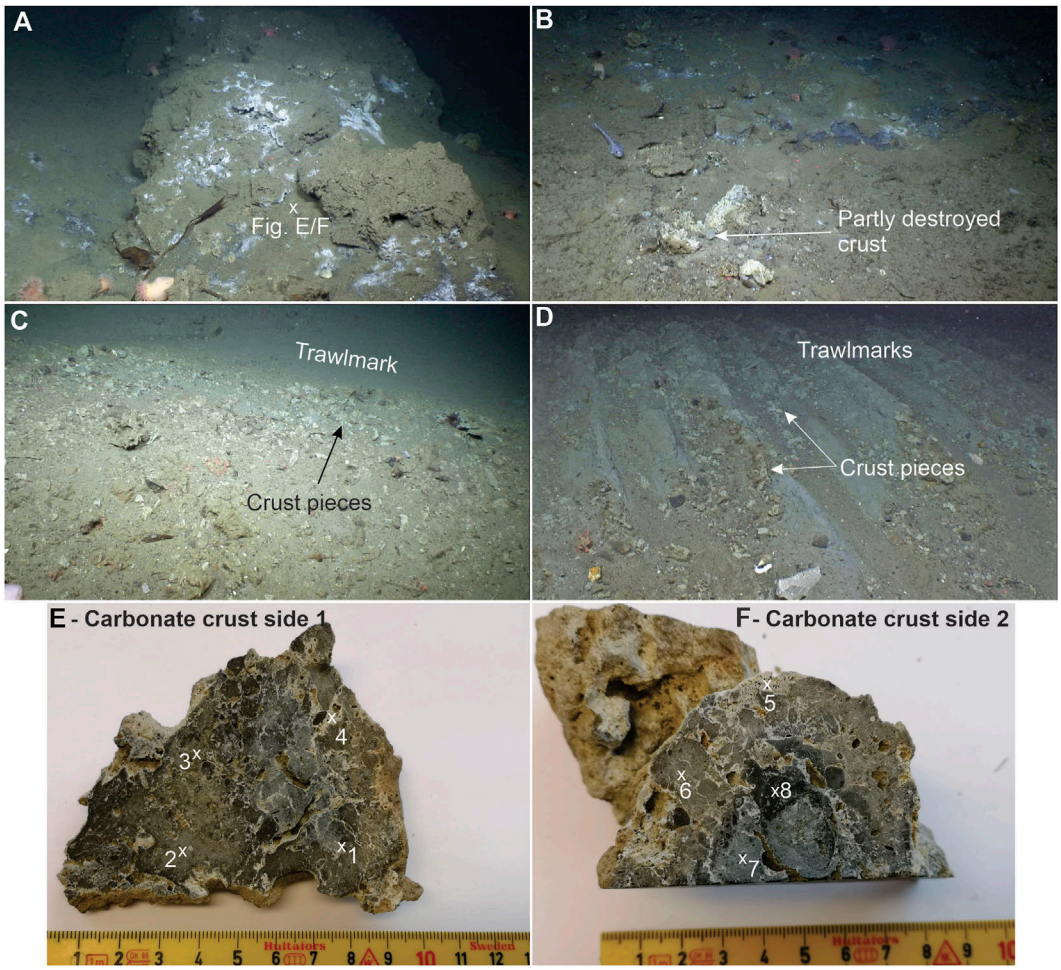

FIGURE 7
Large areas with carbonate crusts occur **(A)** as well as smaller crusts. Crusts were destroyed by trawling in large areas **(B)** and pieces of crusts associated with trawlmarks are interpreted as broken carbonate crusts **(C,D)**. A sample of carbonate crust **(E,F)** were taken on the carbonate crusts of **(A)**. Locations of crust analysis are indicated by numbers on **(E,F)**. Video data supplied by MAREANO/Institute of Marine Research.

southeast areas. In some places, the original mixed coarse sediment is visible at the foot of the hill made by soft sediments, while sediment mounds and chemosynthetic tubeworms are present on the top of the hill (Figure 10E).

On the structure B located at the edge of the dataset, bacterial mats, chemosynthetic tubeworms and small sediment mounds mostly occur close or in an elongated depression at the top of the structure (Figure 4). However, only two video lines have been acquired on this structure, not enough to cover the entire area.

4.3 Seismic observations

The sediments around the protruding structure A show alternating seismic units, either acoustically stratified or transparent (Figure 11). The part right below the protruding structure A is characterised by complete acoustic blanking which can extend horizontally along strata. The top of the structure is marked by chaotic reflections, likely rising from diffractions from the ridges. The along-slope-profile (Figure 11 yy') does not show the same pattern on the two sides of the structure A. One debris flow (marked GDF on Figure 11), about 6 m deep and likely coming from the Storfjorden trough mouth fan, stopped right against the acoustic blanking area.

Carbonate crusts and crust pieces occur on and around the ridges, which are also right above the main acoustic blanking corridor (Figure 12), that we can follow down as deep as the signal penetration. This acoustic blanking widens upwards at about 20 m below the seabed. This part of the acoustic blanking corresponds to the long north depression where little carbonate crusts or bacterial mats have been found and where mostly sediment mounds exist. Sediment mounds also occur on the other side of the structure A, where no acoustic blanking is present.

4.4 Results from the carbonate crust analysis

Carbonate crusts form due to cementation of seafloor sediments via precipitation of authigenic carbonate minerals, and typically

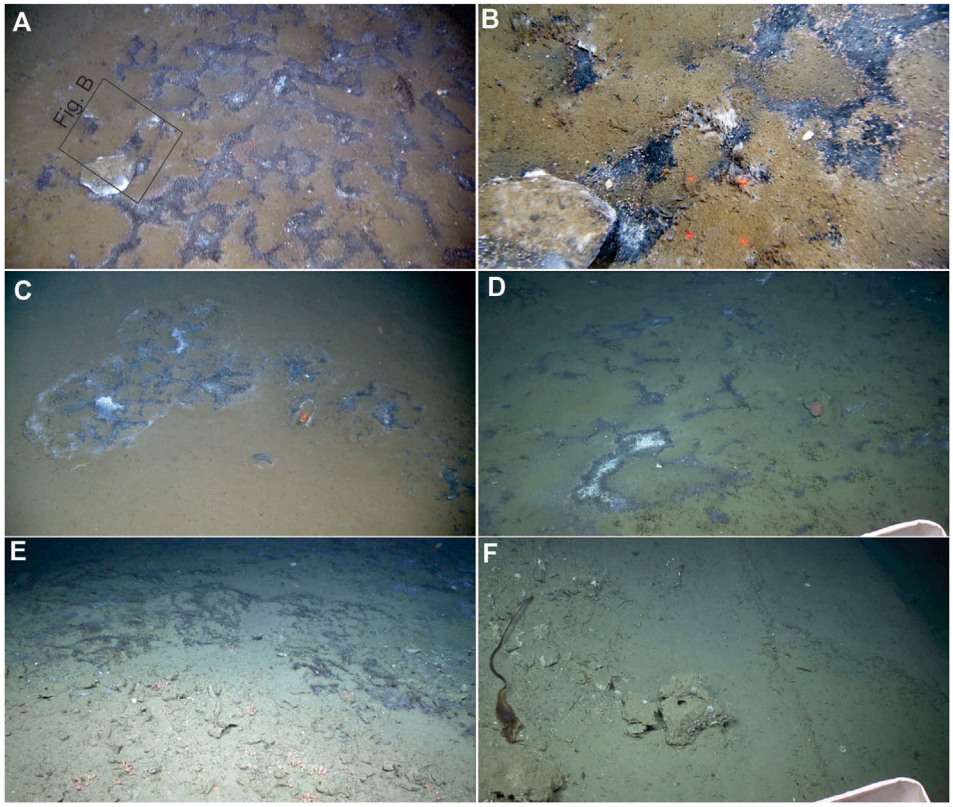

FIGURE 8
Bacterial mats and chemosynthetic tubeworms. **(A)** shows an example of an 18 m long area with bacterial mats, with a zoom in **(B)**. Bacterial mats can also be found in circular structures **(C)** or on top of domes (Figure 9). They are often associated with chemosynthetic siboglinid tubeworms **(D,E)**. Tubeworms can also be found without bacterial mats **(F)**, but also on highs (see also Figure 10). Note the carbonate crust on **(F)** as well as the seafloor layering. 10 cm between red laser dots. Video data supplied by MAREANO/Institute of Marine Research.

TABLE 1 Results of the carbonate crust analysis.

Sample ID	Total silicate (%)	Total carbonate (%)	Dolomite (%)	Calcite (%)	Mg-calcite (%)	Aragonite (%)	δ^{13}CVPDB (‰)	δ^{18}OVPDB (‰)
vg-3082-1	29.9	70	0.6	3.4	1.6	64.4	−52.1	5.0
vg-3082-2	27.7	71.9	tr.	3.5	1.4	67.0	−51.7	5.0
vg-3082-3	27.2	72.5	0.6	4.1	1.2	66.6	−52.5	5.5
vg-3082-4	32.8	66.8	1.4	5.8	0.3	59.3	−49.0	5.2
vg-3082-5	61.8	37.9	1.0	2.3	0.6	34.0	−51.1	4.3
vg-3082-6	22.9	77	0.5	3.8	1.3	71.4	−51.9	4.8
vg-3082-7	27.9	71.7	0.9	4.5	1.5	64.8	−52.7	4.9
vg-3082-8	26.5	73.3	0.5	4.0	1.6	67.2	−48.5	5.2

contain variable propositions of detrital silicate and authigenic carbonate components. Carbonate contents of studied subsamples microdrilled from different parts of the crust taken in the center of the structure A (Figures 7E–F) exhibit minor colour variations range from 67 to 77% wt., except one subsample which carbonate content is 38% wt. Aragonite is the predominant carbonate phase in studied subsamples (ca 90% of carbonate fraction), but trace amounts of dolomite, calcite and Mg-calcite are also present. Stable isotope composition of the eight subsamples is similar with δ^{13}C values ranging between −52.7 and −48.4‰ VPDB and δ^{18}O values ranging between 4.3 and −5.5‰ VPDB (Figure 7; Table 1).

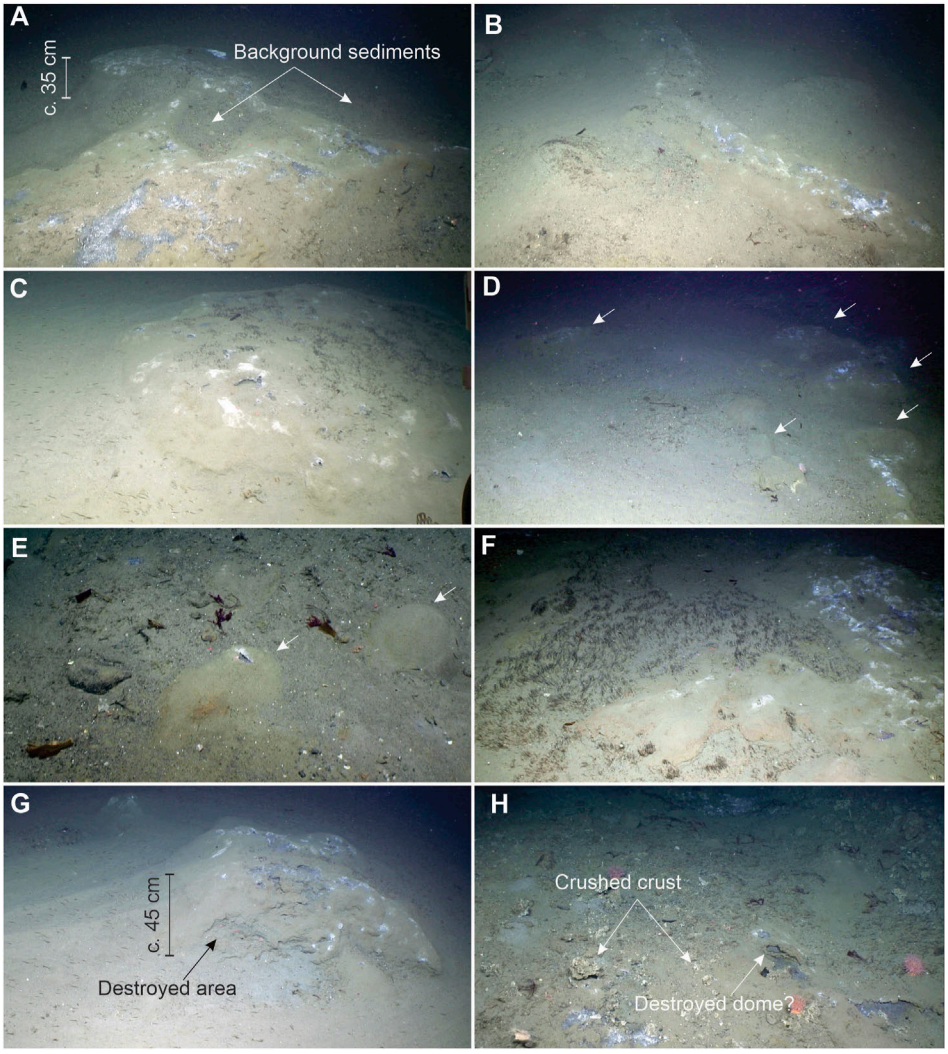

FIGURE 9
Domes show different shapes and sizes and are generally partly covered by bacterial mats **(A–H)**, and more rarely by chemosynthetic tubeworms **(A–C)**. Like for the carbonate crusts, domes can be destroyed and crushed by trawling **(G,H)**. 10 cm between red laser dots. Video data supplied by MAREANO/Institute of Marine Research.

5 Discussion

5.1 Origin of the gas seeps

The seepage may originate from several sources. The middle Miocene organic-rich deposits recovered in the central Fram Strait (Knies and Mann, 2002) is considered to be the most likely source of the ongoing gas and oil seeps on Vestnesa Ridge and Prins Karls Forland (Daszinnies et al., 2021). Southwest of Svalbard, the Storfjorden trough mouth fan is one of the largest and thickest Plio-Pleistocene fans of the western Svalbard-Barents Sea margin (Vorren and Laberg, 1997). Burial of Tertiary organic-rich deposits below these thick wedges of prograding sediment sequences since the intensification of the Barents Sea glaciation (Laberg et al., 2012) may have caused organic matter maturation and eventually expulsion and migration of hydrocarbons (Daszinnies et al., 2021). Indeed, recent data compilation of oil-source rock correlation for the western Svalbard margin indicate an unequivocal correspondence between a Tertiary source rock of deltaic origin and seeping oil at the sea surface (Mattingsdal, 2023). If this Tertiary source rock has reached its maturation window below the trough mouth fan, it may have led to generation of fluids and migration along the limit of the trough mouth fan. Another source of fluids might be older deposits, like gas migrating from Paleocene hydrocarbon reservoirs through the Hornsund fault complex. These reservoirs are likely responsible for the gas-charged sediments at the gas hydrate pingos in Storfjorden trough (Waage et al., 2019), c. 90 km to the south of our study area.

We can rule out any direct link to gas hydrate boundary related seepages, as observed at many locations along the western Svalbard margin (Westbrook et al., 2009; Berndt et al., 2014) as our structures are located much deeper than the upward limit of the gas hydrate stability zone close to 400 m (Vogt et al., 1999; Vadakkepuliyambatta et al., 2017). However, the high $\delta^{13}C$ values, consistent with methane seepage and its anaerobic oxidation as

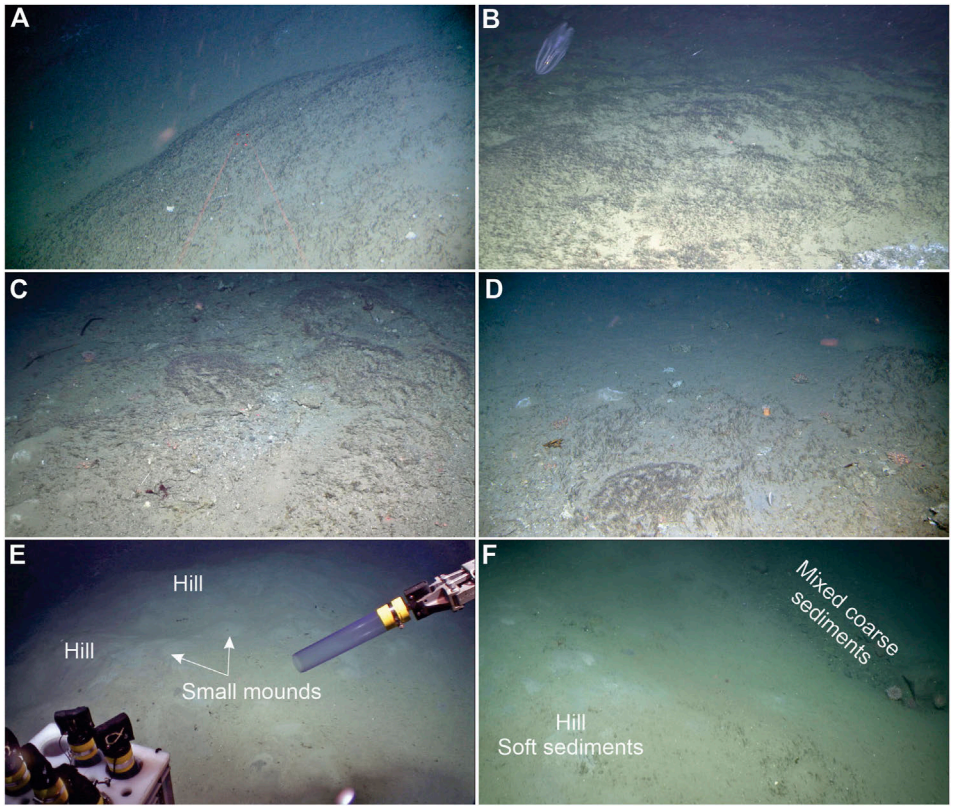

FIGURE 10
Small hills forming hummocky sediments have different sizes, from decimetric to metric, and are generally covered by chemosynthetic tubeworms **(A–D)**. Accumulation of small sediment mounds can also form hills **(E)**. Large hills are also observed covering the background mixed coarse sediments **(F)** with here some sediment mounds and chemosynthetic tubeworms present on top of the hill. 10 cm between red laser dots. Video data supplied by MAREANO/Institute of Marine Research.

the underlying cause for the authigenic carbonate precipitation and crust formation, and the bubbles at the structure A (Figures 3, 5) suggest a breach of free gas through the hydrate stability zone towards the sea surface. This might explain the relatively high $\delta^{18}O$ values which indicate a possible involvement of fluids released by gas hydrate during the carbonate precipitation. The breach of free gas can occur where the hydrate stability parameters are changed, specifically pore fluid temperature altered by seeping fluids or an overpressure buildup due to fluid flow from deeper formations (Paull et al., 2008b), resulting in gas migration from a deep-seated reservoir, below the Plio-Pleistocene trough mouth fan deposits. We cannot rule out that these gases are mixed with gases from microbial origin, as the last ones might occur everywhere.

5.2 Interpretation of the seepage features

No gas flares in multibeam water column data were observed above the structure A in SK01. As the water column data was of poor quality along the slope, we cannot, however, completely rule out the presence of gas flares in this area at the time of surveying. Also, their apparent absence may be due to seepages occurring intermittently rather than continuously. Indeed, a constant bubble stream occurred after sampling a piece of carbonate crusts in the center of the structure A, and several sporadic plumes were observed in its southeast part (Figure 5). Moreover, gas flares only represent free gas emissions, their absence does not mean that dissolved gases are not present and indeed the presence of extensive bacterial mats and siboglinid tubeworms (Figures 3D, E), which depend directly on dissolved gases for their chemosynthesis-based nutrition (see, e.g., Schulze and Halanych, 2003; Sen et al., 2018; Åström et al., 2020), indicate an active and mostly diffuse seepage (Boetius and Wenzhofer, 2013; Panieri et al., 2017). This on-going seepage is also marked by the recolonization by tubeworms and bacterial mats in areas relatively recently disturbed by trawlmarks (Figures 7B, 9H). In fact, the slightly elevated, circular structures with bacterial mats in the centre and siboglinid tubeworms often on the rims indicates a limited chemical impact, with a more focused seepage in one place, in the centre, where the bacterial mats occur, and less, or deeper, chemical reactions supplying sulphide or methane used by the tubeworms' symbionts (e.g., Sen et al., 2018) away from the center where the tubeworms are observed. On the other hand, large areas with bacterial mats, sometimes forming a net of lines, may indicate a more diffuse seepage with gas/fluids migrating upwards through cracks/small faults over larger areas.

Several other features (small sediment mounds, domes, and small hills forming a hummocky surface) have been interpreted as a result of seepages in this area. A common characteristic of these

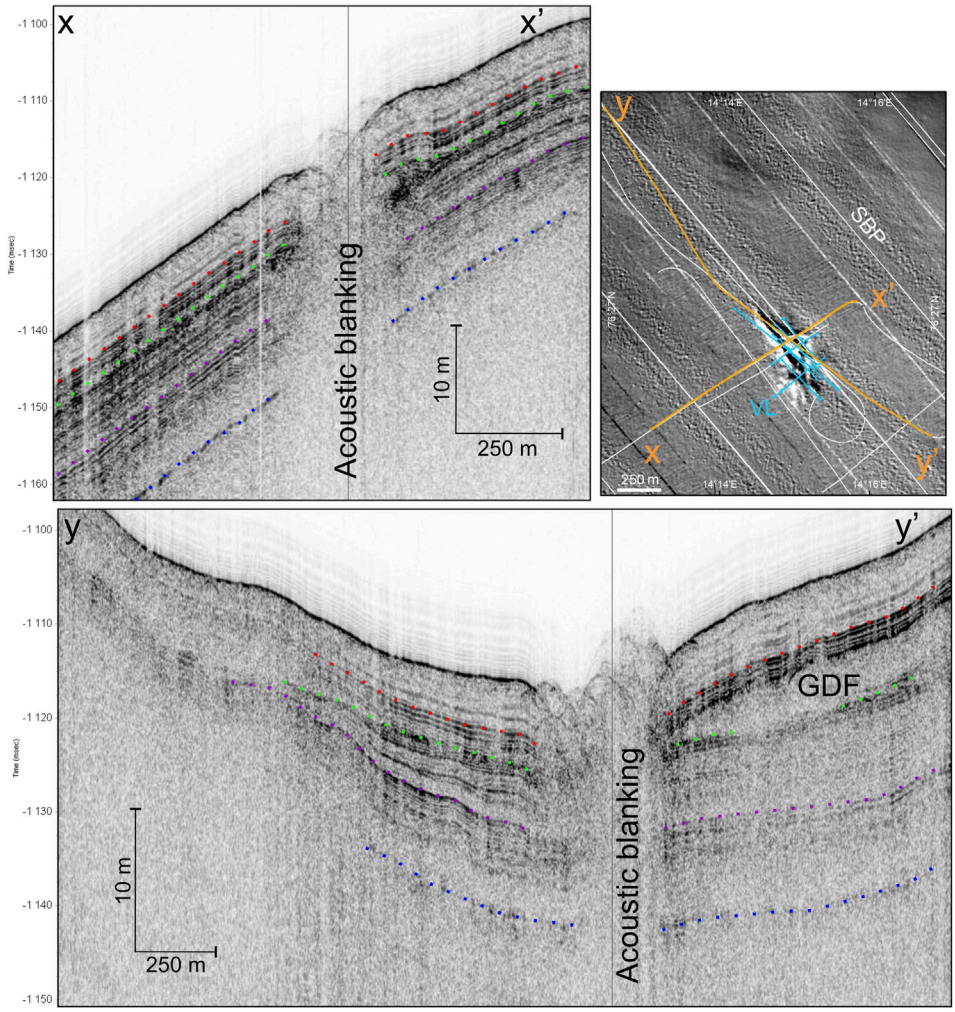

FIGURE 11
TOPAS lines showing the structure A of the SK01 box. Top panel: line perpendicular to the structure and parallel to the regional slope, lower panel: line parallel to the structure. The dotted blue line follows the same reflections on both TOPAS lines. VL, video lines; SBP, sub-bottom profiler. Detailed bathymetry data supplied by MAREANO/Norwegian Hydrographic Survey. TOPAS data: MAREANO/NGU.

features is that all of them show a positive relief. Another common characteristic is that all these features occur only inside the structure A or just at its border.

The small sediment mounds of disturbed sediments with no bacterial mats or siboglinid tubeworms on their tops are the most extended feature, occurring also slightly outside the structure A in the east/southeast but rarely in the center of the structure (Figure 6). They may represent one-time or short-time fluid/gas seep events at the border of the seep area with too little gas to create chemical reactions. On-going short-time seepages have been observed with sporadic plumes leaving behind dark grey sediment lobes (Figures 5A–C). Small sediment lobes have often been observed originating from these mounds, likely linked to these short seepage events, even if not all of them show a dark grey colour. The location of these mounds, mostly observed on the external part of the structure A, supports a lower supply of gas/fluids. Moreover, when checking their location with the imprint of the acoustic blanking (Figure 12), which is interpreted as a blanking linked to gas migration, these mounds occur at the border or outside of the main acoustic blanking corridor. The fact that they do not cover the northern part of the northeast depression while they occur and show active signs of seepage in the east may indicate an actual gas migration towards the east, which is towards the structure B. No correspondences have been found in the literature in the marine domain about these structures. However, they might appear slightly like gryphons found in onshore mud volcano areas. These gryphons are conic features formed from the expulsion of gas, water, oil and mud and gather in cluster or fields in the central part of the mud volcano crater. Their body is made by superposed mud flows resulting from the semi-continuous mud eruption (Mazzini and Etiope, 2017).

Mostly located on the flank and on top of the ridges, the domes show different sizes and shapes with bacterial mats but scarce siboglinid tubeworms on top (Figure 9). They are interpreted as sediments pushed-up by gas/fluids, and they represent areas of more focused and constant seepage pushing the sediments upwards

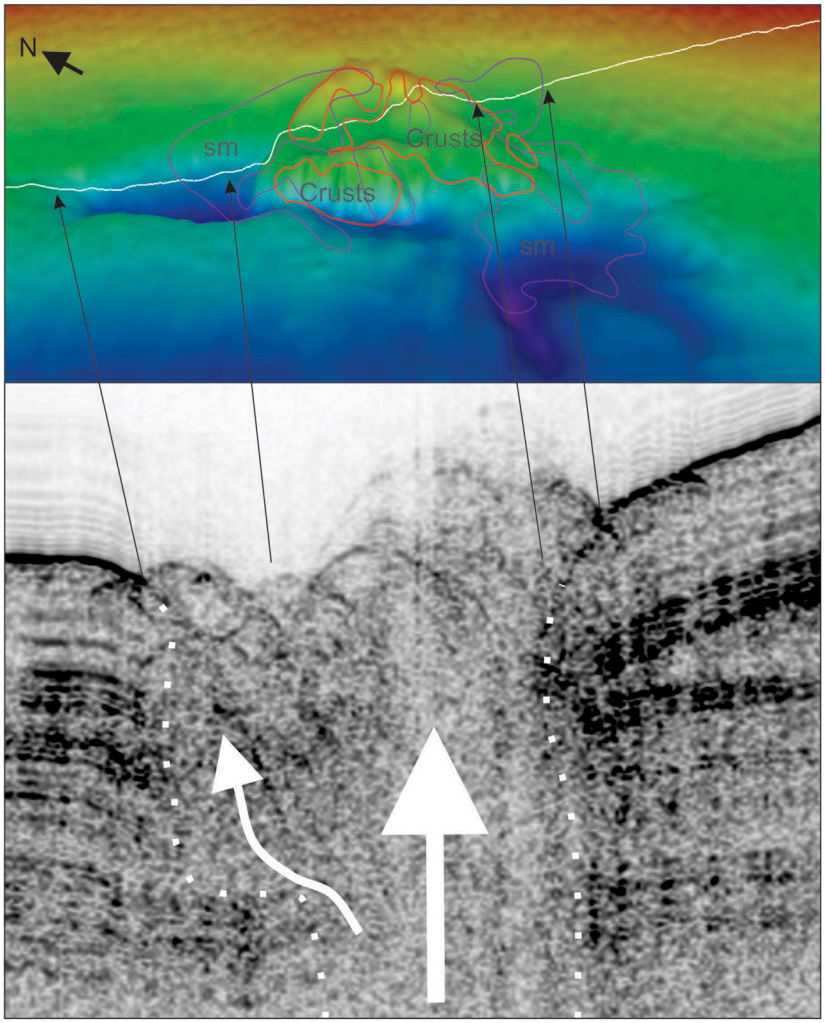

FIGURE 12
Comparison between the acoustic blanking areas (zoom from the yy' TOPAS line of in this figure, lower panel) and the presence of sediment mounds and crusts (large carbonate crusts and small pieces), displayed on top of a 3D view of the structure A [higher panel, white line: TOPAS line, violet lines: limits of the sediment mounds (sm), red lines: limits of the crusts]. The main acoustic blanking (large white arrow) is below the area of carbonate crusts, while the area with a shallower acoustic blanking (smaller arrow) corresponds to the long north depression where the only seepage expressions observed are the sediment mounds. Sediment mounds are also the main sign of seepage on the east border of the structure, where very little acoustic blanking occurs. Detailed bathymetry data supplied by MAREANO/Norwegian Hydrographic Survey. TOPAS data: MAREANO/NGU.

over a more or less long period, which explain why bacterial mats are almost always present on their top. The fact that no signs of mass-movement are visible in the sediment at the surface of the domes may indicate harder/consolidated sediments, which may be confirmed as well by pieces looking like crusts from domes destroyed by trawling. This is also substantiated by the almost total absence of tubeworms on the top on most of the domes, as the worms need softer sediments to settle. The material of these domes might come from the sediments/crust often observed on top of bacterial mats (Figure 8). We do not have enough data to know if these crusts have a chemical origin (like thin layers of carbonate crusts), are originated from bacterial secretions, or simply come from sediments trapped by the bacterial filaments constituting the mats. Once these crusts form a layer, the bacterial mats settle again on top and a new crust starts covering the mats again, and so on until the supply in gas/fluid stops (Figure 13). This kind of formation will explain the empty space between the layers as well as why bacterial mats always occur on top. If the domes are made from carbonate crusts, they might be similar to the small mounds of porous carbonate crusts found at the Nile deep-sea fan (Gontharet et al., 2007). They might also correspond to small gas-hydrate pingos as the ones found in Nyegga (Hovland and Svensen, 2006).

Hills forming a hummocky seafloor are most of the time made of soft sediments, which do not correspond to the mixed coarse background seafloor sediments. As they are often covered by chemosynthetic siboglinid tubeworms, it is likely that some diffuse seepages occur in these areas. If they do not reach the surface, the worms need to dig deeper in the sediments, but these seepages do not create domes or favour the growth of bacterial mats. They might correspond to the accumulation of

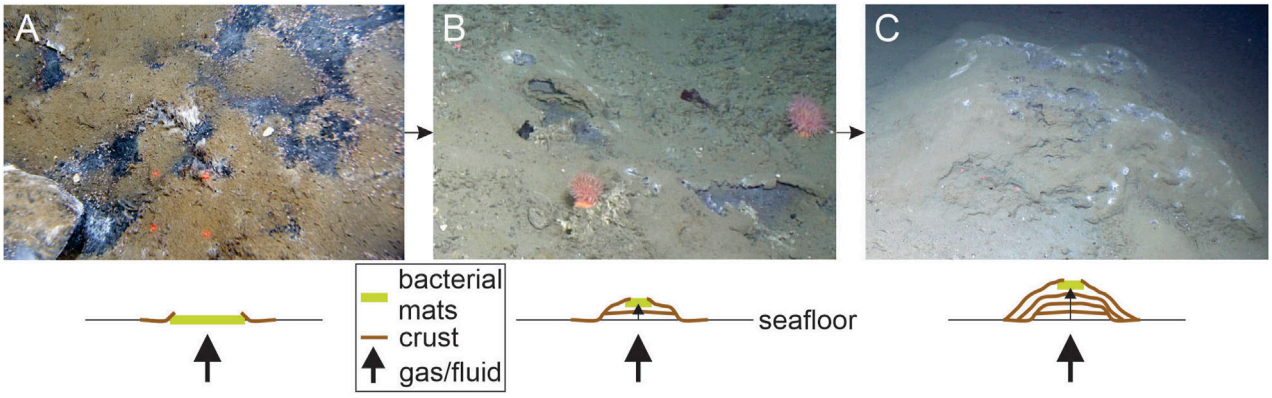

FIGURE 13
Possible formation of the domes. **(A)** Crusts form at the surface of the bacterial mats. **(B)** Bacterial mats. grow again on top of the crusts due to a constant flux of gas. **(A–C)** repeat themselves several times up to forming a dome shape structure. Video data supplied by MAREANO/Institute of Marine Research.

older small sediment mound areas, like the one of the Figure 10A or Figure 10E.

5.3 Formation

The structure A found at about 820 m depth in SK01 is the first of its kind to be observed on the western Svalbard continental margin. The presence of more than 80 cm thick methane-derived authigenic carbonate crusts near the centre of the structure suggests a relatively long seepage history of at least several thousand years (Ye et al., 2019), similar to what it was documented from both theVestnesa Ridge (Himmler et al., 2019) and the southwestern Barents Sea (Crémière et al., 2016). This is further supported by the presence of a glacigenic debris flow stopping nearby the acoustic blanking corridor below the structure A covered by several metres of post-glacial sediments (Figure 11).

The structure A is shaped as an elongated depression with ridges inside. Bacterial mats, siboglinid tubeworms and crusts occur on top and on the sides of these ridges, as well as in the depression southeast to the ridges. These indicate that the ridges may have been the results of sediments pushed upwards by gas migration, quite similar to but much larger than the domes, likely in a comparable way than gas-hydrate pingos (e.g., Hovland and Svensen, 2006; Waage et al., 2019). The ridges and the southeast depression appear more active than the west part of the elongated NW-SE depression where the bottom is filled by muddier sediments.

The sediment distribution along the structure A is interesting, as similar sediments (mud, sand, gravel, cobbles and boulders) occur on the top of the ridges and in the surrounding areas, as well as in the crater, while muddier sediments are found on the flanks of the ridges and in the lower areas. However, in the crater, the mixed sediments alternate with softer sediments often linked to sediments mounds or small hills. This means that the seafloor likely did not collapse at the NW-SE depression (no presence of stones in the deeper areas) but instead opened in the same way that we can see on the southernmost structure, with small cracks, perhaps aided by the regional slope which helps pulling the sediments down the slope (Figure 14). However, as cobbles and boulders are present in the crater, the seafloor likely collapsed in this area.

The first step of the structure A formation would be gas/fluids coming up, disturbing the sediments (Figure 14A) before forming a large positive structure. A partial collapse at the top of the structure might have led to the formation of a crater in the middle, likely linked to stronger gas/fluid seepages at this place (Figure 14B). Around the seepage areas, the sediments might be a little bit more consolidated, either because of carbonate crusts, gas hydrates or because of crusts-like sediments on top of the ridges. Cracks could have occurred along these slightly more consolidated areas (Figure 14C), and as the ridges were going up, cracks opened under the upwards pressure of the ridge and the downwards pressure of the regional slope until the modern structure (Figure 14D). The effect of the slope likely explained why there are no depressions on the shallowest side of the ridges.

Both the structure A and the edge of structure B are located at the limit between the Storfjorden and Hornsund trough mouth fans, out of which the latter is much less developed (Rebesco et al., 2014). The location of the seep structures at the boundary between the Storfjorden and Hornsund trough mouth fan deposits could suggest a loading related fluid seepage where these two deposits are absent or thinner. The overpressure caused by the glacial loading may have driven the fluids upwards to a preferably easier and permeable formation. Indeed, as the glacigenic debris flows constituting the Storfjorden trough mouth fan (Laberg and Vorren, 1996) are less permeable (e.g., Bünz et al., 2003), it is possible that gas have escaped at this boundary due to a low-pressure passage towards the surface.

This model can be compared to that suggested for Nyegga Area where similar features where observed. At Nyegga area, the loading from high sedimentation rate during a glacial advance created an overpressure scenario (Hustoft et al., 2009) which resulted in focussing of fluids to the region outside less permeable glacial debris flow deposits and concentrated escape of fluids creating a region of pockmarks. The enhanced fluid flow activity died out but the structures are preserved, and micro seepage is still

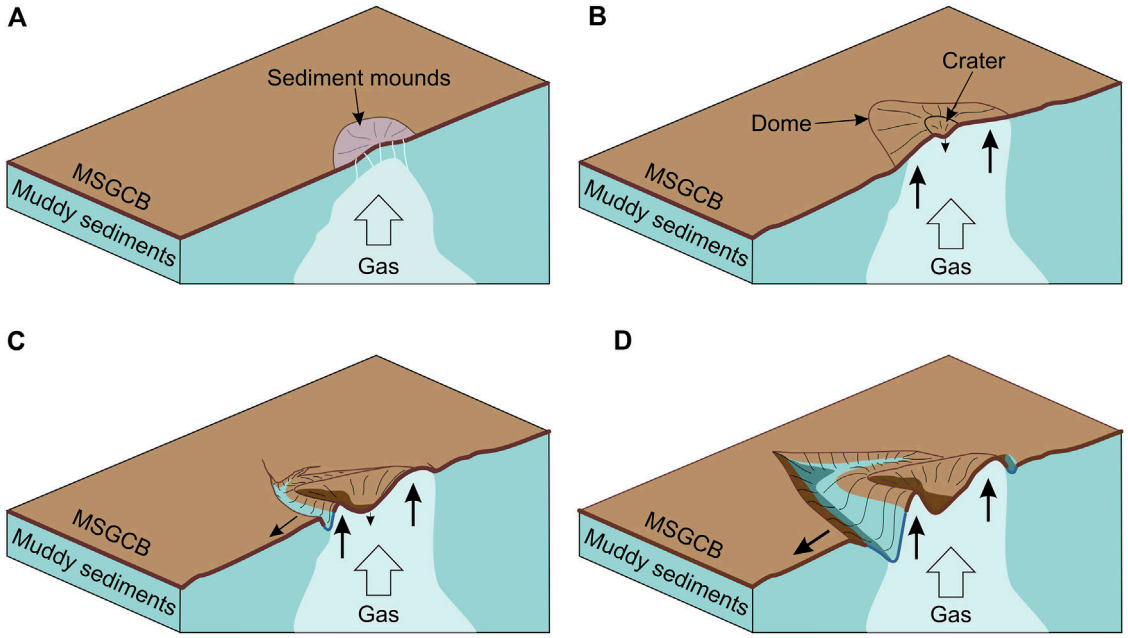

FIGURE 14
Schematic model of the formation of the SK01 structure A. **(A)** Gas (or fluids) migrates upwards forming a small dome. **(B)** Once the gas reaches the surface, the seepage becomes more important, and a larger dome starts forming. A crater may appear at the top of the dome due to the release of pressure below. **(C)** Under the sediment load pressure downslope, cracks start forming parallel to the regional slope. **(D)** Actual shape of the structure, with soft sediments clearly visible on the walls and the bottom of the cracks. MSGCB: Mud, sand, gravel, cobbles and boulders.

reported from some of these pockmarks (Chevalier et al., 2014; Roalkvam et al., 2012; Krylova et al., 2011). This process might be one of the explanations of the formation of the structures right at the border of the two trough mouth fans. Another formation model includes the expulsion of mud or ooze if present along with the fluids. The video and photos indicate fresh flows of material through vents at the sites indicating some material also coming out. This could be also fluids carrying fine particles while they move upwards during the already established conduits. The expulsion of such material also indicates that the overpressure from the loading of two fan deposits are still not accommodated and the processes related to it are still active creating these seafloor features.

Cold seeps occur on both passive and active margins and in different environmental settings (Suess, 2014; Ceramicola et al., 2017). Suess (2014) indicates that, on passive margins, the driving mechanisms for fluid expulsion at passive margins are linked to sediment loading, differential compaction, overpressure and facies changes. And on this, the SK01 cold seeps are not different from the other passive margin seeps.

Some of the environmental settings favouring cold seeps can also be compared with the SK01 cold seep environment: deltaic environments with high sedimentation rate leading to sediment overload, like, for example, the Nile delta where several seeps occur along the fan (e.g., Dupré et al., 2010) or deep-sea fans like the Congo deep-sea fan (e.g., Rabouille et al., 2017; Sen et al., 2017). Glacial trough mouth fans, deltaic fans and deep-sea fans, while occurring at different latitudes or depths, all represent a higher sedimentation rate than the surrounding areas. The major factor triggering the migration of gas or fluids around these fans is likely to be this higher sedimentation rate leading to a sedimentary loading and/or overpressure, like for the Nyegga area (Hustoft et al., 2009).

However, there is a wide range of shapes associated with cold seeps with sediment loading as a primary cause, from pockmarks at the Congo deep-sea fan to mud volcanoes at the Nile delta or possibly ridges and crater at SK01. This indicate that other factors affect the shape of the seeps which might be the flow rate and its upwards migration pathways (e.g., chimneys, faults or through the sediments), the presence of gas hydrates, the composition of the gases/fluids or even the sediment characteristics at the seep location.

6 Conclusion

We report new morphological structures on the southwest continental slope of Svalbard (c. 800 m water depth), which are interpreted as the result of methane seepages. No gas flares were observed in the study area indicating that present seepages, while extensive, might be minimal or intermittent. The structures are located right at the border between two glacial trough mouth fans, Hornsund and Storfjorden, that probably have influenced their formation by the local sediment overpressure they create. Several hypotheses are plausible for the gas origin, either shallow

reservoirs charged by the same middle Miocene organic-rich deposits responsible for the gas seepage at Vestnesa Ridge and Prins Karls Forland, or from older (Paleocene/Eocene) and deeper seated rocks. Video observations show typical features for diffusive gas emission at the seafloor including bacterial mats, chemosynthetic animals, and thick methane-derived authigenic carbonates. Moreover, the micro and mega structures observed within the site such as small mounds, domes, and flow structures indicate that gas seepage is still occurring. Some features seem to indicate a constant and more focused seepage, like the domes, while others like the small mounds appear to be linked to short-time seepages.

Our seep formation hypothesis is that the upwards migration of gas or fluids formed a large dome, likely similar to gas-hydrate pingos, whose the center later collapsed to form the actual crater surrounding by ridges. The mode of seepage is mainly liquid based and is today mostly active when the sediments are disturbed and at the eastern limit of the structure which seems to indicate a migration of the fluids towards this direction.

Extensive diffuse seepages have the potential to release methane in the water column and are known to form special habitats with chemosymbiotrophic fauna. Certainly, more in-depth knowledge from ROV based sampling and multi-scale analytical investigations is needed to fully understand the spatial distribution, controlling processes, chronological constraints and origin of this new discovered seep site.

Data availability statement

The original contributions presented in the study are publicly available. This data can be found here: geo.ngu.no/kart/marin_mobil/ and www.mareano.no.

Author contributions

VB: Investigation, Writing–original draft, Writing–review and editing. SC: Writing–review and editing. JK: Writing–review and editing. LB: Writing–review and editing. AL: Writing–review and editing. AS: Writing–review and editing. TT: Writing–review and editing.

Funding

The author(s) declare that no financial support was received for the research, authorship, and/or publication of this article.

Acknowledgments

We acknowledge all participants of the MAREANO programme (www.mareano.no) for invaluable cooperation. The multibeam data were acquired and supplied by the Norwegian Hydrographic Service at the Norwegian Mapping Authority (Kartverket). The data is released under a Creative Commons Attribution 4.0 International (CC BY 4.0): https://creativecommons.org/licenses/by/4.0/. Fundings for campaigns, research and analysis were supported by the Mareano program. JK was supported by the Research Council of Norway (grant #332635).

Conflict of interest

The authors declare that the research was conducted in the absence of any commercial or financial relationships that could be construed as a potential conflict of interest.

Publisher's note

Supplementary material

The Supplementary Material for this article can be found online at: https://www.frontiersin.org/articles/10.3389/feart.2024.1328357/full#supplementary-material

SUPPLEMENTARY TABLE S1
Locations of the still images shown in this study.

References

Andreassen, K., Hubbard, A., Winsborrow, M., Patton, H., Vadakkepuliyambatta, S., Plaza-Faverola, A., et al. (2017). Massive blow-out craters formed by hydrate-controlled methane expulsion from the Arctic seafloor. *Science* 356 (6341), 948–953. doi:10.1126/science.aal4500

Åström, E. K. L., Sen, A., Carroll, M. L., and Carroll, J. (2020). Cold seeps in a warming Arctic: insights for benthic ecology. *Front. Mar. Sci.* 7, 244. doi:10.3389/fmars.2020.00244

Berndt, C., Feseker, T., Treude, T., Krastel, S., Liebetrau, V., Niemann, H., et al. (2014). Temporal constraints on hydrate-controlled methane seepage off Svalbard. *Science* 343, 284–287. doi:10.1126/science.1246298

Biastoch, A., Treude, T., Rüpke, L. H., Riebesell, U., Roth, C., Burwicz, E. B., et al. (2011). Rising Arctic Ocean temperatures cause gas hydrate destabilization and ocean acidification. *Geophys. Res. Lett.* 38 (8), L08602. doi:10.1029/2011gl047222

Boetius, A., Ravenschlag, K., Schubert, C. J., Rickert, D., Widdel, F., Gieseke, A., et al. (2000). A marine microbial consortium apparently mediating anaerobic oxidation of methane. *Nature* 407 (6804), 623–626. doi:10.1038/35036572

Boetius, A., and Wenzhofer, F. (2013). Seafloor oxygen consumption fuelled by methane from cold seeps. *Nat. Geosci.* 6, 725–734. doi:10.1038/ngeo1926

Bryn, P., Berg, K., Forsberg, C. F., Solheim, A., and Kvalstad, T. J. (2005). Explaining the storegga slide. *Mar. Petroleum Geol.* 22 (1-2), 11–19. doi:10.1016/j.marpetgeo.2004.12.003

Bünz, S., and Mienert, J. (2004). Acoustic imaging of gas hydrate and free gas at the Storegga Slide. *J. Geophys. Res. Solid Earth* 109 (B4), B04102. doi:10.1029/2003jb002863

Bünz, S., Mienert, J., and Berndt, C. (2003). Geological controls on the Storegga gashydrate system of the mid-Norwegian continental margin. *Earth Planet. Sci. Lett.* 209, 291–307. doi:10.1016/s0012-821x(03)00097-9

Bünz, S., Mienert, J., Vanneste, M., and Andreassen, K. (2005). Gas hydrates at the storegga slide: constraints from an analysis of multicomponent, wide angle seismic data. *Geophysics* 70, B19–B34. doi:10.1190/1.2073887

Bünz, S., Polyanov, S., Vadakkepuliyambatta, S., Consolaro, C., and Mienert, J. (2012). Active gas venting through hydrate-bearing sediments on the Vestnesa Ridge, offshore W-Svalbard. *Mar. Geol.* 332-334, 189–197. doi:10.1016/j.margeo.2012.09.012

Ceramicola, S., Dupré, S., Somoza, L., and Woodside, J. (2017). "Cold seep systems," in *Submarine geomorphology*. Editors A. Micallef, S. Krastel, and A. Savini (Charm: Springer), 367–387.

Chevalier, N., Bouloubassi, I., Stadnitskaia, A., Taphanel, M.-H., and Sinninghe Damsté, J. S. (2014). Lipid biomarkers for anaerobic oxidation of methane and sulphate reduction in cold seep sediments of Nyegga pockmarks (Norwegian margin): discrepancies in contents and carbon isotope signatures. *Geo-Marine Lett.* 34, 269–280. doi:10.1007/s00367-014-0363-5

Crémière, A., Lepland, A., Chand, S., Sahy, D., Condon, D. J., Noble, S. R., et al. (2016). Timescales of methane seepage on the Norwegian margin following collapse of the Scandinavian Ice Sheet. *Nat. Commun.* 7 (1), 11509. doi:10.1038/ncomms11509

Daszinnies, M., Plaza-Faverola, A., Sylta, Ø., Bünz, S., Mattingsdal, R., Tømmerås, A., et al. (2021). The Plio-Pleistocene seepage history off western Svalbard inferred from 3D petroleum systems modelling. *Mar. Petroleum Geol.* 128, 105023. doi:10.1016/j.marpetgeo.2021.105023

Dumais, M.-A., Gernigon, L., Olesen, O., Johansen, S. E., and Brönner, M. (2021). New interpretation of the spreading evolution of the Knipovich Ridge derived from aeromagnetic data. *Geophys. J. Int.* 224 (2), 1422–1428. doi:10.1093/gji/ggaa527

Dupré, S., Woodside, J., Klaucke, I., Mascle, J., and Foucher, J.-P. (2010). Widespread active seepage activity on the Nile Deep Sea Fan (offshore Egypt) revealed by high-definition geophysical imagery. *Mar. Geol.* 275, 1–19. doi:10.1016/j.margeo.2010.04.003

Feng, D., Qiu, J.-W., Hu, Y., Peckmann, J., Guan, H., Tong, H., et al. (2018). Cold seep systems in the South China Sea: an overview. *J. Asian Earth Sci.* 168, 3–16. doi:10.1016/j.jseaes.2018.09.021

Ferré, B., Jansson, P. G., Moser, M., Serov, P., Portnov, A., Graves, C., et al. (2020). Reduced methane seepage from Arctic sediments during cold bottom-water conditions. *Nat. Geosci.* 13, 144–148. doi:10.1038/s41561-019-0515-3

Gontharet, S., Pierre, C., Blanc-Valleron, M.-M., Rouchy, J. M., Fouquet, Y., Bayon, G., et al. (2007). Nature and origin of diagenetic carbonate crusts and concretions from mud volcanoes and pockmarks of the Nile deep-sea fan (eastern Mediterranean Sea). *Deep-Sea Res. II* 54, 1292–1311. doi:10.1016/j.dsr2.2007.04.007

Hart, P. E., Pohlman, J. W., Lorenson, T. D., and Edwards, B. D. (2011). "Beaufort Sea deep-water gas hydrate recovery from a seafloor mound in a region of widespread BSR occurrence," in Proceedings of the 7th International Conference on Gas Hydrates (ICGH 2011), Edinburgh, Scotland, United Kingdom, July 17-21, 2011.

Himmler, T., Sahy, D., Martma, T., Bohrmann, G., Plaza-Faverola, A., Bünz, S., et al. (2019). A 160,000-year-old history of tectonically controlled methane seepage in the Arctic. *Sci. Adv.* 5 (8), eaaw1450. doi:10.1126/sciadv.aaw1450

Hovland, M., and Svensen, H. (2006). Submarine pingoes: indicators of shallow gas hydrates in a pockmark at Nyegga, Norwegian Sea. *Mar. Geol.* 228, 15–23. doi:10.1016/j.margeo.2005.12.005

Hughes, A. L. C., Gyllencreutz, R., Lohne, Ø. S., Mangerud, J., and Svendsen, J. I. (2016). The last Eurasian ice sheets – a chronological database and time-slice reconstruction, DATED-1. *Boreas* 45, 1–45. doi:10.1111/bor.12142

Hustoft, S., Dugan, B., and Mienert, J. (2009). Effects of rapid sedimentation on developing the Nyegga pockmark field: constraints from hydrological modeling and 3-D seismic data, offshore mid-Norway. *Geochem. Geophys. Geosystems* 10 (6), Q06012. doi:10.1029/2009gc002409

Jakobsson, M., Mayer, L. A., Bringensparr, C., Castro, C. F., Mohammad, R., Johnson, P., et al. (2020). The international bathymetric chart of the arctic ocean version 4.0. *Sci. Data* 7, 176. doi:10.1038/s41597-020-0520-9

Jones, A. T., Greinert, J., Bowden, D. A., Klaucke, I., Petersen, C. J., Netzeband, G. L., et al. (2010). Acoustic and visual characterisation of methane-rich seabed seeps at Omakere Ridge on the Hikurangi Margin, New Zealand. *Mar. Geol.* 272 (1-4), 154–169. doi:10.1016/j.margeo.2009.03.008

Kim, Y. G., Kim, S., Lee, D.-H., Kim, H. J., Kang, S.-G., Jin, Y. K., et al. (2020). Occurrence of active gas hydrate mounds in the southwestern slope of the Chukchi Plateau, Arctic Ocean. *Arct. Ocean. Episodes* 43 (2), 811–823. doi:10.18814/epiiugs/2020/020053

Knies, J., Daszinnies, M., Plaza-Faverola, A., Chand, S., Sylta, Ø., Bünz, S., et al. (2018). Modelling persistent methane seepage offshore western Svalbard since early Pleistocene. *Mar. Petroleum Geol.* 91, 800–811. doi:10.1016/j.marpetgeo.2018.01.020

Knies, J., and Mann, U. (2002). Depositional environment and source rock potential of Miocene strata from the central Fram Strait: introduction of a new computing tool for simulating organic facies variations. *Mar. Pet. Geol.* 19, 811–828. doi:10.1016/s0264-8172(02)00090-9

Krylova, E. M., Gebruk, A. V., Portnova, D. A., Todt, C., and Haflidson, H. (2011). New species of the genus Isorropodon (Bivalvia: Vesicomyidae: Pliocardiinae) from cold methane seeps at Nyegga (Norwegian Sea, Vøring Plateau, Storrega Slide). *J. Mar. Biol. Assoc. U. K.* 91 (5), 1135–1144.

Laberg, J. S., Andreassen, K., and Vorren, T. O. (2012). Late Cenozoic erosion of the high-latitude southwestern Barents Sea shelf revisited. *GSA Bull.* 124 (1-2), 77–88. doi:10.1130/b30340.1

Laberg, J. S., and Vorren, T. O. (1993). A late Pleistocene submarine slide on the bear Island trough mouth fan. *Geo Mar. Lett.* 13, 227–234. doi:10.1007/bf01207752

Laberg, J. S., and Vorren, T. O. (1996). The glacier-fed fan at the mouth of Storfjorden trough, western Barents Sea: a comparative study. *Geol. Rundsch.* 85, 338–349. doi:10.1007/s005310050079

Loeng, H. (1989). "Ecological features of the Barents Sea," in Proc. 6th Conf. Comité Arct. Internat., E. J. Brill. Leiden, 13-15 May 1985, 327–365.

Lösekann, T., Robador, A., Niemann, H., Knittel, K., Boetius, A., and Dubilier, N. (2008). Endosymbioses between bacteria and deep-sea siboglinid tubeworms from an arctic cold seep (haakon Mosby mud volcano, Barents Sea). *Environ. Microbiol.* 10, 3237–3254. doi:10.1111/j.1462-2920.2008.01712.x

Mattingsdal, R. (2023). "A new young source rock offshore western Svalbard proven with oil seep geochemical results – possible regional implication for the westernmost Barents Sea," in Norwegian Petroleum Directorate, Petroleum Systems Conference, Oslo, Norway, 23-24/05/2023.

Mau, S., Römer, M., Torres, M. E., Bussmann, I., Pape, T., Damm, E., et al. (2017). Widespread methane seepage along the continental margin off Svalbard - from Bjørnøya to Kongsfjorden. *Sci. Rep.* 7, 42997. doi:10.1038/srep42997

Mazzini, A., and Etiope, G. (2017). Mud volcanism: an updated review. *Earth-Science Rev.* 168, 81–112. doi:10.1016/j.earscirev.2017.03.001

Mienert, J., Vanneste, M., Bünz, S., Andreassen, K., Haflidson, H., and Sejrup, H. P. (2005). "Ocean warming and gas hydrate stability on the mid-Norwegian margin at the Storegga Slide," in *Ormen lange–an integrated study for safe field development in the Storegga submarine area*. Editors A. SOLHEIM, P. BRYN, K. BERG, H. P. SEJRUP, and J. MIENERT (Amsterdam, Netherlands: Elsevier), 233–244.

Myhre, C. L., Ferré, B., Platt, S. M., Silyakova, A., Hermansen, O., Allen, G., et al. (2016). Extensive release of methane from Arctic seabed west of Svalbard during summer 2014 does not influence the atmosphere. *Geophys. Res. Lett.* 43, 4624–4631. doi:10.1002/2016gl068999

Nixon, F. C., Chand, S., Thorsnes, T., and Bjarnadóttir, L. R. (2019). A modified gas hydrate-geomorphological model for a new discovery of enigmatic craters and seabed mounds in the Central Barents Sea, Norway. *Geo-Marine Lett.* 39, 191–203. doi:10.1007/s00367-019-00567-1

Orange, D. L., Yun, J., Maher, N., Barry, J., and Greene, G. (2002). Tracking California seafloor seeps with bathymetry, backscatter and ROVs. *Cont. Shelf Res.* 22 (16), 2273–2290. doi:10.1016/s0278-4343(02)00054-7

Ottesen, D., Dowdeswell, J. A., and Rise, L. (2005). Submarine landforms and the reconstruction of fast-flowing ice streams within a large Quaternary ice sheet: the 2500-km-long Norwegian-Svalbard margin (57°–80°N). *GSA Bull.* 117 (7-8), 1033–1050. doi:10.1130/b25577.1

Panieri, G., Ambrose, W., Astrom, E., Carroll, M. L., Fornair, D., George, S. J., et al. (2015). CAGE 15-2 Cruise Report: gas hydrate deposits and methane seepages offshore western Svalbard and Storfjordrenna: biogeochemical and biological investigations. *CAGE – Centre Arct. Gas Hydrate, Environ. Clim. Rep. Ser.* 3. doi:10.7557/cage.6932

Panieri, G., Bünz, S., Fornari, D. J., Escartin, J., Serov, P., Jansson, P., et al. (2017). An integrated view of the methane system in the pockmarks at Vestnesa Ridge, 79°N. *Mar. Geol.* 390, 282–300. doi:10.1016/j.margeo.2017.06.006

Paull, C. K., Normark, W. R., Ussler, W., III, Careass, D. W., and Keaten, R. (2008a). Association among active seafloor deformation, mound formation, and gas hydrate growth and accumulation within the seafloor of the Santa Monica Basin, offshore California. *Mar. Geol.* 250, 258–275. doi:10.1016/j.margeo.2008.01.011

Paull, C. K., Ussler, W., III, Holbrook, W. S., Hill, T. M., Keaten, R., Mienert, J., et al. (2008b). Origin of pockmarks and chimney structures on the flanks of the Storegga Slide, offshore Norway. *Geo Mar. Lett.* 28, 43–51. doi:10.1007/s00367-007-0088-9

Rabouille, C., Olu, K., Baudin, F., Khripounoff, A., Dennielou, B., Arnaud-Haond, S., et al. (2017). The Congolobe project, a multidisciplinary study of Congo deep-sea fan lobe complex: overview of methods, strategies, observations and sampling. *Deep Sea Res. Part II Top. Stud. Oceanogr.* 142, 7–24. doi:10.1016/j.dsr2.2016.05.006

Rebesco, M., Laberg, J. S., Pedrosa, M. T., Camerlenghi, A., Lucchi, R. G., Zgur, F., et al. (2014). Onset and growth of trough-mouth fans on the north-western Barents Sea margin – implications for the evolution of the Barents Sea/svalbard ice sheet. *Quat. Sci. Rev.* 92, 227–234. doi:10.1016/j.quascirev.2013.08.015

Riis, F., Berg, K., Cartwright, J., Eidvin, T., and Hansch, K. (2005). Formation of large crater-like evacuation structures in ooze sediments in the Norwegian Sea. Possible implications for the development of the Storegga Slide. *Mar. Petroleum Geol.* 22, 257–273. doi:10.1016/j.marpetgeo.2004.10.023

Rise, L., Ottesen, D., Longva, O., Solheim, A., Andersen, E. S., and Ayers, S. (2006). The Sklinnadjupet slide and its relation to the Elsterian glaciation

on the mid-Norwegian margin. *Mar. Petroleum Geol.* 23 (5), 569–583. doi:10.1016/j.marpetgeo.2006.05.005

Roalkvam, I., Dahle, H., Chen, Y., Jørgensen, S. L., Haflidason, H., and Steen, I. H. (2012). Fine-scale community structure analysis of ANME in Nyegga sediments with high and low methane flux. *Front. Microbiol.* 3, 216. doi:10.3389/fmicb.2012.00216

Sahling, H., Römer, M., Pape, T., Bergès, B., dos Santos Fereirra, C., Boelmann, J., et al. (2014). Gas emissions at the continental margin west of Svalbard: mapping, sampling, and quantification. *Biogeosciences* 11, 6029–6046. doi:10.5194/bg-11-6029-2014

Schulze, A., and Halanych, K. (2003). Siboglinid evolution shaped by habitat preference and sulfide tolerance. *Hydrobiologia* 496, 199–205. doi:10.1023/a:1026192715095

Sen, A., Andersen, L. W., Kjeldsen, K. U., Michel, L. N., Hong, W. L., Choquet, M., et al. (2023). The phylogeography and ecology of *Oligobrachia* frenulate species suggest a generalist chemosynthesis-based fauna in the arctic. *Heliyon* 9 (3), e14232. doi:10.1016/j.heliyon.2023.e14232

Sen, A., Dennielou, B., Tourolle, J., Arnaubec, A., Rabouille, C., and Olu, K. (2017). Fauna and habitat types driven by turbidity currents in the lobe complex of the Congo deep-sea fan. *Deep Sea Res. Part II Top. Stud. Oceanogr.* 142 (142), 167–179. doi:10.1016/j.dsr2.2017.05.009

Sen, A., Duperron, S., Hourdez, S., Piquet, B., Léger, N., Gebruk, A., et al. (2018). Cryptic frenulates are the dominant chemosymbiotrophic fauna at Arctic and high latitude Atlantic cold seeps. *PLoS ONE* 13 (12), e0209273. doi:10.1371/journal.pone.0209273

Serov, P., Vadakkepuliyambatta, S., Mienert, J., Patton, H., Portnov, A., Silyakova, A., et al. (2017). Postglacial response of Arctic Ocean gas hydrates to climatic amelioration. *Earth, Atmos. Planetar Sci.* 114 (24), 6215–6220. doi:10.1073/pnas.1619288114

Solheim, A., Berg, K., Forsberg, C. F., and Bryn, P. (2005). The Storegga Slide complex: repetitive large scale sliding with similar cause and development. *Mar. Petroleum Geol.* 22 (1-2), 97–107.

Somoza, L., Díaz-del-Río, V., León, M., Ivanov, R., Fernández-Puga, M. C., Gardner, J. M., et al. (2003). Seabed morphology and hydrocarbon seepage in the Gulf of Cádiz mud volcano area: acoustic imagery, multibeam and ultra-high resolution seismic data. *Mar. Geol.* 195 (1-4), 153–176. doi:10.1016/s0025-3227(02)00686-2

Suess, E. (2014). Marine cold seeps and their manifestations: geological control, biogeochemical criteria and environmental conditions. *Int. J. Earth Sci. Geol. Rundsch* 103, 1889–1916. doi:10.1007/s00531-014-1010-0

Talukder, A. R. (2012). Review of submarine cold seep plumbing systems: leakage to seepage and venting. *Terra nova.* 24, 255–272. doi:10.1111/j.1365-3121.2012.01066.x

Thorsnes, T., Chand, S., Bellec, V., Nixon, F. C., Brunstad, H., Lepland, A., et al. (2023). Gas seeps in Norwegian waters – distribution and mechanisms. *Nor. J. Geol.* 103, 202309. doi:10.17850/njg103-2-4

Thorsnes, T., Chand, S., Brunstad, H., Lepland, A., and Lågstad, P. (2019). Strategy for detection and high-resolution characterization of authigenic carbonate cold seep habitats using ships and autonomous underwater vehicles on glacially influenced terrain. *Front. Mar. Sci.* 6. doi:10.3389/fmars.2019.00708

Vadakkepuliyambatta, S., Skeie, R. B., Myhre, G., Dalsøren, S. B., Silyakova, A., Schmidbauer, N., et al. (2017). Climatic impact of Arcitc ocean methane hydrate dissociation in the 21st century. *Eart Syst. Dyn. Discuss.* doi:10.5194/esd-2017-110

Vogt, P. R., Crane, K., Pfirman, S., Sundvor, E., Cherkis, N., Fleming, H., et al. (1991). SeaMarc II sidescan sonar imagery and swatch bathymetry in the Nordic Basin. *EOS* 72, 486.

Vogt, P. R., Crane, K., Sundvor, E., Max, M. D., and Pfirman, S. L. (1994). Methane generated (questionable) pockmarks on young, thickly sedimented oceanic-crust in the Arctic—Vestnesa-Ridge. *Fram Strait. Geol.* 22, 255–258. doi:10.1130/0091-7613(1994)022<0255:mgpoyt>2.3.co;2

Vogt, P. R., Gardner, J., Crane, K., Sundvor, E., Bowles, F., and Cherkashev, G. (1999). Ground-truthing 11- to 12-kHz side-scan sonar imagery in the norwegia-Greenland sea: Part I: pockmarks on the Vestnesa Ridge and storegga slide margin. *Geo-Marine Lett.* 19, 97–110. doi:10.1007/s003670050098

Vorren, T. O., and Laberg, J. S. (1997). Trough mouth fans – palaeoclimate and ice-sheet monitors. *Quat. Sci. Rev.* 16, 865–881. doi:10.1016/s0277-3791(97)00003-6

Waage, M., Portnov, A., Serov, P., Bünz, S., Waghorn, K. A., Vadakkepuliyambatta, S., et al. (2019). Geological controls on fluid flow and gas hydrate pingo development on the Barents Sea margin. *Geochem. Geophys. Geosystems* 20, 630–650. doi:10.1029/2018gc007930

Westbrook, G. K., Thatcher, K. E., Rohling, E. J., Piotrowski, A. M., Pälike, H., Osborne, A. H., et al. (2009). Escape of methane gas from the seabed along the West Spitsbergen continental margin. *Geophys. Res. Lett.* 36, L15608. doi:10.1029/2009gl039191

Ye, T., Jin, G., Wu, D., and Liu, A. L. (2019). Experimental and numerical simulation of the formation of cold seep carbonates in marine sediments. *Int. J. Environ. Res. Public Health* 16 (8), 1433. doi:10.3390/ijerph16081433

frontiers | Frontiers in Earth Science

TYPE Original Research
PUBLISHED 16 April 2024
DOI 10.3389/feart.2024.1347252

OPEN ACCESS

EDITED BY
Muhammad Idrees,
University of Science and Technology of China, China

REVIEWED BY
Michela Giustiniani,
National Institute of Oceanography and Applied Geophysics, Italy
Emanuele Lodolo,
National Institute of Oceanography and Applied Geophysics, Italy

*CORRESPONDENCE
Shyam Chand,
shyam.chand@ngu.no

RECEIVED 30 November 2023
ACCEPTED 21 March 2024
PUBLISHED 16 April 2024

CITATION
Chand S, Knies J, Geissler WH, Plaza-Faverola A and Thorsnes T (2024), Acoustic evidence of hydrocarbon release associated with the Spitsbergen Transform Fault, north of the Molloy Ridge, Fram Strait. *Front. Earth Sci.* 12:1347252. doi: 10.3389/feart.2024.1347252

Acoustic evidence of hydrocarbon release associated with the Spitsbergen Transform Fault, north of the Molloy Ridge, Fram Strait

Shyam Chand[1]*, Jochen Knies[1,2], Wolfram H. Geissler[3], Andreia Plaza-Faverola[2] and Terje Thorsnes[1]

[1]Geological Survey of Norway (NGU), Trondheim, Norway, [2]Department of Geosciences, iC3: Centre for ice, Cryosphere, Carbon and Climate, UiT The Arctic University of Norway, Tromsø, Norway, [3]Alfred Wegener Institute, Helmholtz Centre for Polar and Marine Research (AWI), Bremerhaven, Germany

Hydrocarbon gases formed from biotic and abiotic processes are released through the seafloor at different locations around the world. They have been widely observed directly in video and photo data, and indirectly on echosounder data. Even though biotic gas generation is a very common process, abiotic gas generation is limited to regions where serpentinization of ultramafic rocks occur. Indications of abiotic gas occurrences are therefore sparse and much speculated upon. Here, we investigated the Spitsbergen Transform Fault, the Molloy Ridge, the Molloy Deep, and the Molloy Transform Fault/Fracture Zone, (a transform fault-bounded pull-a-part region offshore western Svalbard) where both processes may be active. Multiple acoustic gas flares, ~1,770 and ~3355 m high above the seafloor (tallest ever recorded), were observed indicating active migration and seepage of hydrocarbons. The proximity to the mid oceanic ridge and the documented high heat flow suggests the influence of high temperatures on organic-rich sedimentary deposits. Deep seismic data and other geological information available indicate that the main source of gas could be from thermal cracking of either pre- or syn-rift source rock organic material, potentially mixed with methane from serpentinization of mantle rocks (peridotites). Correlation with seismic stratigraphy from Ocean Drilling Program (ODP) Sites 910 and 912 on the adjacent Yermak Plateau suggests that the sedimentary source rocks may be present at the northern flank of the Molloy Ridge and within the deep graben along the Spitsbergen Transform Fault. The ~3 km thick sedimentary succession in high heat flow zones within the transform fault and the active bounding faults allow generation and migration of hydrocarbons to the seafloor and sustains present day seepage.

KEYWORDS

gas flare, Molloy Ridge, fluid flow, multibeam, Molloy Deep, deep seismic data

Introduction

Biotic and abiotic processes in sediments lead to the generation and release of hydrocarbons through the seafloor. Biotic gas generation occurs through degradation of organic carbon in sediments through microbial and thermogenic processes (e.g., Milkov

and Etiope, 2018) whereas abiotic gas generation occurs through serpentinization of ultramafic rocks in the presence of water by Fischer-Tropsch-type reactions (Proskurowski et al., 2008). Abiotic methane generation requires circulation of seawater to mantle level and is therefore limited to locations where mantle rocks are shallow or even exposed at the seafloor (Kandilarov et al., 2008). The serpentinization rates are maximal at temperatures between 200°C and 350°C (Martin and Fyfe, 1970) and the process continues for long time periods generating enough methane to have a sustained gas supply. Slow spreading ridges are therefore suggested to be the best locations for elevated methane generation since the mantle remains at shallower depth within the relevant temperature window for a longer time (Charlou et al., 2010). In magma-limited slow and ultra-slow spreading ridges and transform faults, serpentinization occurs along detachment faults which form at young oceanic crust near the active ridge axis and over a period of 1–4 million years (Tucholke et al., 1998; Cannat et al., 2010). Biotic methane generation can also occur with the presence of organic material either through microbial and/or by thermogenic processes since one of these settings could be present due to normal microbial degradation or thermal cracking due to high heat flow.

Our study area is located in the central Fram Strait between Svalbard and Greenland (Figure 1, inset). The Fram Strait is known as the Arctic-Atlantic Gateway between the Norwegian-Greenland Sea and the Arctic Ocean and plays a key role in the deep-water exchange between the Atlantic and Arctic oceans (Hunkins, 1990; Tesi et al., 2021; von Appen et al., 2015). The Molloy Ridge and the Molloy Transform Fault and Fracture Zone System was formed well after the opening of the Norwegian-Greenland Sea ~56 Ma ago (Talwani and Eldholm, 1977). Engen et al. (2008) suggest an early age of ~19.6 Ma for the start of seafloor spreading at the present Molloy Ridge, which coincides with the recent modelling results suggesting 20 Ma for the opening of the Arctic-Atlantic Gateway (Dumais et al., 2021). In this region, the oceanic crust is thin, and the Moho is shallow (<5 km below seafloor) (Czuba et al., 2005). The Molloy Deep is the nodal basin at the intersection of the Molloy Ridge and the Molloy Transform Fault (MTF) (Klenke and Schenke, 2002). The Spitsbergen Transform Fault (STF) in the north and the MTF in the south acts as the boundaries separating the Molloy Ridge spreading zone from the rest of the spreading system further north and south, respectively (Figure 1 inset). The STF also acts as the boundary separating the pre-rift continental sedimentary rocks in the north beneath the SW flank of the Yermak Plateau from the Molloy Ridge spreading oceanic crust and sedimentary deposits further in the south. The Molloy Ridge has three segments with two blocks of highly fractured material filling the space in between and a further deformed zone west of it (Figure 1).

In this study we analysed water column acoustic and seismic reflection data to understand the source and origin of the detected gas flares in the water column, the processes behind the formation of the gases, and the resulting seepage into the water column. The possibility of different mechanisms acting together are critically analysed based on the stratigraphic information available from the nearby Ocean Drilling Program (ODP) Leg 151 boreholes and deep seismic data.

Materials and methods

Seafloor mapping using a multibeam echosounder system (MBES) across the deepest zone of the Norwegian-Greenland Sea, the Molloy Deep (up to 5,569 m deep) and surrounding areas was carried out as part of the MAREANO (mareano.no) program in 2019. The multibeam data were collected by DOF Subsea ship SV Geograph using a hull mounted Kongsberg EM304 MBES which also allowed to image the water column (Figure 1). The MBES transducer system for each ping sends out a fan of 512 beams to the water column and the backscattered energy is received by the transducer array. Since the survey is mainly planned for seafloor bathymetry mapping, the overlap with the nearby line is less than 10%. This results in a fan shaped data coverage with 100% coverage below the ship (nadir zone) and decreasing towards the outermost beam. This results in partial mapping of any anomalies occurring away from the nadir zone (refer Figure 1 in Thorsnes et al., 2023). The MBES operates at frequencies of 26–34 kHz and has a depth range of 10–8,000 m. The MBES data were processed for bathymetry by DOF Subsea as part of the delivery for MAREANO and for backscatter and water column anomalies by Geological Survey of Norway (NGU) to investigate the seafloor and water column. QPS maritime solutions FMGeocoder Toolbox and FM Midwater softwares were used to process, analyse and interpret the backscatter and water column data, respectively. The water column data were inspected visually using FM Midwater where the water column backscattering intensity is filtered to remove background noise. This process will single out higher intensity anomalies from gas flares which are then visible on the inline fan of beams and across line stack (all beams) of data.

Sub bottom profiler (SBP) shallow seismic data was collected using Kongsberg SBP 29 system which operates in the 2–9 kHz frequency range. The MBES receiver array was used to record the data. SBP data were collected across the Molloy Ridge and surrounding seafloor showing the shallow subsurface covering the entire bathymetric range and tectonic regions of the seafloor. Airgun 2D seismic reflection data were acquired by the Alfred Wegener Institute (AWI) and partners during cruise MSM31 onboard R/V Maria S. Merian in 2013. A source array of 6 G guns (each 8 L) and a 3,000 m long digital streamer were deployed (Geissler et al., 2014a). The seismic data are used to define the geological structure across the STF including the northern flank of the Molloy Ridge. The shallow sedimentary cover is seismo-stratigraphically interpreted using the tie towards the nearby ODP sites 910 and 912 (Figure 1) (Spiegler, 1996; Mattingsdal et al., 2014) to provide stratigraphic constraints on sedimentary deposition and development before and after the opening of the Arctic-Atlantic Gateway.

Results

The Molloy Ridge is located between STF and MTF (Figure 1). The Molloy Ridge is a well-developed core complex (Chamov et al., 2010; Thorsnes et al., 2023), with the shallowest part in the centre at ~1,500 m below sea level (Figure 2). The Molloy Ridge core complex includes an oceanic detachment fault forming a hanging

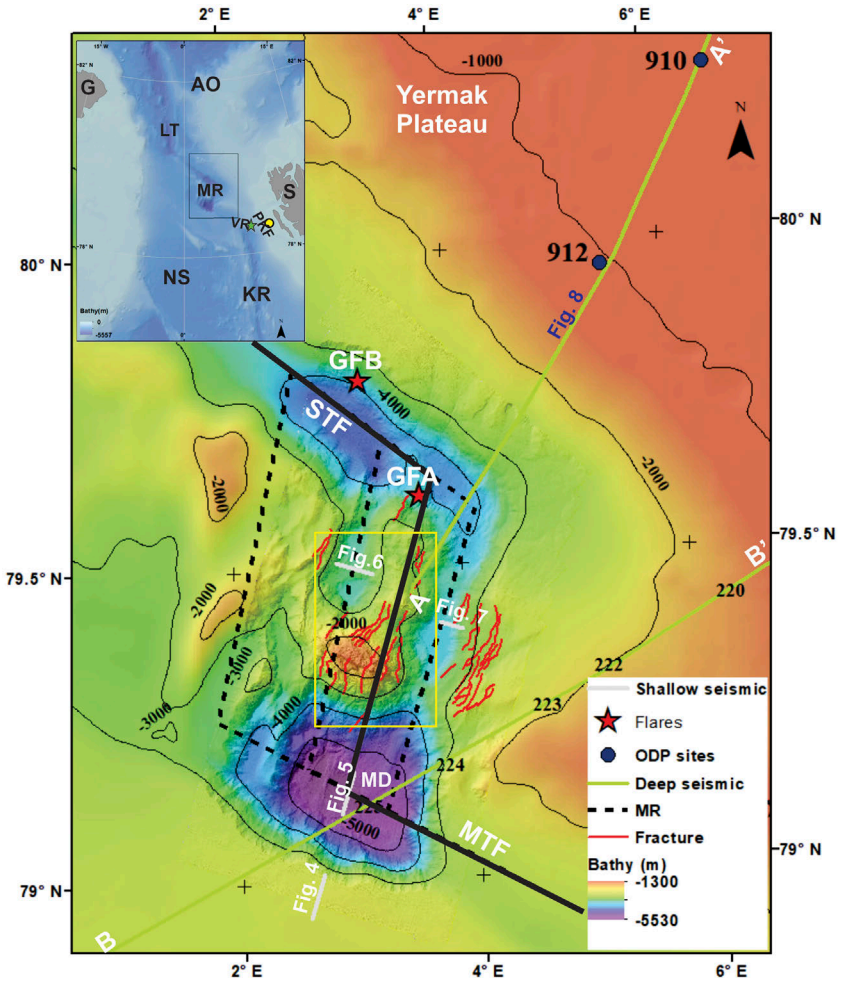

FIGURE 1
Detailed bathymetry of the study area showing faults (red lines), gas flares (red stars; GFA & GFB) and the location of ridge axis (black line) overlayed on regional (IBCAO) and detailed bathymetry. SBP and 2D seismic data are indicated by light grey and light green lines respectively. Seismic line (A-A′) is given Figure 8 and (B-B′) shows the location of seismic line from Czuba et al. (2005). Location of Figure 2 is shown as yellow box. Inset figure shows the locations of the samples in Figure 9 (red dots) from Vestnesa Ridge (VR) and Prins-Karls Forland (PKF). Also shown are the Molloy Ridge/Fracture Zone (MR), Molloy Transform Fault (MTF), Spitsbergen Transform Fault (STF), Molloy Deep (MD), Greenland (G), Norwegian-Greenland Sea (NS), Arctic Ocean (AO), Svalbard (S), Lena Trough (LT) and Knipovich Ridge (KR). Detailed bathymetry supplied by MAREANO/Norwegian Mapping Authority.

wall cut off, a corrugated surface with fault striations and steep brittle fault scarps (Figure 2). Analysis of multibeam data indicates a very complex seafloor with many fractures running parallel to the ridge axis (Figure 1). The presence of numerous slide structures visible along both sides of the Molloy Ridge and Molloy Deep indicates a tectonically very active region with high seismicity (Keiding et al., 2018) (Figure 2). The Molloy Deep, with the deepest part of the area at 5,569 m, ~3,300 m deeper than the surrounding seabed, extends about 15 km x 15 km in dimension (Figure 1).

Two water column acoustic anomalies, GFA and GFB (Figure 1), ~1770 and ~3,355 m high above the seafloor were identified (Thorsnes et al., 2023). They are located at the northern flank of the Molloy Ridge and on the conjugate side of the STF (Figure 3). Stack and fan views of the GFA (Figures 3A,B) and GFB anomalies (Figures 3C,D) show that the GFA anomaly is visible stopping within half-way through in the water column due to lack of MBES coverage in the upper water column and similarly, the top part of the GFB anomaly is also missing. The southern GFA anomaly is close to a fault mapped from the bathymetry data (Figure 1). The water column acoustic anomalies are classic indicators of gas bubble rise through the water column data (e.g., Chand et al., 2016) and verified by AUV and ROV observations (e.g., Chand et al., 2016). The deepest part of the area, the Molloy Deep, does not show any acoustic indications of fluid escape.

SBP data from the region indicate continuous sedimentation during recent times including the basinal part and the depression slopes (Figures 4–7). The sediments occur as stratified layers along the basin flanks (Figure 4) and the deepest parts of the basin (Figure 5). Fault-bounded sub-basins along the Molloy Ridge also contain stratified sediments (Figures 6, 7). The western sub-basin of the Molloy Ridge is tectonically active as indicated by the folding and faulting of stratified sediments up to the seafloor (Figure 6) compared to the eastern sub basin (Figure 7). 2D

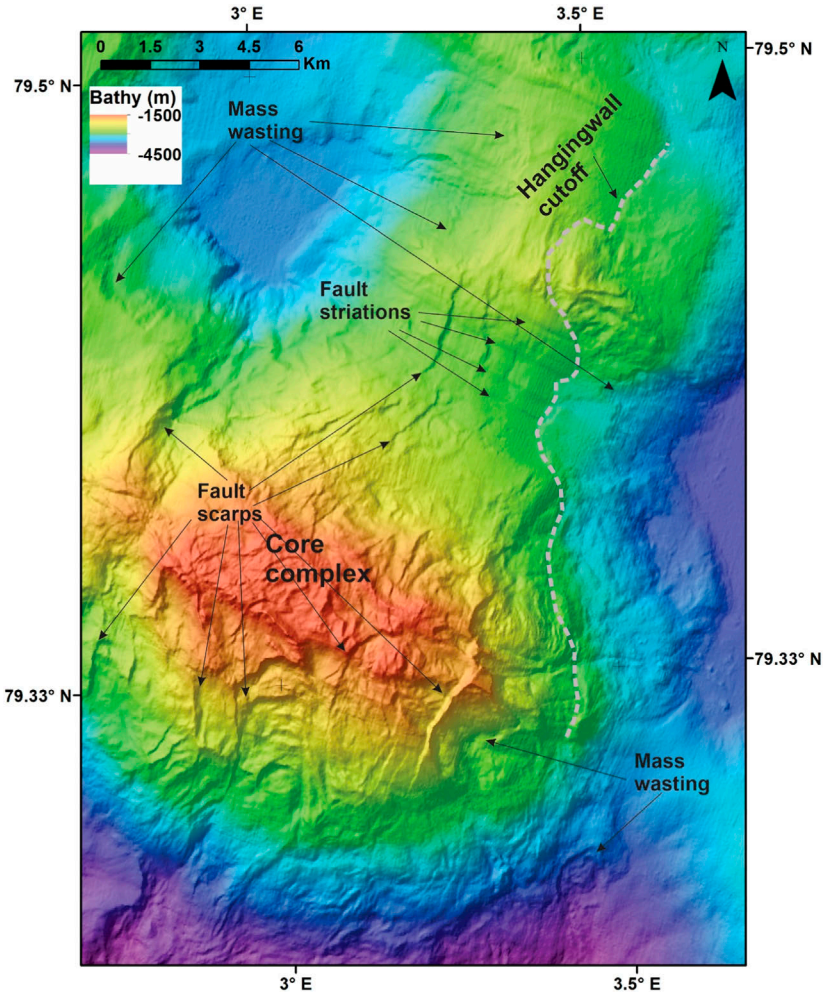

FIGURE 2
Shaded relief bathymetry image showing close-up of the Molloy core complex. The ridge is about 1,000 m high with a hanging wall cut-off, fault striations, fault scarps and mass wasting. Notice is the change in seafloor morphology with the rugged seafloor at core complex changing to smooth seafloor north of it. Detailed bathymetry supplied by MAREANO/Norwegian Mapping Authority. Location shown in Figure 1.

deep seismic data image stratified sediments on the northern flank of the STF (Figure 8). The seismic stratigraphy is traced back towards the northeast along the seismic line and two horizons are correlated with ages ~2.6 and ~5.8 Ma following Mattingsdal et al. (2014) chronostratigraphic framework for the region. The sedimentary succession at the southwestern Yermak Plateau towards STF exhibit similar character to the undisturbed sediments further northeast where they are tied to ODP sites 910 and 912 (Figure 8). A thick succession of sediments extending all the way to the STF can be observed below the 5.8 Ma horizon indicating a high sedimentation rate since the early opening of the Arctic-Atlantic Gateway (Figure 8). The deeper sediments overlying the down faulted segments towards the STF indicate the presence of pre and syn rift sediments on either side of the STF (Figure 8B). Along the seismic profile, the STF itself is covered by more than 3 km of sediments (estimated based on the velocity model in Czuba et al., 2005) with crustal level faults extending all the way up to the seafloor (Figure 8B). The sediments south of the STF flank the Molloy Ridge core complex and thins actually out on to the core complex (Figure 8B). This boundary demarcating the core complex and sediments is clearly visible on bathymetry (Figures 1, 2) where the morphological characteristics changes from very smooth surface in the north to rugged surface in the south. The projected locations of both flares GFA and GFB occurs along the region of deep-seated faults/near vertical sedimentary stratigraphic boundaries interpreted on seismic data (Figure 8).

Discussion

Morphology and gas seepage

The study area consists of a combination of ridge spreading and transform faulting along multiple segments creating a complicated seafloor morphology as well as subsurface structure. The shallow subsurface at the eastern corner of the STF is characterized by stratified sequences within a contourite drift that extends all the

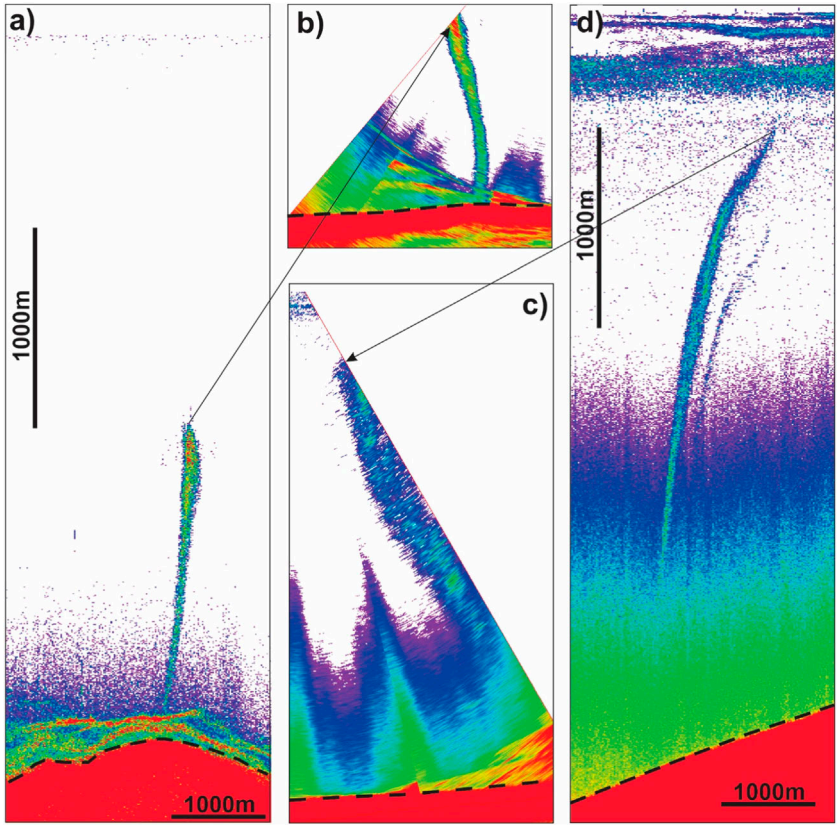

FIGURE 3
Across-track (stack of all beams) and along-track fan (stack of 25 along track pings) views respectively of acoustic gas flares GFA **(A,B)** and GFB **(C,D)**. Notice that the flare GFA is visible only up to half-way through the water column due to the lack of data in the upper part of the water column **(B)**. Similarly, the top part of the GFB is also missing **(C)**. The seafloor is indicated by black dashed line.

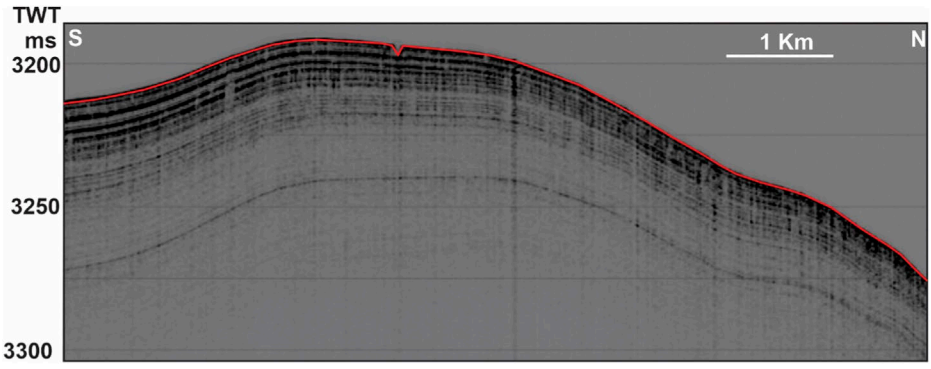

FIGURE 4
SBP line along the southern flank of the Molloy Deep showing the unfaulted stratified units (see Figure 1 for location). SBP data: MAREANO/NGU.

way into the Molloy Ridge associated basins (e.g., Osti et al., 2019). Along the peripheries of Molloy Ridge, more transparent and chaotic facies are observed indicating various episodes of sediment sliding and deformation. This is suggested to be controlled by neotectonics, changes in oceanographic conditions and fluid dynamics among the most likely processes (e.g., Elger et al., 2018; Osti et al., 2019). Submarine sliding is reported along the eastern flank of Molloy Ridge indicating triggering mechanisms mostly from gravitational instability. The latter results from the occurrence of intercalated sedimentary units with differing sedimentary architecture, which is evident in seismic data also (Czuba et al., 2005). At the steepest parts of the northern flank, the shallow sub-surface sediments are

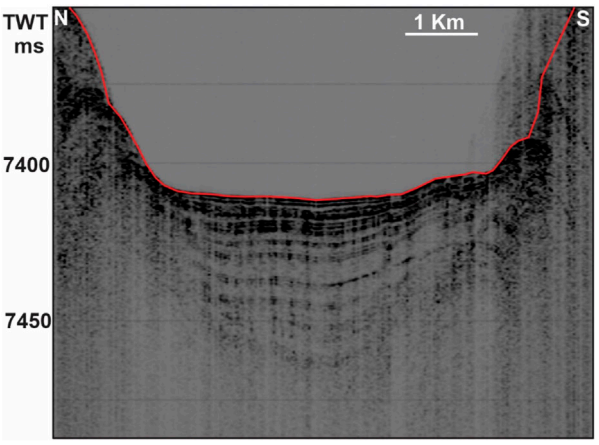

FIGURE 5
SBP line from the Molloy Deep showing the presence of stratified units covering the deepest part of the seafloor (see Figure 1 for location). SBP data: MAREANO/NGU.

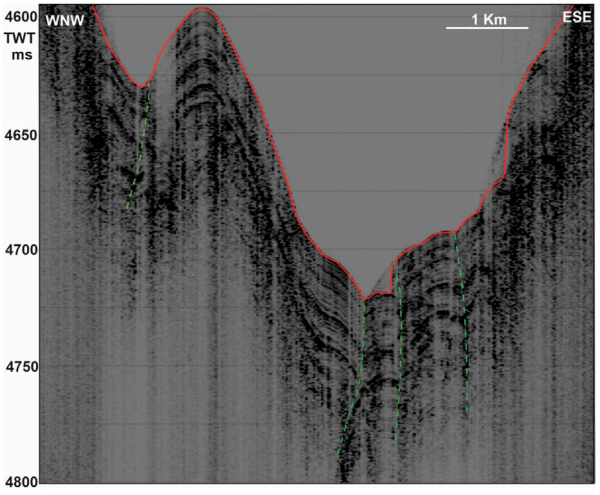

FIGURE 6
SBP line along the western depression of N-S segment of the Molloy Ridge/Fracture Zone showing the presence of heavily faulted and folded stratified units covering the fracture zone (see Figure 1 for location). Green dashed lines indicate faults. SBP data: MAREANO/NGU.

pierced by faults that seemingly extend all the way to the basement (Figure 8). The subsurface sedimentary structure could also consist of pre- and syn-rift sediments at the location of the northernmost flare (GFB) (Figure 8). The 2D deep seismic line (Figure 8) across the northern flank of STF shows pull apart rotated fault segments (pull-apart basin from syn-rift tectonics) containing these sediments and therefore it is likely that similar sediments exist in the relatively undisturbed northern part of the Molloy Ridge (south of STF) (Figure 1). This is suggested by the morphology of the ridge, whereas the southern part of Molloy Ridge consists of rugged seafloor due to a core complex exposed on the seafloor, whereas the northern segment of the ridge is smooth, comparable to normal sediment covered seafloor (Figure 1).

A gas hydrate stability zone (GHSZ) of up to 250 m thickness had been predicted for the flanks of the Molloy Ridge and the region north of STF with varying thickness related to heat flow in different parts of the region (Geissler et al., 2014b). However, a gas hydrate related bottom simulating reflection (BSR) is not visible at the flanks of the STF pull-apart basin (Figure 8). This is consistent with models that predict a non-existent or close to zero gas hydrate stability zone thickness (GHSZ) at the Molloy Ridge and STF boundary region due to high heat flow values (Geissler et al., 2014b). Nevertheless, BSR mapping in the region (Geissler et al., 2014b; Dumke et al., 2016; Osti., et al., 2017; Elger et al., 2018) suggests the existence of a gas hydrate system. Due to high heat flow being near to the mid-ocean ridge (as high as 120 mW/m^2, Klitzke et al., 2016), the thermal gradient could be high thereby proofing high temperatures as we go deep into the sediments assisting the thermal cracking of the organic matter to both gaseous and even liquid hydrocarbons. The flares are located along the peripheries of the Molloy Ridge and along the boundary faults of the STF indicating some influence of fluid flow channelling towards the margin of the ~3 km (based on velocity model from Czuba et al., 2005) thick sediment filled transform fault depression both through boundary faults and stratigraphic boundaries flanking the STF margins. The gas flares GFA and GFB could reach sea surface owing to the high acoustic strength observed at the heights they are cut off in the present data (Figure 3). However, we do not have yet proof by hydro-acoustic or satellite data.

The origin of the seeping gas in Molloy Ridge

Pull-a-part basin structures consisting potentially of pre-rift sedimentary rocks overlayed by syn-rift deposits are observed at the northern flank of STF along the 2D seismic line (Figure 8) suggesting also the presence of syn-rift sediments within the Molloy Ridge and STF area. The deeper sediments here can be seismically correlated to be clearly older than 5.8 Ma based on nearby ODP Sites 910 and 912 (Mattingsdal et al., 2014; Osti et al., 2019). The extension of thick syn-rift sediments, as continuous reflectors on pull-a-part blocks (Figure 8), indicate that the deposition of these sediments continued while the rifting was active. The deep-seated faults could be the reactivated elements from the rifting stage like those observed in analog models and other comparable pull-a-part margins (e.g., Athos and Dungun fault zones [Dooley and McClay, 1997]). The 3D structure of these faults could be even more complicated and therefore the fluid flow along these routes difficult to envisage with just a 2D imaging.

Thorsnes et al. (2023) reported condensate oil seeping gas from the seabed nearby the southern gas flare (GFA). This observation excludes a primary microbial gas origin from CO_2 reduction and methyl-type fermentation, but rather points to secondary microbial gases generated during petroleum biodegradation and thermogenic processes (Whitaker, 1999). Thermogenic gas composition can be delineated in early mature, oil-associated, and late mature thermogenic gas (Milkov and Etiope, 2018). The composition of the so far analysed free seeping gas in

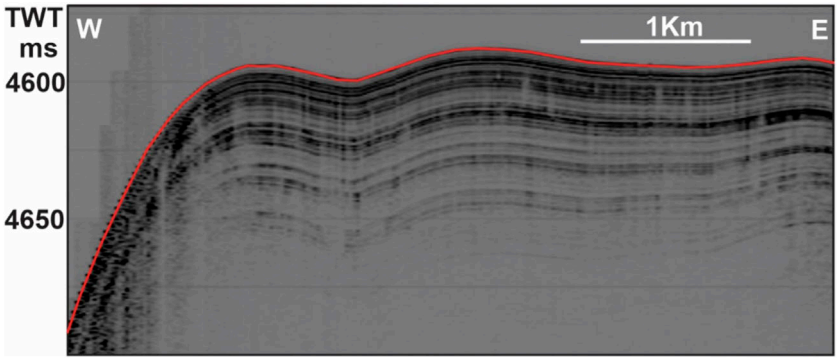

FIGURE 7
SBP line along the eastern depression of N-S segment of Molloy Ridge/Fracture Zone showing the presence of stratified units covering the seafloor. (see Figure 1 for location). SBP data: MAREANO/NGU.

the wider study region including the Vestnesa Ridge, a deep-water gas hydrate system (Plaza-Faverola et al., 2015; 2017), and the oil-seeping gas flare area off Prins Karls Forland, western Svalbard (Panieri et al., 2024) unequivocally point towards the area of oil-associated gas origin (Figure 9). The gas composition from the sub-seafloor on Vestnesa Ridge (δ^{13}C-CH_4: −51.1‰, δ^2H-CH_4: −191‰) (Plaza-Faverola et al., 2017) and oil seeps off Prins Karls Forland (δ^{13}C-CH_4: −48.4‰, δ^2H-CH_4: −196‰ (Panieri et al., 2024), are nearly identical (Figure 9) pointing towards the same petroleum system for the origin of the hydrocarbons in the region.

A likely source of the ongoing gas and oil seepage in the Molloy Ridge area, on Vestnesa Ridge, and the shelf region off Prins Karls Forland could be organic-rich deposits of Middle Miocene (>16–17 Ma; Knies and Mann, 2002) or Late Miocene (>10-11 Ma; Gruetzner et al., 2022), as recovered in ODP Site 909 in the central Fram Strait, south of the Molloy Ridge. Basin modelling (with >16-17 Ma as depositional age) revealed an ongoing hydrocarbon generation potential since the Late Miocene (~6 Ma) (Knies et al., 2018) with first seepage at the seafloor occurring during the early Pleistocene (Plaza-Faverola et al., 2015; Daszinnies et al., 2021).

Based on various palaeo-reconstruction models for the region, the Molloy Ridge was established after 20 Ma (Dumais et al., 2021) and therefore the oldest post rift sediments belong to this age. Indeed, the oldest age for the sediments lying right above the syn-rift rotated blocks and extending all the way to the STF can be assigned to be approximately ~17–18 Ma using similar sedimentation rates and shelf progradation observations as proposed by Hustoft et al. (2009) and Mattingsdal et al. (2014). While immature at the borehole location (ODP Site 909) in central Fram Strait, higher heat flow (>120 mW/m^2; Klitzke et al., 2016) nearby the STF could have increased the maturity level of the organic-rich deposits allowing the expulsion of oil-associated gas in the Molloy region and elsewhere in the region over the past 6 million years until now. Indeed, recent data compilation of oil-source rock correlation for the western Svalbard continental margin indicates an unequivocal correspondence between a Miocene source rock of deltaic/terrestrial origin and oil-associated seeping gas (Mattingsdal et al., 2023). Alternatively, the recovery of organic-rich, early to middle Eocene sediments from the Lomonosov Ridge (Backman et al., 2006), has given rise to speculations that widespread, organic-rich, potential source rocks might be present across the entire Arctic Basin and its adjacent seas (Brinkhuis et al., 2006; Bujak, 2008). These strata are characterised by the widespread occurrence of large quantities of the freshwater fern Azolla deposited during the onset of the middle Eocene (~50 Ma) (Brinkhuis et al., 2006). Basin modelling indicate that this Eocene source rock is potentially prolific close to the Gakkel Ridge with high geothermal gradients (>100°C) (Mann et al., 2009). Moreover, Blumenberg et al. (2016) suggested that the early to middle Eocene source rock is in the early oil window since the Early Miocene along the northern Barents Sea continental margin. However, the kerogen type III/II derived oil seeps from the western Svalbard margin (Mattingsdal et al., 2023; Panieri et al., 2024) rather point to a deltaic/terrestrial source rock of Middle to Late Miocene age (Knies and Mann, 2002; Gruetzner et al., 2022). The potential presence of an Eocene (*Azolla*) source rock along the northern flank of the STF and towards the ODP sites is unlikely to be the source of the condensate oil seeping gas at Molloy Ridge due to its kerogen type II/I character of the organic matter (Stein, 2007).

Slow spreading ridges, and in our case along a transform fault, are proposed to have elevated methane generation and release because of serpentinization (Charlou et al., 2010; Johnson et al., 2015). The Molloy Ridge is suggested to be a slow to ultra-slow spreading ridge and therefore serpentinization could have occurred along detachment faults over a period 1–4 million years (Tucholke et al., 1998; Johnson et al., 2015). Serpentinization due to circulation of seawater into mantle level can occur due to the relatively thin sedimentary cover (<5 km) and faults extending down to mantle exist (Kandilarov et al., 2008). The crust is thinning and shallowing in the NE direction towards the Molloy Ridge and STF from the deepest part at Molloy Deep (Czuba et al., 2005) where the flares are located. Serpentinization is suggested to occur in the region below the STF and northeast of it (Czuba et al., 2005). The occurrence of the flares along the boundary of STF suggests focussing of the fluids towards

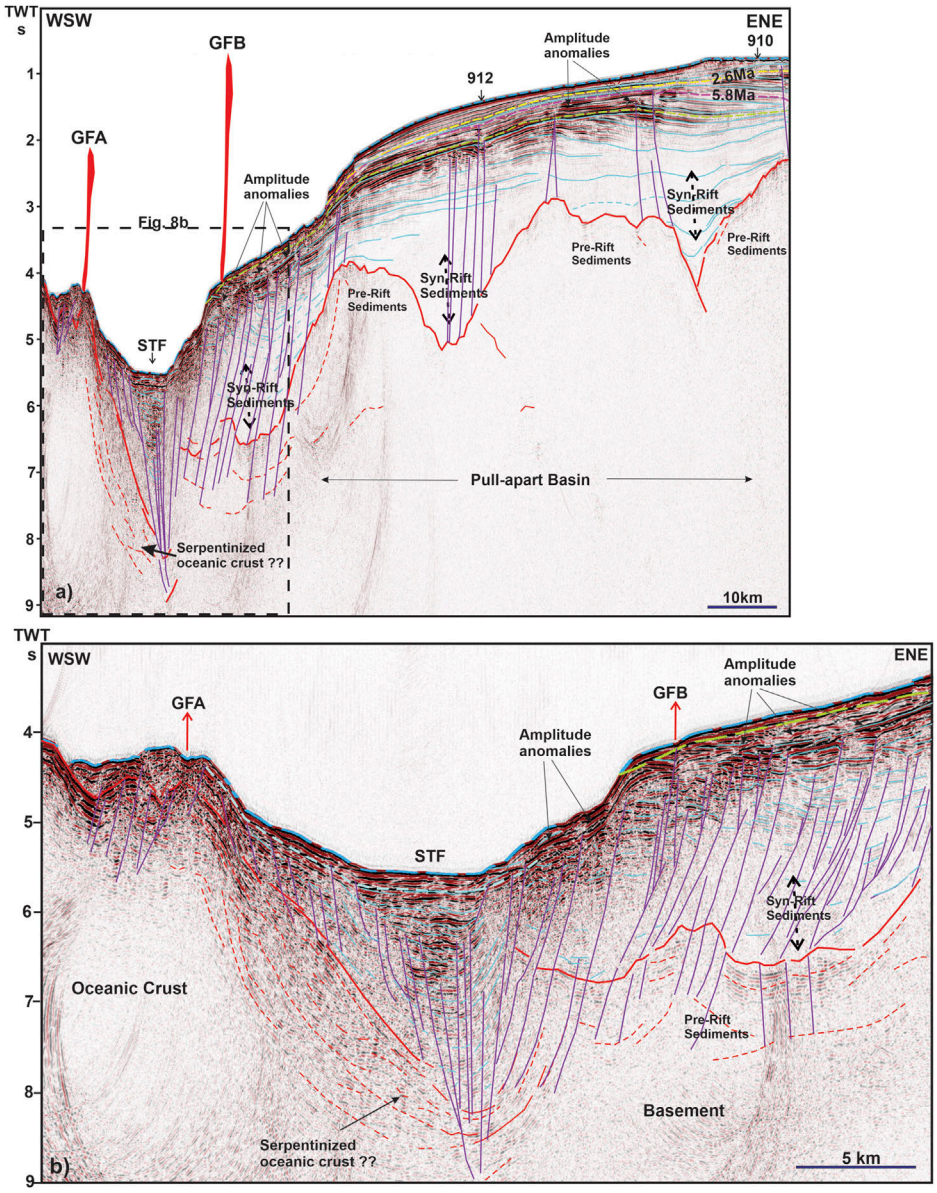

FIGURE 8
2D Seismic section (location in Figure 1) **(A)** from the northern flank of Molloy Ridge showing the pre- and syn-rift sediments along the stretched segments towards the Yermak Plateau. Stratigraphic framework derived from Mattingsdal et al. (2014) based on ODP holes 910 and 912 representing 2.6 Ma (yellow dashed line) and 5.8 Ma (purple dashed line) horizons are also shown. The horizon given in red is the acoustic basement and the sediments above extending to the STF belong to the syn-rift blocks and those deposited later. The projected location of the flare GFA (~8 km) occur along the boundary of oceanic basement towards the STF and GFB (~27 km) occurs along a bounding fault related to the STF. **(B)** Blow up of the location of gas flares and STF showing the faults and thick pack of sediments deposited in the STF. Faults are shown in purple sub-vertical lines and other horizons given in blue in both figures. Acoustic amplitude anomalies due to fluid accumulation can be seen close to boundaries of faults and connected horizons.

the transform boundary. The serpentinized zone proposed by Czuba et al. (2005) is deep but comparing the location of their seismic line (Figure 1) to STF, it is likely that the serpentinized zone could be shallow in the gas flare areas typical of transform fault boundaries where the transition is abrupt (Dooley and McClay, 1997). The gas flares are located where there is a chance for mixing between fluids seeping from different kinds of sources since the flare location is connected to the deep faults, and the transform fault is infilled by ~3 km of sediments potentially diverting the upward migrating fluids (Figure 8B). However, the contribution of abiotic methane to the seepage system may not be significant, compared to high concentrations of thermogenic methane evicted from shallower than oceanic crustal level sources (Lizzaralde et al., 2011).

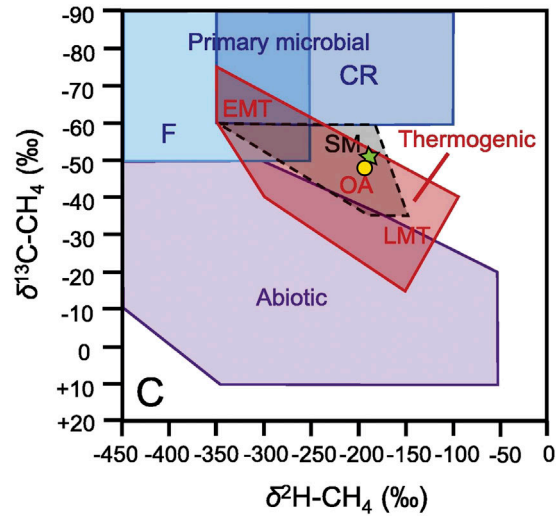

FIGURE 9
Revised methane genetic diagram based on $d^{13}C\text{-}CH_4$ and $d^2H\text{-}CH_4$ (Whiticar, 1999; Milkov and Etiope, 2018). Yellow circle: Oil-coated free seeping gas offshore Prins Karls Forland (Panieri et al., 2024), Green star: Headspace gas extracted from gravity core GC10, Vestnesa Ridge, 200 cm below seafloor (Plaza-Faverola et al., 2017). Abbreviations are: CR: CO2 reduction, F: Methyl-type Fermentation, SM: Secondary microbial, EMT: Early mature thermogenic gas, OA: Oil-associated thermogenic gas, LMT: Late mature thermogenic gas. Locations of samples are shown in Figure 1 (inset).

Currently, we cannot tell the ultimate origin for the release of gas in Molloy Ridge -STF region. More geochemical analyses and basin modelling studies are needed to clarify the source and migration pathways of the seeping hydrocarbons. Clearly, if abiogenic methane is present in the free gas bubbles, its proportions are minor and difficult to detect.

Conclusion

Gas flares rising from the seafloor into the water column from very close to an active mid-ocean ridge with potentially multiple hydrocarbon sources and source rocks offshore Svalbard is reported. The observations from the multibeam echosounder data indicate that methane is generated along the Spitsbergen Transform Fault immediately north of the slow/ultra-slow spreading Molloy Ridge and released through boundary faults of the deep sediment-filled Spitsbergen Transform Fault depression. This region is outside the gas hydrate stability zone due to high heat flow. No other locations in our data set indicated fluid seepage, including the deepest part of the area, the Molloy Deep, at the intersection of the southern part of the Molloy Ridge and the Molloy Transform Fault. The N-S oriented Molloy Ridge in-between the Spitsbergen and Molloy transform faults constitutes a highly fractured region where crustal faults reaching up to the seafloor can be observed. The high heat flow and the likely presence of Middle to Late Miocene source rocks reported from this area makes thermal cracking as the main mechanism producing oil-associated thermogenic gases most plausible, with a possibility of minor contribution from abiotic crustal/mantle sources.

Data availability statement

The datasets presented in this article are not readily available because the raw data is owned by other agencies mentioned in the manuscript. Requests to access the datasets should be directed to www.mareano.no or info.geophysics@awi.de in case of the deep seismic reflection data.

Author contributions

SC: Conceptualization, Data curation, Formal Analysis, Investigation, Methodology, Project administration, Resources, Software, Validation, Visualization, Writing–original draft. JK: Conceptualization, Data curation, Formal Analysis, Methodology, Validation, Visualization, Writing–review and editing. WG: Conceptualization, Data curation, Formal Analysis, Methodology, Software, Visualization, Writing–review and editing. AP-F: Formal Analysis, Validation, Writing–review and editing. TT: Conceptualization, Project administration, Resources, Visualization, Writing–review and editing.

Funding

The author(s) declare that financial support was received for the research, authorship, and/or publication of this article. The multibeam and SBP data were acquired through the MAREANO programme. JK is supported by the Research Council of Norway (grant #332635). AP-F is supported by the Research Council of Norway (grant #287865).

Acknowledgments

The authors thank all participants of the MAREANO programme (www.mareano.no) for invaluable cooperation. The multibeam data were acquired and supplied by the Norwegian Mapping Authority. The data is released under a Creative Commons Attribution 4.0 International (CC BY 4.0). The authors would like to thank Aspen Technology, Inc. for providing software licenses and support.

Conflict of interest

The authors declare that the research was conducted in the absence of any commercial or financial relationships that could be construed as a potential conflict of interest.

Publisher's note

References

Backman, J., Moran, K., McInroy, D. B., Mayer, L. A., and the Expedition 302 Scientists (2006). Proceedings of the integrated Ocean Drilling program. *Arct. Coring Exped. (ACEX)* 302. http://publications.iodp.org/proceedings/302/302/pdf.

Blumenberg, M., Lutz, R., Schlömer, S., Krüger, M., Scheeder, G., Berglar, K., et al. (2016). Hydrocarbons from near-surface sediments of the Barents Sea north of Svalbard – indication of subsurface hydrocarbon generation? *Mar. Petroleum Geol.* 76, 432–443. doi:10.1016/j.marpetgeo.2016.05.031

Brinkhuis, H., Schouten, S., Collinson, M. E., Sluijs, A., Damste, J. S. S., Dickens, G. R., and the Expedition 302 Scientists (2006). Episodic fresh surface waters in the Eocene Arctic Ocean. *Nature* 441, 606–609. doi:10.1038/nature04692

Bujak, J. (2008). From green house to icehouse- the Azolla Trigger: implications for climate change and Arctic petroleum source rocks. *Houst. Geol. Soc. Bull.* 50 (08), 19.

Cannat, M., Fontaine, F., and Escartín, J. (2010). "Serpentinization and associated hydrogen and methane fluxes at slow spreading ridges," in *Geophysical monograph series* (Washington DC, USA: American Geophysical Union), 188. doi:10.1029/2008GM000760

Chamov, N. P., Sokolov, S. Y., Kostyleva, V. V., Efimov, V. N., Peive, A. A., Aleksandrova, G. N., et al. (2010). Structure and composition of the sedimentary cover in the Knipovich Rift valley and Molloy Deep (Norwegian-Greenland basin). *Lithology Mineral Resour.* 45, 532–554. doi:10.1134/s0024490210060039

Chand, S., Cremiere, A., Lepland, A., Thorsnes, T., Brunstad, H., and Stoddart, D. (2016). Long term fluid expulsion revealed by carbonate crusts and pockmarks connected to subsurface gas anomalies and palaeo-channels in the central North Sea. *Geo. Mar. Lett.* 37, 215–227. doi:10.1007/s00367-016-0487-x

Charlou, J. L., Donval, J. P., Konn, C., Ondreas, H., Fouquet, Y., Jean- Baptiste, P., et al. (2010). "High production and fluxes of H2 and CH4 and evidence of abiotic hydrocarbon synthesis by serpentinization in ultramafic-hosted hydrothermal systems on the Mid-Atlantic Ridge, in Diversity of Hydrothermal Systems on Slow Spreading Ocean Ridges," in *Geophys. Monogr. Ser*. Editors P. Rona, C. Devey, J. Dyment, and B. Murton (Washington, DC, USA: AGU), 188, 265–296. doi:10.1029/2008GM000752

Czuba, W., Ritzmann, O., Nishimura, Y., Grad, M., Mjelde, R., Guterch, A., et al. (2005). Crustal structure of northern Spitsbergen along the deep seismic transect between the Molloy Deep and Nordaustlandet. *Geophys. J. Int.* 161, 347–364. doi:10.1111/j.1365-246x.2005.02593.x

Daszinnies, M., Plaza-Faverola, A., Sylta, Ø., Bünz, S., Mattingsdal, R., Tømmerås, A., et al. (2021). The Plio-Pleistocene seepage history off western Svalbard inferred from 3D petroleum systems modelling. *Pet. Geol.* 128, 105023. doi:10.1016/j.marpetgeo.2021.105023

Dooley, T., and McClay, K. (1997). Analog modeling of pull-apart basins. *AAPG Bull.* 81, 1804–1826. doi:10.1306/3b05c636-172a-11d7-8645000102c1865d

Dumais, M. A., Gernigon, L., Olesen, O., Johansen, S. E., and Bronner, M. (2021). New interpretation of the spreading evolution of the Knipovich Ridge derived from aeromagnetic data. *Int.* 224, 1422–1428. doi:10.1093/gji/ggaa527

Dumke, I., Burwicz, E. B., Berndt, C., Klaeschen, D., Feseker, T., Geissler., W. H., et al. (2016). Gas hydrate distribution and hydrocarbon maturation north of the Knipovich Ridge, western Svalbard margin. *J. Geophys. Res. Solid Earth* 121, 1405–1424. doi:10.1002/2015JB012083

Elger, J., Berndt, C., Rupke, L., Krastel, S., Gross, F., and Geissler, W. H. (2018). Submarine slope failures due to pipe structure formation. *Nat. Comm.* 9, 715. doi:10.1038/s41467-018-03176-1

Engen, Ø., Eldholm, O., and Bungum, H. (2003). The Arctic plate boundary. *Geophys Res.* 108 (B2), 2075. doi:10.1029/2002JB001809

Engen, Ø., Faleide, J. I., and Dyreng, T. K. (2008). Opening of the Fram Strait gateway: a review of plate tectonic constraints. *Tectonophysics* 450, 51–69. doi:10.1016/j.tecto.2008.01.002

Escartin, J., Mevel, C., Petersen, S., Bonnemains, D., Cannat, M., Andreani, M., et al. (2017). Tectonic structure, evolution, and the nature of oceanic core complexes and their detachment fault zones (13°20′N and 13°30′N, Mid Atlantic Ridge). *Geochem. Geophys. Geosys.* 18, 1451–1482. doi:10.1002/2016GC006775

Geissler, H. W., Gebhardt, C. A., and Schmidt-Aursch, C. M. (2014a). The Hinlopen/Yermak Megaslide (HYM) – understanding an exceptional submarine landslide, its consequences and relation to the deep structure of the Sophia Basin (Sophia-HYM) – cruise No. MSM31 – august 17 – september 18, 2013 – tromsø (Norway) – bremen (deutschland). *DFG-Senatskommission für Ozeanogr.* 31, 70. MARIA S. MERIAN Berichte. doi:10.2312/cr_msm31

Geissler, W. H., Pulm, P. V., Jokat, W., and Gebhardt, A. C. (2014b). Indications for the occurrence of gas hydrates in the Fram Strait from heat flow and multichannel seismic reflection data. *J. Geol. Res.* 2014, 1–12. doi:10.1155/2014/582424

Gruetzner, J., Matthiessen, J., Geissler, W. H., Gebhardt, C., and Schreck, M. (2022). A revised core-seismic integration in the Molloy Basin (ODP Site 909): Implications for the history of ice rafting and ocean circulation in the Atlantic-Arctic gateway. *Global and Planetary Change*. 215. doi:10.1016/j.gloplacha.2022.103876

Hunkins, K. (1990). "A review of the physical oceanography of Fram Strait," in *The physical oceanography of sea straits*. Editor L. R. Pratt (Dordrecht, Netherlands: Springer), 61–94.

Hustoft, S., Bünz, S., Mienert, J., and Chand, S. (2009). Gas hydrate reservoir and active methane-venting province in sediments on <20Ma young oceanic crust in the Fram Strait, offshore NW-Svalbard. *Earth. Planet. Sci. Lett.* 284, 12–24.

Johnson, J. E., Mienert, J., Plaza-Faverola, A., Vadakkepuliyambatta, S., Knies, J., Buenz, S., et al. (2015). Abiotic methane from ultraslow-spreading ridges can charge Arctic gas hydrates. *Geology* 43, 371–374. doi:10.1130/G36440.1

Kandilarov, A., Mjelde, R., Okino, K., and Murai, Y. (2008). Crustal structure of the ultra-slow spreading Knipovich Ridge, North Atlantic, along a presumed amagmatic portion of oceanic crustal formation. *Mar. Geophys. Res.* 29 (2), 109–134. doi:10.1007/s11001-008-9050-0

Keiding, M., Olesen, O., and Dehls, J. (2018). Neo tectonic map of Norway and adjacent areas, Geological Survey of Norway. https://www.ngu.no/upload/Publikasjoner/Kart/Neotectonic_Map_NGU.pdf.

Klenke, M., and Schenke, H. W. (2002). A new bathymetric model for the central Fram Strait. *Mar. Geophys. Res.* 23, 367–378. doi:10.1023/a:1025764206736

Klitzke, P., Sippel, J., Faleide, J. I., and Scheck-Wenderoth, M. (2016). A 3D gravity and thermal model for the Barents Sea and kara sea. *Tectonophysics* 684, 131–147. doi:10.1016/j.tecto.2016.04.033

Knies, J., Daszinnies, M., Plaza-Faverolla, A., Chand, S., Sylta, Ø., Buez, S., et al. (2018). Modelling persistent methane seepage offshore western Svalbard since early Pleistocene. *Mar. Pet. Geol.* 91, 800–811. doi:10.1016/j.marpetgeo.2018.01.020

Knies, J., and Mann, U. (2002). Depositional environment and source rock potential of Miocene strata from the central Fram Strait: introduction of a new computing tool for simulating organic facies variations. *Mar. Pet. Geol.* 19, 811–828. doi:10.1016/s0264-8172(02)00090-9

Lizarralde, D., Soule, S. A., Seewald, J. S., and Proskurowski, G. (2011). Carbon release by off axis magmatism in a young sedimented spreading centre. *Nat. Geosci.* 4, 50–54. doi:10.1038/ngeo1006

Mann, U., Knies, J., Chand, S., Jokat, W., Stein, R., and Zweigel, J. (2009). Evaluation and modelling of Tertiary source rocks in the central Arctic Ocean. *Mar. Pet. Geol.* 26, 1624–1639. doi:10.1016/j.marpetgeo.2009.01.008

Martin, B., and Fyfe, W. S. (1970). Some experimental and theoretical observations on the kinetics of hydration reactions with particular reference to serpentinization. *Chem. Geol.* 6, 185–202. doi:10.1016/0009-2541(70)90018-5

Mattingsdal, R. (2023). "A new young source rock offshore western Svalbard proven with oil seep geochemical results – possible regional implication for the westernmost Barents Sea," in Norwegian Petroleum Directorate, Petroleum Systems Conference, Oslo, Norway.

Mattingsdal, R., Knies, J., Andreassen, K., Fabian, K., Husum, K., Grøsfjeld, K., et al. (2014). A new 6 Myr stratigraphic framework for the Atlantic-Arctic Gateway. *Quart. Sci. Rev.* 92, 170–178. doi:10.1016/j.quascirev.2013.08.022

Milkov, A. V., and Etiope, G. (2018). Revised genetic diagrams for natural gases based on a global dataset of >20000 samples. *Org. Geochem.* 125, 109–120. doi:10.1016/j.orggeochem.2018.09.002

Osti, G., Franek, P., Forwick, M., and Laberg, J. S. (2017). Controlling factors for slope instability in a seismically active region: the NW-Svalbard continental margin. *Mar. Geol.* 390, 131–146. doi:10.1016/j.margeo.2017.06.005

Osti, G., Waghorn, K. A., Waage, M., Plaza-Faverola, A., and Ferre, B. (2019). Evolution of contourite drifts in regions of slope failures at eastern Fram Strait. *Arktos* 5, 105–120. doi:10.1007/s41063-019-00070-y

Panieri, G., Argentino, C., Ramalho, S. P., Vulcano, F., Savini, A., Fallati, L., et al. (2024). An Arctic natural oil seep investigated from space to the seafloor. *Sci. Total Environ.* 907, 167788. doi:10.1016/j.scitotenv.2023.167788

Panieri, G., Knies, J., Vadakkepuliyambatta, S., Lee, A. L., and Schubert, C. J. (2023). Evidence of Arctic methane emissions across the mid Pleistocene. *Commun. Earth Environ.* 4, 109. doi:10.1038/s43247-023-00772-y

Plaza-Faverola, A., Bunz, S., Johnson, J. E., Chand, S., Knies, J., Mienert, J., et al. (2015). Role of tectonic stress in seepage evolution along the gas hydrate-charged Vestnesa Ridge, Fram Strait. *Geophys. Res. Lett.* 42, 733–742. doi:10.1002/2014GL062474

Plaza-Faverola, A., and Keiding, M. (2019). Correlation between tectonic stress regimes and methane seepage on the western Svalbard margin. *Solid earth.* 10, 79–94. doi:10.5194/se-10-79-2019

Plaza-Faverola, A., Vadakkepuliyambatta, S., Hong, W.-L., Mienert, J., Bünz, S., Chand, S., et al. (2017). Bottom-simulating reflector dynamics at Arctic thermogenic

gas provinces: an example from Vestnesa Ridge, offshore west Svalbard. *J. Geophys. Res. Solid Earth* 122, 4089–4105. doi:10.1002/2016JB013761

Proskurowski, G., Lilley, M. D., Seewald, J. S., Früh-Green, G. L., Olson, E. J., Lupton, J. E., et al. (2008). Abiogenic hydrocarbon production at Lost City hydrothermal field. *Science* 319 (5863), 604–607. doi:10.1126/science.1151194

Rajan, A., Mienert, J., Bünz, S., and Chand, S. (2012). Potential serpentinization, degassing, and gas hydrate formation at a young (<20 Ma) sedimented ocean crust of the Arctic Ocean ridge system. *Jour. Geophys. Res.* 117, B03102. doi:10.1029/2011JB008537

Spiegler, D. (1996). "Planktonic foraminifer Cenozoic biostratigraphy of the Arctic Ocean, Fram Strait (Sites 908e909), Yermak Plateau (Sites 910e912), and East Greenland Margin (Site 913)," in *Proceeding Ocean drilling program, scientific results*. Editors J. Thiede, A. M. Myhre, J. V. Firth, G. L. Johnson, and W. F. Ruddiman (College Station, Texas, USA: Ocean Drilling Program), 151, 153–167.

Stein, R. (2007). Upper Cretaceous/lower Tertiary black shales near the North Pole: organic-carbon origin and source-rock potential. *Mar. Petroleum Geol.* 24 (2007), 67–73. doi:10.1016/j.marpetgeo.2006.10.002

Talwani, M., and Eldholm, O. (1977). Evolution of the Norwegian-Greenland sea. *GSA Bull.* 88, 969–999. doi:10.1130/0016-7606(1977)88<969:eotns>2.0.co;2

Tesi, T., Muschitiello, F., Mollenhauer, G., Miserocchi, S., Langone, L., Ceccarelli, C., et al. (2021). Rapid atlantification along the Fram Strait at the beginning of the 20th century. *Sci. Adv.* 7, eabj2946. doi:10.1126/sciadv.abj2946

Thorsnes, T., Chand, S., Bellec, V., Nixon, F. C., Brunstad, H., Lepland, A., et al. (2023). Gas seeps in Norwegian waters – distribution and mechanisms. *Nor. J. Geol.* 103, 202309. doi:10.17850/njg103-2-4

Tucholke, B. E., Lin, J., and Kleinrock, M. C. (1998). Megamullions and mullion structure defining oceanic metamorphic core complexes on the Mid-Atlantic Ridge. *Jour. Geophys. Res.* 103, 9857–9866. doi:10.1029/98JB00167

von Appen, W.-J., Besczynska-Moller, A., and Fahrbach, E. (2015). Physical oceanography and current meter data from mooring F3-15. *Pangea*. doi:10.1594/PANGAEA.853902

Whiticar, M. J. (1999). Carbon and hydrogen isotope systematics of bacterial formation and oxidation of methane. *Chem. Geol.* 161, 291–314. doi:10.1016/s0009-2541(99)00092-3

frontiers | Frontiers in Earth Science

TYPE Original Research
PUBLISHED 22 April 2024
DOI 10.3389/feart.2024.1338246

OPEN ACCESS

EDITED BY
Jochen Knies,
Geological Survey of Norway, Norway

REVIEWED BY
Muhammed Fatih Sert UiT The Arctic University of Norway, Norway
Kate Schuler,
University of British Columbia, Canada

*CORRESPONDENCE
Ellen Damm,
ellen.damm@awi.de

RECEIVED 14 November 2023
ACCEPTED 20 March 2024
PUBLISHED 22 April 2024

CITATION
Damm E, Thoms S, Angelopoulos M, Von Albedyll L, Rinke A and Haas C (2024), Methane pumping by rapidly refreezing lead ice in the ice-covered Arctic Ocean. *Front. Earth Sci.* 12:1338246. doi: 10.3389/feart.2024.1338246

Methane pumping by rapidly refreezing lead ice in the ice-covered Arctic Ocean

Ellen Damm[1]*, Silke Thoms[2], Michael Angelopoulos[1], Luisa Von Albedyll[2], Annette Rinke[1] and Christian Haas[2]

[1]Alfred Wegener Institute Helmholtz Centre for Polar and Marine Research, Potsdam, Germany, [2]Alfred Wegener Institute Helmholtz Centre for Polar and Marine Research, Bremerhaven, Germany

If and how the sea ice cycle drives the methane cycle in the high Arctic is an open question and crucial to improving source/sink balances. This study presents new insights into the effects of strong and fast freezing on the physical–chemical properties of ice and offers implications for methane fluxes into and out of newly formed lead ice. During the 2019–2020 transpolar drift of the Multidisciplinary Drifting Observatory for the Study of Arctic Climate (MOSAiC), we took weekly samples of growing lead ice and underlying seawater at the same site between January and March 2020. We analyzed concentrations and stable carbon isotopic signatures ($\delta^{13}C–CH_4$) of methane and calculated methane solubility capacities (MSC) and saturation levels in both environments. During the first month, intense cooling resulted in the growth of two-thirds of the final ice thickness. In the second month, ice growth speed decreased by 50%. Both growth phases, disentangled, exposed different freeze impacts on methane pathways. The fast freeze caused strong brine entrapment, keeping the newly formed lead ice permeable for 2 weeks. These physical conditions activated a methane pump. An increased MSC induced methane uptake at the air–ice interface, and the still-open brine channels provided top-down transport to the ocean interface with brine drainage. When the subsurface layer became impermeable, the top-down pumping stopped, but the ongoing uptake induced a methane excess on top. During the second growth phase, methane exchange exclusively continued at the ice–ocean interface. The shift in the relative abundance of the ^{12}C and ^{13}C isotopes between lead ice and seawater toward a ^{13}C-enrichment in seawater reveals brine drainage as the main pathway releasing methane from aging lead ice. We conclude that in winter, refrozen leads temporarily function as active sinks for atmospheric methane and postulate that the relevance of this process may even increase when the Arctic fully transitions into a seasonally ice-covered ocean when leads may be more abundant. To highlight the relevance of methane in-gassing at the air–ice interface as a potential but still unconsidered pathway, we include estimates of the occurrence and frequency of young lead ice from satellite observations of leads during MOSAiC.

KEYWORDS

methane pathways in sea ice, methane exchange at interfaces, refrozen leads, polar winter study, methane isotopic signature, central Arctic Ocean, mosaic drift expedition

1 Introduction

Climate warming impacts Arctic regions 2–4 times faster than the global average (Rantanen et al., 2022). Drastic sea ice losses during summer result in an annual reduction of the September minimum sea ice extent of approximately 25% below the 1981–2010 average and a thinning rate of approximately 10% per decade (Kwok, 2018; Stroeve and Notz, 2018). Most of the thinning is caused by a shift from thicker multiyear ice to thinner first-year ice. Accelerating sea ice drift contributes further to the thinning with shorter residence times of the ice in the central Arctic (Kwok, 2018; Krumpen et al., 2019; Sumata et al., 2023). Sea ice dynamics, that is, the ridging and rafting of colliding floes and ice floes moving apart, create a heterogeneous ice cover with ridges and leads. Leads often cyclically open and close over intervals ranging from days to months (Willmes et al., 2023). Leads are particularly important sites of new ice formation in winter because sea ice growth is faster in open water than below the thicker ice of older floes due to the reduced insulation of ice. Therefore, quick new ice formation in leads contributes up to 30% to the Arctic sea ice mass balance (Kwok et al., 2006; von Albedyll et al., 2022), although leads cover an area of less than 5% of the Arctic sea ice during the freeze period (Wadhams, 2000; Reiser et al., 2020). Recently, the high relevance of leads for the polar climate resulted in increased attention on lead areal fractions in sea ice modeling studies (e.g., Wilchinsky et al., 2015; Zhang et al., 2021; Ólason et al., 2021; Boutin et al., 2023).

In addition to the relevance for the sea ice mass balance, these dynamic processes are associated with a cascade of feedback altering the entire Arctic environmental system, including potential changes in gas and matter fluxes at the air–ocean interfaces (Serreze and Barry, 2011). To date, global coupled models mainly treat the transfer of climate-relevant gases based on fluxes derived from open water measurements and restricted by the area annually or seasonally covered by ice (Torsvik, 2023). Observational studies on methane pathways within sea ice and the exchange at the ocean–ice and air–ice interfaces are scarce and mostly spatially restricted to the marginal ice zone or fast ice areas reported to be affected by local methane sources (Kiditis et al., 2010; Zhou et al., 2013; Zhou et al., 2014; Verdugo et al., 2021; Silyakova et al., 2022; Vinogradova et al., 2022). However, enhanced fluxes of climate-relevant gases from open sea ice leads and cracks in the atmosphere are also described from the central Arctic (Kort et al., 2012; Steiner et al., 2013). More recently, a winter study on refrozen leads revealed physical properties in newly formed lead ice, temporarily favoring an ice-to-air methane flux (Silyakova et al., 2022). While newly formed ice inhibits direct fluxes from the ocean to the atmosphere through leads within hours after opening, refrozen leads exist for days to weeks. Therefore, we suggest that newly formed ice may act as an important pathway for methane transfer in winter. Gas transport

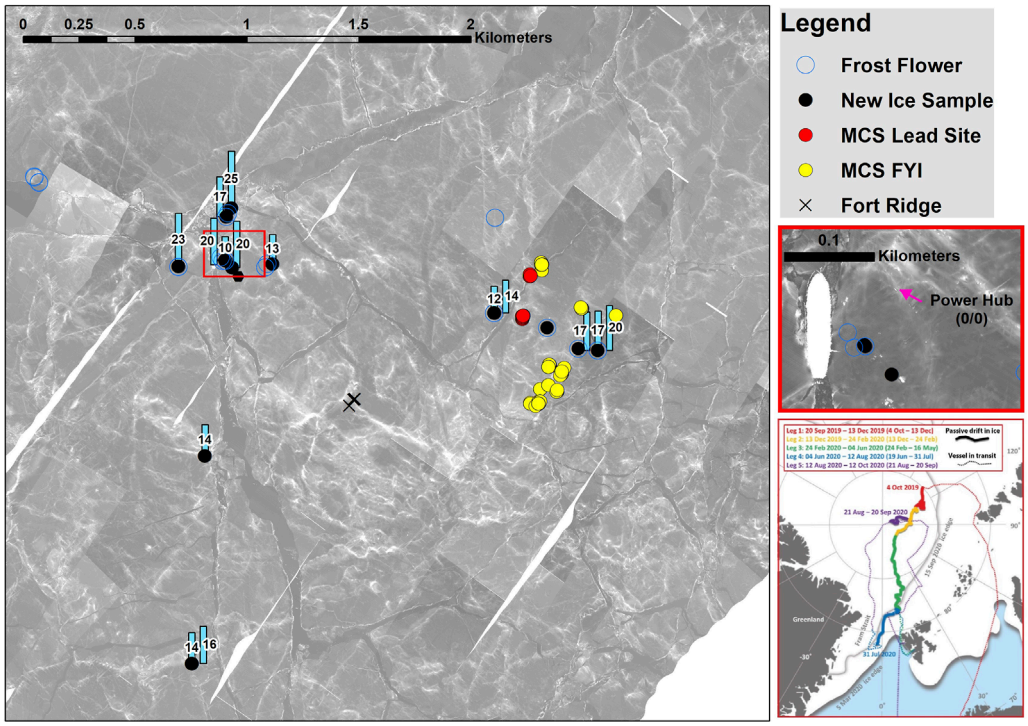

FIGURE 1
Right side, thin red frame: Track of RV Polarstern during the 2019–2020 MOSAiC drift expedition. Colored line segments show the drift trajectory of different cruise legs on the background of the sea ice extent in March 2020 (Nicolaus et al., 2022). Lead ice sampling occurred on Leg 2 and Leg 3 (yellow and green line) north of 85°N. Large panel: Locations of lead ice sampling on the main coring site (MCS) in the Central Observatory (area around the ship). The ship's position is within the red square on the right side. Red dots comprise measurements on the same lead ice site on seven dates between 6 January and 7 March 2020, a 2-month observation period. Sampling started 2 days after lead opening and ended as the sampling site disappeared by ridge formation on 8 March 2020. MCS FYI: sampling position of first-year ice at the main coring site. Black dots and blue circles show spots of thin new ice and frost flowers sampled 2–3 days after formation. The blue rectangles give the surface salinity on new ice spots.

within sea ice strongly depends on brine mobility, which decreases with decreasing temperature (Cox and Weeks, 1983; Weeks and Ackley, 1986; Golden et al., 2007; Tison et al., 2017; Crabeck et al., 2019).

In order to evaluate the potential impact of freeze conditions on methane pathways in lead ice and its interfaces, we carried out *in situ* observations of ice growth during the 2019–2020 Multidisciplinary Drifting Observatory for the Study of Arctic Climate (MOSAiC) drift expedition in the central Arctic (Figure 1). The MOSAiC was a yearlong drift expedition with the purpose of studying the changing Arctic climate system to improve process understanding and model representations of this system (Nicolaus et al., 2022; Rabe et al., 2022; Shupe and Rex, 2022). In a previous study, we described the temporal changes and spatial variability of physical ice properties of different ice types during sea ice growth (Angelopoulos et al., 2022). In the present process study, we investigate changes in physical and chemical properties in newly formed lead ice from the moment of a lead opening through the period of refreezing and ice growth until the closing of the lead by rafting and ridging. Measurements of the same ice were carried out on a weekly basis over a 2-month period from January to March 2020 (Figure 1). These measurements included lead ice temperature and salinity profiles, calculations of the methane solubility capacity (MSC) and methane saturation between lead ice, seawater, and the atmosphere, and the analysis of methane concentration and $\delta^{13}C–CH_4$ values in lead ice and surface seawater. We observed stepwise freeze-induced shifts of the physical properties in lead ice that influenced the methane uptake and release at its interfaces, ultimately affecting methane pathways in winter in the high Arctic.

2 Methods

2.1 Seawater and lead ice sampling

Seawater samples were taken at a 2 m depth underneath the MOSAiC ice floe using a CTD rosette in the main oceanography tent (Rabe et al., 2022). Bubble-free seawater was collected in 500-mL glass vials that were sealed with rubber stoppers and crimped with aluminum caps. Lead ice coring followed the ice coring procedures of MOSAiC (Angelopoulos et al., 2022). In short, at least three lead ice cores 20–50 cm apart were taken using a Kovacs Mark II 9 cm ice core drill. At each sampling site and day, the first ice core was used for *in situ* temperature measurements. Thereafter, two cores for the analyses of methane concentration, the stable carbon isotopic signature of methane ($\delta^{13}C–CH_4$) and salinity, were taken. Once transferred onboard, the cores were immediately cut into 10-cm slices. Each slice was melted in a gas-tight Tedlar bag after evacuating the air therein in darkness at 4°C. Pieces of thin new ice and frost flowers were cut using a knife and collected with a spittle, respectively, and directly saved in Tedlar bags. Once melted, the meltwater was collected in 500-mL glass vials sealed with rubber stoppers and crimped with aluminum caps. In the following, seawater and melted lead ice samples were processed using the same procedure. In the sample bottles, a headspace was created by injecting 20 mL of hydrocarbon-free synthetic air while, at the same time, water was pushed out via a second needle to balance the pressure. After the gas and water were allowed to come to equilibrium by shaking, the headspace was subsampled with a gas-tight syringe (SGE, Victoria, Australia), and the sample was immediately injected into the small sample isotope module (SSIM, see Section 2.2).

2.2 Analyses of methane concentration and $\delta^{13}C–CH_4$ ratios

Methane concentrations and stable carbon isotope ratios ($\delta^{13}C–CH_4$) of seawater and bulk ice samples were determined using a Picarro G2132-i cavity ring-down spectrometer coupled to a small sample isotope module (SSIM) (Picarro, Santa Clara, California, USA). The SSIM is a sample inlet system used to analyze discrete samples. The SSIM coordinator software was run in high-precision mode, with a syringe injection setting, and on dilution with hydrocarbon-free air to account for our analysis procedures. The Picarro G2132-i runs with a flow rate of approximately 25 mL/min. For calibration, we used standard gas mixtures with concentrations of 2 ppm, 5 ppm, and 10 ppm (*Linde Company*) and standard gas mixtures with isotopic ratios of −25‰, −45‰, and −69‰ vs. VPDB (Airgas Company). Considering the complete sampling procedure, the overall total uncertainty was ±5% estimated in duplicate. In addition to this uncertainty, we cannot exclude a concentration-dependent effect on our isotopic ratio measurements (Rella et al., 2015; Uhlig and Loose, 2017; Pohlmann et al., 2021) because many of our measurements were made on samples with mixing ratios <1.2 ppm CH_4 (Supplementary Figure S1). Future studies using a Picarro gas analyzer should use isotopic gas standards spanning the full range of mixing ratios observed in samples in order to isolate the concentration-dependent effect and improve the absolute accuracy of the isotopic ratio measurements.

2.3 Analyses of water and ice temperature and salinity

Surface seawater temperature and salinity at depths of 2 m were continuously measured along the drift track by two thermosalinographs (SBE21, Sea-Bird GmbH) installed in the hull of RV Polarstern (Haas et al., 2021). The temperature and bulk salinity of the lead ice cores were measured according to procedures described in Angelopoulos et al., 2022. In short, ice temperatures were measured in 4.5 cm deep, narrow holes drilled into the core at intervals of 5 cm from the bottom to the top of the ice immediately after the cores were retrieved. Bulk salinity was analyzed on melted subsamples using a WTW 193 Cond 3151 salinometer equipped with a TetraCon 325 four-electrode conductivity cell.

3 Results

3.1 Calculations

3.1.1 Brine volume fraction

The calculation of the brine volume fraction from the ice temperature and salinity data follows Cox and Weeks (1983) according to Eq. 1. To calculate the sea ice density (ρ), the pure ice density as a function of temperature (T) was first estimated from Fukusako (1990). The equation for sea ice density considers

temperature-dependent phase equilibrium relationships from Assur (1960) for brine salinity (B_s) and the ratio (k) of the mass of solid salts to the mass of dissolved salts in the brine. We assumed no air volume when implementing the sea ice density. The BVF was calculated from Eq. 1, where ρ is sea ice density, S_i is sea ice salinity, $F_1(T) = \rho_b B_s(1+k)$, and ρ_b is brine density. Brine salinity, density, and the amount of solid salts all vary as a function of temperature (see also Angelopoulos et al., 2022).

$$BVF = \frac{\rho S_i}{F_1(T)} \tag{1}$$

The BVF decreases as the temperature and bulk salinity of ice decrease. Here, we adopt the hypothesis of the law of fives, which states that when BVF is above 5%, the ice is permeable, and brine moves in channels, but when BVF falls below 5%, the ice becomes impermeable for brine movement, and brine inclusions disconnect (Golden et al., 2007).

3.1.2 Rayleigh number

The Rayleigh (Ra) number is a dimensionless value that characterizes a fluid's flow regime and describes the susceptibility of sea ice to brine convection (e.g., Notz and Worster, 2009; Zhou et al., 2013). In the literature, the critical Ra number for which the sea becomes unstable to convection varies between 2 and 10. However, lower values are typically used for field studies (Gourdal et al., 2019). We calculate a local Ra number for different sampling points in the ice column to help determine how and when brine gravity drainage influenced the lead ice salinity profiles. The driving variables affecting the local Ra number are the ice depth, the brine salinity gradient between the ice depth and seawater, and the effective sea ice permeability. We followed the same approach from Angelopoulos et al. (2022) to ensure consistency between the characterizations of first-year ice (FYI), second-year ice, and new lead ice at the different MOSAiC sites. Like Angelopoulos et al. (2022), the physical constants needed for the Ra calculation were adopted from Gourdal et al. (2019).

3.1.3 Methane solubility capacity in seawater and lead ice

In this work, we have defined the methane solubility capacity (MSC in $molL^{-1}$) as the thermodynamic capacity to dissolve methane in a liquid. Following the dependency of Henry's solubility coefficient (K_H in mol L^{-1} atm^{-1}) on temperature T) and salinity S), the equilibrium MSC in seawater is given by

$$MSC_{SW} = P * K_{H(T,S)}, \tag{2}$$

where P is the partial pressure of methane in the overlying atmosphere (in atm). The T and S dependency of K_H can be derived from the measured Bunsen solubility coefficient (β), which describes the volume of pure dry gas reduced to standard temperature and pressure (STP; 0°C and 1 atm) that will dissolve in a volume of water at ambient T exposed to a gas partial pressure of 1 atm. The Bunsen coefficients for methane have been measured for various temperatures and salinities (Wiesenburg and Guinasso, 1979) and can be easily converted into Henry's solubility by $K_H = \beta/V_M$, where V_M is the molar volume of the gas at STP (L/mol). Assuming that the total atmospheric pressure is equal to 1 atm and the relative humidity is 100%, Eq. 2 can be written in the form most often used for solubility calculations of methane in moist air:

$$MSC = \frac{\beta}{V_M} * \left(1 - P_{vp}\right) * f_G, \tag{2a}$$

where P_{vp} is the saturation vapor pressure of the water (atm) and f_G is the dry mole fraction of the gas in the atmosphere. Based on measured Bunsen solubility coefficients reported in the literature, Wiesenburg and Guinasso (1979) have shown that MSC can be described as a function of temperature, salinity, and mole fraction of methane in a dry atmosphere by using a single equation. For the calculation of MSC in nmol L^{-1}, we use Equation 7 along with the coefficients in the second row of Table VI in Wiesenburg and Guinasso (1979) to obtain the equation for the atmospheric equilibrium solubility:

$$\begin{aligned} \ln MSC = {} & \ln f_G - 415.2807 + 596.8104 * \left(\frac{100}{T}\right) \\ & + 379.2599 * \ln\left(\frac{T}{100}\right) - 62.0757 * \left(\frac{T}{100}\right) \\ & + S * \left[-0.05916 + 0.032174 * \left(\frac{T}{100}\right) - 0.0048198 * \left(\frac{T}{100}\right)^2\right], \end{aligned} \tag{2b}$$

where T is the absolute temperature in Kelvin and S is the salinity in parts per thousand. MSC increases with decreasing temperature and salinity. However, the temperature effect clearly outweighs the salinity effect when cooling to the freezing point occurs in polar surface water. Note that K_H (or β) is defined within the range of $-2 < T < 40$°C and $0 < S < 40$ (Wiesenburg and Guinasso, 1979), but it has been postulated to remain valid for the potentially much lower temperatures of brine found in sea ice (Zhou et al., 2013; Crabeck et al., 2019).

When seawater begins to freeze, the methane dissolved in seawater becomes incorporated in liquid brine at the ice–seawater interface, and the brine temperature is equal to the temperature of the surrounding ice. Within the liquid brine, dissolved methane migrates within the brine channels as long as the ice is still permeable. With decreasing ice and brine temperatures, BVF decreases, and the ice becomes impermeable when BVF <5% (Golden et al., 2007). Brine is then trapped in discrete pockets. Therein, liquid brine remains in thermodynamic equilibrium with the ice matrix, whose temperature controls the brine volume and salinity. During ongoing cooling, brine pockets shrink as water freezes onto the walls of the pockets, thereby increasing the internal brine salinity (iB_S). The increase in iB_S due to the decrease in temperature is described by

$$iB_s = 1.2 - 21.8 * T - 0.919 * T^2 - 0.0178 * T^3. \tag{3}$$

As exclusively defined by ambient ice temperature, iB_s increases with decreasing temperature (Notz, 2005). Replacing S by iB_s, Eq. 2b predicts a reduced MSC in enclosed brine pockets compared to the MSC in seawater (MSC-I; Figure 2A).

The situation is different, however, in bottom ice, at the ice–seawater interface, and also in new lead ice that is still permeable. During the transition period from seawater conditions to conditions present in impermeable ice, dissolved methane still migrates with the brine in open brine channels as long as the BVF is above 5%. In an open brine channel system, brine salinity might still be

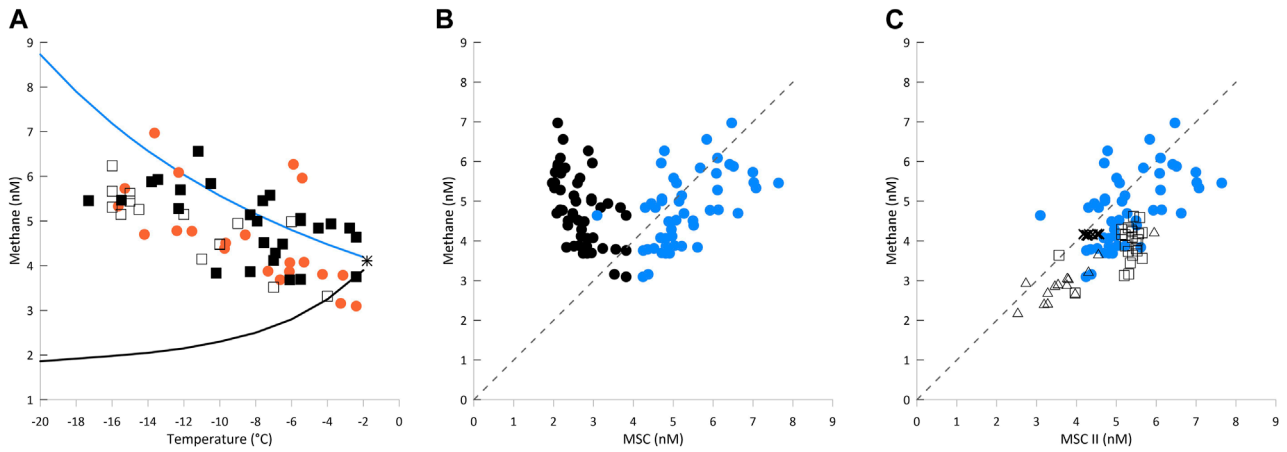

FIGURE 2
(A): Calculated methane solubility capacity (MSC) and measured methane concentrations in lead ice *versus* brine temperature. The black star shows the MSC of seawater calculated for the freezing point. Curved lines show MSCs calculated using the two methods. MSC-I (black line) with brine salinity in equilibrium with ambient temperature (iB_s; Eq. 3; related to closed brine pockets in impermeable ice) and MSC-II (blue line) with brine salinity equal to seawater salinity (32 PSU, Eq. 2; related to open brine channels in permeable ice). Orange dots and black squares represent measured concentrations of all ice samples from the first and second month of the time series, respectively. Open squares are related to 2–3-day-old lead ice spots (for locations, see Figure 1). **(B)** Measured methane concentrations vs. calculated MSCs (MSC-I in black; MSC-II in blue dots). The dotted line represents 100% saturation. Areas to the left and right of this line represent super- and undersaturation, respectively. Calculations with MSC-I result in clear supersaturation, while with MSC-II, they result in scattering around the saturation line. **(C)** Methane concentration in seawater (crosses), thin new ice (open squares), lead ice from the time series (blue dots), and triangles (frost flowers) vs. MSC-II. The gray line represents 100% saturation. A strong freeze induced enhanced MSC-II levels in thin new ice relative to seawater. The increase in concentration reflects an uptake of gaseous/re-dissolved methane initiated by the increase in MSC-II during a freeze.

close to seawater salinity. Furthermore, a fast and strong decrease in temperature could place the brine out of the equilibrium state with the ice matrix because diffusion of temperature is faster than diffusion of salt; that is, brine salinity adjusts more slowly to colder ambient conditions than brine temperature. Therefore, the brine could become temporarily supercooled below its equilibrium freezing point. This mechanism would decrease the temperature in the liquid brine faster than it increases the brine's salinity. Then, the MSC in brine is still mainly controlled by temperature comparable to MSC in seawater. Because there is no liquid-to-ice phase transition in the formation of supercooled water, we assume that the calculation of MSC following Wiesenburg and Guinasso (1979) remains valid. This is similar to cloud water droplets, which can persist in a supercooled state to below −37°C (Rosenfeld and Woodley, 2000), and to sodium chloride at the interface of snow, which can exist as supercooled liquid down to −32°C (Bartels-Rausch et al., 2021). However, it is not known if a supercooled phase occurs at the interface of brine with the ice matrix. Here, we assume the possibility of a transient (metastable) supercooled state of the liquid brine, which will eventually destabilize to form ice and thereby trap methane in the ice matrix or liquid brine. In particular, we suggest that this process is important in the beginning of sea ice formation in leads before the time of complete brine entrapment, where brine is basically seawater of salinity 32 PSU in contact with the very cold atmosphere. Supercooling was also observed in seawater underneath Arctic winter sea ice (Katlein et al., 2020). The observed water temperatures of only 0.01–0.02 K below the respective seawater freezing point (Katlein et al., 2020) probably represent a final residual supercooled state at the end of ice floe formation.

Using seawater salinity instead of brine salinity for the calculation of MSC (MSC-II) results in a net increase in MSC in permeable lead ice compared to seawater, which is in good agreement with our measured concentrations (Figure 2A). By comparison, calculations carried out for MSC-I and MSC-II show the range between the lowest and highest solubility capacity that can be expected in newly forming lead ice (Figure 2A). We suggest experimental analyses to validate the relationship between changing freeze conditions and the MSC under special consideration of sea ice permeability.

3.1.4 Methane saturation in seawater and lead ice

The ratio between measured and calculated concentrations at the atmospheric equilibrium gives the methane saturation (Figure 2B). As atmospheric equilibrium concentration, we used an atmospheric mole fraction $f_G = 1.95 \times 10^{-6}$ (NOAA global sampling networks http://www.esrl.noaa.gov). Differences in saturation reflect the contrasting effect of assuming equilibrium with brine salinity (MSC-I; Eq. 3) or seawater salinity (MSC-II; Eq. 2). The balancing net effect of decreasing temperature and increasing iB_s on MSC results in MSC-I being smaller than MSC_{SW}, ultimately causing supersaturation in brine.

By comparison, MSC-II reflects the dominance of the temperature effect on MSC in newly formed and still-permeable lead ice. Using MSC-II promotes scattering along the saturation line, which mirrors the effect of temperature decrease and reveals the trend of increasing concentration during ongoing cooling. In the following, we are using the MSC-II calculations because they better agree with our measurements. That is, MSC-II better describes the effect of relative changes in MSC induced by

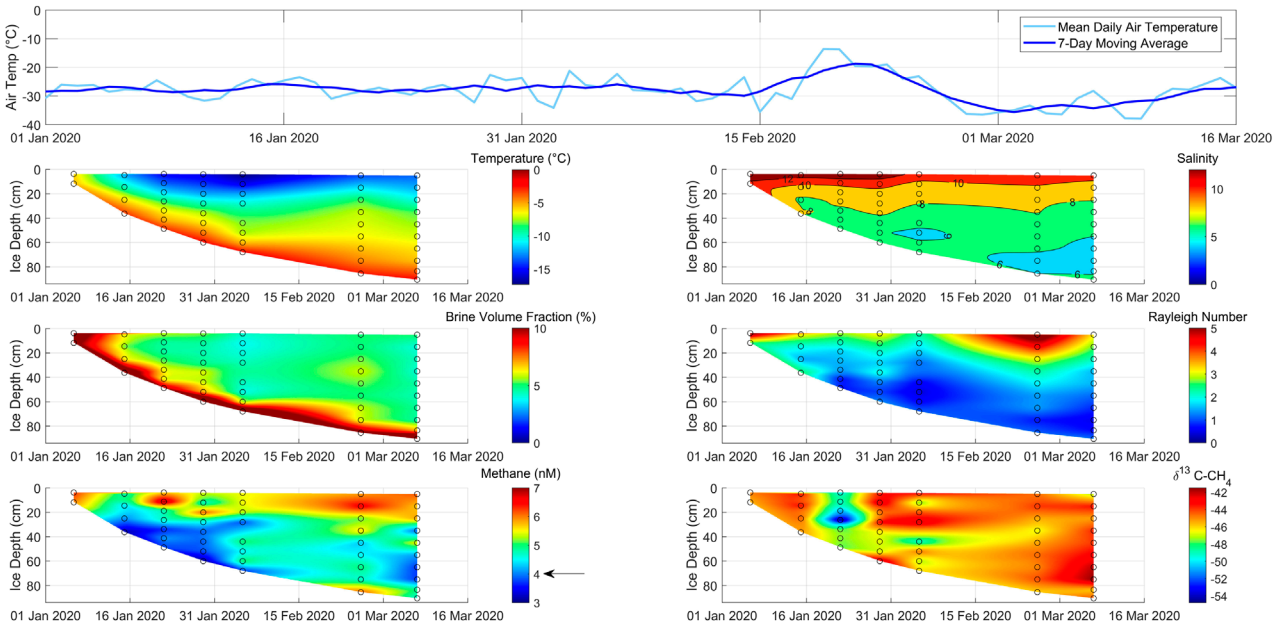

FIGURE 3
Time series of air temperature above and physical and chemical properties within growing lead ice at our main sampling site between 6 January and 7 March 2020 (location: see Figure 1). The black arrow in the bottom left panel marks the methane concentration in seawater.

fast, strong cooling in still-permeable lead ice (see Discussion) (Figure 2B).

3.2 Phases of lead ice formation—the time series

We analyzed the concentration and stable carbon isotope ratio of methane in lead ice and used the methane concentration and $\delta^{13}C–CH_4$ ratio in surface seawater immediately measured before lead opening as our values at time zero (t = 0). Surface seawater was in equilibrium or slightly supersaturated (less than 10%) relative to the atmosphere, while the $\delta^{13}C–CH_4$ ratios of dissolved methane in seawater deviated by 8‰–10‰ ^{13}C-enrichment from the Arctic atmospheric equilibrium $\delta^{13}C–CH_4$ signature (≈−47.5‰; White et al., 2018).

Figure 3 shows lead ice measurements during the 2-month sampling period. We divided this period into five different phases to highlight different predominant processes of lead ice evolution in the following subsections.

3.2.1 Phase I: initial lead ice formation

The first sampling occurred 2 days after the lead opened on 4 January. During this 2-day period, the ice grew 15 cm thick, and its surface temperature decreased from seawater temperature to −5.9°C. The complete ice layer was still permeable with BVFs >10% (Figures 3, 4). The temperature decrease increased the MSC-II therein by approximately 20% compared to the MSC in seawater (Figure 2A). However, our measurements show that methane was not undersaturated during this time. In addition, we observed $\delta^{13}C–CH_4$ values depleted in ^{13}C in lead ice compared to the marine methane background (Figure 3).

3.2.2 Phase II: brine drainage

A week later, on January 15, the surface-ice temperature had dropped to −12°C while the ice thickness increased to 36 cm. Due to the strong cooling, the BVF decreased from approximately >10% to 6% in the uppermost layer (Figure 3). While this represented the strongest BVF decrease over the whole observation period, the lead ice was still permeable. The linear decrease in salinity down to 25 cm revealed brine rejection over most of Phase II, which was initiated by the strong negative temperature gradient. Attributed to the salinity decrease, the methane concentration decreased as well, reflecting the discharge of dissolved methane coupled to brine loss. Remarkably, the methane concentration decreased by approximately 20% compared to the concentration during Phase I. Accordingly, lead ice changed from being saturated during Phase I to being undersaturated during Phase II related to MSC-II (Figure 2). The $\delta^{13}C–CH_4$ ratio shifted to values slightly enriched in ^{13}C compared to the $\delta^{13}C–CH_4$ ratio during Phase I (Figure 3).

3.2.3 Phase III: formation of an impermeable subsurface layer

Another week later, on 22 January, the surface ice temperature had dropped to −16°C, and the ice thickness increased to 48 cm. The ongoing cooling resulted in a decrease in the BVF to less than 5% between 10 and 20 cm. Thus, a subsurface impermeable layer (SSIL) had started to form, while due to slightly higher bulk salinity, the surface layer remained permeable (Figures 3, 4). The interrupted vertical brine exchange influenced the vertical gradients of methane concentration and $\delta^{13}C–CH_4$ ratios. At the interface between the upper permeable layer and the SSIL, we detected a peak in concentration, which resulted in a level of concentration similar to Phase I. Below the SSIL, the concentration

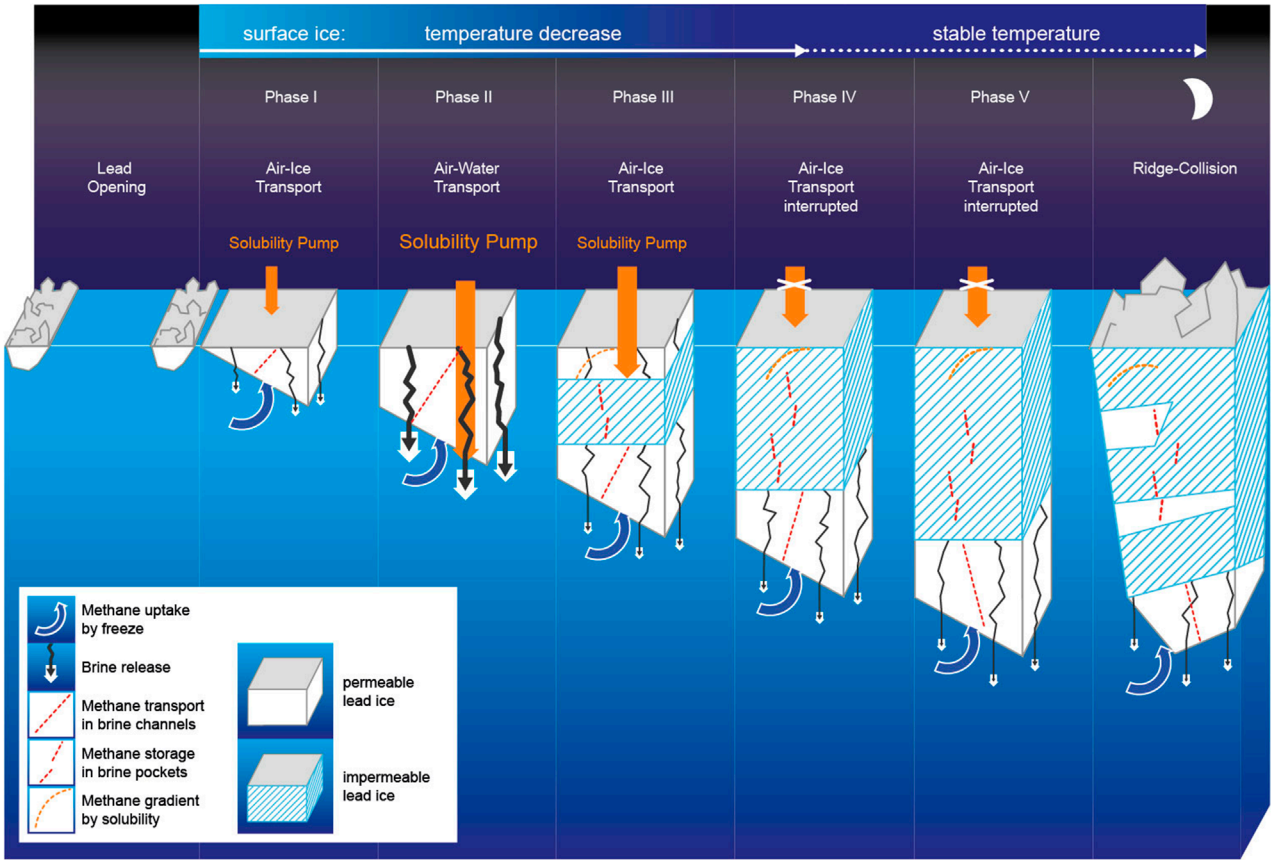

FIGURE 4
Temporal development of growing lead ice between lead opening and closing. The temperature decrease in surface ice is most pronounced during the first 10 days. Gradients of methane concentration (dashed red lines) in lead ice result from 1) the entrapment of dissolved methane at the ice–seawater interface (methane uptake), 2) the loss to seawater triggered by brine release, and 3) methane uptake at the ice–air interface. Strong cooling initiated a methane pump. The top-down transport stopped when a subsurface impermeable layer formed, while ongoing uptake at the ice–air interface created the methane excess in the upper, still-permeable lead ice layer.

remained similar to that during Phase II. The lead ice also remained slightly undersaturated due to MSC-II conditions similar to Phase II (Figure 2). The $\delta^{13}C$–CH_4 gradient showed the most evident shift toward a depletion in ^{13}C related to earlier phases at the interface between the SSIL and the lower permeable layer (Figure 3).

3.2.4 Phase IV: lead ice consolidation

After 3 weeks of continuous decrease at the ice surface, the temperature remained stable at about −16°C for the first time while the ice thickness increased to 60 cm. Changes in BVF remained small and restricted to the layer between 20 cm and 35 cm, causing a thickening of the SSIL. The concentration profile was comparable to Phase III. The $\delta^{13}C$–CH_4 profile strongly deviated from the profile from the previous phase but conformed to the profile of Phase II. In addition, this profile showed large variations from the surface up to the bottom of the SSIL, but changes were less pronounced in the permeable layer underneath the SSIL (Figure 3).

3.2.5 Phase V: formation of C-shaped concentration profiles

The ice temperature at the surface reached a minimum at the beginning of February, while within the bottom ice, the temperature minimum was reached 4 weeks later at the beginning of March. In total, lead ice grew to 90 cm. Although the impermeable layer comprised up to 75% of the whole thickness, the thickness of the permeable bottom layer slightly increased relative to the first month. Accordingly, the concentration profiles developed from half-C-shaped to mainly C-shaped (Figures 3, 4). The methane excess related to the seawater background that developed at the lead ice surface during the first month was preserved. Within the impermeable layer, the concentration profiles showed vertical, small-scaled variations. Although the methane concentration increased relative to the first month, the permeable bottom layer remained undersaturated relative to MSC-II. The $\delta^{13}C$–CH_4 ratio varied less. In general, we observed a ^{13}C-enrichment during phase V compared to previous phases in the permeable bottom layer (Figure 3).

3.3 Short-lived ice structures

In addition to ice collected from the same lead during the 2-month observation period, we sampled thin new ice less than a week old and frost flowers at several other places between January and the beginning of May to evaluate the impact of the first freeze phase on methane uptake and discharge, respectively (Figures 1, 2C).

4 Discussion

This study presents methane concentration and $\delta^{13}C–CH_4$ ratio measurements in lead ice grown in winter. On the one hand, we observed how the freeze up conditions during the first weeks of ice growth influenced the incorporation of dissolved methane in lead ice. On the other hand, we noted how the growth conditions during a 2-month period shaped the methane distribution therein. To evaluate spatial variabilities during the freeze up phase, we sampled several additional spots of newly formed, thin lead ice and frost flowers spread on the same floe (Figure 1).

Seawater underneath the floe was in equilibrium or slightly supersaturated (10%) relative to the atmospheric methane background concentration during the whole study period (Figures 3, 4). Hence, methane uptake from seawater into growing lead ice remained unaffected by methane transported from remote sources toward the interior Arctic (Xin et al., 2013; Damm et al., 2018; Manning et al., 2022; Vinogradova et al., 2022). Furthermore, as our study was carried out during the dark season, we exclude any potential influence on our results from photochemical methane production or oxidation (Li et al., 2020) and postulate that methane-related microbial activities (Valentine, 2002; Damm et al., 2010; Damm et al., 2015; Uhlig et al., 2018) therein remain negligible due to the short life cycle of lead ice.

Although time-invariant in seawater, we discovered pronounced shifts in methane distribution in aging lead ice, reflecting the impact of changes in freezing conditions during different ice growth phases. Intense cooling occurred during the first month when two-thirds of the complete ice thickness grew, while the speed of growth decreased by 50% during the second month when cooling ceased at the ice surface and clearly slowed within the lead ice (Figure 5). Differentiation of two distinct temperature regimes during lead ice formation exposed counterintuitive impacts of freezing on methane circulation within lead ice. The chronology of cooling appeared to be especially relevant for the temporally restricted uptake of methane by the ocean from the atmosphere.

4.1 Strong freeze initiating a methane pump

Lead opening in winter exposes the relatively warm underlying seawater to the cold air, resulting in rapid ice formation and growth by heat loss to the atmosphere. Strong brine entrapment affected by fast freeze causes high bulk salinities within the newly formed lead ice (Perovich and Gow, 1996). Indeed, we detected bulk surface salinities higher than those in FYI grown at the same time on this floe (Figure 6; Angelopoulos et al., 2022). A fast freeze favors upward brine expulsion to the surface ice layer (Notz and Worster, 2009). Pronounced half-C-shaped profiles of bulk salinity confirmed this upward-directed brine transport (Figures 3, 6). Exposing the highest-saline layer to the cold ice surface provoked counterintuitive physical properties: despite an ongoing strong freeze, the newly formed lead ice remained permeable for longer than 2 weeks (Figures 3, 4). Considering permeable ice as an open system (Golden et al., 2007), newly formed lead ice favors gas exchange coupled with brine migration between both interfaces, that is, to the atmosphere and ocean during that period.

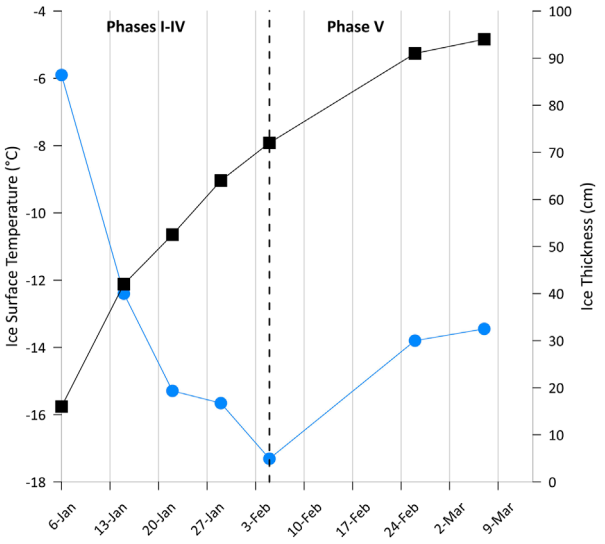

FIGURE 5
Decrease in ice surface temperature (blue dots) and increase in ice thickness (black squares) during the 2-month time series. Intense cooling resulted in a growth of more than 2/3 of the entire ice thickness in the first month.

In addition to affecting the physical properties, strong cooling also influenced the chemical properties, increasing the methane solubility at the ice surface and promoting in-gassing from the atmosphere (Figure 2). An eventual strong freeze induced a pronounced shift in the MSC-II in permeable lead ice compared to the MSC in seawater underneath. More precisely, accounting for the cooling of migrating brine to approximately −6°C causes an increase in MSC-II by approximately 20% related to the MSC of seawater (Figure 2). Therefore, seawater saturated with methane should induce an undersaturation related to MSC-II when the uptake of dissolved marine methane in permeable lead ice occurs. However, we observed methane saturation relative to MSC-II in lead ice, while methane was supersaturated relative to MSC in seawater. Consequently, the increase in solubility in permeable lead ice induced a solubility pump transporting methane downward through lead ice. Uptake at the ice surface might occur directly by dissolution of gaseous atmospheric methane or via an intermediate step, that is, indirectly by re-dissolution of methane previously released from high-saline frost flowers.

Cooling to −12°C further increased MSC-II (Figure 2), promoting continued dissolution of gaseous methane at the lead

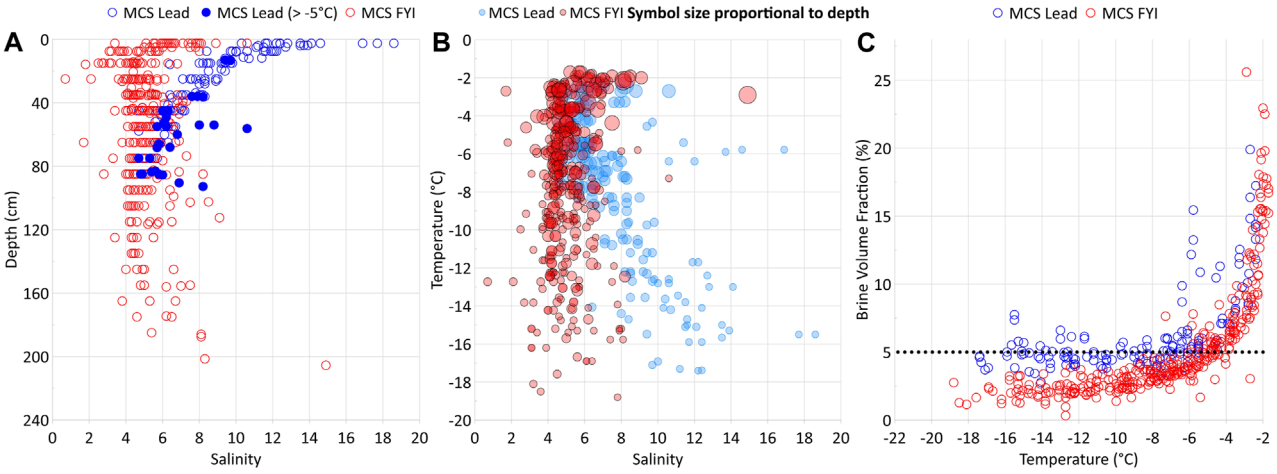

FIGURE 6
Salinity versus ice depth **(A)**, temperature versus salinity **(B)**, and brine volume fraction (BVF) versus temperature **(C)** in lead ice (blue dots) compared to first-year ice (red dots) from the main coring site (MCS FYI) in the Central Observatory during the MOSAiC drift expedition (locations see Figure 1). Salinities and BVF in lead ice grown in winter were generally higher than in FYI that developed on the same floe in early autumn. Lead ice remained completely permeable for more than 2 weeks.

ice–air interface but also causing squeezing and subsequent gravity brine drainage. The "squeezing" caused a loss of methane by brine rejection, shown by the reduced concentration compared to the former phase at the lead ice surface. The interaction of the two processes initiated an incipient top-down transport of dissolved methane through the more than 30-cm-thick permeable lead ice layer (Figure 4). The ongoing uptake at the surface partly counterbalanced the loss by brine drainage and initiated a brief steady state period reflected in linear concentration and solubility gradients (Figures 3, 4). However, this period ceased before the end of Phase II. The convex-shaped concentration gradient pointed to an interrupted downward transport when the bottom layer grew.

Finally, cooling to −16°C resulted in the formation of a subsurface impermeable layer (SSIL), while the surface layer remained permeable due to the slightly higher bulk salinity. The SSIL separated the formerly complete permeable lead ice into an upper and lower permeable layer, interrupted the top-down brine drainage, and stopped the methane pump (Figures 3, 4). In impermeable ice, brine movement stops, but the brine is stored in isolated pockets (Golden et al., 2007; Crabeck et al., 2019). Hence, the formation of the SSIL caused a temporal offset in terms of methane stored in lead ice. While the SSIL preserves "frozen-in relicts" of earlier phases of ice formation, the permeable top and bottom layers mirror the impact of ongoing exchange at the interfaces between the ice surface and atmosphere on the one side and seawater on the other side. Indeed, methane uptake at the permeable top layer proceeded as cooling continued. Because the SSIL from that point on inhibited the downward transport, a methane excess on top of the SSIL developed (Figures 3, 4). By comparison, underneath the SSIL, methane loss by brine discharge continued from the permeable bottom layer to seawater. As uptake at the air–ice interface and loss at the ice–ocean interface took place contemporaneously, the concentration profiles changed from linear to half-C-shaped. This shift in gradients clearly assigned counter-rotating methane pathways when lead ice started to convert from completely permeable to partly impermeable (Figures 3, 4).

4.2 The shift from half-C- to C-shaped methane profiles

After a month, cooling at the surface ceased, disrupting the increase in solubility, and therefore, methane uptake at the air–ice interface stopped. At the same time, the lead ice surface became impermeable, enclosing the methane excess formed in the first month in disconnected brine pockets (Figures 3, 4). By comparison, cooling slowed but continued in subsurface lead ice. Consequently, the thicknesses of both the SSIL and the permeable bottom layer still increased, but brine release from the permeable layer weakened, as shown by the low Rayleigh numbers (Figure 3). The restricted brine release also reduced the loss of methane. Due to the gradient between MSC in seawater and MSC-II in open brine channels, methane replenishment from seawater into the highly permeable bottom layer started to occur at this point (Figures 2, 4). Accordingly, the former half-C-shaped concentration profiles developed toward rather C-shaped concentration profiles during the fifth and last phase, that is, the second month (Figure 4). Remarkably, this shift reflects how the strong freeze during the first month shaped the concentration profiles compared to the second month when mainly ice growth shaped the profiles, that is, either brine/methane release or ice growth/methane uptake dominated.

4.3 Isotopic fractionation effects during a strong freeze

While surface seawater was saturated to just slightly supersaturated, the $\delta^{13}C$–CH_4 ratios in seawater clearly deviated

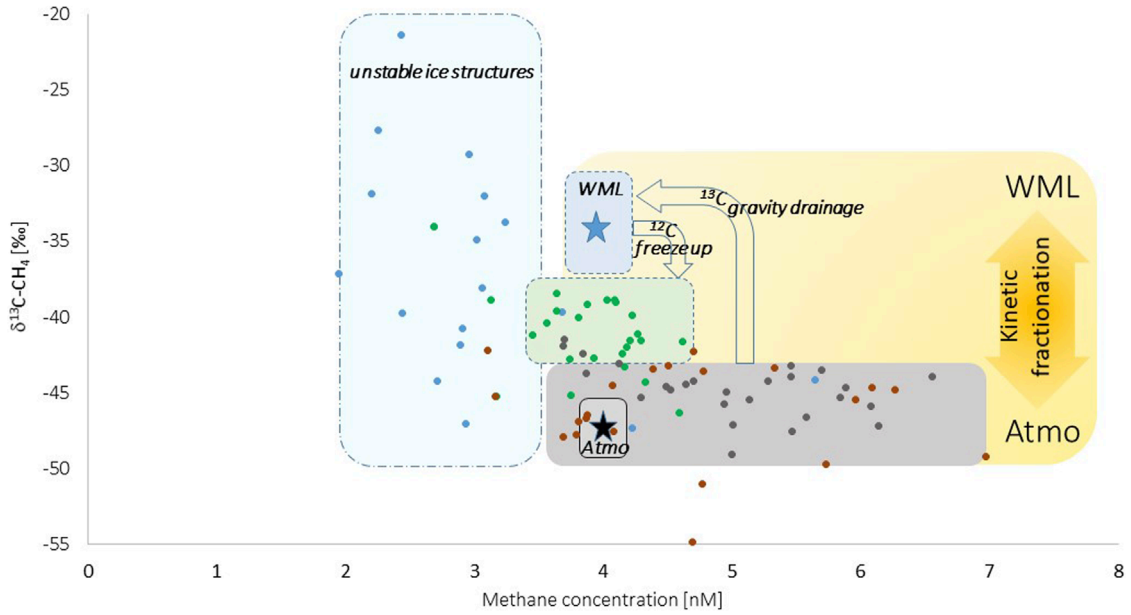

FIGURE 7
$\delta^{13}C–CH_4$ ratios related to methane concentration in newly formed lead ice (green dots) and lead ice from the time series (first and second month: brown and gray dots, respectively). The blue star in the blue field represents the range in surface seawater, that is, the winter mixed layer (WML), and the black star represents the atmospheric background. Freeze up and brine discharge induced shifts in $\delta^{13}C–CH_4$ ratios between methane dissolved in seawater and brine. Seawater was saturated to slightly supersaturated with methane, while the $\delta^{13}C–CH_4$ ratio in seawater was clearly enriched in ^{13}C compared to the atmospheric background signature. This pattern points to gravity-triggered brine drainage as the main pathway for losing methane from lead ice. Note: The analyses of $\delta^{13}C–CH_4$ ratios might be influenced by the low concentrations in frost flowers (unstable ice structures; blue dots), finally contributing to the large variations in $\delta^{13}C–CH_4$ ratios.

from the atmospheric equilibrium. Based on the atmospheric background of −47.5‰ (White et al., 2018) and taking into account up to 1‰ ^{13}C-enrichment in seawater by kinetic isotopic fractionation (KIF) at the water–air interface (Knox et al., 1992; Happell et al., 1995), the $\delta^{13}C–CH_4$ ratio in surface seawater equilibrated with the atmosphere results in −46.5‰ VPDB. However, the $\delta^{13}C–CH_4$ ratio in seawater deviated by 8‰–10‰ ^{13}C-enrichment from the atmospheric equilibrium value during the winter study. Remarkably, this pronounced shift even exceeded up to 5‰ of the ^{13}C-enrichment detected during the melt season in this area (Damm et al., 2015; Verdugo et al., 2021). Seasonally altering $\delta^{13}C–CH_4$ ratios in seawater points to impacts of the sea ice life cycle on the marine methane pool by KIF effects. KIF effects are caused by the higher binding energy of the heavier isotopic molecule (^{13}C), resulting in a lower mobility than the lighter isotopic molecule (^{12}C) (Mook, 1994). Consequently, seasonal variations in $\delta^{13}C–CH_4$ ratios reveal a shift in the relative abundance of the ^{12}C and ^{13}C isotopes obviously related to melting and freezing processes.

Indeed, a ^{13}C-depletion by at least 2‰ in newly formed lead ice related to the methane pool in seawater points to a higher abundance of the lighter (^{12}C) isotope when marine methane became enclosed in brine (Figure 7). The ^{13}C-depletion evidently strengthened when brine discharge occurred, as shown by the shift in $\delta^{13}C–CH_4$ ratios between newly formed and older lead ice (Figure 7). As occurring in the opposite direction than uptake, gravity favored the higher abundance of the heavier (^{13}C) isotope on its way back to seawater, reinforcing on one side ^{13}C-depletion in brine-methane and on the other side ^{13}C-enrichment in marine methane.

At the ice–air interface, methane dissolution induced by the solubility pump also contributed to $\delta^{13}C–CH_4$ ratio shifts in lead ice. Caused by differences in the molecular transfer rates of the lighter and heavier isotope (Mook, 1994), dissolution initiates a shift toward a ^{13}C-enrichment in the relative abundance of the ^{12}C and ^{13}C isotopes, ultimately weakening the ^{13}C-depletion in lead ice formerly induced by the KIF effect during ice formation. Consequently, because brine drainage and dissolution take place simultaneously and both processes partly counterbalance each other, $\delta^{13}C–CH_4$ ratios just vary less in aging lead ice.

4.4 Fast phase changes in frost flowers

Ice growth under winter conditions results in highly saline surface skim, often additionally covered by frost flowers. Frost flowers frequently develop at the surface of new sea ice, especially when the temperature gradient between surface ice and the overlaying atmosphere is large, and wind speeds are low. Initially, frost flowers are frozen freshwater, as they grow from the vapor phase, but the ice crystals wick up the brine from the surface of the sea ice, producing salinities of up to 180 PSU (Perovich and Richter-Menge, 1994; Domine et al., 2005). Their crystal-shaped configuration tends to provide a high total surface area of up to

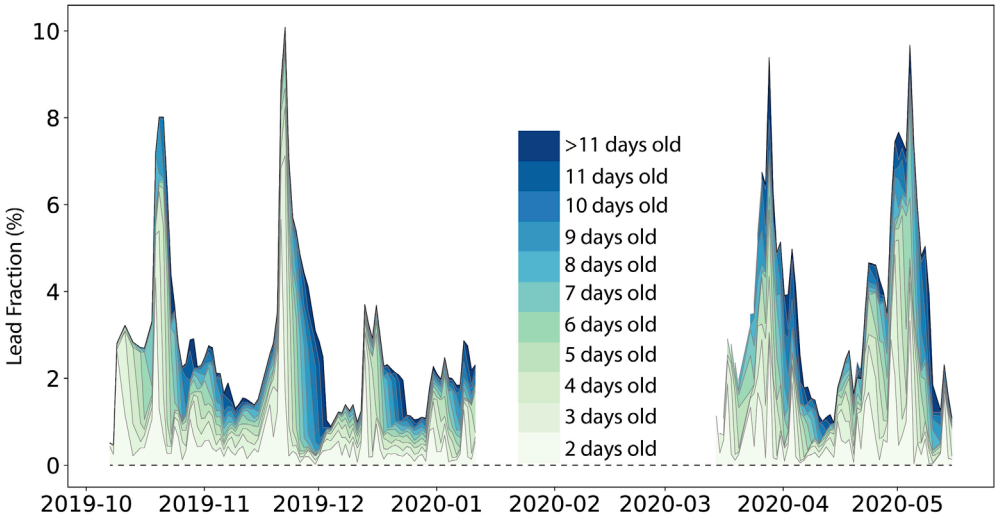

FIGURE 8
Lead fractions averaged in a circle with a 10 km radius around the RV *Polarstern* during the MOSAiC drift from 7 Oct 2019 to 15 May 2020. Colors indicate the percentage of leads of different ages between 2 days and > 11 days.

1000 m^2 of ice surface (Domine et al., 2002), suggesting that frost flowers are sites for enhanced exchanges and chemical reactions (Rankin et al., 2002). These circumstances might also induce fast but pronounced shifts in the methane solubility capacity at the ice surface. Consequently, lead ice covered by frost flowers is a favored environment for phase changes between gaseous and dissolved methane. However, in opposition to the one-way direction of phase changes due to temperature decrease, the high variability in salinity at the ice surface during the life cycle of frost flowers enables phase changes in both directions. While low salinities in freshly formed frost flowers favor the dissolution of gaseous methane, increasing salinity induces a backward phase change, that is, a shift from dissolved to gaseous methane despite strong freezing. Large variations in $\delta^{13}C–CH_4$ ratios in frost flowers compared to those in lead ice potentially might refer to pronounced KIF effects by phase changes (Figure 7). However, we cannot exclude that the low concentrations affected the analyses of the $\delta^{13}C–CH_4$ ratios, finally inducing the large variations in $\delta^{13}C–CH_4$ ratios. To prove the proposed processes, *in situ* studies on frost flowers are required in the future.

4.5 Lead ice fraction in the new Arctic—an outlook

To estimate the Arctic-wide relevance of methane uptake at the ice surface on newly formed lead ice, we upscale our results with satellite observations of leads during MOSAiC. We use lead observations based on divergence previously presented in von Albedyll et al. (2023). With this dataset, we analyze the aerial coverage and lifetime of up to 10-day-old leads in a circle with a 10 km radius around MOSAiC and compare the results to circles with radii of 50 km, 100 km, and 150 km.

The mean aerial fraction (10-km scale) of up to 10-day-old leads was 3.2%, with a maximum of 10% (Figure 8). On 50% of the days, at least 2.5% of the area was covered by leads. Consequently, thin lead ice was an abundant feature of the sea ice cover. As shown above, the physical and chemical properties of up to 10–14-day-old lead ice mostly favored methane uptake at the lead ice surface. Von Albedyll et al. (2023) also showed that most of the leads during MOSAiC were short-lived (Figure 8). The median lifetime of leads was only 3 days, while only 2% of all leads did not close within 11 days. Thus, most of the leads during MOSAiC were an open system between the atmosphere and the ocean until an impermeable subsurface layer formed after this period.

The mean lead fractions from the MOSAiC expeditions on the 10 km scale (3.2%) are representative of the larger (50 km, 100 km, and 150 km) surroundings with a lead fraction of 3.1%–3.2%. However, some spatial lead dynamics differences emerge when the time series data are compared on a daily basis, resulting in a Pearson correlation coefficient of R = 0.6–0.7 (not shown).

Analyzing datasets from different Arctic regions, other studies found similar average lead fractions and maximum lifetimes of leads (Wadhams, 2000; Reiser et al., 2020; Hutter et al., 2023). Thus, we consider our estimates of lead aerial fraction and lifetime representative for a larger region and time beyond the drift of MOSAiC. Consequently, uptake at the ice surface and pumping through thin lead ice is a significant yet unconsidered methane pathway in the Arctic. The relevance of this process may even increase when the Arctic fully transitions into a seasonally ice-covered ocean where leads may be more abundant than in the central ice pack (Kwok et al., 2006).

5 Conclusion

Estimates of the occurrence and frequency of young lead ice from satellite observations highlight the relevance of this ice type in a warming Arctic. Our process study of rapid lead ice growth conditions and properties in winter has identified some

previously unconsidered methane pathways between sea ice, ocean, and atmosphere.

1) Fast brine entrapment can keep newly formed lead ice completely permeable for up to 2 weeks. During that period, the imbalanced effect of temperature decrease and salinity increase on the methane solubility capacity leads to physical conditions that support a top-down methane pump. The decrease in surface temperature triggers how long methane uptake can occur.
2) The time variable onset of impermeable conditions in the ice column results in vertical methane gradients that reflect concurrent ongoing transport processes and storage of methane in "frozen-in" zones. Identifying temporal delays of those freeze effects on methane gradients in ice cores will contribute to an improved interpretation of the methane "history" stored in single, "snapshot" ice cores taken later in the season.
3) We show for the first time that freeze strongly affects the $\delta^{13}C–CH_4$ ratios in seawater and newly formed lead ice, resulting, on the one hand, in seasonal shifts of the isotopic signature in the marine methane pool and, on the other hand, in a clear enrichment of the ^{13}C isotope of marine methane compared to the atmospheric background signature.
4) The revealed methane pathways highlight an intense circulation of methane between seawater and sea ice during freeze. In comparison, the air–ice interaction is restricted to phases when physical conditions enable air-to-ice in-gassing.

Data availability statement

The raw data presented in the study are available in PANGAEA. Further inquiries can be directed to the corresponding author.

Author contributions

ED: conceptualization, data curation, formal analysis, funding acquisition, investigation, methodology, project administration, resources, visualization, and writing–original draft. ST: conceptualization, formal analysis, funding acquisition, methodology, and writing–original draft. MA: data curation, investigation, methodology, visualization, writing–review and editing, and formal analysis. LV: conceptualization, methodology, visualization, and writing–original draft. AR: data curation, validation, and writing–review and editing. CH: funding acquisition, validation and writing–review and editing.

Funding

The author(s) declare that financial support was received for the research, authorship, and/or publication of this article. The work was funded by the German Federal Ministry for Education and Research (BMBF) through financing the Alfreds Wegener-Institut Helmholtz Zentrum für Polar-und Meeresforschung (AWI) and the RV Polarstern expedition PS122 under grant N-2014-H-060_ Dethloff and the AWI through its project: AWI_BGC. The work carried out and data used in this manuscript were produced as part of the International Multidisciplinary Drifting Observatory for the Study of the Arctic Climate (MOSAiC) with the tag MOSAiC20192020. ST was supported by DFG—priority program SPP 1158 by the following grant: TH744/7-1.

Acknowledgments

We thank all persons involved in the expedition of the Research Vessel RV Polarstern during MOSAiC in 2019–2020 (AWI_PS122_ 00) as listed in Nixdorf et al. (2021). We highly thank all the participants for the fieldwork in the Central Observatory, especially Patric Simones Pereira, Adela Dumitrescu, Torsten Sachs, and Hans Werner Jacobi, who contributed to sampling thin new ice and frost flowers in the field.

Conflict of interest

The authors declare that the research was conducted in the absence of any commercial or financial relationships that could be construed as a potential conflict of interest.

Publisher's note

Supplementary material

The Supplementary Material for this article can be found online at: https://www.frontiersin.org/articles/10.3389/feart.2024.1338246/full#supplementary-material

References

Angelopoulos, M., Damm, E., Simões Pereira, P., Abrahamsson, K., Bauch, D., Bowman, J., et al. (2022). Deciphering the properties of different arctic ice types during the growth phase of MOSAiC: implications for future studies on gas pathways. *Front. Earth Sci.* 10. doi:10.3389/feart.2022.864523

Assur, A. (1960). *Composition of sea ice and its tensile strength*, 44. Wilmette, Illinois: US Army Snow, Ice and Permafrost Research Establishment.

Bartels-Rausch, T., Kong, X., Orlando, F., Artiglia, L., Waldner, A., Huthwelker, T., et al. (2021). Interfacial supercooling and the

precipitation of hydrohalite in frozen NaCl solutions as seen by X-ray absorption spectroscopy. *Cryosphere* 15, 2001–2020. doi:10.5194/tc-15-2001-2021

Boutin, G., Ólason, E., Rampal, P., Regan, H., Lique, C., Talandier, C., et al. (2023). Arctic sea ice mass balance in a new coupled ice–ocean model using a brittle rheology framework. *Cryosphere* 17, 617–638. doi:10.5194/tc-17-617-2023

Cox, G. F. N., and Weeks, W. F. (1983). Equations for determining the gas and brine volumes in sea-ice samples. *J. Glaciol.* 29, 306–316. doi:10.1017/s0022143000008364

Crabeck, O., Galley, R. J., Mercury, L., Delille, B., Tison, J. L., and Rysgaard, S. (2019). Evidence of freezing pressure in sea ice discrete brine inclusions and its impact on aqueous-gaseous equilibrium. *J. Geophys. Res. Oceans* 124, 1660–1678. doi:10.1029/2018JC014597

Damm, E., Bauch, D., Krumpen, T., Rabe, B., Korhonen, M., Vinogradova, E., et al. (2018). The transpolar drift conveys methane from the siberian shelf to the central Arctic Ocean. *Sci. Rep.* 8, 4515. doi:10.1038/s41598-018-22801-z

Damm, E., Helmke, E., Thoms, S., Schauer, U., Nöthig, E., Bakker, K., et al. (2010). Methane production in aerobic oligotrophic surface water in the central Arctic Ocean. *Biogeosciences* 876, 1099–1108. doi:10.5194/bg-7-1099-2010

Damm, E., Rudels, B., Schauer, U., Mau, S., and Dieckmann, G. (2015). Methane excess in arctic surface water- triggered by sea ice formation and melting. *Sci. Rep.* 5, 16179. doi:10.1038/srep16179

Domine, F., Cabanes, A., and Legagneux, L. (2002). Structure, microphysics, and surface area of the Arctic snowpack near Alert during the ALERT 2000 campaign. *Atmos. Environ.* 36, 2753–2765. doi:10.1016/s1352-2310(02)00108-5

Domine, F., Taillandier, A. S., Simpson, W. R., and Severin, K. (2005). Specific surface area, density and microstructure of frost flowers. *Geophys. Res. Lett.* 32, L13502. doi:10.1029/2005GL023245

Fukusako, S. (1990). Thermophysical properties of ice, snow, and sea ice. *Int. J. Thermophys.* 11, 353–372. doi:10.1007/BF01133567

Golden, K. M., Eicken, H., Heaton, A. L., Miner, J., Pringle, D. J., and Zhu, J. (2007). Thermal evolution of permeability and microstructure in sea ice. *Geophys. Res. Lett.* 34. doi:10.1029/2007GL030447

Gourdal, M., Crabeck, O., Lizotte, M., Galindo, V., Gosselin, M., Babin, M., et al. (2019). Upward transport of bottom-ice dimethyl sulfide during advanced melting of arctic first-year sea ice. *Elem. Sci. Anthr.* 7. doi:10.1525/elementa.370

Haas, C., Hoppmann, M., Tippenhauer, S., and Rohardt, G. (2021). Continuous thermosalinograph oceanography along RV POLARSTERN cruise track PS122/2. *PANGAEA*. doi:10.1594/PANGAEA.930024

Happell, J. D., Chanton, J. P., and Showers, W. J. (1995). Methane transfer across the water-air interface in stagnant wooded swamps of Florida: evaluation of mass-transfer coefficients and isotropic fractionation. *Limnol. Oceanogr.* 40 (2), 290–298. doi:10.4319/lo.1995.40.2.0290

Hutter, N., Hendricks, S., Jutila, A., Ricker, R., von Albedyll, L., Haas, C., et al. (2023). Digital elevation models of the sea-ice surface from airborne laser scanning during MOSAiC. *Sci. Data* 10, 729. doi:10.1038/s41597-023-02565-6

Katlein, C., Mohrholz, V., Sheikin, I., Itkin, P., Divine, D. V., Stroeve, J., et al. (2020). Platelet ice under arctic pack ice in winter. *Geophys. Res. Lett.* 47, e2020GL088898. doi:10.1029/2020GL088898

Kiditis, V., Upstill-Goddard, R. C., and Anderson, L. (2010). Methane and nitrous oxide in surface water along the north-west passage, Arctic Ocean. *Mar. Chem.* 121 (issue 1-4), 80–86. doi:10.1016/j.marchem.2010.03.006

Knox, M., Quay, P. D., and Wilbur, D. (1992). Kinetic isotopic fractionation during air-water gas transfer of 0_2, N_2, CH_4, and H_2. *J. Geophys. Res.* 97 (C12), 335–343.

Kort, E. A., Wofsy, S. C., Daube, B. C., Diao, M., Elkins, J. W., Gao, R. S., et al. (2012). Atmospheric observations of Arctic Ocean methane emissions up to 82° north. *Nat. Geosci.* 5, 318–321. doi:10.1038/ngeo1452

Krumpen, T., Belter, H. J., Boetius, A., Damm, E., Haas, C., Hendricks, S., et al. (2019). Arctic warming interrupts the Transpolar Drift and affects long-range transport of sea ice and ice-rafted matter. *Sci. Rep.* 9, 5459. doi:10.1038/s41598-019-41456-y

Kwok, R. (2006). Contrasts in sea ice deformation and production in the Arctic seasonal and perennial ice zones. *J. Geophys. Res.* 111, C11S22. doi:10.1029/2005jc003246

Kwok, R. (2018). Arctic sea ice thickness, volume, and multiyear ice coverage: losses and coupled variability (1958–2018). *Environ. Res. Lett.* 13 (10), 105005. doi:10.1088/1748-9326/aae3ec

Li, Y., Fichot, C. G., Geng, L., Scarratt, M. G., and Xie, H. (2020). The contribution of methane photoproduction to the oceanic methane paradox. *Geophys. Res. Lett.* 47. doi:10.1029/2020GL088362

Manning, C. C. M., Zheng, Z., Fenwick, L., McCulloch, R. D., Damm, E., Izett, R. W., et al. (2022). Interannual variability in methane and nitrous oxide concentrations and sea-air fluxes across the north American Arctic Ocean (2015–2019). *Glob. Biogeochem. Cycles* 36 (4), e2021GB007185. doi:10.1029/2021GB007185

Mook, W. (1994). Principles of isotope hydrology. Introductory course on Isotope Hydrology. *Dep. Hydrogeol. Geogr. Hydrol.* VU Amsterdam, Amsterdam.

Nicolaus, M., Perovich, D. K., Spreen, G., Granskog, M. A., Albedyll, L., Angelopoulos, M., et al. (2022). Overview of the MOSAiC expedition-Snow and sea ice. *Elem. Sci. Anthropocene* 10 (1). doi:10.1525/elementa.2021.000046

Nixdorf, U., Dethloff, K., Rex, M., Shupe, M., Sommerfeld, A., Perovich, D. K., et al. (2021). MOSAiC extended acknowledgement. doi:10.5281/zenodo.5179739

Notz, D. (2005). *Thermodynamic and fluid-dynamical processes in sea ice*. University of Cambridge. Ph. D. thesis.

Notz, D., and Worster, M. G. (2009). Desalination processes of sea ice revisited. *J. Geophys. Res.* 114. doi:10.1029/2008JC004885

Ólason, E., Rampal, P., and Dansereau, V. (2021). On the statistical properties of sea-ice lead fraction and heat fluxes in the Arctic. *Cryosphere* 15, 1053–1064. doi:10.5194/tc-15-1053-2021

Perovich, D. K., and Gow, A. J. (1996). A quantitative description of sea ice inclusions. *J. Geophys. Res.* 101 (C8), 18327–18343. doi:10.1029/96jc01688

Perovich, D. K., and Richter-Menge, J. A. (1994). Surface characteristics of lead ice. *J. Geophys. Res.* 99 (C8), 16341–16350. 16,341-16,350. doi:10.1029/94jc01194

Pohlmann, J. W., Casso, M., Magen, C., and Bergeron, E. (2021). Discrete sample introduction Module for quantitative and isotopic analysis of methane and other gases by cavity ring-down spectroscopy. *Environ. Sci. Technol.* 55 (17), 12066–12074. 12,066-12,074. doi:10.1021/acs.est.1c01386

Rabe, B., Heuzé, C., Regnery, J., Aksenov, Y., Allerholt, J., Athanase, M., et al. (2022). Overview of the MOSAiC expedition- Physical oceanography. *Elem. Sci. Anthropocene* 10 (1). doi:10.1525/elementa.2021.00062

Rankin, A. M., Wolff, E. W., and Martin, S. (2002). Frost flowers: implications for tropospheric chemistry and ice core interpretation. *J. Geophys. Res.* 107 (D23), 4683. doi:10.1029/2002JD002492

Rantanen, M., Karpechko, A. Y., Lipponen, A., Nordling, K., Hyvärinen, O., Ruosteenoja, K., et al. (2022). The Arctic has warmed nearly four times faster than the globe since 1979. *Commun. Earth Environ.* 3, 168. doi:10.1038/s43247-022-00498-3

Reiser, F., Willmes, S., and Heinemann, G. (2020). A new algorithm for daily sea ice lead identification in the arctic and antarctic winter from thermal-infrared satellite imagery. *Remote Sens.* 12, 1957. doi:10.3390/rs12121957

Rella, C. W., Hoffnagle, J., He, Y., and Tajima, S. (2015). Local- and regional-scale measurements of CH₄, δ¹³CH₄, and C₂H₆ in the Uintah Basin using a mobile stable isotope analyzer. *Atmos. Meas. Tech.* 8, 4539–4559. doi:10.5194/amt-8-4539-2015

Rosenfeld, D., and Woodley, W. (2000). Deep convective clouds with sustained supercooled liquid water down to -37.5 °C. *Nature* 405 (6785), 440–442. doi:10.1038/35013030

Serreze, M. C., and Barry, R. G. (2011). Processes and impacts of Arctic amplification: a research synthesis. *Glob. Planet. Change* 77, 85–96. doi:10.1016/j.gloplacha.2011.03.004

Shupe, M. D., Rex, M., Blomquist, B., Persson, P. O. G., Schmale, J., Uttal, T., et al. (2022). Overview of the MOSAiC expedition—atmosphere. *Elem. Sci. Anthropocene* 10 (1). doi:10.1525/elementa.2021.00060

Silyakova, A., Nomura, D., Kotovich, M., Fransson, A., Delille, B., Chierici, M., et al. (2022). Methane release from open leads and new ice following an Arctic winter storm event. *Pol. Sci.* 33, 100874. doi:10.1016/j.polar.2022.100874

Steiner, N. S., Lee, W. G., and Christian, J. R. (2013). Enhanced gas fluxes in small sea ice leads and cracks: effects on CO2 exchange and ocean acidification. *J. Geophys. Res. Oceans* 118, 1195–1205. doi:10.1002/jgrc.20100

Stroeve, J., and Notz, D. (2018). Changing state of Arctic sea ice across all seasons. *Environ. Res. Lett.* 13 (10), 103001. doi:10.1088/1748-9326/aade56

Sumata, H., de Steur, L., Divine, D. V., Granskog, M. A., and Gerland, S. (2023). Regime shift in Arctic ocean sea ice thickness. *Nature* 615, 443–449. doi:10.1038/s41586-022-05686-x

Tison, J. L., Delille, B., and Papadimitriou, S. (2017). "Gases in sea ice," in *Gases in sea ice* (Chichester, UK: John Wiley and Sons), 433–471. Chap. 18. doi:10.1002/9781118778371.ch18

Torsvik, T. (2023). Modeling influence of sea ice on gas exchanges between atmosphere and ocean in a global. *Earth Syst. Model.* Assembly 2023. doi:10.5194/egusphere-egu23-9684EGU

Uhlig, C., Kirkpatrick, J. B., D'Hondt, S., and Loose, B. (2018). Methane-oxidizing seawater microbial communities from an Arctic shelf. *Biogeosciences* 15, 3311–3329. doi:10.5194/bg-15-3311-2018

Uhlig, C., and Loose, B. (2017). Using stable isotopes and gas concentrations for independent constraints on microbial methane oxidation at Arctic Ocean temperatures. *Limnol. Oceanogr. Methods* 15, 737–751. doi:10.1002/lom3.10199

Valentine, D. L. (2002). Biogeochemistry and microbial ecology of methane oxidation in anoxic environments: a review. *Antonie Leeuwenhoek* 81, 271–282. doi:10.1023/a:1020587206351

Verdugo, J., Damm, E., and Nikolopoulos, A. (2021). Methane cycling within sea ice; results from drifting ice during late spring, north of svalbard. *Cryosphere* 15, 2701–2717. doi:10.5194/tc-15-2701-2021

Vinogradova, E., Damm, E., Pnyushkov, A. V., Krumpen, T., and Ivanov, V. (2022). Shelf-sourced methane in surface seawater at the eurasian continental slope (Arctic Ocean). *Front. Envir. Sci.* 8, 811375. doi:10.3389/fenvs.2022.811375

Von Albedyll, L., Hendricks, S., Grodofzig, R., Krumpen, T., Arndt, S., Belter, H. J., et al. (2022). Thermodynamic and dynamic contributions to seasonal Arctic sea ice thickness distributions from airborne observations. *Elem. Sci. Anthropocene* 10. doi:10.1525/elementa.2021.00074

Von Albedyll, L., Hendricks, S., Hutter, N., Murashkin, D., Kaleschke, L., Willmes, S., et al. (2023). Lead fractions from SAR-derived sea ice divergence during MOSAiC. *Cryosphere (Disc,)*. doi:10.5194/tc-2023-123

Wadhams, P. (2000). *Ice in the ocean*. London (UK): Gordon and Breach Science Publishers. 90-5699-296-1.

Weeks, W. F., and Ackley, F. S. (1986). "The growth, structure and properties of sea ice," in *Geophysics of sea ice*. Editor N. Untersteiner (London: Plenum press), 9–164. (NATO ASI series, B: Physics 146).

White, J., Vaughn, B. H., and Michel, S. (2018). University of Colorado, institute of arctic and alpine research (INSTAAR), stable isotopic composition of atmospheric methane (13C) from the NOAA ESRL carbon cycle cooperative global air sampling network, 1998–2017 (version 2018-09-24). Available at: ftp://aftp.cmdl.noaa.gov/data/trace_gases/ch4c13/flask/.

Wiesenburg, D. A., and Guinasso, N. L. (1979). Equilibrium solubilities of methane, carbon monoxide, and hydrogen in water and seawater. *J. Chem. Eng. Data* 24, 356–360. doi:10.1021/je60083a006

Wilchinsky, A. V., Heorton, H. D. B. S., Feltham, D. L., and Holland, P. R. (2015). Study of the impact of ice formation in leads upon the sea ice pack mass balance using a new frazil and grease ice parameterization. *J. Phys. Oceanogr.* 45, 2025–2047. doi:10.1175/jpo-d-14-0184.1

Willmes, S., Heinemann, G., and Schnaase, F. (2023). Patterns of wintertime Arctic sea-ice leads and their relation to winds and ocean currents. *Cryosphere* 17, 3291–3308. doi:10.5194/tc-17-3291-2023

Xin, He, Sun, L., Xie, Z., Huang, W., Long, N., Li, Z., et al. (2013). Sea ice in the Arctic Ocean: role of shielding and consumption of methane. *Atmos. Environ.* 67, 8–13. doi:10.1016/j.atmosenv.2012.10.029

Zhang, F., Pang, X., Lei, R., Zhai, M., Zhao, X., and Cai, Q. (2021). Arctic sea ice motion change and response to atmospheric forcing between 1979 and 2019. *Int. J. Climatol.* 42, 1854–1876. doi:10.1002/joc.7340

Zhou, J., Delille, B., Eicken, H., Vancoppenolle, M., Brabant, F., Carnat, G., et al. (2013). Physical and biogeochemical properties in landfast sea ice (barrow, Alaska): insights on brine and gas dynamics across seasons. *J. Geophys. Res. Oceans* 118, 3172–3189. doi:10.1002/jgrc.20232

Zhou, J., Tison, J.-L., Carnat, G. N., Geilfus, X., and Delille, B. (2014). Physical controls on the storage of methane in landfast sea ice. *Cryosphere* 8, 1019–1029. doi:10.5194/tc-8-1019-2014

frontiers | Frontiers in Environmental Science

TYPE Review
PUBLISHED 26 April 2024
DOI 10.3389/fenvs.2024.1382621

OPEN ACCESS

EDITED BY
Carolyn Ruppel,
US Geological Survey (USGS), United States

REVIEWED BY
Peter Swarzenski,
United States Geological Survey, United States
Patrick Crill,
Stockholm University, Sweden

*CORRESPONDENCE
Xin Lan,
xin.lan@noaa.gov

RECEIVED 05 February 2024
ACCEPTED 08 April 2024
PUBLISHED 26 April 2024

CITATION
Lan X and Dlugokencky EJ (2024), Atmospheric constraints on changing Arctic CH_4 emissions. *Front. Environ. Sci.* 12:1382621. doi: 10.3389/fenvs.2024.1382621

Atmospheric constraints on changing Arctic CH_4 emissions

Xin Lan[1,2]* and Edward J. Dlugokencky[3]

[1]Global Monitoring Laboratory, National Oceanic and Atmospheric Administration, Boulder, CO, United States, [2]Cooperative Institute for Research in Environmental Sciences, University of Colorado, Boulder, CO, United States, [3]Formerly with Global Monitoring Laboratory, National Oceanic and Atmospheric Administration, Boulder, CO, United States

Rapid warming in the Arctic has the potential to release vast reservoirs of carbon into the atmosphere as methane (CH_4) resulting in a strong positive climate feedback. This raises the concern that, after a period of near-zero growth in atmospheric CH_4 burden from 1999 to 2006, the increase since then may be in part related to increased Arctic emissions. Measurements of CH_4 in background air samples provide useful, direct information to determine if Arctic CH_4 emissions are increasing. One sensitive first-order indicator for large emission change is the Interpolar Difference, that is the difference in surface atmospheric annual means between polar northern and southern zones (53°–90°), which has varied interannually, but did not increase from 1992 to 2019. The Interpolar Difference has increased moderately during 2020–2022 when the global CH_4 burden increased significantly, but not yet to its peak values in the late-1980s. For quantitative assessment of changing Arctic CH_4 emissions, the atmospheric measurements must be combined with an atmospheric tracer transport model. Based on multiple studies including some using CH_4 isotopes, it is clear that most of the increase in global atmospheric CH_4 burden is driven by increased emissions from microbial sources in the tropics, and that Arctic emissions have not increased significantly since the beginning of our measurement record in 1983 through 2022.

KEYWORDS

atmospheric methane, Arctic, methane emissions, climate change, climate feedbacks

1 Introduction

Atmospheric methane (CH_4) has wide-ranging impacts on climate and air quality. The increase in CH_4's atmospheric burden since pre-industrial (usually taken as 1750) is responsible for 0.55 W m^2 direct effective radiative forcing (https://gml.noaa.gov/ccgg/ghgpower/). Its atmospheric chemistry produces tropospheric O_3 and stratospheric H_2O, two additional important GHGs), which add ~0.4 W m^{-2} (IPCC Assessment Report 6, hereafter AR6) to CH_4's forcing. Tropospheric O_3 is also a regulated pollutant that affects human health and agricultural productivity. Increases in atmospheric CH_4 burden impact the atmospheric concentration of hydroxyl radical (OH), which affects the lifetime of CH_4 and other reduced long-lived greenhouse gases (LLGHG).

From paleoclimate studies, we know that the changing atmospheric burden of CH_4 (along with CO_2, primarily) is a key driver in transitions from glacial to interglacial periods (Bock et al., 2017). Small changes in Earth's orbital parameters have little impact on Earth's radiation budget, but they impact the geographical and seasonal distribution of solar radiation, which affects ice sheets and GHGs (Lorius et al., 1990). As ice sheets shrink, the darker surface underneath absorbs more radiation, warming Earth. A warming planet also releases GHGs from the ocean and land, acting as a climate feedback.

Similar to ancient times, current Arctic environmental conditions are especially worrisome for potential climate feedback that will accelerate the impacts of anthropogenic emissions of CO_2 from fossil fuel combustion and other LLGHG emissions. Arctic landmasses hold huge stores of carbon, on order 1000 Pg C, in the top 3 m of permafrost. For comparison, the current atmosphere holds ~4 Pg C as CH_4. While frozen in permafrost (permanently frozen ground), Earth's climate is immune to this carbon, as long as it remains frozen in permafrost. But if the permafrost thaws, this carbon can be released where it can be converted to CO_2 or CH_4 by microbes, depending on hydrology. Additionally, there is a large amount of CH_4 in clathrates on land and under the Arctic Ocean, but we consider these as potential impacts over millennial time scales rather than an immediate threat (Ruppel and Kessler, 2017; Ruppel and Waite, 2020).

We also know the Arctic is warming rapidly, at ~0.73 K decade^{-1} since 1979, about a factor of 3 faster than the global average (Rantanen et al., 2022), in part because of decreasing snow and ice cover that affects albedo. This has potentially large impacts on carbon cycling in the Arctic. Thawing permafrost accelerates formation of thermokarst lakes and generally increases wetland area; flux measurements in Siberia show these lakes can strongly emit CH_4 (Wik et al., 2016). Warmer temperatures are likely to increase the length of the growing season, also increasing the depth of the active layer at the permafrost surface. As newly formed wetlands drain, flow of dissolved organic carbon into the Arctic Ocean increases, where it can be converted to CH_4 by microbes in carbon-rich sediments. These changes may also affect vegetation, e.g., as tree growth occurs further north, which affects Arctic albedo. For this paper, we ignore the substantial impacts of thawing permafrost on Arctic infrastructure, e.g., crumbling of building foundations and pipeline footings. CH_4 production and emission is also sensitive to temperature. This sensitivity is typically characterized by a Q_{10} value, which quantifies the relative change in production or emissions for a 10 K increase in temperature. Reported Q_{10} is typically in the range of 2–15 with large uncertainties (e.g., Change et al., 2021). Methane production and loss through oxidation by soil bacteria also depend on inundation; so changes in precipitation magnitude, type, and distribution caused by climate change and local hydrology will also impact CH_4 emission rates.

So how can we determine if CH_4 emissions in the Arctic are increasing as a result of climate change? Detailed field studies are useful for improving understanding of processes responsible for CH_4 fluxes (both emission and soil sink), but they are still limited in their footprint (Röβger et al., 2023) or temporal extent or both. Satellite GHG monitoring looks at sunlight reflected from Earth's surface, which is limited to estimating atmospheric CH_4 only in daytime with strong sunlight and under cloud-free conditions that are not possible during polar night. Other remote sensors look at thermal infrared radiation to retrieve atmospheric CH_4, so they allow extension of the measurement coverage to nighttime conditions (including polar night), but are most sensitive to high altitudes, far from emissions. High-quality ground and vertical observations (often called *in situ* observations) of the temporal and spatial distributions of atmospheric CH_4 provide strong (i.e., with small uncertainty) constraints on CH_4's budget of emissions and sinks and how they change over time. Here we give some examples of how NOAA GML surface atmospheric observations are used to quantify potential changes in Arctic CH_4 emissions.

2 Methods

2.1 Atmospheric sampling

This study is based on measurements of atmospheric CH_4 from air samples collected at sites in NOAA GML's Cooperative Global Air Sampling Network. The sampling network has been described elsewhere (Dlugokencky et al., 1994), so only a brief description is given here. Sites are located so sampled air is free of local or regional contamination of CH_4 and other climate-related anthropogenic gases and represents a large, well-mixed volume of background atmosphere. This is important to ensure the observations can be compared with output of atmospheric chemical transport models, where the model grid is relatively large (larger than 1° latitude x 1° longitude for the model described below), and for meaningful trends from weekly sampling. Most discrete air samples have been collected in 2.5 L borosilicate glass flasks at approximately weekly frequency. Each flask has two glass-piston stopcocks, an inlet and outlet, sealed with polytetrafluoroethylene O-rings. Flasks are sent to sampling sites filled with dry gas containing no CH_4 (fill gas). A battery-powered portable sampler is used to flush a pair of flasks in series for ~10 min before the flasks are pressurized to a small overpressure of ~0.4 atm. The lack of CH_4 in the fill gas provides an excellent tool to ensure the flasks are sufficiently flushed with ambient air; insufficient flushing combined with sensitive measurement methods would result in a significant difference in CH_4 measured between members of the sample pair. Once sampled, the flasks are returned to Boulder, CO for analysis. Various other sampling methods and flask types have also been used since CH_4 measurements began in 1983, but they account for a very small percentage of samples, and we have ensured all agree by direct comparisons.

2.2 Analytical methods

From the start of measurements in 1983 until mid-2019, CH_4 was measured by gas chromatography with flame ionization detection (GC/FID) (Dlugokencky et al., 1994). Since mid-2019, a commercial laser-based spectrometer utilizing cavity ring-down spectroscopy (CRDS) has been used. Air samples are physically dried to a dew point of −70°C with a cold trap. The CH_4 quantity reported is *amount of substance fraction* and it is in units of mole fraction, dry air. We use the abbreviation *ppb* for nmol mol^{-1}. Analyzer response (both GC/FID and CRDS) has been calibrated with a suite of CH_4 in natural air standards. This suite of standards, which is maintained by NOAA GML, defines the WMO X2004A scale (maintained by NOAA) with a nominal range from 300 to 5000 ppb [Dlugokencky et al., 2005; https://gml.noaa.gov/ccl/scales.html]. Measurement uncertainties (reported as 68% confidence interval) range from ~3 ppb in 1983 to ~0.6 ppb in 2023. With careful attention to analytical details, we are confident that our reported trends and spatial patterns are meaningful.

2.3 Calculation of global and zonal averages

Before NOAA CH_4 data are analyzed, they undergo a two-step procedure to ensure temporal variability is representative of large, well-

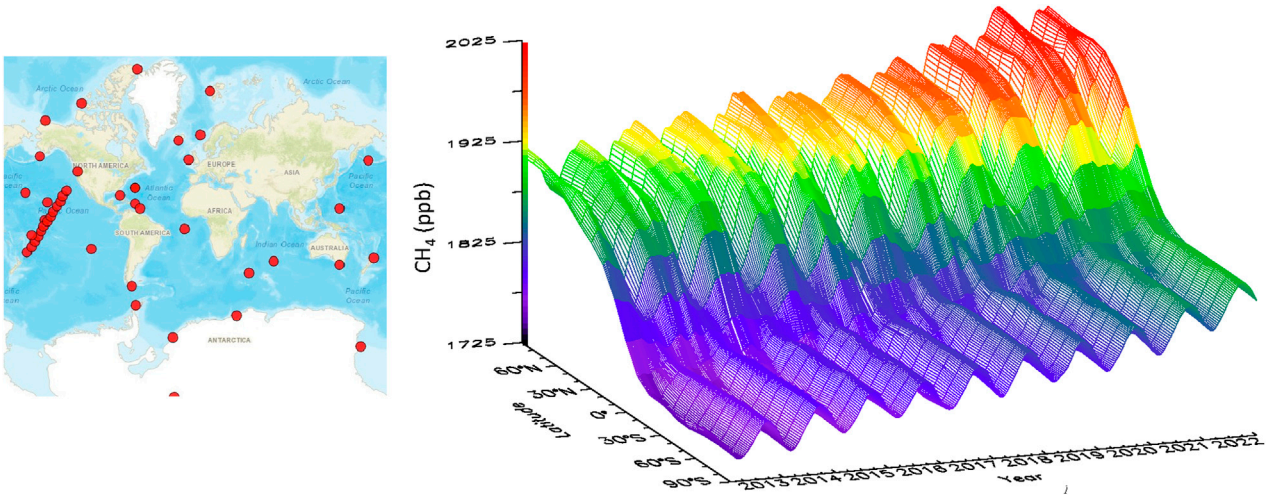

FIGURE 1
Left: subset of atmospheric sampling sites used in the construction of the Marine Boundary Layer (MBL) Reference for CH_4. Right: atmospheric CH_4 abundance at Earth's surface based on NOAA's Marine Boundary Layer measurements (Lan et al., 2023).

mixed atmospheric volumes and not the result of sampling or analytical errors, or local contamination. In the first quality control step, all data with clear sampling or analysis errors are flagged and excluded from further analysis. The second step, which is based on statistical analysis and behavior of other species measured in the same air sample (e.g., CO), ensures the sample meets our background condition. To calculate large scale averages, measurements from a subset of background network sites (Figure 1) are first smoothed in time. From these smoothed curves, values are extracted at approximately weekly synchronized intervals, and new curves are fitted with an iterative process as a function of latitude. The latitude fits at each weekly time step are used to create a matrix of CH_4 as functions of time and latitude. Values in the matrix are stored at latitudinal spacing of sine (latitude) = 0.05 (Figure 1), so each represents an equal volume of atmosphere. Averages of atmospheric CH_4 over specific latitude zones are calculated by averaging the appropriate values from the matrix.

3 Results and discussion

3.1 Global scale

We start at the global scale to illustrate how observations are used to constrain the atmospheric CH_4 budget of sources and sinks. Given that atmospheric CH_4's lifetime is long relative to atmospheric mixing, global changes will broadly reflect atmospheric changes observed over smaller regions, although, by themselves, global changes in atmospheric CH_4 abundance are poor indicators of the processes causing the change.

At the global scale, the time series of measured atmospheric burden can be used in a mass-balance calculation with an estimate of CH_4's lifetime to constrain total global emissions to within ~10% (with most of the uncertainty in the lifetime).

$$E = \frac{d[CH_4]}{dt} + \frac{[CH_4]}{\tau}$$

Here, $[CH_4]$ is the global CH_4 burden determined from atmospheric observations with the conversion 1 ppb = 2.763 Tg CH_4 (based on atmospheric mass and CH_4 distributions in TM5 (The Global Atmospheric Tracer Model, version 5), Lan et al., 2021) and τ is the budget lifetime, 8.8 years (not to be confused with the perturbation lifetime (11.8 ± 1.8 years in AR6) used by IPCC to calculate Global Warming Potential). In 2020–2022, we observed the largest increase in CH_4 since our systematic measurements started in 1983, with an average annual increase of 15.2 ppb/yr, and the atmospheric burden reached 5316 Tg CH_4 in 2023 (Lan et al., 2024). Global total emission increased to 642 Tg/yr CH_4 in 2020–2023, almost 15% greater than the 1983–2006 average of 560 Tg/yr. The time series of emissions calculated with global mass balance is plotted in Figure 2.

Atmospheric mixing is not instantaneous, so gradients in the measured abundances of gases remain in the background atmosphere that reflect the large-scale distributions of emissions. Figure 1 shows the latitude gradient of atmospheric CH_4 at background sites. These patterns can be exploited directly, or in more sophisticated approaches using atmospheric tracer transport models, to quantify the spatial distribution of emissions and how they change with time. Because vertical mixing in the Arctic is much less rapid than in the tropics, surface measurements are quite sensitive to changing emissions. Accounting only for differences in horizontal vs. vertical atmospheric transport, Bousquet et al. (2011) found that measurements of atmospheric CH_4 at the surface in the Arctic were about a factor of 2–3 more sensitive to surface emissions than the tropics.

3.2 Arctic scale

Interpretation of the atmospheric measurements alone informs us of potential changes in CH_4 emissions in the Arctic. Figure 3 plots the interpolar difference (IPD) between annual mean CH_4 values calculated for polar northern (PNH = 53° to 90°N) and polar

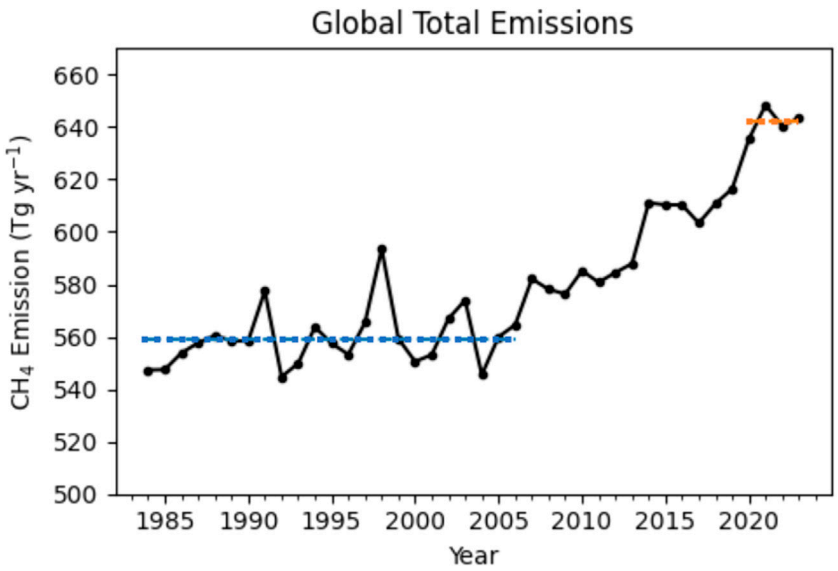

FIGURE 2
Global total annual CH_4 emissions calculated using a mass-balance approach constrained by measured atmospheric burden and increase (τ = 8.8 years). Blue and orange dash lines show the average levels in 1984–2006 and 2020–2023, respectively.

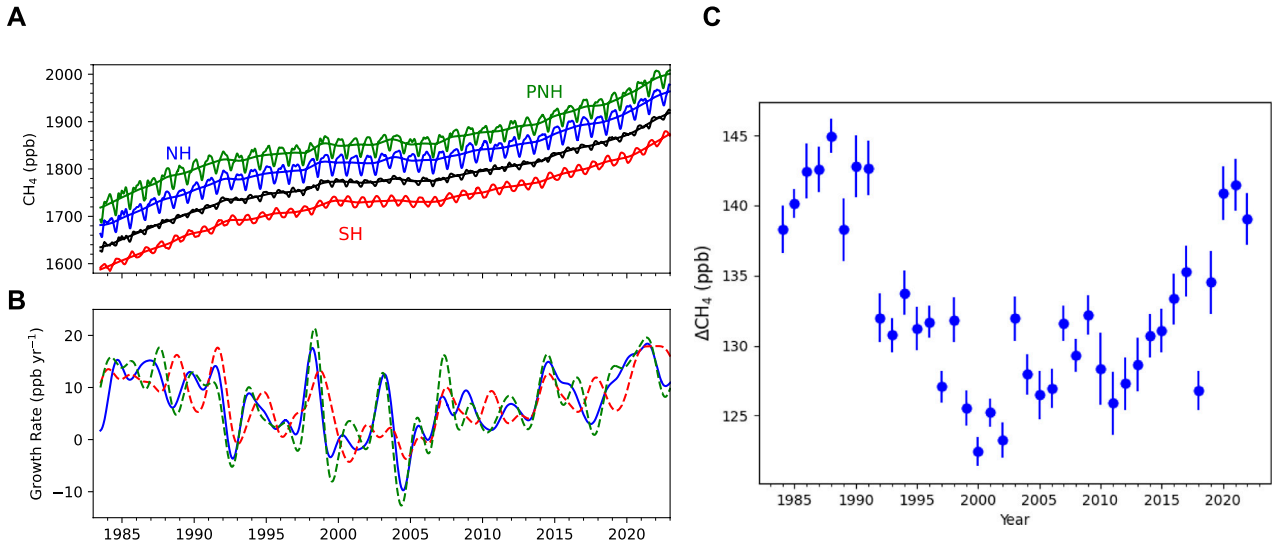

FIGURE 3
(A) Large-scale average time evolution of CH_4 determined from surface measurements in Figure 1. Plotted are Polar Northern Hemisphere (PNH; 53° to 90°N), Northern Hemisphere (NH), global, and Southern Hemisphere (SH) averages, from top to bottom. Deseasonalized trend lines are also plotted for each. **(B)** Instantaneous CH_4 growth rates determined as time-derivatives of the trend lines in **(A)**. **(C)** Differences in annual averaged atmospheric CH_4 between polar northern (53°–90°N) and polar southern latitudes (53°–90°S).

southern (PSH = 53° to 90°S) latitude zones. The largest signal is the step change between 1991 and 1992 of ~10 ppb, which is consistent in timing with the economic collapse of the former Soviet Union. Following that, IPD trends downward or remains approximately level, until ~2020 when it recovers to pre-1992 levels. While IPD provides strong observational evidence for a potential change in Arctic emissions, it reflects changes in both emissions and transport. To account for transport effects, Dlugokencky et al. (2003) used an atmospheric tracer transport model (The Global AtmosphericTracer Model, version 3; TM3) and anthropogenic emissions from a global inventory to simulate atmospheric CH_4 at NOAA observing sites. The emission inventory captured a decrease in annual emissions of ~10 Tg CH_4 from the former Soviet Union through the 1991–92 anomaly in IPD.

While it is useful to analyze atmospheric observations to try to qualitatively assess CH_4 emissions at high northern latitudes and how they change with time, a tracer transport model is necessary to quantify those emissions and their changes. The Global Carbon

Project - CH_4 (the Global Methane Budget) summarized top-down inversion results for CH_4 from a few atmospheric tracer transport models that assimilate atmospheric CH_4 measurements to inform emissions (Saunois et al., 2020). They found that (shown in their Table 5) total Arctic methane emissions (60–90°N) were stable when comparing 2008–2017 with 2000–2009 periods. Extended inversion results until 2022 from the Copernicus Atmosphere Monitoring Service (CAMS; https://atmosphere.copernicus.eu/) model show that average Arctic total methane emissions are 57 Tg/yr in 2020–2022, slightly greater than the 54.3 Tg/yr average in 2010–2019 (Segers and Houwelling, 2024), which may partially explain the increase in observed IPD since 2020 (Figure 3). Arctic total emissions for 2020–2022, however, are similar to the 57.9 Tg/yr average estimated for 2000–2009, which does not support a large long-term emission increase from natural processes in the Arctic.

Atmospheric measurements of stable carbon isotopes of CH_4 (denoted as $\delta^{13}C\text{-}CH_4$) provide additional constraints on emissions from different source sectors, given that different CH_4 sources have distinct $\delta^{13}C\text{-}CH_4$ signatures driven by different fundamental processes (Schwietzke et al., 2016; Lan et al., 2021). Microbially-driven CH_4 emissions tend to be more depleted in $\delta^{13}C\text{-}CH_4$ (range of emission-weighted globally averaged values −60 to −62‰) while thermogenic emissions (predominated by fossil fuel emissions) tend to be slightly enriched in $\delta^{13}C\text{-}CH_4$ (−43 to −45‰) compared with the atmosphere. Methane emitted through biomass burning (pyrogenic) retains the $\delta^{13}C$ signature in the biofuels, which results in highly enriched $\delta^{13}C\text{-}CH_4$ signatures (−24 to −25‰). As atmospheric CH_4 began increasing in 2007 after near-zero growth from 1999 through 2006, measurements of the relative amount of $\delta^{13}C\text{-}CH_4$ at Alert (82.45°N, 62.51°W) suggested that warm, wet conditions in the Arctic during 2007 enhanced natural CH_4 emissions from wetlands (Dlugokencky et al., 2009). The post-2006 global CH_4 increase is accompanied by a significant decreasing trend in atmospheric $\delta^{13}C\text{-}CH_4$ (Michel et al., 2021), suggesting a dominant contribution from microbial CH_4 emissions, which can include both anthropogenically influenced microbial sources such as livestock, landfill/waste, and rice cultivation, and natural sources such as wetlands and shallow lakes. Atmospheric inverse modeling that assimilates both atmospheric CH_4 and $\delta^{13}C\text{-}CH_4$ measurements suggests a major emission increase in 2006–2016 from tropical regions, while total emissions from the Arctic remain stable (Basu et al., 2022). These conclusions are consistent with GCP-CH_4 results. Basu et al. (2022) found a more significant contribution from microbial emission increase to post-2006 global increase than the GCP- CH_4 study, but mainly from the tropics. Extended modeling results until 2021 from joint atmospheric CH_4 and $\delta^{13}C\text{-}CH_4$ inversions provided by NOAA's CarbonTracker-CH_4 modeling system (Oh et al., 2023) also found a dominant role of global microbial emission increases since 2006, but no significant increase in total Arctic methane emissions or Arctic microbial emissions.

4 Summary and conclusion

There is, without question, potential for significant amplification of climate change resulting from disturbance of large carbon reservoirs in the Arctic. Thawing permafrost releases carbon into newly formed inundated regions that can be converted to CH_4 or CO_2, depending on hydrology. Such changes were a major contributor to transitions from glacial to interglacial periods in the paleoclimate record. Are changes to Arctic CH_4 emissions already significantly altering Earth's climate? Our best constraint comes from high-quality atmospheric measurements of CH_4 abundance at background surface measurement sites, both for assessing changes in CH_4 emissions and determining the reasonableness of estimates from particular Arctic sources.

We, and other participants in the World Meteorological Organization, Global Atmosphere Watch program (https://community.wmo.int/en/activity-areas/gaw) of GHG and related tracer observations, put great effort into ensuring high-quality measurements where spatial and temporal gradients are meaningful. These gradients are used in the range of analysis methods and scales to quantify emissions and how they change with time. Total Arctic methane emissions north of 53°N are estimated to account for about 10% of global total emissions, while north of 60°N accounts for about 4%. Based on the difference in surface atmospheric CH_4 between polar northern and polar southern latitudes, and interpretation of such observed features by various atmospheric tracer transport models, a significant increase in Arctic emissions has not yet been detected.

Author contributions

XL: Conceptualization, Data curation, Formal Analysis, Funding acquisition, Investigation, Methodology, Writing–original draft, Writing–review and editing. ED: Conceptualization, Data curation, Formal Analysis, Investigation, Methodology, Writing–original draft, Writing–review and editing.

Funding

The author(s) declare financial support was received for the research, authorship, and/or publication of this article. This research was supported in part by NOAA Climate Program Office AC4 program NA23OAR4310283 and NOAA cooperative agreement NA22OAR4320151.8.

Acknowledgments

We thank all the organizations and individuals who have assisted us with our cooperative global air sampling network and measurements, and we are grateful for the conscientious efforts of all network observers.

Conflict of interest

The authors declare that the research was conducted in the absence of any commercial or financial relationships that could be construed as a potential conflict of interest.

Publisher's note

References

Basu, S., Lan, X., Dlugokencky, E., Michel, S., Schwietzke, S., Miller, J. B., et al. (2022). Estimating emissions of methane consistent with atmospheric measurements of methane and δ 13 C of methane. *Atmos. Chem. Phys.* 22 (23), 15351–15377. doi:10.5194/acp-22-15351-2022

Bock, M., Schmitt, J., Beck, J., Seth, B., Chappellaz, J., and Fischer, H. (2017). Glacial/interglacial wetland, biomass burning, and geologic methane emissions constrained by dual stable isotopic CH4 ice core records. *Proc. Natl. Acad. Sci.* 114 (29), E5778–E5786. doi:10.1073/pnas.1613883114

Bousquet, P., Ringeval, B., Pison, I., Dlugokencky, E. J., Brunke, E.-G., Carouge, C., et al. (2011). Source attribution of the changes in atmospheric methane for 2006–2008. *Atmos. Chem. Phys.* 11 (8), 3689–3700. doi:10.5194/acp-11-3689-2011

Chang, K.-Y., Riley, W. J., Knox, S. H., Jackson, R. B., McNicol, G., Poulter, B., et al. (2021). Substantial hysteresis in emergent temperature sensitivity of global wetland CH4 emissions. *Nat. Commun.* 12, 2266. doi:10.1038/s41467-021-22452-1

Dlugokencky, E. J., Houweling, S., Bruhwiler, L., Masarie, K. A., Lang, P. M., Miller, J. B., et al. (2003). Atmospheric methane levels off: temporary pause or a new steady-state? *Geophys. Res. Lett.* 30 (19). doi:10.1029/2003GL018126

Dlugokencky, E. J., Myers, R. C., Lang, P. M., Masarie, K. A., Crotwell, A. M., Thoning, K. W., et al. (2005). Conversion of NOAA atmospheric dry air CH4 mole fractions to a gravimetrically prepared standard scale. *J. Geophys. Res. Atmos.* 110, D18. doi:10.1029/2005JD006035

Dlugokencky, E. J., Paul Steele, L., Lang, P. M., and Masarie, K. A. (1994). The growth rate and distribution of atmospheric methane. *J. Geophys. Res. Atmos.* 99 (D8), 17021–17043. doi:10.1029/94JD01245

Lan, X., Basu, S., Schwietzke, S., Bruhwiler, L. M. P., Dlugokencky, E. J., Michel, S. E., et al. (2021). Improved constraints on global methane emissions and sinks using δ13C-CH4. *Glob. Biogeochem. Cycles* 35 (6), e2021GB007000. doi:10.1029/2021GB007000

Lan, X., Tans, P., Thoning, K., and NOAA Global Monitoring Laboratory (2023). *NOAA greenhouse gas marine boundary layer reference - CH4*. Boulder, Colorado: NOAA GML. doi:10.15138/TJPQ-0D69

Lan, X., Thoning, K. W., and Dlugokencky, E. J.: Trends in globally-averaged CH4, N2O, and SF6 determined from NOAA global monitoring laboratory measurements. 2024, doi:10.15138/P8XG-AA10

Michel, S. E., Vaughn, B. H., Tans, P., Thoning, K., and Lan, X. (2021). Atmospheric δ13C-CH4 data from the institute of arctic and alpine Re- search (INSTAAR) at the university of Colorado. *Boulder Coop. NOAA Glob. Monit.* doi:10.15138/79jq-qc24

Oh, Y., Bruhwiler, L., Lan, X., Basu, S., Schuldt, K., Thoning, K., et al. (2023). *CarbonTracker CH4 2023* (Boulder, Colorado: NOAA Global Monitoring Laboratory).

Rantanen, M., Karpechko, A. Y., Lipponen, A., Nordling, K., Hyvärinen, O., Ruosteenoja, K., et al. (2022). The Arctic has warmed nearly four times faster than the globe since 1979. *Commun. Earth Environ.* 3, 168. doi:10.1038/s43247-022-00498-3

Rößger, N., Sachs, T., Wille, C., Boike, J., and Kutzbach, L. (2022). Seasonal increase of methane emissions linked to warming in Siberian tundra. *Nat. Clim. Change* 12 (11), 1031–1036. doi:10.1038/s41558-022-01512-4

Ruppel, C., and Kessler, J. D. (2017). The interaction of climate change and methane hydrates. *Rev. Geophys.* 55, 126–168. doi:10.1002/2016RG000534

Ruppel, C. D., and Waite, W. F. (2020). Timescales and processes of methane hydrate formation and breakdown, with application to geologic systems. *J. Geophys. Res. Solid Earth* 125, e2018JB016459. doi:10.1029/2018JB016459

Saunois, M., Stavert, A. R., Poulter, B., Bousquet, P., Canadell, J. G., Jackson, R. B., et al. (2020). The global methane budget 2000–2017. *Earth Syst. Sci. data* 12 (3), 1561–1623. doi:10.5194/essd-12-1561-2020

Schwietzke, S., Sherwood, O. A., Bruhwiler, L. M. P., Miller, J. B., Etiope, G., Dlugokencky, E. J., et al. (2016). Upward revision of global fossil fuel methane emissions based on isotope database. *Nature* 538 (7623), 88–91. doi:10.1038/nature19797

Segers, A., and Houweling, S. (2024). Description of the CH4 inversion production chain. *CAMS Copernic. Atmos. Monit. Serv. Rep.*, Available at: https://ads.atmosphere.copernicus.eu/cdsapp#!/dataset/cams-global-greenhouse-gas-inversion?tab=overview.

Wik, M., Varner, R., Anthony, K., MacIntyre, S., and Bastviken, D. (2016). Climate-sensitive northern lakes and ponds are critical components of methane release. *Nat. Geosci.* 9, 99–105. doi:10.1038/ngeo2578

frontiers | Frontiers in Earth Science

TYPE Original Research
PUBLISHED 14 May 2024
DOI 10.3389/feart.2024.1346645

OPEN ACCESS

EDITED BY
Michael Lehning,
Swiss Federal Institute of Technology Lausanne, Switzerland

REVIEWED BY
Alexey Portnov,
Spanish National Research Council (CSIC), Spain
Pavel Serov,
UiT The Arctic University of Norway, Norway

*CORRESPONDENCE
Shyam Chand,
shyam.chand@ngu.no

RECEIVED 29 November 2023
ACCEPTED 23 April 2024
PUBLISHED 14 May 2024

CITATION
Chand S, Brunstad H, Lepland A, Thorsnes T and Pedersen JH (2024), Fluid flow at the Loppa High results from the seabed laboratory and test site.
Front. Earth Sci. 12:1346645.
doi: 10.3389/feart.2024.1346645

Fluid flow at the Loppa High results from the seabed laboratory and test site

Shyam Chand[1]*, Harald Brunstad[2], Aivo Lepland[1], Terje Thorsnes[1] and Jon Halvard Pedersen[2]

[1]Geological Survey of Norway (NGU), Trondheim, Norway, [2]Expres Aker BP, Lysaker, Norway

The Loppa High is a subsurface structural high located in SW Barents Sea flanked by regional fault complexes where many hydrocarbon discoveries have been made along its peripheries during recent years. Since the petroleum exploration started in the late 1970's, extensive studies have been undertaken giving a good understanding of the subsurface stratigraphy and the presence and maturation of hydrocarbon sources, fluid migration processes into hydrocarbon traps and seabed seeps. Many shallow gas anomalies are observed in this region due to fluid migration from the deeper reservoirs. Taking advantage of modern echo sounder and sonar technology, a more precise mapping of shallow subsurface became possible as well as detection of seafloor seeps to be inspected and sampled by advanced ROV technology. Presence of thermogenic hydrocarbons in seeps would indicate remobilisation from reservoirs in the subsurface that remained after the Late Paleogene/Neogene tectonism and the Pleistocene glacial rebound. Results of multibeam echosounder mapping of selected areas have been used to select seep sites for detailed investigation using ROV's, and HUGIN AUV equipped with synthetic aperture sonar (HISAS), methane sniffers and optical cameras. This has aided the selection of optimal sampling sites and the collection of a large amount of sample material including seeping fluids, carbonate crusts and sediments which has been used for geochemical characterization and geochronology. Here, we present the evidence of the hydrocarbon migration and seepage from reservoirs mainly of deep thermogenic origin and altered by shallow storage during and after glaciation. The thermogenic signature of the seeping fluids indicates the long term and large-scale supply of methane to the global methane budget also from similar areas of potential natural leakage from the subsurface to the water column.

KEYWORDS

fluid flow, Barents Sea, Loppa High, pockmark, multibeam, gas flare, gas hydrate, methane

Introduction

Seafloor observations of fluid flow features have become more of interest recently since they have provided many clues not only about what has happened in the past but a peep in to the present subsurface hydrocarbon potential and its relation to the geological formations (Capozzi et al., 2017; Crémière et al., 2018). The seafloor anomalies also give an insight into the relation between fluid seepage and habitats for different life-forms, and geo hazards that

might be relevant to future drilling (Sen et al., 2016; Sen et al., 2018). Fluid seepage at the seafloor is often associated with circular seabed depressions called pockmarks which are generated when the strength of fluid flow is sufficient to remove surface sediments and/or prevent sedimentation (King and MacLean, 1970; Judd and Hovland, 2007). It has been suggested that pockmarks are not necessary criteria for tracking fluid seepage since they are only formed where there is a recording medium present in the form of soft sediments (Rise et al., 2015). Hence, even though the seepage can be marked by the presence of acoustic gas flares in the water column (Leifer and MacDonald, 2003; Römer et al., 2014; Dupré et al., 2015), many flares do not associate with pockmarks (Chand et al., 2012). The fluid seepage along passive margins is linked to many factors depending on the structural, geological and palaeo geographic evolution history of the region. These include the proximity to active plate boundaries, active zones of sediment loading, faulting and the effects of glaciations in the form of ice loading and unloading (Einsele, 2013; Khader and Novakowski, 2014; Fjeldskaar and Amantov, 2018).

At high latitudes, waxing and waning of glaciers have the most important direct and indirect effect on seepage. Most of the studies from the Norwegian offshore regions link fluid flow anomalies to glacial loading and unloading cycles (Chand et al., 2008; Chand et al., 2012; Crémière et al., 2016a; Portnov et al., 2016; Winsborrow et al., 2016; Andreassen et al., 2017; Serov et al., 2023) or to sudden sediment loading resulting from glacial retreat melt water inflows and associated sediment discharges during glacial retreat (Hustoft et al., 2009; Karstens et al., 2018). Moreover, the glacial cycles create or expand a hydrate stable zone in sediments during loading, holding a reservoir of gas and hydrates. Gases from such reservoirs are released during and after the glacial unloading due to the removal of the load which is needed to keep the hydrates in stable form (Sloan and Koh, 2007). Glacial loading can also affect the fluid flow in the fault systems and result in the sealing of normal faults causing a quiescent period of no movements followed by enhanced activity during and after unloading (Hampel and Hetzel, 2006). Analysis using fault stress modelling from North Sea area indicates that the reactivation of faults might have happened during Pleistocene deglaciations and therefore potential hydrocarbon seepage might have occurred (Grollimund and Zoback, 2000). The large-scale erosion and uplift that has happened during the past glaciations resulted in overturned formations and near seafloor subcropping of source and reservoir rocks (Henriksen et al., 2011) influencing the fluid flow.

Seafloor and water column data collected during number of surveys have yielded important observations about the seabed features such as pockmarks, iceberg ploughmarks, glacial prodmarks, carbonate crusts, bacterial mats and ongoing/past gas seepage of SW Barents Sea (Chand et al., 2009; Chand et al., 2012; Chand et al., 2014; Crémière et al., 2016a; Crémière et al., 2016b; Crémière et al., 2018). The prodmarks are formed when detached icebergs plunges making a rounded depression on seafloor and when these icebergs plough away creating a ploughmark in seafloor sediments can be many tens of meters deep affecting the subsurface stratigraphy also. The subsurface has also been investigated many years through the acquisition of 2D and 3D seismic data and resulted in many important hydrocarbon discoveries (Vadakkepuliyambatta et al., 2013; NPD, 2016). Geochemical analysis of seeping free gas, methane derived authigenic carbonate crusts and biomarkers indicated a deep seated origin of fluids that is leaking/leaked through the Barents Sea seafloor (Nickel et al., 2013; Crémière et al., 2016b; Thiagarajan et al., 2022) showing the importance in using these proxies for hydrocarbon exploration.

This study focuses on the Loppa High, a fault bounded structural high in the SW Barents Sea and the surrounding basins and fault structures (Figure 1). Based on the geological and geophysical information from many surveys, this site was chosen as a laboratory site to investigate various factors related to fluid flow. Properties of the gases released at the seafloor and associated carbonate crusts can be linked to the sources of the gases and thereby analyse the possibility that the hydrocarbons were leaking during and after the glaciations. Comparison of results from seep to the reservoir gases can give a direct information of source to seep relationships and gas modifications along the migration pathways. Here, we have the unique opportunity to compare results from reservoir level to the seafloor thereby envisage the entire route for the gases. The influence of faults and properties of near seafloor sediments are analysed to study their impact on the formation of the present focussed fluid flow locations. Results from the nearby area are also presented to compare the regional development of the fluid flow.

Geological setting

The Barents Sea is a shallow epicontinental sea surrounded by a Tertiary rifted margin to the west and the Norway, Russia and Svalbard landmasses lying on the south, east and north respectively (Eldholm et al., 1984). The SW Barents shelf formed in late Devonian and is underlain by metamorphic basement formed during Caledonian orogeny (Smelror et al., 2009) (Figure 2). Extensional tectonic movements dominated the late Palaeozoic and Mesozoic tectonic history of the region (Johansen et al., 1993), locally influenced by wrench tectonics (Brunstad and Rønnevik, 2022). The late Devonian to early Carboniferous crustal extension resulted in the formation of Hammerfest Basin followed by extension faulting affecting the Loppa High area during late Carboniferous to early Permian period (Faleide et al., 1993; Cavanagh et al., 2006). The main depocenters were located in intra-cratonic basins in the Mesozoic and early Cenozoic, shifting to the continental margin following the early Eocene opening of the Norwegian Sea (Spencer et al., 1984). The late Jurassic Hekkingen Formation is the major source rock along the Loppa High and Hammerfest Basin area (Doré, 1995), even though, Lower to Middle Triassic shales (mainly Klapmyss and Kobbe formations) also have hydrocarbon potential (Bjorøy et al., 2010) (Figure 2). In the flanking Hammerfest, Tromsø and Bjørnøya basins and the Fingerdjupet, higher levels of TOC are present in the Hauterivian-Cenomanian intervals of Cretaceous (Hagset et al., 2022) and are considered as gas and locally oil sources. Moreover, there are indications that source rocks of Eocene and possibly Miocene age (Daszinnies et al., 2021) are present west of Svalbard margin, and could potentially be present also along the western Barents Sea margin further south. The Selis Ridge of the crestal parts of the Loppa high acts as the major divide separating the pre-Triassic sediments on either sides and therefore the likelihood of potential traps prior to this age along the flanks of the Loppa High (Figure 2A).

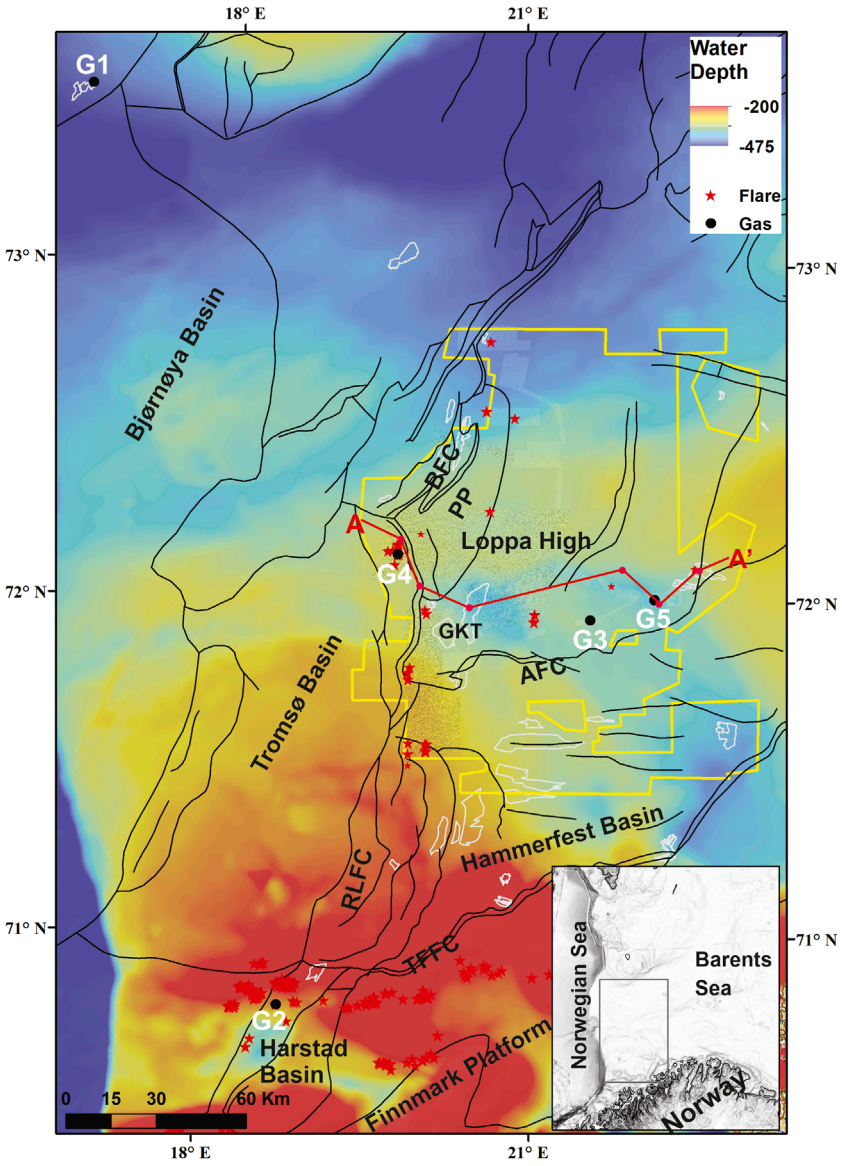

FIGURE 1
Regional bathymetry of the SW Barents Sea showing the boundaries of structural blocks (black lines). Also shown are the locations of gas flares (red stars) (Thorsnes et al., 2023), sites (black dots with white labels) where gas samples for geochemical studies were collected (G1-Well 7316/5-1, G2-Harstad Basin, G3-Håbrann, G4-Loppa High, G5-Svanefjell), seismo-geological section A-A' (red line, Figure 2), exploration wells along the line (red dots), hydrocarbon discoveries (white polygons) and 3D seismic cube LN12M01 (yellow polygon, Figure 5). The high-resolution bathymetry indicates the new locations where multibeam water column data were interpreted. BFC- Bjørnoyrenna Fault Complex, AFC-Asteria Fault Complex, TFFC-Tromsø Finnmark Fault Complex, RLFC- Ringvassøy Loppa Fault Complex, PP–Polheim Platform, GKT-Gohta.

Seafloor geomorphology of the SW Barents Sea has been shaped by several glacial-interglacial cycles since the Pliocene. Glaciers have reached the shelf edge many times with the most extensive coverage occurring during the last glacial maximum (Vorren et al., 1991; Laberg et al., 2010; Laberg et al., 2012). Numerous erosional channels were carved in to the lithified sedimentary rocks with the main channel being the Bjørnøyrenna resulting in deposition of more than 3000 m sediments at the Bear Island Fan (Eidvin and Riis, 1989; Vorren et al., 1991; Riis and Fjeldskaar, 1992; Faleide et al., 1996; Laberg et al., 2012). The glacial and erosional unloading resulted in 900–1,400 m of late Cenozoic uplift (Riis and Fjeldskaar, 1992) and the formation of a prominent erosional surface known as the upper regional unconformity (URU) which represents the base of the glacial sediments (Solheim and Kristoffersen, 1984; Vorren et al., 1986). On the westward transect from the Tromsø and Bjørnøya basins to the shelf margin, there is a transition from areas of net erosional uplift to that of net deposition. The area west of this transition to net deposition consists of a thick wedge of Pleistocene sediments. This change from net erosional uplift to net burial has implications on the hydrocarbon generation history. In general, the areas of net erosional uplift are believed to have reached maximum burial in the Eocene/Oligocene ending petroleum

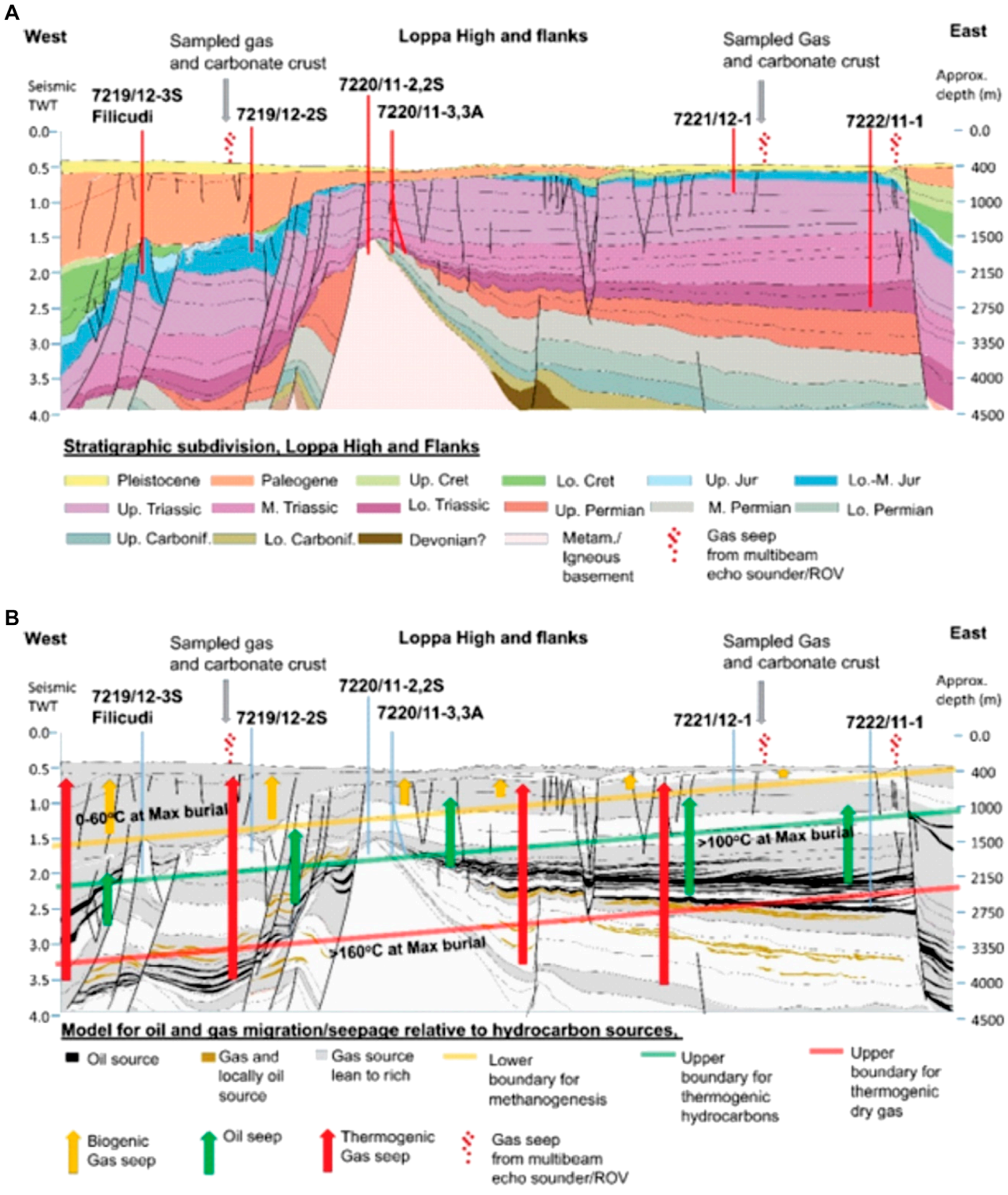

FIGURE 2
(A) Geological section across the study area showing the major structural features and the seepage routes. The sites of two surface gas samples are also indicated. **(B)** Section showing the hydrocarbon generation and seepage history across the study area. Petroleum generation and escape history was modelled by Lundin Petroleum AS using information from the exploration wells and sedimentation history of various formations established from palaeo-geographic modelling (Thiagarajan et al., 2022).

generation. The areas of net burial have their petroleum source rocks at maximum burial today and are believed to have ongoing petroleum generation (Henriksen et al., 2011). Seismo-stratigraphic interpretations and glacial modelling indicate that grounded glaciers may have reached the shelf break of the southern Barents Sea 5–10 times during the Pleistocene (Solheim and Kristoffersen, 1984;

Vorren et al., 1988; Sættem et al., 1991; Siegert and Dowdeswell, 2004; Patton et al., 2015a; 2015b), with ice thickness estimated at 800–2000 m during the last glacial maximum (Siegert et al., 2001; Svendsen et al., 2004; Patton et al., 2015a; 2015b; Auriac et al., 2016). Dating of carbonate crusts and sediments cores from various locations of the SW Barents Sea indicate that the deglaciation started ~17.5 kyr ago (Winsborrow et al., 2010; Crémière et al., 2016a). This was followed/coincident with pockmark formation in the Loppa High area around 15 kyr ago (Pau et al., 2014), by which time the entire Barents Sea was ice-free. Sedimentation decreased from 40–70 cm/kyr during deglaciation to ~6 cm/kyr during the last 9 kyr (Aagaard-Sørensen et al., 2010).

Material and methods

Multibeam echosounder (MBE) data collected using EM710 MBE by the Norwegian Defence Research Establishment (FFI) ship RV H.U. Sverdrup II have been used to generate terrain models and identify water column acoustic gas flares (hereafter referred as flares) (Figure 1). Fledermaus (FM) Midwater package was used to detect and analyse water column gas anomalies. Details about water column analysis can be found in Thorsnes et al. (2023). The autonomous underwater vehicle (AUV) HUGIN, equipped with a high-resolution interferometric synthetic aperture sonar (HISAS 1030) and MBE EM2040 was used to map the seabed in detail in selected areas with detected gas flares (Figures 3, 4). The HISAS system gives a range-independent resolution of approximately 3x3 cm and swath of 400 m at a speed of 2 m/s. The data were merged into high-resolution mosaics using Reflection software from Kongsberg Maritime. Methane sniffer (Franatech) installed on HUGIN was used to detect methane seepage in the water column at identified flare locations using EM710 data. Still photos were also collected using the TFish Black & White camera onboard HUGIN at selected locations. High resolution Topas and sub bottom profiler (SBP) seismic data were also collected from selected locations using Ship's Topas PS18 system and EdgeTech 2200 full spectrum chirp SBP system on HUGIN respectively. Details about sampling and analyses of seep and reservoir gases from the study area can be found in Crémière et al. (2018) and Thiagarajan et al. (2022), respectively.

The gas samples from the flare sites were collected using a gas sampler connected to the manipulator arm of the ROV and the reservoir gas sample using MDT (modular formation tester) and DST (drill stem tester) fluid sampling tools. The stable isotope ratios and molecular proportions hydrocarbons were analyzed at the Applied Petroleum Technology labs in Oslo, Norway. As described by Thiagarajan et al. (2022), aliquots of gas sample were transferred to exetainers and 0.1–1.0 mL of each sample was as extracted using a Gerstel MPS2 autosampler and injected into an Agilent 7890 RGA GC equipped with Mol sieve 5A, 4–8 mesh and Poraplot Q columns, a flame ionisation detector (FID) and 2 thermal conductivity detectors. Hydrocarbon concentrations were measured by FID. The carbon isotope compositions of hydrocarbons were determined using a GC-CIRMS system. Repeated analyses of standards indicate that the reproducibility of δ13C values is better than 1‰ (2 RSD).

Regional stratigraphic and structural boundaries were mapped using available 2D and 3D seismic data and presented in Chand et al. (2012). Spatial subsurface coverage was obtained for most of the Loppa High area with data interpretation based on 2D and 3D seismic data using Petrel software. The 2D and 3D seismic data were provided by Lundin Petroleum AS and consists of mega merged 3D cube LN12M01 covering many surveys from the study area and 2D lines available in DISKOS database. The 3D seismic is with 4 ms sampling interval and 25 m horizontal resolution. Resolution was sufficiently high to identify the position and vertical extent of deep local fault structures. Petroleum generation and escape history was modelled by Lundin Petroleum AS using information from the exploration wells and sedimentation history of various formations established from palaeogeographic modelling (details given in Thiagarajan et al., 2022). Different phases of petroleum generation and expulsion have been suggested based on the modelling (Figure 2B). The sources of gases from different generation scenarios and probable locations of their escape are indicated on a composite seismic section along the geological section given in Figure 2A (Figure 2B).

Results

Seafloor and water column inspection

Multibeam echosounder and HISAS data were used to inspect the water column and seafloor for fluid flow features. The study area consists of locations covering different structural, stratigraphic and glacial features which can control fluid flow. The seafloor consists of iceberg ploughmarks and glacial features such as eskers and end morains (Figure 3). Partially covered retreat moraine (RM) ridges can be observed indicating the region was influenced by multiple glacial advances during the last glaciation (Figure 3A). The eskers observed are also partially covered by the retreat moraines indicating that they belong to an early stage (Figure 3A). The pockmarks are concentrated along iceberg ploughmarks either due to the presence of soft sediments as recording medium in these depressions or that the ploughmarks acts as easier pathways for fluid escape being an incision into the relatively less permeable glacial deposits (Figure 3B). Glacio-tectonic depressions (GDR) are also observed in the study area indicating the influence from grounded ice (Figure 3C). The pockmarks vary in sizes and depths occurring close to each other indicating difference mechanisms or intensity in fluid flow creating them (Figures 3D, E). As observed elsewhere, the pockmarks consist of relatively coarser/harder sediments indicated by high backscatter (Figure 3E). Flares are observed to be associated with some of the large pockmarks but not always as noted earlier (Figure 3E). Close inspection of the large pockmark using high resolution HISAS data indicate the presence of carbonate crusts and very small pockmarks inside them (Figure 4). The detailed morphology of the pockmark indicates that the fluids are deflected to the rims of the pockmarks creating the small pockmarks probably due to blockage of conduits by authigenic carbonate precipitation cementing fine grain sediments (Figure 4). The carbonate crusts occur as massive pavements covering hundreds of square meters indicating long term release and focussed flow of fluids through the seafloor. In many areas the carbonate crusts fields are seen to be associated with pockmarks. However, there are also numerous pockmarks without any indication of carbonate crusts or current fluid flow.

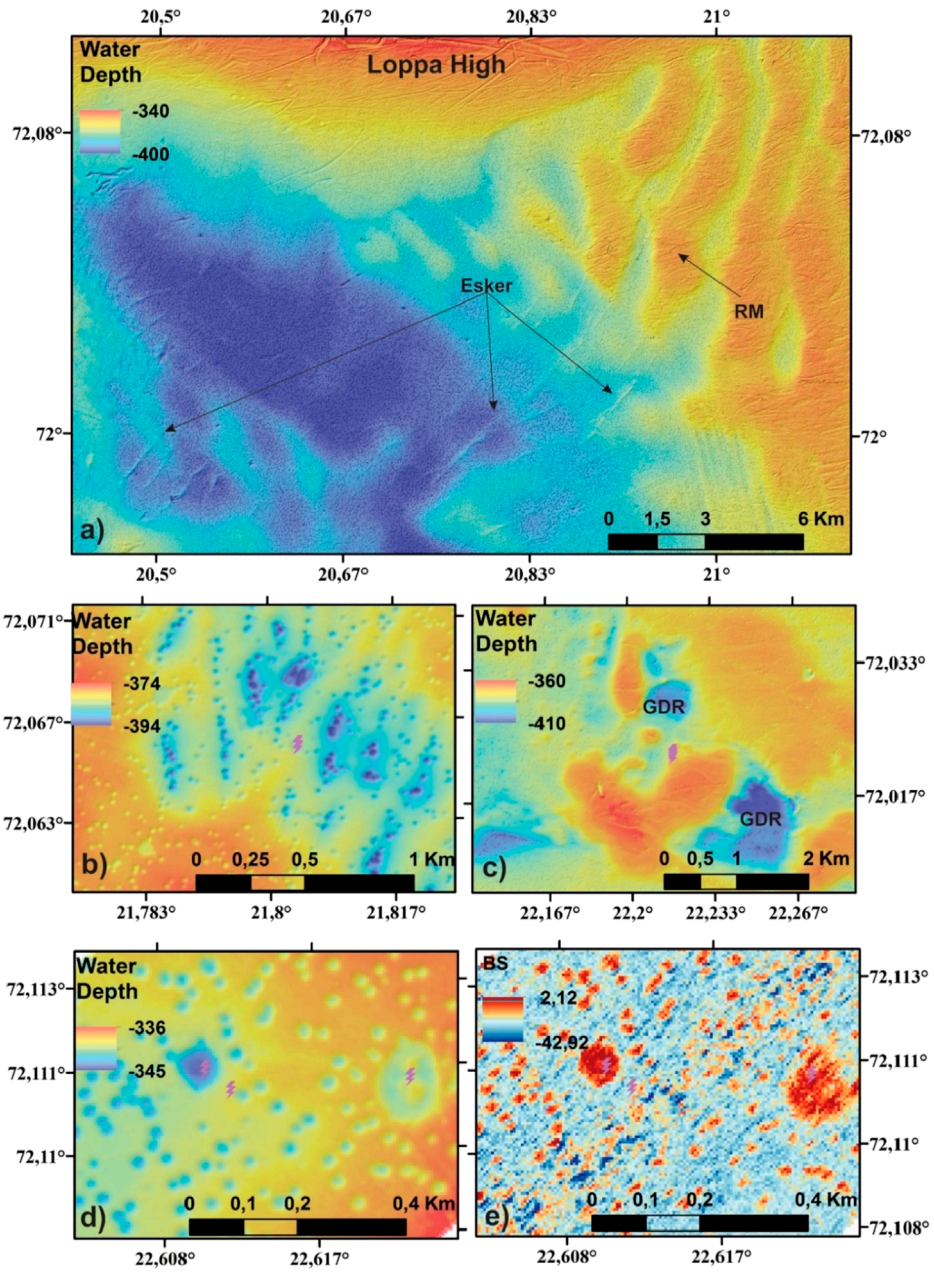

FIGURE 3
Multibeam bathymetry from four areas **(A–D)** showing the locations of pockmarks, flares (pink lightning symbol) in coexistence with various glacial seafloor features such as eskers, retreat moraine ridges (RM), glacio-tectonic depressions (GDR, hill-hole pairs). **(A)** Notice that the eskers cross the retreat moraines indicating that they formed after RM. **(B)** The pockmarks occur as chains in ploughmarks due to the availability of more soft sediments. **(C)** The GDRs appear to be depression formed after blocks of sediments moved from east to west. **(D)** bathymetry and **(E)** backscatter map showing the properties associated with small and mega pockmarks and the flare locations.

We have interpreted ~3800 km^2 of water column data and observed 28 flares of varying sizes and magnitudes from the study area. The northernmost flare location of the study area is part of the Bjørnøyrenna fault complex where one flare is observed (Figure 1). The flare occurs close to the Filicudi (well 7219/12-1) hydrocarbon discovery (Figure 1). Three flares are identified in the region along the eastern boundary of the Polhem Platform with Loppa High (Figure 1). Two flares occur close to the boundary whereas one is found ~10 km west of the boundary (Figure 1). Further south, eight flares occur bounding the Ringvassøy Loppa fault complex (RLFC) along the southwestern part of the Polhem Platform, (Figure 1). Along the southern part of the RLFC bounding the Gohta-Komse Terrace and Hammerfest Basin, eleven flares are observed mostly concentrated along the fault locations (Figures 1, 5). Further east, five flares are observed along the Bjørnøyrenna glacial advance grounding zone wedge deposits (Figure 1).

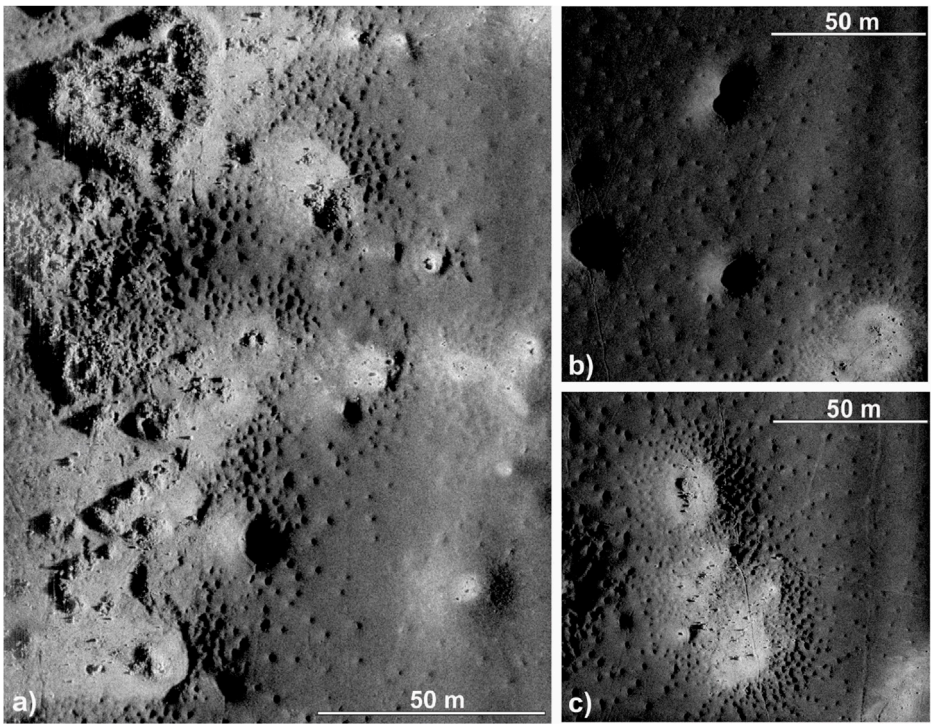

FIGURE 4
HISAS image from Hammerfest basin flare area showing **(A)** carbonate crust with micro pockmarks (~1 m), **(B)** normal pockmarks (~15 m) and micro pockmarks, **(C)** normal pockmarks closer to the HUGIN AUV nadir showing high resolution image from the inside of pockmarks with stones and carbonates.

Fluid flow and the subsurface

The subsurface structure and geology are investigated using 2D and 3D seismic data. The subsurface along northern part of Bjørnøyrenna fault complex indicates the presence of N-S oriented faults in line with the direction of the fault complex (Figure 5). Faults of several other structural trends and directions can also be seen in the variance slice taken at 800 ms TWT from sea level indicating the heavily faulted nature of the subsurface (Figure 5). The flare here is situated above the faults corresponding to the Bjørnøyrenna fault complex (Figure 6A) where the high amplitude anomalies associated with presence of gas can be seen at different stratigraphic levels of the subsurface (Figure 6A). The flare seems to be located ~5 km away from the traceable deep-seated fault location. The URU surface appears to be blotted with gas leaking from the faults which is probably moving upslope along it to the flare location (Figure 6A). The post URU sediments show a chaotic pattern below the flare compared to either side indicating that the sediments are probably of different character allowing fluid flow through them (Figure 6A).

Further south along the eastern boundary of Polhem Platform, the seismic data indicate a dome structure (the Selis Ridge) associated with numerous faults (Figure 6B). Some very strong amplitude anomalies are observed at the URU surface at the shallowest part of the dome where the glacial sediments are thick (~100 ms TWT) and non-tectonized (Figure 6B). The sub-URU stratigraphy is sloping towards west in the west side of the dome whereas it shallows from east to west in the eastern side of the dome. One of the two flares in this area occurs above the fault with a marked high amplitude anomaly close to the URU surface. Many high amplitude anomalies can be seen fringing to the eastern side of the fault below the URU surface as well (Figure 6B). The URU surface is blotted with high amplitude anomaly towards the west of the flare and close to the western end of the seismic line where a second flare is observed (Figure 1). The variance slice (Figure 5) indicates heavy faulting with fault orientations shifting from N-S in the south to NE-SW orientation in the north with the faults becoming more and more bifurcated covering larger areas (Figure 5).

Along the central eastern boundary between the Polhem Platform and Loppa High, the subsurface is faulted with N-S oriented faults (Figures 5, 6C). This location is peculiar with a mixed type of stratigraphic and structural control since the sub-URU sedimentary wedge from the west at the Polhem Platform is pinching out close to this area. The faulted Triassic deposits of Loppa High reach the URU surface here (Figure 6C). The flare observed in this area is located above one of the faults which has a high amplitude anomaly in the subsurface, but dipping strata also pinch out directly below this flare. The presence of deep-seated faults, and the high amplitude anomaly deeper than URU close to the fault, suggests a fault related fluid supply to this flare and the shallow dipping permeable beds serving as fluid conduits (Figure 6C).

The western flare on the Polhem Platform also suggests a similar fluid flow mechanism with direct link to faults but intermediate permeable beds facilitating the fluid flow to the URU level (Figure 6D). Here, many flares occur above the large high

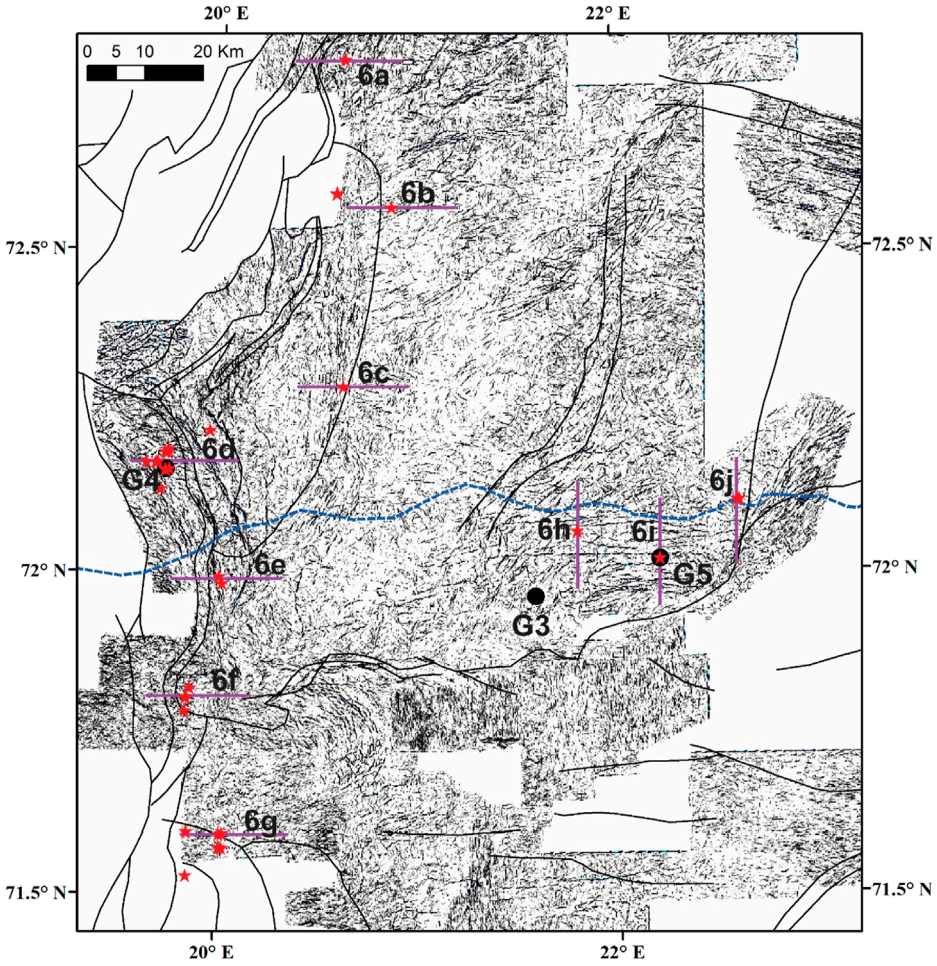

FIGURE 5
Variance cube slice at 800 ms TWT from sea surface of LN12M01 3D seismic data showing the location of flares (red stars), boundary of Bjørnøyrenna glacial advance grounding zone (blue dashed line), seismic sections in Figure 6 (purple lines), gas sample locations (black dots) and regional faults (black lines). Notice the good correlation of flares with faults locations. Figure location is given in Figure 1.

amplitude anomaly close to the URU surface. The gas sample G4 is collected from the seep in this area. The flares along the eastern boundary of RLFC are located above the base Cretaceous pinchout boundary with faults linking the subsurface to seafloor (Figures 6D–G). The subsurface high amplitude anomalies, even though located along a westward dipping stratigraphic boundary, indicate a clear connection to faults below it. The Gohta and Komse Terraces also show the association with flares (Figures 1, 6E). The fluids seem to be accumulating at the top boundary of the faults creating the high amplitude anomaly which is then moving upwards to the URU level through sloping layers of the fault complex (Figure 6E). The triple junction between RLFC and Asterias fault complex along the southern part of the Gohta-Komse terrace appears to be chaotic with many high amplitude anomaly pockets occurring at different level with no apparent connection shown by faults (Figure 6F). The presence of faults as the major mechanism for gas transport can be inferred at the southernmost location along the RLFC where all the flares occur away from the pinch out zones but on top of faults (Figure 6G). The URU surface and sediments above it may be acting as a partially compromised cap rock regulating the fluid transfer from the URU to the seafloor (Figure 6G).

A series of high amplitude anomalies occur along the top of Triassic close to the pinch out zone. But there is no real connectivity between these anomalies and each of these anomalies can be directly linked to faults in the subsurface (Figures 6H–J). As noticeable in seismic data, the fluid flow is controlled by the glacial sediments which in this case are pinching out towards south. Further south, on top of E-W oriented faults, four flares have been identified (Figures 6H–J). The flares appear to be directly connected to the faults with little quaternary sediments overlying these faults (Figures 6H–J). The gas sample G5 is collected from this flare along the line given in Figure 6I. High amplitude anomalies due to the presence of gas can be seen at different levels of stratigraphy along the flanks of the faults (Figures 6H–J). The anomalies are concentrated on one side of the fault and on foot wall part of the permeable layer which is acting as the reservoir.

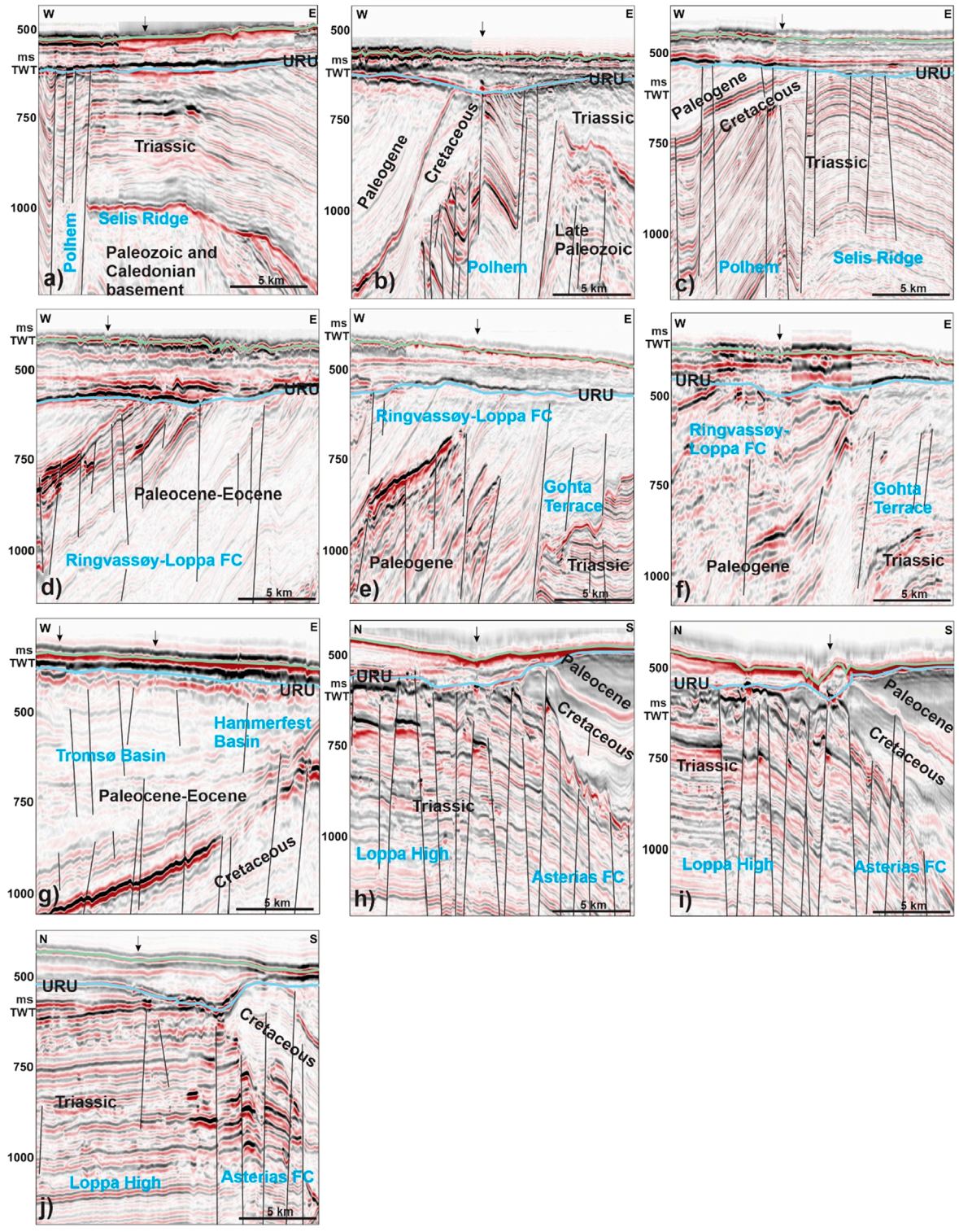

FIGURE 6
Seismic sections **(A–J)** showing examples of high amplitude anomalies related to acoustic gas flares (arrows) observed in the study area (Location in Figure 5). Blue line indicates URU surface, and green line for seafloor. The major faults are marked by black lines. The location of two gas samples, G4 and G5, coincides with flare locations shown on 6d and 6i.

The two easternmost flares located above Svanefjell discovery have a similar model of fluid flow where the faults are bringing fluids to the URU surface and the URU surface act as horizontal cap rock layer with large gas accumulation at the URU level (Figure 6J). The seismic data indicates that the chances of finding a gas flare is very high along the southern part of the seismic data since the gas

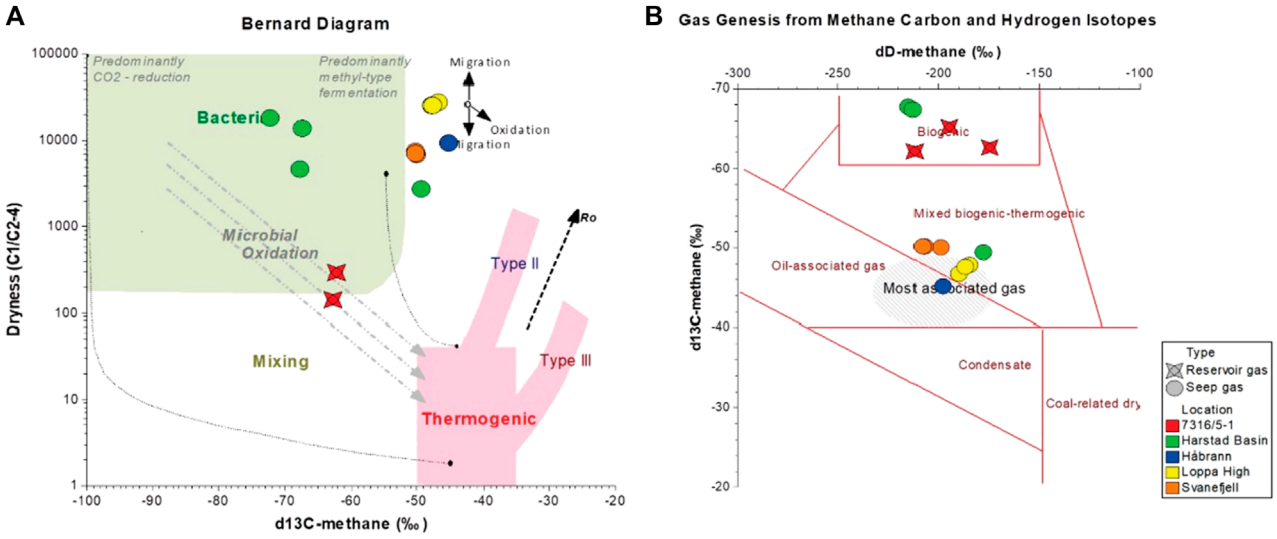

FIGURE 7
Gas composition and isotope data from samples collected from the study area and nearby locations plotted as **(A)** Bernard diagram and **(B)** gas genesis diagram based on methane carbon and hydrogen isotope composition. Locations shown as G1-Well 7316/5-1, G2-Harstad Basin, G3-Håbrann, G4-Loppa High and G5-Svanefjell in Figure 1.

accumulation is having a clear route to the surface from the high amplitude anomaly located at the URU level (Figure 6J).

Geochemical results

Gas composition and isotope data of samples collected from the study area indicate variably mixed thermogenic and bacterial origins of gases (Figure 7). The relationships of methane dD vs. d13C (Figure 7B) are consistent with predominantly thermogenic origin of gases in locations G3, G4 and G5 (δ^{13}C-CH_4: 45.2‰ to −50.2‰, dD-CH_4: 185‰ to −208‰) whereas microbial source dominates in G1 and G2 (δ^{13}C-CH_4: 49.4‰ to −67.8‰, dD-CH_4: 175‰ to −215‰). All seep samples plot in or near the bacterial field on the Bernard diagram (Figure 7A) due to very low abundance of higher molecular-weight components (ethane, propane, butane). The reservoir sample from G1 stands out and plots between the thermogenic and bacterial fields in the Bernard diagram showing that there is some mixing happening at the reservoir level too (Figure 7A) which is clear in the methane isotopic ratios indicating a biogenic origin (Figure 7B). Despite indications of bacterial origin of seep gases based on the Bernard plot relationships, the predominantly thermogenic origin as indicated by methane data (Figure 7B) appears fully feasible given that methane migrates more readily from reservoirs compared to higher-molecular weight components that tend to be retained in the rock (Prinzhofer and Huc, 1995; Martini et al., 1996). Such compositional fractionation along the migration pathway from the reservoir to the seep may result in high C1/(C2-C4) and placement outside the thermogenic field in the Bernard plot (Figure 7B) of G3, G4 and G5 gases that have predominantly thermogenic origin. Still, isotope data of methane suggest that there is a minor bacterial component present in G3, G4 and G5, and a bacterial component is dominant in G1 and G2 as suggested earlier (Crémière et al., 2018).

Discussion

The fluid flow processes in the Loppa High and surrounding region are of special interest to investigate given the forcing of the glacial loading and unloading after deglaciation on the faulted shallow source rocks of Jurassic and Triassic age. The Loppa High is bounded by regional fault complexes of various ages (the Asterias, the Ringvassøy-Loppa, the Bjørnøyrenna and the Hoop fault complexes) on all sides and the sedimentary rocks encompassing the high are also heavily faulted making the region prone for fluid flow from deep source levels. The fault orientations might have changed in directions and dips due to the combined effects of sedimentary loading and various glaciations including erosion and glacio-isostatic uplift resulting in frequent opening and closing of various pathways. The glaciers were ~1,500–2000 m thick during the last glaciation (Siegert et al., 2001; Auriac et al., 2016) reached the maximum extent 25 Ka and started retreating 17 ka ago (Peltier, 2004; Siegert and Dowdeswell, 2004; Svendsen et al., 2004). The loading effect during last glacial maximum spanned over a period of about 8000 years resulting in a thick hydrate stability zone (Chand et al., 2008) and consequent fluids expulsion from the subsurface reservoirs due to the load. Whether the thick and deep gas hydrate stability zone acted as a seal or not is unclear since there are many factors affecting the situation, such as, 1) the rate of grounded ice sheet growth (pressure buildup) vs. intensity of fluid seepage towards the surface, 2) the pore saturation and morphology of the hydrate formed controlling the fluid flow, 3) the temperature of the fluids vs. hydrate stability parameters, 4) proximity of the location to glacial front. In simple terms we can assume that the hydrate layer acted as a barrier, and with the deglaciation, the layer was removed resulting in intense fluid flow to the seafloor immediately followed by long term fluid flow as observed now as flares.

The results from the analysis of seep gas samples from the flare areas indicate that they, except G2, have a deep thermogenic origin, but the reservoir gas in G1 indicates a significant microbial contribution. This can be attributed to microbial degradation of thermogenic gas altering the isotopic composition of the methane gas (Milkov, 2011) most probably resulting from water percolation through open faults. The water percolation can be due to the existence of hydraulic under pressures either due to glacial unloading after hydraulic equilibration during grounded ice loading or due to an inherent under pressure generated due to large scale erosion during various ice ages which got equilibrated with opening of faults (Vinard et al., 2001). Both scenarios exhibit an open system at least for a short duration, consistent with the seepage from the reservoirs. All other samples except those from the Harstad Basin indicates an oil associated existence also implying the possibility of seepage from oil reservoirs. The four study areas are close to hydrocarbon discoveries and therefore such a signature indicates the possibility of past and present seepage from these reservoirs. Results from previous studies (Crémière et al., 2016a) suggest an enhanced seepage scenario after glacier retreat.

Since the fluids are leaking from the shallow sources, the originally deep sourced fluids probably have changed in properties by microbial degradation and hence the original source properties are partly hidden. The acoustic gas flares observed in the study can be related to the location of deep-seated faults in seismic data (Figure 5) and different levels of accumulation can be observed (Figure 6). The glacial deposits cover a major part of the study area, but flares occur wherever a subsurface fault is bringing fluids to the base of these deposits. The Cretaceous and older Mesozoic sediments are shallowing towards the area with the presence of fluid flow anomalies with fluid transfer happening along faults and unconformities. But no apparent single fluid focussing routes can be pointed out indicating a general seepage through heavy faulted sediments bringing the fluids to the URU. On the other hand, the glacial deposits act as a major control in redirecting the upward movement of fluids to the seafloor.

Conclusion

2. Fluid flow in the SW Barents Sea is occurring through faults mediated by glacial sediments.
3. The fluid leaking locations with soft sediments are associated with larger pockmarks (>30 m) than the usual ones and occurrence of carbonate crusts.
4. Geochemical results from the samples indicate that the fluids are mainly deep thermogenic origin and altered by shallow storage during and after glaciation.
5. The thermogenic signature of the seeping fluids indicates the long term and large-scale supply of methane to the global methane budget also from similar areas of potential natural leakage from the subsurface to the water column.

Data availability statement

The datasets presented in this article are not readily available because the raw data is not distributable. Requests to access the datasets should be directed to shyam.chand@ngu.no.

Author contributions

SC: Conceptualization, Data curation, Formal Analysis, Funding acquisition, Investigation, Methodology, Project administration, Resources, Software, Validation, Visualization, Writing–original draft, Writing–review and editing. HB: Investigation, Project administration, Resources, Supervision, Visualization, Writing–review and editing. AL: Data curation, Investigation, Methodology, Validation, Writing–review and editing. TT: Funding acquisition, Investigation, Project administration, Supervision, Visualization, Writing–review and editing. JP: Formal Analysis, Investigation, Resources, Visualization, Writing–review and editing.

Funding

The author(s) declare that financial support was received for the research, authorship, and/or publication of this article. This study was funded by Lundin Norway AS (now Aker BP) and Geological Survey of Norway (NGU).

Acknowledgments

Geological Survey of Norway (NGU): data collection, processing, analysis, research, support and reporting.

Conflict of interest

Authors HB and JP were employed by Expres Aker BP.

The remaining authors declare that the research was conducted in the absence of any commercial or financial relationships that could be construed as a potential conflict of interest.

The authors declare that this study received funding from Lundin Norway AS. The funder had the following involvement in the study: data collection, processing, analysis and reporting.

Publisher's note

References

Aagaard-Sørensen, S., Husum, K., Hald, M., and Knies, J. (2010). Paleoceanographic development in the SW Barents Sea during the Late Weichselian–Early Holocene transition. *Quat. Sci. Rev., APEX Arct. Palaeoclim. its Extrem.* 29, 3442–3456. doi:10.1016/j.quascirev.2010.08.014

Andreassen, K., Hubbard, A., Winsborrow, M., Patton, H., Vadakkepuliyambatta, S., Plaza-Faverola, A., et al. (2017). Massive blow-out craters formed by hydrate-controlled methane expulsion from the Arctic seafloor. *Science* 356, 948–953. doi:10.1126/science.aal4500

Auriac, A., Whitehouse, P. L., Bentley, M. J., Patton, H., Lloyd, J. M., and Hubbard, A. (2016). Glacial isostatic adjustment associated with the Barents Sea ice sheet: a modelling inter-comparison. *Quat. Sci. Rev., Special Issue PAST Gatew. (Palaeo-Arctic Spatial Temporal Gatew.)* 147, 122–135. doi:10.1016/j.quascirev.2016.02.011

Bjorøy, M., Hall, P. B., Ferriday, I. L., and Mørk, A. (2010). Triassic source rocks of the Barents Sea and Svalbard. *Search Discov. Artic.* 10219, 7–10.

Brunstad, H., and Rønnevik, H. C. (2022). Loppa High composite tectono-sedimentary element, Barents Sea. *Geol. Soc.* 57. doi:10.1144/M57-2020-3

Capozzi, R., Oppo, D., and Taviani, M. (2017). Cold seepages: an economic tool for hydrocarbon appraisal. *AAPG Bull.* 101, 617–623. doi:10.1306/011817dig17041

Cavanagh, A. J., Di Primio, R., Scheck-Wenderoth, M., and Horsfield, B. (2006). Severity and timing of Cenozoic exhumation in the southwestern Barents Sea. *J. Geol. Soc.* 163, 761–774. doi:10.1144/0016-76492005-146

Chand, S., Knies, J., Baranwal, S., Jensen, H., and Klug, M. (2014). Structural and stratigraphic controls on subsurface fluid flow at the Veslemøy High, SW Barents Sea. *Mar. Pet. Geol.* 57, 494–508. doi:10.1016/j.marpetgeo.2014.06.004

Chand, S., Mienert, J., Andreassen, K., Knies, J., Plassen, L., and Fotland, B. (2008). Gas hydrate stability zone modelling in areas of salt tectonics and pockmarks of the Barents Sea suggests an active hydrocarbon venting system. *Mar. Pet. Geol.* 25, 625–636. doi:10.1016/j.marpetgeo.2007.10.006

Chand, S., Rise, L., Ottesen, D., Dolan, M., Bellec, V., and Bøe, R. (2009). Pockmark-like depressions near the Goliat hydrocarbon field, Barents Sea: morphology and genesis. *Mar. Pet. Geol.* 26, 1035–1042. doi:10.1016/j.marpetgeo.2008.09.002

Chand, S., Thorsnes, T., Rise, L., Brunstad, H., Stoddart, D., Bøe, R., et al. (2012). Multiple episodes of fluid flow in the SW Barents Sea (Loppa High) evidenced by gas flares, pockmarks and gas hydrate accumulation. *Earth Planet. Sci. Lett.* 331, 305–314. doi:10.1016/j.epsl.2012.03.021

Crémière, A., Chand, S., Sahy, D., Thorsnes, T., Martma, T., Noble, S. R., et al. (2018). Structural controls on seepage of thermogenic and microbial methane since the last glacial maximum in the Harstad Basin, southwest Barents Sea. *Mar. Pet. Geol.* 98, 569–581. doi:10.1016/j.marpetgeo.2018.07.010

Crémière, A., Lepland, A., Chand, S., Sahy, D., Condon, D. J., Noble, S. R., et al. (2016a). Timescales of methane seepage on the Norwegian margin following collapse of the Scandinavian Ice Sheet. *Nat. Commun.* 7, 11509. doi:10.1038/ncomms11509

Crémière, A., Lepland, A., Chand, S., Sahy, D., Kirsimäe, K., Bau, M., et al. (2016b). Fluid source and methane-related diagenetic processes recorded in cold seep carbonates from the Alvheim channel, central North Sea. *Chem. Geol.* 432, 16–33. doi:10.1016/j.chemgeo.2016.03.019

Daszinnies, M., Plaza-Faverola, A., Sylta, Ø., Bünz, S., Mattingsdal, R., Tømmerås, A., et al. (2021). The Plio-Pleistocene seepage history off western Svalbard inferred from 3D petroleum systems modelling. *Mar. Petroleum Geol.* 128, 105023. doi:10.1016/j.marpetgeo.2021.105023

Doré, A. (1995). Barents Sea geology, petroleum resources and commercial potential. *Arctic* 48, 207–221. doi:10.14430/arctic1243

Dupré, S., Scalabrin, C., Grall, C., Augustin, J.-M., Henry, P., Şengör, A. M. C., et al. (2015). Tectonic and sedimentary controls on widespread gas emissions in the Sea of Marmara: results from systematic, shipborne multibeam echo sounder water column imaging. *J. Geophys. Res. Solid Earth* 120, 2891–2912. doi:10.1002/2014JB011617

Eidvin, T., and Riis, F. (1989). Nye dateringer av de tre vestligste borehullene i Barentshavet. Resultater og konsekvenser for den Tertiære hevingen. *Nor. Pet. Dir. Contr.* 27, 1–62.

Einsele, G. (2013). *Sedimentary basins: evolution, facies, and sediment budget*. Berlin, Germany: Springer Science and Business Media.

Eldholm, O., Sundvor, E., Myhre, A. M., and Faleide, J. I. (1984). "Cenozoic evolution of the continental margin off Norway and western Svalbard," in *Petroleum geology of the north European margin*. Editor A. M. Spencer (Netherlands: Springer), 3–18. doi:10.1007/978-94-009-5626-1_2

Faleide, J. I., Solheim, A., Fiedler, A., Hjelstuen, B. O., Andersen, E. S., and Vanneste, K. (1996). Late Cenozoic evolution of the western Barents Sea-Svalbard continental margin. *Glob. Planet. Change, Impact Glaciat. Basin Evol. Data Models Nor. Margin Adjacent Areas* 12, 53–74. doi:10.1016/0921-8181(95)00012-7

Faleide, J. I., Vågnes, E., and Gudlaugsson, S. T. (1993). Late Mesozoic-Cenozoic evolution of the south-western Barents Sea in a regional rift-shear tectonic setting. *Mar. Pet. Geol.* 10, 186–214. doi:10.1016/0264-8172(93)90104-z

Fjeldskaar, W., and Amantov, A. (2018). Effects of glaciations on sedimentary basins. *J. Geodyn.* 118, 66–81. doi:10.1016/j.jog.2017.10.005

Grollimund, B., and Zoback, M. D. (2000). Post glacial lithospheric flexure and induced stresses and pore pressure changes in the northern North Sea. *Tectonophysics* 327, 61–81. doi:10.1016/s0040-1951(00)00162-1

Hagset, A., Grundvåg, S. A., Badics, B., Davies, R., and Rotevatn, A. (2022). Tracing lower cretaceous organic-rich units across the SW Barents shelf. *Mar. Petroleum Geol.* 140, 105664. doi:10.1016/j.marpetgeo.2022.105664

Hampel, A., and Hetzel, R. (2006). Response of normal faults to glacial-interglacial fluctuations of ice and water masses on Earth's surface. *J. Geophys. Res. Solid Earth* 111. doi:10.1029/2005jb004124

Henriksen, E., Bjørnseth, H., Hals, T., Heide, T., Kiryukhina, T., Kløvjan, O., et al. (2011). Chapter 17 Uplift and erosion of the greater Barents Sea: impact on prospectivity and petroleum systems. *Geol. Soc. Lond. Mem.* 35, 271–281. doi:10.1144/m35.17

Hustoft, S., Dugan, B., and Mienert, J. (2009). Effects of rapid sedimentation on developing the Nyegga pockmark field: constraints from hydrological modeling and 3-D seismic data, offshore mid-Norway. *Geochem. Geophys. Geosystems* 10. doi:10.1029/2009gc002409

Johansen, S., Ostisty, B., Fedorovsky, Y., Martirosjan, V., Christensen, O. B., Cheredeev, S., et al. (1993). "Hydrocarbon potential in the Barents Sea region: play distribution and potential," in *Norwegian petroleum society special publications* (Amsterdam, Netherlands: Elsevier), 273–320.

Judd, A., and Hovland, M. (2007). *Seabed fluid flow: the impact on geology, biology and the marine environment*. Cambridge: Cambridge University Press.

Karstens, J., Haflidason, H., Becker, L. W., Berndt, C., Rüpke, L., Planke, S., et al. (2018). Glacigenic sedimentation pulses triggered post-glacial gas hydrate dissociation. *Nat. Commun.* 9, 635. doi:10.1038/s41467-018-03043-z

Khader, O., and Novakowski, K. (2014). Impacts of Pleistocene glacial loading on abnormal pore-water pressure in the eastern Michigan Basin. *Geofluids* 14, 200–220. doi:10.1111/gfl.12074

King, L. H., and MacLean, B. (1970). Pockmarks on the Scotian shelf. *GSA Bull.* 81, 3141–3148. doi:10.1130/0016-7606(1970)81[3141:potss]2.0.co;2

Laberg, J. S., Andreassen, K., Knies, J., Vorren, T. O., and Winsborrow, M. (2010). Late Pliocene–Pleistocene development of the Barents Sea ice sheet. *Geology* 38, 107–110. doi:10.1130/G30193.1

Laberg, J. S., Andreassen, K., and Vorren, T. O. (2012). Late Cenozoic erosion of the high-latitude southwestern Barents Sea shelf revisited. *Geol. Soc. Am. Bull.* 124, 77–88. doi:10.1130/b30340.1

Leifer, I., and MacDonald, I. (2003). Dynamics of the gas flux from shallow gas hydrate deposits: interaction between oily hydrate bubbles and the oceanic environment. *Earth Planet. Sci. Lett.* 210, 411–424. doi:10.1016/S0012-821X(03)00173-0

Martini, A. M., Budai, J. M., Walter, I. M., and Schoell, M. (1996). Microbial generation of economic accumulations of methane within a shallow organic-rich shale. *Nature* 383, 155–158. doi:10.1038/383155a0

Milkov, A. V. (2011). Worldwide distribution and significance of secondary microbial methane formed during petroleum biodegradation in conventional reservoirs. *Org. Geochem.* 42, 184–207. doi:10.1016/j.orggeochem.2010.12.003

Nickel, J. C., di Primio, R., Kallmeyer, J., Hammer, Ø., Horsfield, B., Stoddart, D., et al. (2013). Tracing the origin of thermogenic hydrocarbon signals in pockmarks from the southwestern Barents Sea. *Org. Geochem.* 63, 73–84. doi:10.1016/j.orggeochem.2013.08.008

NPD (2016). Fact pages, Norwegian petroleum directorate. Available at: http://www.npd.no/no/Tema/.

Patton, H., Andreassen, K., Bjarnadóttir, L. R., Dowdeswell, J. A., Winsborrow, M. C. M., Noormets, R., et al. (2015a). Geophysical constraints on the dynamics and retreat of the Barents Sea ice sheet as a palaeo benchmark for models of marine ice sheet deglaciation. *Rev. Geophys.* 53, 2015RG000495. doi:10.1002/2015RG000495

Patton, H., Andreassen, K., Bjarnadóttir, L. R., Dowdeswell, J. A., Winsborrow, M. C. M., Noormets, R., et al. (2015b). Geophysical constraints on the dynamics and retreat of the Barents Sea Ice Sheet as a palaeo-benchmark for models of marine ice-sheet deglaciation: geophysical constraints on the BSIS. *Rev. Geophys. n/a-n/a* 53, 1051–1098. doi:10.1002/2015RG000495

Pau, M., Hammer, Ø., and Chand, S. (2014). Constraints on the dynamics of pockmarks in the SW Barents Sea: evidence from gravity coring and high-resolution, shallow seismic profiles. *Mar. Geol.* 355, 330–345. doi:10.1016/j.margeo.2014.06.009

Peltier, W. (2004). Global glacial isostasy and the surface of the ice-age Earth: the ICE-5G (VM2) model and GRACE. *Annu. Rev. Earth Planet Sci.* 32, 111–149. doi:10.1146/annurev.earth.32.082503.144359

Portnov, A., Vadakkepuliyambatta, S., Mienert, J., and Hubbard, A. (2016). Ice-sheet-driven methane storage and release in the Arctic. *Nat. Commun.* 7, 10314. doi:10.1038/ncomms10314

Prinzhofer, A. A., and Huc, A. Y. (1995). Genetic and post genetic molecular and isotopic fractionations in natural gases. *Chem. Geol.* 126, 281–290. doi:10.1016/0009-2541(95)00123-9

Riis, F., and Fjeldskaar, W. (1992). "On the magnitude of the Late Tertiary and Quaternary erosion and its significance for the uplift of Scandinavia and the Barents Sea," in *Structural and tectonic modeling and its application to the petroleum geology* (Amsterdam: NPF Special Publication. Elsevier), 163–185.

Rise, L., Bellec, V., Chand, S., and Bøe, R. (2015). Pockmarks in the southwestern Barents Sea and Finnmark fjords. *Nor. J. Geol.* 94, 263–282. doi:10.17850/njg94-4-02

Römer, M., Sahling, H., Pape, T., dos Santos Ferreira, C., Wenzhöfer, F., Boetius, A., et al. (2014). Methane fluxes and carbonate deposits at a cold seep area of the central Nile deep sea fan, eastern Mediterranean Sea. *Mar. Geol.* 347, 27–42. doi:10.1016/j.margeo.2013.10.011

Sættem, J., Rise, L., and Westgaard, D. A. (1991). Composition and properties of glacigenic sediments in the southwestern Barents Sea. *Mar. Geotechnol.* 10, 229–255. doi:10.1080/10641199109379893

Sen, A., Åström, E. K. L., Hong, W.-L., Portnov, A. D., Waage, M., Serov, P., et al. (2018). Geophysical and geochemical controls on the megafaunal community of a high Arctic cold seep. *Biogeosciences* 15, 4533–4559. doi:10.5194/bg-15-4533-2018

Sen, A., Ondréas, H., Gaillot, A., Marcon, Y., Augustin, J.-M., and Olu, K. (2016). The use of multibeam backscatter and bathymetry as a means of identifying faunal assemblages in a deep-sea cold seep. *Deep Sea Res. Part Oceanogr. Res. Pap.* 110, 33–49. doi:10.1016/j.dsr.2016.01.005

Serov, P., Mattingsdal, R., Winsborrow, M., Patton, H., and Andreassen, K. (2023). Widespread natural methane and oil leakage from sub-marine Arctic reservoirs. *Nat. Commun.* 14, 1782. doi:10.1038/s41467-023-37514-9

Siegert, M. J., and Dowdeswell, J. A. (2004). Numerical reconstructions of the Eurasian ice sheet and climate during the Late Weichselian. *Quat. Sci. Rev.* 23, 1273–1283. doi:10.1016/j.quascirev.2003.12.010

Siegert, M. J., Dowdeswell, J. A., Hald, M., and Svendsen, J.-I. (2001). Modelling the Eurasian ice sheet through a full (Weichselian) glacial cycle. *Glob. Planet. Change, late Quat. Stratigr. Environ. North. Eurasia adjacent Arct. seas - new contributions QUEEN* 31, 367–385. doi:10.1016/S0921-8181(01)00130-8

Sloan Jr, E. D., and Koh, C. (2007). *Clathrate hydrates of natural gases*. United States: CRC Press.

Smelror, M., Petrov, O., Larssen, G. B., and Werner, S. (2009). Geological history of the Barents Sea. *Nor. Geol. Unders.*, 1–135.

Solheim, A., and Kristoffersen, Y. (1984). The physical environment, Western Barents Sea; Sediments above the upper regional unconformity: thickness, seismic stratigraphy and outline of the glacial history. *Nor. Polarinst. Skr.* 179B, 26.

Spencer, A. M., Home, P. C., and Berglund, L. T. (1984). "Tertiary structural development of the western Barents shelf: Troms to Svalbard," in *Petroleum geology of the north European margin*. Editor A. M. Spencer (Netherlands: Springer), 199–209. doi:10.1007/978-94-009-5626-1_14

Svendsen, J. I., Alexanderson, H., Astakhov, V. I., Demidov, I., Dowdeswell, J. A., Funder, S., et al. (2004). Late Quaternary ice sheet history of northern Eurasia. *Quat. Sci. Rev.* 23, 1229–1271. doi:10.1016/j.quascirev.2003.12.008

Thiagarajan, N., Pedersen, J. H., Brunstad, H., Rinna, J., Lepland, A., and Eiler, J. (2022). Clumped isotope constraints on the origins of reservoir methane from the Barents Sea. *Pet. Geosci.* 28. doi:10.1144/petgeo2021-037

Thorsnes, T., Chand, S., Bellec, V., Nixon, F. C., Brunstad, H., Lepland, A., et al. (2023). Gas seeps in Norwegian waters – distribution and mechanisms. *Nor. J. Geol.* 103, 202309. doi:10.17850/njg103-2-4

Vadakkepuliyambatta, S., Bünz, S., Mienert, J., and Chand, S. (2013). Distribution of subsurface fluid-flow systems in the SW Barents Sea. *Mar. Pet. Geol.* 43, 208–221. doi:10.1016/j.marpetgeo.2013.02.007

Vinard, P., Bobet, A., and Einstein, H. H. (2001). Generation and evolution of hydraulic underpressures at Wellenberg, Switzerland. *Jour. Geophys. Res.* 106 (B12), 30593–30605. doi:10.1029/2001jb000327

Vorren, T. O., Hald, M., and Lebesbye, E. (1988). Late Cenozoic environments in the Barents Sea. *Paleoceanography* 3, 601–612. doi:10.1029/PA003i005p00601

Vorren, T. O., Kristoffersen, Y., and Andreassen, K. (1986). Geology of the inner shelf west of North Cape, Norway. *Geol. Tidsskr.* 66.

Vorren, T. O., Richardsen, G., Knutsen, S.-M., and Henriksen, E. (1991). Cenozoic erosion and sedimentation in the western Barents Sea. *Mar. Pet. Geol.* 8, 317–340. doi:10.1016/0264-8172(91)90086-g

Winsborrow, M., Andreassen, K., Hubbard, A., Plaza-Faverola, A., Gudlaugsson, E., and Patton, H. (2016). Regulation of ice stream flow through subglacial formation of gas hydrates. *Nat. Geosci.* 9, 370–374. doi:10.1038/ngeo2696

Winsborrow, M. C., Andreassen, K., Corner, G. D., and Laberg, J. S. (2010). Deglaciation of a marine-based ice sheet: late Weichselian palaeo-ice dynamics and retreat in the southern Barents Sea reconstructed from onshore and offshore glacial geomorphology. *Quat. Sci. Rev.* 29, 424–442. doi:10.1016/j.quascirev.2009.10.001

frontiers | Frontiers in Earth Science

TYPE Original Research
PUBLISHED 14 June 2024
DOI 10.3389/feart.2024.1287226

OPEN ACCESS

EDITED BY
Carolyn Ruppel,
US Geological Survey (USGS), United States

REVIEWED BY
Casey R. J. Hubert,
University of Calgary, Canada
Wolfram Geissler,
Alfred Wegener Institute Helmholtz Centre for Polar and Marine Research (AWI), Germany

*CORRESPONDENCE
Tim R. de Groot,
tim.de.groot@nioz.nl

RECEIVED 01 September 2023
ACCEPTED 08 May 2024
PUBLISHED 14 June 2024

CITATION
de Groot TR, Kalenitchenko D, Moser M, Argentino C, Panieri G, Lindgren M, Dølven KO, Ferré B, Svenning MM and Niemann H (2024), Methanotroph activity and connectivity between two seep systems north off Svalbard.
Front. Earth Sci. 12:1287226.
doi: 10.3389/feart.2024.1287226

Methanotroph activity and connectivity between two seep systems north off Svalbard

Tim R. de Groot[1]*, Dimitri Kalenitchenko[2,3], Manuel Moser[2], Claudio Argentino[2], Giuliana Panieri[2], Matteus Lindgren[2], Knut Ola Dølven[2], Benedicte Ferré[2], Mette M. Svenning[2,4] and Helge Niemann[1,2,5]

[1]Marine Microbiology and Biogeochemistry, NIOZ Royal Netherlands Institute for Sea Research, Texel, Netherlands, [2]CAGE – Centre of Arctic Gas Hydrate, Environment and Climate, Department of Geosciences, UiT the Arctic University of Norway, Tromsø, Norway, [3]LIttoral ENvironnement et Sociétés (LIENSs)—UMR 7266, La Rochelle, France, [4]Department of Arctic and Marine Biology, UiT the Arctic University of Norway, Tromsø, Norway, [5]Department of Earth Sciences, Utrecht University, Utrecht, Netherlands

Understanding methane flux dynamics in Arctic cold seep systems and the influence of oceanic currents on microbial methane-oxidizing bacteria (MOB) is crucial for assessing their impact on Arctic methane emissions. Here, we investigate methane dynamics and associated microbial communities at two cold seep areas, Norskebanken and Hinlopen Trough, North of Svalbard. Methane concentrations and methane oxidation rates (MOx) were measured in bottom and surface waters, with higher values observed in bottom waters, particularly at Hinlopen Trough. Dominant water column MOB clusters were Milano–WF1B–03 and *Methyloprofundus*. Methane availability drove MOx activity, as indicated by higher concentrations in bottom waters and sediments where MOx was elevated, too. Sediment MOB communities varied among locations, with Hinlopen featuring higher diversity and abundance. Similarities between sediments and water column MOBs suggest potential recruitment from sediments, possibly via a bubble shuttle mechanism. In addition, bottom water MOB community composition also showed similarities between the Norskebanken and Hinlopen seeps, implying an exchange of water column microbes between the two seep areas, which may likely be driven by the regional current regime. Together, our results show that bubble-mediated transport and translocation via currents are important processes shaping the community structure and efficiency of the microbial methane filter in the water column.

KEYWORDS

Arctic, cold seep, methane, methane oxidation, microbial connectivity

1 Introduction

Methane, a potent greenhouse gas with a much higher global warming potential than carbon dioxide, is a key component in planed strategies to reduce global warming (Etminan et al., 2016; IPCC, 2021). In marine environments, methane production is primarily attributed to microbial or thermogenic processes in sediments. At cold seeps, this methane migrates upwards through stratigraphic or structural pathways, frequently accompanied by geofluids and other reduced chemical

compounds such as sulfide (Reeburgh, 2007). At these systems, the reduced compounds and electron acceptors (oxygen, nitrite/nitrate, metal oxides and sulfate) form steep geochemical gradients close to the seafloor because a substantial amount of methane is reduced by a cascade of different modes of microbial methane oxidation. Most importantly, methane is oxidized with sulfate as a terminal electron acceptor in deeper sediment layers followed by other alternative electron acceptors and finally oxygen at the sediment surface (James et al., 2016). The geochemical gradients also play a vital role in supporting ecosystems that rely on chemosynthesis (Fisher et al., 1997; Gibson et al., 2005; Argentino et al., 2022).

On a global scale, most methane is retained in mare sediments, but substantial amounts typically circumvent the benthic microbial methane filter at cold seeps. Cold seeps thus release methane into the water column, but the activity of methane efflux at these geo structures can vary on geological (Suess, 2020), seasonal (Mau et al., 2013; Berndt et al., 2014; Silyakova et al., 2020; Dølven et al., 2022) and diel to hourly time scales (Römer et al., 2016; Sultan et al., 2020; Dølven et al., 2022). Net methane emissions from the ocean into the atmosphere are relatively low compared to other natural sources, but highly skewed towards higher emissions at shallow coastal areas. Here the vertical distance between the seafloor and sea surface is short, providing only a limited time window for microbial oxidation to efficiently consume methane before reaching the atmosphere (James et al., 2016; Weber et al., 2019; de Groot et al., 2023). In the water column, the aerobic oxidation of methane (MOx) is the most important methane sink. This is facilitated by aerobic methane–oxidizing bacteria (MOB), commonly referred to as methanotrophs. MOx can be summarized by the following equation (Reeburgh, 2007):

$$CH_4 + 2\,O_2 \rightarrow CO_2 + 2\,H_2O \quad (1)$$

Known MOBs belong to the Gammaproteobacteria (type I and type X), Alphaproteobacteria (type II), Verrucomicrobia and members of the candidate division NC10 (Knief, 2015). MOB communities substantially mitigate the release of methane intro the atmosphere (Boetius and Wenzhöfer, 2013; Steinle et al., 2016; Gründger et al., 2021). However, the efficiency of MOx can be modulated by multiple environmental factors such as nutrient and methane availability, redox dynamics, water temperature and water depth (Reeburgh, 2007; Crespo-Medina et al., 2014; de Groot et al., 2023). Additionally, deep mixing and currents have been identified as important agents in the translocation of MOBs, thereby impacting the efficiency of the microbial methane filter (Steinle et al., 2015; James et al., 2016; Gründger et al., 2021). Methanotrophic activity in the water column can also be hampered by the availability of methane, oxygen, and nutrients (Reeburgh, 2007; Crespo-Medina et al., 2014; Steinle et al., 2017).

In the Arctic, currents play a vital role in introducing nutrients and biomass to higher latitudes (Oziel et al., 2020). The West Spitsbergen Current (WSC) carries warm nutrient–rich Atlantic Water (AW) north into the North Svalbard Current (NSC), passing Norskebanken and the Hinlopen Trough (Menze et al., 2020), where numerous cold seeps were reported (Geissler et al., 2016) (Figure 1). The WSC also passes by the seep systems West of Svalbard, which release methane of a mixed thermogenic/microbial origin to the water column (Graves et al., 2015; Mau et al., 2017; Sauer et al., 2021).

In this study, we focused on methane dynamics above two cold seep systems at Norskebanken and Hinlopen Trough, where we found extremely high methane concentrations but contrasting methane oxidation rates—low at Norskebanken but high in Hinlopen Trough. The aim of our study was to investigate the microbial communities associated with these seep sites and unravel whether the contrasting methane oxidation patterns are influenced by regional and local transport and exchange of microbial communities due to ocean currents.

2 Materials and methods

2.1 Site description and sampling

Samples were acquired during a research expedition with R/V Kronprins Haakon (CAGE 20-7) from November 2nd until 16 November 2020. Our study areas are located north of Svalbard, (i) a flat rocky section on the Yermak plateau called Norskebanken (~200 m water depth) and (ii) a deep trench between the islands of Spitsbergen and Nordaustlandet on Svalbard's northern margin called the Hinlopen Trough (500-meter water depth; Figure 1). Both sites are known to feature cold seep locations (Geissler et al., 2016) and could be a potential sources of methane to the atmosphere. During our cruise, we detected 288 acoustic "flares" indicative of bubble emission sites at Norskebanken and 239 at Hinlopen Trough during multibeam echosounder surveys. The flares extended 6—97 m (average = 35 m) from the seafloor at Norskebanken and 13—222 m (average = 98 m) at Hinlopen Trough. Our study areas are highly influenced by incoming Atlantic water (AW) that flows along the Western Svalbard shelf as part of the West Spitsbergen Current (WSC; Menze et al., 2020). The incoming AW can influence microbial diversity in the Arctic Ocean by introducing heat, nutrients, and (re) introducing bacterial communities (Steinle et al., 2015; Gründger et al., 2021).

Samples were taken from two locations at Norskebanken designated as Norskebanken West (80°37.397 N, 14°06.302 E) and Norskebanken East (80°37.398 N, 14°24.725 E), and from three locations in the Hinlopen Trough designated as Hinlopen West (80°30.395 N, 16°04.391 E), Hinlopen South (80°28.885 N, 16°09.311 E), and Hinlopen East (80°30.520 N, 16°10.194 E) (Figure 1B). The distance between Norskebanken (Norskebanken E) and in the Hinlopen Trough (Hinlopen W) was approximately 50 km.

Seafloor observations were conducted with the remotely operated vehicle (ROV) ÆGIR 6000 from the Norwegian Marine Robotics Laboratory at the University of Bergen. During hydro casts, we continuously measured water mass properties (temperature, salinity, pressure, oxygen) using a Sea–Bird (SBE911) + conductivity–temperature–depth (CTD) system. The CTD frame also featured a rosette sampler with 24 × 12 L Niskin bottles, which were used to acquire discrete water samples at each hydro cast location. At Norskebanken West, water samples were collected from five depths, while at Norskebanken East and in the Hinlopen Trough, samples were collected from six and eight depths, respectively. Immediately upon recovery, we subsampled Niskin

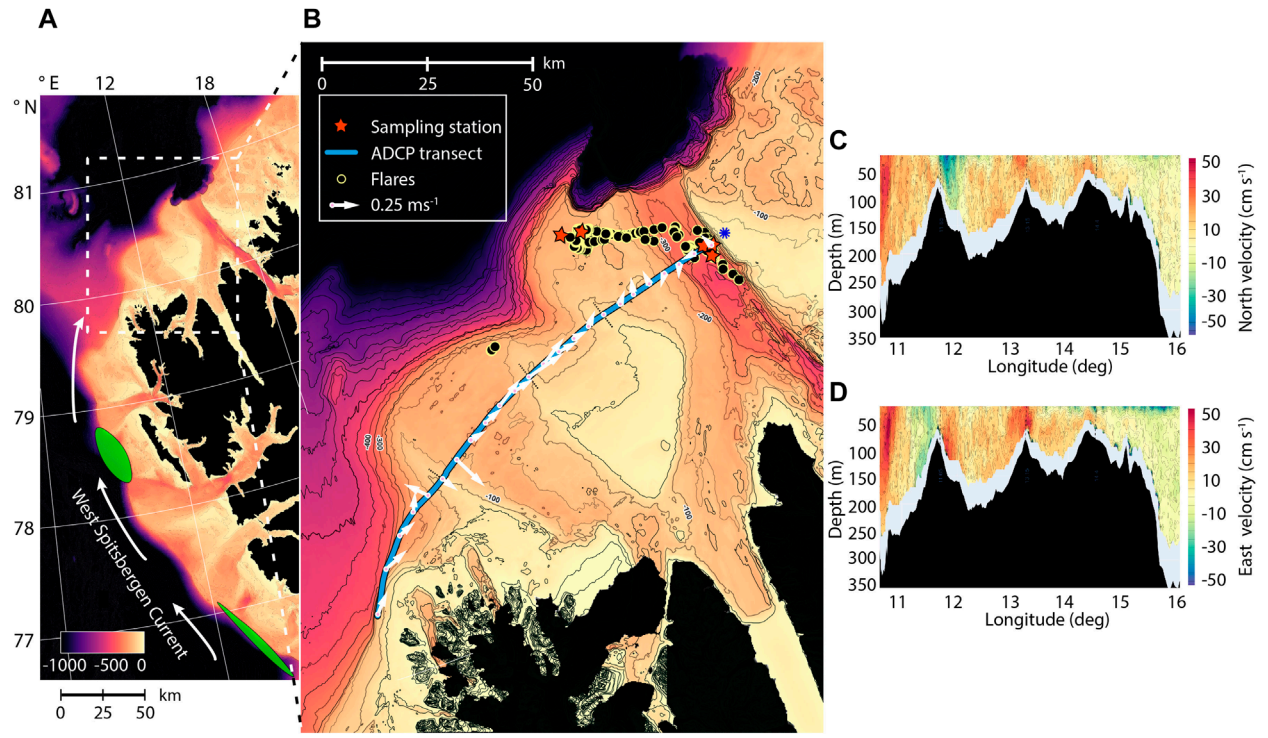

FIGURE 1
(A) Northwestern Spitsbergen, with arrows indicating the northward flow of the West Spitsbergen Current along the western side of Svalbard. Green ellipses denote extensive seep areas west of Prins Karls Forland, previously studied for MOB (Steinle et al., 2015; Mau et al., 2017; Gründger et al., 2021). **(B)** Map of Norskebanken (80˚37 N, 14˚06 E) and Hinlopen Trough (80˚30 N, 16˚04 E), showing sampling stations, flare observations, and the ADCP transect. Arrows represent bottom water velocity and direction at discrete locations. The easternmost velocity, denoted by a blue star, was derived from an earlier ADCP section (Supplementary Figure S1). **(C)** ADCP transect data illustrating the northward velocity component. **(D)** ADCP transect data displaying the eastward velocity component. Note that this ADCP transect was collected over a 9–h measurement period and velocities can be influenced by processes on short timescales such as tidal effects and surface wind forcing.

bottles for subsequent analyses of water column constituents as well as microbial activity and microbial community composition. At Norskebanken East and Hinlopen East, the ROV was used to grab–and then position the CTD frame directly into the plume of rising bubbles close to the sea floor (hereafter, these samples are denoted as ROV–grab).

Suspended particulate organic matter (POM) was sampled from two depths at Norskebanken East (60 m and 160 m), Hinlopen West (120 m and 330 m), South (100 m and 345 m) and East (350 m) using two McLane *in situ* pumps (WTS–LV) equipped with glass fibre filters (142 mm, 0.3 µm nominal mesh size, Advantec MFS).

2.2 Sediments

We employed two different sampling methods to collect sediment samples from various locations at Hinlopen Trough and Norskebanken East. The choice of sampling method depended on the sediment characteristics at each site. The fine sediments in Hinlopen Trough allowed us to sample them with push core samplers operated by the ROV. At Norskebanken East, the high proportion of sand and rocks/carbonate crusts prevented the collection of sediments by push coring. Instead, we used a multiple corer deployed from the ship. Immediately after retrieval, the sediment cores were sliced into one–centimeter sections. Aliquots for microbiological analysis were taken with a sterile spatula and immediately frozen at −20°C for further analysis.

2.3 Dissolved methane concentrations

Dissolved methane concentrations were quantified using a headspace technique (Green, 2005). Immediately after CTD recovery, 120 mL flasks were filled headspace–free with seawater, and the samples were fixed with 1 mL 1M NaOH. The flasks were then crimp top–sealed and stored at 4°C. Before analysis, a headspace was introduced by replacing 5 mL of water with 5 mL N_2 gas, and the samples were allowed to equilibrate for minimum 24 h. The headspace methane concentrations were measured using a gas chromatograph (Thermo Scientific Trace 1310 GC, FID detector, Thermo Scientific TG–BOND MSieve 5A column).

Sediments for methane concentration measurements were subsampled with cut–off syringes from sediment cores immediately upon core recovery. Methane concentrations were determined from 5 mL sediment aliquots fixed in 5 mL 1M NaOH solution in a 20 mL glass vials. All samples for methane concentration measurement were stored upside–down at 4°C. The headspace methane concentrations were measured using a gas chromatograph (Thermo Scientific Trace 1310 GC, FID detector, Restek Rt–Alumina BOND/Na_2SO_4 column).

2.4 Methane oxidation rate measurements

Methane oxidation rates were determined by *ex–situ* incubations with trace amounts of ^{3}H-labelled methane as described previously (Niemann et al., 2015). Briefly, from each Niskin bottle, sea water aliquots were filled headspace free in 20 mL glass vials in quadruplicates and sealed with grey–bromobutyl stoppers that are known to not hamper methanotrophic activity and amended with 5 µL of ^{3}H-CH_4 in N_2 (4.5 kBq, American Radiolabeled Chemicals, United States). Samples were incubated for 2–3 days in the dark at 4°C. Activities of residual C^3H_4 and the MOx product ^3H_2O were measured by liquid scintillation counting.

First order rate constants (k) were determined from fractional tracer turnover (Reeburgh, 2007):

$$k = \frac{^3H_2O}{^3H_2O + C^3H_4} \times \frac{1}{t} \quad (2)$$

Where t is the incubation time in days. k was corrected for (insubstantial) tracer turnover in killed controls (k_{KC}, fixed with 50 µL $HgCl_2$ directly after sampling). Together with methane concentrations [CH_4], ($k–k_{KC}$) yields MOx:

$$MOx = (k - k_{KC}) \times [CH_4] \quad (3)$$

2.5 DNA extraction and 16S rRNA gene amplicon library preparation

DNA was extracted from filters (suspended POM) and sediment samples using the PowerSoil Pro DNA extraction kit (Mo Bio Laboratories, Carlsbad, CA, United States) and stored at −20°C until further analysis. Gene amplification was performed in triplicate with the universal SSU primer pair 515F-Y/926R targeting the V4 and V5 hypervariable regions (Parada et al., 2016) as described earlier (Vaksmaa et al., 2021) but with an adaptation to the PCR program: 5 min initial enzyme activation/DNA denaturation at 98°C, followed by 25 cycles of 98°C for 1 min, 58°C for 1 min, 72°C for 2 min, with a final elongation of 72°C for 10 min. The 16S rRNA gene products, comprising approximately 400 bp with unique Golay barcodes incorporated into the forward and reverse primers, underwent gel purification. Subsequently, library preparation, pooling, and Illumina MiSeq 2 × 300 sequencing were performed at Integrated Microbiome Resource (IMR).

To analyze the bacterial and archaeal 16S amplicon reads, we utilized the DADA2 algorithm (Callahan et al., 2016), implemented in Qiime2 (v2021.8.0). The following steps were performed on the raw reads: filtering, merging, denoising, and removal of chimeric sequences. Truncation lengths of 270 bp (forward) and 210 bp (reverse) were used during the process. This allowed us to obtain high–quality sequences for downstream analysis. Taxonomy assignment of the resulting inferred Amplicon Sequence Variants (ASVs) was done using Mothur (v1.43.0) (Schloss et al., 2009) and the SILVA non–redundant SSU database version 138 (Quast et al., 2013). ASVs assigned to Eukaryotes, mitochondria, chloroplasts, or those lacking domain–level taxonomy were excluded from further analysis to focus specifically on Bacteria and Archaea. Alpha and beta diversity was estimated using the R programming language with the vegan package (v. 2.5–6). Dispersed alpha diversity values were calculated as means of 25 iterations to account for potential variation. Hierarchical clustering and Non–Metric Multidimensional Scaling (NMDS) analyses were performed based on the Bray–Curtis dissimilarity index. These approaches allowed us to assess the similarity and dissimilarity of microbial communities across samples. To investigate potential correlations between bacterial phyla at the family level and selected environmental variables, Spearman's rank correlation was conducted using the R package Hmisc (v.4.4–0). Only family–level clades (SILVA taxonomy v.132) that accounted for at least 0.5% of the total sequences in at least one sample were considered for the analysis. Furthermore, to evaluate differences between groups, we employed PERMANOVA (Permutational Multivariate Analysis of Variance) tests. This statistical approach allowed us to assess the significance of dissimilarities in microbial community composition between different sample groups. Additionally, an analysis was conducted using the DADA2–generated ASV abundance tables. A Venn diagram was constructed to visualize the distribution and overlap of ASVs across sampling regions. This analysis aimed to identify shared ASVs between sediment and water column habitats within specific sampling regions.

2.6 ADCP

Current velocities were measured with a 150 kHz Teledyne RD 206 Ocean Surveyor Acoustic Doppler Current Profiler (ADCP). The ADCP was set to operate in narrowband configuration with 60 ping ensemble over a 2-min ensemble interval. The blanking distance was 27 m (including ship draft), and bin size was set to 8 m. The data was averaged with a 500 m horizontal bin size. We calculated mass transport in the bottom 100 m of water column since this is where the main stock of methane oxidizing bacteria are situated.

The transect started from the Hinlopen Trough at 16.07°E, 80.50°N at 07:00 the 11th of November traversing Norskebanken from east to west, ending at the shelf break at the northwest corner of Spitsbergen at 10.42°E, 79.82°N at 17:00 the 11th of November. It covers the shelf break in the west then follows two depressions, the first one being part of a depression that connects to the Hinlopen Trough slightly south of the Hinlopen South/East/West sampling stations (Figure 1). The second depression is a shallow trough that tapers off into the shallowest central part of Norskebanken. The easternmost part of the transect goes into the Hinlopen and ends at the Hinlopen East sampling station.

3 Results

3.1 Water column properties and water masses

At Norskebanken, water temperatures were ~3.5°C in the surface and increased relatively gradually with depth to 5.1°C in

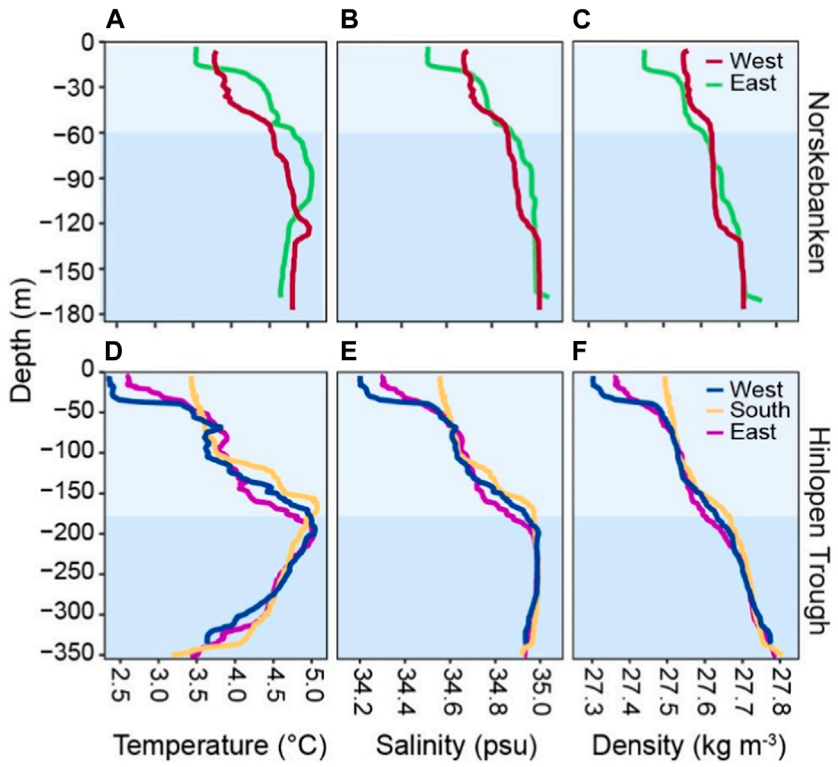

FIGURE 2
Water column characteristics of Norskebanken **(A–C)** and Hinlopen Trough **(D–F)**; different water layers are highlighted as light (surface waters) and darker blue (bottom waters). At Norskebanken, the colors for surface and bottom waters correspond to water depths of 0–55 m, and 55–175 m, while at Hinlopen Trough, they correspond to depths of 0–180 m, and 180–350 m.

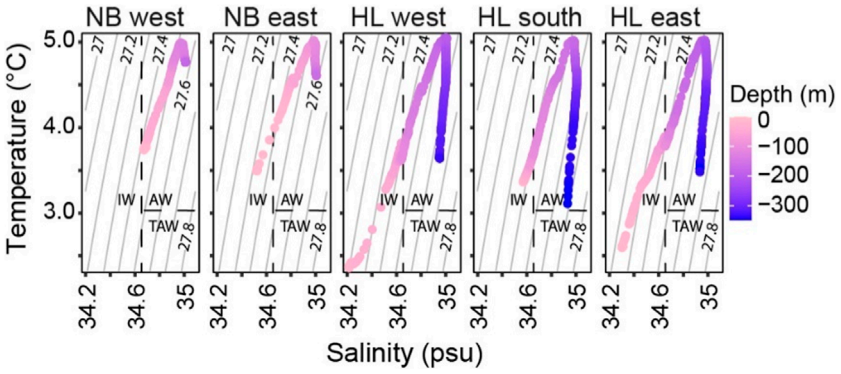

FIGURE 3
Temperature and salinity profiles of Norskebanken (NB) and Hinlopen Trough (HL) showing distinct water properties. The warm and saline Atlantic waters (AW) with temperatures above 3°C and salinities above 34.65 psu dominate the deeper layers, while intermediate waters (IW) with temperatures above 1°C and salinities between 34 and 34.65 psu are only present in surface layers.

bottom waters. Hinlopen displayed lower surface temperatures of 2.4°C (West), 3.2°C (South), and 2.6°C (East), with increasing temperatures up to a maximum of 5.0°C at Hinlopen West and East, and 5.1°C at Hinlopen South at ~180 m depth. Below this depth, temperatures decreased to ~3.5°C in the bottom water at ~350 m depth. Salinity showed a similar pattern, with values at Norskebanken ranging from 34.5 psu (surface) to 35.1 psu (bottom). At Hinlopen, salinity was 34.2 psu (surface) and reached a maximum of 35.0 psu at ~180 m depth but were constant (rather than decreasing) from this depth to the bottom.

The two areas shared common water masses at specific depths, following the classification by previous studies (Cottier et al., 2005). At the Norskebanken stations, the water column featured relatively warm and saline Atlantic Water (AW: >3°C, >34.65 psu) below a

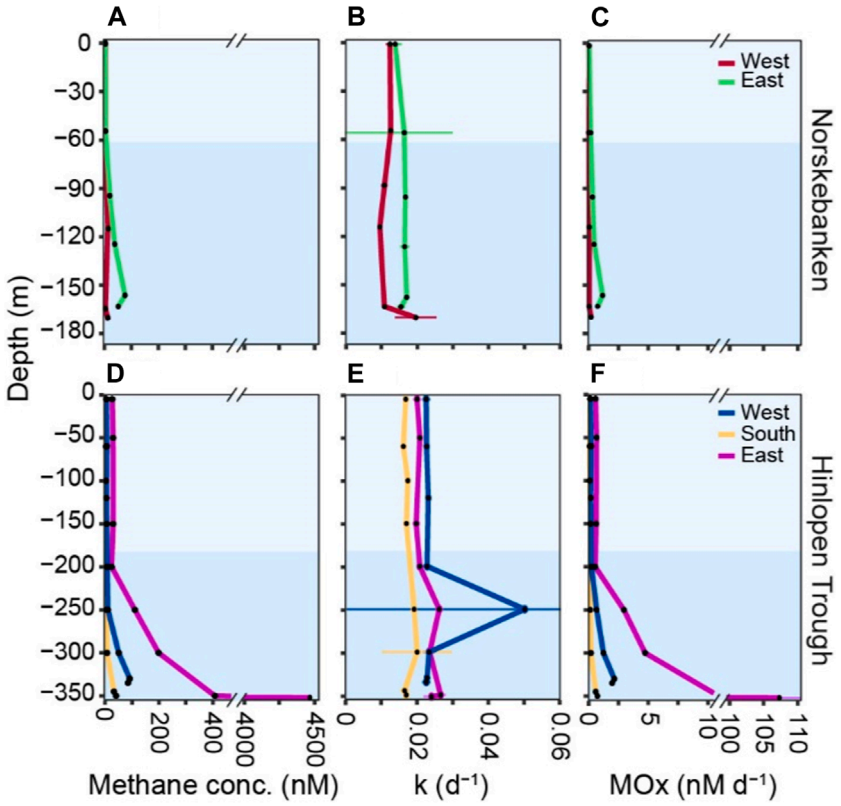

FIGURE 4
Methane concentrations, first–order rate constant (*k*), and MOx activity at Norskebanken **(A–C)** and Hinlopen Trough **(D–F)**. Note the axis break on the *x*-axis for methane concentrations and MOx. The water column is divided into surface waters, also referred to as intermediate waters (IW), and bottom waters, also referred to as Atlantic waters (AW), based on distinct temperature and salinity characteristics (Figure 3). At Norskebanken, the colors correspond to water depths of 0–55 m, and 55–175 m, while at Hinlopen Trough, they correspond to depths of 0–180 m, and 180–350 m.

~25 m deep surface layer (Figures 2, 3). At the Hinlopen stations, AW occupied waters below ~105 m with similar densities as observed in the bottom waters of Norskebanken (~1,027.5 kg m^{-3}). This supports an assumption of recent/frequent exchange of water masses between the sampling stations.

At the western extension of the ADCP transect, we observed a robust northeastern flow with velocities reaching up to 50 cm/s associated with the West Spitsbergen Current situated at the western shelf break of Spitsbergen (Figure 1B, <11°E). Following the transect eastward onto Norskebanken, the western depression at ~12–13°E featured a vigorous southeastward current into the depression (up to 40 cm s^{-1}) on its western side, transitioning to a northeastward flow slightly further east (Figures 1C,D). From here, the whole central part of Norskebanken (from ~12.5 to 14.5°E) exhibited a substantial east/northeastward current (>40 cm s^{-1}). At the shallow northern/eastern part of Norskebanken and western slopes of the Hinlopen Trough (~14.5–15.5°E), currents/transport were much weaker and pointing in various directions. Currents within the Hinlopen Trough were also comparatively weak (<~10 cm s^{-1}). However, we did observe a strong (up to ~40 cm s^{-1}) along–trough current core in the upper part of the water column associated with the eastern bank of Hinlopen in a separate ADCP section we collected during the CTD sampling in Hinlopen between 23:20 November 10 and 02:00 November 11 (Supplementary Figure S1).

3.2 Methane dynamics

At all stations, except Norskebanken West, which is situated at a greater distance from cold seeps (Figure 1), surface water methane concentrations were supersaturated in comparison to the atmospheric equilibrium (~3 nM) (Figure 4; Table 1); in particular, Hinlopen East was characterized by high surface water methane concentrations. Dissolved methane concentrations generally increased with depth, with maximum values in bottom waters (Figure 4; Table 1). Comparing all sampling locations, minimum methane concentrations in bottom waters were found at Norskebanken West (average: 6.6 ± 3.5 nM), whereas Hinlopen East featured the highest methane concentrations in bottom waters (average: 874.1 ± 1763 nM, note that bottom waters were sampled with a CTD–grab, i.e., the sampler was positioned directly into the bubble plume, see Materials and Methods section). Methane concentrations in sediment porewaters at Hinlopen South ranged from 1.4—3.4 mM, while at Hinlopen East, methane concentrations ranged from 1—10.8 mM (Supplementary Table S1).

10.3389/feart.2024.1287226

TABLE 1 Methane concentrations, dissolved methane inventories, and methane oxidation (MOx) activity in different water column layers. The water column is divided into surface waters (referred to as intermediate waters, IW) and bottom waters (referred to as Atlantic waters, AW; Figure 3). MOx efficiency is assessed as the fractional turnover of the methane pool per day and the turnover time of the methane pool. All values are presented as the arithmetic mean ± standard deviation.

	Norskebanken		Hinlopen trough		
	West	East	West	South	East
	Averages				
Methane conc. (nM)					
Surface waters (IW)	3.3 ± 1.6	6.6 ± 5.0	8.2 ± 1.9	6.3 ± 0.9	30.6 ± 2
Bottom waters (AW)	6.6 ± 3.5	41.5 ± 22.1	44.3 ± 39.6	21 ± 17.0	874.1 ± 1763
Water column average	5.3 ± 3.2	29.8 ± 25.0	35.3 ± 37.4	15.5 ± 15.0	663.2 ± 1,540.3
k (d^{-1})					
Surface waters (IW)	0.012 ± 0.0001	0.015 ± 0.002	0.023 ± 0.0001	0.017 ± 0.001	0.020 ± 0.001
Bottom waters (AW)	0.013 ± 0.01	0.016 ± 0.001	0.028 ± 0.01	0.018 ± 0.002	0.024 ± 0.003
Water column average	0.013 ± 0.004	0.016 ± 0.001	0.026 ± 0.01	0.018 ± 0.001	0.023 ± 0.003
MOx (nM d^{-1})					
Surface waters (IW)	0.04 ± 0.01	0.11 ± 0.1	0.19 ± 0.1	0.10 ± 0.02	0.63 ± 0.1
Bottom waters (AW)	0.10 ± 0.1	0.68 ± 0.4	1.08 ± 0.9	0.36 ± 0.3	21.19 ± 42.4
Water column average	0.08 ± 0.1	0.49 ± 0.4	0.85 ± 0.8	0.27 ± 0.2	16.05 ± 37.1
Inventories					
Methane (μmol m^{-2} d^{-1})					
Surface waters (IW)	202 ± 105	375 ± 244	1,004 ± 263	623 ± 161	4,757 ± 1,556
Bottom waters (AW)	543 ± 96	3,514 ± 507	6,088 ± 739	3,050 ± 336	46,362 ± 5,553
Total water column	745 ± 201	3,889 ± 751	7,092 ± 1,002	3,673 ± 498	51,118 ± 7,109
MOx (μmol m^{-2} d^{-1})					
Surface waters (IW)	2.5 ± 1.3	5.9 ± 8.7	22.9 ± 6.0	10.2 ± 2.6	97 ± 32
Bottom waters (AW)	6.9 ± 0.9	58.5 ± 3.9	158.3 ± 18.4	55.7 ± 6.0	1,142 ± 141
Total water column	9.3 ± 2.2	64.4 ± 12.6	181.2 ± 24.4	64.9 ± 8.6	1,238 ± 172
Efficiency MOx					
Oxidation of methane pool (% d^{-1})	1.3%	1.7%	2.6%	1.8%	2.4%
Methane pool turnover time (d)	80	60	39	57	41

3.3 Aerobic methane oxidation

MOx was generally lowest in surface waters but, just as methane concentrations, increased in bottom waters (Figure 4; Table 1). MOx in surface waters ranged from 0.04 to 0.19 nM d^{-1} and 0.10–1.08 nM d^{-1} in bottom waters at Norskebanken West and East, and Hinlopen West and South. At Hinlopen East, MOx was higher with 0.63 nM d^{-1} in surface waters and increased more substantially in bottom waters to a maximum of 107 nM d^{-1}. Water column MOx was approximately 33-fold higher at Hinlopen East compared to Norskebanken East, while the rate constant (k) only increased 1.5-fold. Methane turnover time (i.e., the time it would take to fully

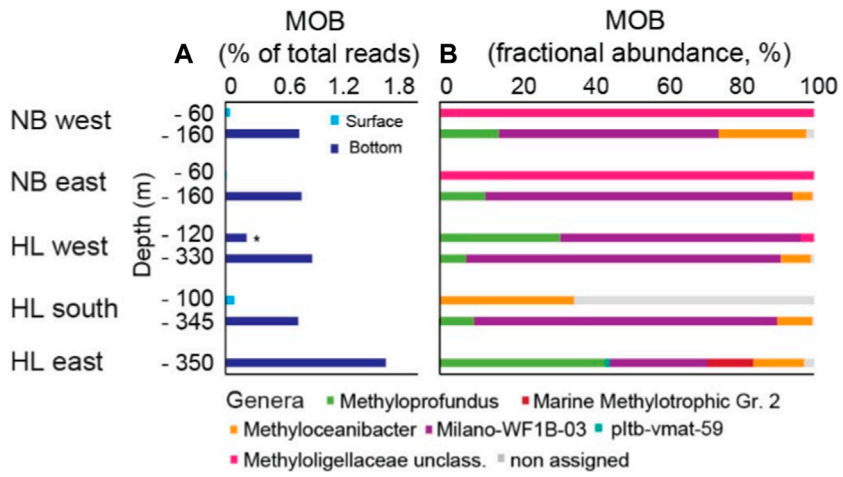

FIGURE 5
Methane–oxidizing bacteria (MOB) at Norskebanken (NB) and Hinlopen Trough (HL). **(A)** Proportion of MOB reads in relation to total bacterial reads. **(B)** Fractional abundance of MOB genera per water layer. See Supplementary Table S2 for comprehensive details on sequencing reads. ∗ Note that at Hinlopen West, MOB samples were taken at two depths within the bottom water layer.

oxidize the methane pool by MOx) was highest at Norskebanken West (80 days) and two–fold lower at Hinlopen West and East (39–41 days; Table 1).

3.4 Community of methane oxidizing bacteria

3.4.1 Water column

At Norskebanken, surface waters exhibited a relatively low presence of putative MOBs, accounting for only 0.05% (West) and 0.01% (East) of total bacterial reads (Figure 5A; Supplementary Table S2). In contrast, surface waters at Hinlopen South and West featured substantially higher MOB abundances, comprising 0.1% and 0.2% MOBs of total bacterial reads (note that no surface water samples were taken at Hinlopen East). However, we found strongest differences in MOB abundance when comparing surface and bottom waters: At Norskebanken, the MOB abundance in bottom waters amounted to 0.81% (West) and 0.83% (East) of total bacterial reads. At Hinlopen, MOB abundances similarly amounted to 0.8% (South), 0.95% (West), and 1.76% (East) of total bacterial reads.

The composition of the MOB community varied between surface and bottom waters at different sampling locations (Figure 5B). At Norskebanken West and East, the majority of putative surface water MOBs belonged to unclassified genera within the *Methyloligellaceae* family. This contains both type II MOB and methylotrophs that metabolize C_1 compounds other than methane (see discussion). At Hinlopen South, the assigned MOBs in surface waters belonged to the genus *Methyloceanibacter* (36%), which is part of this *Methyloligellaceae* family, while the remaining 64% of MOB reads were non–assigned.

In general, bottom waters featured a more diverse MOB community that was shared among locations, with the most abundant MOBs being the type I genera *Methyloprofundus* and Milano–WF1B–03, and the type II genus *Methyloceanibacter*. Other MOBs present in bottom waters belonged to the genera *Marine methylotrophic* group 2 (Hinlopen East). The community composition was similar in shallow and deeper bottom waters at Hinlopen West (Figure 5B).

3.4.2 Sediments

The assessment of MOB abundance within sediments revealed distinct patterns across the study sites. At Norskebanken and Hinlopen West, the abundances of MOB did not show significant variation with depth, representing approximately 0.3%–0.9% and 0.1%–0.6% of total reads, respectively. In contrast, at Hinlopen South and East, MOB were more abundant, particularly in the top 5 cm of sediment, with abundances ranging from 0.1% to 3.9% and 0.1%–4.2% of total reads, respectively (Figure 6; Supplementary Figure S2; Supplementary Table S2).

The community composition of MOB in sediments differed among the locations. At Norskebanken and Hinlopen West, this was dominated by type II MOB, specifically *Methyloceanibacter*, with the presence of other genera such as pltb–vmat–59 and unclassified genera of the family *Methyloligellaceae*. At Hinlopen West, the diversity of MOB was higher, with the additional presence of *Methyloprofundus*, lheB2–23, *Methylomonas*, and unclassified genera of the family *Methylomonadaceae*. At Hinlopen South, the sediments were dominated by *Methyloprofundus*, with a decrease in its abundance with depth, and the presence of MOB from other genera such as *Methyloceanibacter*, *Marine methylotrophic* group 2, pltb–vmat–59, and unclassified genera of MOB families *Methylomonadaceae* and *Methyloligellaceae*. At Hinlopen East, we found the largest MOB diversity. *Methyloprofundus* was the most abundant genus, followed by *Marine methylotrophic* group 2 and *Methyloceanibacter*. Additionally, reads of Milano–WF1B–03 were found in sediment layers at different depths (Figure 6; Supplementary Figure S2). Methane

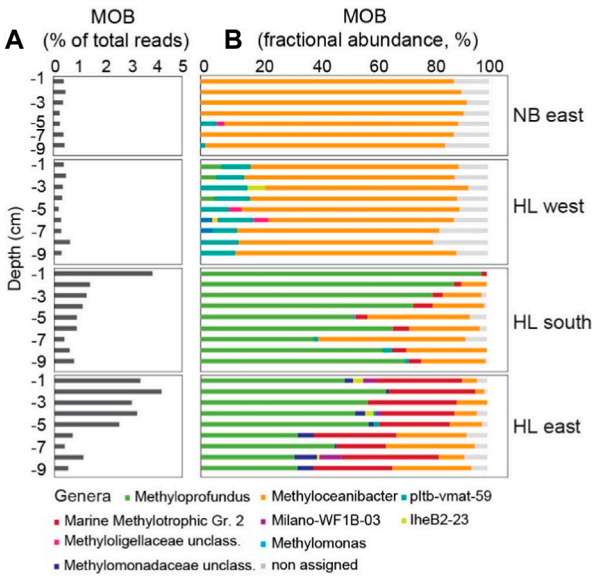

FIGURE 6
Methane oxidizing bacteria (MOB) in sediments at Norskebanken (NB) and Hinlopen (HL). **(A)** Proportion of total reads assigned to MOB in sediments at different depths and locations. **(B)** Fractional abundance of MOB genera in sediments at Norskebanken and Hinlopen. Supplementary Material (Supplementary Figure S2) shows MOB communities below 9 cm depth. See Supplementary Table S2 for comprehensive details on sequencing reads.

concentrations within sediments were notably higher at Hinlopen East, potentially influencing the observed higher diversity of MOB.

3.5 Statistical analysis

Comparison of the bacterial community composition (i.e., methanotrophs and other microbes) in the water column and in sediments was performed by a non–metric multidimensional scaling (NMDS) analysis. For this, the microbial community ASV data were converted to Bray–Curtis community dissimilarities. The NMDS results (Figure 7) reveal similarities between sediment samples from Norskebanken and Hinlopen West, that contrast Hinlopen East and Hinlopen South. Within these groups, surface sediments (<15 cm) and the deeper sediments (>15 cm) form distinct clusters (in particular at Hinlopen South and East). The water column samples form a separate group, with a clear differentiation between the surface and bottom water communities. Notably, the bacterial communities in the bottom waters were more similar to surface sediment communities, particularly at Hinlopen East.

We further visualized overlaps in microbial community structures with the aid of Venn diagrams. For instance, 59% of ASVs in bottom waters at Norskebanken East and the Hinlopen region were the same (Figure 8). Similarly, we found a substantial overlap in ASVs when comparing sediments and bottom waters. At Hinlopen East, 36% of ASV in bottom waters and surface sediments were the same, while the percentage of shared ASVs was ~20% at the other stations.

4 Discussion

In this study, we investigate methane dynamics and associated microbial communities at two large cold seep areas, Norskebanken and Hinlopen Trough, which are located on the shelf North of Svalbard (Figure 1). The WSC transports relatively warm Atlantic water, crosses the large seep areas West of Svalbard before a side branch of the current deviates and flows North of Svalbard to the East. This side branch then crosses the Yermak plateau and the Norskebanken seep area before entering into the Hinlopen Trough area (Menze et al., 2020).

4.1 Methane dynamics at the cold seeps at Norskebanken and Hinlopen Trough

The studied areas at Norskebanken and Hinlopen Trough feature many active seepage sites where methane bubbles are released from the sea floor, as previously documented during a research expedition in 2013 (Geissler et al., 2016). This suggests that seepage in the two areas has been ongoing for at least a decade. The total number of detected flares was similar at Norskebanken (n = 288) and Hinlopen Trough (n = 239). However, flare heights between the two locations were substantially different, 35 m at Norskebanken and 98 m at Hinlopen Trough. We also found higher methane concentrations in the water column at Hinlopen Trough (Figure 4; Table 1) suggesting a higher seepage activity there. The water column at Hinlopen Trough also appears to support a higher standing stock and activity of MOBs. The maximum methane concentration (4,461 nM) and methane oxidation rates (107 nM d^{-1}) that we measured at Hinlopen East are, to the best of our knowledge, the highest measured values in the Arctic Ocean. These concentrations and rates are comparable to measurements at sites of accidental, large scale gas release events at offshore hydrocarbon exploitation facilities (Valentine et al., 2010; Schneider von Deimling et al., 2015). Nevertheless, the horizontal extent of waters with high methane concentration and high MOx remains unknown as we positioned the CTD frame in the gas plume but did not measure across the gas release site (e.g., along a transect).

Independent of the sampling area, methane concentrations increased with depth, and methane inventories showed that between 73% and 90% of the dissolved methane was present in bottom waters. Rising bubbles constantly exchange gases with the surrounding sea water so that their initial methane content decreases during ascent, thus with distance from the sea floor (Leifer and Patro, 2002). The vertical methane profile, as well as transport in pure gas form, is mainly dependent on gas bubble size, flow rate (at the seabed) and vertical exchange of water masses (Jansson et al., 2019). We did not measure the size of methane bubbles, but the ROV video footage suggests that they are a few mm, likely <5 mm in diameter, when they escape from small orifices at the seafloor. Model simulations in similar conditions (offshore Western Spitsbergen, temperature ~4°C and salinity ~35 psu), using a Gaussian bubble size distribution peaking at 6 mm show that most (>90%) if not all of the methane will be exchanged with ambient water masses within ~100 m of water column (Jansson et al., 2019). Density stratification reduces water mass exchange between well mixed surface and deeper

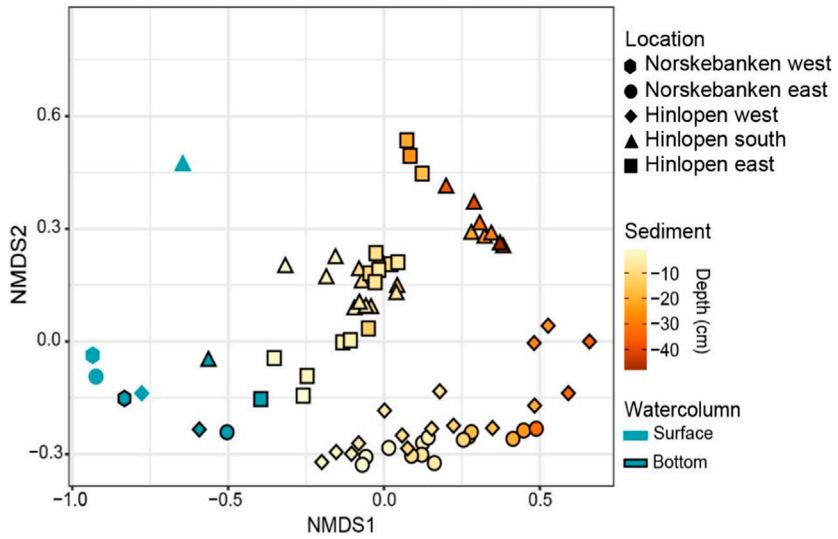

FIGURE 7
Non–metric multidimensional scaling (NMDS) plot based on Bray–Curtis's dissimilarities using log–transformed ASV reads. Each sampling site is represented by a unique symbol shape. Sediment data are color–coded according to sediment depth, while water column samples are indicated by blue color with bottom samples having a black outline.

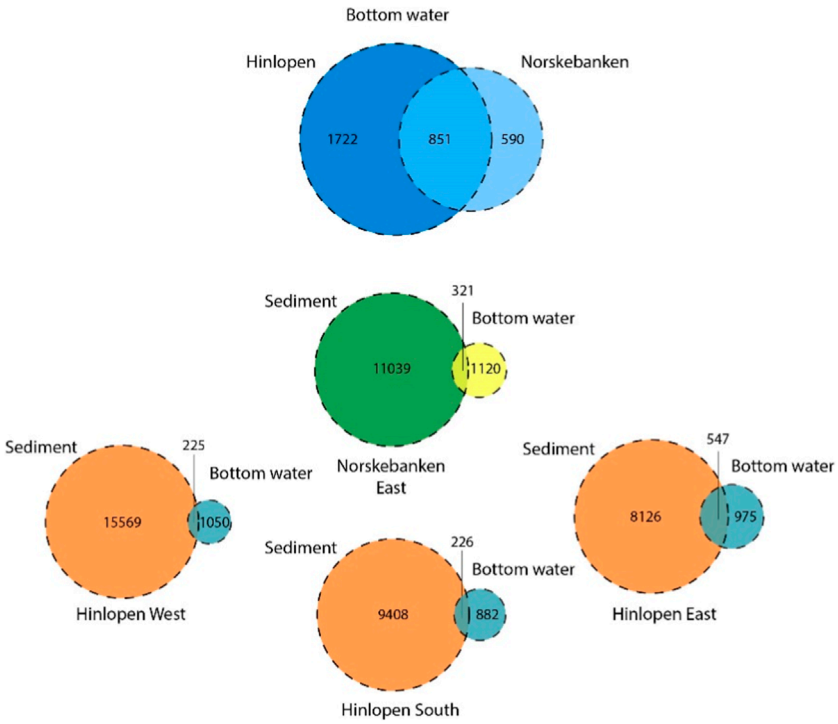

FIGURE 8
Venn diagram visualizing the distribution and overlap of ASVs across sampling regions. The blue circles indicate ASVs found in bottom waters from Norskebanken and Hinlopen (all stations combined). The orange/blue circles indicate ASVs present in sediments, with overlap observed in bottom waters from Hinlopen West, East, and South. The green/yellow circles indicate ASVs identified in sediments overlapping with bottom waters from Norskebanken East. Circle size reflects the number of ASVs within each group, with overlapping regions indicating shared ASVs between different groups.

water layers so that dissolved methane primarily remains in bottom waters (Rudels et al., 1991; James et al., 2016; Silyakova et al., 2020). Though bubbles may cross the pycnocline at our seep areas, it seems unlikely that they still contain high amounts of methane at the sea surface. This also explains the only slightly oversaturated methane concentrations when compared to the atmospheric equilibrium (~3 nM) - with the exception of Hinlopen East, where we found much higher surface water methane concentrations (~30 nM). Since the vertical stratification is similar between the Hinlopen sampling stations, this indicates that the gas flow from the seabed at Hinlopen East was comparably high, potentially accompanied by a larger bubble sizes. This aspect needs to be further investigated in the future, for example, through geometrically calibrated video analysis, calibrated hydroacoustic, air measurements and/or model simulations.

Similar to methane concentrations, MOx was generally highest in bottom waters and at the more active sites in Hinlopen Trough, foremost Hinlopen East. With the exception of Hinlopen East bottom waters, MOx was typically in the range of a few nM d^{-1}; these values are consistent with previous studies investigating MOx in Arctic bottom waters at other locations around Svalbard (Mau et al., 2013; Gentz et al., 2014; Steinle et al., 2015; Gründger et al., 2021). On average, MOx in bottom waters was about 3 to 6 −fold (Norskebanken and Hinlopen south and east) and 33-fold (Hinlopen east) higher than in surface waters, indicating a more active MOB community in bottom waters. Dissolved methane availability was approximately 2–6 -fold (Norskebanken and Hinlopen South and East) and 29-fold (Hinlopen east) higher in bottom waters, indicating that MOx activity was primarily driven by substrate availability. However, the first−order rate constant, *k*, was only 7%–20% higher in bottom waters suggesting that MOx approaches (pseudo) zero order kinetics. We argue that this is caused by the very high access of methane in bottom waters which is not matched by a proportional increase in the standing stock of MOB in this water layer (Czepiel et al., 1996). In this situation, MOx is limited by the lack of available reaction sites (enzymes/MOB cells), so an increase in methane concentration does not result in a proportional increase in MOx. Furthermore, MOB also contends with other substrate limitations, such as the availability of essential elements like nitrogen, phosphorus, and trace metals, which are crucial for their growth. Nevertheless, the efficiency of MOx was high, particularly at Hinlopen South and East; methane turnover times were on the order of months at all locations (Table 1), which is much lower when compared to the seeps west of Svalbard (Gründger et al., 2021), but similar to findings from hydrothermal vents and maximum turnover times at other cold seeps (James et al., 2016).

4.2 Community of methane oxidizing bacteria

MOBs comprised a minor, though substantial fraction of the overall microbial community (up to 1.76%, Figure 5) and the relative abundance of MOBs was higher in bottom waters compared to surface waters. While DNA extraction and amplification protocols vary, it is worth noting that the abundance of MOBs observed in this study was somewhat higher compared to previous investigations of marine MOBs amounting to <1% at the highly active and spatially extensive seep sites west off Svalbard (Steinle et al., 2015; Gründger et al., 2021). However, the dominant MOBs found in our study, i.e., members of the Milano−WF1B cluster and *Methyloprofundus* are Type I MOB that are often found in the water column of cold seeps (Pop Ristova et al., 2015; Savvichev et al., 2018; Mau et al., 2020).

We found strong differences in MOB abundance when comparing surface and bottom waters, matching the segregation of these water layers (see below). The community composition of MOB also varied among the locations. Most prominently, we detected members of the *Marine Methylotrophic* group 2 in bottom waters at Hinlopen East, but not at the other sites. Members of this group are typically found in methane−rich waters and surface sediments (Ruff et al., 2013; Steinle et al., 2016; Uhlig et al., 2018). Indeed, we also found members of this group in high abundance in sediments at Hinlopen East, where seepage activity was particularly high. Our results thus suggest that members of the *Marine Methylotrophic* group 2 might be recruited from sediments, i.e., transported with rising bubbles into bottom waters and in the wake of the bubbles further upwards (see below).

Other strong differences in MOB community composition were the almost exclusive presence of *Methyloceanibacter* at Norskebanken and, to a lesser degree, at Hinlopen West. Some members of this genus may oxidize methane with a soluble methane monooxygenase (sMMO) similar to classical Type II MOB (Vekeman et al., 2016). The relative abundance of this group was much lower at Hinlopen South and East, where, instead, we found higher proportions of *Methyloprofundus*. These sites, in particular Hinlopen East, featured the highest sediment MOB diversity of all sites. With our data set, we cannot determine which environmental factors drive MOB community composition at Norskebanken and Hinlopen Trough. Nevertheless, the sites differ in (apparent) methane availability and sediment characteristics with coarser/more rocky sediments with relatively low methane levels at Norskebanken and finer and methane enriched sediments in Hinlopen Trough, which could be a key factor selecting for distinct MOBs.

MOBs were consistently present within the top decimeter of surface sediments (i.e., the section that we could target at Norskebanken and Hinlopen Trough). However, O_2 in marine sediments is typically consumed within the upper millimeters of the sediment surface (Jørgensen and Kasten, 2006). Unless that bio−irrigation through larger marine benthic organisms introduces O_2 to deeper sediment layers (Kristensen, 2000; Dauwe et al., 2001; Niemann et al., 2006), or that some of the detected MOBs can utilize electron acceptors other than O_2 (Kits et al., 2015; Martinez-Cruz et al., 2017; Su et al., 2023), it seems likely that MOBs in subsurface sediments at Norskebanken and Hinlopen Trough are mostly dormant *in situ*. Nevertheless, at Hinlopen Trough (specifically station East), we found a maximum in MOB abundance close to the sediment surface (Figure 6; Supplementary Figure S2) suggesting that MOB cell numbers near the sediment−water interface in this region are elevated, too. Notably, this pattern aligns with the observed higher methane availability, reaching 11 mM, in this area. Such elevated MOB abundance near the sediment surface is consistent with earlier reports on high MOB abundances at highly active seeps (Niemann et al., 2006; Steinle et al., 2016).

Overall, the MOB community composition was more diverse at Hinlopen East, implying a comparably greater range of methane–consuming processes and/or associated microbial interactions. This increased diversity and complexity could be driven by larger substrate availability, which matches the overall high values of MOx at Hinlopen East. The observed variations in MOB abundance and community composition among the different locations highlight the heterogeneity of seep environments. These differences are likely influenced by various environmental conditions, including sediment characteristics, availability of methane sources, essential elements, and local hydrodynamic factors. The unique combination of these factors at each seep location investigated here likely shapes the MOB community structure and its functioning in methane oxidation.

4.3 Segregation and connectivity

Across multiple locations in Norskebanken and Hinlopen Trough, this study explores MOBs and other microbes that are, potentially, involved in methane cycling in the water column and sediments. Our findings indicate a notable dissimilarity in community composition when contrasting sediment and water column samples from Norskebanken and Hinlopen West, while revealing a more pronounced similarity in the communities within Hinlopen South and East. This pattern was also visible when considering the entire bacterial community. Previous research has shown that MOBs, along with other microbes, can be transported from sediments into the water column via drag induced by rising bubbles – a phenomenon that has been coined as 'the bubble shuttle' (Schmale et al., 2015). This bubble mediated transport has been shown for a few marine seeps at different marine locations (Schmale et al., 2015; Steinle et al., 2016; Jordan et al., 2020; 2021). As a result of this transport process, water column MOBs may be recruited, at least in parts, from sediments. Our NMDS and Venn diagram analysis (Figures 7, 8) indeed indicates a higher degree of similarity of surface sediment and bottom water communities (while this similarity decreases when comparing the microbial community in deeper sediment layers with bottom waters). This was mostly pronounced at Hinlopen East, where we also found the highest seepage activity. At this site, we also found all of the water column MOBs in sediments. For the seeps North of Svalbard, our data consequently suggest that sedimentary microbes, including MOBs, are translocated from surface sediments to the water column via a 'bubble shuttle' effect.

The observed variations in the overlap of the microbial community structure in bottom waters versus surface sediments when comparing the different locations might be related to differences in sediment characteristics and seep activity. Norskebanken features rocky sediments, while sediments at Hinlopen are predominantly muddy, with a greater abundance of benthic megafauna (Supplementary Figure S3). The variation in sediment composition likely influences the mobilization of sediment particles through rising bubbles and whether MOBs, potentially attached to particles/surfaces, are dragged into the water column where they are subsequently dispersed.

MOB communities in bottom waters exhibited similar characteristics across all locations (Figure 5). This observation prompted us to investigate the potential for hydrological connectivity, i.e., for frequent and substantial water mass exchange between the seep areas at Norskebanken and Hinlopen. Previous studies by (Menze et al., 2020) measured and modelled current dynamics north of Svalbard showing a profound eastern branch of the West Spitsbergen Current following the northern shelf break of Norskebanken with inflow into Hinlopen straight as well as onto Norskebanken proper at its western depression. Our ADCP transect (Figure 1B) provided *in situ* measurements approximately at sampling time. It has to be noted that our ADCP measurements (Figures 1C,D) only provide a snapshot of the situation at transect time and are influenced by tidal and other short–term effects, such as, e.g., wind forcing. They do not resolve net transport trajectories over longer time scales across Norskebanken. Nonetheless, this transect clearly highlights water mass flow crossing Norskebanken from West to East and we observed a strong out–trough plume associated with the eastern bank of Hinlopen in a separate ADCP transect. This is generally in line with observations and model simulations in (Menze et al., 2020). Similarities in water mass properties at the two sampling stations support the notion that there is considerable exchange of water masses between the Hinlopen and Norskebanken stations. It is also important to consider the potential for periodic and frequent exchange of water masses between the sampling sites due to tidal and/or eddy activity. The distance between the Norskebanken and Hinlopen station is approximately 50 km, which is on the high end of typical eddy length scales in the region (Wekerle et al., 2020). However, considerable baroclinic and atmospheric forcing, as well as freeze/melt processes and energy provided by the West Spitsbergen Current, make the frequent presence of eddies and turbulent flows, which can drive water mass exchange between the sites, likely. This notion is further supported by our ADCP data, which show strong currents not only in the West Spitsbergen Current core but also across large portions of Norskebanken.

Furthermore, our Venn diagram analysis (Figure 8) shows a substantial overlap in the microbial community composition in bottom waters at Norskebanken and Hinlopen (Figure 5), indicating a hydrological connection. This suggests that, along with water masses, MOBs are likely transported between the two seep areas. Hence, some of the MOBs in bottom waters at Hinlopen (in addition to a sedimentary origin) may indeed be recruited from the Norskebanken seep area.

Approximately 250 km away of Norskebanken and Hinlopen lies the massive seep area off Prins Karls Forlandet (West of Svalbard). There, MOBs in bottom waters were dominated by Milano–WF1B–03 and *Methyloprofundus* (Steinle et al., 2015; Gründger et al., 2021), matching our observations at Norskebanken and Hinlopen Trough. Also, Verrucomicrobia of the families *Rubritaleaceae* and Luteolibacter were detected in bottom waters West of Svalbard (Gründger et al., 2021) and in bottom waters at our sites (Supplementary Figure S4). Previous studies by (Menze et al., 2020) and our data show that AW water from the WSC enters Hinlopen facilitated through generally eastward water mass transport North of Svalbard. Tentatively, we therefore suggest that water column microbes that drift with the WSC (Steinle et al.,

2015) towards the North might be transported East to the Yermak plateau North of Svalbard. The West Spitsbergen current is consequently a potential conduit for the dispersal and redistribution of microbial populations across geographically distant seep habitats.

5 Summary and conclusion

This study investigates methane dynamics and associated microbial communities at cold seep areas North of Svalbard, Norskebanken and Hinlopen Trough. The activity of MOBs in the water column was mostly determined by the availability of methane; under conditions of extremely high methane concentrations, to the point that MOx approaches pseudo zero order kinetics. The MOB community composition in the water column and in sediments at Hinlopen Trough showed similarities, indicating that MOBs in the water column are, at least partially, recruited from sediments. This could not be observed at Norskebanken, potentially related to the rocky sea floor there. In addition to a bubble–mediated transport, the high degree of similarity when comparing MOBs from North and West of Svalbard suggests that the major current system in the region, the WSC, translocate a seeding community of MOBs from the seeps West of Svalbard towards those North of Svalbard. Ocean currents thus facilitate long–range transport and hydrologically connect spatially segregated 'submarine island habitats' such as cold seeps. Additionally, the microbial community structures on local/regional scales may be influenced by advective transport of microbes facilitated through the ascent of bubbles or through currents. This mechanism holds the potential to regulate crucial microbial processes, including trace gas cycling.

Data availability statement

All data will be archived and made publicly available in the NIOZ data base DAS (Data Archive System, https://doi.org/10.25850/nioz/7b.b.pf). The sequence data generated in this study have been deposited in the NCBI BioProject database under accession number PRJNA1118678.

Author contributions

TG: Conceptualization, Formal Analysis, Investigation, Methodology, Software, Validation, Visualization, Writing–original draft. DK: Formal Analysis, Investigation, Methodology, Writing–review and editing. MM: Writing–review and editing, Formal Analysis, Investigation, Software. CA: Writing–review and editing, Formal Analysis, Investigation. GP: Supervision, Writing–review and editing, Investigation. ML: Formal Analysis, Investigation, Writing–review and editing. KD: Data curation, Formal analysis, Visualization, Writing–review and editing. BF: Writing–review and editing, Conceptualization, Funding acquisition, Supervision. MS: Supervision, Writing–review and editing, Funding acquisition. HN: Conceptualization, Funding acquisition, Methodology, Project administration, Resources, Supervision, Validation, Writing–review and editing.

Funding

The author(s) declare that financial support was received for the research, authorship, and/or publication of this article. We would like to extend our sincere appreciation to Utrecht University and NIOZ for their generous internal grant that played a pivotal role in supporting this project. Additionally, we wish to express our profound gratitude to the Center for Arctic Gas Hydrate Environment and Climate (CAGE), which provided essential financial support through RCN grant No. 223259 for our research. Furthermore, we would like to acknowledge the invaluable contribution of the AKMA project, also funded by RCN grant No. 287869, to our research efforts.

Acknowledgments

The unwavering support from the captain, crew, and onboard scientific team of R/V Kronprins Haakon, as well as the operators of ROV ÆGIR 6000, played an instrumental role in the success of our research. We wish to express our profound gratitude to Marie Stetzler from CAGE for her invaluable contribution to the molecular work carried out in this study. All support has been instrumental in the success of our work, and we are genuinely thankful for the received contributions.

Conflict of interest

The authors declare that the research was conducted in the absence of any commercial or financial relationships that could be construed as a potential conflict of interest.

Publisher's note

Supplementary material

The Supplementary Material for this article can be found online at: https://www.frontiersin.org/articles/10.3389/feart.2024.1287226/full#supplementary-material

References

Argentino, C., Savini, A., and Panieri, G. (2022). "Integrating fine-scale habitat mapping and pore water analysis in cold seep research: a case study from the SW barents sea," in *World atlas of submarine gas hydrates in continental margins*. Editors J. Mienert, C. Berndt, A. M. Tréhu, A. Camerlenghi, and C.-S. Liu (Cham: Springer International Publishing), 505–514.

Berndt, C., Feseker, T., Treude, T., Krastel, S., Liebetrau, V., Niemann, H., et al. (2014). Temporal constraints on hydrate-controlled methane seepage off svalbard. *Science* 343, 284–287. doi:10.1126/science.1246298

Boetius, A., and Wenzhöfer, F. (2013). Seafloor oxygen consumption fuelled by methane from cold seeps. *Nat. Geosci.* 6, 725–734. doi:10.1038/ngeo1926

Callahan, B. J., Mcmurdie, P. J., Rosen, M. J., Han, A. W., Johnson, A. J. A., and Holmes, S. P. (2016). DADA2: high-resolution sample inference from Illumina amplicon data. *Nat. Methods* 13, 581–583. doi:10.1038/nmeth.3869

Cottier, F., Tverberg, V., Inall, M., Svendsen, H., Nilsen, F., and Griffiths, C. (2005). Water mass modification in an Arctic fjord through cross-shelf exchange: the seasonal hydrography of Kongsfjorden, Svalbard. *J. Geophys. Res. Oceans* 110. doi:10.1029/2004jc002757

Crespo-Medina, M., Meile, C. D., Hunter, K. S., Diercks, A. R., Asper, V. L., Orphan, V. J., et al. (2014). The rise and fall of methanotrophy following a deepwater oil-well blowout. *Nat. Geosci.* 7, 423–427. doi:10.1038/ngeo2156

Czepiel, P. M., Mosher, B., Crill, P. M., and Harriss, R. C. (1996). Quantifying the effect of oxidation on landfill methane emissions. *J. Geophys. Res. Atmos.* 101, 16721–16729. doi:10.1029/96jd00222

Dauwe, B., Middelburg, J. J., and Herman, P. M. (2001). Effect of oxygen on the degradability of organic matter in subtidal and intertidal sediments of the North Sea area. *Mar. Ecol. Prog. Ser.* 215, 13–22. doi:10.3354/meps215013

De Groot, T. R., Mol, A. M., Mesdag, K., Ramond, P., Ndhlovu, R., Engelmann, J. C., et al. (2023). Diel and seasonal methane dynamics in the shallow and turbulent Wadden Sea. *EGUsphere* 2023, 3857–3872. doi:10.5194/bg-20-3857-2023

Dølven, K. O., Ferré, B., Silyakova, A., Jansson, P., Linke, P., and Moser, M. (2022). Autonomous methane seep site monitoring offshore western Svalbard: hourly to seasonal variability and associated oceanographic parameters. *Ocean. Sci.* 18, 233–254. doi:10.5194/os-18-233-2022

Etminan, M., Myhre, G., Highwood, E. J., and Shine, K. P. (2016). Radiative forcing of carbon dioxide, methane, and nitrous oxide: a significant revision of the methane radiative forcing. *Geophys. Res. Lett.* 43 (12), 614–612. doi:10.1002/2016gl071930

Fisher, C., Urcuyo, I., Simpkins, M., and Nix, E. (1997). Life in the slow lane: growth and longevity of cold-seep vestimentiferans. *Mar. Ecol.* 18, 83–94. doi:10.1111/j.1439-0485.1997.tb00428.x

Geissler, W. H., Gebhardt, A. C., Gross, F., Wollenburg, J., Jensen, L., Schmidt-Aursch, M. C., et al. (2016). Arctic megaslide at presumed rest. *Sci. Rep.* 6, 38529. doi:10.1038/srep38529

Gentz, T., Damm, E., Schneider Von Deimling, J., Mau, S., Mcginnis, D. F., and Schlüter, M. (2014). A water column study of methane around gas flares located at the West Spitsbergen continental margin. *Cont. Shelf Res.* 72, 107–118. doi:10.1016/j.csr.2013.07.013

Gibson, R., Atkinson, R., and Gordon, J. (2005). Ecology of cold seep sediments: interactions of fauna with flow, chemistry and microbes. *Oceanogr. Mar. Biol. Annu. Rev.* 43, 1–46. doi:10.1201/9781420050943

Graves, C. A., Steinle, L., Rehder, G., Niemann, H., Connelly, D. P., Lowry, D., et al. (2015). Fluxes and fate of dissolved methane released at the seafloor at the landward limit of the gas hydrate stability zone offshore western Svalbard. *J. Geophys. Res. Oceans* 120, 6185–6201. doi:10.1002/2015jc011084

Green, J. D. (2005). "Headspace analysis | static," in *Encyclopedia of analytical science*. Editors P. Worsfold, A. Townshend, and C. Poole (Oxford: Elsevier), 229–236.

Gründger, F., Probandt, D., Knittel, K., Carrier, V., Kalenitchenko, D., Silyakova, A., et al. (2021). Seasonal shifts of microbial methane oxidation in Arctic shelf waters above gas seeps. *Limnol. Oceanogr.* 66, 1896–1914. doi:10.1002/lno.11731

IPCC (2021). "Climate Change 2021: The Physical Science Basis," in *Contribution of Working Group I to the Sixth Assessment Report of the Intergovernmental Panel on Climate Change*. Editors Masson-Delmotte, V. P., Zhai, A., Pirani, S. L., Connors, C., Péan, S., Berger, N., et al.(Cambridge, United Kingdom and New York, NY, United States: Cambridge University Press) (In press). doi:10.1017/9781009157896

James, R. H., Bousquet, P., Bussmann, I., Haeckel, M., Kipfer, R., Leifer, I., et al. (2016). Effects of climate change on methane emissions from seafloor sediments in the Arctic Ocean: a review. *Limnol. Oceanogr.* 61, S283–S299. doi:10.1002/lno.10307

Jansson, P., Ferré, B., Silyakova, A., Dølven, K. O., and Omstedt, A. (2019). A new numerical model for understanding free and dissolved gas progression toward the atmosphere in aquatic methane seepage systems. *Limnol. Oceanogr. Methods* 17, 223–239. doi:10.1002/lom3.10307

Jordan, S. F. A., Gräwe, U., Treude, T., Van Der Lee, E. M., Schneider Von Deimling, J., Rehder, G., et al. (2021). Pelagic methane sink enhanced by benthic methanotrophs ejected from a gas seep. *Geophys. Res. Lett.* 48, e2021GL094819. doi:10.1029/2021gl094819

Jordan, S. F. A., Treude, T., Leifer, I., Janssen, R., Werner, J., Schulz-Vogt, H., et al. (2020). Bubble-mediated transport of benthic microorganisms into the water column: identification of methanotrophs and implication of seepage intensity on transport efficiency. *Sci. Rep.* 10, 4682. doi:10.1038/s41598-020-61446-9

Jørgensen, B. B., and Kasten, S. (2006). "Sulfur cycling and methane oxidation," in *Marine geochemistry*. Editors H. D. Schulz, and M. Zabel (Berlin, Heidelberg: Springer Berlin Heidelberg), 271–309.

Kits, K. D., Klotz, M. G., and Stein, L. Y. (2015). Methane oxidation coupled to nitrate reduction under hypoxia by the Gammaproteobacterium M*ethylomonas denitrificans*, sp. nov. type strain FJG1. *Environ. Microbiol.* 17, 3219–3232. doi:10.1111/1462-2920.12772

Knief, C. (2015). Diversity and habitat preferences of cultivated and uncultivated aerobic methanotrophic bacteria evaluated based on pmoA as molecular marker. *Front. Microbiol.* 6, 1346. doi:10.3389/fmicb.2015.01346

Kristensen, E. (2000). Organic matter diagenesis at the oxic/anoxic interface in coastal marine sediments, with emphasis on the role of burrowing animals. *Hydrobiologia* 426, 1–24. doi:10.1007/978-94-011-4148-2_1

Leifer, I., and Patro, R. K. (2002). The bubble mechanism for methane transport from the shallow sea bed to the surface: a review and sensitivity study. *Cont. Shelf Res.* 22, 2409–2428. doi:10.1016/s0278-4343(02)00065-1

Martinez-Cruz, K., Leewis, M.-C., Herriott, I. C., Sepulveda-Jauregui, A., Anthony, K. W., Thalasso, F., et al. (2017). Anaerobic oxidation of methane by aerobic methanotrophs in sub-Arctic lake sediments. *Sci. Total Environ.* 607-608, 23–31. doi:10.1016/j.scitotenv.2017.06.187

Mau, S., Blees, J., Helmke, E., Niemann, H., and Damm, E. (2013). Vertical distribution of methane oxidation and methanotrophic response to elevated methane concentrations in stratified waters of the Arctic fjord Storfjorden (Svalbard, Norway). *Biogeosciences* 10, 6267–6278. doi:10.5194/bg-10-6267-2013

Mau, S., Römer, M., Torres, M. E., Bussmann, I., Pape, T., Damm, E., et al. (2017). Widespread methane seepage along the continental margin off Svalbard - from Bjørnøya to Kongsfjorden. *Sci. Rep.* 7, 42997. doi:10.1038/srep42997

Mau, S., Tu, T.-H., Becker, M., Dos Santos Ferreira, C., Chen, J.-N., Lin, L.-H., et al. (2020). Methane seeps and independent methane plumes in the south China sea offshore taiwan. *Front. Mar. Sci.* 7. doi:10.3389/fmars.2020.00543

Menze, S., Ingvaldsen, R. B., Nikolopoulos, A., Hattermann, T., Albretsen, J., and Gjøsæter, H. (2020). Productive detours – Atlantic water inflow and acoustic backscatter in the major troughs along the Svalbard shelf. *Prog. Oceanogr.* 188, 102447. doi:10.1016/j.pocean.2020.102447

Niemann, H., Losekann, T., De Beer, D., Elvert, M., Nadalig, T., Knittel, K., et al. (2006). Novel microbial communities of the Haakon Mosby mud volcano and their role as a methane sink. *Nature* 443, 854–858. doi:10.1038/nature05227

Niemann, H., Steinle, L., Blees, J., Bussmann, I., Treude, T., Krause, S., et al. (2015). Toxic effects of lab-grade butyl rubber stoppers on aerobic methane oxidation. *Limnol. Oceanogr. Methods* 13, 40–52. doi:10.1002/lom3.10005

Oziel, L., Baudena, A., Ardyna, M., Massicotte, P., Randelhoff, A., Sallée, J. B., et al. (2020). Faster Atlantic currents drive poleward expansion of temperate phytoplankton in the Arctic Ocean. *Nat. Commun.* 11, 1705. doi:10.1038/s41467-020-15485-5

Parada, A. E., Needham, D. M., and Fuhrman, J. A. (2016). Every base matters: assessing small subunit rRNA primers for marine microbiomes with mock communities, time series and global field samples. *Environ. Microbiol.* 18, 1403–1414. doi:10.1111/1462-2920.13023

Pop Ristova, P., Wenzhöfer, F., Ramette, A., Felden, J., and Boetius, A. (2015). Spatial scales of bacterial community diversity at cold seeps (Eastern Mediterranean Sea). *ISME J.* 9, 1306–1318. doi:10.1038/ismej.2014.217

Quast, C., Pruesse, E., Yilmaz, P., Gerken, J., Schweer, T., Yarza, P., et al. (2013). The SILVA ribosomal RNA gene database project: improved data processing and web-based tools. *Nucleic Acids Res.* 41, D590–D596. doi:10.1093/nar/gks1219

Reeburgh, W. S. (2007). Oceanic methane biogeochemistry. *Chem. Rev.* 107, 486–513. doi:10.1021/cr050362v

Römer, M., Riedel, M., Scherwath, M., Heesemann, M., and Spence, G. D. (2016). Tidally controlled gas bubble emissions: a comprehensive study using long-term monitoring data from the NEPTUNE cabled observatory offshore Vancouver Island. *Geochem. Geophys. Geosystems* 17, 3797–3814. doi:10.1002/2016gc006528

Rudels, B., Larsson, A.-M., and Sehlstedt, P.-I. (1991). Stratification and water mass formation in the Arctic Ocean: some implications for the nutrient distribution. *Polar Res.* 10, 19–32. doi:10.3402/polar.v10i1.6724

Ruff, S. E., Arnds, J., Knittel, K., Amann, R., Wegener, G., Ramette, A., et al. (2013). Microbial communities of deep-sea methane seeps at hikurangi continental margin (New Zealand). *PLOS ONE* 8, e72627. doi:10.1371/journal.pone.0072627

Sauer, S., Hong, W.-L., Yao, H., Lepland, A., Klug, M., Eichinger, F., et al. (2021). Methane transport and sources in an Arctic deep-water cold seep offshore NW Svalbard (Vestnesa Ridge, 79°N). *Deep Sea Res. Part I Oceanogr. Res. Pap.* 167, 103430. doi:10.1016/j.dsr.2020.103430

Savvichev, A. S., Kadnikov, V. V., Kravchishina, M. D., Galkin, S. V., Novigatskii, A. N., Sigalevich, P. A., et al. (2018). Methane as an organic matter source and the trophic basis of a laptev sea cold seep microbial community. *Geomicrobiol. J.* 35, 411–423. doi:10.1080/01490451.2017.1382612

Schloss, P. D., Westcott, S. L., Ryabin, T., Hall, J. R., Hartmann, M., Hollister, E. B., et al. (2009). Introducing mothur: open-source, platform-independent, community-supported software for describing and comparing microbial communities. *Appl. Environ. Microbiol.* 75, 7537–7541. doi:10.1128/aem.01541-09

Schmale, O., Leifer, I., Deimling, J. S. V., Stolle, C., Krause, S., Kießlich, K., et al. (2015). Bubble Transport Mechanism: indications for a gas bubble-mediated inoculation of benthic methanotrophs into the water column. *Cont. Shelf Res.* 103, 70–78. doi:10.1016/j.csr.2015.04.022

Schneider Von Deimling, J., Linke, P., Schmidt, M., and Rehder, G. (2015). Ongoing methane discharge at well site 22/4b (North Sea) and discovery of a spiral vortex bubble plume motion. *Mar. Petroleum Geol.* 68, 718–730. doi:10.1016/j.marpetgeo.2015.07.026

Silyakova, A., Jansson, P., Serov, P., Ferré, B., Pavlov, A. K., Hattermann, T., et al. (2020). Physical controls of dynamics of methane venting from a shallow seep area west of Svalbard. *Cont. Shelf Res.* 194, 104030. doi:10.1016/j.csr.2019.104030

Steinle, L., Graves, A. C., Treude, T., Ferré, B., Biastoch, A., Bussmann, I., et al. (2015). Water column methanotrophy controlled by a rapid oceanographic switch. *Nat. Geosci.* 8, 378–382. doi:10.1038/ngeo2420

Steinle, L., Maltby, J., Treude, T., Kock, A., Bange, H. W., Engbersen, N., et al. (2017). Effects of low oxygen concentrations on aerobic methane oxidation in seasonally hypoxic coastal waters. *Biogeosciences* 14, 1631–1645. doi:10.5194/bg-14-1631-2017

Steinle, L., Schmidt, M., Bryant, L., Haeckel, M., Linke, P., Sommer, S., et al. (2016). Linked sediment and water-column methanotrophy at a man-made gas blowout in the North Sea: implications for methane budgeting in seasonally stratified shallow seas. *Limnol. Oceanogr.* 61, S367–S386. doi:10.1002/lno.10388

Su, G., Lehmann, M. F., Tischer, J., Weber, Y., Lepori, F., Walser, J.-C., et al. (2023). Water column dynamics control nitrite-dependent anaerobic methane oxidation by Candidatus "Methylomirabilis" in stratified lake basins. *ISME J.* 17, 693–702. doi:10.1038/s41396-023-01382-4

Suess, E. (2020). "Marine cold seeps: background and recent advances," in *Hydrocarbons, oils and lipids: diversity, origin, chemistry and fate*. Editor H. Wilkes (Cham: Springer International Publishing), 747–767.

Sultan, N., Plaza-Faverola, A., Vadakkepuliyambatta, S., Buenz, S., and Knies, J. (2020). Impact of tides and sea-level on deep-sea Arctic methane emissions. *Nat. Commun.* 11, 5087. doi:10.1038/s41467-020-18899-3

Uhlig, C., Kirkpatrick, J. B., D'hondt, S., and Loose, B. (2018). Methane-oxidizing seawater microbial communities from an Arctic shelf. *Biogeosciences* 15, 3311–3329. doi:10.5194/bg-15-3311-2018

Vaksmaa, A., Knittel, K., Abdala Asbun, A., Goudriaan, M., Ellrott, A., Witte, H. J., et al. (2021). Microbial communities on plastic polymers in the mediterranean sea. *Front. Microbiol.* 12, 673553. doi:10.3389/fmicb.2021.673553

Valentine, D. L., Kessler, J. D., Redmond, M. C., Mendes, S. D., Heintz, M. B., Farwell, C., et al. (2010). Propane respiration jump-starts microbial response to a deep oil spill. *Science* 330, 208–211. doi:10.1126/science.1196830

Vekeman, B., Kerckhof, F.-M., Cremers, G., De Vos, P., Vandamme, P., Boon, N., et al. (2016). New Methyloceanibacter diversity from North Sea sediments includes methanotroph containing solely the soluble methane monooxygenase. *Environ. Microbiol.* 18, 4523–4536. doi:10.1111/1462-2920.13485

Weber, T., Wiseman, N. A., and Kock, A. (2019). Global ocean methane emissions dominated by shallow coastal waters. *Nat. Commun.* 10, 4584–4610. doi:10.1038/s41467-019-12541-7

Wekerle, C., Hattermann, T., Wang, Q., Crews, L., Von Appen, W. J., and Danilov, S. (2020). Properties and dynamics of mesoscale eddies in Fram Strait from a comparison between two high-resolution ocean–sea ice models. *Ocean. Sci.* 16, 1225–1246. doi:10.5194/os-16-1225-2020

frontiers | Frontiers in Earth Science

TYPE Original Research
PUBLISHED 11 July 2024
DOI 10.3389/feart.2024.1404027

OPEN ACCESS

EDITED BY
Nir Krakauer,
City College of New York (CUNY),
United States

REVIEWED BY
Ang Li,
Qingdao Institute of Marine Geology (QIMG),
China
Jinxiu Yang,
China University of Petroleum, China
Xiaoming Miao,
Ocean University of China, China
Tobias Himmler,
University of Bremen, Germany

*CORRESPONDENCE
Pavel Serov,
pavel.russerov@uit.no

RECEIVED 20 March 2024
ACCEPTED 17 June 2024
PUBLISHED 11 July 2024

CITATION
Serov P, Andreassen K, Winsborrow M, Mattingsdal R and Patton H (2024), Geological and glaciological controls of 21,700 active methane seeps in the northern Norwegian Barents sea.
Front. Earth Sci. 12:1404027.
doi: 10.3389/feart.2024.1404027

Geological and glaciological controls of 21,700 active methane seeps in the northern Norwegian Barents sea

Pavel Serov[1,2]*, Karin Andreassen[1,2], Monica Winsborrow[1,2], Rune Mattingsdal[3] and Henry Patton[1,2]

[1]CAGE, Centre for Arctic Gas Hydrate, Environment and Climate, UiT–The Arctic University of Norway, Tromsø, Norway, [2]Department of Geosciences, UiT–The Arctic University of Norway, Tromsø, Norway, [3]Norwegian Offshore Directorate (NOD), Harstad, Norway

Due to tectonic uplift in the Cenozoic and numerous shelf-wide glaciations during the Quaternary, ~1–2.5 km of sedimentary overburden has been eroded from the Barents Sea shelf, leading to the exhumation and partial uncapping of hydrocarbon accumulations. Widespread natural gas and oil leakage from the glacially eroded middle-upper Triassic reservoir directly into the water column has been documented at the Sentralbanken high in the northern Norwegian Barents Sea. However, it remains unclear whether the hydrocarbon leakage occurs only from the middle-upper Triassic reservoir units in geological settings exceptionally conducive to hydrocarbon leakage, or if other reservoir formations contributed to the release of hydrocarbons into the water column. It is also not clear whether complete erosion of the caprock is a prerequisite for widespread liberation of natural gas and oil from glacially eroded reservoirs across Arctic continental shelves. Here we analyze multibeam echosounder data covering ~5,000 km^2 and a suite of high-resolution P-cable seismic lines from a range of geological structures across the northern Norwegian Barents Sea. Our analyses reveal that ~21,700 natural gas seeps originate from exhumed, faulted and variably eroded structural highs bearing a range of Mesozoic reservoir formations. All investigated structural highs fuel seabed methane release hotspots with no exception. Evident from observations of seismic anomalies, fluid accumulations are pervasive in the subsurface and likely to continue fuelling seabed gas seepage into the future. We also document that gas seepage through faults piercing overburden, caprocks and reaching potential reservoir levels is pervasive at all investigated structural highs. On the Storbanken high and the Kong Karl platform, such fault-controlled seepage is more prevalent than seepage from reservoir formations subcropping below the seafloor. Using a simple parametrization approach, we estimate that seeps identified within our multibeam data coverage produce a seabed methane flux of 61 x 10^7 mol/yr (9,803 ton/yr), which is one to two orders of magnitude higher than other globally known submarine methane seepage provinces. Fluxes of methane from sea water to the air above the thermogenic gas seep provinces in the northern Norwegian Barents Sea remain to be determined.

KEYWORDS

methane, hydrocarbons, seepage, Arctic, Barent sea

1 Introduction

Methane (CH_4) is the third most abundant greenhouse gas in Earth's atmosphere after water vapor and carbon dioxide (CO_2) and has a ~25 times stronger greenhouse effect per molecule compared to carbon dioxide on a 100-year timescale. Understanding, quantifying, and mitigating its emissions has attained significant attention in recent decades. The lifetime of methane in the atmosphere is >10 times shorter than that of carbon dioxide, which makes it an increasingly important target for urgent anthropogenic emission reductions (Staniaszek et al., 2022; Shoemaker et al., 2013; Nisbet et al., 2020; Asadnabizadeh, 2022). While reducing anthropogenic emissions may lead to rapid 0.2°C reduction in warming by 2050 (CCAC, 2021), neither precise quantification of natural methane sources, nor discrimination between some categories of anthropogenic and natural sources has been achieved. Furthermore, a ~30% gap remains between global methane emission assessments following a bottom-up approach, where discrete near-surface emission measurements are upscaled to larger areas, and those following a top-down approach where the contribution of individual sources is parceled from the bulk atmospheric methane reservoir (Saunois et al., 2020). Bottom-up assessments likely overestimate emissions due to the paucity of observational data, the temporal variability of sources, and inherent biases in near-surface measurements (Ruppel and Kessler, 2017; Vaughn et al., 2018). However, bottom-up assessments may provide precise discrimination of geographically overlapping sources or sources with similar isotopic characteristics of the emitted methane, and attempts to improve them remain important. Mapping natural methane emissions and tying them to settings conducive to the liberation of methane with a certain isotopic signature could be an important step towards more precise bottom-up assessments.

The ability of submarine-sourced methane to reach the atmosphere, such as from microbial production in bottom sediments, dissociating methane hydrates, thawing subsea permafrost, leaking petroleum basins, and submarine hot vents, is dampened by the anaerobic oxidation of methane in bottom sediments (Egger et al., 2018) and aerobic oxidation of methane in the water column. Because rates of methane oxidation may change in response to tidal cycles, currents and seasons (Steinle et al., 2015; Gründger et al., 2021) and an existing lack of systematic air measurements above submarine sources of methane, their contribution to the atmospheric budget remains highly uncertain (Masson-Delmotte et al., 2021). Furthermore, the global distribution of seabed methane discharge hotspots is still poorly known. New submarine methane emission sites continue to be discovered, including those in climatically sensitive polar regions in Greenland (Nielsen et al., 2014), offshore Svalbard (Mau et al., 2017) and Antarctica (Thurber et al., 2020). Recently, the formerly glaciated Barents Sea shelf has been documented emitting fossil thermogenic methane into the water column, a small fraction of which reaches the sea surface and is liberated into the air (Serov et al., 2023). Here, gas seepage correlates with structural highs exhumed close to the seafloor due to tectonic uplift in the Cenozoic and >40 highly erosive Quaternary glacial cycles removing ~1–2.5 km sediments from the shelf (Lasabuda et al., 2021; Patton et al., 2022). Such naturally uncapped hydrocarbon reservoirs may release thermogenic gas with a heavy stable isotopic composition, similar to the composition of methane emitted during hydrocarbon production, refining and transportation yet different from methane microbially produced in bottom sediments and in the water column (Mao et al., 2024) which are depleted in heavy carbon and hydrogen isotopes (Whiticar, 1993, Whiticar, 1999). Thermogenic signature of sediment bound gas ($\delta^{13}C_{methane}$ = −50.8‰ ± 5.2‰ V-PDB (n=18)) has been revealed in samples from a periphery of a glacially eroded Sentralbanken high in the northern Norwegian Barents sea (Weniger et al., 2019). Paleo seepage of thermogenic gas has also been inferred from analyses of methane-derived authigenic carbonates in several locations in the Norwegian Barents Sea (Himmler et al., 2019). Understanding the geological settings conducive to the release of such thermogenic gas, and quantifying its fluxes to the water column, may be an important step towards deciphering the potential contribution of such natural sources to a total atmospheric pool of isotopically heavy and old methane carbon.

Although the spatial relation of seepage to exhumed structural highs has been shown, the migration pathways of fluids from shallow accumulations to the seafloor are poorly understood. It is also unclear whether seepage occurs through fractured or partly eroded cap rocks, what fraction of seepage is related to faults, and if overlying glacigenic deposits prohibit fluid discharge. A lack of knowledge on how hydrocarbons escape from the shallow subsurface prevents a prognosis of whether other uplifted and formerly glaciated continental margins may also leak thermogenic methane gas.

2 Geological settings

The northern Norwegian Barents Sea hosts several basins and numerous structural highs that together form an extensive petroleum province (Lundschien et al., 2023). The Norwegian Offshore Directorate in 2024 estimated that it may contain significant 1,125 million standard cubic meters of recoverable oil equivalents of undiscovered resources (Norwegian Offshore Directorate, 2024). However, the area is not open for petroleum activity (Figure 1) and information on its structural settings, stratigraphy, lithological and geochemical properties is scarce compared to the Norwegian Barents Sea south of the current limit for exploration at 74° 30' N, where 49 hydrocarbon discoveries have so far been found.

Structural outlines of the northern Norwegian Barents Sea are defined by the Timanian and Caledonian Basement (Faleide et al., 2008). Regional extension in the Late Devonian–Carboniferous formed a system of NE-SW oriented rifts (Grogan et al., 1999) that were inverted by several episodes of compressional tectonism forming a suite of structural high and anticline structures. Inversion of the Sentralbanken and Storbanken structural highs, and large (up to 100 km long) anticline structures on the Kong Karl platform started in the Late Jurassic and continued during the Early Cretaceous and Cenozoic tectonic episodes. Due to erosion of Cenozoic and Cretaceous sequences in our study areas, some of the younger tectonic events of potential importance for the development of these structural highs cannot be dated stratigraphically. Nevertheless, more complete sediment successions in the southern Barents Sea (e.g., Fingerdjupet subbasin and Hoop

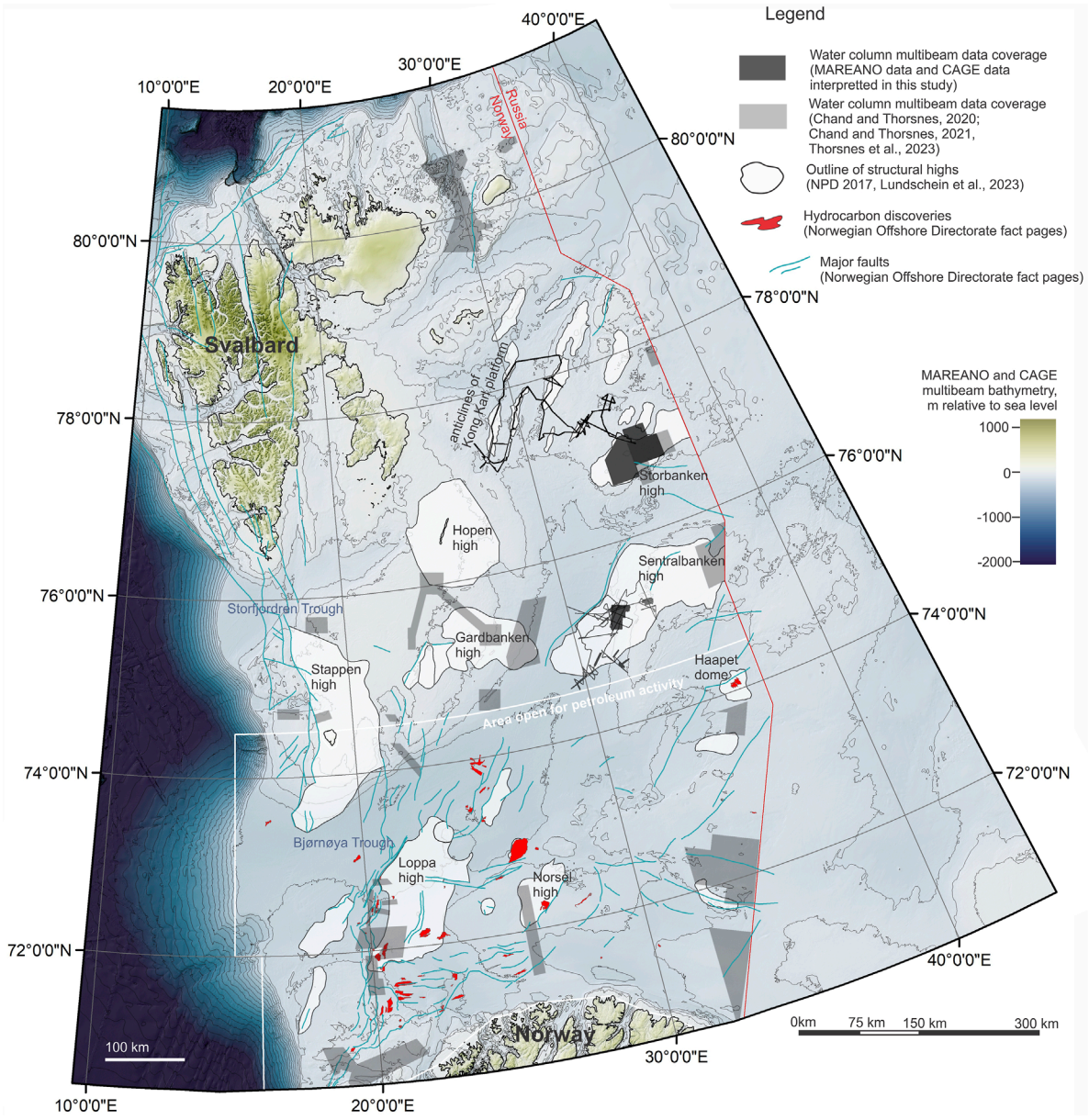

FIGURE 1
outlines of the main structural elements and relevant multibeam echosounder data coverage in the northern Norwegian Barents Sea. Seafloor and land topography is from GEBCO (Jakobsson et al., 2020). Multibeam echosounder data processed for this study is from the MAREANO program and the following research cruises: CAGE 18–1 (Plaza-Faverola, 2018), CAGE 19–2 (Andreassen et al., 2019), CAGE 20–2 (Patton et al., 2020), CAGE 21–4 (Winsborrow et al., 2021), CAGE 21–6 (Winsborrow and Knies, 2021), CAGE 22–6 (Serov et al., 2022).

fault complex) reflect systems of faults demonstrating rhomboidal or orthogonal pattern attributed to late Mesozoic–Cenozoic rifting (Collanega et al., 2017; Serck et al., 2017) Two important fault orientation previously reported in these areas are NE-SW inherited from Paleozoic rifting and NW-SE established in Cenozoic (Serck et al., 2017).

Petroleum systems of the northern Norwegian Barents Sea contain a suite of potential source rocks: Lower Carboniferous shales and coal (likely gas generating due to significant burial depth), upper Carboniferous and lower Permian carbonate-rich muds and marine shales (potentially oil-generating), and Olenekian, Anisian and Ladinian shales representing the most significant source rocks of the region. Due to tectonic uplift and glacial erosion in Cenozoic, the Triassic successions are currently located close to the seafloor and are partially visible on our seismic data. In the northern Norwegian Barents Sea, the Triassic strata host both, a potent source rock Steinkobbe formation and a suite of formations with reservoir qualities: Havert, Klappmyss, Kobbe and Snadd.

Sediment deposition in Triassic is largely defined by regional subsidence and progradation of a delta system sourced from the Ural Mountains. The Triassic delta system in the Barents Sea prograded to the northwest and reached the Sentralbanken high in the Induan

and Svalbard in the Carnian (Riis et al., 2008; Høy and Lundschien, 2011; Klausen et al., 2019). On the Sentralbanken high and in the Olga basin, four progradational upward coarsening units have been identified: Havert, Klappmyss, Kobbe, and Snadd Formations. The three former of these formations have time equivalent organic rich shales of Seinkobbe formation deposited in marine conditions prevailing close to Svalbard. Deposition of marine shales prevailed when subsidence of the basing over-paced sediment deposition and caused delta front to retract. Thus, in Sentralbanken and Storbanken highs, the middle-upper Triassic succession represents an interbedding of organic-rich marine shales of Steinkobbe formation and coarser-grained Havert, Klappmyss and Kobbe formations. Kong Karl platform has not been significantly affected by the prograding delta and marine shales prevail. Snadd Formation is the most prominent and thick prograding sequence which deposited across the entire basin, including Kong Karl platform. Clastic sedimentation related to the delta system was interrupted by a regional transgression during the Norian, which corresponds to the deposition of shales of the Flatsalen Formation in the Barents Sea (Worsley, 2008).

Potential reservoirs may also occur in lower - middle Jurassic fluvial, deltaic and shallow-marine sandstones (Lundschien et al., 2023). The sandstones are overlain with middle-upper Triassic anoxic black shales of the Fuglen and Hekkingen Formations (Stemmerik and Worsley, 2005; Worsley, 2008). These organic-rich shales are immature in the northern Norwegian Barents Sea due to insufficient burial depth, but demonstrate good cap rock potential.

Outside the Kong Karl and Edgøya platforms and the Olga basin, Cretaceous strata are extensively eroded. Cretaceous successions preserved in these platforms and basins comprise silty shales and mudstones deposited in predominately open-marine conditions with turbidites and debris flows surrounding structural highs. Cenozoic sediments were subaerially eroded from the northern Norwegian Barents Sea shelf during the Neogene and at a faster rate by ice sheets during the Quaternary.

Thus, the elements of the petroleum systems that likely play a significant role in modulating shallow subsurface fluid flow in the northern Norwegian Barents Sea are source rock formation Steinkobbe, reservoirs in Havert, Klappmyss, Kobbe, Snadd formations and in lower-middle Jurassic sandstones. Middle-upper Triassic marine shale units (e.g., Flatsalen formation) and middle-upper Jurassic deep-marine organic reach shales (Fuglen and Hekkingen formations) may act as caprocks.

3 Materials and methods

3.1 Acquisition, processing, and interpretation of multibeam echosounder data

Due to the high acoustic impedance contrast between gas bubbles and sea water, submarine gas seeps are excellent targets for identification with multibeam echosounder sonars. For identifying gas seeps in the water column and mapping seafloor topography, we used multibeam echosounder data acquired during six research cruises onboard RV Helmer Hanssen and RV G.O. Sars conducted by CAGE–Centre for Arctic Gas Hydrate, Environment and Climate (Plaza-Faverola, 2018; Andreassen et al., 2019; Patton et al., 2020; Winsborrow et al., 2021; Winsborrow and Knies, 2021; Serov et al., 2022) and data provided by the MAREANO seafloor mapping program (Thorsnes et al., 2008).

All CAGE data sets were acquired with Kongsberg EM302 multibeam echosounders operated at 30 kHz nominal signal frequency and 120° opening angle encompassing 432 beams. A 120° opening angle provided off-track coverage of the seafloor ~3 times greater than the water depth, while maintaining good resolution of the data (Figure 2). The ping rate automatically varied from 0.5 to 2 Hz depending on the water depth. During the research cruises, we regularly collected sound velocity profiles of the water column with an SBE 19plus CTD sensor to convert the acoustic signal travel time to water depth accurately.

MAREANO data were acquired by a third-party with Kongsberg EM710 multibeam echosounder system (see https://www.mareano.no/for details on data acquisition).

Backscatter data in the water column has persistent side lobe artefacts due to strong signal reflections from the seafloor on the peripheral sectors of the swath (Figure 2). These artefacts are inherent features of multibeam data regardless of the sonar model or acquisition settings and have been previously reported (Urban et al., 2017; Thorsnes et al., 2023). Parts of the swath affected by the side lobe artefacts are not suitable for reliable gas seep identification. Therefore, the footprint of the swath sector useable for gas seep detection in data acquired with both Kongsberg EM302 and Kongsberg EM710 echosounder systems, is ~50% of the total footprint (Figure 2). For mapping gas flares across large areas without data gaps, a total swath overlap between parallel survey lines should be at least 30%. In the large MAREANO data set covering the Storbanken structural high, 88.2% of the total insonified area is suitable for gas flare detection. The CAGE 21–4 data set in Sentralbanken high also demonstrates 88.2% water column data coverage (Figure 11). Other CAGE data sets used in this study consist of discrete survey lines and do not intend to provide continuous spatial coverage (Figure 3). Of note, side lobe artifacts do not obstruct mapping seafloor topography and the entire swath width has been used to produce bathymetric maps.

To compensate for ship movements, the transmit fans of the EM302 and EM710 echosounders are split in four sectors with independent steering. Because peripheral sectors have a slight ping offset compared to the central sectors, static artifacts occur near the seafloor (Figure 2). The static artifacts decrease the quality of data in the peripheral sectors of the swath, yet do not obstruct flare identification completely. In EM710 data, static artefacts are weaker and the sectors where they occur are narrower compared to EM302 data.

For processing and interpretation of echosounder data in the water column we used QPS FMMidwater software. To identify locations of gas flares we replayed all acquired lines in a single fan view' and a fan view showing five consecutive fan images stacked together, which helped identify weaker acoustic signals. The coordinates of where the gas flares originate at the seafloor were picked manually with the geopicking tool (Figure 2). In cases of swath overlaps, flare coordinates were picked only at the first passage. Identified water column anomalies were categorized as weak, medium or strong based on raw amplitude of the anomalies and the appearance of the flares on echograms. All lines and all data

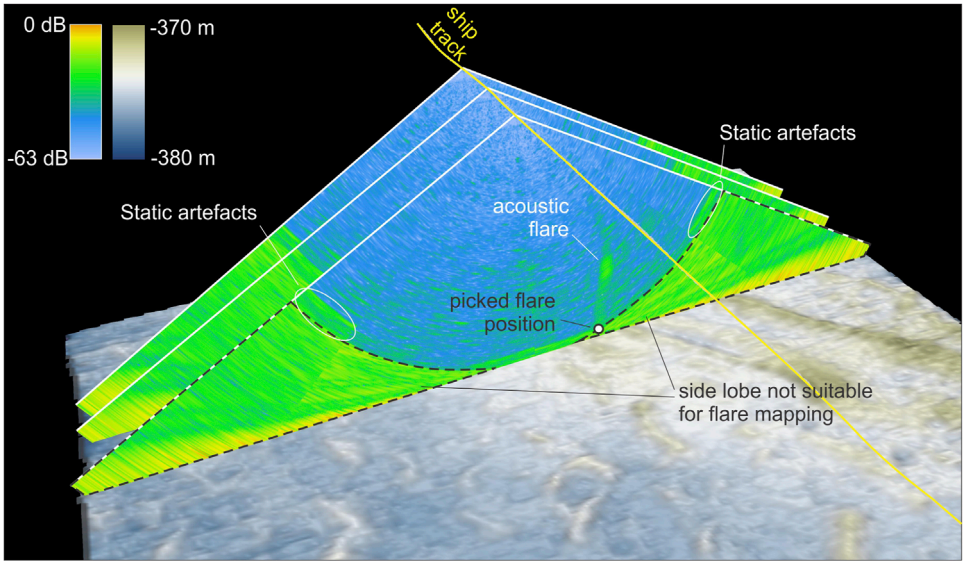

FIGURE 2
example of swath images acquired with Kongsberg EM302 echosounder.

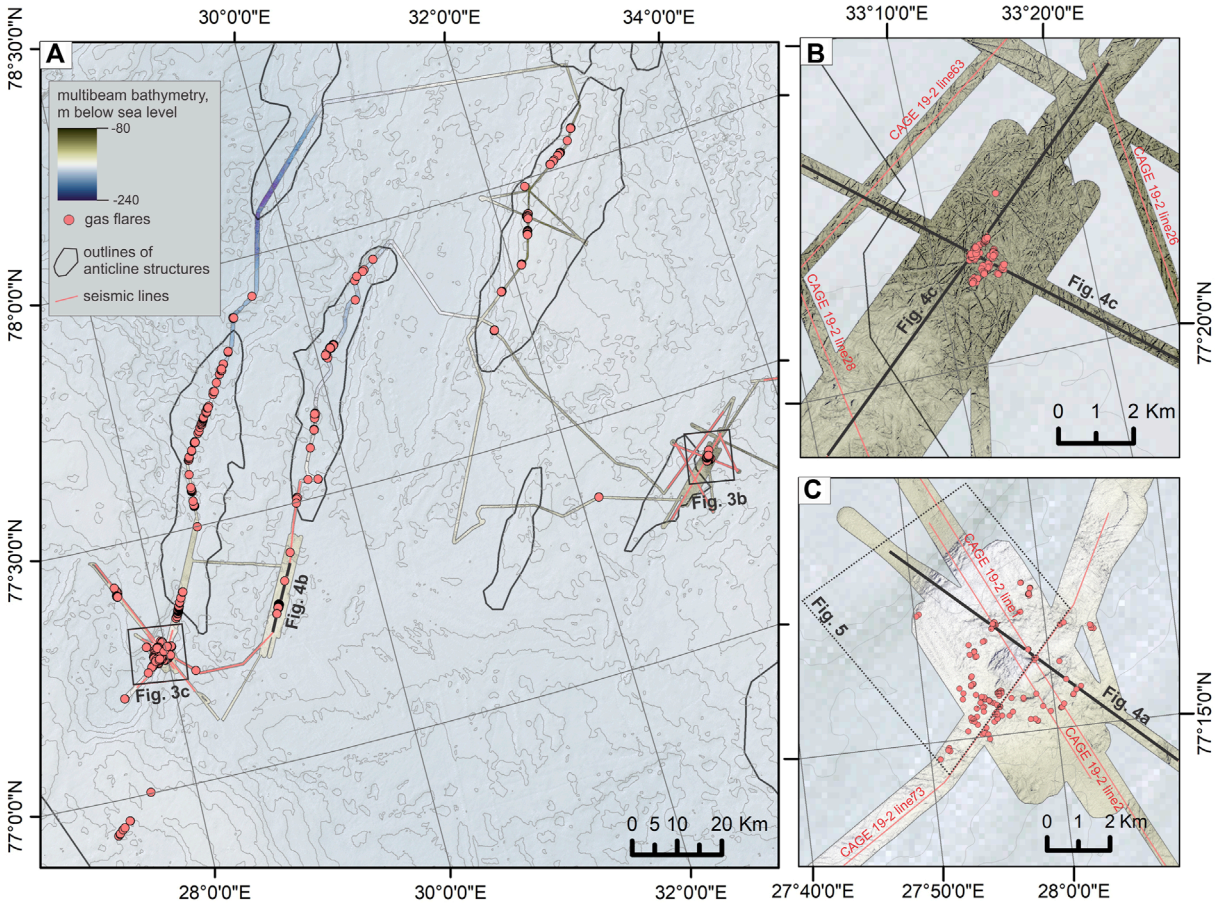

FIGURE 3
data coverage, gas seepage locations (Andreassen et al., 2019) and structural outlines (Lundschien et al., 2023) within Kong Karl platform. Background seafloor topography is from GEBCO (Jakobsson et al., 2020).

TABLE 1 tentative mass flux of free methane from the seabed into the water column at three investigated areas in the northern Norwegian Barents Sea.

Area	Multibeam coverage, km^2	Weak flares	Medium flares	Strong flares	All gas flares	Mass flux of methane, mol/min			Total mass flux of methane, mol/min	Total mass flux of methane, mol/yr
						Weak flares	Medium flares	Strong flares		
Kong Karl platform	602	547	287	61	895	9.3 (4.9–27.4)	29,3 (5.2–57.5)	12.4 (1.6–22.9)	51 (11.7–107.7)	26.8 x 10^6 (6.1–57 x 10^6)
Storbanken high	2,435	2,215	626	153	3,004	37.7 (19.9–110.8)	63.9 (11.3–125.2)	31.2 (4.1–57.4)	132.7 (35.3–293.3)	69.8 x 10^6 (18.5 x 10^6–15.4 x 10^7)
Sentralbanken high	1,855	11,890	4,213	1,701	17,804	202.1 (107–594.6)	429.7 (75.8–842.5)	347 (45.9–637.9)	978.9 (228.8–2,074.9)	51.4 x 10^7 (12 x 10^7–10.9 x 10^8)
all surveyed areas	4,892	14,652	5,126	1,915	21,703	249.1 (131.9–732.8)	522.9 (92.3–1,025.8)	390.7 (195.3–718.1)	1,162.6 (275.8–2,476)	61 x 10^7 (14.5 x 10^7–13 x 10^8)

sets were processed in the same manner, using uniform color scale and screen settings for better equability of interpretation.

To produce gridded seafloor topography from data acquired during CAGE research cruises, we used QPS Qimera software. During the processing, we applied static shifts, rejected outliers and removed pieces of data with a poor quality, such as data acquired during ship turns and sediment and water column sampling. MAREANO data is available for users in a gridded format already. Gridded seafloor topography data and picked locations of gas flares were subsequently imported to ArcMap software to produce maps.

To identify trends in the orientation of flare clusters we calculated the standard deviation of the flare coordinates x and y from the mean center using the Directional Distribution tool from the ArcMap toolbox (Figure 12).

3.2 Gas flux quantification

We estimate the flux of free methane gas using a modified version of the simple upscaling method used by Sahling et al. (2014) and replicated by Ferré et al. (2020). Sahling et al. (2014) used a remotely operated vehicle on the formerly glaciated western Svalbard margin (240 m water depth) to find out that an acoustic gas flare on multibeam echosounder data represents six bubble streams on average. This is because the footprint of the multibeam echosounder at ~240 m water depth is >4 m (1.7% water depth) and, thus, cannot parcel closely located bubble streams.

Lacking direct quantification of bubble release in our study areas, we rely on average gas flux of 17 ± 8 mmol/min (n = 15) from each bubble stream reported offshore Svalbard by Sahling et al. (2014). This well-known seep cluster has similar size to individual clusters within our study areas, similar seep density and is located at similar water depth of 240 m. In contrast to Sahling et al. (2014), we parametrize the gas fluxes based on a qualitative assessment of acoustic flare strength. Here we assume that a weak gas flare corresponds to one bubble stream, a medium gas flare corresponds to six bubble streams, and a large gas flare–to twelve bubble streams, with each of the bubble streams releasing 17 mmol of methane gas per minute.

We further estimate minimum and maximum methane fluxes accounting for large uncertainties in both the flux at each bubble stream and the number of bubble streams stacked in one acoustic gas flare. The minimum scenario assumes the lowest individual bubble stream flux of 9 mmol/min reported by Sahling et al. (2014) and that the weak, medium and strong flares represent one, two and three streams of gas bubbles, respectively (Table 1). The maximum scenario assumes the upper range of methane flux (25 mmol/min) at each bubble stream and that the weak, medium and strong flares represent two, eight and fifteen bubble streams.

3.3 Acquisition and processing of high-resolution 2D seismic data

Reflection seismic data was acquired in three research cruises: CAGE 18–1, CAGE 19–2, and CAGE 22–6. One or two generator-injector air guns were used as the seismic source and a 100 m long streamer with 32 channels separated by 3.125 m as the

receiver. Shooting range, sampling rate and the number of guns varied between the surveys and are described in the respective cruise reports in detail (Plaza-Faverola, 2018; Andreassen et al., 2019; Serov et al., 2022).

The data was processed onboard using RadEx Pro software. All data have gone through simple bandpass filtering, bubble removal, normal moveout (NMO) correction and stacking, migration using Kirchhoff Migration Algorithm, post-migration filtering such as band-pass filtering, butterworth filtering, etc. and SEG-Y output (See cruise reports for more detail on seismic processing) (Plaza-Faverola, 2018; Andreassen et al., 2019; Serov et al., 2022). Seismic data was interpreted in Schlumberger Petrel software.

4 Results

4.1 Kong Karl platform

On Kong Karls platform we identified 895 gas flares within a ~602 km^2 seafloor footprint of useable multibeam echosounder data and where the water column was unaffected by side-lobe artifacts (see Methods for details on data acquisition, processing and interpretation) (Figure 3). All data were acquired during the CAGE 19–2 research cruise (Andreassen et al., 2019) in July 2019. The majority of identified gas seeps correlate to the outlines of the anticline structures previously established based on the network of conventional seismic lines (Lundschien et al., 2023) and boundaries identified on our new 2D seismic lines (Figure 4). The study area is located in water depths <200 m which results in a shallow first-seafloor-multiple reflection, limiting the thickness of interpretable seismic cross sections to 200–250 ms. This was sufficient to identify lower-middle Jurassic sandstone formations with reservoir potential, the upper Jurassic Hekkingen and Fuglen formations with good sealing properties, and the Cretaceous overburden (Figures 4, 5). Lower-middle Jurassic sandstone units are problematic to discriminate and correlate because they appear only within short fragments of seismic lines and are otherwise masked by the first-seafloor-multiple reflection (Figure 4).

Different from the Sentralbanken structural high described by Serov et al. (2023), where the seismic data show that reservoir intervals of the Kobbe Formation presumably subcrop at the seafloor, on the Kong Karl platform we did not acquire seismic lines at zones where the Upper Jurassic cap rock has been fully eroded. The most prominent gas seepage clusters relate to faults piercing lower-middle Jurassic sandstones overlain by a seal of upper Jurassic shales of Hekkingen and Fuglen formations and Cretaceous overburden (Figures 4, 5). The highest seep density we observed in such settings is at least an order of magnitude lower than in Sentralbanken (Serov et al., 2023).

Within anticlines, upper sections of middle Jurassic sandstones exhibit 0.2–2.5 km wide amplitude enhancement zones (Figures 4B–D) pointing towards fluid accumulations. The enhanced reflectors appear within tilted blocks isolated with juxtaposition seals. Bright spots likely related to fluid accumulations also occur in the overburden at the hinges of the anticline structures (Figure 4C). A suite of shallow faults in the overburden and deeper faults penetrating to the reservoir level correlate well with the seafloor seeps.

The capping potential of upper Jurassic shales and Cretaceous overburden appears to be compromised without visible faulting in at least one location (Figure 4B). Here a 6 km wide anticline structure (potentially a four-way closure structure) containing middle Jurassic sandstone with enhanced reflection fuels a pronounced vertical zone of acoustic blanking, leading to a cluster of seafloor seeps (Figure 4B). The acoustic blanking zone features push-down of the reflectors likely due to the presence of free gas, which lowers the seismic velocity. Available data suggest that the upper Jurassic seal has been breached leading to the escape of fluids from the accumulation in the middle Jurassic sandstone reservoir.

A prominent seafloor depression of ~1 km in diameter and 20 m deep is located on the southern part of a large NE-SW trending anticline (Figure 3C; Figure 5). The depression has similar dimensions and morphology to the craters in the Bear Island Trough (Andreassen et al., 2017; Waage et al., 2020). Resonating with findings of Waage et al. (2020) and Andreassen et al. (2017), the depression represents a small graben and its walls are delimited by normal faults. Gas seepage corresponds to the faults framing the graben, while no free gas is found liberating from its bottom (Figure 5). The seafloor at the Kong Karl platform is densely scattered with iceberg ploughmarks (Figure 3B) and we see no indications of pockmarks, pingo-like features or any other common seafloor manifestations of fluid release.

4.2 Storbanken high

Excellent spatial coverage of multibeam echosounder data on the Storbanken high (Figure 1) acquired by MAREANO (Thorsnes et al., 2008; Bøe et al., 2022) allows for precise outlining of gas seep clusters. Here the footprint coverage of multibeam echosounder data suitable for gas seep identification is ~90% of the total insonified seafloor area. We identified 3,004 gas seeps, most of which form elongated clusters with two orientations normal to each other: NE-SW and NW-SE.

Seismic and multibeam water column data interpretations suggest that NW-SE trending clusters are fault controlled (Figure 7). Notably, MAREANO multibeam data reveals seafloor lineaments which correlate to faults mapped on 2D seismic data and gas seepage occurs along these (Figures 6B,C, 7). The lineaments are unlikely to be mistaken with glacial lineations because the latter have distinctively different orientation evident from both our data (Figure 6D) and literature (Sejrup et al., 2022). Within the NW-SE trending seep clusters, the gas flares correlate well to the fault lineaments. In the absence of such visible lineaments, gas flares often form distinctive linear clusters of the same orientation (Figure 6D). We found that 1,309 gas seeps (43.5% of total number observed in Storbanken) relate to this NW-SE trending generation of faults.

NE-SW oriented seep clusters appear to be controlled by exhumed, and subcropping, lower-middle Jurassic and upper Triassic rocks with potential of bearing hydrocarbons (Stø and Snadd Formation, respectively) (Figure 7; Figure 8A, B). The Jurassic reservoir within several large, uplifted blocks contains a prominent flat spot seismic anomaly extending for >6 km (Figure 7). The flat spot is indicative of a high acoustic impedance contrast on the boundary between gas-saturated porous rocks (above) and liquid-saturated porous rocks (below) (Gluyas and Swarbrick,

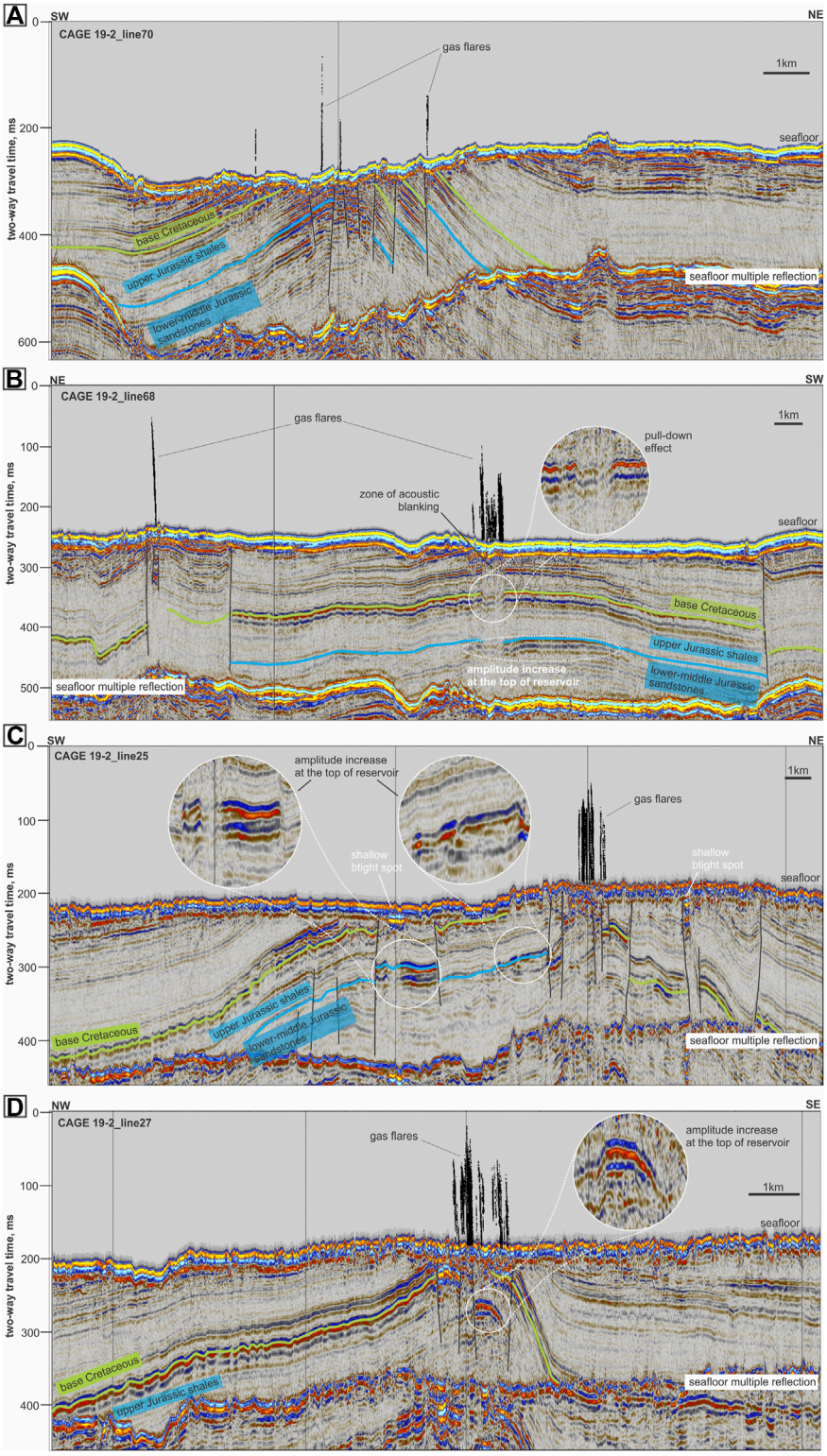

FIGURE 4
(A–D) P-Cable 2D seismic data and multibeam echosounder data showing evidence of gas accumulations and leakage into the water column on the Kong Karl platform.

2021). Seepage from the faults between the blocks is hampered (Figure 6B; Figure 7) and the shallow fluid accumulation might be sufficiently sealed.

In total, we attributed 541 seeps (18% of the total number) to NE-SW oriented clusters associated with subcropping Triassic and Jurassic sandstones with reservoir qualities. Seafloor bathymetry

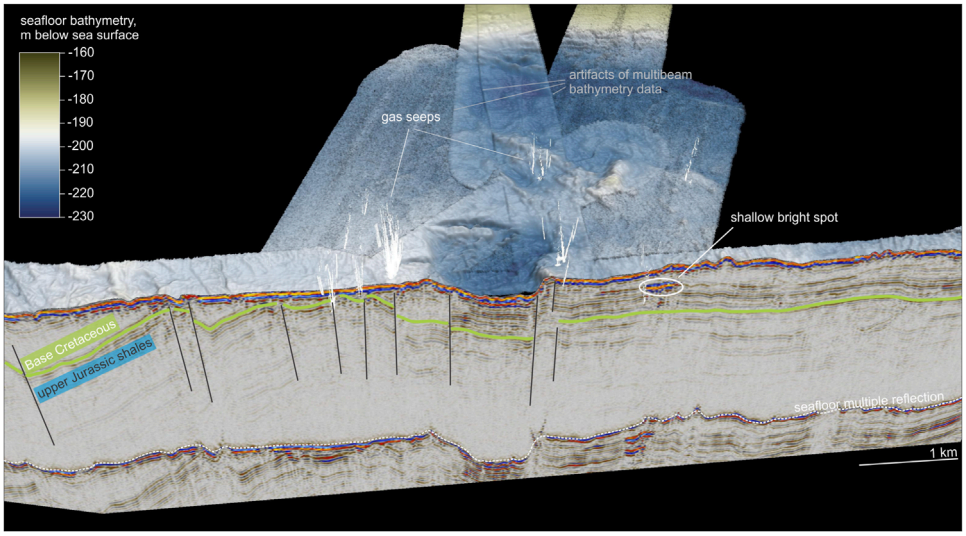

FIGURE 5
gas seepage surrounding the crater on the Kong Karl platform.

does not reveal any distinctive lineaments or other seabed features associated with subcropping of the lower-middle Jurassic and upper Triassic reservoir units, apart from one occasion where an uplifted block of upper Triassic sandstone strata forms a mound 800 m in diameter and ~15 m high (Figure 8A). Gas seeps are strictly linked to the flank of the mound, where the upper Triassic sandstone reservoir outcrops. Unlike submarine gas hydrate pingos reported at several locations on the Barents Sea shelf (Andreassen, 2016; Serov et al., 2017; Serov et al., 2023), the mound is composed of lithified sedimentary rocks. As gas seepage is strictly limited to subcropping sandstone reservoirs, and the mound represents an uplifted and tilted block of sedimentary rocks, it is unlikely that its genesis is driven by fluid flow. Both seafloor seepage and the mound itself are likely a result of the tectonic evolution of the area and its erosional history leading to exhumation of gas-bearing strata onto the seafloor.

Southern sectors of the Storbanken high for the first time described in Nixon et al. (2019) exhibit a group of 35 seabed craters (Figure 6A, E; Figure 9) resembling craters in the Bear Island Trough (Andreassen et al., 2017) and a crater we found on the Kong Karl platform. The craters are 200–600 m in diameter and 3–15 m deep. They have sharp edges, steep walls, often flat bottoms, and are engraved in lithified upper Triassic sedimentary rocks. These characteristics make them distinct from seafloor pockmarks occurring in soft sediments, which tend to have smoother edges and gentler walls (Judd and Hovland, 2009). Seven gas seeps forming two groups occur within the Storbanken crater field (Figure 9). The seepage is related to faults piercing the upper Triassic cap rock formation and reaching the sandstone unit of the Snadd formation (Figure 9A). Available seismic data indicate that the crater walls correlate with shallow and deep faults striking through 50 to >300 ms of seismic cross sections (Figure 9A). Blocks of Triassic strata beneath the craters are often subsided and tilted (such as the craters 1, 2,3,6 on Figure 9A), yet on some occasions do not clearly correspond to subsidence and are underlain by flat basal reflectors (crater 5). Nevertheless, shallow faults correlate to the walls of such craters. Our observations alone cannot rule out possible contribution of gas blow-out events upon destabilization of subglacial gas hydrates proposed in Andreassen et al. (2017) But tectonic processes have likely played a major role in crater formation as all craters correlate to faults and some are surface manifestations of deeper graben or half-graben structures. Notably, the entire 55 km^2 crater area in Storbanken hosts only seven seeps, which is significantly lower than both the average seep density in the mapped Storbanken area and the seep density in the Bear Island Trough crater area (Andreassen et al., 2017; Waage et al., 2020).

4.3 Sentralbanken high

Serov et al. (2023) reported extensive seafloor hydrocarbon gas and oil release in the central part of the Sentralbanken high. Here we use new multibeam echosounder data with sufficient continuous spatial coverage to estimate the total number of gas seeps and outline seep clusters in detail (Figure 11). We focused our mapping on the central part of the structural high where seismic data previously indicated 2–5 km wide zones where the middle Triassic Kobbe formation with reservoir potential subcrops at the seafloor (Serov et al., 2023). Other zones of the structural high have been characterized with discrete survey lines only and lack continuous spatial data coverage (Figure 10).

Our results show that 15,105 acoustic gas flares (73% weak, 23% medium and 4% strong) occur within the 465 km^2 polygon at the hinges of the eroded structural high (Figure 11). The entire data set from Sentralbanken (Figure 10) reveals 17,804 acoustic flares within 1,855 km^2 of water column multibeam data.

The majority of flares within the hinges of the structure form densely populated elongated clusters with a NE-SW orientation (Figure 11). Such clusters are often segmented by zones with no gas seepage possibly explained by small grabens which contain internal

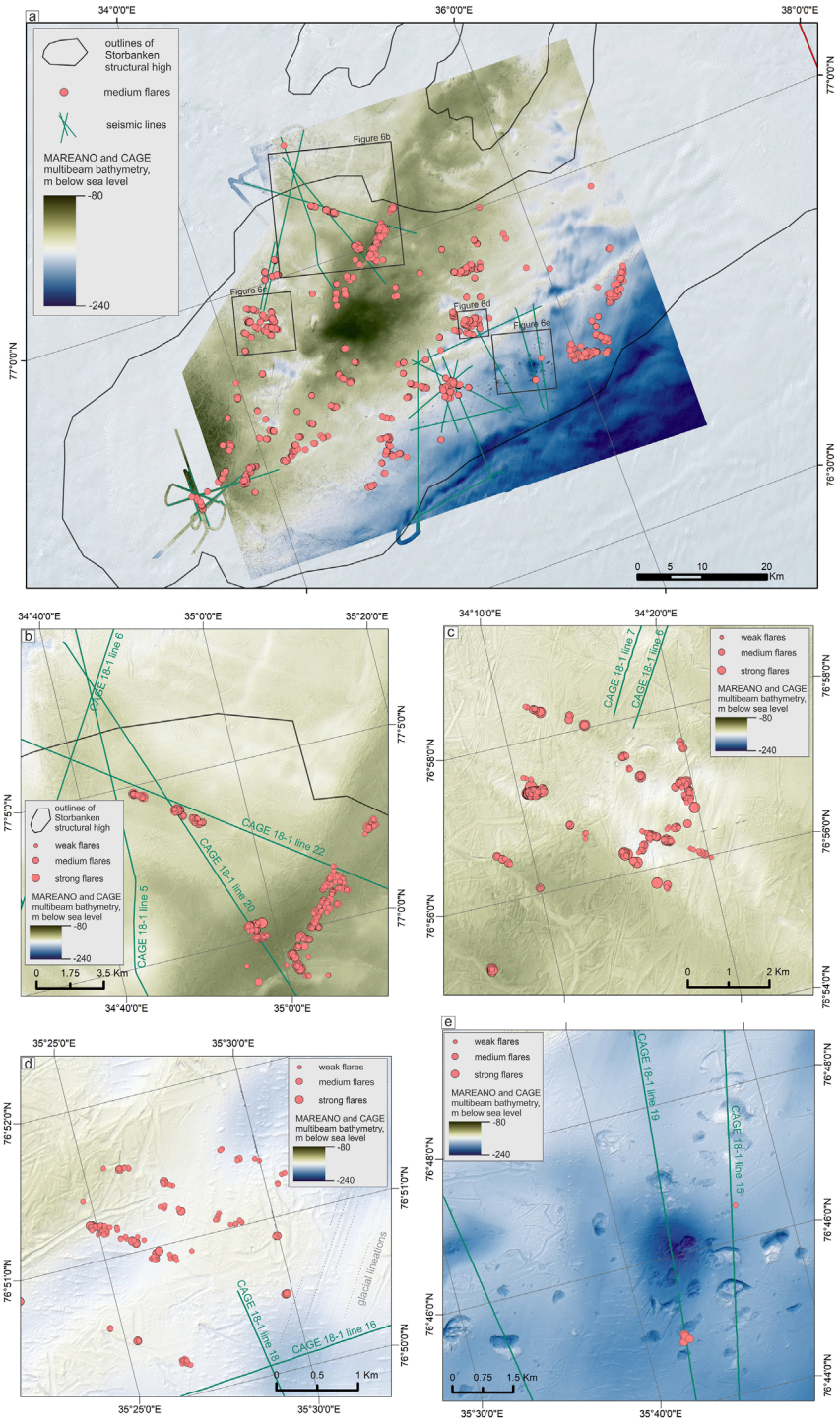

FIGURE 6
(A) The distribution of gas flares on the Storbanken high and locations of seismic lines. Multibeam echosounder data was acquired by the MAREANO project (Thorsnes et al., 2008) and the CAGE 18–1 research cruise (Plaza-Faverola, 2018).; **(B–D)** elongated seep clusters on the Storbanken high; **(E)** gas seeps snd seafloor depressions on the Storbsnken high.

Kobbe Formation cap rock shales and younger overburden (lower Ladinian shales). Newly acquired high-resolution P-Cable seismic data on the Sentralbanken high (Serov et al., 2022) demonstrated poor signal penetration in areas where acoustically hard Triassic and Jurassic formations subcrop at the seafloor and could not be used to correlate seep cluster boundaries with structural elements on a finer scale than previously done by Serov et al. (2023).

Coupling seafloor bathymetry and gas flare mapping allowed investigation of whether gas seepage correlates with glacial landforms or potential manifestations of seabed fluid flow such

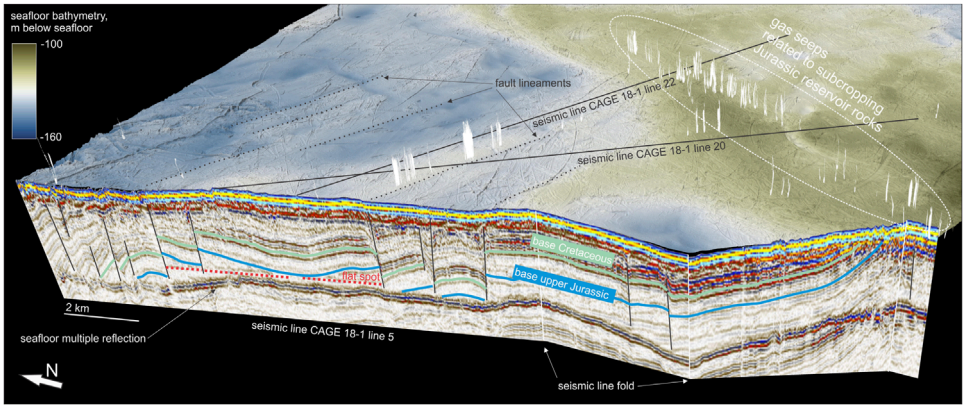

FIGURE 7
Seismic line 'CAGE 18–1 line 05' (Plaza-Faverola, 2018) showing a flat spot seismic anomaly, combined with seafloor topography and gas flares (MAREANO data).

as pockmarks, mounds, craters, etc. Geomorphological mapping of the seafloor bathymetry has revealed a prominent tunnel valley and esker system crossing the study site from NE to SW (Figure 12) (Shackleton et al., 2023). Both the tunnel valley and the esker are imprints of subglacial water drainage during the last deglaciation some 15,000 years ago (Patton et al., 2017; Shackleton et al., 2023). Tunnel valleys are erosional features formed by the subglacial flow of meltwater. Overprinted eskers are time-transgressive depositional features that typically form near the former ice-sheet margin and are composed of a wide variety of glaciofluvial facies ranging from sorted silts to boulders (Livingstone et al., 2020).

In our data set, eskers do not correlate with gas flare locations. This may be expected given that the eskers are up to 50 m thick and potentially contain a significant sediment volume unfavorable to fluid migration. However, eskers occupy a small fraction of the total mapped area and happen to lie outside of large flare clusters (Figure 11; Figure 12A). Therefore, it is probable that esker deposits do not emit gas flares due to the absence of fluid source, and not due to their sealing lithological properties.

The network of tunnel valleys demonstrates an erratic relation to gas seepage. In the northern part of the area (Figures 12A, B), the tunnel valley crosscuts a pronounced flare cluster with NE-SW orientation and does not cause an apparent change in flare density compared to surrounding areas. However, in the central part of the area, flare density within the valley is visibly less compared to the surrounding areas (Figure 12C). Locally, edges of the valley coincide with sharp transitions between densely populated flare clusters and areas with no seepage. While widespread gas seepage within the valley is somewhat expected considering its erosional origin, decreased gas seepage and even a complete absence, is surprising. We hypothesize that this section of the meltwater stream followed structural elements of the underlying strata (such as a small graben or the axis of a syncline) which act as a barrier for seepage, and the valley itself does not constrain fluid escape. Alternatively, this section of the valley network might have accumulated a thicker section of glaciofluvial sediments constraining gas leakage.

The northern part of the area features a ~40 km^2 densely populated pockmark field (locally, >40 pockmarks/km^2). Seafloor pockmarks are a widespread manifestation of seabed fluid escape formed by gases or fluids mobilizing soft sediments for subsequent removal with currents (Hovland et al., 2002; Forwick et al., 2009). On Sentralbanken, the pockmarks are 0.5–3 m deep and 10–50 m in diameter. The pockmarks are distributed randomly and are abundant within and outside the tunnel valley (Figures 12A, B). Present-day seepage, however, shows no clear correlation with them. While gas flares demonstrate clustering, the pockmarks do not, and are equally widespread within and outside gas seeping areas (Figure 12B). Furthermore, very few gas flares originate from pockmarks. The extensive field of extinct pockmarks whose distribution does not resemble the structurally controlled distribution of seeps may indicate a different nature of fluids forming the pockmarks than thermogenic gas discharge. Escape of sediment pore water (Harrington, 1985), or release of microbial methane gas generated beneath the ice sheet (Wadham et al., 2012) are possible explanations for the pockmark field. While the type of fluid mobilizing sediments is uncertain, the pockmark field and abundant iceberg ploughmarks indicate with certainty that a drape of soft sediments exists in this zone. Gas seepage is abundant in the area despite this sedimentary veneer.

5 Discussion

5.1 Seep clusters correlating with structural framework

At Storbanken and Sentralbanken structural highs, the excellent spatial coverage of multibeam echosounder data suitable for gas flare detection exhibits two distinct trends in flare cluster orientation (Figures 13A, B): NE-SW and NW-SE. On Storbanken, elongated fault-controlled NW-SE clusters dominate (27 clusters), while on Sentralbanken the majority of the gas flares appear within five large NE-SW oriented clusters controlled by the subcropping of middle-Triassic reservoirs. A different Jurassic reservoir formation subcrops on Storbanken, yet the orientation of the seep clusters is the same. The NE-SW orientation may be dictated by general structural trend

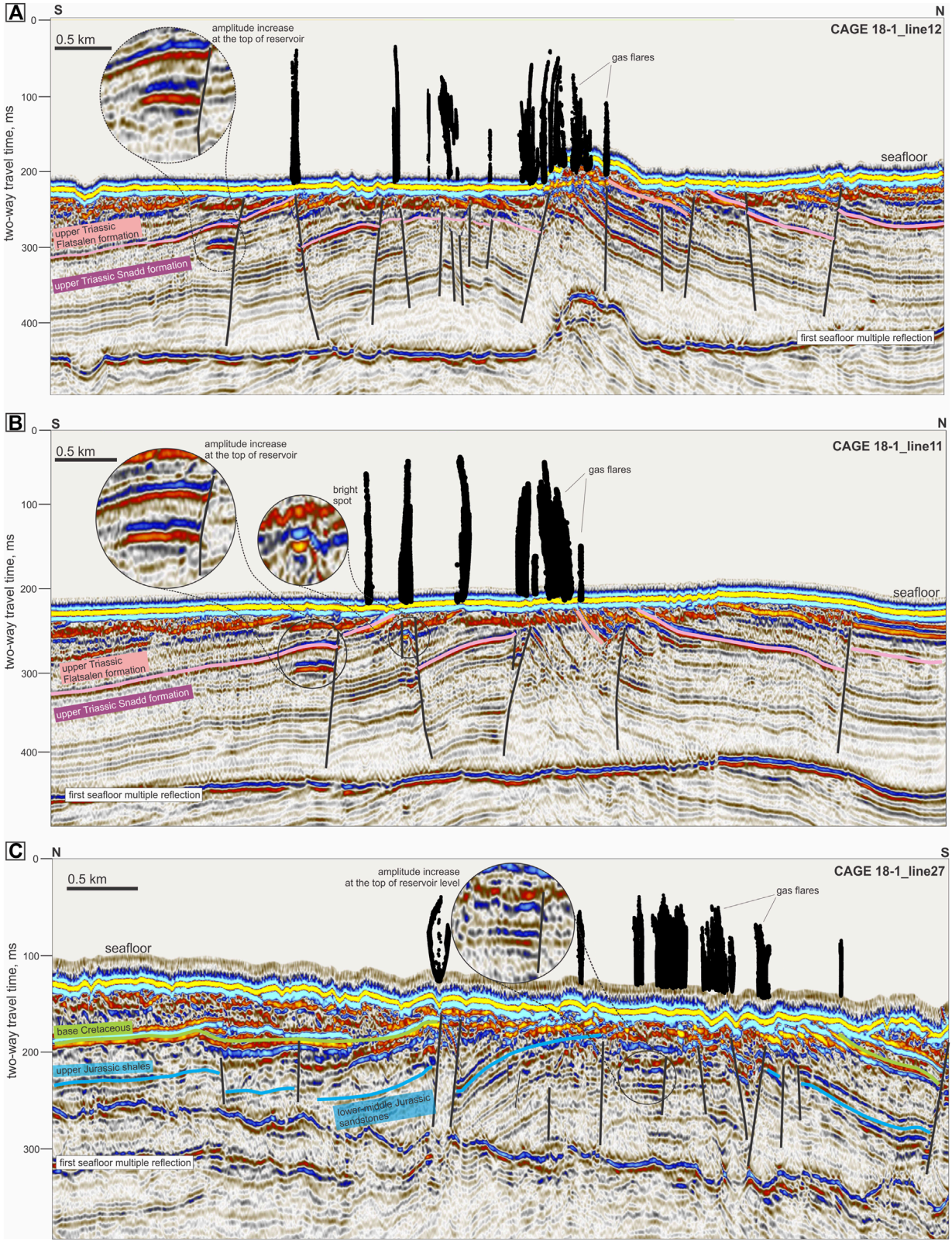

FIGURE 8
(A–C) P-Cable 2D seismic data and multibeam echosounder data showing evidence of gas accumulations and seepage into the water column at Storbanken high.

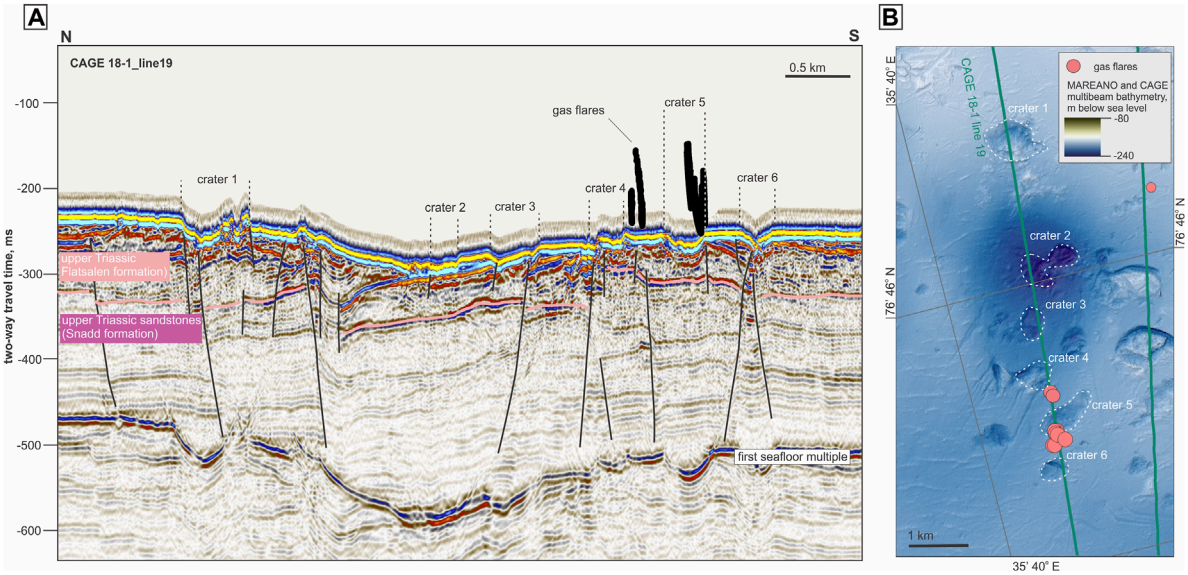

FIGURE 9
Geological controls of seafloor craters on Storbanken high. **(A)** fragment of a seismic line CAGE 18–1 line 19 crossing six seafloor craters; **(B)** location of the seismic line and gas flares on seafloor topographic map.

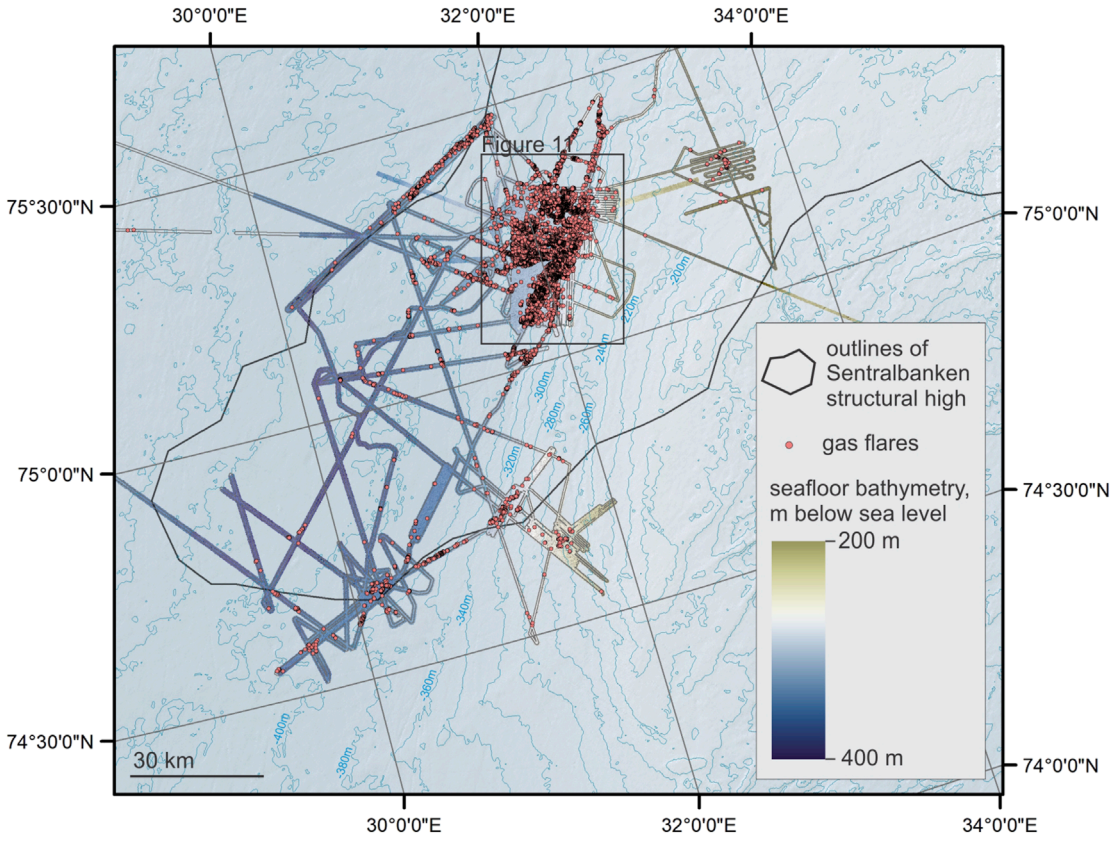

FIGURE 10
Data coverage and distribution of gas glares in Sentralbanken high. Data were acquired in CAGE 20–2 (Patton et al., 2020), CAGE 21–4 (Winsborrow et al., 2021), CAGE 21–6 (Winsborrow and Knies, 2021) and CAGE 22–6 (Serov et al., 2022).

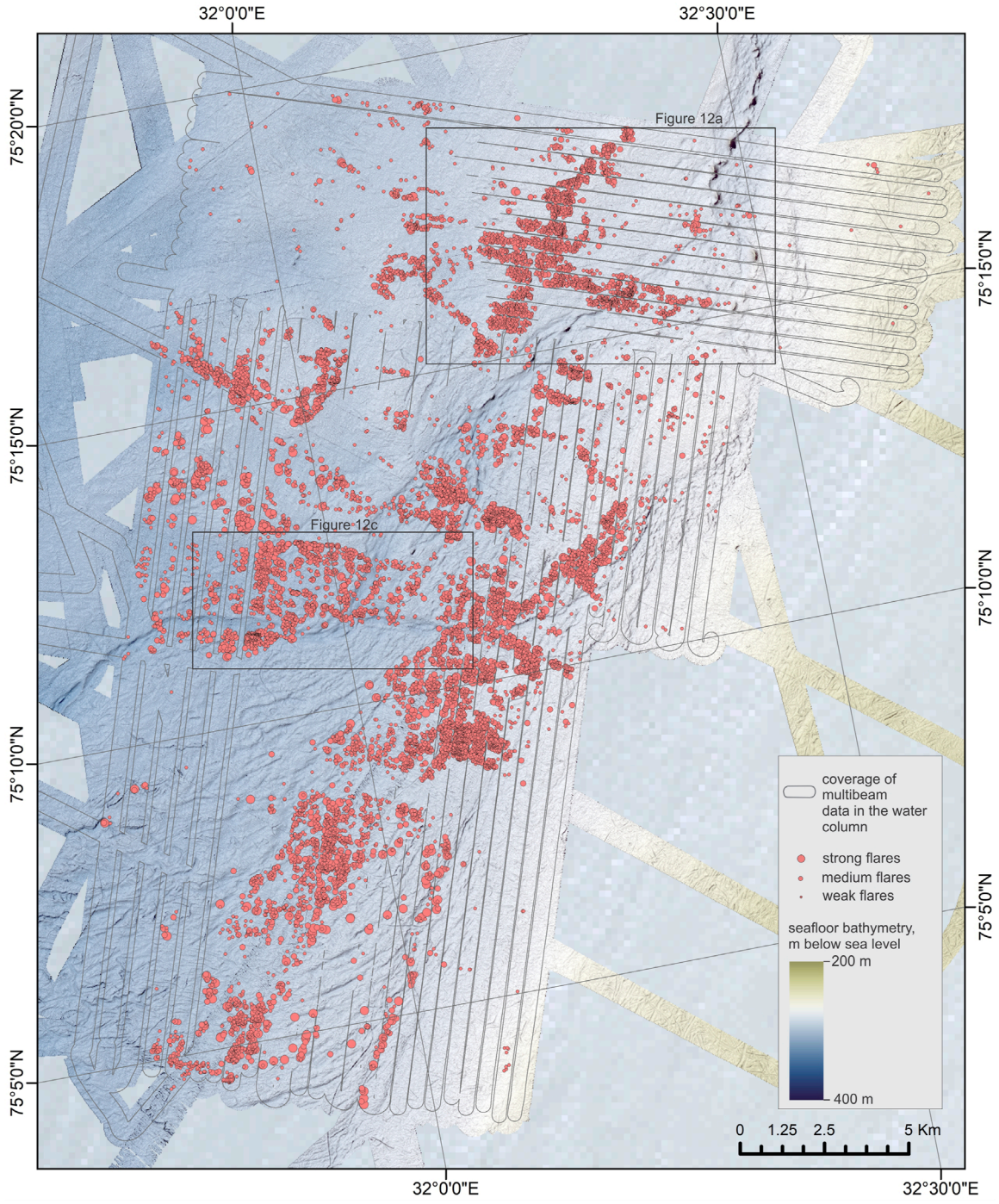

FIGURE 11
Distribution of weak, medium and strong gas flares in central part of the Sentralbanken gas seep area based on CAGE 21–4 multibeam data (Winsborrow et al., 2021). Total coverage of data suitable for flare mapping is 465 km^2.

of Paleozoic rift basins elongated in this direction (Faleide et al., 2008), while the NW-SW orientation corresponds to faults likely associated to late Mesozoic - Cenozoic rifting episodes.

The seeps grouped within NW-SE clusters are most frequent near the top of the structure where seismic data point toward fluid accumulations (Figures 4, 7, 8). This suggests that the seeping gas is likely of thermogenic nature and predominantly leaks from the same exhumed reservoir units as in the NE-SW clusters. However, or data alone cannot rule out a possibility that some larger faults may penetrate the shallowest reservoir and reach lower Triassic successions and beyond. Such faults could promote migration of gas of the same thermogenic nature, yet, potentially, different origin. It is also possible that in areas where sedimentary overburden remains, particularly on the Kong Karl platform and Storbanken

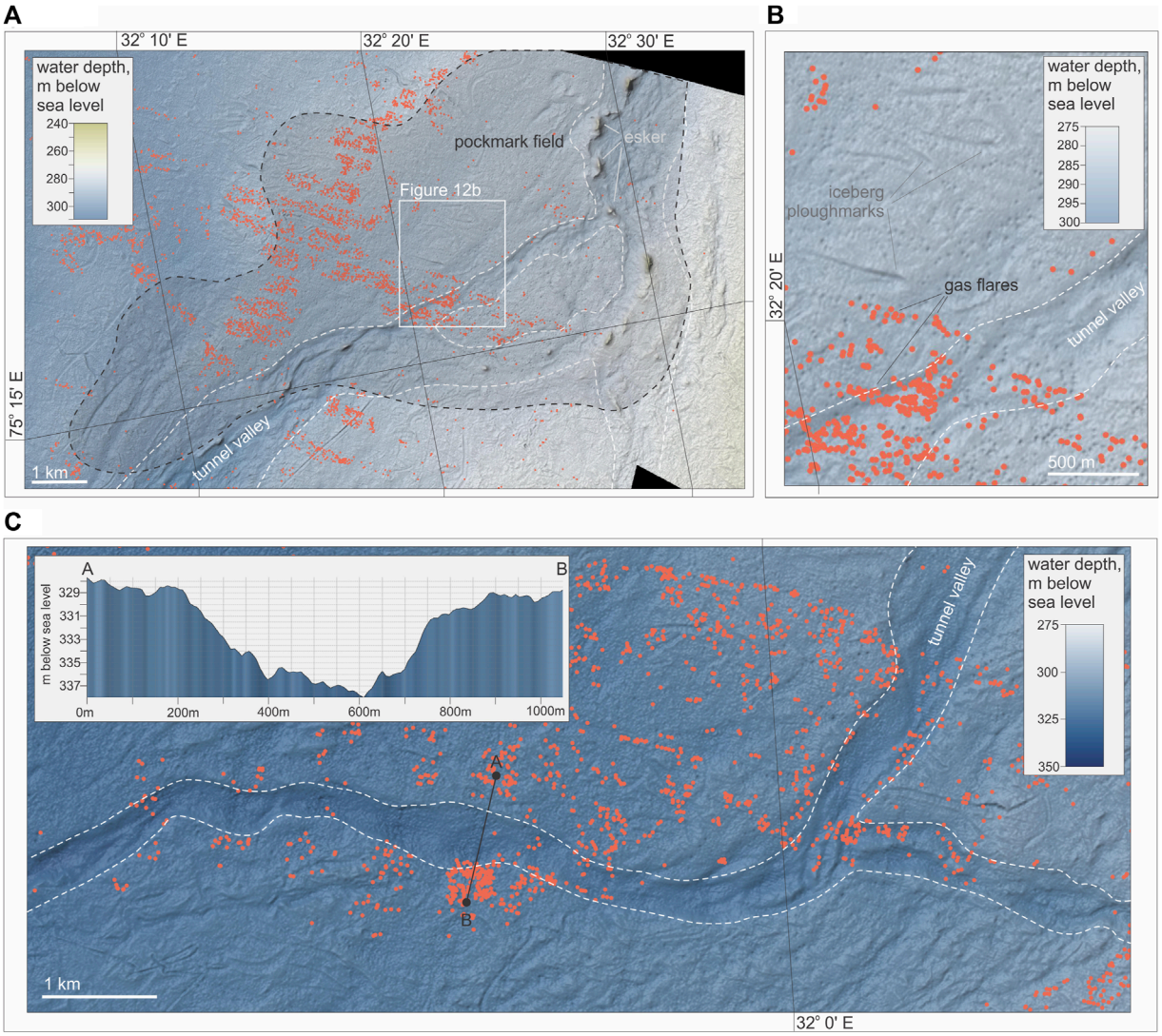

FIGURE 12
bathymetric features potentially modifying seabed gas leakage, and possibly caused by it. Note that weak, medium and strong gas flares are shown by the same symbol. **(A)** distribution of gas seeps within the field of pockmarks. See Figure 11 for location; **(B)** uniformly distributed pockmarks and clusters of gas flares; **(C)** gas seep distribution around a fragment of the main tunnel valley. See Figure 11 for location.

high (Figures 4, 5, 7), the fault conduits may be exploited by the locally generated microbial gas.

On Storbanken the fault-controlled clusters prevail, while on Sentralbanken clusters outlining eroded cap rock dominate. This reflects a variable state of exhumation and erosion of the structural highs. While on Storbanken, younger middle Jurassic successions subcrop locally (Figure 7), on Sentralbanken large patches (>5 km across) of older Triassic succession appear at, or very close to, the seafloor (Serov et al., 2023). It is possible that the fault-related seepage trend is also widespread on Sentralbanken but is masked within large, densely populated seep clusters (Figure 11).

Fault lineaments visible on multibeam bathymetry data on Storbanken show a close correlation to seepage. Other landforms prevalent across the northern Norwegian Barents Sea shelf generally show less apparent or no relation to free gas release. Only 9% of all seabed craters on Storbanken high and Kong Karl platform show seepage from their edges and no gas release was observed at the bottoms of the craters. Pockmarks on Sentralbanken do not correlate with today's seepage (Figures 12A, B). Glacial landforms such as beaded esker, glacial lineations, and iceberg plougmarks do not control free gas release, apart from the tunnel valley system in the Sentralbanken area, some sections of which demonstrate a negative correlation with seepage density (Figure 12C). Therefore, we suggest that the distribution of free gas release within glacially eroded structural highs in the northern Norwegian Barents Sea is not largely modulated by seabed geomorphological features, all of which are rather small scale. Structural configuration of the subseafloor (e.g., the subcropping of reservoir formations and faulting) is the dominant factor controlling gas seepage distribution.

Our study areas lie within the 100–400 m water depth interval, though the hypsometry shows a distinct skew towards shallower

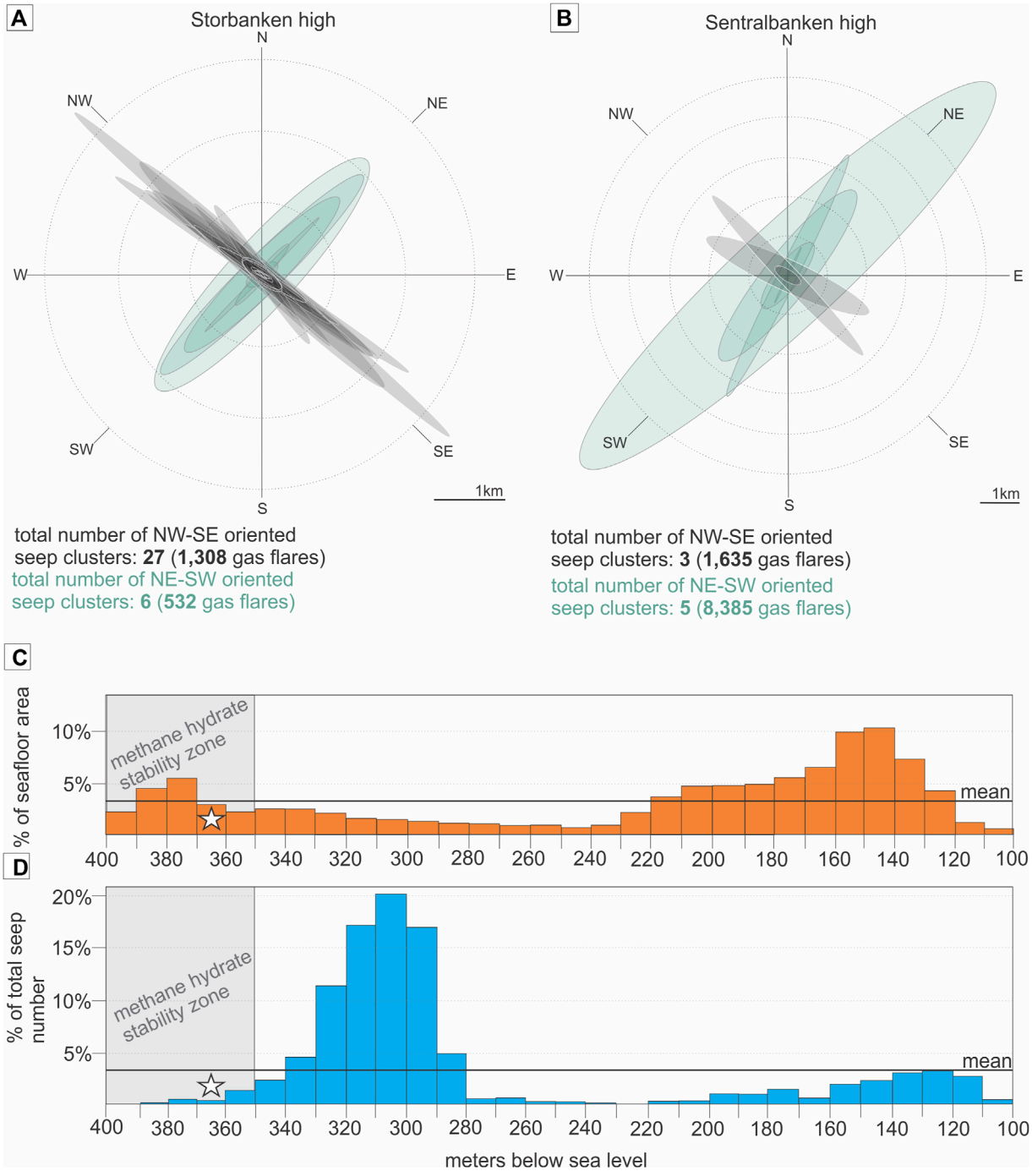

FIGURE 13
Orientation of seep clusters and distribution of seepage across water depth intervals. **(A)** orientation of seep clusters at Storbanken high shown as standard deviation of coordinates x and y from the mean center; **(B)** orientation of seep clusters at Sentralbanken high shown as standard deviation of coordinates x and y from the mean center; **(C)** distribution of seafloor depth (10 m intervals) at all studied areas. The grey square shows theoretical gas hydrate stability zone calculated assuming pure methane gas composition, a 1.5 C bottom water temperature and 3.5% salinity (Sloan and Koh, 2007). The white star indicates a gas hydrate recovery at 363 m water depth (Patton et al., 2020); **(D)** distribution of flare numbers at all studied areas (10 m intervals).

depths (120–220 m water depth) (Figure 13C). The distribution of acoustic gas flares is, on the contrary, centered around water depths of 290–330 m, primarily due to the extremely large seep abundance on the Sentralbanken high. We did not identify a water-depth control on seepage distribution and the seeps are predominately conjugate to the underlying geology.

The seafloor region deeper than 350 m hosts a gas hydrate stability zone, which is an area where temperature and pressure conditions are appropriate to form a solid crystalline mixture of natural gas and water called gas hydrate. Gas hydrates were also recovered in shallow sediment cores at 363 m water depth on Sentralbanken (Patton et al., 2020; Serov et al., 2023). Within the theoretical gas hydrate stability field, the seepage is less abundant compared to other water depth intervals (Figure 13D). However, this deep-water part of the data sets (mostly within the Sentralbanken high) is also lying outside of the exhumed hydrocarbon reservoir and is not conducive to fluid release. Seismic indications of gas hydrates have not been observed. Therefore, our data alone cannot be conclusive as to whether shallow gas hydrate accumulations capture and preserve a fraction of hydrocarbon gases migrating through the subsurface. Of note, gas hydrate samples were recovered on the Sentralbaken high from an extensively leaking gas-hydrate pingo resembling the ones previously reported at 360–380 m water depth in the Barents Sea (Serov et al., 2017). In this case, stable gas hydrates are not blocking ascending gas entirely.

5.2 Quantification of methane bubble emissions

Quantification of ebullitive fluxes of methane from the seabed into the water column remains challenging because it requires the use of seafloor observatories or remotely operated vehicles conducting visual observations of bubble release, or operating equipment which measures volume of emitted gas over time (flowmeters, gas chambers, etc.). Such investigations are time consuming and costly, leading to very few direct gas-flux measurements acquired worldwide (Römer et al., 2014; Sahling et al., 2014; Weber et al., 2014; Veloso-Alarcón et al., 2022). Flux quantification of large seep regions with direct near-seafloor observations and measurements is practically not possible. Alternatively, fluxes of free gas may be inferred from splitbeam echsounder data through sonar signal inversion (Veloso et al., 2015). However, the footprint of splitbeam systems is narrow (typically <5% of the water depth) leading to >30 times longer time required to achieve the same spatial coverage compared to multibeam echosounders.

Here, we tentatively estimate the flux of free methane gas using a modified version of the simple upscaling method used by Sahling et al. (2014) and replicated by Ferré et al. (2020) (see Methods). Sahling et al. (2014) concluded that, on average, six bubble streams with a methane gas flux of 17 ± 8 mmol/min (n=15) corresponds to one gas flare recorded by the echosounder on the formerly glaciated western Svalbard margin. The total flux from the seep area was estimated by multiplying the number of acoustic gas flares identified on multibeam data by the average number of gas streams 6) and the average flux (17 ± 8 mmol/min). Single seep fluxes of the same order of magnitude, or one order of magnitude higher, are commonly reported worldwide (Römer et al., 2012; Römer et al., 2014; Skarke et al., 2014; Higgs et al., 2019; Razaz et al., 2020; Veloso-Alarcón et al., 2022).

We estimate that the eroded structural highs on the Kong Karl platform, the Sentralbanken and Storbanken highs may release 61 x 10^7 mol/yr (9,803 ton/yr) (Table 1). This is a rather conservative estimate given that the original upscaling method in Sahling et al. (2014), which does not account for relative strength of the flares and assumes all seeps contain six streams of bubbles, would result in total flux of 11 x 10^8 mol/yr.

A large range of uncertainty is inherent to the upscaling method primarily dictated by uncertainty in methane fluxes from individual gas seep. Therefore, we further estimate minimum and maximum methane fluxes accounting for possible variations of the flux at each bubble stream and the number of bubble streams appearing as one acoustic gas flare on echosounder data. The resulting minimum total flux is 14.5 x 10^7 mol/yr and a maximum estimated flux of 13 x 10^8 mol/yr.

The base scenario seabed flux of 61 x 10^7 mol/yr generated by > 21,700 seeps within a <5,000 km^2 study area might be one to two orders of magnitude higher compared to other vast seep provinces, primarily due to a large total number of seeps (Serov et al., 2023). For comparison, Skarke et al. (2014) estimated that the 94,000 km^2 area of the northern US Atlantic margin hosts 512 seeps which produce a seabed methane flux of 0.95–5.66 x 10^6 mol/yr. On the Makran continental margin offsore Pakistan, an area similar in size to our study areas in the Barents Sea, has been estimated to release 40 ± 32 x 10^6 mol/yr of methane gas (Römer et al., 2012). Ferré et al. (2020) used both inversion of split beam echosounder data and upscaling of few *in situ* measurements to a larger area to find out that the flux from a ~8 km^2 localized seep area offshore western Svalbard varies from 17.3 to 40.4 x 10^6 mol/yr depending on the season.

Previously published measurements of methane concentrations in surface seawater in the Sentralbanken region revealed that a flux of methane from the water column into the air may occur (Serov et al., 2023). Assuming that the average methane flux of 0.2 μmol/(m^2 x d) reported by Serov et al. (2023) remains constant throughout a year, and relying on our tentative flux estimate approach (Table 1), we estimate that in this actively seeping region (Figure 11) only 0.05% of methane gas emitted from the seafloor into the water column reaches the air. Repeated sea water sampling campaigns at different seasons and oceanographic conditions as well as air sample analyses are necessary to verify our preliminary estimates. Nevertheless, it is very likely that aerobic oxidation of methane utilizes most of the emitted gas, which has also been repeatedly documented across Arctic continental margins and elsewhere (Valentine et al., 2001; Graves et al., 2015; Steinle et al., 2015; Gründger et al., 2021; Mao et al., 2022).

The last episode of erosion which could contribute to uncapping hydrocarbon-bearing natural geological reservoirs occurred in the northern Barents Sea during the last glaciation (Patton et al., 2017; Patton et al., 2022). Numerical modeling constrained with empirical observations suggests that grounded ice retreated from our study sites ~14 ka BP (Patton et al., 2017). Several studies have found that hydrocarbon seepage across the Barents Sea started shortly after cryospheric systems (grounded ice, subglacial permafrost and gas hydrates) retreated and warmer submarine conditions prevailed across the shelf (Crémière et al., 2016; Portnov et al., 2016; Himmler et al., 2019; Argentino et al., 2021; Argentino et al., 2022). Assuming the gas discharge rates similar to present were constant since deglaciation, ~137 (32.6–201.8) million tons of methane from

thermogenic sources has been released into the seawater from our <5,000 km^2 study sites alone. Putting this into perspective, the production and use of fossil fuels is estimated to emit 108 (91–121) million tons of methane into the atmosphere annually (Saunois et al., 2020).

The wider Norwegian Barents Sea shelf likely host more seepage provinces beyond the ones mentioned in our study. We estimate that echosounder data presented in Thorsnes et al. (2023) (Sahling et al., 2014; Mau et al., 2017; Chand and Thorsnes, 2020; Chand and Thorsnes, 2021), and in our study cover only 10% of the Norwegian sector of the Barents Sea shelf. Excluding data overlaps, ~27,000 gas flares have been identified within the mapped territories. Notably, only 17% of the structural highs that may be conduced to strong hydrocarbon seepage (Serov et al., 2023) have been mapped. Therefore, it is possible that the total number of seeps actively injecting methane gas in the water column may be up to one magnitude higher than what today's mapping revealed.

Today, most of the gas released into the seawater from glacially eroded hydrocarbon bearing structures in the northern Norwegian Barents Sea is unlikely to reach the atmosphere (Serov et al., 2023). However, the amount of gas bypassing microbial oxidation in the water column at different seasons, oceanographic and meteorological conditions remains to be quantified precisely. As evident from our geophysical data, large subseafloor hydrocarbon sources are sustaining the water column methane plume, and even a short episode of decreased efficiency of the microbial filtering due to currents or storms (Steinle et al., 2015) may result in potentially significant emissions to the atmosphere. Furthermore, it is important to characterize a stable isotopic signature of the sea-air methane emissions originating from eroded hydrocarbon reservoirs to identify whether such methane gas fluxes are practically distinguishable from other isotopically similar sources, which may be worth considering in future top-down assessments. Finally, understanding the future efficacy of the microbial oxidation filters in bottom sediments and in the water column of the rapidly changing polar regions and, especially at the newly emerging seep sites in Antarctica and Greenland, will be important because it is the single most efficient barrier between active and widespread submarine methane sources, like the ones we have documented in the Barents Sea, and the atmosphere.

6 Conclusion

1. ~21,700 methane gas emissions sites occur within ~5,000 km^2 of seafloor area in the northern Norwegian Barents Sea
2. Gas seepage correlates with Triassic and Jurassic formations with potential of bearing hydrocarbons subcropping beneath the seafloor and outcropping at the seafloor.
3. Gas seeps form elongated clusters with two distinct orientations: NW-SE and NE-SW
4. NW-SE clusters correlate with faults located near the top of the hydrocarbon bearing structures, while NE-SW clusters correspond to subcropping of Triassic and Jurassic hydrocarbon-bearing reservoir formations.
5. We estimate that the investigated areas in the northern Norwegian Barents Sea, produce methane flux from the seafloor into the water column of 61 x 10^7 (14.5 x 10^7–13 x 10^8) mol/yr.

Data availability statement

The raw data supporting the conclusions of this article will be made available by the authors, without undue reservation.

Author contributions

PS: Writing–review and editing, Writing–original draft, Visualization, Methodology, Investigation, Formal Analysis, Data curation, Conceptualization. KA: Writing–review and editing, Supervision, Resources, Project administration, Funding acquisition, Conceptualization. MW: Writing–review and editing, Supervision, Investigation, Conceptualization. RM: Writing–review and editing, Visualization, Methodology, Investigation, Funding acquisition, Formal Analysis, Data curation, Conceptualization. HP: Writing–review and editing, Investigation, Data curation, Conceptualization.

Funding

The author(s) declare that financial support was received for the research, authorship, and/or publication of this article. The research is supported by the Research Council of Norway through its Centres of Excellence funding scheme (Grant 223259), and through the large-scale interdisciplinary project ReGAME (Grant 325610).

Acknowledgments

We would like to acknowledge Dr. Andreia-Plaza Faverola from CAGE, UiT for leading research cruise CAGE 18-1 and sharing multibeam echosounder and seismic data acquired. We thank the crew of research vessels Helmer Hanssen and G. O. Sars for providing invaluable support for acquisition of the empirical data.

Conflict of interest

The authors declare that the research was conducted in the absence of any commercial or financial relationships that could be construed as a potential conflict of interest.

Publisher's note

References

Andreassen, K. (2016). CAGE16-2 cruise report: marine geological cruise to the maud basin and crater area, bjørnøyrenna. *CAGE–Centre Arct. Gas Hydrate, Environ. Clim. Rep. Ser.* 4. doi:10.7557/cage.6925

Andreassen, K., Hubbard, A., Winsborrow, M., Patton, H., Vadakkepuliyambatta, S., Plaza-Faverola, A., et al. (2017). Massive blow-out craters formed by hydrate-controlled methane expulsion from the Arctic seafloor. *Science* 356, 948–953. doi:10.1126/science.aal4500

Andreassen, K., Patton, H., Mattingsdal, R., Moser, M., Cooke, F. A., Jansson, P., et al. (2019). CAGE19-2 Cruise Report: hunting gas flares and launching seafloor observatory. *CAGE–Centre Arct. Gas Hydrate, Environ. Clim. Rep. Ser.* 7. doi:10.7557/cage.6910

Argentino, C., Lee, A., Fallati, L., Sahy, D., Birgel, D., Peckmann, J., et al. (2022). Biogeochemistry and timing of methane-derived carbonate formation at Leirdjupet fault complex, SW Barents sea. *Front. Earth Sci.* 10. doi:10.3389/feart.2022.1029471

Argentino, C., Waghorn, K. A., Vadakkepuliyambatta, S., Polteau, S., Bünz, S., and Panieri, G. (2021). Dynamic and history of methane seepage in the SW Barents Sea: new insights from leirdjupet fault complex. *Sci. Rep.* 11, 4373. doi:10.1038/s41598-021-83542-0

Asadnabizadeh, M. (2022). Critical findings of the sixth assessment report (AR6) of working Group I of the intergovernmental panel on climate change (IPCC) for global climate change policymaking a summary for policymakers (SPM) analysis. *Int. J. Clim. Change Strateg. Manag.*

Bøe, R., Bjarnadóttir, L. R., Elvenes, S., Dolan, M., Bellec, V., Thorsnes, T., et al. (2022). "Revealing the secrets of Norway's seafloor – geological mapping within the MAREANO programme and in coastal areas," in *From continental shelf to slope: mapping the oceanic realm*. Editors K. ASCH, H. KITAZATO, and H. VALLIUS (London: Geological Society of).

CCAC, U. (2021). "United nations environment programme and climate and clean air coalition", in *Global methane assessment: benefits and costs of mitigating methane emissions* (Nairobi: United Nations Environment Programme).

Chand, S., and Thorsnes, T. (2020). *Processing and interpretation of water column data from the polarrev high, Barents Sea*.

Chand, S., and Thorsnes, T. (2021). Processing and interpretation of water column data from the gardarbankhøgda, bjarmelandplattformen, sentralbankhøgda and Kong Karls land-plattformen. *Barents Sea*.

Collanega, L., Massironi, M., Breda, A., and Kjølhamar, B. E. (2017). Onset of N-atlantic rifting in the Hoop fault complex (SW Barents Sea): an orthorhombic dominated faulting? *Tectonophysics* 706-707, 59–70. doi:10.1016/j.tecto.2017.04.003

Crémière, A., Lepland, A., Chand, S., Sahy, D., Condon, D. J., Noble, S. R., et al. (2016). Timescales of methane seepage on the Norwegian margin following collapse of the Scandinavian Ice Sheet. *Nat. Commun.* 7, 11509. doi:10.1038/ncomms11509

Egger, M., Riedinger, N., Mogollón, J. M., and Jørgensen, B. B. (2018). Global diffusive fluxes of methane in marine sediments. *Nat. Geosci.* 11, 421–425. doi:10.1038/s41561-018-0122-8

Faleide, J. I., Tsikalas, F., Breivik, A., Mjelde, R., Ritzmann, O., Engen, O., et al. (2008). Structure and evolution of the continental margin off Norway and the Barents Sea. *Episodes* 31, 82–91. doi:10.18814/epiiugs/2008/v31i1/012

Ferré, B., Jansson, P. G., Moser, M., Serov, P., Portnov, A., Graves, C. A., et al. (2020). Reduced methane seepage from Arctic sediments during cold bottom-water conditions. *Nat. Geosci.* 13, 144–148. doi:10.1038/s41561-019-0515-3

Forwick, M., Baeten, N., and Vorren, T. (2009). Pockmarks in spitsbergen fjords. *Nor. Geol. Tidsskr.* 89.

Gluyas, J. G., and Swarbrick, R. E. (2021). *Petroleum geoscience*. John Wiley and Sons.

Graves, C. A., Steinle, L., Rehder, G., Niemann, H., Connelly, D. P., Lowry, D., et al. (2015). Fluxes and fate of dissolved methane released at the seafloor at the landward limit of the gas hydrate stability zone offshore western Svalbard. *J. Geophys. Res. - Oceans* 120, 6185–6201. doi:10.1002/2015jc011084

Grogan, P., Østvedt-Ghazi, A. M., Larssen, G. B., Fotland, B., Nyberg, K., Dahlgren, S., et al. (1999). "Structural elements and petroleum geology of the Norwegian sector of the northern Barents Sea. Petroleum Geology of Northwest Europe," in Proceedings of the 5th Conference 5, 247–259.

Gründger, F., Probandt, D., Knittel, K., Carrier, V., Kalenitchenko, D., Silyakova, A., et al. (2021). Seasonal shifts of microbial methane oxidation in Arctic shelf waters above gas seeps. *Limnol. Oceanogr.* 66, 1896–1914. doi:10.1002/lno.11731

Harrington, P. K. (1985). Formation of pockmarks by pore-water escape. *Geo-Marine Lett.* 5, 193–197. doi:10.1007/bf02281638

Higgs, B., Mountjoy, J. J., Crutchley, G. J., Townend, J., Ladroit, Y., Greinert, J., et al. (2019). Seep-bubble characteristics and gas flow rates from a shallow-water, high-density seep field on the shelf-to-slope transition of the Hikurangi subduction margin. *Mar. Geol.* 417, 105985. doi:10.1016/j.margeo.2019.105985

Himmler, T., Sahy, D., Martma, T., Bohrmann, G., Plaza-Faverola, A., Bünz, S., et al. (2019). A 160,000-year-old history of tectonically controlled methane seepage in the Arctic. *Sci. Adv.* 5, eaaw1450. doi:10.1126/sciadv.aaw1450

Hovland, M., Gardner, J. V., and Judd, A. G. (2002). The significance of pockmarks to understanding fluid flow processes and geohazards. *Geofluids* 2, 127–136. doi:10.1046/j.1468-8123.2002.00028.x

Høy, T., and Lundschien, B. (2011). "Triassic deltaic sequences in the northern Barents Sea," in *Geological Society, London, Memoirs* 35, 249–260.

Klausen, T. G., Nyberg, B., and Helland-Hansen, W. (2019). The largest delta plain in Earth's history. *Geology* 47, 470–474.

Jakobsson, M., Mayer, L. A., Bringensparr, C., Castro, C. F., Mohammad, R., Johnson, P., et al. (2020). The international bathymetric chart of the arctic ocean version 4.0. *Sci. Data* 7, 176. doi:10.1038/s41597-020-0520-9

Judd, A., and Hovland, M. (2009). *Seabed fluid flow: the impact on geology, biology and the marine environment*. Cambridge University Press.

Lasabuda, A. P. E., Johansen, N. S., Laberg, J. S., Faleide, J. I., Senger, K., Rydningen, T. A., et al. (2021). Cenozoic uplift and erosion of the norwegian barents shelf—a review. *Earth Sci. Rev.* 217, 103609.

Livingstone, S. J., Lewington, E. L. M., Clark, C. D., Storrar, R. D., Sole, A. J., Mcmartin, I., et al. (2020). A quasi-annual record of time-transgressive esker formation: implications for ice-sheet reconstruction and subglacial hydrology. *Cryosphere* 14, 1989–2004. doi:10.5194/tc-14-1989-2020

Lundschien, B. A., Mattingsdal, R., Johansen, S. K., and Knutsen, S.-M. (2023). North Barents composite tectono-sedimentary element. *Geol. Soc.* 57, M57–M2021. doi:10.1144/m57-2021-39

Masson-Delmotte, V., Zhai, P., Priani, A., Connors, S., Péan, C., and Berger, S. (2021). "IPCC, 2021: climate change 2021: the physical science basis," in *Contribution of working group I to the sixth assessment report of the intergovernmental panel on climate change*. Cambridge, United Kingdom: Cambridge University Press.

Mao, Y., Lin, T., Li, H., He, R., Ye, K., Yu, W., et al. (2024). Aerobic methane production by phytoplankton as an important methane source of aquatic ecosystems: reconsidering the global methane budget. *Sci. Total Environ.* 907, 167864.

Mao, S.-H., Zhang, H.-H., Zhuang, G.-C., Li, X.-J., Liu, Q., Zhou, Z., et al. (2022). Aerobic oxidation of methane significantly reduces global diffusive methane emissions from shallow marine waters. *Nat. Commun.* 13, 7309. doi:10.1038/s41467-022-35082-y

Mau, S., Römer, M., Torres, M. E., Bussmann, I., Pape, T., Damm, E., et al. (2017). Widespread methane seepage along the continental margin off Svalbard - from Bjørnøya to Kongsfjorden. *Sci. Rep.* 7, 42997. doi:10.1038/srep42997

Nielsen, T., Laier, T., Kuijpers, A., Rasmussen, T. L., Mikkelsen, N. E., Nørgård-Pedersen, N., et al. (2014). Fluid flow and methane occurrences in the Disko Bugt area offshore West Greenland: indications for gas hydrates?. *Geo-Mar. Lett.* 34, 511–523.

Nisbet, E., Fisher, R., Lowry, D., France, J., Allen, G., Bakkaloglu, S., et al. (2020). Methane mitigation: methods to reduce emissions, on the path to the Paris agreement. *Rev. Geophys.* 58, e2019RG000675.

Nixon, F. C., Chand, S., Thorsnes, T., and Bjarnadóttir, L. R. (2019). A modified gas hydrate-geomorphological model for a new discovery of enigmatic craters and seabed mounds in the Central Barents Sea, Norway. *Geo-Marine Lett.* 39, 191–203. doi:10.1007/s00367-019-00567-1

Norwegian Offshore Directorate (2024). Resource Accounts for the Norwegian continental shelf as per 31 December 2023. *Norwegian Offshore Directorate*.

Patton, H., Hubbard, A., Andreassen, K., Auriac, A., Whitehouse, P. L., Stroeven, A. P., et al. (2017). Deglaciation of the Eurasian ice sheet complex. *Quat. Sci. Rev.* 169, 148–172. doi:10.1016/j.quascirev.2017.05.019

Patton, H., Hubbard, A., Heyman, J., Alexandropoulou, N., Lasabuda, A. P. E., Stroeven, A. P., et al. (2022). The extreme yet transient nature of glacial erosion. *Nat. Commun.* 13, 7377. doi:10.1038/s41467-022-35072-0

Patton, H., Mattingsdal, R., Pavel, S., Cooke, F. A., and Alexandropoulou, N. (2020). CAGE20-2 cruise report: hunting flares in hopendjupet and glacigenic sediments in sentralbankrenna. *CAGE–Centre Arct. Gas Hydrate, Environ. Clim. Rep. Ser.* 8. doi:10.7557/cage.6745

Plaza-Faverola, A. (2018). CAGE18-1 cruise report: marine geophysical cruise to storbanken and Olga basin in the Barents Sea. *CAGE–Centre Arct. Gas Hydrate, Environ. Clim. Rep. Ser.* 6. doi:10.7557/cage.6846

Portnov, A., Vadakkepuliyambatta, S., Mienert, J., and Hubbard, A. (2016). Ice-sheet-driven methane storage and release in the Arctic. *Nat. Commun.* 7, 10314. doi:10.1038/ncomms10314

Razaz, M., Di Iorio, D., Wang, B., and Macdonald, I. (2020). Temporal variations of a natural hydrocarbon seep using a deep-sea camera system. *J. Atmos. Ocean. Technol.* 37, 1737–1751. doi:10.1175/jtech-d-19-0137.1

Riis, F., Lundschien, B. A., Høy, T., Mørk, A. E., and Mørk, M. B. (2008). Evolution of the Triassic shelf in the northern Barents Sea region. *Polar Res.* 27, 318–338.

Römer, M., Sahling, H., Pape, T., Bohrmann, G., and Spieß, V. (2012). Quantification of gas bubble emissions from submarine hydrocarbon seeps at the Makran continental margin (offshore Pakistan). *J. Geophys. Res. Oceans* 117. doi:10.1029/2011jc007424

Römer, M., Sahling, H., Pape, T., Dos Santos Ferreira, C., Wenzhöfer, F., Boetius, A., et al. (2014). Methane fluxes and carbonate deposits at a cold seep area of the central nile deep sea fan, eastern mediterranean sea. *Mar. Geol.* 347, 27–42. doi:10.1016/j.margeo.2013.10.011

Ruppel, C. D., and Kessler, J. D. (2017). The interaction of climate change and methane hydrates. *Rev. Geophys.* 55, 126–168.

Sahling, H., Römer, M., Pape, T., Bergès, B., Dos Santos Fereirra, C., Boelmann, J., et al. (2014). Gas emissions at the continental margin west of Svalbard: mapping, sampling, and quantification. *Biogeosciences* 11, 6029–6046. doi:10.5194/bg-11-6029-2014

Saunois, M., Stavert, A. R., Poulter, B., Bousquet, P., Canadell, J. G., Jackson, R. B., et al. (2020). The global methane budget 2000–2017. *Earth Syst. Sci. Data* 12, 1561–1623. doi:10.5194/essd-12-1561-2020

Sejrup, H. P., Hjelstuen, B. O., Patton, H., Esteves, M., Winsborrow, M., Rasmussen, T. L., et al. (2022). The role of ocean and atmospheric dynamics in the marine-based collapse of the last Eurasian Ice Sheet. *Commun. Earth Environ.* 3, 119. doi:10.1038/s43247-022-00447-0

Serck, C. S., Faleide, J. I., Braathen, A., Kjølhamar, B., and Escalona, A. (2017). Jurassic to early cretaceous basin configuration(s) in the fingerdjupet subbasin, SW Barents Sea. *Mar. Petroleum Geol.* 86, 874–891. doi:10.1016/j.marpetgeo.2017.06.044

Serov, P., Mattingsdal, R., Winsborrow, M., Patton, H., and Andreassen, K. (2023). Widespread natural methane and oil leakage from sub-marine Arctic reservoirs. *Nat. Commun.* 14, 1782. doi:10.1038/s41467-023-37514-9

Serov, P., Patton, H., Mazzini, A., Mattingsdal, R., Shephard, G., Cooke, F. A., et al. (2022). CAGE22-6 cruise report: GEO-3144/8144 Teaching Cruise: geologically controlled hydrocarbon seepage in Hopendjupet and the wider Barents Sea. *CAGE–Centre Arct. Gas Hydrate, Environ. Clim. Rep. Ser.* 10. doi:10.7557/cage.6769

Serov, P., Vadakkepuliyambatta, S., Mienert, J., Patton, H., Portnov, A., Silyakova, A., et al. (2017). Postglacial response of Arctic Ocean gas hydrates to climatic amelioration. *Proc. Natl. Acad. Sci.* 114, 6215–6220. doi:10.1073/pnas.1619288114

Shackleton, C., Patton, H., Winsborrow, M., Esteves, M., Bjarnadóttir, L., and Andreassen, K. (2023). Distinct modes of meltwater drainage and landform development beneath the last Barents Sea ice sheet. *Front. Earth Sci.* 11. doi:10.3389/feart.2023.1111396

Shoemaker, J., Schrag, D., Molina, M., and Ramanathan, V. (2013). What role for short-lived climate pollutants in mitigation policy?. *Science* 342, 1323–1324.

Skarke, A., Ruppel, C., Kodis, M., Brothers, D., and Lobecker, E. (2014). Widespread methane leakage from the sea floor on the northern US Atlantic margin. *Nat. Geosci.* 7, 657–661. doi:10.1038/ngeo2232

Sloan, E. D., and Koh, C. A. (2007). *Clathrate hydrates of natural gases*. CRC Press.

Staniaszek, Z., Griffiths, P. T., Folberth, G. A., O'Connor, F. M., Abraham, N. L., and Archibald, A. T. (2012). The role of future anthropogenic methane emissions in air quality and climate. *npj Clim. Atmos. Sci.* 5, 21.

Steinle, L., Graves, C. A., Treude, T., Ferré, B., Biastoch, A., Bussmann, I., et al. (2015). Water column methanotrophy controlled by a rapid oceanographic switch. *Nat. Geosci.* 8, 378–382. doi:10.1038/ngeo2420

Stemmerik, L., Worsley, D., et al. (2005). 30 years on-Arctic Upper Palaeozoic stratigraphy, depositional evolution and hydrocarbon prospectivity. *Norw. J. Geol./Norsk Geologisk Forening*, 85.

Thorsnes, T., Buhl-Mortensen, L., and Skyseth, T. (2008). Integrated mapping of the seafloor and ecosystems in the Arctic–the MAREANO programme. *Gråsteinen* 12, 115–125.

Thorsnes, T., Chand, S., Bellec, V. K., Nixon, C., Brunstad, H., Lepland, A., et al. (2023). *Gas seeps in Norwegian waters–distribution and mechanisms*.

Thurber, A. R., Seabrook, S., and Welsh, R. M. (2020). "Riddles in the cold: antarctic endemism and microbial succession impact methane cycling in the Southern Ocean," in Proceedings of the royal society B: biological sciences 287, 20201134.

Urban, P., Köser, K., and Greinert, J. (2017). Processing of multibeam water column image data for automated bubble/seep detection and repeated mapping. *Limnol. Oceanogr.: Methods* 15, 1–21.

Valentine, D. L., Blanton, D. C., Reeburgh, W. S., and Kastner, M. (2001). Water column methane oxidation adjacent to an area of active hydrate dissociation, Eel River Basin. *Geochimica Cosmochimica Acta* 65, 2633–2640. doi:10.1016/s0016-7037(01)00625-1

Vaughn, T. L., Bell, C. S., Pickering, C. K., Schwietzke, S., Heath, G. A., Pétron, G., et al. (2018). "Temporal variability largely explains top-down/bottom-up difference in methane emission estimates from a natural gas production region," in Proceedings of the National Academy of Sciences 115, 11712–11717.

Veloso-Alarcón, M. E., Urban, P., Weiss, T., Köser, K., She, M., and Greinert, J. (2022). Quantitatively monitoring bubble-flow at a seep site offshore Oregon: field trials and methodological advances for parallel optical and hydroacoustical measurements. *Front. Earth Sci.* 10. doi:10.3389/feart.2022.858992

Veloso, M., Greinert, J., Mienert, J., and Batist, M. (2015). A new methodology for quantifying bubble flow rates in deep water using splitbeam echosounders: examples from the Arctic offshore NW-Svalbard. *Limnol. Oceanogr. Methods* 13, 267–287. doi:10.1002/lom3.10024

Waage, M., Serov, P., Andreassen, K., Waghorn, K. A., and Bünz, S. (2020). Geological controls of giant crater development on the Arctic seafloor. *Sci. Rep.* 10, 8450. doi:10.1038/s41598-020-65018-9

Wadham, J., Arndt, S., Tulaczyk, S., Stibal, M., Tranter, M., Telling, J., et al. (2012). Potential methane reservoirs beneath Antarctica. *Nature* 488, 633–637. doi:10.1038/nature11374

Weber, T. C., Mayer, L., Jerram, K., Beaudoin, J., Rzhanov, Y., and Lovalvo, D. (2014). Acoustic estimates of methane gas flux from the seabed in a 6000 km2 region in the Northern Gulf of Mexico. *Geochem. Geophys. Geosystems* 15, 1911–1925. doi:10.1002/2014gc005271

Weniger, P., Blumenberg, M., Berglar, K., Ehrhardt, A., Klitzke, P., Krüger, M., et al. (2019). Origin of near-surface hydrocarbon gases bound in northern Barents Sea sediments. *Mar. Petroleum Geol.* 102, 455–476. doi:10.1016/j.marpetgeo.2018.12.036

Whiticar, M. (1993). "Atmospheric methane: sources, sinks, and role in global change," in *Atmospheric methane: sources, sinks, and role in global change*. Berlin: Springer, 138–167.

Whiticar, M. J. (1999). Carbon and hydrogen isotope systematics of bacterial formation and oxidation of methane. *Chem. Geol.* 161, 291–314.

Winsborrow, M., and Knies, J. (2021). CAGE21-6 cruise report: hydrocarbon leakage in hopendjupet, central Barents Sea. *CAGE–Centre Arct. Gas Hydrate, Environ. Clim. Rep. Ser.* 9. doi:10.7557/cage.6675

Winsborrow, M., Patton, H., Jakobsen, F., Pau, M., Akinselure, A., and Jensen, A. (2021). CAGE21-4 Cruise Report: oil slicks, gas flares and glacial landforms in Hopendjupet and Sentralbanken. *CAGE–Centre Arct. Gas Hydrate, Environ. Clim. Rep. Ser.* 9. doi:10.7557/cage.6703

Worsley, D. (2008). The post-Caledonian development of Svalbard and the western Barents Sea. *Polar res.* 27, 298–317.

Frontiers in Earth Science

Investigates the processes operating within the major spheres of our planet

Advances our understanding across the earth sciences, providing a theoretical background for better use of our planet's resources and equipping us to face major environmental challenges.

Discover the latest Research Topics

See more →

Frontiers

Avenue du Tribunal-Fédéral 34
1005 Lausanne, Switzerland
frontiersin.org

Contact us

+41 (0)21 510 17 00
frontiersin.org/about/contact